HIGH FREQUENCY SOLID-STATE POWER SOURCES FOR INDUCTION HEATING

by

YAVUZ AHISHALILAR, B.Sc.

A Doctoral Thesis

Submitted in partial fulfilment of the requirements for the award of the degree of Doctor of Philosophy of the Loughborough University of Technology

April, 1978

Supervisor: I.R. Smith, DSc, CEng, FIEE

Department of Electronic and Electrical Engineering

"To the memory of my father"

ACKNOWLEDGEMENTS

The author wishes to express his sincere gratitude to his supervisor Professor I.R. Smith for his constant encouragement and guidance during the course of the project and for the generous help he has provided in many other fields.

The author would like to thank Mr. H. Barber for his valuable advice and suggestions on induction heating. Thanks are also extended to close friends Mr. G. Ocal, Mr.A. Aksel, Dr. S.E. Tez and Mr. M. Serter for various forms of assistance they have given.

The author is indebted to his mother and brother for their continual encouragement and financial support; without their sacrifices this work would never have been completed.

Special mention should also be made for the Turkish National Electricity Board (TEK) for their financial contribution.

Finally many thanks are due to Mrs. Janet Smith who patiently carried out the typing of this thesis.

SYNOPSIS

Induction heating and melting applications often require a power source to convert 3-phase mains input power to single-phase output power at a higher and variable frequency. Amongst various power conversion schemes, solid-state power converters using the most modern devices provide the best power control techniques available for this application. In designing for this purpose, careful consideration must be given to the characteristics of the load, which presents a very low power factor and an impedance possibly varying widely as the heating cycle proceeds.

From the variety of thyristor commutation techniques commonly employed in high-power inverters, series load commutation is particularly suited to high-frequency applications, as it has an intrinsically high turn-off time for the circuit thyristors (clearly essential at high operational frequencies) and much reduced switching losses. However, series commutation circuits are load sensitive, and therefore require careful design, especially with an induction heating load.

Recent developments in power conversion techniques have led to the elimination of the d.c. link in a.c. to a.c. power conversion, enabling both high operational efficiencies and substantial savings in the initial cost of the device to be achieved. This new type of converter (called a cycloinverter)

employs series commutation and offers an inherent output power and frequency control facilities. However, in a cycloinverter, since high-frequency switching is performed simultaneously with rectification, these control schemes are dependent on the operational frequency. The direct power conversion in a cycloinverter causes, unfortunately, distortion currents in the input lines and the output circuit, and it is the designer's task to minimise these undesirable components.

The project aims to investigate the potential uses, both of the series inverter in its high-frequency form and of the cycloinverter, as power sources for induction heating. Design criteria are established for each circuit, with consideration given to turn-off time, efficiency, power factor, component ratings and predicted load variations. Computer simulations of the converters are employed to investigate the different voltage and current waveforms in the circuits, and to establish how the performance of each inverter may be optimised, and these are verified by results obtained on experimental prototypes.

LIST OF PRINCIPAL SYMBOLS

General

C_o	compensating capacitor of the induction heating load
D	diode
DD	diode derating
DELX	increment of the quantity X
DF	distortion factor
DP	displacement factor
DR	rectifier derating
DS	thyristor derating
E	source voltage (d.c)
f	frequency
f_I	input (supply) frequency
f_o	output frequency
f_r	damped resonant frequency of the output circuit
F[g]	Fourier series of g(t)
i	instantaneous current
I	r.m.s. current
$i_{1,2,3}$	3-phase input line currents
L_o	heating coil inductance
P	power
P_{cLoss}	conduction losses
P_{CT}	total power delivered to the heating coil
P_w	power wasted due to undesired output current harmonics
PF	power factor
Q_L	tank-load selectivity
R_{eq}	equivalent tank-load resistance at output frequency

R_o	heating coil resistance
S	thyristor
t	time
T	period; temperature
t_c	commutation time
TH_{off}	minimum thyristor turn-off time
t_{off}	turn-off time
T_r	$= 1/f_r$
v	instantaneous voltage
V	r.m.s. voltage
$v_{1,2,3}$	3-phase input voltages
VA	volt-ampere rating
w	angular frequency
w_o	output angular frequency
X	reactance
Z	impedance; state variable
Z_L	tank-load impedance
θ	power control angle, firing angle

Subscripts

ab	across points A and B
av	average value
B,base	base value
C,L,R	pertaining to circuit elements C, L and R
D	diode
d.c.	pertaining to d.c. source; average value
F	filter component; pertaining to full output power
I	pertaining to input

LN	line-to-neutral
max	maximum
min	minimum
o	pertaining to output
off	pertaining to thyristor turn-off; when the circuit thyristors are all non-conducting
p	peak
p-p	peak-to-peak
S	thyristor
T	total
1,2,3,n	(as a first subscript) pertaining to input mains phases 1,2, ..N; (as an end subscript) pertaining to harmonic frequencies w(fundamental), 2w, 3w, ... nw

CHAPTER I

A_1	area corresponding to energy dissipated during turn-off
$C_{1,2}$	commutating capacitors
L_d	smoothing choke
$g(V_{d.c},R_o)$	function of the d.c. source voltage $V_{d.c.}$ and the load resistance R_o
V_{Ro}	r.m.s. voltage across the load resistance R_o

CHAPTER II

d_m	workpiece diameter
G	geometrical factor
g	airgap
H	magnetic field strength

$K_{1,2}$	constants, as described in Section 2.4.2
ℓ	coil length
L_o', R_o'	L_o and R_o after the Curie temperature
N	number of heating coil turns
w_n	resonant frequency of the tank-load
δ	skin depth
μ	permeability
ρ	resistivity
η	efficiency
ϕ	flux
X_o	total heating coil reactance = $X_g + X_m + X_c$
Z_o	total heating coil impedance = $R_o + j X_o$

Subscripts

g	airgap
m	workpiece
c	coil

CHAPTER III

a,b	real and imaginary parts of the impedance of the tank-load circuit Z_L
E,F,G,H,	$\alpha_{1,2}$ as defined in Section 3.3.2
ILIMIT	limiting value of the output current i_L
Z_{In}, Z_{Ln}	see Figure 3.6
V_{oa}	driving voltage

β, ϕ phase angles as defined in Section 3.3.1

ψ_1 $= \tan^{-1} \frac{b_1}{a_1}$

CHAPTER IV

E_1 generated voltage at the supply frequency

$P_{0,1,2,3}$ switch positions as defined in Figure 4.5

V_{na} driving voltage

X_s source reactance

$\beta\ \alpha\ \sigma\ \rho\ \phi\ \zeta$: phase angles as defined in Section 4.2.2.3

$\psi\ \delta\ \lambda$: phase angles as defined in Section 4.2.2.4

Subscript

h distortion harmonic

CHAPTER V

A,A',B,B' sideband harmonic amplitudes

r(t), u(t), z(t), s(t), h(t): Boolean functions as defined in Figures 5.5 and 5.6

w_s sideband harmonic frequency

Subscripts

C-I cycloinverter

F-B full-bridge cycloinverter

H-B half-bridge cycloinverter

R rectifier

CHAPTER VI

A	= S(1) + S(2) + S(3) + S(4) + S(5) + S(6)
a_k, b_k	cosine and sine coefficients of a Fourier series
D_j, D(J)	binary logic variable for Jth diode D_j, 1 or 0
h	step size
LD_j,LDJ,LS_j,LSJ:	binary variable corresponding to the permissible conduction interval of Jth diode or thyristor, 1 or 0
LJPOZ, LJNEG	Logic variables to define the sequence of the positive and negative group thyristors respectively
LISJ	logic variable indicating the presence of positive current from anode to cathode of Jth thyristor, TRUE or FALSE
LVSJ	logic variable indicating the presence of positive anode to cathode voltage across Jth thyristor, TRUE or FALSE
R_c, R_s	see Figure 6.2
S_j, S(J)	binary logic variable for Jth thyristor, 1 or 0
V_s	on-state thyristor voltage
V_D	on-state diode voltage

CHAPTER VII

a,b	real and imaginary parts of cycloinverter input impedance
C_F	filter capacitor
$i_{a,b,c}$	filter capacitor currents
$i'_{1,2,3}$	input line currents to the cycloinverter alone
I_{1n}	nth harmonic of the input current in line 1
I'_{1n}	nth harmonic of the input line current to the cycloinverter alone
I_{1loff}	supply frequency harmonic of the input line current when the circuit thyristors are all non-conducting
$L_{F,F1,F2}$	filter inductors
R_F	filter resistance
R_{I1}	input resistance of the filter-cycloinverter configuration at the supply frequency

V_a	input phase voltage to the cycloinverter
V_{aloff}	supply frequency input phase voltage to the cycloinverter when all the circuit thyristors are non-conducting
Z_{Il}	input impedance of the cycloinverter at the supply frequency
Z'_{Il}	input impedance of the cycloinverter
θ'	firing angle w.r.t. the source phase voltage
$\alpha_{V_1 - V_a}$	phase difference between V_1 and V_a

TABLE OF CONTENTS

CHAPTER 1

INTRODUCTION

1.1 Background

Induction heating and melting applications generally require a power source of high efficiency, to convert the 3-phase mains frequency input to a high-frequency single-phase output. In the past, this conversion has been achieved by motor-generator sets, magnetic multipliers, spark gap converters and radio-frequency oscillators, but recent developments in solid-state technology have led to the use of static power converters to supply the medium-frequency power normally required in these applications.

The first static power sources, introduced in the early 1960s, enabled low-frequency units of 150-700 Hz to be constructed and operated economically, up to a power level of about 100 kW. The frequency could not be higher than about 700 Hz, due to the limited switching speed of the solid-state devices then available. As devices of higher current rating became available, converters of several hundred kilowatts rating were designed, at frequencies up to 1 kHz. At present, 300A, 1000V high-speed thyristors are marketed, with turn-off times around 12 μs, and this has resulted in the development of frequency converters in single power modules up to 0.2 MW, operating at frequencies up to 10 kHz. Today, megawatt size induction heating installations operating at around 1 kHz are commonplace, while the number of submegawatt systems operating at

higher frequencies is increasing rapidly.

The spectrum of induction heating applications covers a range[1] from mains frequency (50 Hz) to VHF (e.g. 5 MHz). Figure 1.1 shows how the present practical range for solid-state inverters, which is 150 Hz to 10 kHz, covers the broad spread from melting furnaces and billet heating prior to forging and a major section of the heat treatment field. As seen in its application range, the static inverter has to compete primarily with magnetic frequency-multipliers and motor-generator sets.

Magnetic multipliers[2] comprise a combination of transformers operating at high saturation, and rely on the principle that when non-linear devices are driven from sinusoidal voltage or current sources, harmonic frequency components are produced in their currents and voltages respectively. Multi-phase transformer connections enable the separation of the required component of the generated harmonics to be achieved. Due to their simplicity, reliability and reasonable efficiency, magnetic frequency converters have been commonly used at low frequencies, particularly at 150 Hz in the form of the magnetic tripler. However, it is suggested[3] that they are subject to the following limitations:

i) a large magnetising current is required to obtain a high degree of saturation and the input power factor is therefore low (typically 0.4 lagging),

ii) for reasons of economy, the output frequency is restricted to low-order odd-harmonics of the supply frequency,

iii) the output power changes with fluctuations in the input mains supply,

iv) undesirable oscillations may be generated by ferro-resonance and subharmonic oscillations,

v) the physical size is generally large.

When used as a high-frequency source, a motor-generator set (Figure 1.2) requires a motor starter and generator control and output stations, where the latter includes load compensating capacitors, an output transformer and a series of mechanical contactors. The advantages of a static frequency converter over such an installation are[4] :

a) higher efficiency,

b) smaller size,

c) lighter weight,

d) less maintenance,

e) fast response giving quick power control during changing load conditions or line voltage fluctuations,

f) soft starting.

(The motor generator always demands more than its full load kVA at start-up, which is an important disadvantage in plants of

limited kVA capacity). In addition to this list, static converters are quiet and easier to install, while parallel operation of any number of units does not present appreciable difficulty. In terms of overall conversion economics, motor generators run at about 75-85% efficiency[5]with an input power factor of from 0.8-0.9 at full load. Because the intermediate step of producing mechanical energy is eliminated,the overall efficiency of the static converter is higher, at around 75-95% depending on the design and the operational frequency.

One major advantage of static converters over their magnetic and rotary counterparts is that they offer a variable output frequency, which substantially simplifies the apparatus and the operation of an induction heating system. A loaded induction heating coil presents a low power factor, and both the inductance and the reactance change considerably during a cycle of operation. The inherently low power factor of the loaded coil is generally compensated by the use of parallel connected capacitors. Clearly, for best utilisation of the power source available, the tank load circuit thus formed must be kept in tune with the output frequency. Magnetic frequency multipliers and motor-generator systems both operate at a fixed output frequency,and tuning of the tank load circuit during a heating cycle is therefore achieved by step-wise switching of the compensating capacitors using mechanical contactors. Although automatic contactors are available for this purpose,

they are costly and of limited life. However, in static converters the output frequency is determined mainly by the switching rate of the circuit thyristors and it is relatively easy to vary this to overcome the power factor variations of the work coils. In fact, thyristor inverters for induction heating are usually equipped with a load-tracking frequency control, which automatically adjusts the output frequency to the resonant frequency of the work coil and tuning capacitor. With this control feature, capacitor switching during the cycle of operation is usually unnecessary.[5]

Static Power Converters for Induction Heating

There are two basic types of inverter usually used in induction heating; the parallel inverter[6-12] and the series inverter.[12-19] The parallel or current-fed inverter, shown in Figure 1.3, uses parallel-connected tank capacitors for commutating the current between the thyristors of the inverter. A current of rectangular waveform is fed to the tuned tank circuit, producing a reasonably sinusoidal load voltage. On the other hand, the series or voltage-fed inverter of Figure 1.4 uses a series-resonant load circuit for commutation. The unidirectional thyristor characteristics allow a single half cycle of damped resonant current to flow, at the end of which the series capacitor reverse biases the conducting thyristor. The use of forced commutation techniques for induction heating inverters is not favoured,[3]

as they involve higher power circuit ratings than the alternative techniques. With forced commutation, the commutating capacitor supplies twice the load current during a thyristor turn-off, and causes high commutating component and thyristor ratings which may become excessive in high power high-frequency applications.

Conventional high-frequency power sources convert a d.c. input to an a.c. output, by using one of the commutation techniques described above in an overall a.c./d.c./a.c. conversion, as shown in Figure 1.5. Since such converters separate the low frequency (slow) rectifier thyristors (or diodes) from the more sophisticated high frequency (fast) inverter thyristors, by the d.c. *reservoir*, a large number of switching elements are therefore needed to achieve the dual conversion and to generate a controllable output power. The process of dual conversion also results in a reduced overall efficiency. It is, however, possible to convert the supply frequency input to a higher output frequency, without specifically using a d.c. link. Such a frequency converter, called a cycloinverter, eliminates the d.c. link by employing thyristors to perform simultaneously both the rectification and high frequency switching processes. In so doing, each half cycle of the alternating supply voltage is effectively treated as a temporary d.c. supply for the inverter and, as the next supply voltage half cycle becomes more positive, a fresh pair of thyristors takes over the inversion duty in the same load components.

The technique of cycloinversion was developed in the late 1930s, soon after the introduction of the industrial mercury-arc valves, primarily for the supply of medium-frequency power to induction melting furnaces.[20] The term, cycloinverter, originates from the structure of early prototypes, where 3-phase power is used as the input supply for a set of three bi-phase inverters without preliminary rectification.[20] Figure 1.6 shows a 2-anode mercury arc valve in the basic bi-phase inverter circuit, whereby a sinusoidal voltage is maintained across the inverter output terminals by firing the anodes H and K successively to alter the direction of the primary current.

Smart and Weaver improved the basic cycloinverter operation by devising a 6-anode, steel-tank mercury arc inverter for the generation of medium-frequency power in the range up to 250 kW. Figure 1.7 shows the basic circuit for this arrangement, where the output current flows from the input phase whose potential is most positive at that instant, to feed its associated inverter circuit. The grid control is arranged so that when any phase is operative, no current flows through the others. It was also suggested that, by improving the grid circuit, activation of a phase couldbe delayed, to vary the average power delivered to the load during the conduction period.

Since solid-state power devices became economic, various cycloinversion schemes utilising thyristors have been devised. Figure 1.8 shows a single phase step-up cycloinverter[22,23] where

the low-frequency source is inverted to the desired high frequency, and the resulting waveform, which has an input frequency modulation, is fed to the synchronous tap changer and filter to improve its harmonic content. The synchronous tap changer, shown in Figure 1.8b, is a transformer, in which the turns ratio can be varied by switching taps in either the primary or secondary circuits to minimise the distortion content of the high frequency output power. The inverter recommended for this scheme is a high frequency version[24] of the basic half-bridge series inverter of Figure 1.4, and is supplied from a fully rectified (but not filtered) input source. Although this system provides an efficient source for induction heating, its application has been limited to low output powers since it requires a large number of high-frequency thyristors for tap changing and was devised for a single-phase input.

In the early 1960s, semiconductor versions of many mercury-arc devices were developed. The thyristor version of the circuit of Smart and Weaver, shown in Figure 1.9, was introduced by Wurm and Stratton.[25] By analogy with the principles of operation of the earlier circuit, the solid-state cyclo-inverter employed parallel commutation, and since it utilised separate switching devices the output transformer was simplified to a single centre-tapped primary winding. The capacitor C in the output circuit is used both to compensate the load and

to provide the lead angle required for thyristor commutation, as in the basic parallel inverter of Figure 1.3. With this arrangement, Wurm and Stratton achieved frequencies as high as 3200 Hz, although they noted various shortcomings in their proposal. During commutation of a pair of thyristors, a time of overlap exists, when the incoming thyristor has just turned on and before the outgoing thyristor has completely turned off. (This is typical of parallel commutation and is caused by the series-stray or di/dt-inductor in the output current path. In Figure 1.9, this series inductor is the leakage reactance of the power transformer). During the overlap time, both thyristors conduct and, as can be seen from the circuit diagram, this results in zero voltage across the primary of the transformer. Since there is no output voltage, the current then flowing results only in a power loss. At high operational frequencies, the overlap time becomes a significant part of the output period, which clearly results in very inefficient operation. To avoid this serious shortcoming Dewan[26,27] modified the power circuit of the cycloinverter, to employ the series commutation shown in Figure 1.10. The arrangement has an additional advantage in that it does not require a centre-tapped output transformer or, if an output transformer is not used, a centre-tapped heating coil. Dewan showed also that, by further modifying the commutation circuit to the form shown in Figure 1.11, a higher input power factor could be achieved. The reduction of the input terminals from 4 to 3 also eliminated the centre-tapped input transformer.

As suggested earlier, in relation to the 6-anode mercury-arc inverter, performing the rectification and inversion processes simultaneously in a cycloinverter provides an inherent power control facility, which can be exploited by delaying the power control angle introduced in the firing sequence of the switching elements. The output frequency of the cycloinverter can also be controlled by varying the firing frequency of the thyristors. Although for efficient operation the available range of variation is narrow, it is nevertheless sufficient for most induction heating applications.

Due to the rectifying function of the circuit thyristors, the cycloinverter possesses an inherent short circuit protection capability. When a short circuit occurs, the circuit functions as a phase-controlled rectifier, for a worst case duration of less than one-half a mains cycle.

As can be clearly seen from the brief survey given above of cycloinverter techniques, the series cycloinverter is particularly advantageous as it offers a high operational efficiency and a simple power circuit, without the need for centre-tapped input and output transformers or a centre-tapped work coil. On the other hand, as the cycloinverter employs this form of series commutation, it has certain inherent disadvantages.
In this respect, the following critical consideration on the use of parallel and series commutation in induction heating will be helpful in assessing the full potential of the series commutated cycloinverter in this field

Use of Parallel and Series Inverters in Induction Heating

In a parallel inverter, the output voltage is related to a variable d.c. input voltage obtained from a controlled rectifier, independently of the timing control which determines its output frequency. Because of its variable output frequency characteristics, a parallel inverter is capable of supplying a wide range of loads having large impedance variations. However, starting presents an initial problem, since the then uncharged compensating capacitor cannot provide sufficient reverse voltage to commutate the pair of conducting thyristors at the end of the first current reversal. This problem is usually solved[28] either by using an auxiliary starting circuit or by permanently introducing a capacitor in series with the parallel resonant load, though this latter solution is at the expense of a slight narrowing of the operational frequency range.

Unlike the parallel inverter, the series inverter has received little attention in the field of induction heating. It is said[29,30] to suffer from the following shortcomings:

i) high load sensitivity and poor load-voltage regulation,

ii) low efficiency,

iii) it is basically a fixed frequency source,

iv) excessive voltage rise in the commutating circuit at low resistance loads.

The differences in load sensitivity in the parallel and series inverters results from their inherently different power circuit characteristics. The parallel inverter is normally fed from a d.c. source in series with an inductor L_d, used as a short-term constant-current device. As there may be no mean voltage drop across L_d during steady-state conditions, the output amplitude is determined by the supply voltage. However, in the series inverter, it can be shown[31] that the output voltage is given by:

$$V_{Ro} = [2 f_o g(V_{d.c}, R_o) R_o (C_1 + C_2)]^{\frac{1}{2}} \qquad (1.1)$$

which characterises the load sensitivity (at a fixed frequency f_o), since V_{Ro} is a function of R_o.

The claim that the series inverter is less efficient that the parallel inverter (i.e. item (ii)) is based on the argument that when the output frequency of a series inverter approaches the natural resonant frequency of the series L-C combination, a resonant rise of voltage appears across the heating coil. The coil voltage becomes therefore large in comparison with the inverter voltage, although its current remains the same as the inverter current. On the other hand, when the parallel L-C tank circuit in a parallel inverter (with selectivity Q_L) is excited close to its natural resonance, this results in a multiplication (approximately by Q_L) of the

current through the coil. The coil voltage is thus the same as the inverter voltage, while its current is higher than the inverter current. Since,for a heating coil,Q_L is typically around 5-20, the above argument can be justified. However, it cannot be generalised, since most series inverters at present used in induction service do not employ the same series capacitor for both tuning and commutation, but have a parallel compensated load and a separate series capacitor and inductor for commutation.[1,5,32] During operation the tank load circuit is kept tuned by continuous adjustment of the output frequency, so that it behaves, in effect, as a pure or nearly pure resistance. In this arrangement, as in the parallel inverter, the coil current (increased by Q_L) circulates within the tank only, and it is not carried by the inverter and the supplying conductors. An additional advantage of this configuration is that the commutating componentscan be selected to provide the optimum inverter performance for a particular application. Based on the considerations above, the series inverter does not necessarily have a lower efficiency than the parallel inverter. In fact, as will be explained later, the series inverter produces a better operational efficiency than its counterparts,[31] particularly at high operational frequencies.

The output frequency of the series inverter (referring back to item (iii) of the shortcomings listed earlier) can be made to vary within a range, although for a given commutating circuit it only produces an optimum inverter performance at a

specific output frequency. When so doing, the output frequency must always be lower than the damped resonant frequency of the output current, so that sufficient turn-off time is always available to ensure successful commutation of the circuit thyristors. The lower limit of the output frequency is defined by the deteriorating inverter performance. As the output frequency is reduced, the output current becomes distorted due to the long zero intervals, and the input power factor of the inverter falls. On the other hand, if the commutating inductor varies during application, as in the series-tuned circuit of Figure 1.3, the inverter frequency can be made to shift automatically with the load characteristics, with the turn-off behaviour determined by a controlled de-tuning between the inverter operating frequency and the resonant frequency of the load circuit, so as to maintain a constant thyristor extinction time. Although the output frequency range of a series inverter with a parallel compensated load is unfortunately limited, it is still compatible with the operational frequency range requirement of most induction heating applications.

As stated earlier (item (iv) on page 11), the commutating circuit voltages in a series inverter rise, excessively if the load resistance (i.e. the equivalent tank load resistance in the case of parallel compensated load) drops. This is caused by the resonant rise of voltage across the reactive elements in a series resonant circuit of increased selectivity, and means

increased voltage ratings for both the commutating capacitor and the inverter thyristors. The minimum load resistance for a given commutating circuit is therefore limited and a short-circuit load condition leads to a hazardous situation. (On the other hand, the maximum load resistance for the resonant action of the commutating circuit to be effective is also obviously limited). An excessive voltage rise in the commutation circuit can be avoided to a significant extent by:

i) feeding the reactive energy stored in the commutating components back to the source,

ii) limiting the input current to the inverter,

iii) step-wise load matching via a multi-tap output transformer.

The sine-wave bridge inverter of Figure 1.12 makes use of the first method. The anti-parallel feedback diodes across the thyristors feed back the excessive reactive energy of the load and, in so doing, provide the turn-off conditions to the thyristors. Clearly, in this arrangement the maximum thyristor voltage is limited to the supply voltage.

[24]

The second method can be realised by supplying the series inverter from a current source in parallel with a capacitor, as shown in Figure 1.13. By analogy with the parallel inverter, where an approximately constant output voltage is achieved by supplying the inverter from a voltage source in series with an

inductor (i.e. a short-term current source), an approximately constant output current is obtained from a series inverter by supplying it from a constant current source in parallel with a capacitor (i.e. a short-term voltage source).

The two previous methods avoid excessive commutating circuit voltage rises by, in effect, limiting the variation of the output current at the expense of the output voltage regulation. However, by load matching, both of these desired operating conditions can be achieved simultaneously. Figure

33

1.14 shows a typical scheme, with a multi-tap auto-transformer used for load impedance matching. As shown, the compensating capacitor is placed at the secondary terminals to save transformer rating, since it now needs only to supply the real power to the tuned load. This is further advantageous, since a change in the impedance transformation ratio need not be accompanied by a retuning of the load. The output transformer may be provided with a large number of taps, in order to track closely the load impedance changes. However, in a high power cyclic application of short period, frequent tap changing may cause severe interruptions and prove costly in terms of contactor wear. Although, in a series inverter tap changing can be performed at zero output current (resulting in a longer contactor lifetime, etc), the tap changing should be avoided wherever possible.

29

It was once claimed that in a series inverter an unscheduled initiation of thyristor conduction by spurious signals

could cause a short circuit, and thereby lead to the ultimate destruction of the inverter. However, it has since been demonstrated[31] that this idea is erroneous, and that when the control circuit is properly designed and constructed the thyristors will not fire accidentally. On the other hand, it is difficult in induction heating systems employing series inverters to guard entirely against an occasional shutdown, if the load fluctuates violently or if there are faults in the output circuit.

So far, only the *shortcomings* of the series inverter have been considered. These circuits do, however, also possess important features which make them particularly suitable for high-frequency induction heating and melting applications. Inverters with series commutation offer:

i) higher operational efficiency and reliability than their counterparts,

ii) approximately sine-wave output current,

iii) an intrinsically high turn-off time to output period ratio, which enables them to be used at higher operational frequencies.

These significant advantages stem basically from the stresses on thyristors using a series commutation circuit being considerably lighter than when other commutation techniques[31,34-36] are used. Clearly, the losses and the damage suscepti-

bility of switching elements during on-off operation both increase with the ratio of transient to steady-state stresses. Common inverter circuits, such as parallel inverters, employ modes of operation based on the forced interruption of the load currents as part of their cyclic operation. This mode of operation imposes considerable stresses on the switching components, especially at the end of the quasi-rectangular current pulses. A typical power dissipation curve for a power transistor operating in the indicated switching mode is given in Figure 1.15a.[31,37] The *tail* of this occurs as the switching element undergoes the transition from the conducting to the nonconducting state, and its shape and size depend solely on the network and the device characteristics, and are independent of the frequency of operation. The area under this part of the curve (A_1) corresponds to the energy dissipated per cycle which constitutes the frequency heat barrier for efficient inverter operation.

During a series commutation, the thyristor open circuits naturally when zero current flows, with the cessation of the underdamped resonant load current pulse, and the power dissipation is therefore near zero during the turn-off process. Also, on initiation of current conduction in the thyristor, the rate of rise of current is limited by the series inductor, such that it cannot attain any significant value during this process. Figure 1.15b (Ref.31) shows a typical power dissipation curve for a thyristor undergoing series commutation. Since the power

dissipation in the switching element is confined mainly to the conduction time, it is almost independent of the frequency of operation for a given current level and of the conduction time to period ratio.

In a series inverter, the time for which the thyristors are switched off can be a substantial part (up to 25%) of the full commutation cycle, which makes it adaptable to high frequency operation. In the parallel inverter, the ratio of the circuit turn-off time to the output period is inherently low.

In general, the achievement of operational frequencies of 10 kHz and above in static power converters is rather difficult, because of the turn-off time and switching loss limitations of existing thyristors. For applications at these frequencies, various conversion techniques have been developed which rely basically on:

i) some means of frequency multiplication, to enable the load to operate at a frequency above the capability of the thyristor [5,38-41],

ii) the time-sharing principle [5,11,42-45].

When using the first method to obtain, for example, a 10 kHz output frequency, the tuned tank load circuit is supplied from a 3 kHz inverter, with half-cycle 10 kHz pulses of 0.333 duty cycle. The load is required to be of high selectivity Q_L

to minimise voltage waveform distortion. The second method uses a number of low-frequency inverters on a time sharing basis, to achieve a high output frequency. In this case,the 10 kHz output frequency is obtained by using three 3 kHz invertersdelivering time-shared 10 kHz pulses, with each inverter operating on a 0.333 duty cycle. With the continuous 10 kHz output current thus obtained, this arrangement overcomes the voltage waveform distortion problem. It should be noted that a time-sharing scheme only eliminates the problem of thyristor recovery time, and,since the thyristors still have to generate the output frequency current pulses,the maximum operational frequency becomes limited by factors normally of secondary importance (such as turn-on time and the rate of rise of forward voltage). Both parallel and series commutation can be used to generate high-frequency power in time-shared inverters as shown in Figures 1.16 and 1.17 respectively. As can be seen, the high output frequency is achieved at the cost of an increase in both the complexity and the number of thyristors,which obviously adversely affects the operational efficiency and reliability and results in a high initial cost. The time sharing principle can also be applied to a cycloinverter, but this would be merely of academic interest as it requires a very complicated power circuit.

1.2 Scope of the Project

The series inverter, although suitable for high-frequency applications, cannot be used to its full potential with the varying load conditions of induction heating, because of its load sensitivity. However, this problem can to a considerable extent be overcome in most induction heating applications, if the commutation circuit is carefully designed to match the varying load conditions of a heating cycle.

The principal aim of the project presented in this thesis is to study the performance of the series commutated cyclo-inverter when used as a power source for induction heating, and to establish an optimum design criteria for the power circuit. The operational characteristics of the cycloinverter do not appear to be fully documented, although it is in extensive use. By analogy with a controlled rectifier, the power circuit of the cycloinverter may be simplified to its half-bridge form, the operational characteristics of which are also studied. The theoretical investigations undertaken when searching for an efficient power source in the early stages of the project (prior to the course of the research being fully directed to the study of the cycloinverter), finally gave way to a subproduct; the analysis and optimisation of the sine-wave inverter. This was also found to develop the understanding of series commutation necessary for the latter stages of this work.

When proceeding with the project, there was a need to determine the load characteristics and their variation throughout a typical induction heating application. Unfortunately, induction heating loads require a very complicated equivalent circuit, with a large number of non-linear parameters which vary substantially during a cycle of operation. Since a detailed theoretical study is clearly beyond the scope of the project, this task is tackled empirically. By examining the available literature on recent induction heating applications, a set of load conditions are derived and assumed to be typical of induction heating applications.

When optimising the performance of an inverter for a given load condition, the following systematic approach is adopted:

i) Develop an understanding of the operational principles involved.

ii) Develop a reliable and *flexible* method of analysis to study the inverter in different operational modes.

iii) Fix the inverter design variables.

iv) Establish a set of parameters to describe the important aspects of the inverter performance.

v) Investigate fully the variation of the inverter performance parameters with the design parameters for varying load conditions.

vi) Select the values of the design parameters which produce the best inverter performance on the basis of the optimised criteria.

The method of analysis required in item (ii) can be developed by establishing a complete digital simulation of the inverter. However, it was found that relying solely on the digital simulation of the investigation of the inverter performance usually demanded an excessive computation time. The inverters were therefore also investigated using an approximate but appreciably faster method of analysis, that is a steady-state harmonic analysis. The availability of the two different methods of analysis provided an additional check on the validity of the theoretical results obtained.

For the sake of clarity in presentation, the thesis is divided into 9 chapters, and the scope of the remaining chapters is:

In Chapter 2, the load conditions of an induction heating application are described and classified. Some important parameters of the load are introduced and their variations in typical induction heating applications are derived.

In Chapter 3, the sine-wave inverter is analysed and its commutation circuit is optimised by following the steps described above.

In Chapter 4, the operational and theoretical principles of a cycloinverter operating at relatively low output frequencies (i.e. 120 Hz - 450 Hz) are described. The performance

of a 150 Hz cycloinverter delivering controlled power to an induction heating load with stable characteristics is investigated, and its power circuit is optimised. It is shown that the performance of the cycloinverter operating at low non-multiple input frequencies tends to deteriorate as high modulation appears in the output current.

Chapter 5 provides an optimisation analysis of the cycloinverter performance operating at high frequencies (i.e. around 900 - 1050 Hz). This range is chosen because, although it is a very common induction heating frequency range, the design of an efficient cycloinverter at these frequencies presents some additional difficulties.

In Chapter 6, some techniques for the digital simulation of the switching networks are introduced, and a complete digital simulation of the cycloinverter is developed for investigating the inverter performance at different output frequencies, power control modes and varying load conditions.

In Chapter 7, an input filter for the cycloinverter is considered. By analysing the overall performance of the filter-cycloinverter configuration optimum design criteria for the filter components are established. A carefully designed input filter not only improves the input power factor and eliminates the distortion harmonics at the input lines, but also provides means of preventing excessive voltage rises in the commutating circuit at high loads.

Chapter 8 describes an experimental investigation to verify the theoretical findings previously presented. For this purpose experimental prototypes of both a 150 Hz cycloinverter and a 900 - 1050 Hz cycloinverter with an input filter are constructed and their performances when delivering power to a simulated induction load with stable and varying load characteristics are investigated.

The final chapter of the thesis records the conclusions derived from the project and suggests how the work might be developed and extended in the future.

FREQUENCY	EQUIPMENT	APPLICATION
10 Hz – 100 Hz	Supply mains Frequency Induction Heating	Melting Pre-heating billets Billet heating for forging Press Platten heating
1 kHz – 10 kHz	Magnetic Multipliers, Solid State and Motor Generator Equipment	Billet heating for forging Deep case hardening Melting air type furnaces Melting vacuum furnaces
100 kHz – 1 MHz	Thermionic Vacuum Tube Equipment (Induction)	Soldering, Brazing, Annealing, Hardening, Levitation Melting, Float-zone Refining—Semi-conductor Materials, Crystal pulling under vacuum, Plasma torch, Ionization of gases, Analysis of metals by fusion in vacuum, Graphite heating to high temperatures
10 MHz – 100 MHz	Thermionic Vacuum Tube Equipment (Dielectric)	Pre-heating moulding powders Wood gluing Biscuit baking, Fish and meat thawing Plastic sheet welding
1 kMHz – 10 kMHz	Magnetron Tube Equipment	Food re-heating and cooking Food de-frosting Pre-heating low loss materials Processing liquids

Figure 1.1 Frequency spectrum - generating equipment - application

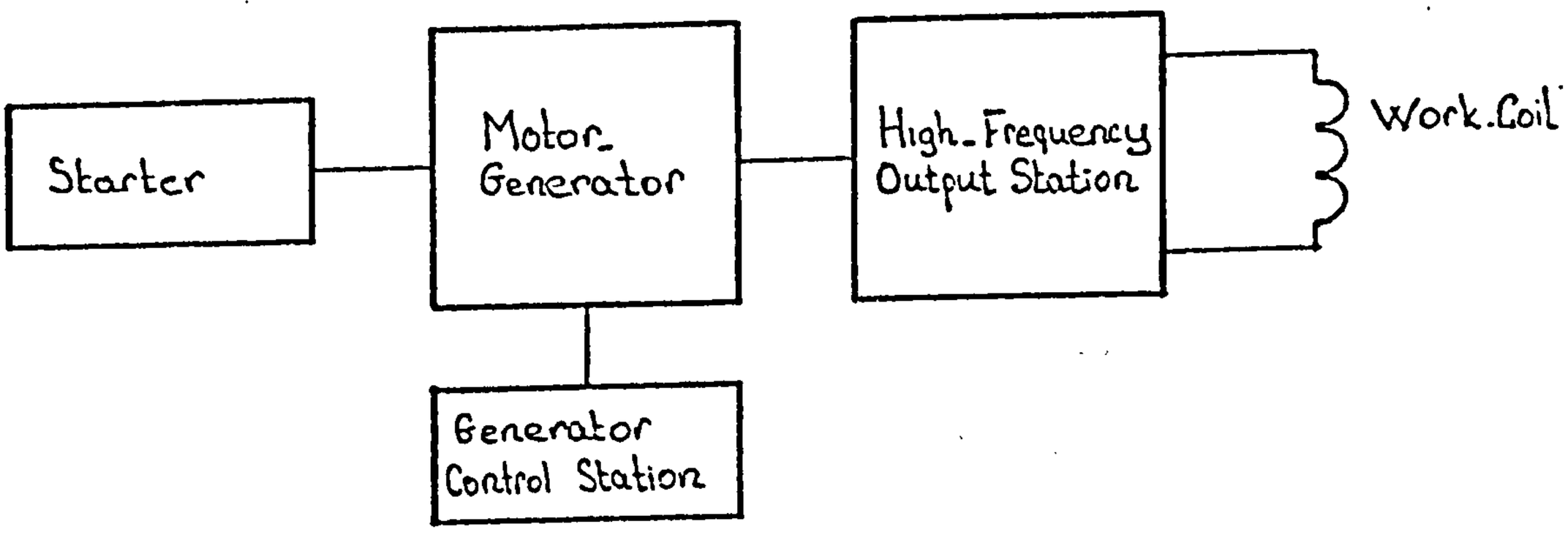

Figure 1.2 A typical high power motor-generator installation

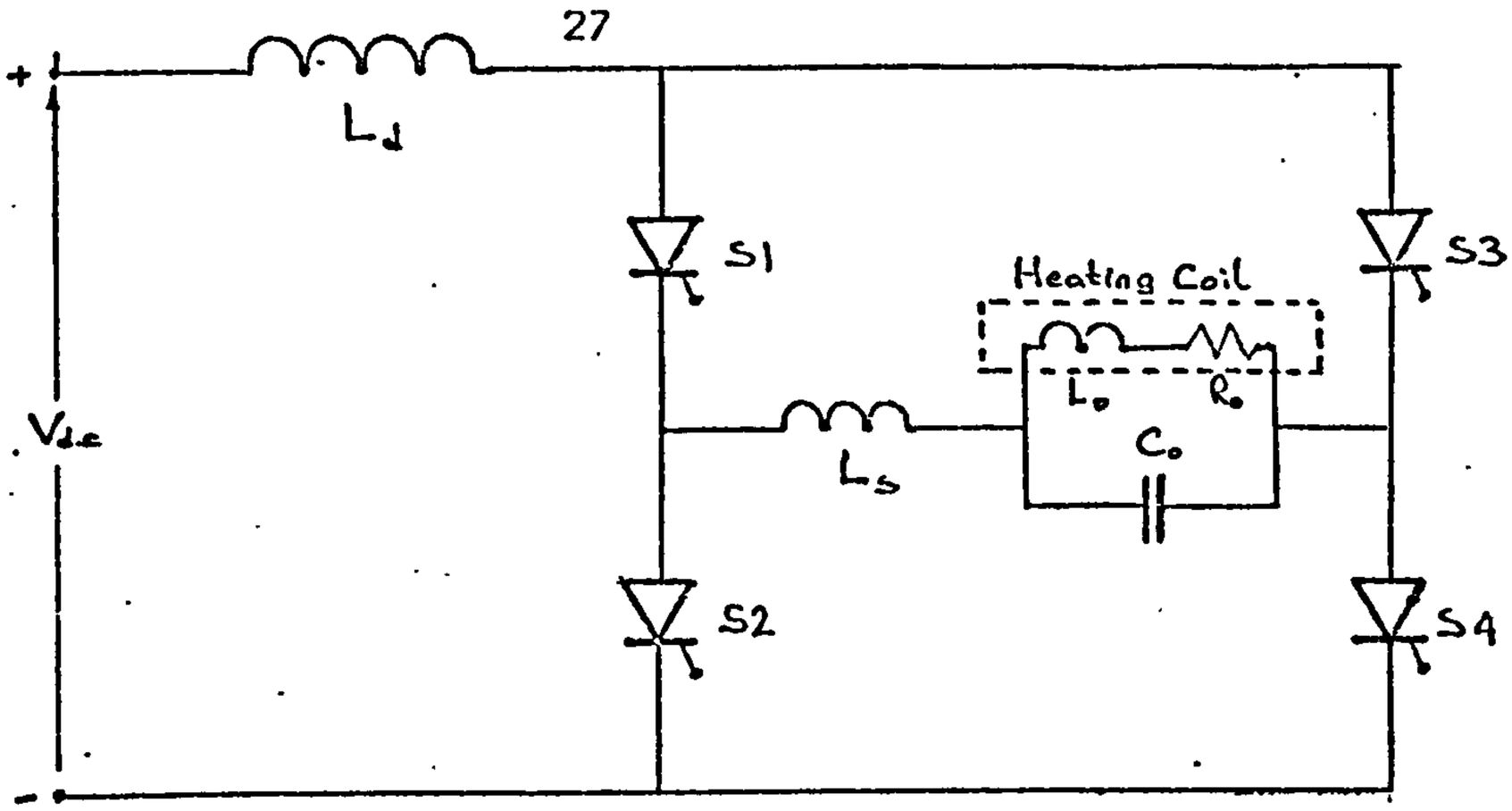

Figure 1.3 A parallel inverter for induction heating (L_s is the di/dt limiting inductor)

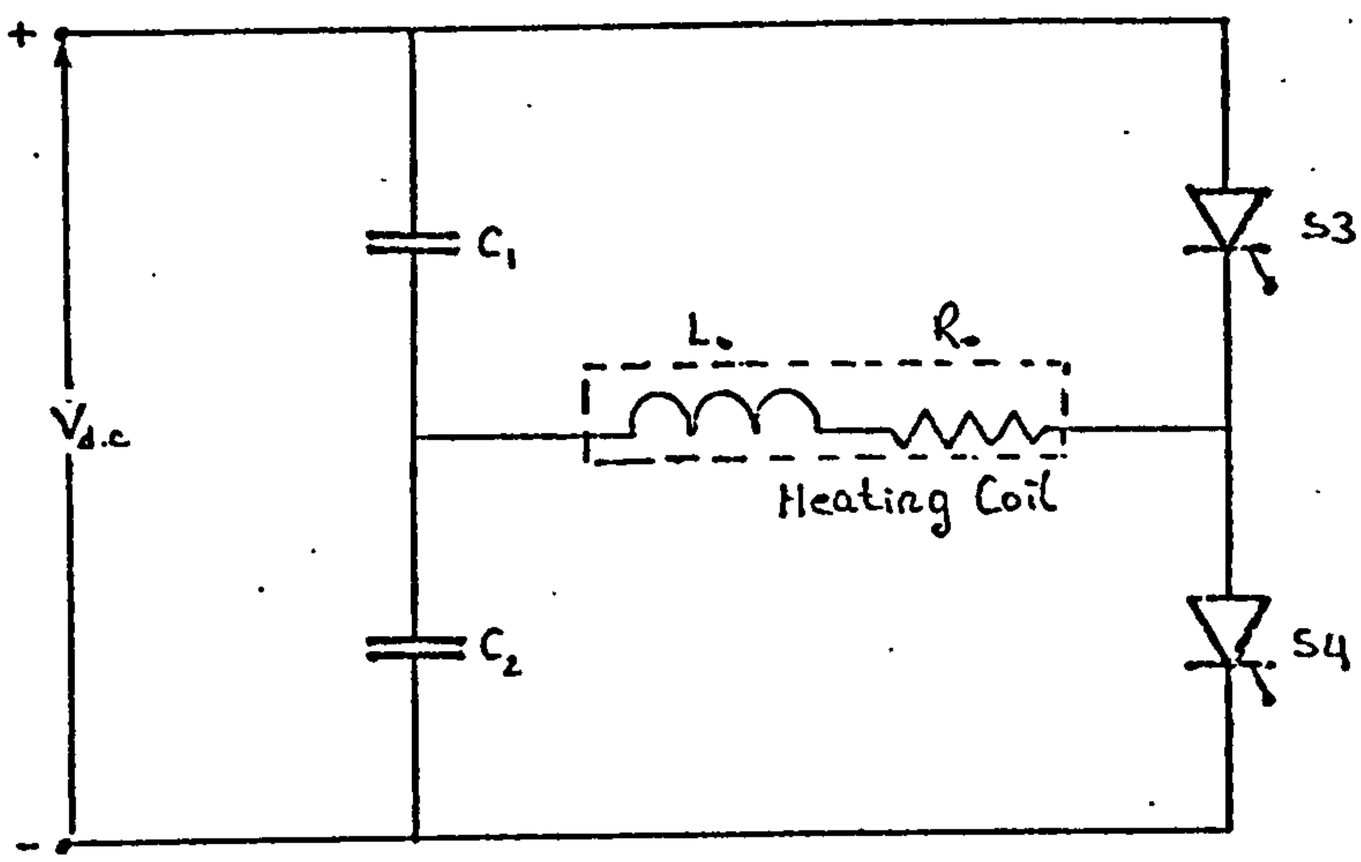

Figure 1.4 The basic series inverter with an induction heating load

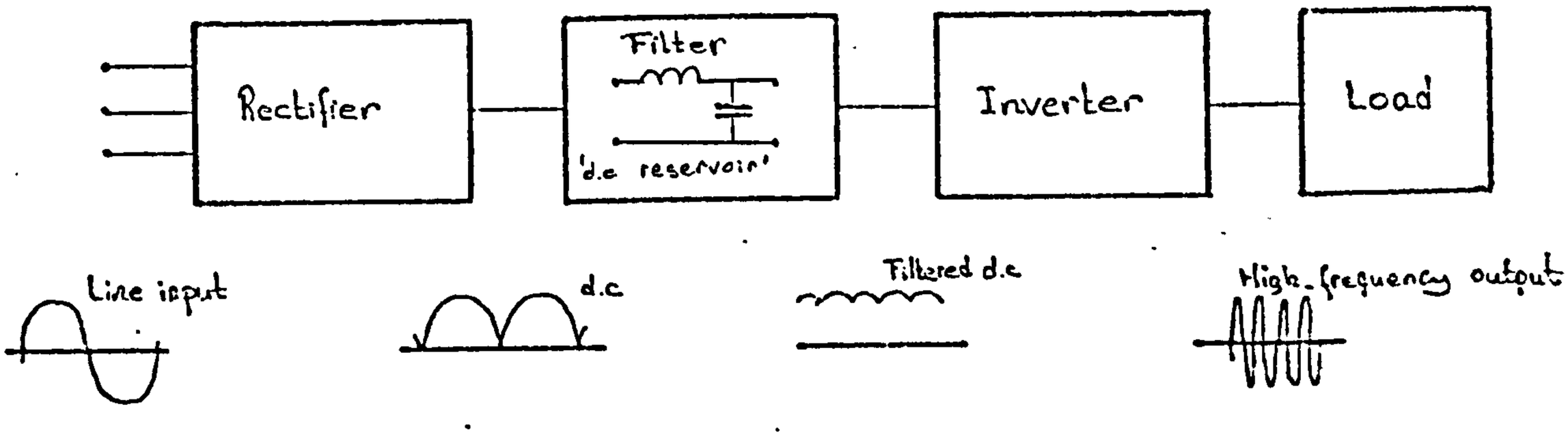

Figure 1.5 Conventional ac-dc-ac frequency conversion

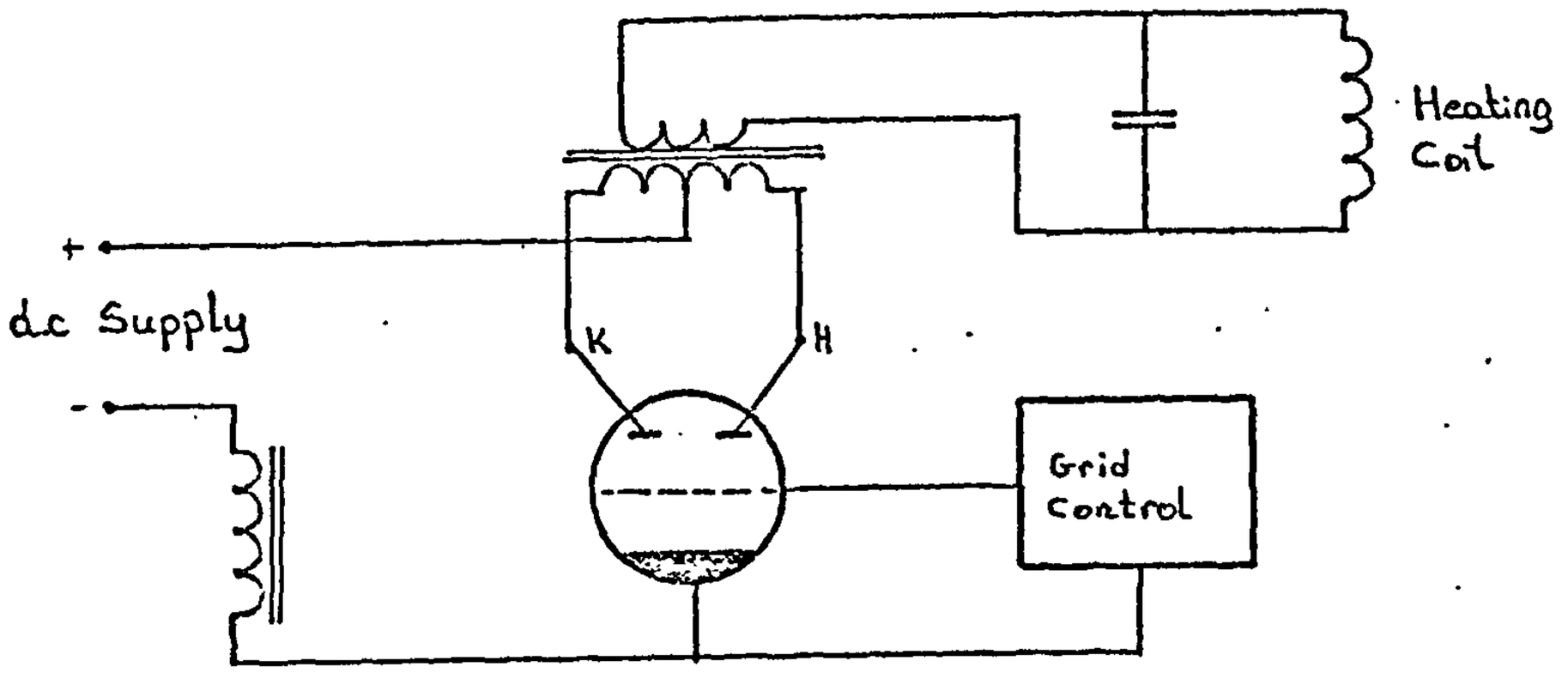

Figure 1.6 Bi-phase mercury-arc inverter circuit

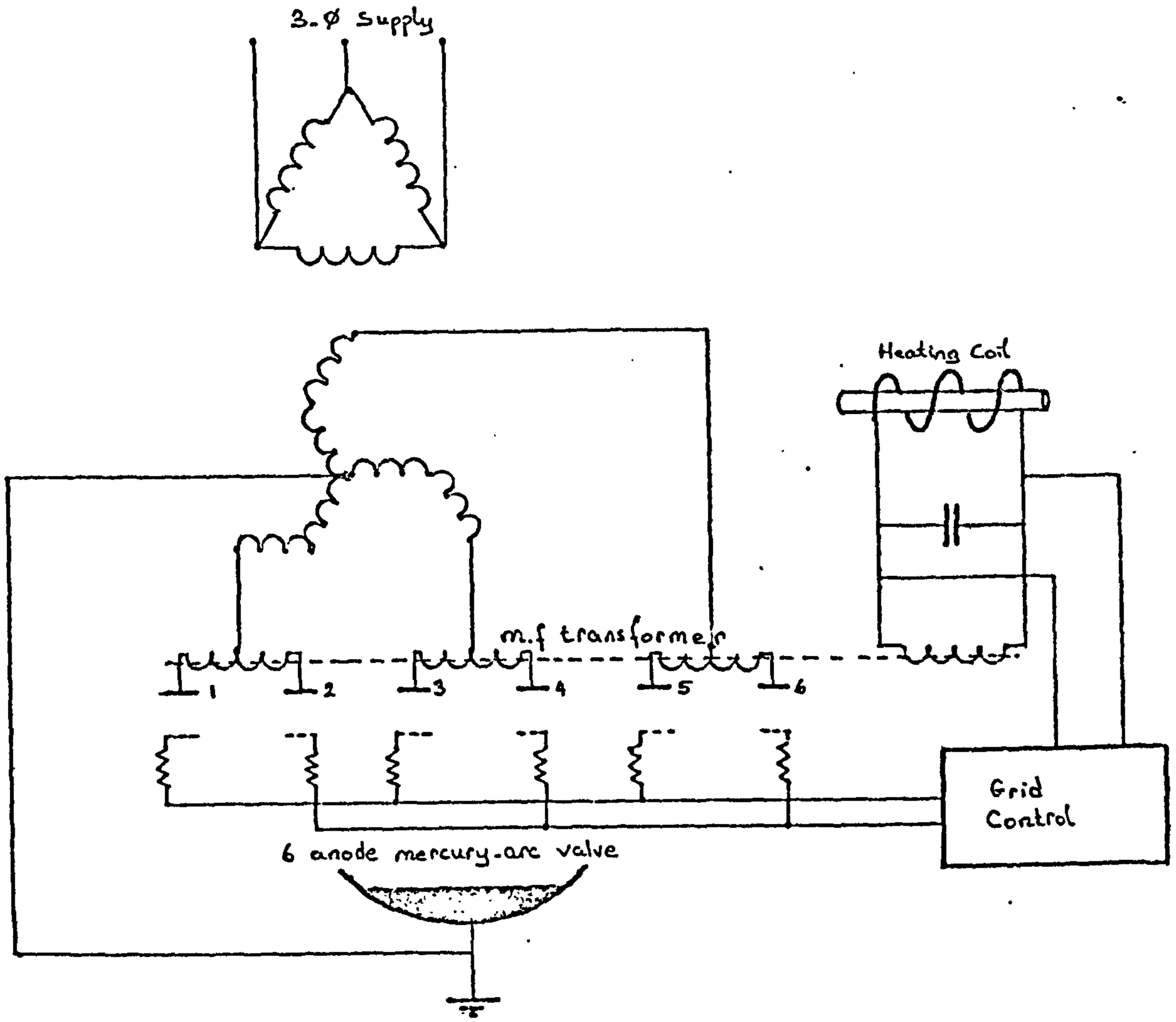

Figure 1.7 Simplified diagram of 6-anode mercury-arc inverter (devised by Smart and Weaver)

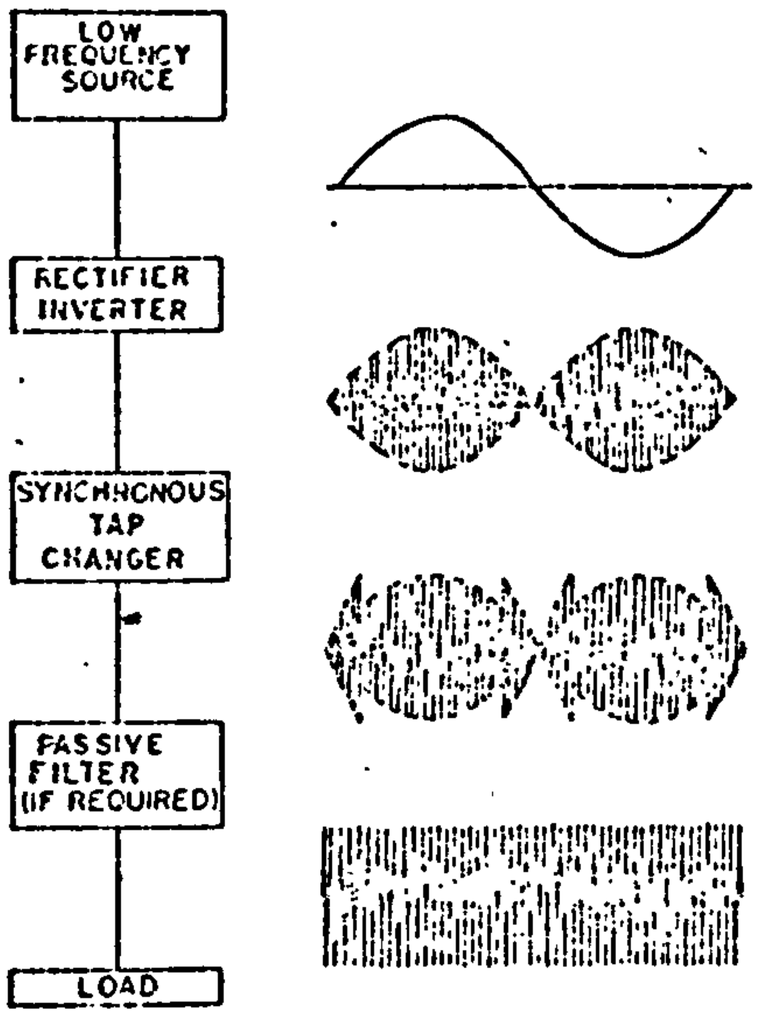

(a)

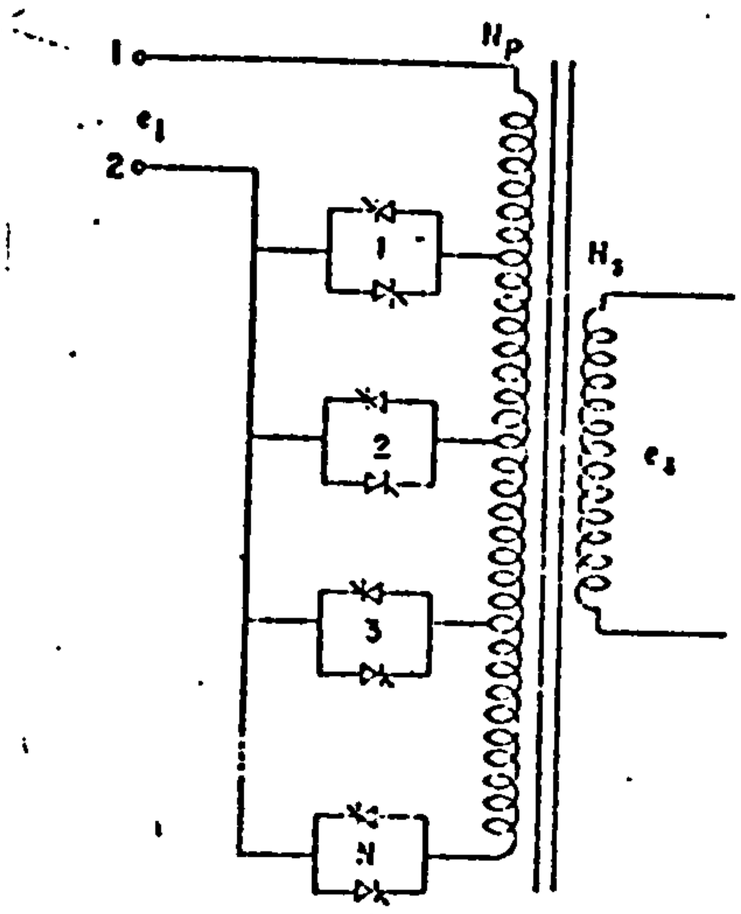

(b)

Figure 1.8 Single phase cycloinversion:
a) block diagram b) the synchronous tap changer

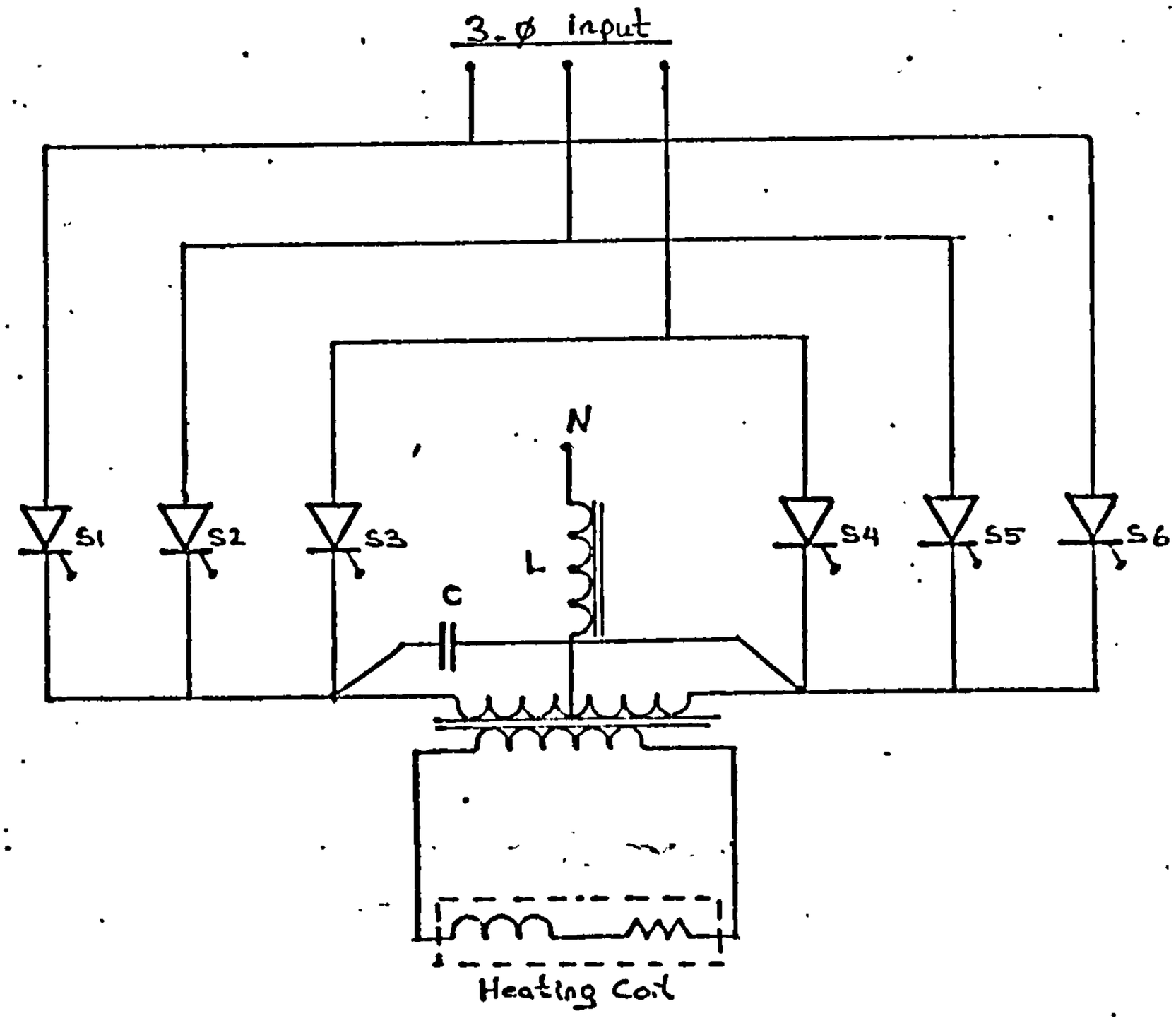

Figure 1.9 The parallel load commutated cycloinverter (devised by Wurm and Stratton)

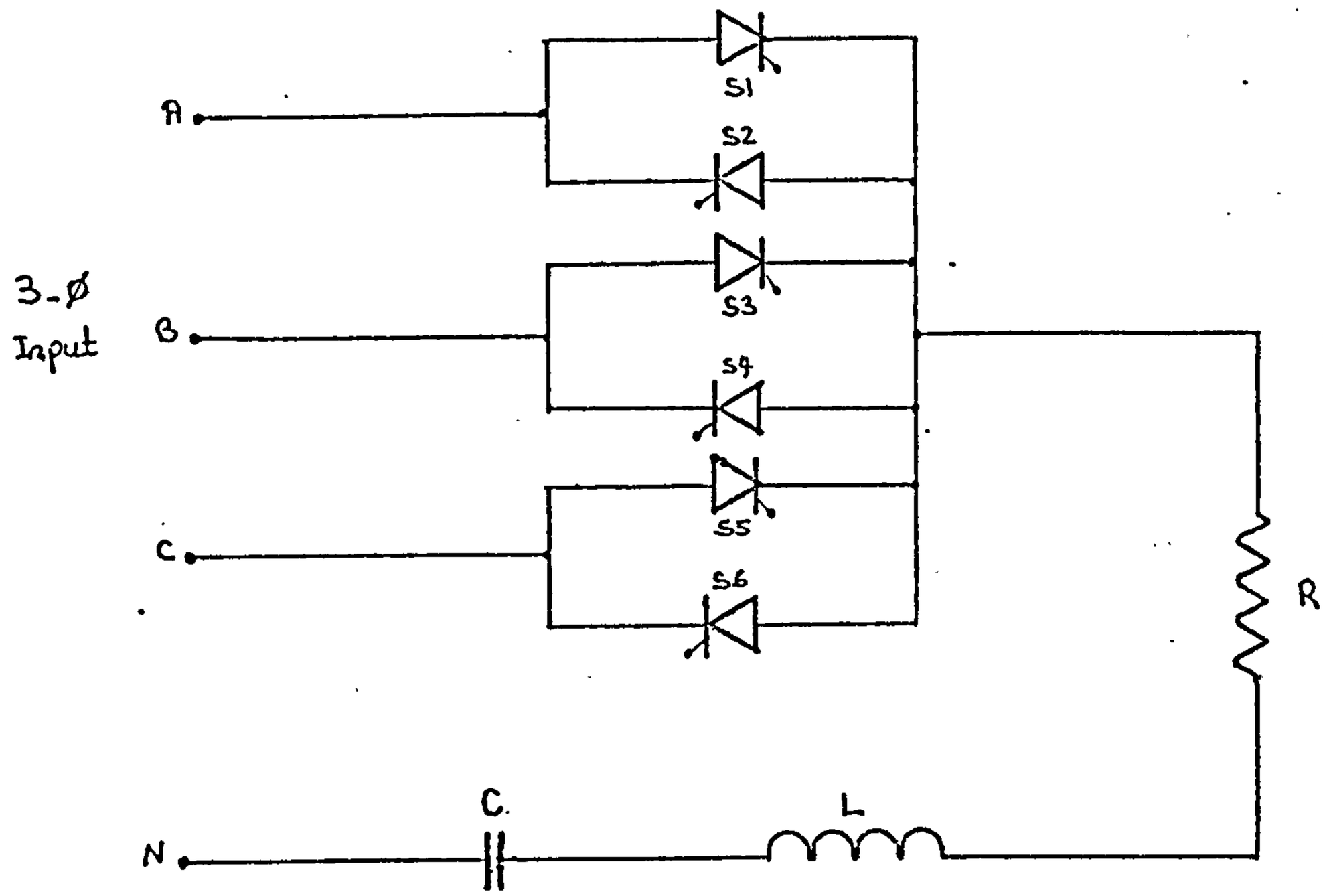

Figure 1.10 The series commutated cycloinverter

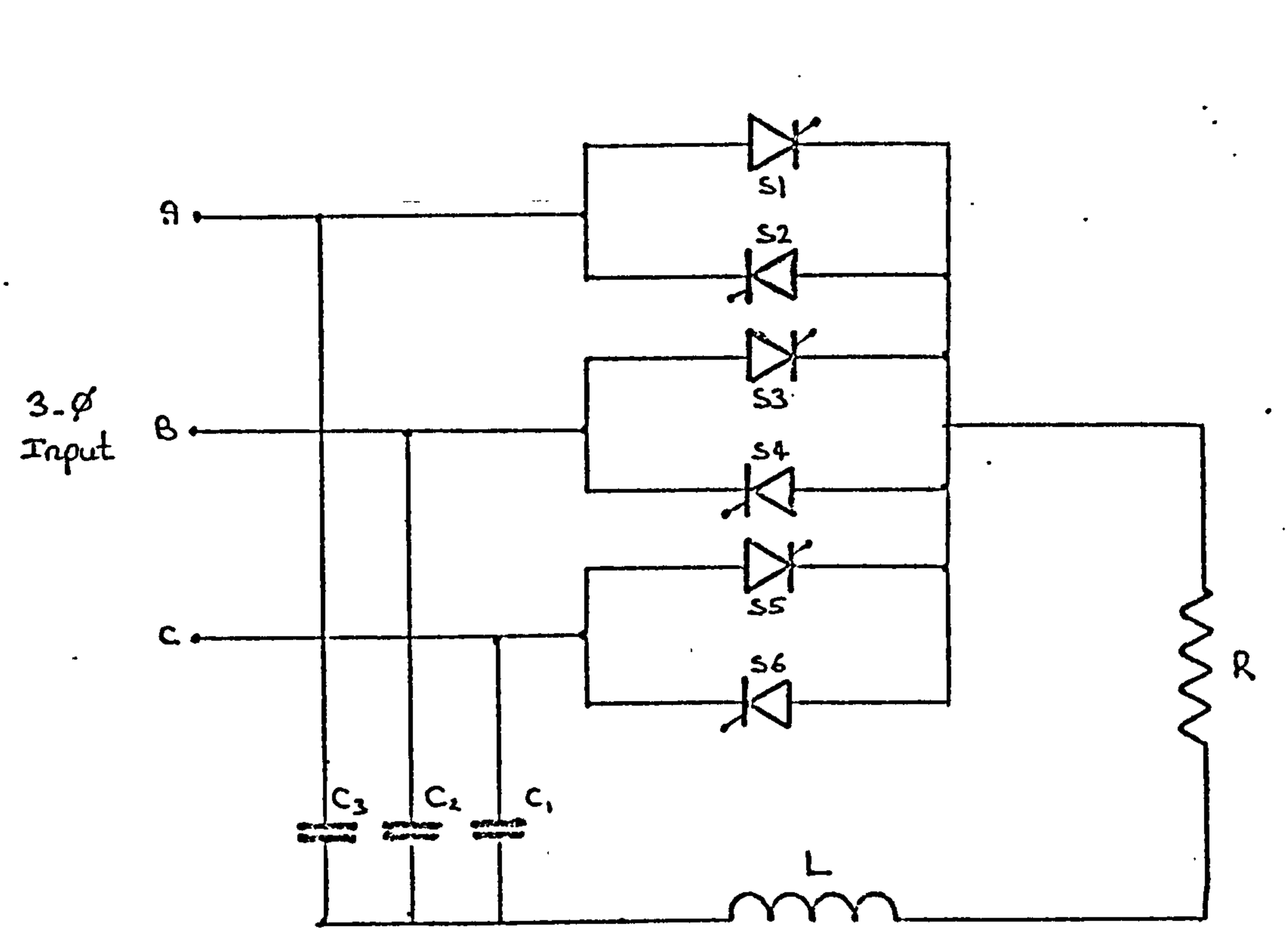

Figure 1.11 The improved series inverter with 3-phase input

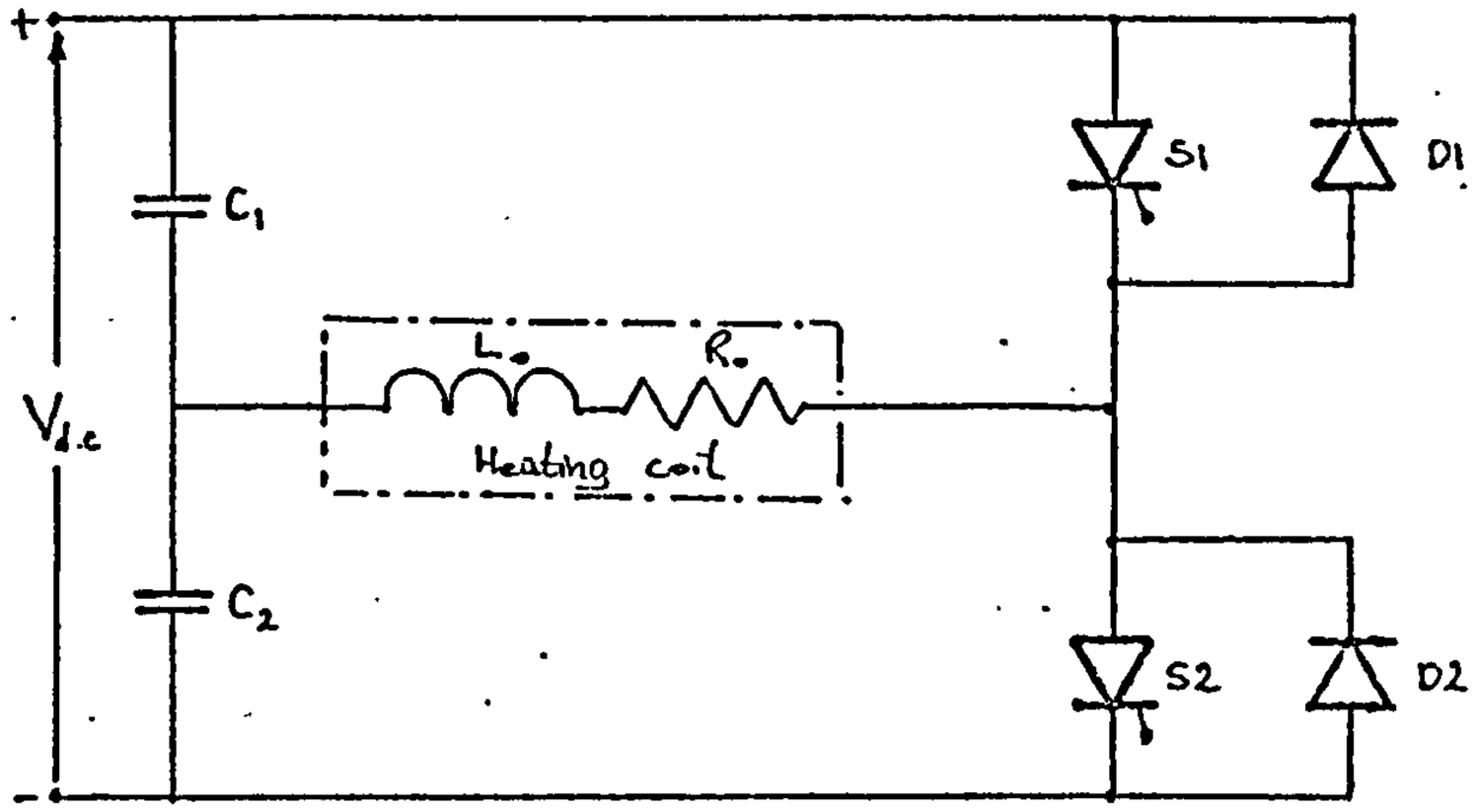

Figure 1.12 The sine-wave inverter

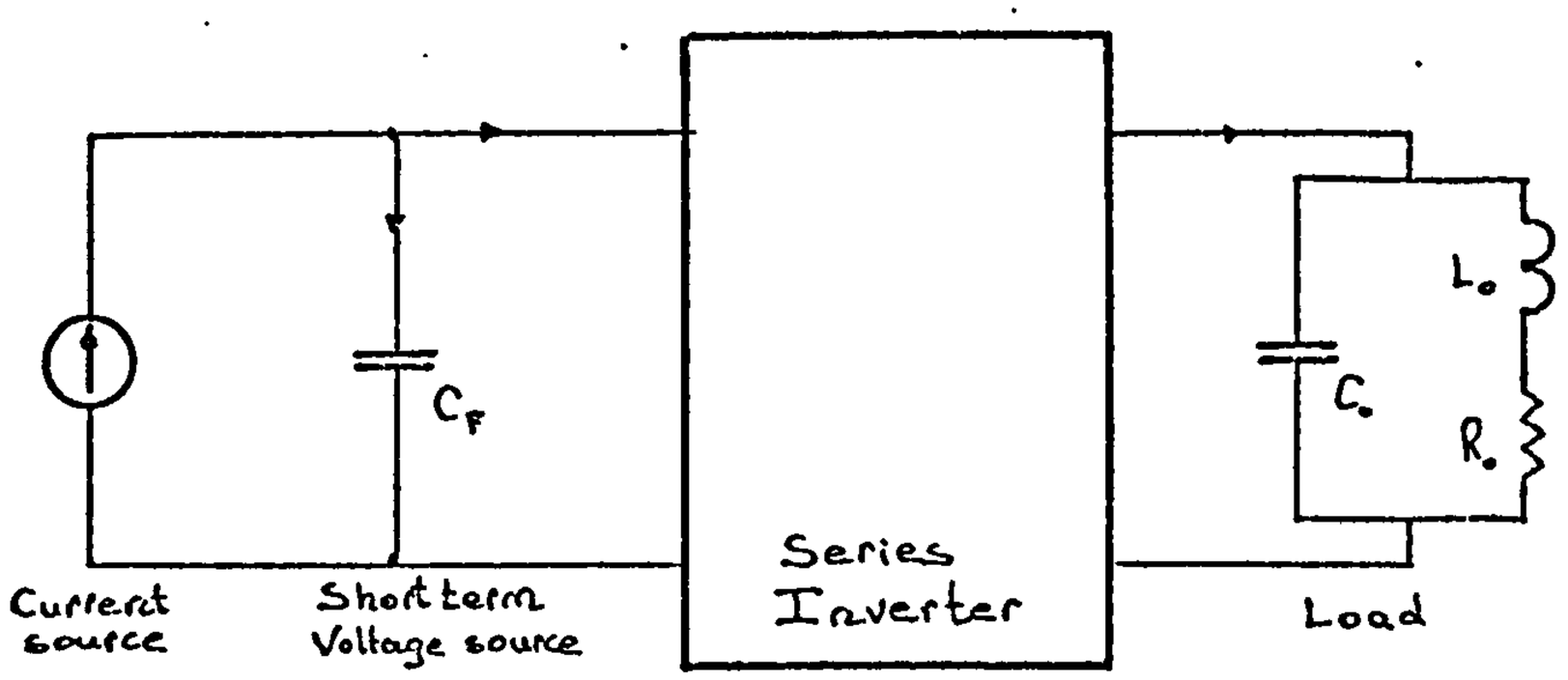

Figure 1.13 In a series inverter excessive commutating circuit voltages at high loads can be prevented by supplying the inverter from a capacitor in parallel with a current source

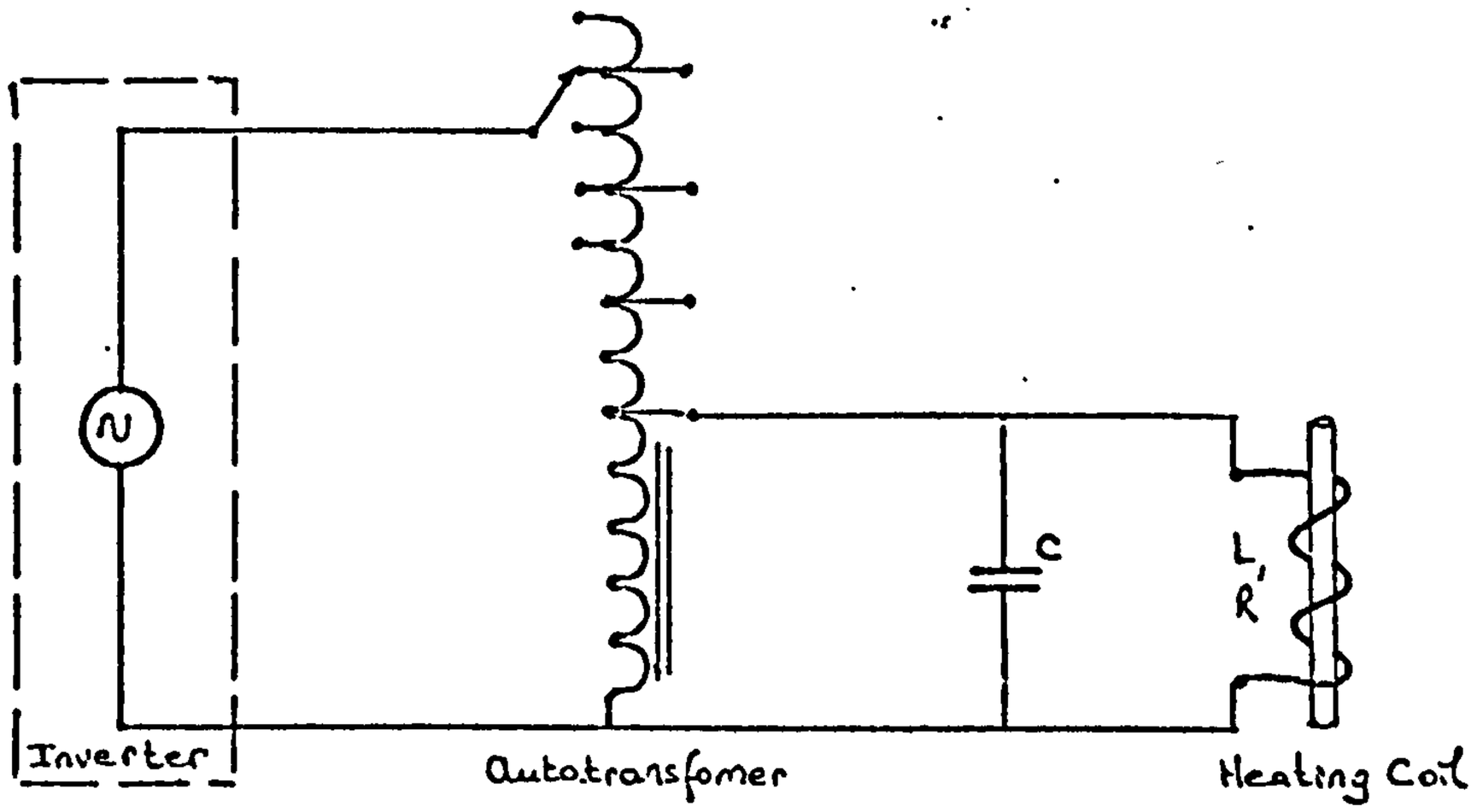

Figure 1.14 A typical load impedance matching scheme for an induction heating load.

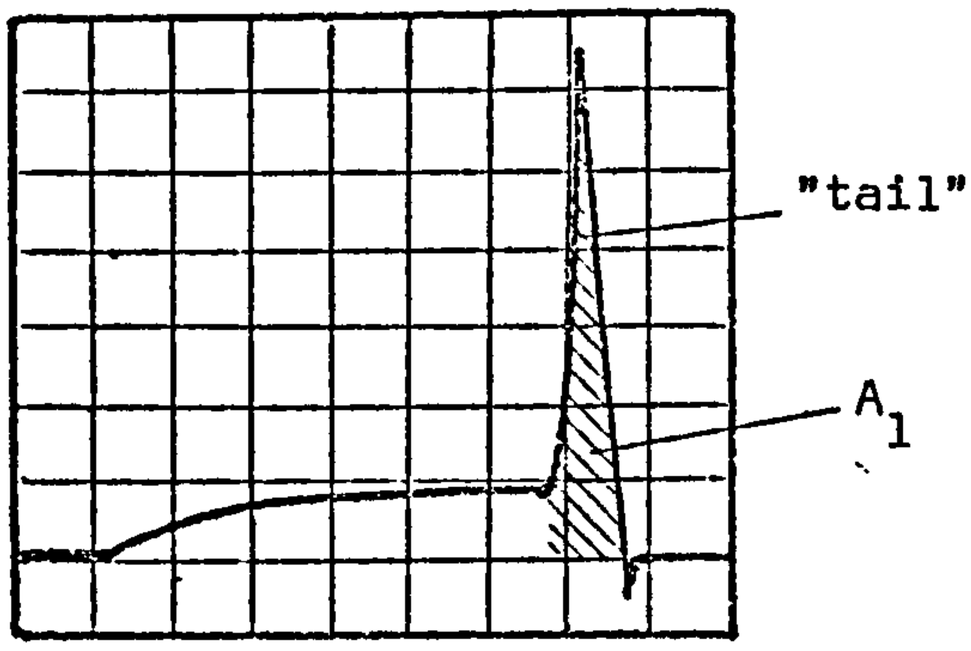

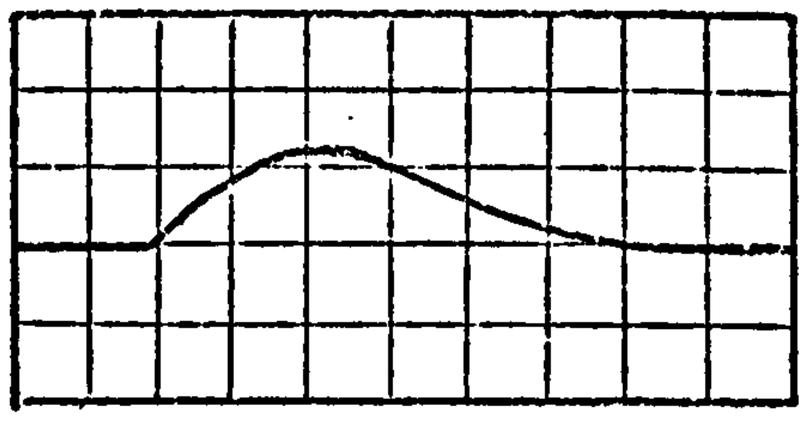

(a) (b)

Figure 1.15 Power dissipation of the switching element.
(Scales: vertical - 5 watt/div; horizontal - 5 μs/div)

a) transistor in an inductive circuit (maximum collector current = 5A, series inductor = 10 μH).

b) thyristor in a series resonant circuit (maximum thyristor current = 7A)

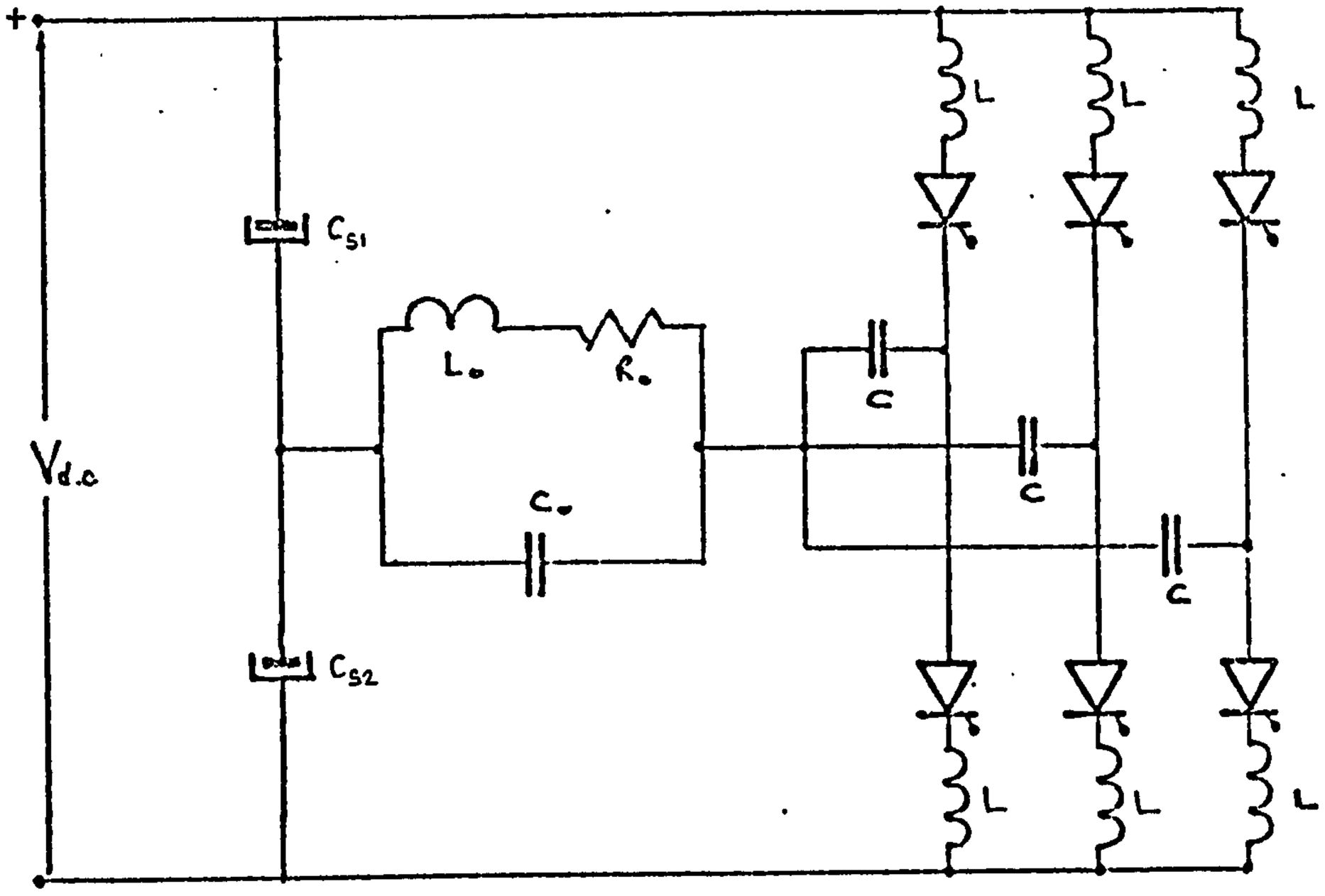

Figure 1.16 A high frequency, time-shared, series inverter
(L,C - commutating components,
C_{s1} , C_{s2} - centre tap d.c. source capacitors)

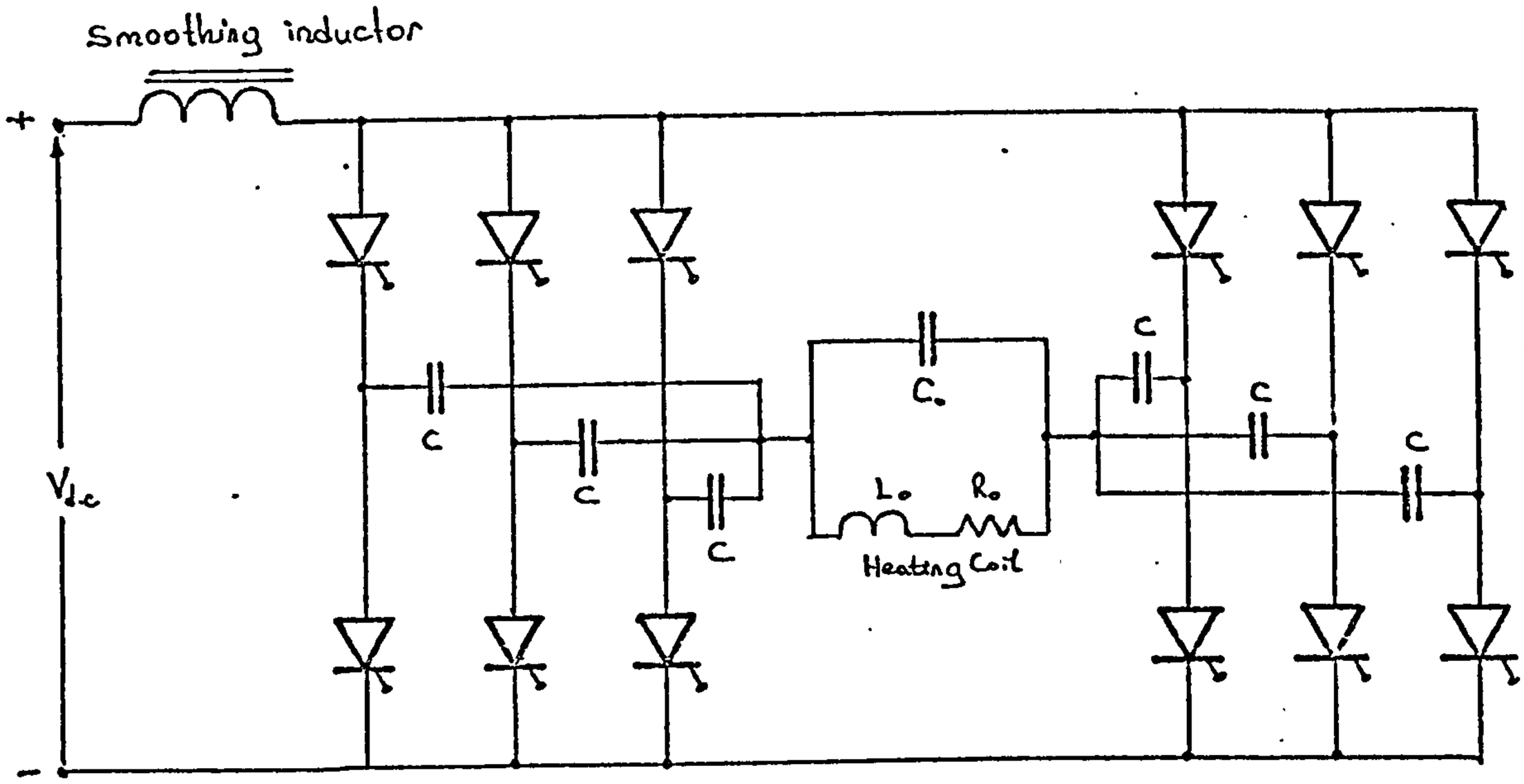

Figure 1.17 A high frequency, time-sharing, current-fed inverter

CHAPTER 2

LOAD CHARACTERISTICS OF INDUCTION HEATING

Any attempt to select and design an efficient power source for a particular application naturally requires a thorough study of the load conditions experienced while operational. This is particularly important when designing a power source for induction heating applications, since most power sources at present available are unfortunately load sensitive.

This chapter investigates the dynamic characteristics of induction heating loads, by pursuing the following steps. Firstly, the general principles and theoretical considerations of an induction heating load are outlined, to enable an approximate equivalent load circuit to be established. Secondly, the load characteristics of typical induction heating and melting applications are examined. Finally, based on experimental evidence and on approximate theoretical estimations, a dynamic load equivalent circuit for a typical induction heating load is developed.

2.1 General Principles and Theoretical Considerations

The theoretical analysis of an induction heating load is an advanced subject, generally requiring computer analysis and outside the scope of this thesis. Nevertheless, in this section,

some parameters of a loaded induction heating coil are introduced, and their possible variations as a result of the changing physical and electrical conditions of the load circuit during an operational cycle are discussed, although a detailed mathematical analysis is avoided.

In an induction heating application, energy is transferred into the workpiece from an induction coil via an electromagnetic field. In most cases, a water-cooled induction heating coil encircles the furnace containing the metal charge being heated, melted or treated, and in this respect the induction coil may be approximated to a transformer short-circuited on the secondary side. The heating of the workpiece arises by virtue of the power losses associated with the electrical resistance of the material, when this carries the induced current. The workpiece may involve magnetic or non-magnetic conductive materials, that are normally heated from room temperature 70°F, to 1700°F or 2300°F, depending on the application.

Methods for calculating the various parameters of a loaded induction heating coil may be conveniently subdivided into accurate and approximate techniques. The former include the finite-element numerical method, simulation and the method of induced e.m.f,[48] all of which require computer solutions. The latter[44,49,50] are based on separate determination of the impedances of the workpiece and of the coil, with subsequent approximate considerations of the final dimensions of the system elements and their mutual arrangement.

Figure 2.1a shows a typical induction heating load, where the coil and the workpiece are uniform and of equal length. Due to skin effect, the currents in Figure 2.1b are concentrated near the internal surface of the induction coil and the external shell of the workpiece.

The sum of the three component fluxes of Figure 2.1a (i.e. the air gap flux ϕ_g, the workpiece flux ϕ_m, and the coil flux ϕ_c) gives the total flux linking the coil ϕ_o. The reactances due to these fluxes (X_g, X_m and X_c respectively) are as shown in the equivalent circuit diagram of Figure 2.2, together with the coil resistance R_c and the reflected workpiece resistance R_m. In high-frequency applications, the air gap component of the coil reactance X_g represents the largest numerical factor, because the coupling between the coil and the workpiece is far from ideal and a large quantity of flux is wasted. In a melting furnace, the charge is normally covered with a rammed refractory lining to withstand high temperatures, the thickness of the lining being of the order of a few centimetres and designed to prevent excessive heat losses to the coil. This wasted flux draws a very large reactive power from the source, and results in a low coil power factor of the order of 0.1 to 0.2 lagging. On the other hand, in high frequency applications the reactance X_c is often small in comparison with the total reactance X_o, when it may conveniently be neglected. Considering the equivalent circuit of Figure 2.2, the coil power factor PF_c, and the coil efficiency η_c are respectively given by

$$PF_c = \frac{R_o}{Z_o} \qquad (2.1)$$

and $$\eta_c = \frac{R_m}{R_o} \qquad (2.2)$$

Naturally, the flux paths in different types of loads - with a short coil or a short workpiece load - may differ, but nevertheless the approximate equivalent circuits can still be reduced to the form of series resistance and reactance.[49] Expressions for R_o and X_o for different applications are derived in many publications.[44,49,50] Although different approximate methods are employed, the expressions for R_o and X_o are found to have the following common form:

$$R_o \cong \frac{\pi\, d_m}{\ell}\; N^2 \sqrt{\frac{\rho_m\, \mu_o}{2}}\; [\sqrt{\mu_{mr}} + \sqrt{\rho_c/\rho_m}]\; \sqrt{w_o} \qquad (2.3)$$

$$X_o \cong \mu_o \frac{\pi\, d_m}{\ell}\; g\, N^2\; [1 + \frac{\mu_{mr}}{2}\; \frac{\delta_m}{g} + \frac{1}{2}\; \frac{\delta_c}{g}\;]\; w_o \qquad (2.4)$$

As equations (2.3) and (2.4) suggest, the most important variables in the load parameters include the magnetic permeability μ, the resistivity of the workpiece ρ_m, the coil material ρ_c, and the operational frequency w_o.[51]

Resistivity: For all metals the resistivity increases with temperature. Although for pure metals the increase is linear up to the melting point, the alloys exhibit non-linearities due to the individual properties of the constituents. Figure 2.3 shows that the resistivity of various types of steel changes in excess of 4 times in the temperature range 200° - 1400°C. As the equation[51]

$$\delta = \sqrt{\frac{2\rho}{w_o \mu}} \qquad (2.5)$$

suggests, this increase in resistivity results in an increase in the skin (penetration) depth, δ.

Permeability: For all practical purposes, the relative permeability of non-magnetic materials may be taken as constant and equal to unity. However, the permeability of magnetic materials is a function of both the magnetic field strength H, and the temperature, T. As shown in Figure 2.4, once the material is saturated any further increase in H causes a considerable fall in the value of μ_r. However, a much more significant effect is that materials which are magnetic at room temperature, with a high value of μ_r, become non-magnetic with their relative permeability reverting to unity, at a temperature corresponding to the Curie point. The temperature at which this occurs varies widely from material to material.

Frequency: The depth of current penetration in the workpiece is proportional to $1/\sqrt{w_o}$, with the source frequency being selected in accordance with the nature of the application (i.e. low frequencies for heating and melting purposes-high frequencies for surface hardening etc). It is an important factor in determining the coupling between the coil and the workpiece, and significantly affects the coil power factor. In most applications, the source frequency is varied manually or by a closed loop control, in order to maintain a maximum load power factor despite the adverse effects of varying R_o and X_o. As will be made clear later, w_o varies with $1/\sqrt{L_o}$ in such systems.

The functional dependence of the important characteristics of a loaded induction heating may thus be summarised by

$$\rho(T)$$

$$\mu_r\ (H,T)$$

$$Z_o\ (R_o,\ X_o) \quad \text{or} \quad Z_o(\rho,\ \mu_r,\ w_o,\ H,\ T,\ G)$$

Since the magnetic field strength is a function of the coil current, i_{Lo},

$$H\ (i_{Lo})$$

On the other hand, the static inverter is a load sensitive source, therefore

$$i_{Lo}\ (Z_o,\ w_o)$$

while for a high output power factor

$$w_o \alpha \frac{1}{\sqrt{L_o}}$$

The above relations are further complicated by their dependence on the geometrical arrangement factor G, which, for many cases, is indeterminate and varies significantly as the heating cycle progresses (e.g. in the case of scrap metal melting). Moreover, in most static power sources the relation i_{Lo} (Z_o), is not a simple analytical function but may involve considerable numerical complexity.

2.2 Compensated Load Equivalent Circuit

The low power factor of an induction heating load poses important application problems, such as the need for a power source of increased VA capacity, together with higher running costs. It is therefore common practice to supply all the reactive component of the load current from capacitors, generally connected in parallel with the work coil,as shown in Figure 2.5, so that the power source supplies mainly the power component of the load current.

A further advantage of using a power factor compensating capacitor C_o is that, due to the high selectivity of the tank load, the load voltage becomes closely sinusoidal at the fundamental frequency of the source. The higher harmonic currents

flow predominantly through the capacitor, providing a negligible contribution to the total voltage. This parallel tuning is also beneficial in reducing an error introduced into the equivalent load circuit of Figure 2.2, when the source contains distortion frequencies. Since both the resistance R_o and the inductance L_o reflected from the coil are frequency dependent, the equivalent load circuit is applicable only at the operational frequency, and calculations assuming that the distortion frequencies flow through the coil will clearly be inaccurate. By providing a low impedance path for these harmonics through the compensating capacitor this inaccuracy is substantially reduced.

The impedance of the tank load to a sine wave of angular frequencyw_o is:

$$Z_{Ln} = \frac{R_o Q_L}{(1 - m^2)^2 Q_L^2 + m^2} [Q_L - j(m Q_L^2 (1 - m^2) - m)] \quad (2.6)$$

where: $m = w_d / w_n$, and if the coil power factor is from 0.1 - 0.2 lagging the corresponding range for the selectivity Q_L is approximately from 5-10. For this range, the resonant frequency of the load ω_n is approximately $1/\sqrt{L_o C_o}$.

Maximum output power is delivered to the load when the tank load circuit is tuned to the source frequency - i.e. $w_o = w_n$ For this case the tank load may be approximately represented by an equivalent resistance R_{eq}, where:

$$R_{eq} = R_o Q_L^2 = \frac{L_o}{R_o C_o} \qquad (2.7)$$

if the source waveform has a low harmonic content.

Due to the high selectivity of the tank load, the output power obviously depends critically on the source frequency (see Figure 2.6). Any variations in the resonant frequency of the tank circuit, due to variations in L_o as the heating cycle progresses, result in a significant change in the output power. As previously mentioned, this is overcome, in applications employing static power sources, by causing the source frequency to trace the varying load resonant frequency, so that $\omega_o \alpha 1/\sqrt{L_o}$ approximately. On the other hand, in some inverters this relation is utilised to control the output power.[1]

2.3 Effect of an Output Transformer on the Equivalent Load Circuit

In practice, load matching may require an output transformer (which may also serve to isolate the work coil where there is no input isolation) and which should be included in the equivalent load circuit. Figure 2.7a shows the equivalent circuit of a common output arrangement with a tuning capacitor in the secondary circuit of the transformer. To a first approximation, the components representing the core losses and the

magnetising flux of the transformer may be neglected, and since the leakage inductance is generally at least 10 times the equivalent series resistance of the windings, the equivalent output circuit reduces to the form of Figure 2.7b.[5] Due to better coupling between their primary and secondary windings, auto-transformers have lower leakage inductances than isolating transformers. Thus the minimum practical leakage inductance for a toroidal auto-transformer (e.g. 800V, 525A rating) is 2 μH (at around 1 kHz) and about 7-10 μH for a toroidal isolation type.[5] For the sake of simplicity in the circuit analysis and design of a series inverter, this leakage inductance may be considered as a part of the series commutating inductor.

2.4 Evaluation of Load Characteristics

2.4.1 Load behaviour in typical applications

For the purpose of simplification, induction heating applications may be divided into three broad groups; continuous heating, static heating, and melting.

In continuous heating applications, the load presented to the power source is relatively stable and, as in billet heating, once the equipment is started it produces parts continuously throughout the daily work schedule. If the size or production rate requires adjustment to meet operational requirements, some

changes in tuning may be necessary, but once the equipment has been restarted, the characteristics of the load are again stable. In continuous heating applications, the load is therefore relatively simple to analyse, as it presents a constant impedance to the inverter at all times.[52]

Most static heating applications involve heating of magnetic materials, usually carbon steels, to beyond the Curie temperature. Although the load characteristics throughout the work cycle are well-defined, their variation is wide and presents a difficult task to the inverter designer.

Melting loads present an even more widely varying load condition, for either a magnetic or a non-magnetic charge. The nature of the initial charge (whether light or heavy scrap) and how it is positioned in the furnace both have a strong influence on the load characteristics in the early stages of the melt cycle. Although once the material is molten,the coil characteristics can be precisely defined, this considerable variation in load conditions makes the melting furnace the most difficult load of all to analyse. Possible differences in the make up of the charge and the charge density, and in any accompanying ranges of resistivity and permeability etc. must also be considered when defining the maximum limits of the load variation.

2.4.2 Approximate estimation of load variations

Although there are a number of publications which discuss the evaluation of the equivalent circuit for an induction heating load, none appears to investigate the way in which the dynamic load characteristic varies during the heating cycle. Some effort has therefore been made in this direction, as follows.

On introducing the penetration depth δ, equations (2.3) and (2.4) may be rewritten:

$$R_o = K_1 \left[\frac{\rho_m}{\delta_m} + \frac{\rho_c}{\delta_c}\right] \qquad (2.8)$$

and $$L_o = K_2 \left[1 + \frac{\mu_{mr}\,\delta_m}{2g} + \frac{1}{2}\,\frac{\delta_c}{g}\right] \qquad (2.9)$$

where $K_1 = \pi d_m N^2/\ell$ and $K_2 = \mu_o \pi d_m q N^2/\ell$

respectively, and despite the complexity of the parameter interaction involved, these equations may be utilised to obtain a first approximation to some typical load characteristics.

It might be anticipated that since the relative permeability of some magnetic materials drops sharply, from several hundreds to unity, after the transition at the Curie temperature, significant changes in L_o will occur. However, as empirical evidence shows, the variation in L_o is in fact relatively small. This apparent abnormality arises primarily because the work coil mmf is always sufficiently high[53] to saturate the (magnetic) workpiece for at least 4/5 of the magnetisation cycle, so that the actual relative

permeability is considerably smaller than the maximum possible cycle. In a method suggested for calculating μ_r during heating,[53] it is shown that μ_r usually lies between 20 and 40 for through-heating applications, and may even approach unity at the very high field intensities used for surface hardening. Another reason for the small variation in L_o is the low ratio of the penetration depth in the workpiece to the air gap. For the case of a 1 kHz melting furnace the following values are typical[44,54]

$$\frac{\delta_m}{g} \simeq \left(\frac{1}{10} \cdot\cdot \frac{1}{12}\right) \text{ and } \frac{\delta_c}{g} \simeq \left(\frac{1}{40} \cdot\cdot\cdot \frac{1}{45}\right) \qquad (2.10)$$

and these become even smaller with increasing frequency. Based on these typical values, the average value for L_o before the Curie temperature may be obtained from equation (2.9) as

$$L_o \simeq 2.4\ K_2 \qquad (2.11)$$

Assuming that δ_m is increased five fold[33] after the transition at the Curie temperature, but that the factor K_2 (which includes parameters such as the geometrical factor) remain unchanged, the value of L_o after the Curie temperature becomes L_o', where

$$L_o' \simeq 1.2\ K_2 \qquad (2.12)$$

indicating a relatively small variation of $L_o/L_o' \simeq 2.0$.

Assuming further that the work coil has a high efficiency, the term ρ_c/δ_c in equation (2.8) may be neglected; and by substituting the values of ρ_m and δ_m given above it can be shown that the relationship between the reflected load resistance above and below the Curie temperature is

$$R_o' \simeq \frac{R_o}{2.5} \tag{2.13}$$

In static heating applications, the field intensities are generally higher than those in melting applications, which results in a lower value for μ_r. Assuming μ_r between 10-20, and using the remaining coil parameters as above, it follows that the average variation in L_o in a static heating application is even smaller, being about $L_o/L_o' \simeq 1.4$. The relatively small change in the ratio of the reflected coil reactances between static heating and melting applications results mainly from a neglect of the change in the load geometry during heating, which is an extremely important factor in some melting applications.

Because of the considerable simplifications and approximations made in considering the ranges of variation of R_o and L_o, various empirical results documented for similar applications are investigated next.

2.4.3 Data on load variations in typical applications

Numerical data giving actual values for R_o and L_o is available in only a few publications.[52,55] Nevertheless, using some of that presented for thyristor inverter fed induction heating applications, a typical range of variation of L_o may be predicted.

The following information is presented in relation to magnetic material melting applications:

Power Source	Load Material	Output Frequency Range (Hz)	$\frac{w_o}{w'_o}$	$\frac{L_o}{L'_o}$	Ref.
100 kW Thyristor inverter	Steel	700 - 800	0.82	1.47	3
	Steel	2650 - 3000	0.86	1.33	33
100 kW Thyristor inverter	Ferrous charge	2700 - 3000	0.9	1.21	1
25 kW Thyristor inverter	Cast Iron	2700 - 3300	0.81	1.49	10
750 kW Thyristor inverter	Ferrous charge	800 - 1000	0.76	1.56	56

Assuming a tuned load and a high load selectivity for all cases, the ratio L_o/L'_o is obtained from the relationship $w_o^2 \alpha 1/L_o$. The variations of X_{Lo} and R_o with heating time in a static heating, bar end heating application is given in Figure 2.8.[52] The figure also illustrates an additional feature of the variable

frequency drive in reducing load impedance variations, since X_{Lo} is proportional to $\sqrt{L_o}$ instead of L_o, as in a fixed frequency drive. From Figure 2.7, the following information can be obtained,

	Start (base)	Peak (p.u)	End (p.u)	Max/Min
L_o	1.0	1.23	0.87	1.41
R_o	1.0	1.8	0.70	2.57

As an example of a typical static heating application, the following values of L_o and R_o are suggested,[55] for carbon steel raised through the Curie temperature, by a 3 kHz thyristor inverter,

	Start (base)	Peak (p.u)	End (p.u)	Max/Min
L_o	1.0	1.24	0.94	1.32
R_o	1.0	2.3	0.71	3.2

This section could be further extended with similar application information.[42,57] However, as the data presented are broadly in agreement, and tend to confirm the approximate theoretical estimates of the previous section, it will suffice to derive some general conclusions concerning the dynamic characteristics of an induction heating load.

2.4.4 Dynamic load equivalent circuit

Based on the content of sections 2.4.2 and 2.4.3, the general characteristics of induction heating loads may be summarised as:

i) In continuous heating applications, the load may be assumed stable, so that a constant frequency power source can be used. For such loads, power source selection, optimisation and design pose relatively easy tasks.

ii) In static heating applications the load varies considerably, but the variations can nevertheless be predicted. By combining the application data and the results of the approximate estimation, the dynamic load characteristics of a typical application may be assumed to be as in Figure 2.9, where the maximum variations in the equivalent load inductance and resistance with heating time are approximately 35% and 320% respectively. The practical data examined earlier indicates that these ranges can be safely assumed for applications with operational frequencies between approximately 700-5000 Hz, and with reasonable coil selectivities, i.e. $5<Q_L<15$. Since most static power sources produce optimum performance at only a fixed condition of operation, the varying load conditions of static heating applications may cause some deterioration of the source performance. Nevertheless, with careful design of the power source, such adverse effects may be kept to a minimum.

iii) In melting applications, the load variations are substantial and in most cases cannot easily be predicted. Although the application data quoted suggests that the load changes in induction melting are close to those in static heating, this cannot be generalised. This resemblance arises mainly because the available data of induction melting are obtained for applications with well behaved loads - i.e. the load is homogeneous and changes in the geometrical factor G with melting are small. In general, however, when designing power sources for melting applications (which may include scrap metal melting etc) a considerably larger load variation margin should be assumed to ensure the reliability of the operation, though the price paid for this is usually a deterioration in the inverter performance. Some compensation for this can nevertheless be achieved by using step-wise load matching via a multi-tap work coil or an output transformer.

2.5 Conclusion

As the dynamic load equivalent circuit for induction heating applications is not available, an attempt has been made to develop a simple, approximate equivalent circuit. In so doing, complex theoretical analysis has been avoided, although some theoretical consideration has been given to the various parameters involved, and to their inter-relation and variation throughout the heating cycle. Despite the number of simplifying assumptions involved, the formulae adopted for the equivalent load circuit components yield a reasonable estimate of their load variations.

However, the actual plots of load impedance variation for a typical application, where the load is heated through the Curie temperature, is developed empirically by studying the application data available.

In the following chapters, the performances of the power sources studied are optimised in accordance with the load models provided in this chapter.

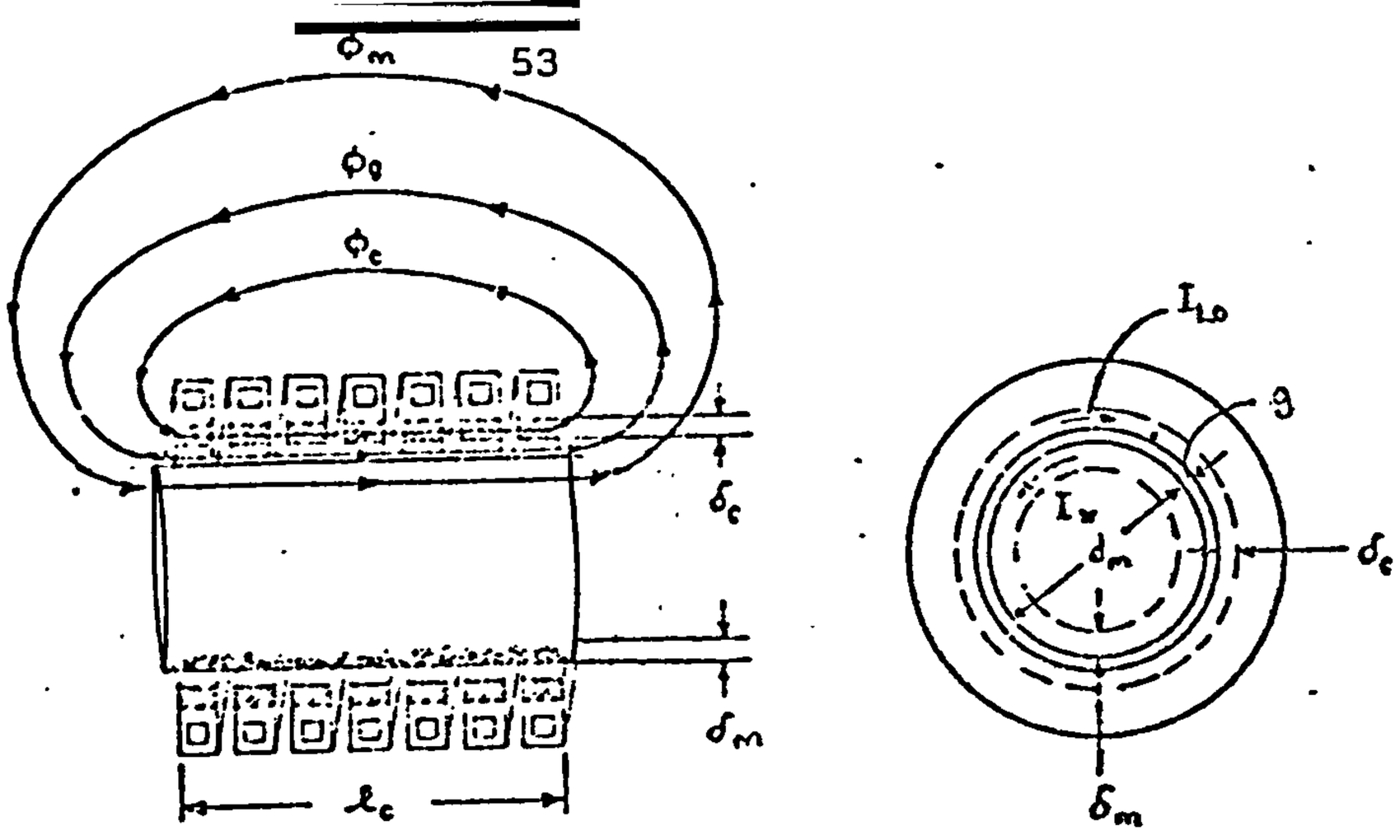

(a) (b)

Figure 2.1 A typical induction heating load

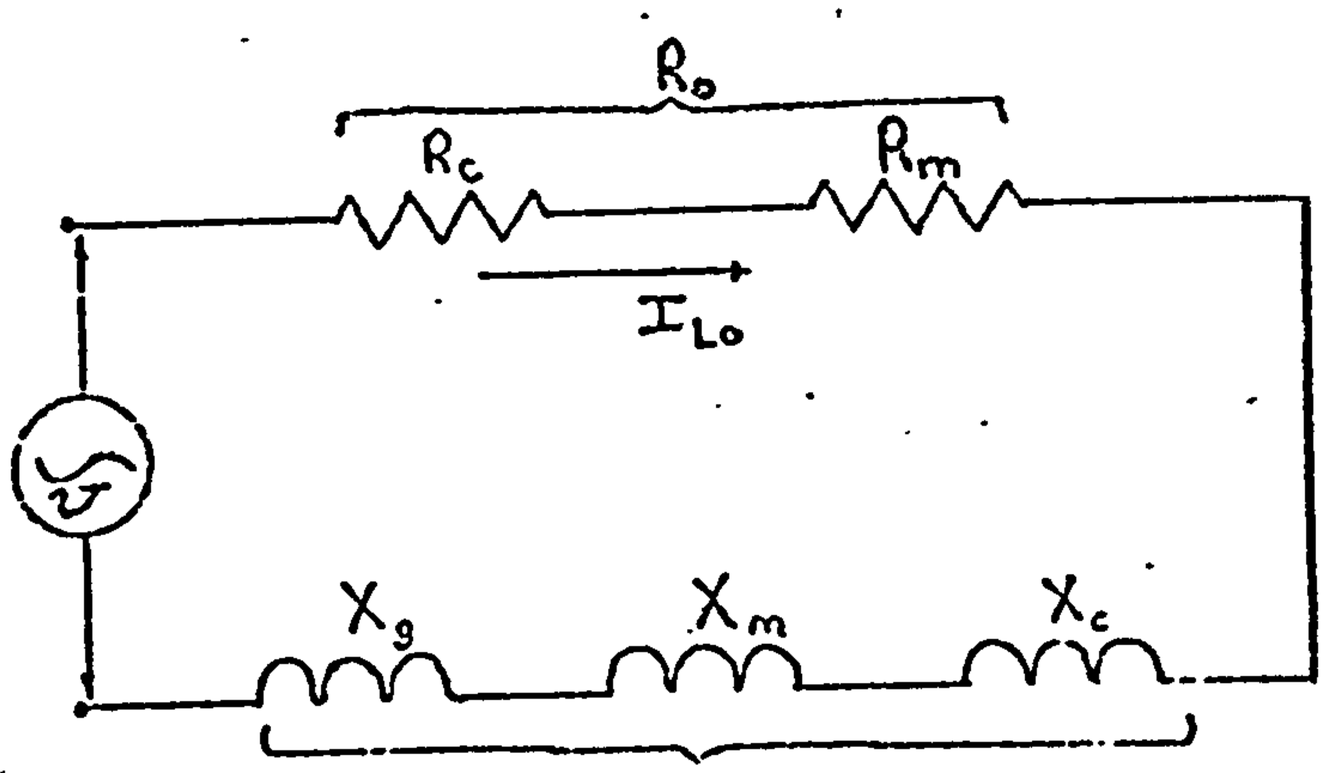

Figure 2.2 Equivalent circuit to a induction heating load

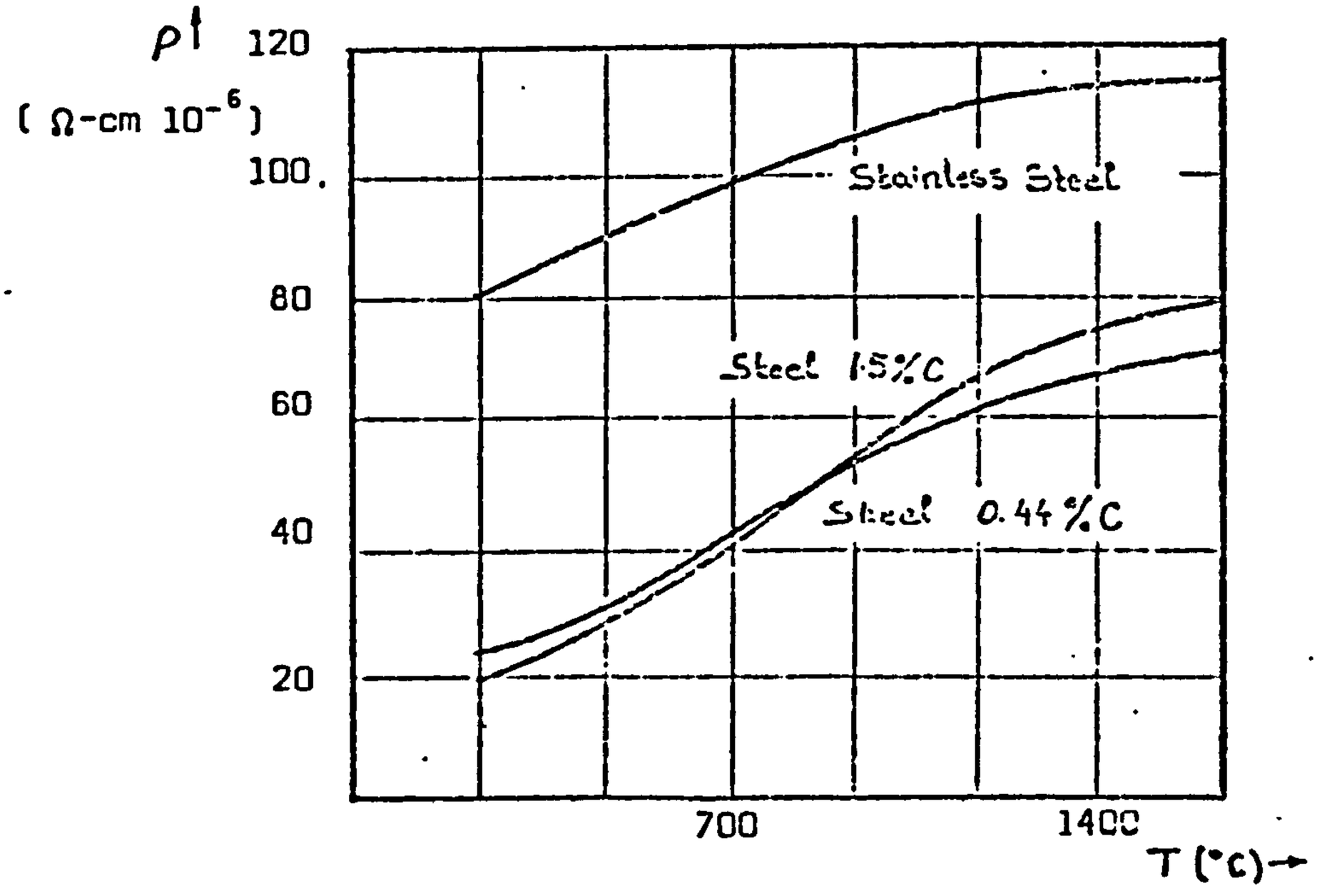

Figure 2.3 Variation of resistivity with temperature

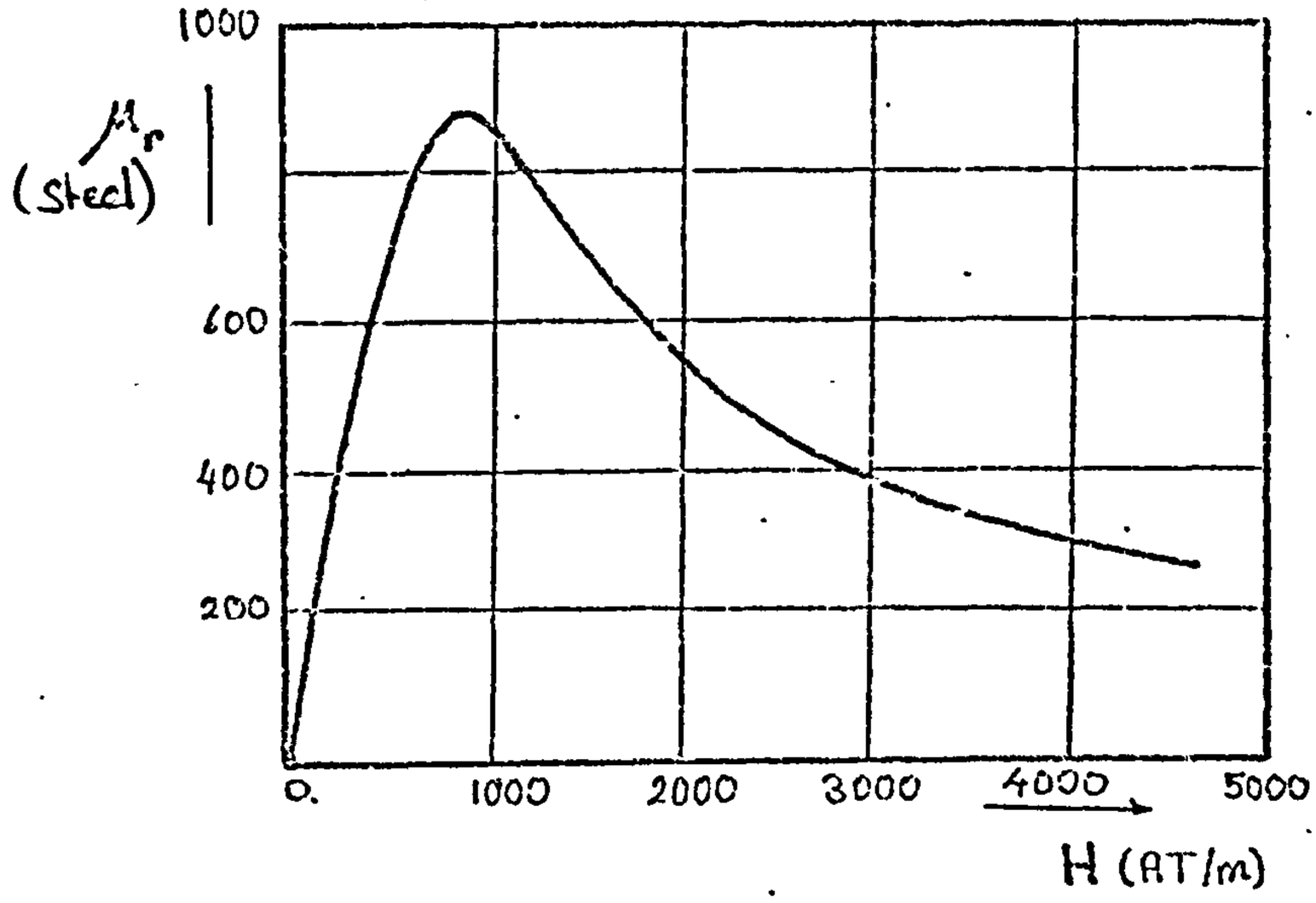

Figure 2.4 Variation of the relative permeability with field strength

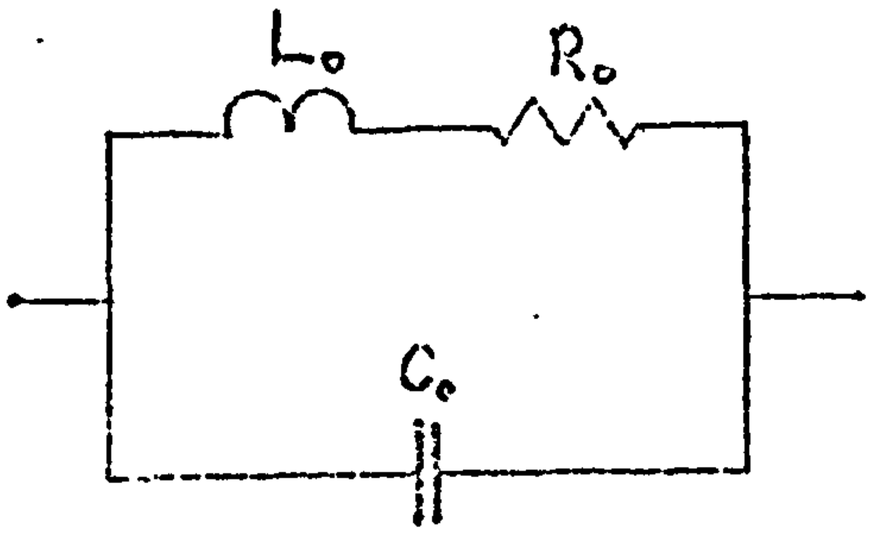

$$w_n \simeq \frac{1}{\sqrt{L_o C_o}}$$

$$Q_L = \frac{1}{R_o}\sqrt{\frac{L_o}{C_o}}$$

$$R_{eq} = \frac{L_o}{R_o C_o}$$

Figure 2.5 Compensated induction heating load

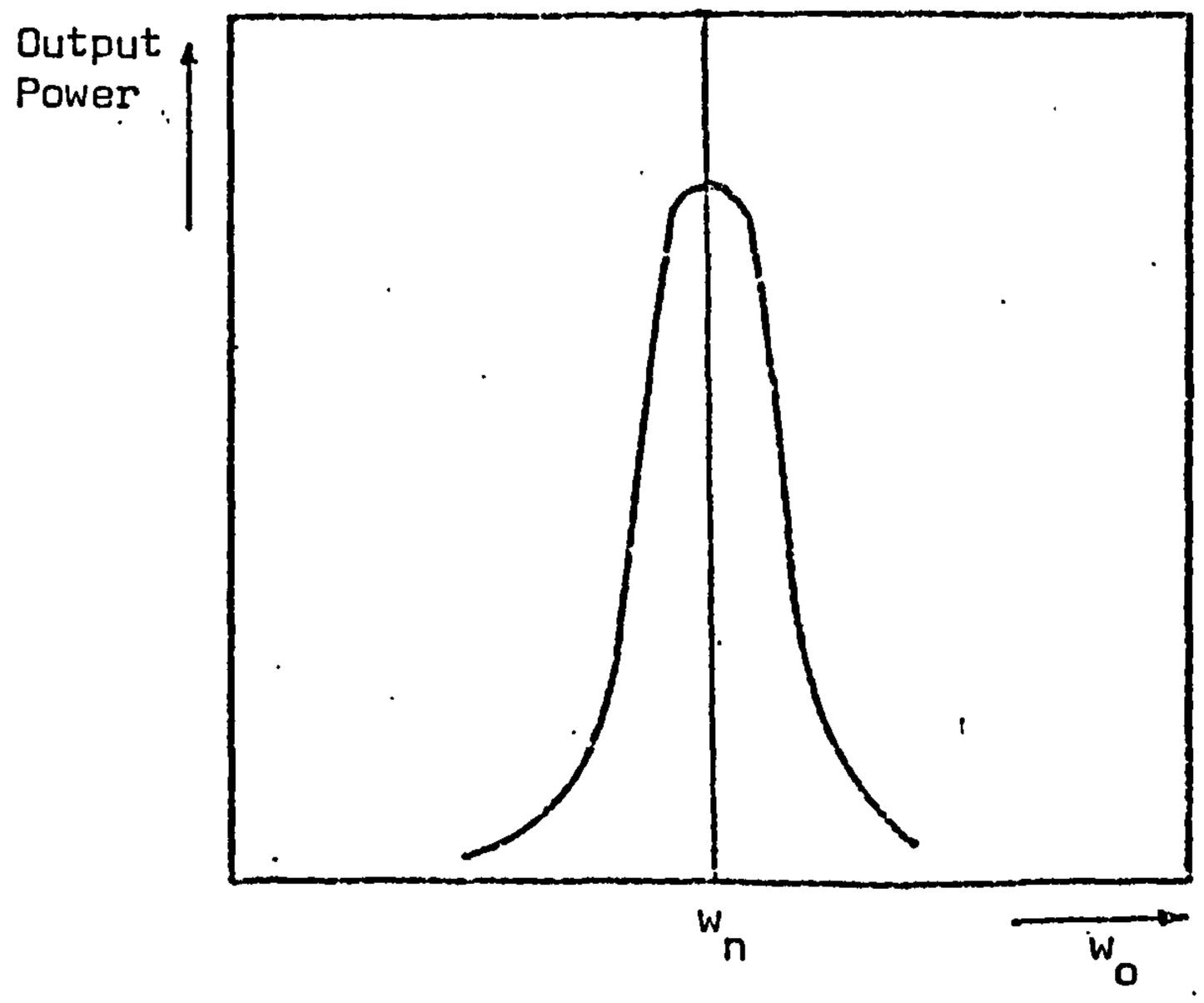

Figure 2.6 Load characteristics of a compensated load

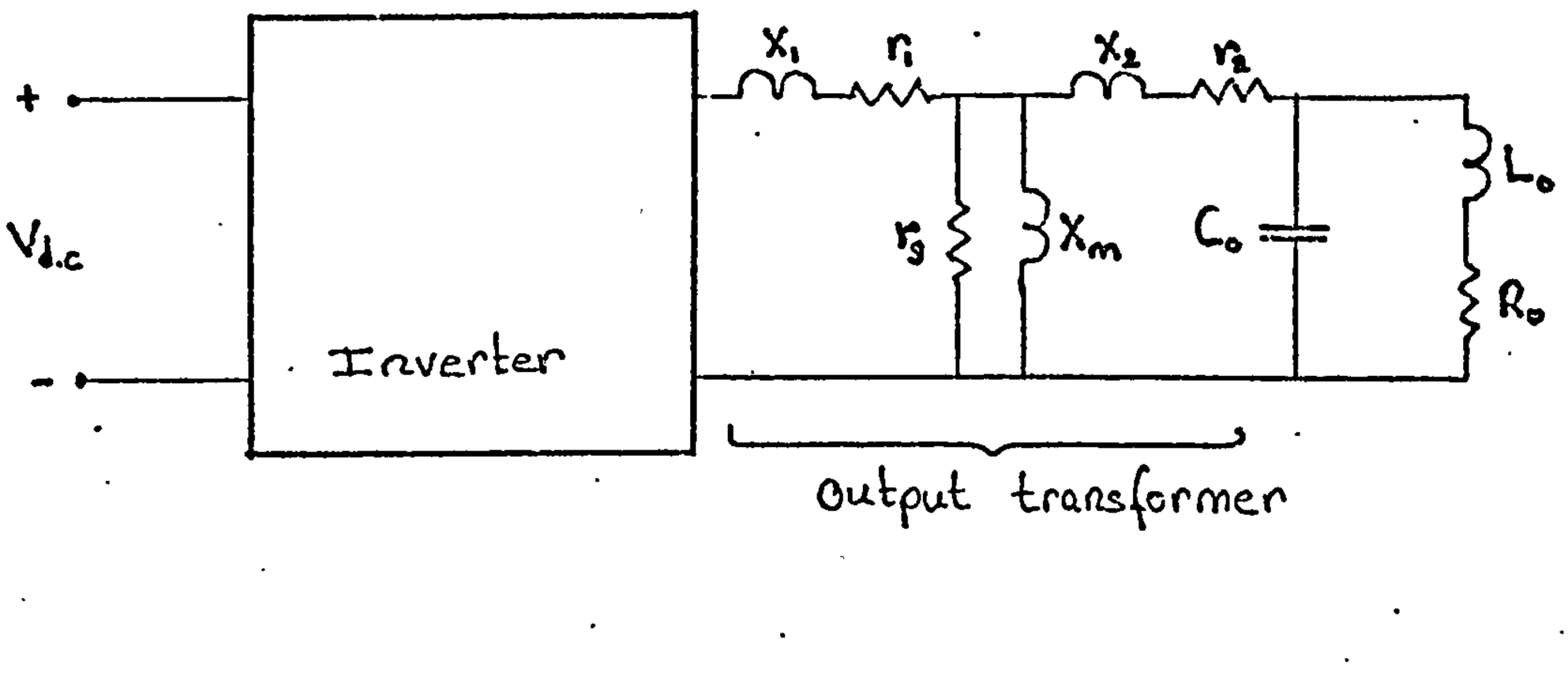

(a)

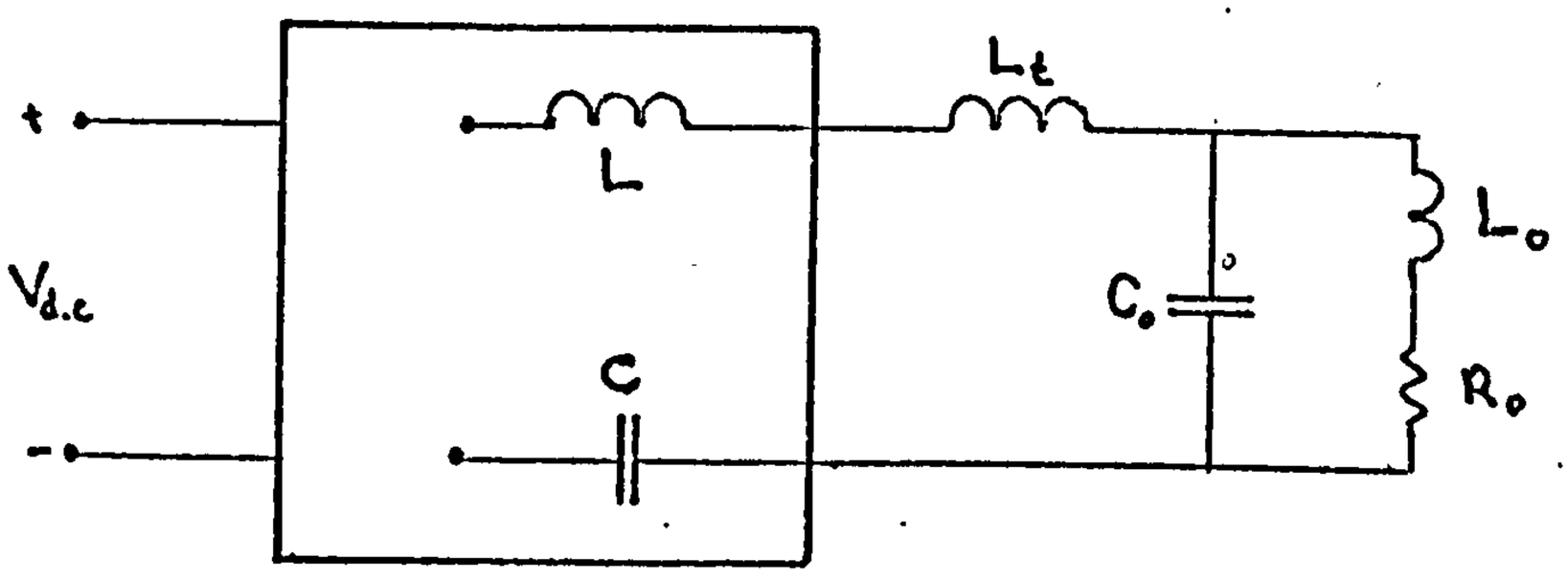

(b)

Figure 2.7 (a) Equivalent circuit of a transformer coupled induction heating load

(b) Simplified output circuit (L, C - commutating components; L_t - equivalent leakage transformer inductor)

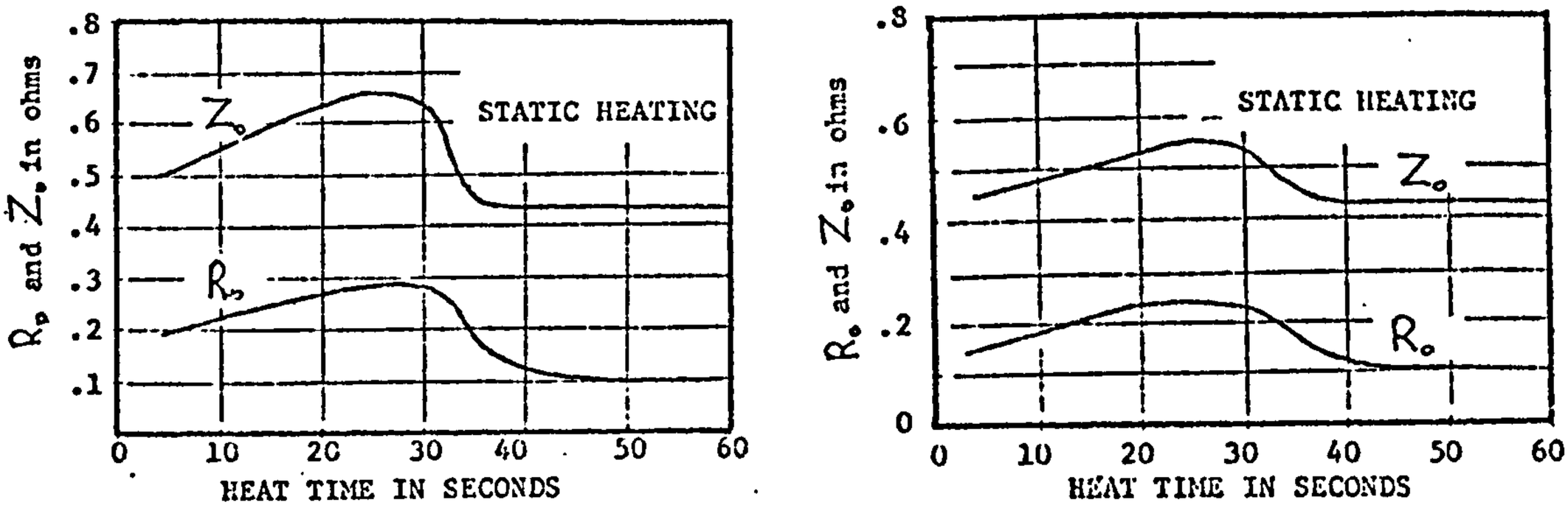

Figure 2.8 Load characteristics during heating cycle with

a) fixed source frequency
b) variable source frequency

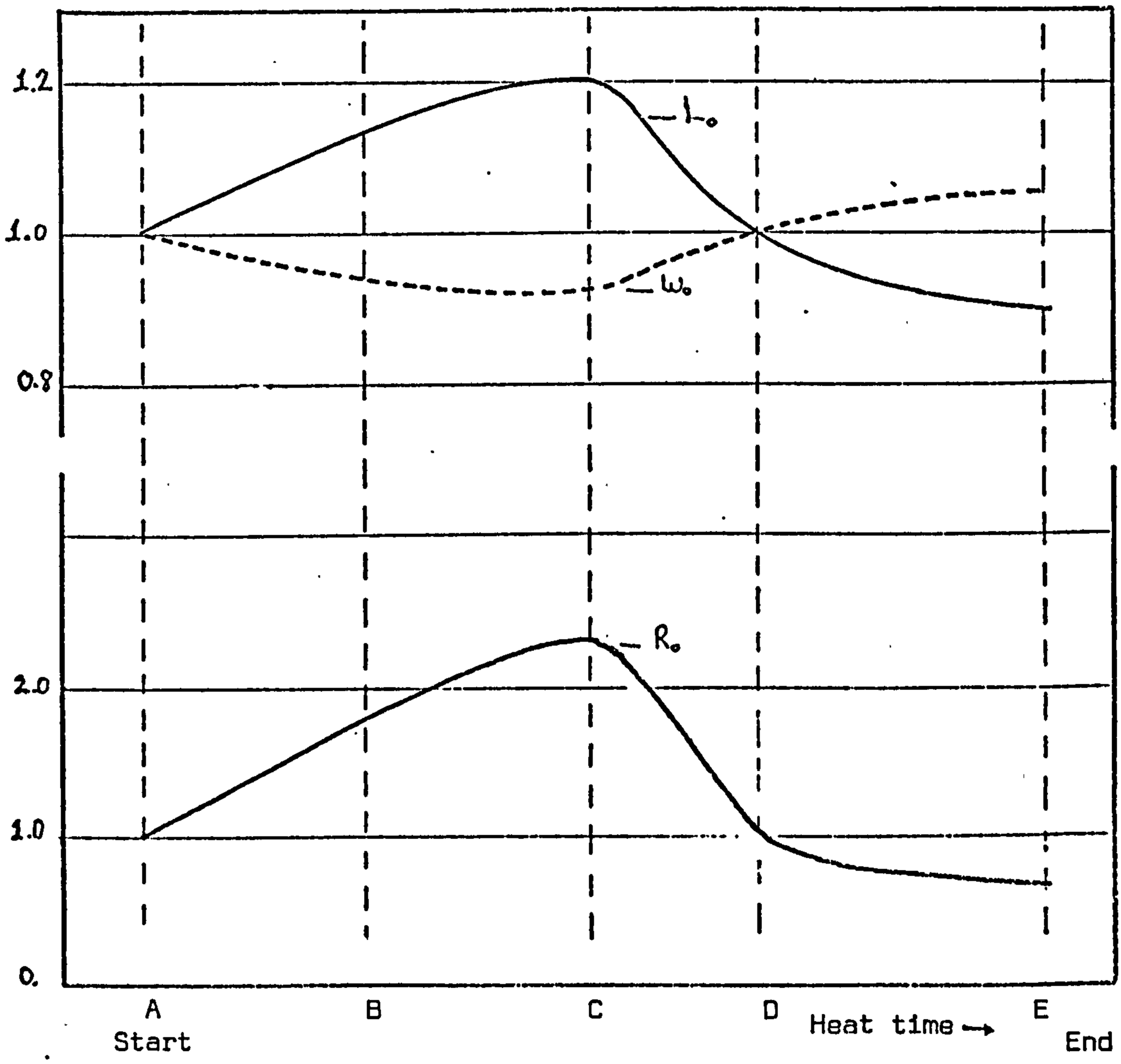

Figure 2.9 Variation of the load characteristics of a typical static heating application during a heating cycle.relative coil resistance, R_o and inductance, L_o.

CHAPTER 3

THE ANALYSIS OPTIMISATION OF THE PERFORMANCE OF THE SINE-WAVE INVERTER AS APPLIED TO INDUCTION HEATING

This chapter investigates the performance of the sine-wave inverter as applied to high frequency induction heating. The sine-wave inverter is particularly suited to induction heating as it overcomes some of the problems encountered in a series inverter, without losing its advantages of good output waveform, low switching losses and reliable operation.

Owing to the desirable characteristics at high-operational frequencies, the sine-wave inverter is gaining increasing acceptance for various applications, besides those of induction heating and melting. Important among these are the inverter stage of dc-to-dc power converters for sophisticated space[34,57,58] and submegawatt power applications[31,34,58]. As a result of this growing interest, the analysis of the sine-wave inverter is now reasonably well documented,[31,34,57-73] although this literature does not appear to include a thorough study of its performance with an induction heating load, particularly when it is used to drive a parallel-compensated heating coil. The need for the following treatment is further justified, as in all high-power applications the optimisation of the inverter performance in accordance with the particular requirements of the job poses an important problem which has received only scant previous consideration.

In the following sections of this chapter, the sine-wave inverter when supplying a parallel-compensated load (Figure 3.1) is analysed in both the frequency and the time domain, with the later analysis performed by establishing a digital simulation of the inverter. The analyses are then used to investigate the variation of the inverter performance parameters (i.e. input power factor, thyristor derating, etc.) with design variables and varying load conditions, in order to obtain a design criteria that produces an optimum inverter performance during a complete cycle of operation. To perform this task, in an efficient and systematic manner, a procedure for the optimisation of the inverter performance for a given induction heating is established, on the basis of the general guidelines described in Section 1.3, and a computer program which executes some important steps of this procedure is suggested. The application of the optimisation procedure by making use of this program is subsequently demonstrated for a static heating application. Some application aspects of the sine-wave inverter are briefly considered in Appendix 2.

Before proceeding further, the following brief discussion on some selected literature may be found useful.

3.1 Discussion of Selected Literature on the Sine-Wave Inverter

In general, inverters that supply only leading power factor loads do not require special commutation means. Where filters

are used to ensure the load presents a leading power factor, these can be used as the commutating circuit, and the use of a complex output filter can provide additional advantages. Thus, in reference (73), the output circuit of the sine-wave bridge inverter is treated as a complex filter, and it is shown that a 4-element filter (Figure 3.2) has the minimum number of elements needed to approach the desired characteristics of load-independent transfer functions at the fundamental frequency, a capacitive input impedance and sufficient harmonic attenuation. However, examination of the results presented suggests that the inverter design by making use of filter synthesis is more useful if accompanied by considerations of other inverter parameters (i.e. thyristor derating, input p.f. etc) and the important operational aspects of a particular application. Otherwise, as in reference (73), the price paid for these desirable characteristics may be too high (high component rating, low input p.f. etc). On the other hand, the achievement of load insensitivity at the fundamental frequency may not in itself be a sufficient advantage in applications such as induction heating, where the output frequency is subject to change.

In the bridge inverter, a good output regulation may also be achieved without any additional circuitry[65,68], by over-compensating the load at all times and increasing the ratio of the damped resonant frequency w_r of the output circuit to the firing frequency, w_o . For this purpose, it is suggested that $w_r = 1.35\, w_o$ produces the lowest distortion in the load voltage

waveform. However due to the highly distorted (and indeed discontinuous) output current waveform caused by the high w_r/w_o ratio, the inverter efficiency drops significantly.and the component rating increases by about 50%.

Many recent publications[62,63] on the sine-wave inverter have been devoted to investigations of the performance of the inverter with a series tuned load (in the form of Figure 1.12). However, as mentioned previously, such configurations have several important disadvantages; for example, the equivalent coil inductance is determined by the nature of the application, (coil shape, operational frequency, etc) and this may not necessarily correspond to the optimum commutating inductance in that particular application. A possibly more important consideration is that the highly reactive current,confined within the tank circuit in compensated load applications, now circulates through the inverter, causing a low input power factor and efficiency and high component ratings. It is therefore clear that these publications are of limited practical importance.

In predicting the steady-state characteristics of the sine-wave inverter, a harmonic analysis using a Fourier series expansion of the square output voltage waveform may be performed. In doing so it is necessary to include a sufficient number of harmonic components to achieve a reasonable accuracy, due to the Gibb's phenomenon and to the crucial importance of the output current waveform. An analysis, basically of this type is presen-

ted in reference* (74), although since only the fundamental component is considered, the resulting accuracy is low. The optimisation procedure outlined is also not entirely satisfactory, since the selection of the commutating components is based solely on design criteria such as the upper and lower limits of the working frequency range. An integral part of an optimisation procedure should be the variation of various performance parameters (input power factor, power component ratings, current distortion factor, etc.) with varying design values of commutating components and under varying load conditions, and this is completely omitted. Thus, instead of optimising the inverter performance, an inverter is designed to perform a given task.

In performing the analysis and optimising the performance of the sine-wave inverter in this chapter, the points mentioned above are given full consideration. Before proceeding with this analysis, a brief description of the operation of the inverter is presented.

---

* The only publication traced which treats the sine-wave inverter supplying a parallel-compensated load.

3.2 Principle of Operation

As already stated, successful commutation in a naturally commutated inverter requires the thyristor current to lead the output voltage at an angle determined by the turn-off time of the switching thyristor. During a design, the commutating inductor L and capacitor C are selected to over-compensate the output circuit throughout all operational conditions. The inverter output frequency is determined by the triggering frequency of the thyristors, which in practice is automatically controlled to follow the varying resonant frequency of the tank load.

As is well known, a complete cycle of inverter operation circuits of four modes, during which S1, D1, S2 and D2 conduct successively (see Figure 3.3). In some applications, for current limiting and power control purposes, the inverter operation may include another mode, during which none of the rectifiers conduct and only the load current within the tank circuit flows.

In a high-frequency sine-wave inverter, the turn-off time is a critical characteristic. For thyristors designed specifically for inverter applications, the need for good dynamic capability requires a full description of the minimum turn-off time under specified conditions of waveform and temperature. Wide deviations from the typical values may result in circuit failures. In the sine-wave inverter, the use of feedback diodes is a disadvantage from the standpoint of the thyristor turn-off time.

By limiting the reverse voltage of the thyristor to the forward diode voltage, it produces the adverse effect of increasing the minimum thyristor turn-off time, with a decreasing reverse voltage available for turn off. Other parameters which significantly affect the turn-off time, and demand consideration in optimisation and design, are the peak forward current and the rate of reapplication of forward blocking voltage, and an increase in either of these will cause an increased turn off time[75]. In any prospective design, an unnecessarily high peak forward current may be avoided by keeping the ratio

$$\frac{\text{peak output current, } I_{Lp}}{\text{r.m.s. fundamental output current, } I_{L1}}$$

as small as possible. On the other hand, the adverse effect of the intrinsically high rate of rise of forward blocking voltage may be substantially reduced, by modifying the basic circuit as in Figure 3.4a. However, the penalty paid for this improvement is an increase in the thyristor voltage rating, from E to v_{c1}. By further modifying the circuit, as shown in Figure 3.4b, a higher reverse voltage for turn-off may be obtained, although this is applicable only if the inverter is designed to cause the incoming thyristor to fire before the current in the conducting diode reaches its maximum value. Otherwise the introduction of an inductance within the diode-thyristor loop undesirably shortens the circuit turn-off time. The steady-state thyristor voltages corresponding to the

modifications of Figures 3.4a and 3.4b are computed in a digital simulation program presented in the following section and shown in Figures 3.5b and 3.5c respectively.

However, in future sine-wave inverter applications the modifications described above may not be required. Recent developments[76] in thyristor and diode technology have aimed to exploit the anti-parallel thyristor-diode combination of a high-frequency sine-wave inverter in a positive manner. Thyristor and free-wheeling diodes both contain stored charge at the end of the conduction interval, and the way in which this is recovered critically affects the performance of high-speed circuits. The development mentioned is an optimisation of the reverse recovery characteristic of both the thyristor and its companion rectifier, to eliminate the need for the dv/dt or di/dt limiting components (such as shunt RC-snubbers or series reactors), and simultaneously to achieve a low minimum thyristor turn-off time.

3.3 Theory of Operation

3.3.1 Steady-state harmonic analysis

In order to pursue a linear analysis of the steady-state operation, of the sine-wave inverter, the following assumptions are made:

1. The thyristors and diodes switch state instantaneously, with zero voltage drop during conduction and no reverse current.

2. The power circuit components are ideal.

3. The inverter output voltage v_{oa} may be represented by the Fourier series expansion of a square waveform, and a sufficiently close approximation to steady-state conditions is obtained from the first 7 harmonics of this series.

4. The output frequency is tuned to the resonant frequency of the tank load circuit.

The harmonic equivalent circuit of the inverter is shown in Figure 3.6. The driving voltage function v_{oa} is a square waveform with a peak-to-peak amplitude equal to the d.c. source E. The equivalent commutating capacitor, $C = 2C_1$, since the output current sees the equal commutating capacitances C_1 and C_2 of Figure 3.1 as if they are in parallel.

Based on assumption (3) above, the driving function has the form

$$v_{oa} = \frac{2E}{\pi} \left[\sin \omega_o t + \frac{1}{3} \sin 3\omega_o t + \frac{1}{5} \sin 5\omega_o t + \frac{1}{7} \sin 7\omega_o t\right] \qquad (3.1)$$

During steady-state conditions, a d.c. voltage equal to E/2 appears at the junction of C_1 and C_2. However, because it does not affect the output current waveform, it is omitted in the driving voltage equation above.

The impedance of the tank circuit at an angular frequency $n\omega_o$ may be expressed as:

$$Z_{Ln} = a_n + j\, b_n \qquad (3.2)$$

where a_n and b_n are defined in equation (2.6), and the total input impedance of the equivalent circuit at this frequency is:

$$Z_{In} = a_n + j\,(n\omega_o L - \frac{1}{n\omega_o C} + b_n) \qquad (3.3)$$

The r.m.s. value of the n^{th} harmonic of the output current, I_{Ln}, is therefore:

$$I_{Ln} = \frac{\sqrt{2}E}{n\pi} \frac{1}{|Z_{In}|} \Big/ - \tan [(n\omega_o L - \frac{1}{n\omega_o C} + b_n)/a_n] \qquad (3.4)$$

and the output current is:

$$i_L = \sum_{n=1,3,5,7} I_{Ln} \sin (n\omega_o t + \beta_n) \qquad (3.5)$$

where

$$\beta_n = - (n\omega_o L - \frac{1}{n\omega_o C} + b_n)/a_n$$

The n^{th} harmonic of the tank load voltage is:

$$v_{con} = \sqrt{2}\, V_{con} \sin (n\omega_o t + \phi_n) \qquad (3.6)$$

where: $V_{con} = |Z_{Ln}|\, I_{Ln}$

$$\phi_n = \beta_n + \tan^{-1} \frac{b_n}{a_n}$$

and the total load voltage is hence:

$$v_{co} = \sqrt{2} \sum_{n=1,3,5,7} V_{con} \sin (n\omega_o - \phi_n) \qquad (3.7)$$

As outlined above, a harmonic analysis provides a quite simple solution. However, its application is restricted to inverter operation in which the output current is continuous. For a more general and accurate analysis a transient analysis must be performed.

3.3.2 Transient analysis and digital simulation

A transient analysis is performed by solving the circuit differential equations, using either operational or numerical methods.

Operational methods may be applied in the form of the *Laplace* and *Inverse-Laplace* transformation techniques, or in the form of the *Heaviside* Method or its modification, the *Haiyashi*

Method. When employing these methods, the circuit equations are derived in the matrix form [I], [Z] = [V], and the determinant of the impedance matrix [Z] is evaluated to determine the roots of the denominator of the operational expression for the current. Finally, and with the help of the Heaviside expansion formula, the inverse Laplace transform of the current expression is determined to obtain its time domain solution.

When using numerical methods, the sets of circuit differential equations are first converted to the first-order form $y' = f(y)$, and the calculation is then pursued iteratively, with a step length selected according to the accuracy requirements. Various digital simulation algorithms based on numerical analysis methods, and developed specially for thyristor circuits, are presented in detail in Chapter 6.

A comparison of the operational and numerical techniques, indicates that an operational method has the advantages of providing solutions in analytical form and of requiring less computation time. However, much analytical effort is needed, and the approach is most suited to relatively simple circuit configurations. With the many standard subroutines now readily available, the application of numerical techniques is extremely simple, and since these operate iteratively, they offer the advantage of being more adaptive.

For the analysis of the sine-wave inverter, the operational method is preferred, to provide a fuller understanding of the

circuit with a considerable saving in computation time. The steps in the analysis are presented in detail in Appendix 1, where the steady-state equation for the output current is shown to be of the form:

$$i_L = 2\,(E\,e^{\alpha_1 t}\cos w_1 t - F\,e^{\alpha_1 t}\sin w_1 t + G\,e^{\alpha_2 t}\cos w_2 t$$

$$- H\,e^{\alpha_2 t}\sin w_2 t) \qquad 0 < t < \frac{T_o}{2} \qquad (3.8)$$

where: α_n and w_n are respectively the real and imaginary parts of the n^{th} root of the determinant of the impedance matrix, and the coefficients E, F, G and H are the Heaviside coefficients defined in Appendix 1.

Digital Simulation

The flow chart of a computer program developed for simulation of the inverter is given in Figure 3.7. As shown, the flow chart is reasonably self-explanatory and only some of the more important steps are described here.

In the program, identification of the incoming mode of the inverter operation is performed in the following manner:

Rectifier	Firing Pulse	Forward Voltage	Mode
S1	Present	$v_{c_1} - v_{co} > 0$	1
S2	Present	$v_{c_2} + v_{co} > 0$	3
D1	-	$v_{c_2} + v_{co} > E$	2
D2	-	$v_{c_2} + v_{co} < 0$	4
For all other cases			5

Once the mode of the operation is identified, the appropriate current expressions are determined, as described in Appendix 1.

The program includes a current-limiting facility for power control and over-current protection purposes. In operating this, the output current is continually checked, so that whenever it exceeds a preset limit, the firing pulse to the incoming thyristor is cancelled.

The program is also equipped with the following failure-warning facilities:

SYMPTOM	FAILURE
If $i_L > 0$ and duration of Mode 1 or 3 $> T_o/2$	Both S1 and S2 are simultaneously on
duration of Mode 2 or 4 $< TH_{off}$	Insufficient turn-off time

In the program, steady-state conditions are checked at the beginning of both Modes 1 and 3. Whenever the values of v_{c1}, i_L and v_{co} are detected as approximating to their corresponding values stored at the end of the previous steady-state check, within a specified error margin, the steady state is decided. With the complete analytical descriptions of the circuit quantities to hand, whichever output quantity is required may be readily calculated.

Some graphical results of the digital simulation for an inverter with design values of $X_{LB} = 1.4$ and $X_{CB} = 2.5$, and operating at 5 kHz, are shown in Figure 3.8.

3.3.3 Comparison of the results of the transient and harmonic analysis techniques

The steady-state output current waveforms, as provided by both the harmonic and the transient analysis methods are shown in Figure 3.9, and the agreement between the results is quite satisfactory. The small discrepancies are, of course, mainly due to neglect of output current harmonics higher than the seventh, and to errors in obtaining an accurate steady-state response from the digital simulation. Figure 3.9 indicates therefore that the results of the harmonic analysis are quite reliable for optimisation and design purposes. On the other hand, for a better accuracy and for investigation of the various modes of the inverter operation for which the harmonic analysis is inapplicable, the transient analysis is needed.

3.4 Performance Parameters

Output power

The useful output power developed is due to the fundamental output current, i.e.

$$P_o = I_{L1}^2 . R_{eq} \qquad (3.9)$$

In general, for any load or source:

$$PF = \frac{\text{total power}}{\text{total r.m.s. VA}}$$

Clearly, the harmonics of the output current increase the total apparent power delivered to the load. Taking this and the stiff voltage characteristic of the tuned load into account, the power factor expression may be modified as:

$$PF_o = \frac{V_{co_1} . I_{L_1} \cos\psi_1}{V_{co} I_L}$$

or since $V_{co_1} \simeq V_{co}$

$$PF_o = \cos\psi_1 . \frac{I_{L1}}{I_L} \qquad (3.10)$$

Conventionally, the ratio I_{L1}/I_L is defined as the current distortion factor and $\cos\psi_1$ as the displacement factor.

Hence output power factor = (output displacement factor)

x (output current distortion factor).

The current distortion factor is also an important practical parameter, since it provides a measure of the penalty of processing the charge through the inverter in the form of a current that does not contribute to the useful output power.

Input power factor

The input power of the inverter is the sum of the power associated with all the individual harmonics, i.e.

$$P_I = \sum V_{oan} I_{Ln} \cos \beta_n$$

Alternatively, since the inverter is assumed lossless:

$$P_I = \text{total output power } (P_{oT})$$

Input volt-ampere are

$$VA = E I_I$$

and since

$$I_I = \frac{I_L}{2}$$

the input power factor becomes:

$$PF_I = \frac{2\,P_{oT}}{E\,I_L}$$

However, since some of the output power is due to the higher harmonics, the expression for PF_I may be modified to the more useful form

$$PF_I = \frac{2\,P_o}{E\,I_L} \qquad (3.11)$$

Solid-state component derating

The solid-state component or rectifier derating DR required in a circuit is a measure of the utilisation efficiency of the devices (thyristors, diodes etc) in that particular configuration. The thyristor derating is defined[27] as

$$DS = \frac{\text{(Peak thyristor voltage)}\quad\text{(r.m.s. thyristor current)}}{\text{(useful output power)}}\quad\text{(No. of thyristors}$$

(3.12)

which may also be used for the diode derating.

The r.m.s. thyristor and diode currents may be calculated from

$$I_s = \sqrt{\frac{1}{T_o} \int_o^{t_c} \left[\sum_{n=1,3}^{7} i_{Ln}^2 \right] dt}$$

and

$$I_D = \sqrt{\frac{1}{T_o} \int_{t_c}^{\frac{T_o}{2}} \left[\sum_{n=1,3}^{7} i_{Ln}^2 \right] dt}$$

respectively, where t_c is the instant of current changeover from a thyristor to the incoming diode.

According to equation (3.12), the total rectifier derating is:

$$DR = \frac{2 E I_s}{P_o} + \frac{2 E I_D}{P_o}$$

Thyristor derating Diode derating (3.13)

Thyristor di/dt rating

The di/dt rating of a thyristor can be found be evaluating the maximum value of di/dt corresponding to the time $t = t_m$, from

$$\left| \frac{d^2 i_L}{dt^2} \right|_{t=t_m} = 0$$

giving

$$\left(\frac{d\, i_L}{dt}\right)_{max} = \sum_{n=1,3}^{7} n\omega_o\, I_{Ln} \cos\left(n\omega_o\, t_m + \beta_n\right) \qquad (3.14)$$

Commutating component ratings

The VA ratings of the commutating inductor VA_L and the capacitor VA_C are:

$$VA_L = \sum_{n=1,3}^{7} I_{Ln}^2\ X_L\ n \qquad (3.15)$$

and

$$VA_C = \sum_{n=1,3}^{7} I_{Ln}^2\ X_C/n \qquad (3.16)$$

respectively.

The instantaneous voltage across the commutating capacitor is:

$$v_{c1} = \frac{\sqrt{2}\, X_C}{n} \sum I_{Ln} \cos\left(n\omega_o\, t + \beta\right) + \frac{E}{2} \qquad (3.17)$$

which reaches a maximum before a feedback diode begins to conduct. The peak-to-peak capacitor voltage is therefore:

$$v_{c1\ p\text{-}p} = v_{c1}\left(-t_{off}\right) = v_{c1}\left(-t_{off} + \frac{T_o}{2}\right) \qquad (3.18)$$

Turn-off time

Since the minimum thyristor turn-off time TH_{off} is fixed, the minimum lead angle β between the output current i_L and the output circuit voltage v_{oa} increases as the operational frequency increases, with the result that the input power factor drops. To maintain a high input power factor in high frequency application, the designer must therefore ensure that the turn-off time does not exceed a specified minimum.

The turn-off time is calculated from the relations:

$$\left| \sum_{n=1}^{7} I_{Ln} \sin (n\omega_o t + \beta_n) \right|_{t=t_c} = 0$$

and $$t_{off} = \frac{T}{2} - t_c \qquad (3.19)$$

Per unit bases

For convenience, the parameters in the above equations are expressed in per unit form, with basic values of 1.0 p.u. being

$$\text{resistance base} = \text{Req.} = \frac{L_o}{R_o C_o}$$

$$\text{voltage base} = E/2$$

$$\text{angular frequency base} = \omega_o$$

Hence: $$\text{current base} = \frac{E}{2 R_{eq}}$$

$$\text{power base} = \frac{E^2}{4 R_{eq}}$$

$$\text{inductive reactance } X_L = \frac{\omega_o L}{R_{eq}}$$

$$\text{capacitive reactance } X_c = \frac{1}{2 C R_{eq} \omega_o} \qquad (3.20)$$

When analysing the inverter performance under varying load conditions during the heating cycle, the values of R_{eq} and ω_o at the end of the cycle are taken, for simplicity, as the base values. The values of X_L and X_c corresponding to these base values are denoted by X_{LB} and X_{CB} respectively.

3.5 Optimisation of the Inverter Performance

3.5.1 The optimisation criteria

The criteria used to select the commutating inductor and capacitor to provide an optimum inverter performance throughout the heating cycle are

i) maximum possible input power factor.

ii) minimum output current harmonics.

iii) minimum possible ratings for commutating inductor and capacitor.

iv) minimum rectifier derating.

v) minimum circuit losses.

Clearly, the weightings of these items differ considerably, depending on the nature of the application. For example, in high-frequency applications the size of the commutating components decreases significantly, and item (iii) carries less weight than otherwise. Further, in high-power applications, the long-term operational costs (due to losses, low input power factor, etc) are appreciably greater than the cost of an increased derating on the initial investment, and terms (i), (ii) and (v) often take priority in the performance of the inverter.

A high level of distortion in the output current seriously affects the inverter performance in several different ways. It causes a reduction in the input power factor and increases the ratings of the power circuit components. Additionally, for a sine-wave inverter with a highly-distorted output current, the difference between the total power output and the useful output power widens. Besides resulting in a lower efficiency, this may also produce undesirable effects in the workpiece. However, the worst effect is that with increased conduction losses a distorted output current produces a lower efficiency.

Since the inverter is assumed to be lossless, the calculation and comparison of the efficiencies of different designs naturally presents a serious problem. This may be partially tackled by using the distortion factor of the output current as a measure of the conduction losses in the following way:

$$\frac{P_{CLoss}}{P_o} \alpha \frac{I_L^2}{I_{L1}^2}$$

or $$\frac{P_{CLoss}}{P_o} \alpha \frac{1}{DF_{iL}^2} \qquad (3.21)$$

A comparison of the switching losses in different designs is, however, more difficult. It is known that the thyristor dissipation per commutation depends on the waveform of its current, and although special charts are available,[77,78] the calculation of the actual power loss per commutation is a lengthy procedure. On the other hand, the switching losses with series commutation are already low, and if changes in the output current waveform of different designs are not sufficient to produce wide variations, the switching losses may be neglected in the optimisation procedure.

3.5.2 The optimisation procedure

For an induction heating application, optimisation of the inverter performance must be performed on the basis of the inverter performance throughout the heating cycle. In other words, those values of the design variables (X_{LB} and X_{CB}) which provide the best inverter performance throughout the cycle must be selected as the optimum.

The following procedure may be adopted for the optimisation:

1. Identify the worst operation conditions which occur during the heating cycle. The prospective design values of X_{LB} and X_{CB} are obviously expected to produce successful commutation even at the worst possible operating conditions,

where the circuit turn-off time is a minimum. In induction heating applications, the worst operating condition is at the highest output frequency with the maximum equivalent load resistance, which occurs towards the end of the heating cycle after the Curie temperature is passed.

The first task for the designer is therefore to identify the worst operating condition (w.o.c.) in the load characteristics of the application. In a continuous heating application, the stable operating condition may be assumed to be the w.o.c.

2. Calculate the variation of X_{CB} with X_{LB}, to ensure successful commutation at the w.o.c.. Clearly, designs that produce an unnecessarily high turn-off time result in unsatisfactory inverter performance, as they cause

low input power factors and a distorted output current waveform. Hence, as an important step of the optimisation, such design values of X_{CB} and X_{LB} should be eliminated. This may be accomplished by calculating a series of values of X_{LB} and X_{CB} which provide the minimum thyristor turn-off time at the w.o.c..

3. Calculate the variation of the inverter performance (i.e. the changes of the steady-state circuit waveforms, their harmonic content and the inverter performance parameters) with X_{LB} and the corresponding value of X_{CB}.

4. Calculate the variation of the inverter performance at varying operational conditions of the heat cycle, for a series of values of X_{LB} and X_{CB}. Ignore this step if the load has a stable characteristic.

5. By comparing the variation of the inverter performance throughout the cycle of operation with the optimisation criteria, select the optimum design values of X_{LB} and X_{CB}.

It is possible to perform steps 2, 3 and 4 of the above procedure with the computer program presented in the next section.

3.5.3 A computer program for the optimisation procedure

As described above, the optimisation procedure requires considerable effort, involving performance investigation of the inverter with different design values and when operating under varying load conditions. Nevertheless, a substantial part of this work can be efficiently performed by a digital computer analysis.

For the performance analysis of the inverter, either the harmonic or the transient analysis techniques of the previous sections can be employed. However, since the analysis is repeated, the harmonic approach is more suitable, as it offers a very substantial saving in computation time. If on the other hand, the load changes are considerable and a discontinuous

output current is predicted, the computer program must be based on the transient analysis. A computer program prepared for the systematic investigation of the inverter performance by performing certain steps of the optimisation procedure is presented in Appendix 2. The important steps of the computation are as follows.

Calculation of a series of values of X_{LB} and X_{CB} to produce minimum circuit turn-off time.

As equation (3.19) suggests, there is no simple analytical solution for the circuit turn-off time for a given X_{LB} and X_{CB}. Nevertheless, some relation between these parameters may be established through a numerical analysis, and a flow chart of the section of the program which performs this is shown in Figure 3.10 . As seen, X_{LB} is incremented through its expected range, and for each increment the corresponding value of X_{LB} is calculated to produce a circuit turn-off time t_{off} equal to the minimum thyristor turn-off time TH_{off} at the worst operating condition. In so doing, the process is speeded by elimination of the values of X_{CB} which produces

$$i_L\ (t = 0) < 0$$

where t = 0 corresponds to the beginning of a positive half-cycle of the output current, or cause equation

$$i_L(t) = 0$$

to have more than one root within $0 < t < T_o/2$ are disregarded without further consideration.

Analysis of the inverter performance

The values of X_{LB} and X_{CB} calculated in the previous step are returned to the program, for the analysis of the performance of the inverter. In performing this, the output circuit waveforms are constructed by a summation of the first 7 harmonics, and the circuit performance parameters are calculated by using the equations derived in section 3.4.

Analysis of the inverter performance throughout the heating cycle

For this purpose some *characteristic load conditions* occurring during a heat cycle are selected and the procedure of the previous step is repeated for each of these.

The use of the program is demonstrated by the example in the next section.

3.5.4 Optimisation of the inverter performance for a typical static heating load

In this section, the performance of the sine-wave inverter is optimised for a 5 kHz static heating application.

The variations of the load parameters and the operating frequency for a typical static heating load throughout a complete

cycle of operations were obtained in Figure 2.9 of the previous chapter. In this figure, the highest output frequency and the maximum equivalent load resistance clearly corresponds to the load condition at the end of the heating cycle i.e. E. This condition is therefore identified as corresponding to the worst operational condition of the inverter during a full heating cycle. Some other characteristic load conditions may be selected as A, B, C and D, among which C corresponds to the minimum operating frequency. Let us assume that the 5 kHz output frequency corresponds to points A and D.

The optimisation procedure requires a knowledge of the minimum turn-off time of the thyristors to be used in the inverter. The selection of low turn-off time, high-frequency switching thyristors is of paramount importance. However, for the sake of demonstration, a moderate thyristor turn-off time TH_{off} of 25 μs is assumed, and this is fed into the program together with the description of the characteristic load conditions (i.e. the coil inductance L_o, the reflected load resistance R_o and the operational frequency w_o at A, B, C, D, E).

The computed results giving the variation of X_{CB} with X_{LB}, to produce a circuit turn-off time of 25 μs at the w.o.c. are plotted in Figure 3.11. The minimum value of X_{LB} is limited to approximately 0.6 p.u., since lower values will not produce a sensible answer. The reason for this becomes apparent when the output current waveform shown in Figure 3.12 for X_{LB} = 0.55 p.u.

is examined, which shows the impractical requirement that the diode current shall change in sign. This indicates a weakness of the mathematical model used, and results from a violation of the assumption that the output current is continuous (i.e. the driving voltage does not anymore have a square waveform). Nevertheless, this current waveform indicates that, for $X_{LB} < 0.6$ p.u. (approximately), there is insufficient reactive energy stored in the commutating circuit to provide the turn-off conditions when the feedback diodes begin to conduct. Because of these restrictions, future considerations will neglect $X_{LB} < 0.6$ p.u.

Figure 3.13 shows the variation of the circuit turn-off time during a heating cycle, for different values of X_{LB} (for reasons of clarity, only results for some interesting values of X_{LB} are presented). Obviously, as the values of X_{LB} and X_{CB} correspond to the curve of Figure 3.11, the circuit turn-off time of all designs at the operating point E is 25 μs. These curves illustrate that the maximum turn-off time for each design occurs when the output frequency and the equivalent resistance of the tank load circuit are a minimum (i.e. at C).

The variation of the harmonic content of the output current throughout the heating cycle is given in Figure 3.14. As expected, the harmonic content deteriorates at load conditions which produces an increased turn-off time. On the other hand, the variation of the fundamental output current illustrates an important characteristic of the sine-wave inverter. As clearly

shown, the fundamental changes considerably with changes of up to 50% in the equivalent tank load resistance. However, for values of X_{LB} around 1.2, the inverter behaves as a constant current source, which is beneficial in preventing an excessive rise of commutating capacitor voltage, etc. However, it also causes a poor output voltage regulation and produces a low output power with low impedance loads. The curves of Figures 3.15 and 3.16 show the variation of both the output power and the input power factor with the load conditions. As can be seen, at a given supply voltage high values of X_{LB} produce a lower output power than do low values of X_{LB}.

During the heat cycle, the ratio of the conduction power losses to the useful output power varies with X_{LB}, in proportion to the curves shown in Figure 3.17.

The total rectifier derating (i.e. the sum of the thyristor and diode derating) at different design values of X_{LB} can be compared by plotting the worst value occurring throughout the cycle of operation against X_{LB}, as shown in Figure 3.18. Figure 3.19 shows the variation with X_{LB} of the highest peak-to-peak commutating capacitor voltage occurring during a heating cycle.

3.5.5 Selection of X_{LB} and X_{CB}

It is evident from an investigation of the performance curves presented above that there is no universal optimum value for X_L. The results indicate that low design values of X_L cause higher power losses, although producing a better input power factor and reduced output power variations throughout the cycle of operation. On the other hand, if X_L is high the harmonic content of the output current is satisfactory and the losses are low, although the inverter has a low input power factor, reducing even further near the Curie temperature and with higher power component ratings. The selection of X_{LB} is therefore a matter for engineering judgement, as it depends on the requirements of a particular application. For example, if the power output is controlled by the input source voltage, a low X_{LB} may be preferred, since the required variation of the input voltage may otherwise be unacceptably high (e.g. for X_{LB} = 3.0 p.u., a 150% input voltage increase is required to keep the output power constant during the heating cycle).

Based on the considerations above, X_{LB} = 1.4 p.u. may be selected as the optimum for a high-frequency high-power inverter. This will achieve reasonably low conduction losses and a good output current harmonic content, but will to some extent worsen the input power factor and increase the power component derating. From Figure 3.11, the corresponding value of X_{CB} is 2.2 p.u.

With these design values for X_{LB} and X_{CB}, the performance of the inverter may easily be evaluated, giving the results in Table 3.1. Variation of the output current waveform with selected characteristic load conditions (A, C and E) are obtained from the digital simulation of the inverter as shown in Figure 3.20.

3.6 Discussion

Because the output current must lead the output circuit voltage by an angle $\beta > w_o T_{off}$, the maximum possible input power factor of the sine-wave inverter is limited to, approximately:

$$PF_{Im} = 0.9 \text{ Cos } w_o TH_{off}$$

when only the fundamental current is considered and 0.9 is the 1/form factor of the sine-wave. This expression gives:

f_o, kHz	(TH_{off} = 20 μs) PF_{Imax}	(TH_{off} = 12 μs)
10	0.27	0.66
7.5	0.522	0.76
5	0.73	0.83

which clearly indicates the very significant effect of the minimum thyristor turn-off time on the maximum input power factor. In the performance optimisation example presented in section 3.5.4., the high $TH_{off}/(T_o/2)$ ratio assumed to be 25% is therefore responsible for the low input power factor of the inverter (in Table 3.1 PF_I = 0.68). A low input power factor will, of course, result in an increased inverter VA rating and hence in a higher initial cost. Nevertheless, at high operational frequencies, this increase in VA rating is a less serious problem. At present, a sine-wave inverter employing thyristors with 12 μs turn-off time is economically viable[59] for submegawatt power applications at frequencies as high as 10 kHz. On the other hand, as far as the supply is concerned, this low input power factor is corrected, as the harmonic components of the input current are reduced by the low pass filter in the ac-to-dc converter preceding the inverter.

As indicated in Table 3.1, the output power of the inverter drops approximately by 50% at around the Curie temperature. This scale of output power variation is not uncommon in induction heating.[42,57] It can, nevertheless, be reduced substantially by step-wise load matching, as mentioned in earlier chapters. If the feasibility of the system operation permits the use of tap changing in the output transformers* ,Figure 3.16 suggests that

---

*This scheme involves additional initial and operational costs, and has the disadvantage of interrupting a process which already has a short heating cycle (the majority of heat treatment applications at these operational frequencies have heating cycles of the order of a few minutes).

the output power characteristics of the inverter can be improved significantly by only changing the transformer taps twice, at instants corresponding to load conditions somewhere between A and B and C and D. Load matching performed in this manner would also be advantageous in reducing the power component derating.

If a load matching scheme is to be used, the optimisation procedure presented in this chapter can still be employed although the effect of varying load impedance with the tap changing must of course be further considered.

The analysis of this chapter indicates that the sine-wave inverter has the advantages of:

1. An approximately sinusoidal output current.
2. Well defined circuit waveforms.
3. Low circuit losses (i.e. both conduction and switching) and hence a high operational efficiency.
4. Simplicity in construction.
5. Small size in high-frequency applications, which enables high-power densities (i.e. P_o/kg) to be achieved with low initial cost.

Whereas the disadvantages are:

1. The practical range of operational frequency is narrow. The highest operational frequency is limited by the minimum thyristor turn-off time, while low operational frequencies cause a distorted (discontinuous) output current waveform

and a worsened input power factor.

2. The output voltage is load sensitive.

3. Complicated control circuitry is required for the short-circuit protection essential in high-frequency applications (see Appendix 3).

From these features, it can be deduced that the sine-wave inverter is particularly suited to stable-load continuous heating applications. Fortunately, the operational frequency range of a typical static heating application is also compatible with the inverter performance, and a satisfactory inverter performance can be achieved by performing the optimisation procedure established in this chapter.

Design values: X_{LB} = 1.4 p.u., X_{CB} = 2.2 p.u.

Load: Static-heating load, with characteristic load conditions,

	w_o(p.u)	Q_L	Req.(p.u)
A,D	1.00 (5000 Hz)	5.0	1.0
B	0.940	3.03	0.64
C	0.912	2.43	0.53
E	1.056	6.77	1.29

Inverter Parameters:		Maximum	Minimum
t_{off}	:	47 μs at C	25 μs at E
P_o	:	0.34 p.u at E	0.14 at C
PF_I	:	0.68 at E	0.22 at C
DF	:	0.99 at E	0.98 at C
I_D	:	0.31 p.u.	
I_s	:	0.17 p.u.	
DR	:	12.4 at C	

Harmonics of i_L (r.m.s)

1st	:	0.54 p.u at E	0.51 p.u at C
3rd	:	0.11 p.u at C	0.08 p.u at E

Table 3.1 Performance of the optimum inverter with a static heating load

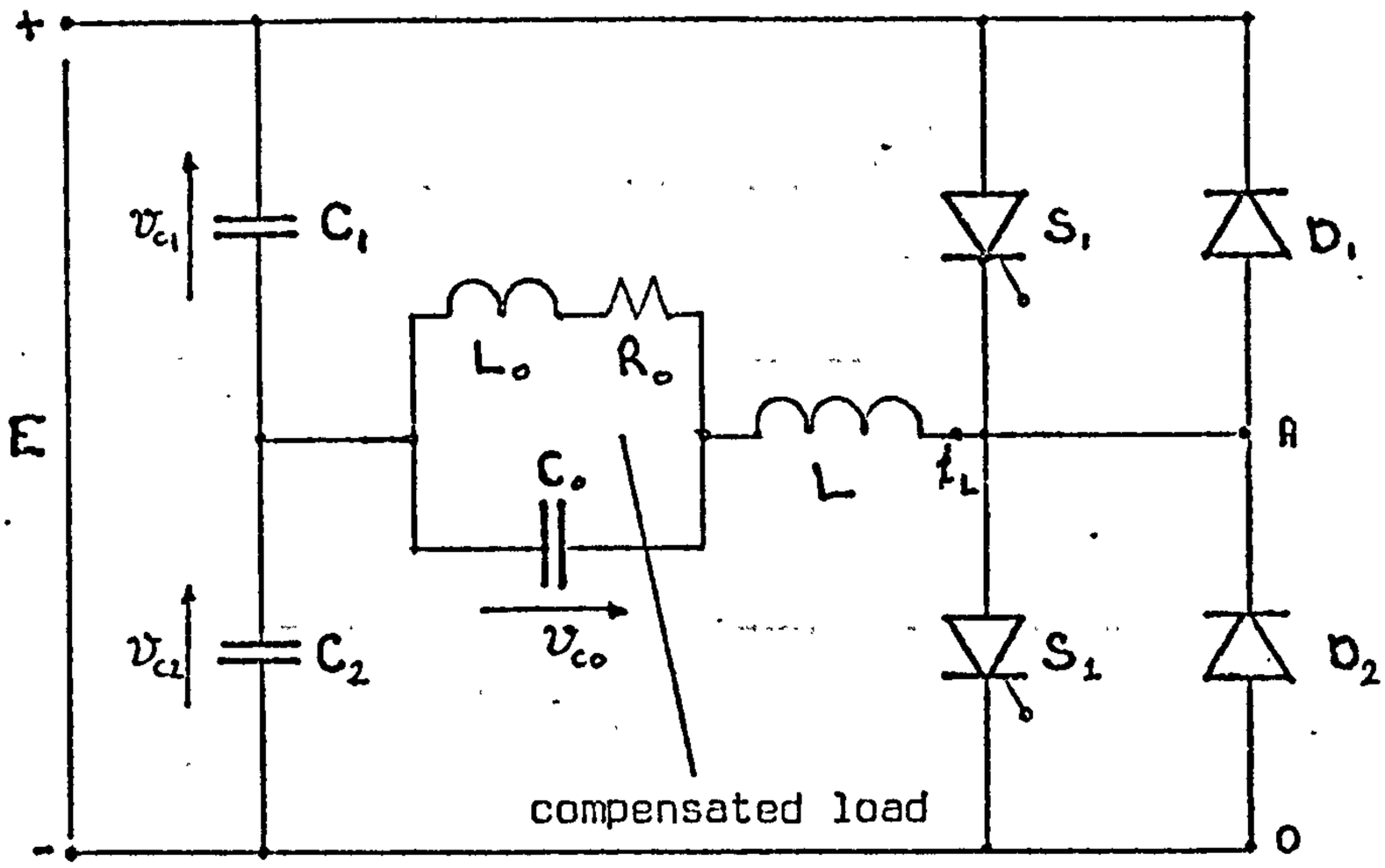

Figure 3.1 Basic sine-wave inverter with a compensated induction heating load

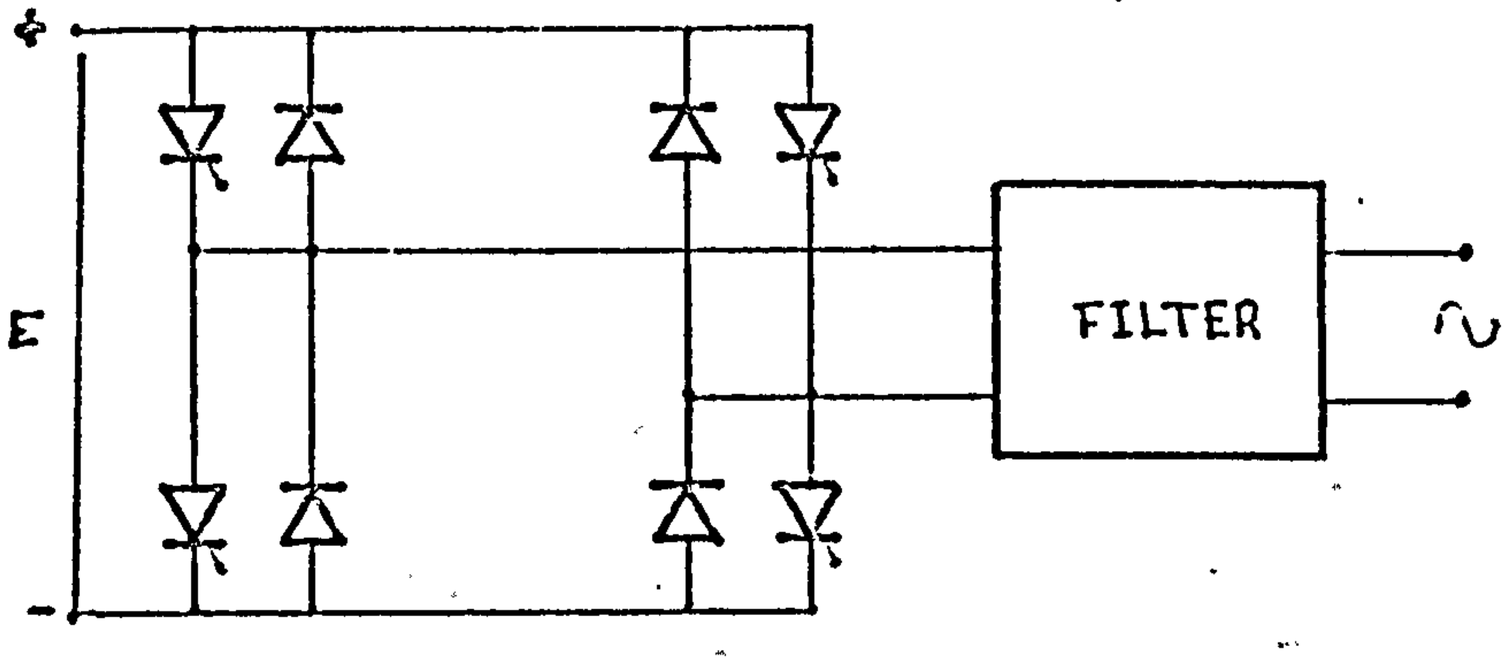

(a)

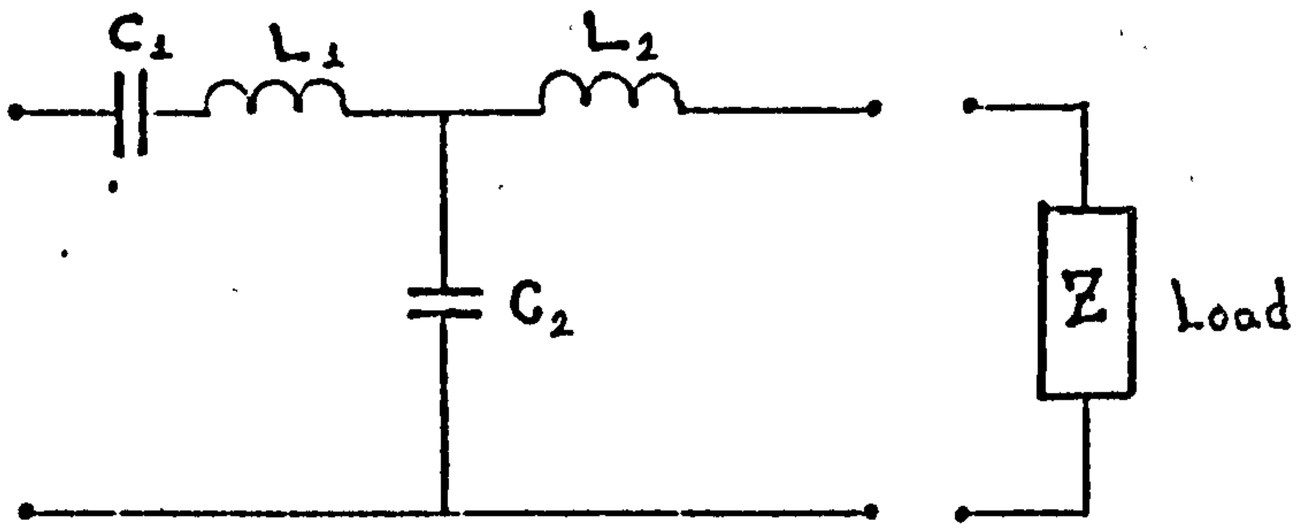

(b)

Figure 3.2 a) Full bridge sine-wave inverter.
b) 4 element commutating filter

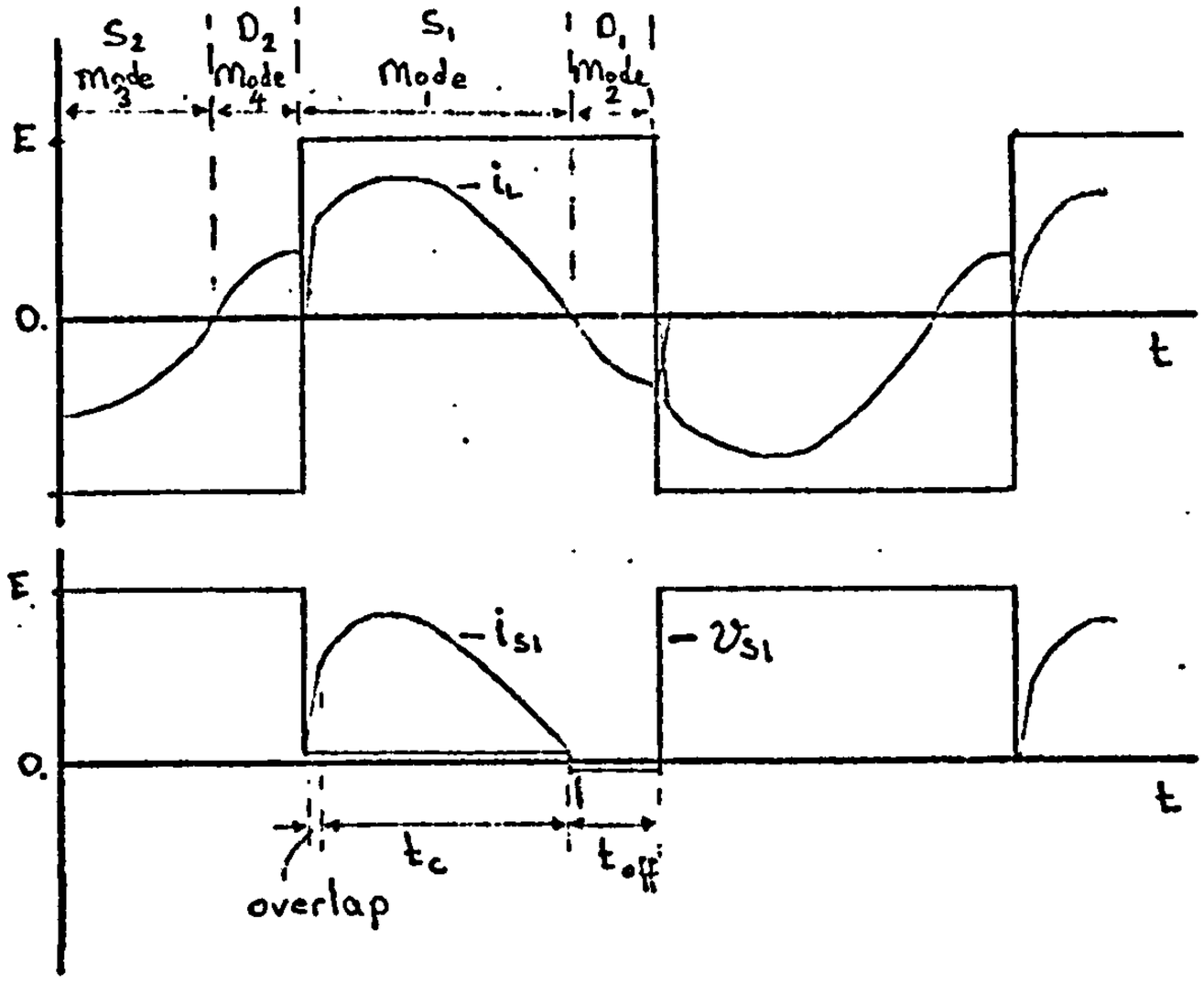

Figure 3.3 Steady state waveforms of the output current i_L, thyristor voltage v_{s1} and the thyristor current i_{s1} in the basic inverter

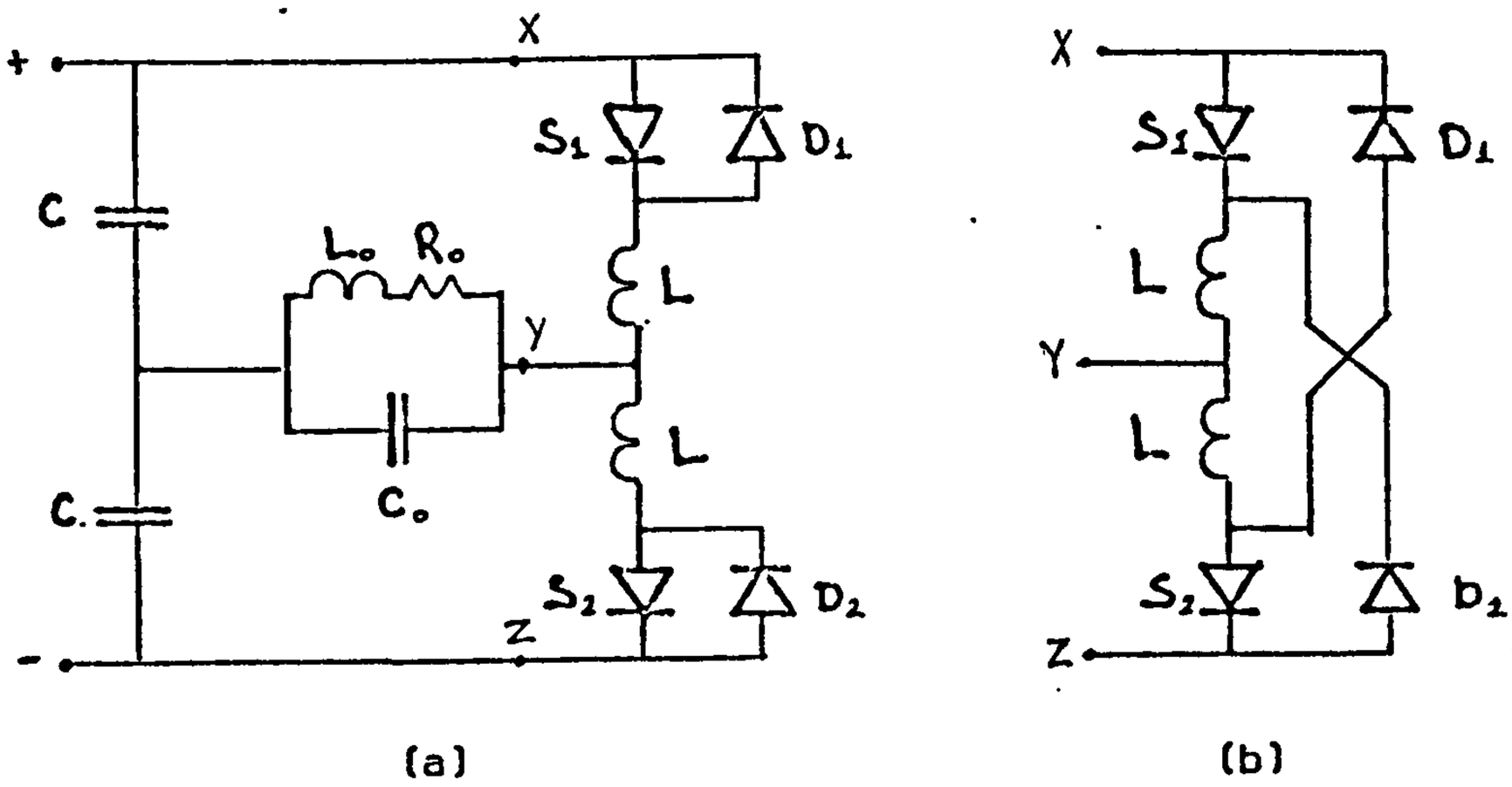

Figure 3.4 Some circuit modifications for the sine-wave inverter to achieve a lower rate of rise of thyristor voltage

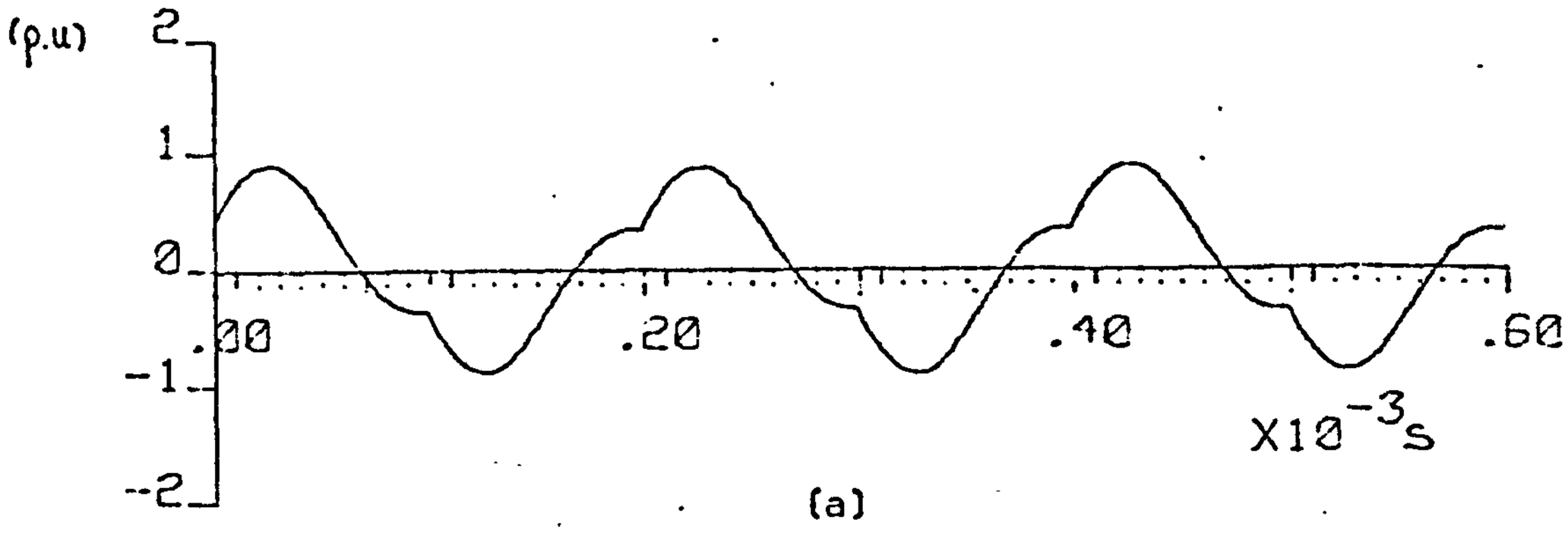

(a)

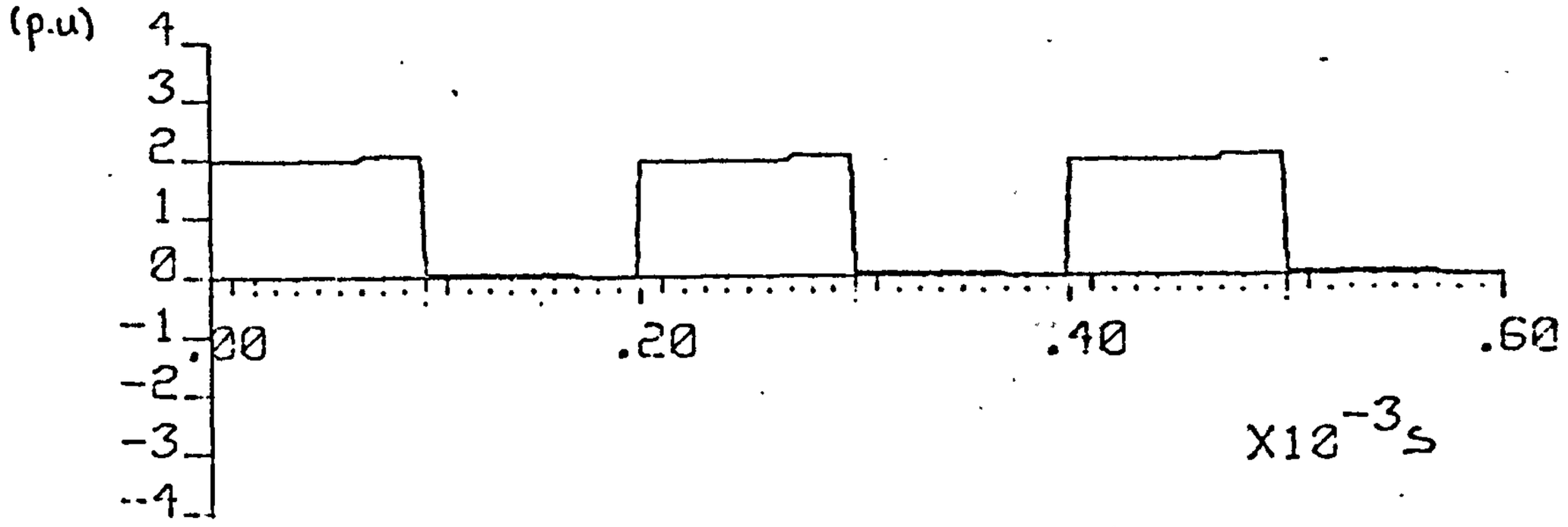

(b)

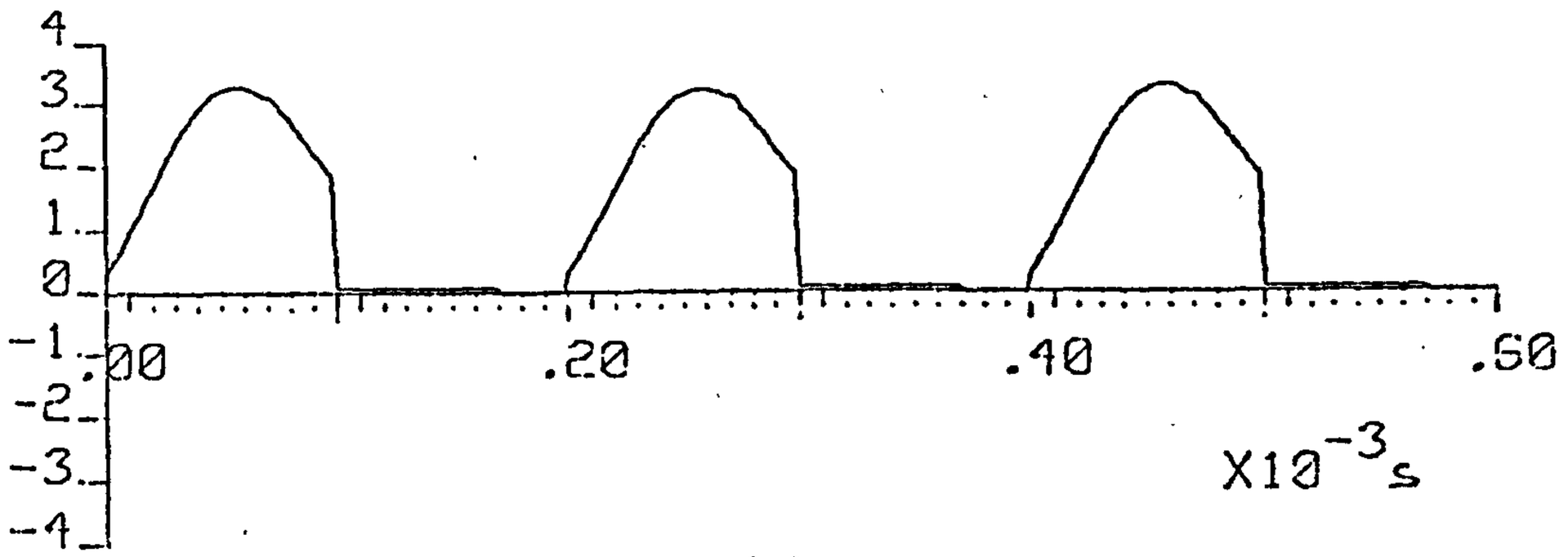

(c)

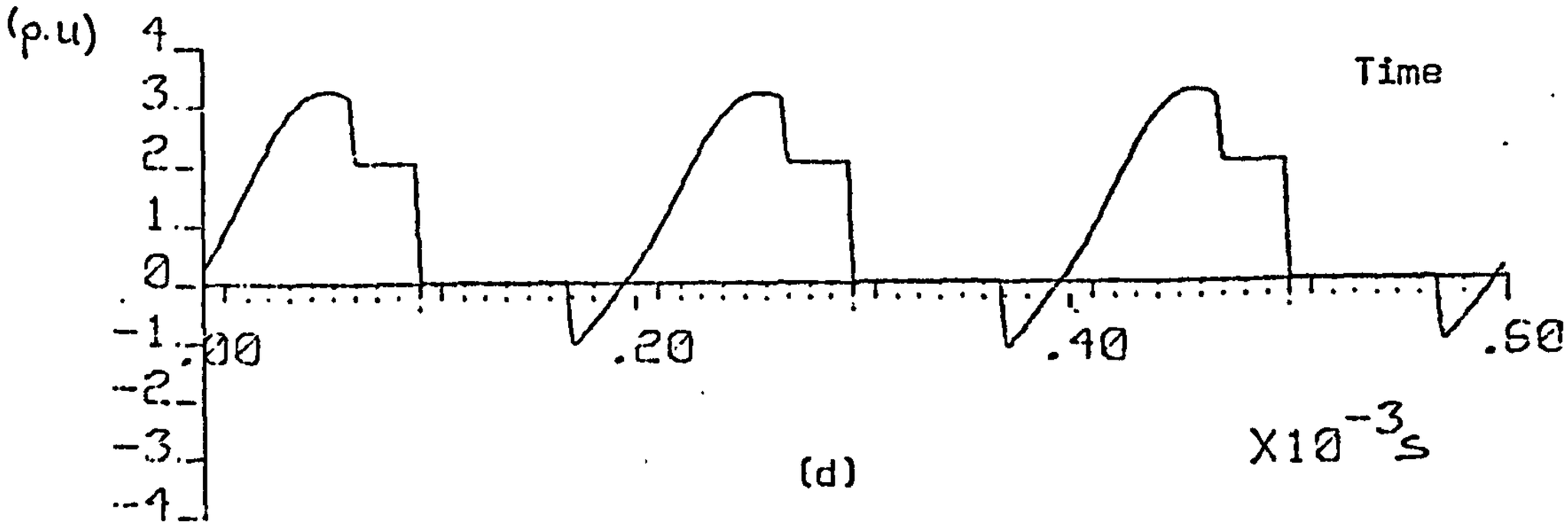

(d)

Figure 3.5 Thyristor voltages in different versions of the sine-wave inverter for same output current (f_o = 5 kHz)

a) the output current - i_L

b) v_{s1} in the basic inverter

c) v_{s1} in Figure 3.4a

d) v_{s1} in Figure 3.4b

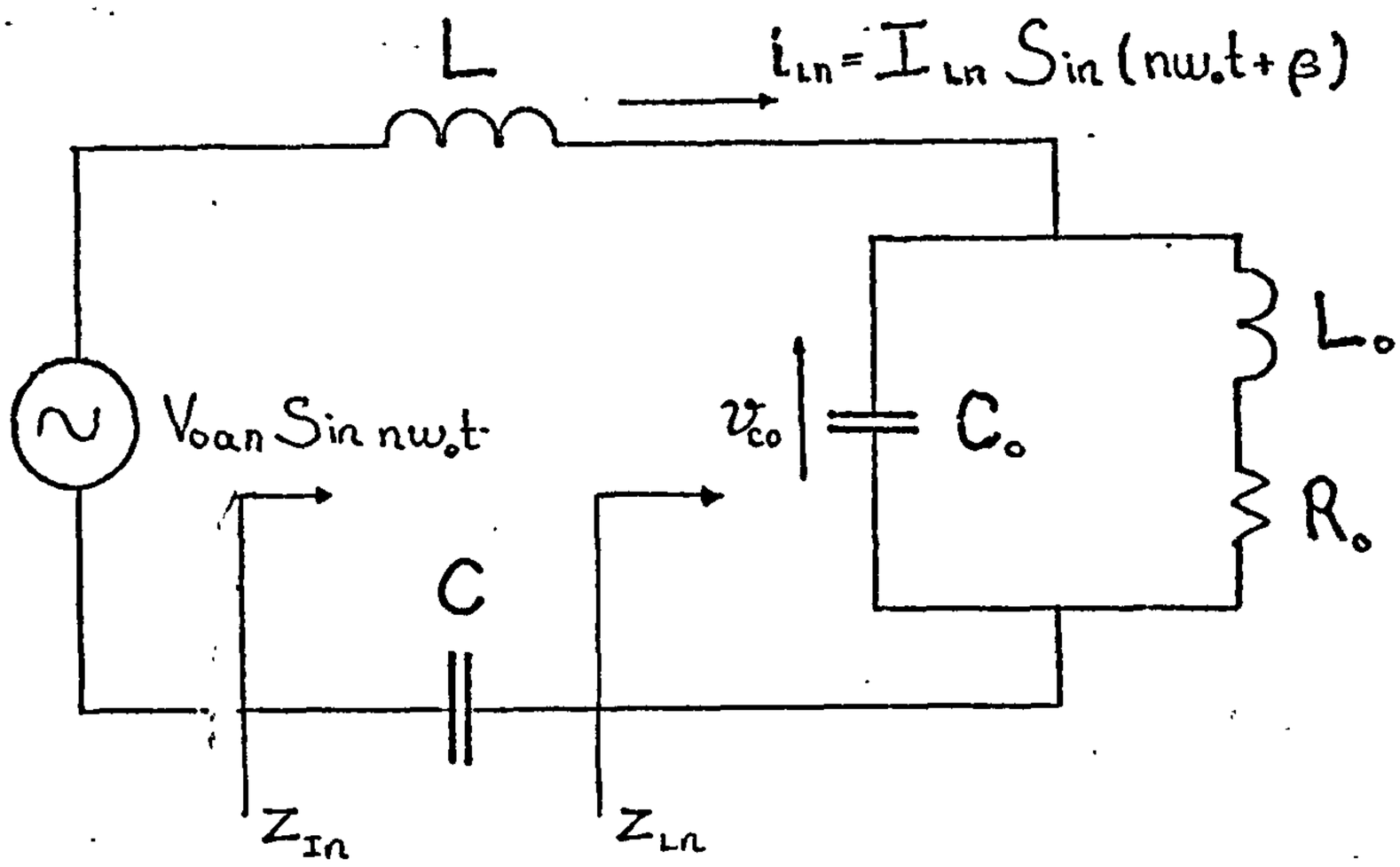

Figure 3.6 The n^{th} harmonic equivalent circuit

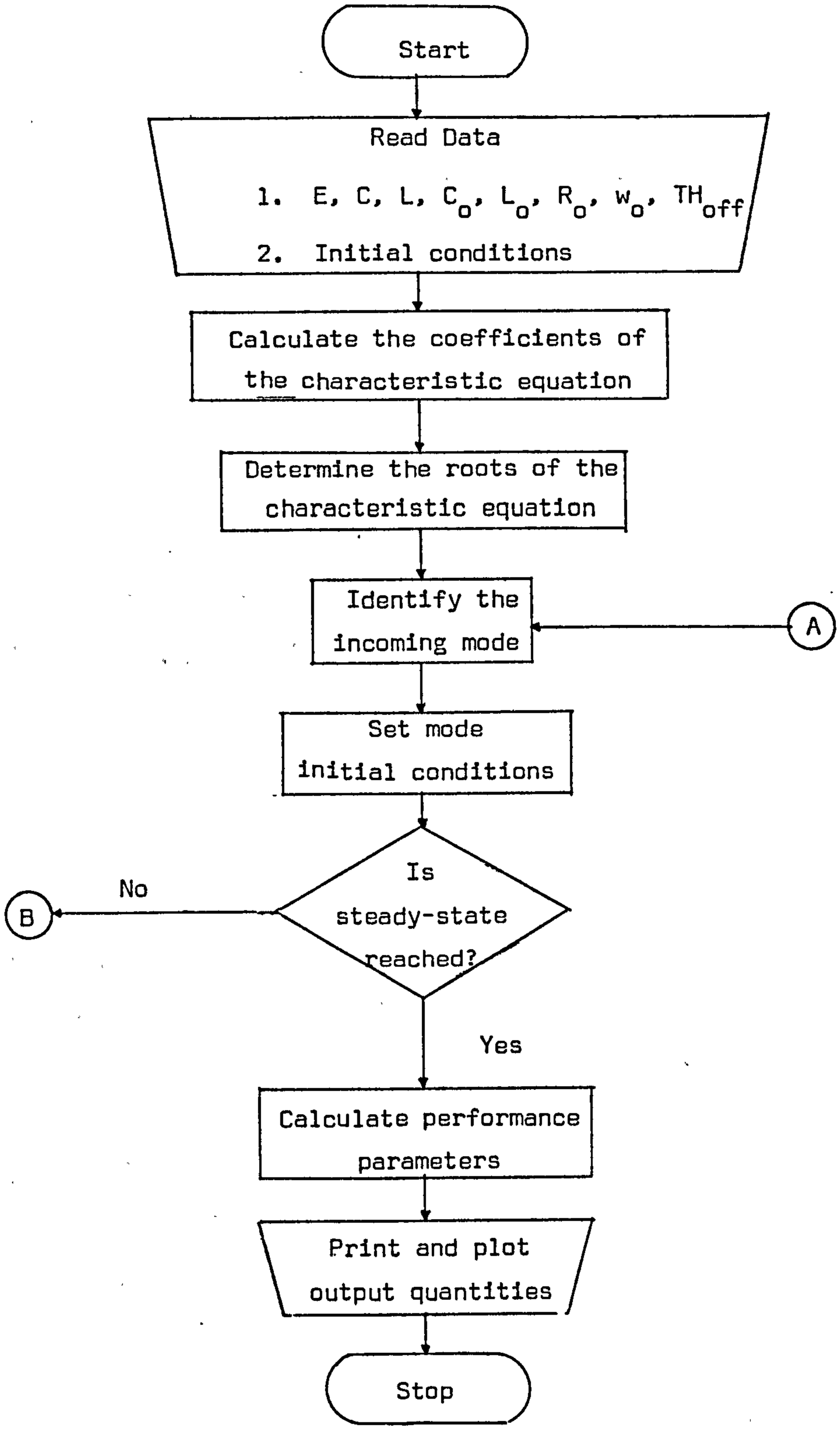

Figure 3.7 Flow chart of the computer program prepared for the digital simulation of the sine-wave inverter

/Continued

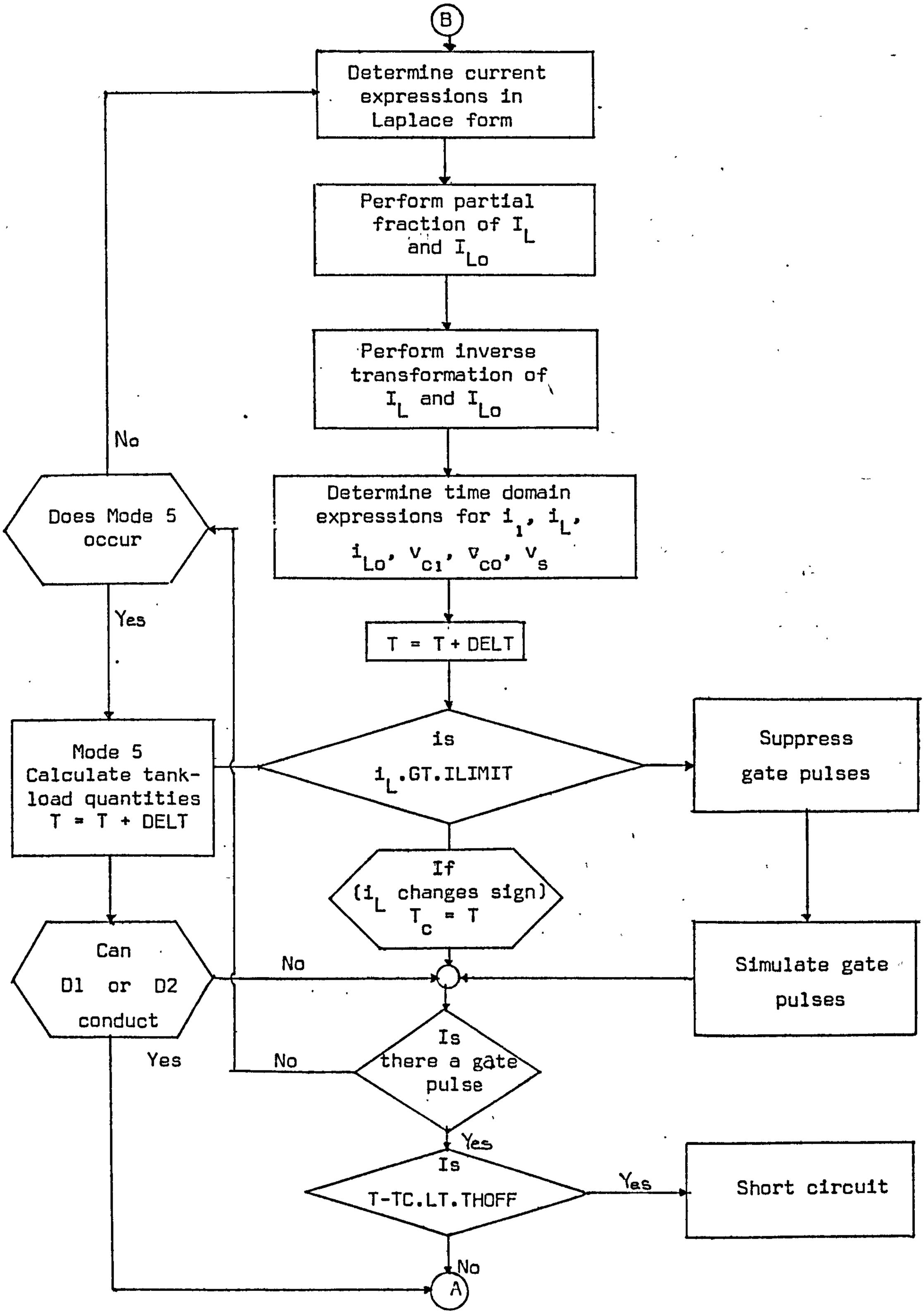
B
Determine current expressions in Laplace form
Perform partial fraction of I_L and I_{Lo}
Perform inverse transformation of I_L and I_{Lo}
Determine time domain expressions for i_1, i_L, i_{Lo}, v_{c1}, v_{co}, v_s
T = T + DELT
is i_L.GT.ILIMIT
Suppress gate pulses
Simulate gate pulses
If (i_L changes sign) T_c = T
No
Does Mode 5 occur
Yes
Mode 5 Calculate tank-load quantities T = T + DELT
Can D1 or D2 conduct
Yes
No
Is there a gate pulse
No
Yes
Is T-TC.LT.THOFF
Yes
Short circuit
No
A

Figure 3.7

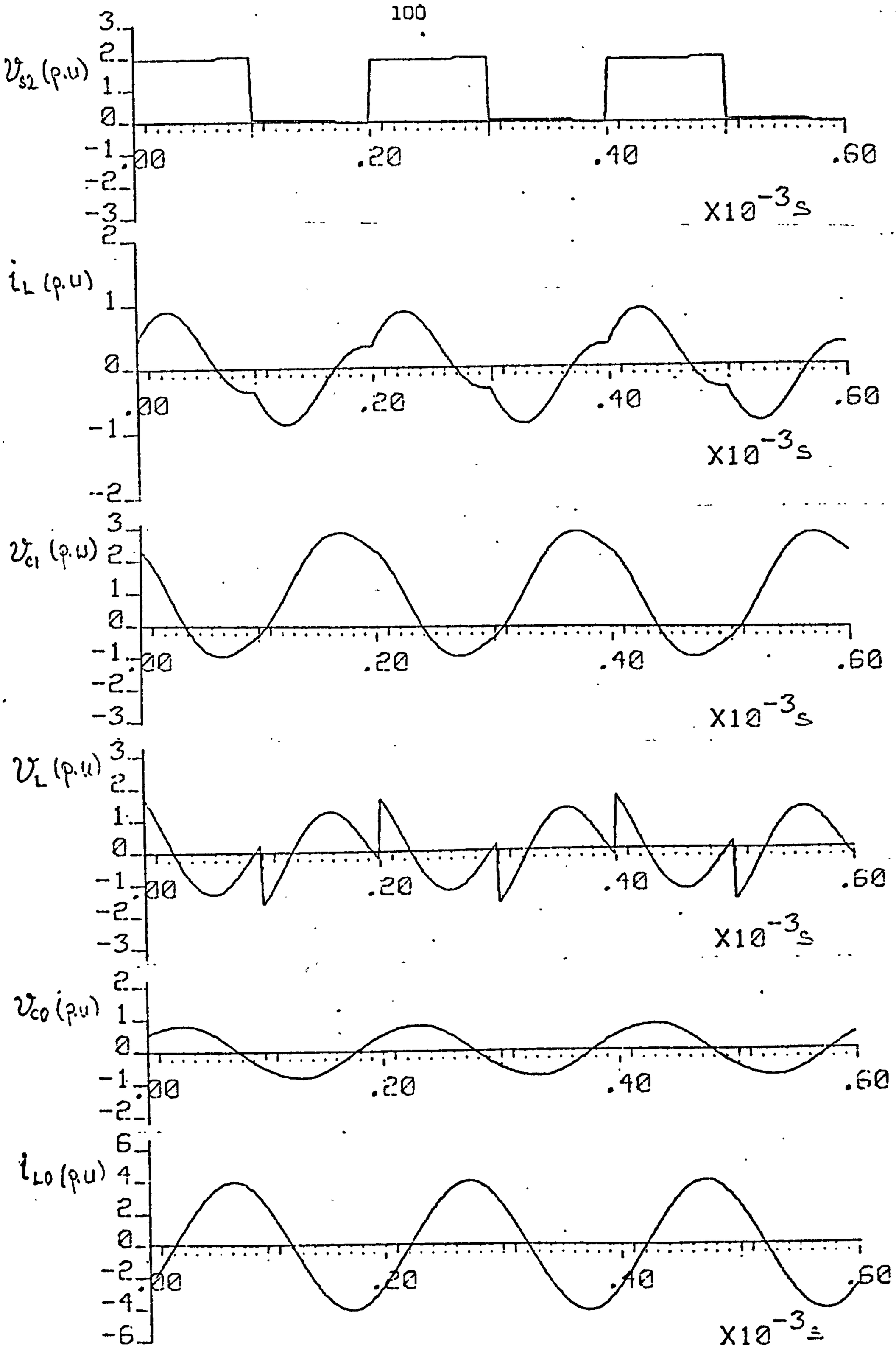

Figure 3.8 Graphical results of the digital simulation of the sine-wave inverter (f_o = 5 kHz, X_{LB} = 1.4 p.u., X_{CB} = 2.5 p.u., Q_L = 5).

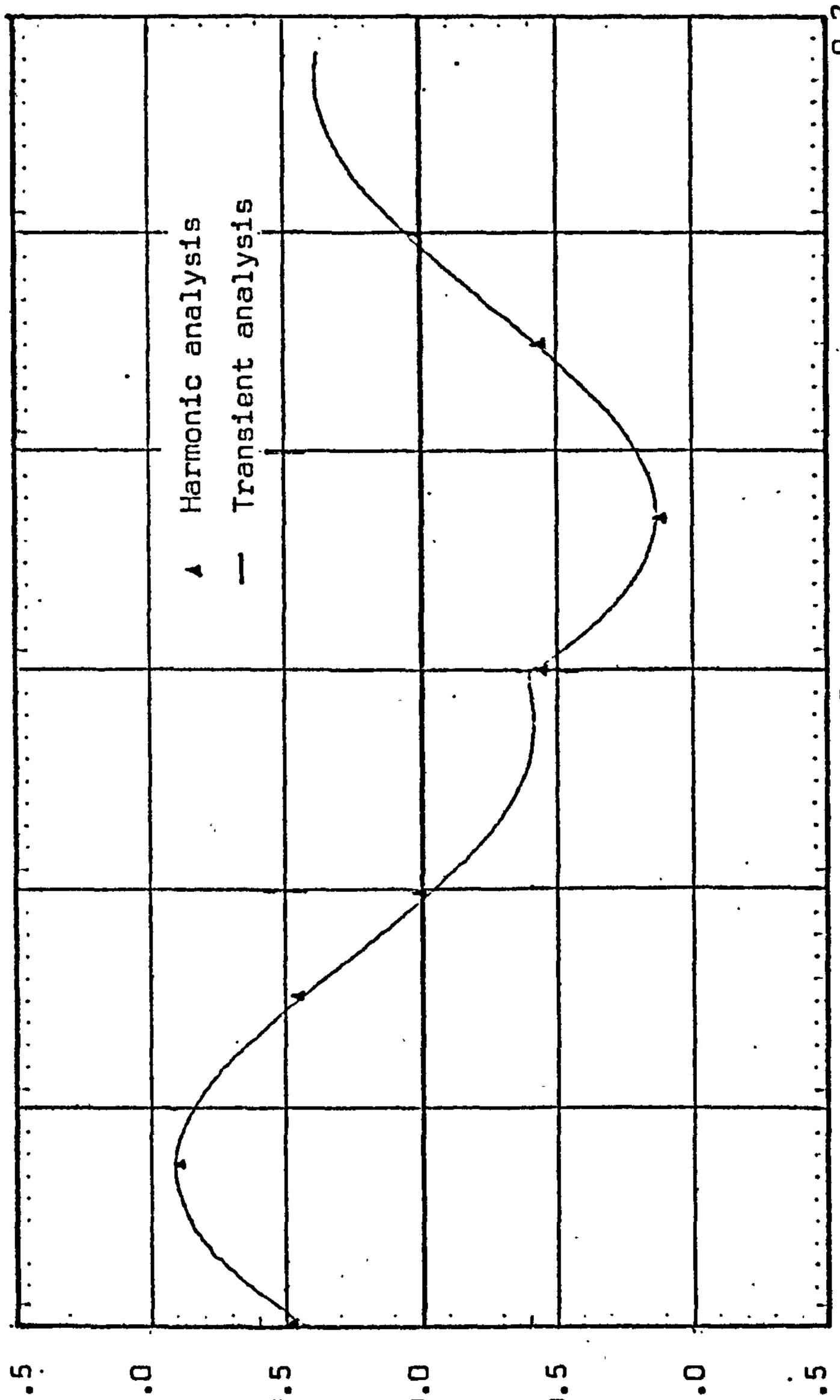

Figure 3.9. Comparison of the output current waveforms obtained from transient and harmonic analysis (X_L = 1.4, X_c = 2.5, f_o = 5 kHz)

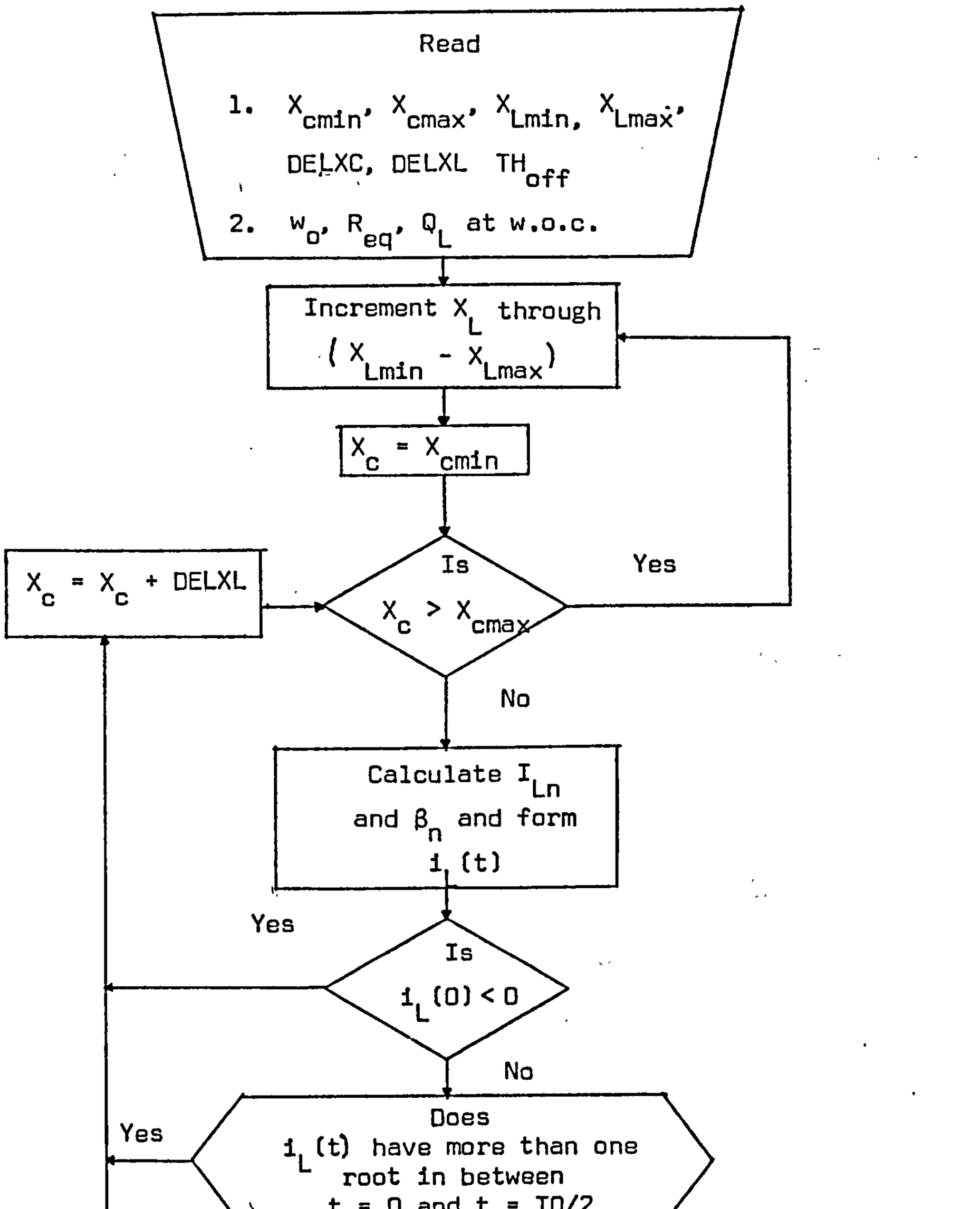

Figure 3.10 Flow chart for the execution of step 2 of the optimisation procedure

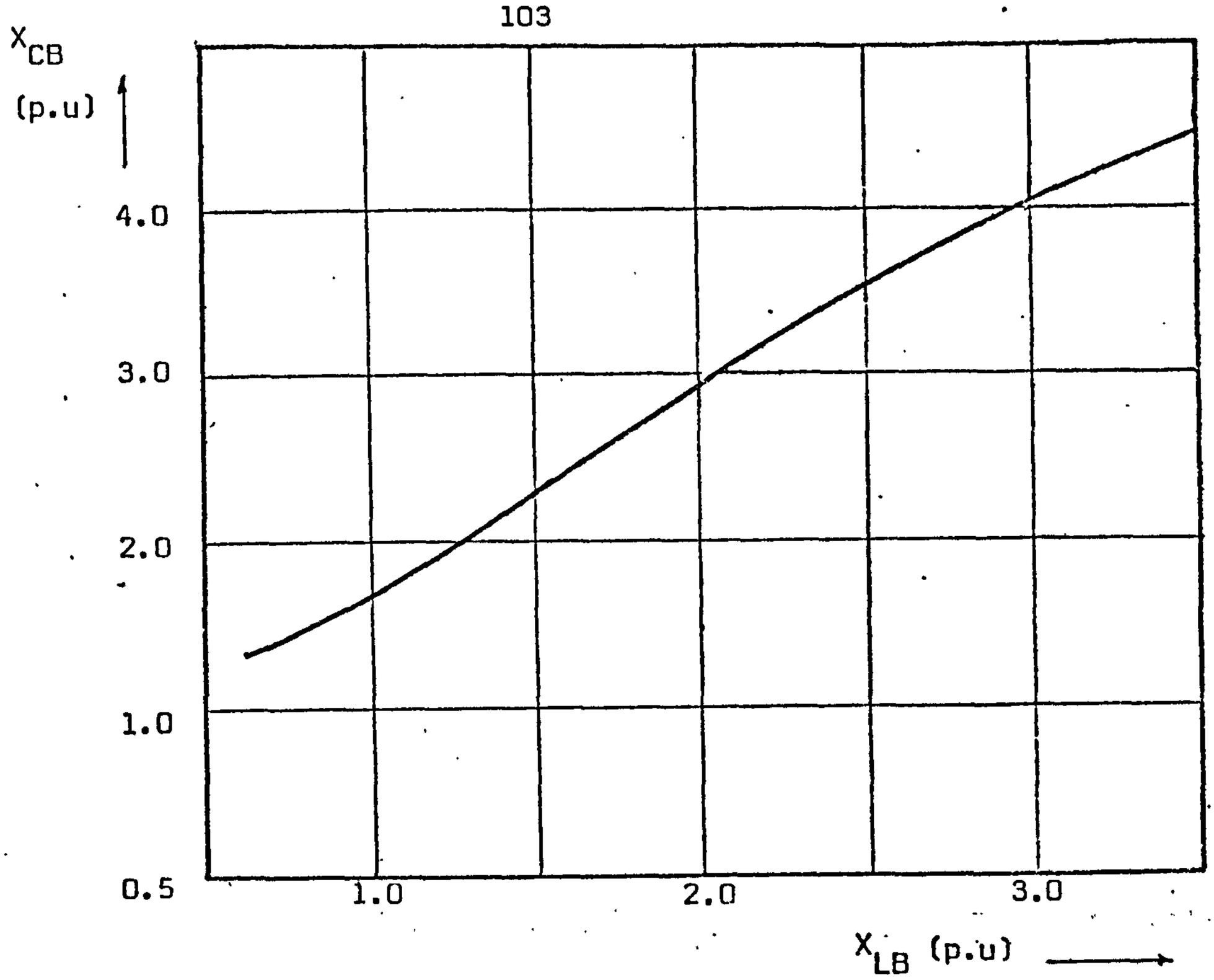

Figure 3.11 Variation of X_{CB} with X_{LB} to produce t_{off} = 25 µs at the load condition E (i.e. at w.o.c).

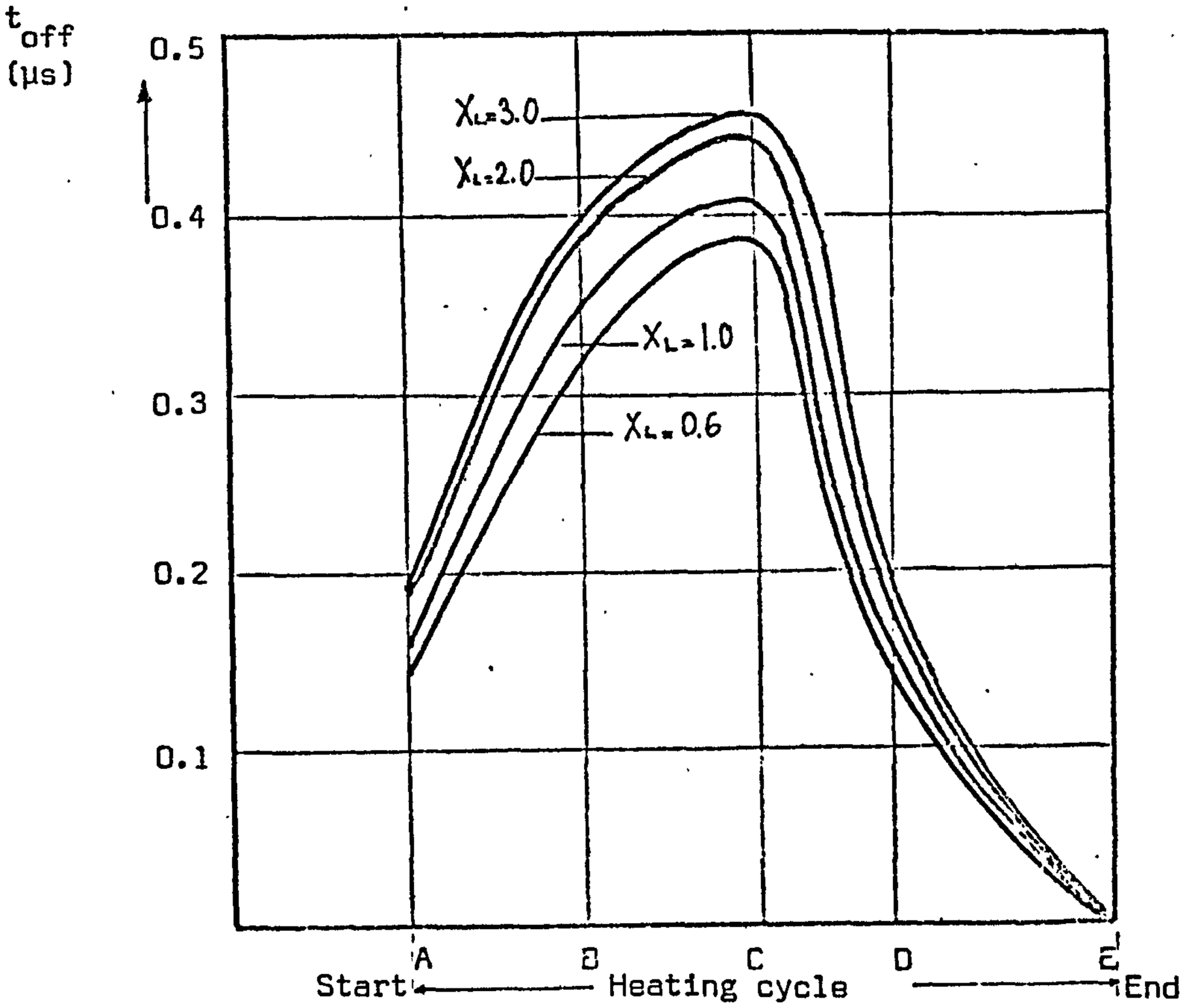

Figure 3.13 Variation of circuit turn-off time t_{off} for different designs during a complete cycle of operation (f_o = 5 kHz, Q_L = 5)

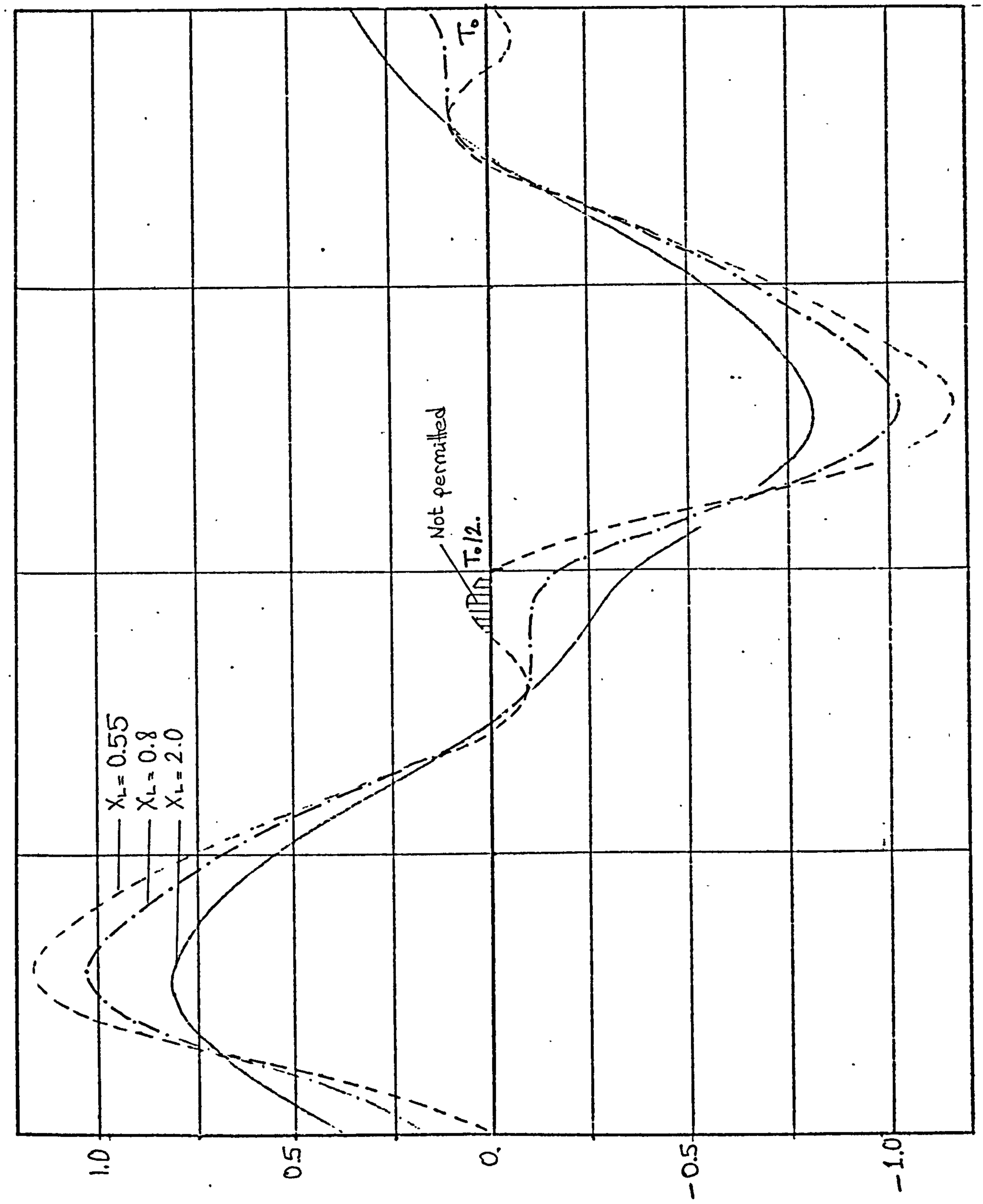

Figure 3.12 Output current waveforms for various values of X_L (obtained from the harmonic analysis performed at the load condition E).

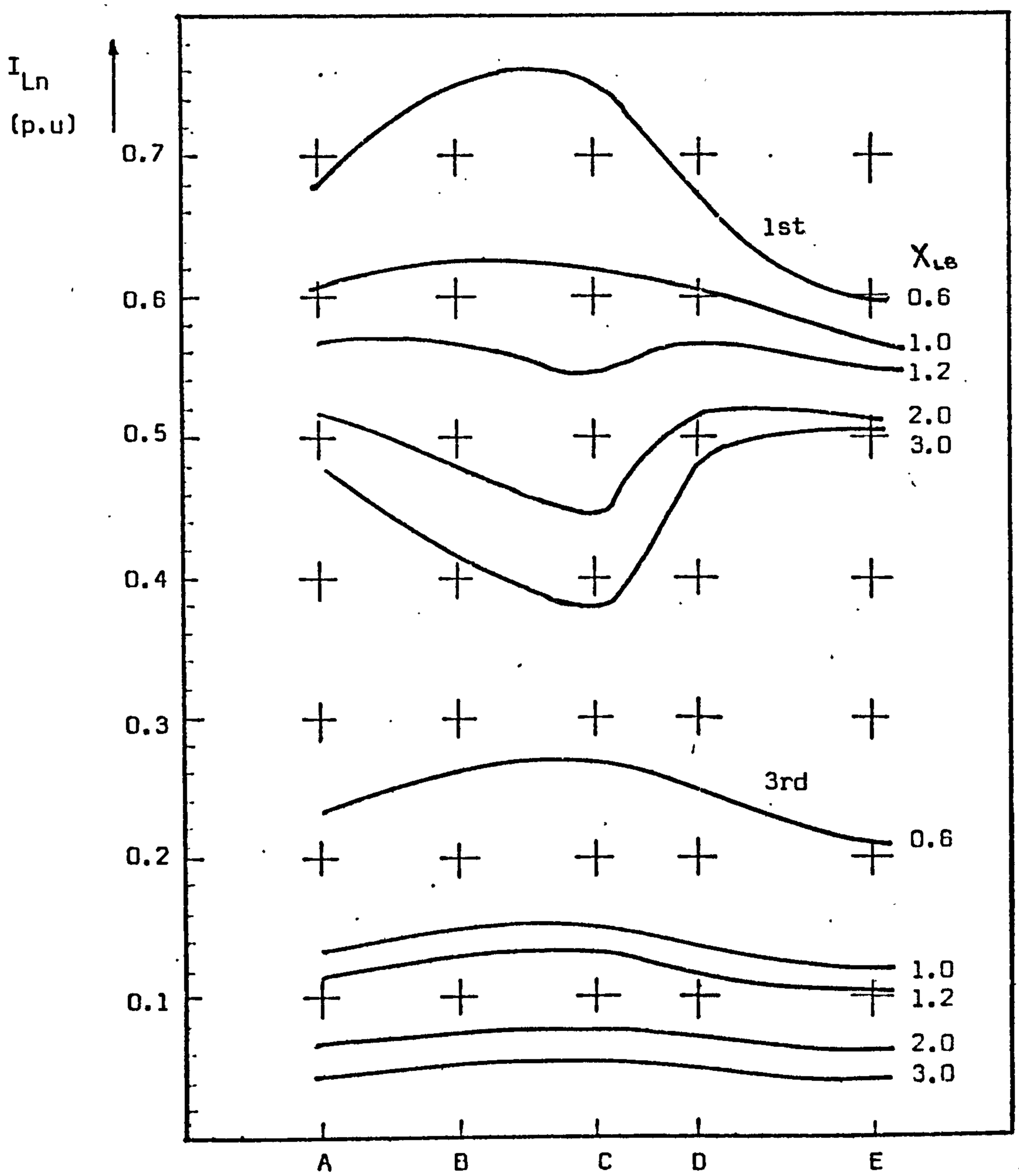

Figure 3.14 Variation of peak output current harmonics for different designs as the heat cycle progresses (f_o = f kHz)

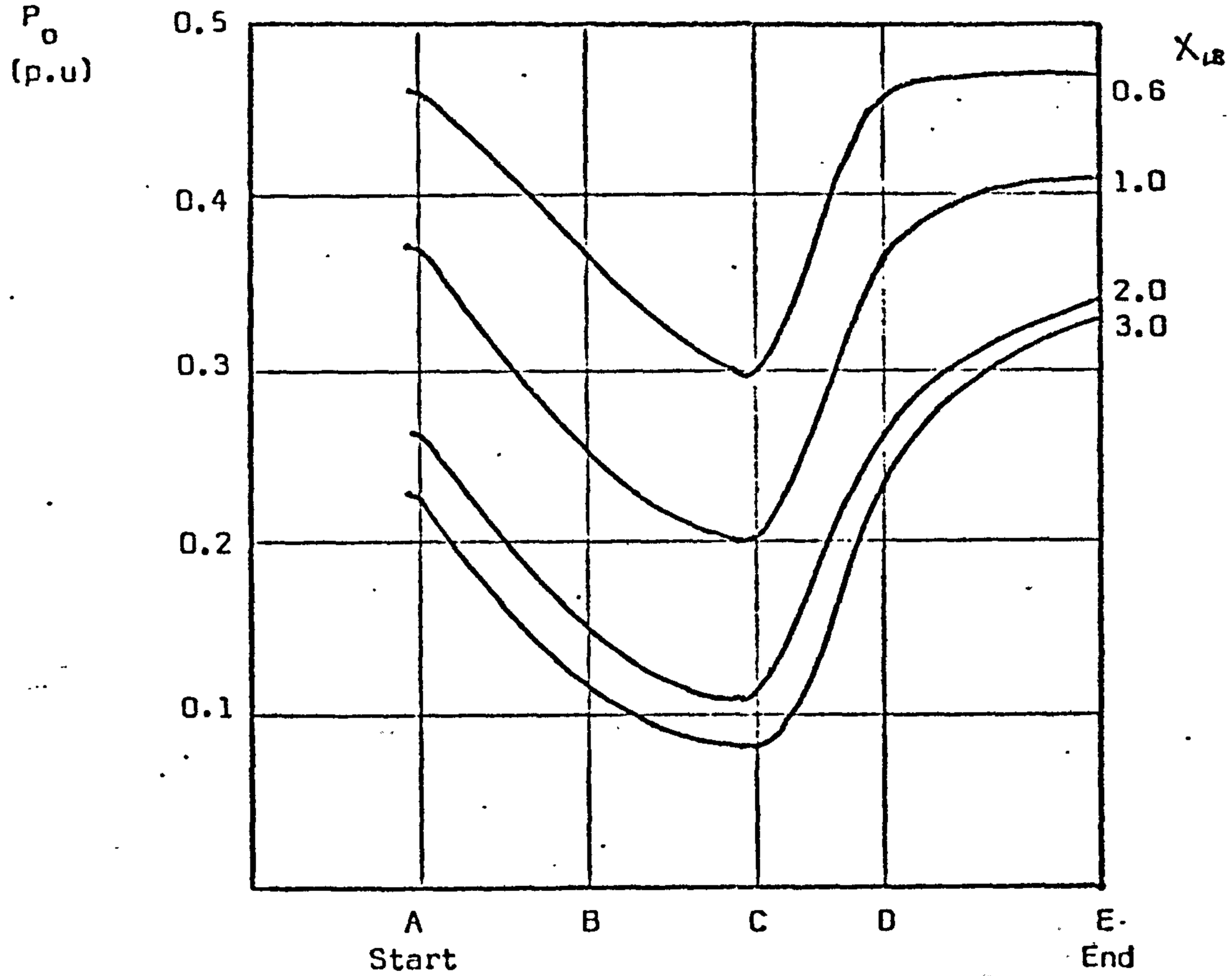

Figure 3.15 Variation of input power factor for different designs as the heat cycle progresses.

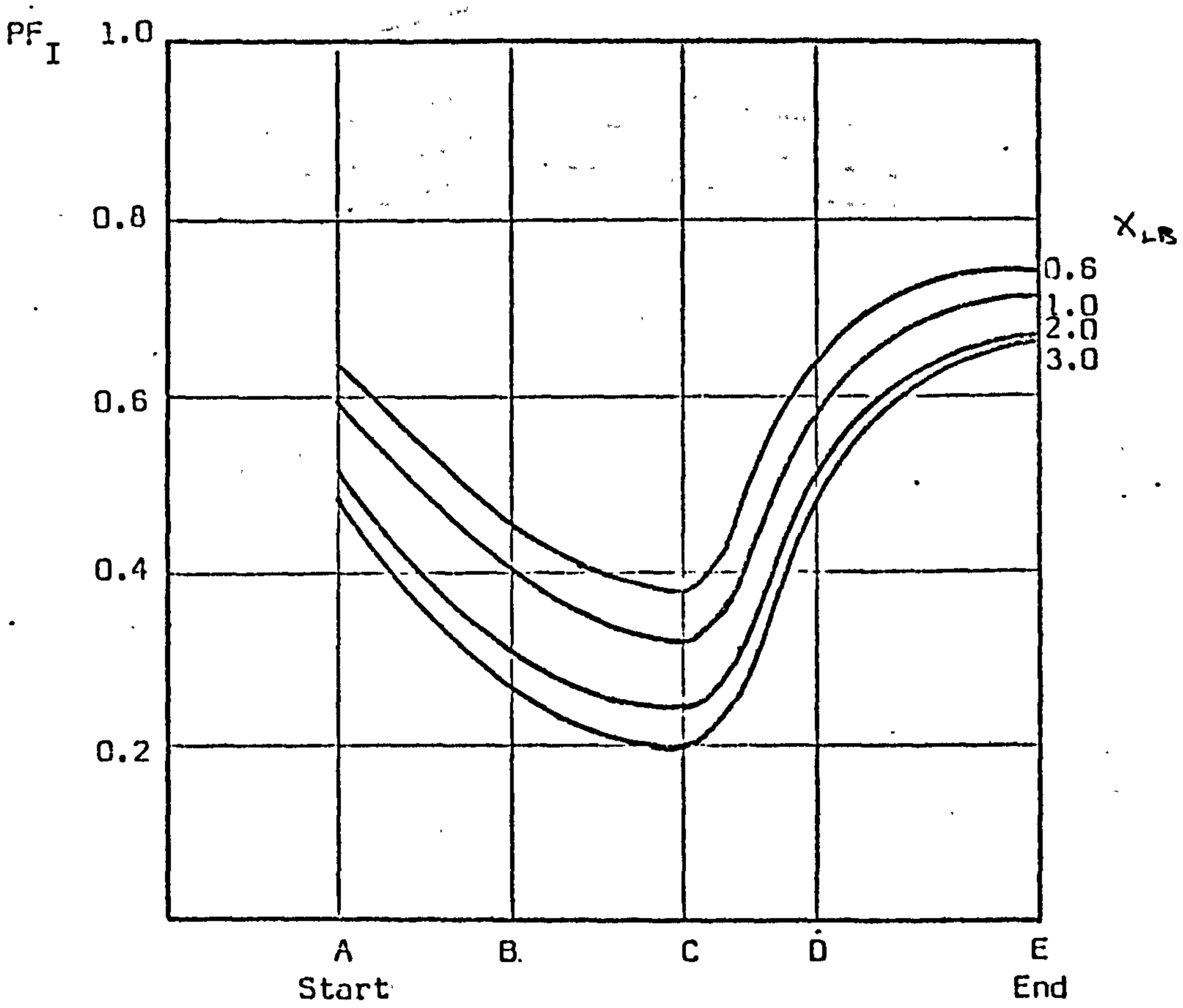

Figure 3.16 Variation of output power for different designs as the heat cycle progresses

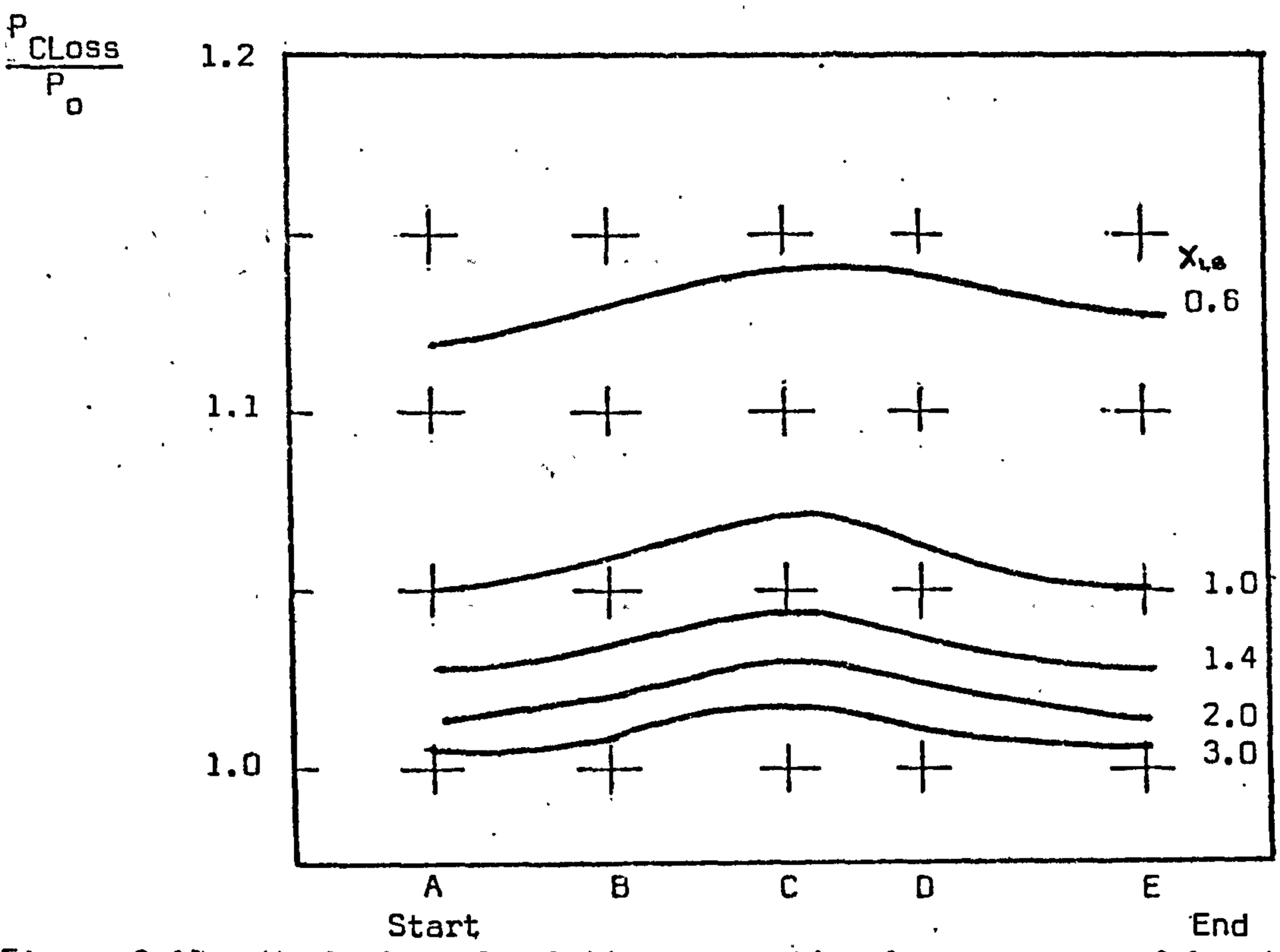

Figure 3.17 Variation of relative conduction losses per useful output power P_{cLoss}/P_o during a heating cycle for different designs

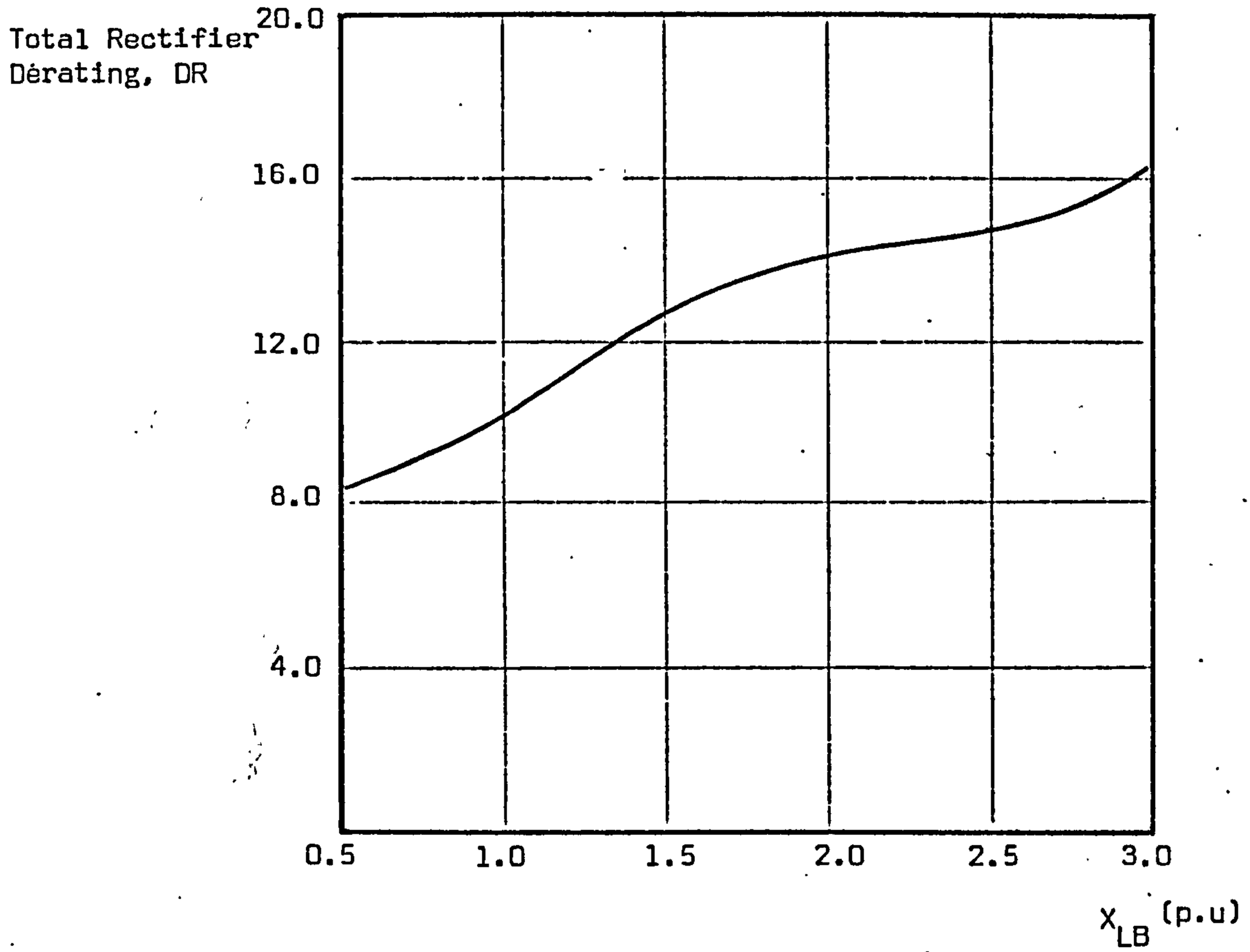

Figure 3.18 Variation of total rectifier derating with X_{LB}

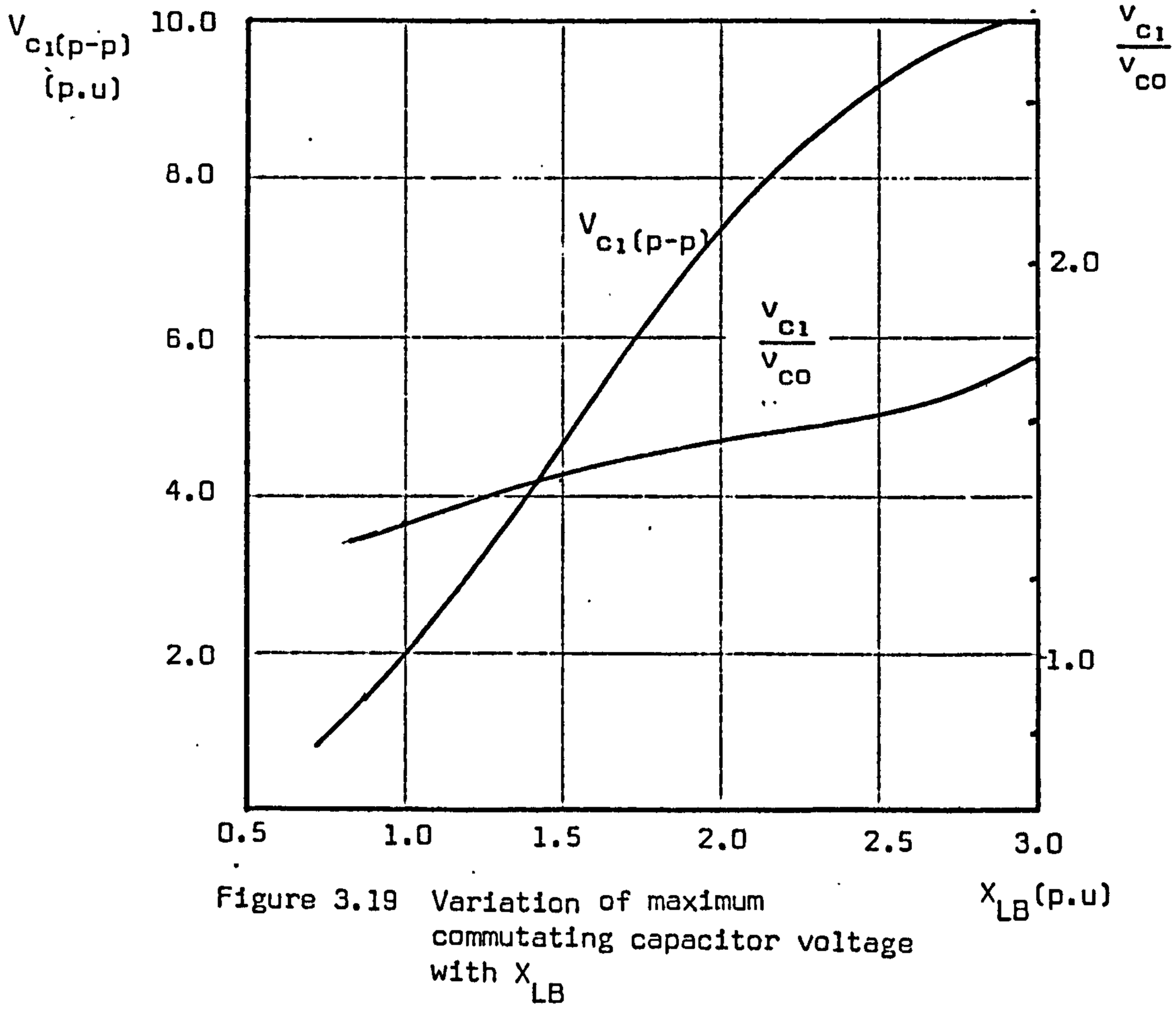

Figure 3.19 Variation of maximum commutating capacitor voltage with X_{LB}

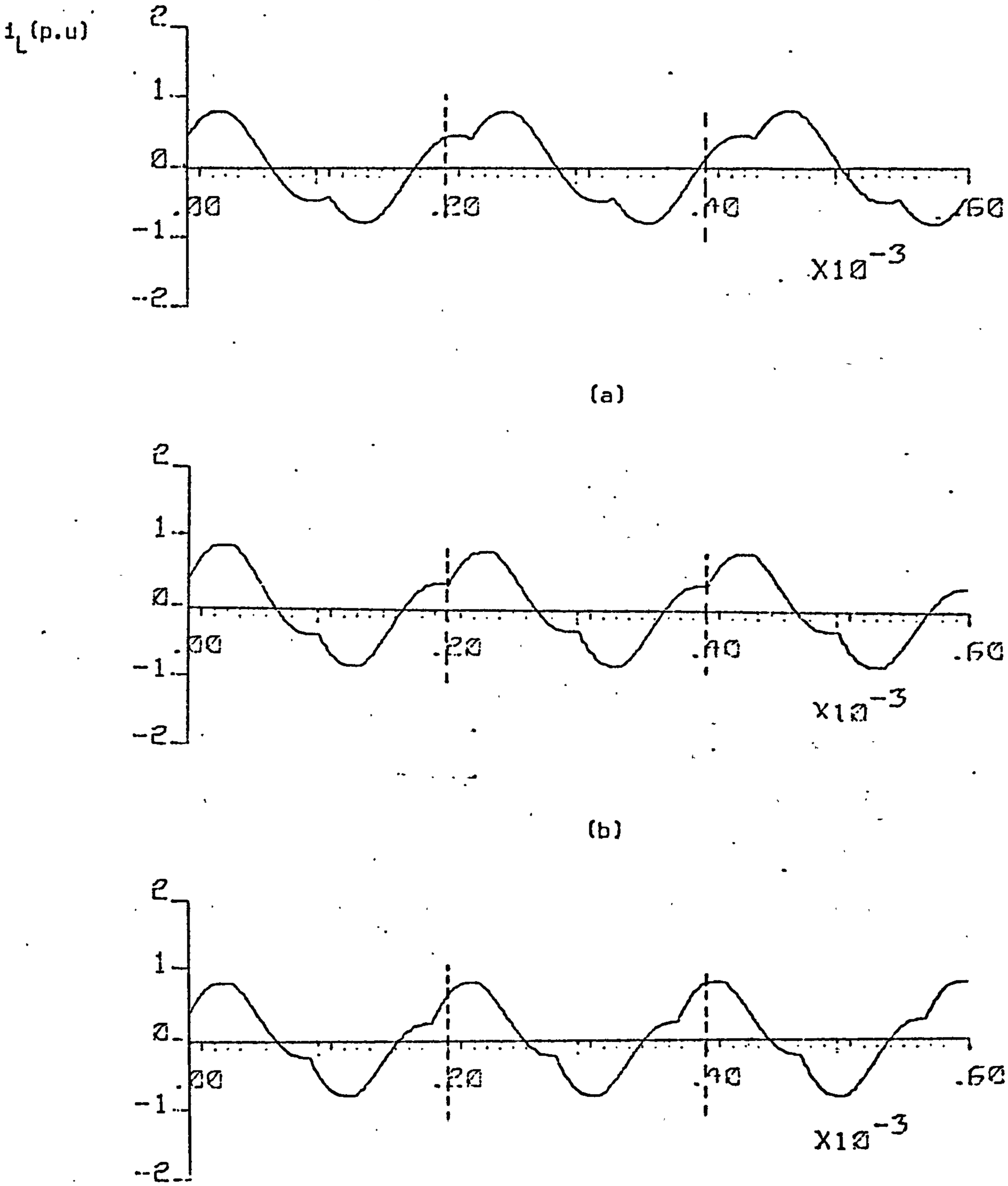

Figure 3.20 Variation of the output current waveform during a heating cycle

a - at the load condition C

b - at the load condition A

CHAPTER 4

THE LOW-FREQUENCY CYCLOINVERTER

The series 3-phase to single-phase cycloinverter of Figure 4.1 exhibits operational characteristics dependent upon the output frequency. This chapter is confined to an investigation of these characteristics, as applied to induction heating applications at low operational frequencies of around 120-450 Hz.

Following a discussion of the general principles and the theory of operation of both full- and half-bridge versions, the inverter operation is described quantitatively, by employing various techniques including steady-state harmonic considerations and a transient analysis. The former is pursued basically to investigate the effects of the variations of various design parameters on the overall circuit performance, and thereby to provide the information needed for an optimisation investigation. The transient analysis is performed by establishing a complete digital simulation of the cycloinverter, and is needed for an examination of the inverter behaviour under power control and varying load conditions when the harmonic analysis is inapplicable.

After an introduction to the parameters needed for a description of the device performance, the inverter operation is investigated for variable output power and frequency modes. Finally, a criteria is established for the selection of the commutating circuit components to produce an optimum performance

when supplying an induction heating load with stable characteristics.

4.1 Principle of Operation

In Figure 4.1, thyristors S1, S3 and S5 form a positive group giving an output when the corresponding supply voltage is the most positive,and thyristors S2, S4 and S6 a negative group giving an output when the corresponding voltage is the most negative. During inverter operation, the two groups are alternately turned on and sequenced from one phase to another as the voltage of that phase becomes either most positive or most negative. The firing sequence of the thyristors is shown in Figure 4.2, where the permissible firing range of each thyristor is, as shown, equal to $T_I/3$. A thyristor will only receive a firing pulse during its firing range, and when this arrives the thyristor turns on (assuming forward bias conditions) and conducts for a duration determined by the commutating circuit components. Clearly, if a thyristor in one group is turned on , while a thyristor in another group is still conducting,a short circuit occurs, and the conduction time of a given thyristor must inevtiably be less than $T_o/2$. A complete cycle of inverter operation may include 7 different operational modes; six of these arising since one - but only one- thyristor conducts at a time, with the 7th mode occurring when the thyristors are simultaneously all in a non-conducting state.

The inductor L and the capacitors C_1, C_2 and C_3 of Figure 4.1, together with the tuned load, form a series resonant circuit to provide the familiar series-type load commutation for the thyristors. Figure 4.3 shows typical circuit waveforms from a 150 Hz inverter, when the output current waveform (at triple the input frequency) is formed by the positive and negative current pulses supplied by each input phase, when the voltage of this is the most positive or the most negative respectively. Evidently,the input line current contains a component at the input frequency, which is responsible for the per phase input power.

Output power control of a 3-phase cycloinverter does not require any external power circuitry, and it is readily achieved by controlling the thyristor firing sequence. When the thyristor groups are gated to commutate alternatively between the most positive and the most negative phases, the full output power is developed, as the envelope of the voltage at the input to the thyristor blocks is always a maximum. If, however, a delay is introduced into the full output power sequence,the envelope of the input line voltage, and hence the voltage available for commutation, can be varied to provide output power control. In Figure 4.3 this delay angle (hereafter referred to as the firing or power control angle) is denoted by θ and is measured from the positive-going zero crossing of a given phase. To achieve full output power control, θ needs

to be varied through the range:

$$\theta_{min} < \theta < 180^{o} \qquad (4.1)$$

where the minimum power control angle θ_{min} is determined by the operational frequency. As is shown later, θ_{min} for 150 Hz operation is 60^{o}. The power control characteristics of the inverter depend upon the output frequency. At triple output frequencies a smooth power control can be achieved, whereas for output frequencies not an integral multiple of the input frequency (i.e. non-multiple output frequencies) the output power fluctuates around a mean value.

The half-bridge version of the cycloinverter is shown in Figure 4.4. Modifications made to the cycloinverter power circuit in forming this version do not affect the principle of commutation of the thyristors. One difference, however, is that thyristor S4 and diodes D1, D2, and D3 now perform the duty of the negative group thyristors S2, S4 and S6 of the full-bridge inverter. Hence, when developing output power, thyristor S4 is fired alternately with one of the thyristors of the positive group (i.e. S1, S2 and S3), in the order of their phase sequence. Obviously, due to the rectifying function of the diodes during conduction of thyristor S4, only the most negative phase supplies the input current.

Both the half-bridge and the full-bridge cycloinverters possess an inherent short-circuit protection ability. If a short circuit occurs, the power circuit functions as a bridge-

rectifier, so that the worst case duration of the short circuit is 10.0 ms and 6.66 ms for half- and full-bridge configurations respectively.

More detailed considerations of the operational characteristics of both types of cycloinverter are presented in later sections, after methods of analysis available for the study of these configurations have been established.

4.2 Theory of Operation

This section aims to develop methods of analysis for use in studying various aspects of both half- and full-bridge cycloinverters, as used in induction heating applications. Due to the nature of this application, the methods of analysis are required to be suitable for investigations under operating conditions of variable output frequency and power.

The methods of analysis presented here are:

1. Transient analysis.

and 2. Steady-state harmonic analysis

with each method offering certain advantages over the other, when some particular aspects of the circuit operation are investigated.

Besides the approximations and assumptions made specifically in each analysis, the following considerations are common to both:

1. The thyristors are effectively ideal switches, and the power circuit components are also ideal,
2. Input filtering is neglected,
3. The 3-phase input is balanced,
4. The induction heating load can be represented by its equivalent tank circuit, which is tuned to the output frequency.

4.2.1 Transient Analysis

4.2.1.1 Analysis of the full-bridge cycloinverter

The simplified power circuit diagram of the full-bridge cycloinverter is shown in Figure 4.5, with the switch S assumed to perform the duty of the thyristors in the actual circuit. The load circuit is connected to the phase voltages via S in the correct sequence and at a frequency equal to that required from the cycloinverter output, so as to simulate the thyristor conduction in the actual circuit. Using this model, an equivalent circuit diagram with switch S in position P1 and thyristor S1 conducting (the remaining thyristors are now open circuit) can easily be obtained, as shown in Figure 4.6. The circuit differential equations for operation in this mode can be derived using Kirchhoff's laws, as follows.

The 3-phase input voltages are:

$$v_1 = V_{1p} \sin w_I t$$

$$v_2 = V_{2p} \text{Sin } (w_I t - 2\pi/3)$$

$$v_3 = V_{3p} \text{Sin } (w_I t + 2\pi/3)$$

while from the input voltage loops,

$$v_1 - v_2 = \frac{1}{C} \int (i_{C1} - i_{C2})\, dt$$

$$v_2 - v_3 = \frac{1}{C} \int (i_{C2} - i_{C3})\, dt$$

$$v_3 - v_1 = \frac{1}{C} \int (i_{C3} - i_{C1})\, dt \qquad (4.2)$$

Applying the nodal current law to the floating neutral point O gives:

$$i_{C1} + i_{C2} + i_{C3} = - i_L \qquad (4.3)$$

while the instantaneous sum of the 3-phase line-to-neutral input voltage is zero, i.e.

$$v_1 + v_2 + v_3 = 0 \qquad (4.4)$$

Eliminating i_{C2} and i_{C3} from the above equations, and making the necessary substitutions yields:

$$v_{c1} = v_1 - \frac{1}{C}\int_0^t i_L \, dt \qquad (4.5)$$

From the output circuit loop,

$$L\,\dot{i}_L = v_{c1} - v_{co} \qquad (4.6)$$

Equation (4.6) holds when either thyristor S1 or thyristor S4 is conducting (i.e. switch S is in position P_1). When either thyristor S3 or S6 is conducting (i.e switch S is in position P_2) the corresponding equation is:

$$L\,\dot{i}_L = v_2 - v_1 + v_{c1} - v_{co}$$

and when thyristor S2 or S5 is conducting (i.e. switch S is in position P_3)

$$L\,\dot{i}_L = v_3 - v_1 + v_{c1} - v_{co} \qquad (4.7)$$

On the other hand, for all modes of operation:

$$v_{co} = \frac{1}{C_o}\int_0^t (i_L - i_{Lo}) \, dt \qquad (4.8)$$

and from the loop forming the tank circuit

$$L_o\,\dot{i}_{Lo} = v_{co} - R_o i_{Lo} \qquad (4.9)$$

By choosing the following state variables

$$Z_1 = v_{C1}$$

$$Z_2 = i_L$$

$$Z_3 = v_{CO}$$

$$Z_4 = i_{LO}$$

the circuit differential equations (equations (4.4) to (4.9))

can be rewritten as:

$$\dot{Z}_1 = \dot{v}_1 - Z_2/3C$$

$$\dot{Z}_2 = \frac{1}{L}(Z_1 - Z_3) \text{ when either S1 or S4 is on}$$

$$= \frac{1}{L}(v_3 - v_1 + Z_1 - Z_3) \text{ when either S2 or S5 is on}$$

$$= \frac{1}{L}(v_2 - v_1 + Z_1 - Z_3) \text{ when either S3 or S6 is on.}$$

$$\dot{Z}_3 = \frac{1}{C_O}(Z_2 - Z_4)$$

$$\dot{Z}_4 = \frac{1}{L_O}(Z_3 - RZ_4) \qquad (4.10)$$

The initial conditions at $t = T_s$ are:

$$Z_1 = V_{c1}$$

$$Z_2 = 0$$

$$Z_3 = V_{co}$$

$$Z_4 = I_{Lo}$$

From Figure 4.6 and equation (4.5), the instantaneous input line current i_1 is:

$$i_1 = i_{c1} + i_L$$

$$= C\dot{V}_1 + \frac{2}{3} Z_2 \quad \text{when either S1 or S4 is on (switch position } P_1)$$

or

$$i_1 = i_{c1}$$

$$= C\dot{V}_1 - Z_2/3 \quad \text{when any of the remaining thyristors are on (switch positions } P_2 \text{ and } P_3)$$

or

$$i_1 = C\dot{V}_1 \quad \text{when all of the thyristors are OFF. (Switch position } P_0).$$

Similarly, the equations for the currents i_2 and i_3 in the input lines 2 and 3 are:

i_2	i_3	Switch position
$C\dot{v}_2 - Z_2/3$	$C\dot{v}_3 - Z_2/3$	P_1
$C\dot{v}_2 + \frac{2}{3} Z_2$	$C\dot{v}_3 - Z_2/3$	P_2
$C\dot{v}_2 - Z_2/3$	$C\dot{v}_3 - \frac{2}{3} Z_2$	P_3
$C\dot{v}_2$	$C\dot{v}_3$	P_0

(4.11)

The voltages across the circuit thryistors are:

$v_{S1,S4}$ (line 1)	$v_{S3,S6}$ (line 2)	$v_{S2,S5}$ (line 3)	Switch Position
0	$v_2 - v_1$	$v_3 - v_1$	P_1
$v_1 - v_3$	0	$v_3 - v_2$	P_2
$v_1 - v_3$	$v_2 - v_3$	0	P_3
$Z_1 - Z_3 - L\dot{Z}_2$	$v_2 - v_1 + Z_1 - Z_3 - L\dot{Z}_2$	$v_3 - v_1 + Z_1 - Z_3 - L\dot{Z}_2$	P_0

(4.12)

4.2.1.2 Transient analysis of the half-bridge cycloinverter

Clearly, the equivalent circuit of the half-bridge inverter during a particular mode is the same as that of the low-frequency full-bridge cycloinverter in the corresponding mode, and the model described in Figure 4.5 is therefore fully applicable. However, the sequence of the modes of the inverter operation (i.e. the sequence of the switching action of S) is changed. Moreover, an additional constraint is imposed on S, so as to ensure connection of only the most negative phase to the load circuit, in order to supply the negative output current pulse. If a phase crossover occurs when a negative output current pulse is flowing, an instantaneous changeover to the corresponding switch position is assumed, so as to simulate the takeover of the output current by the diode in the phase with the most negative voltage.

From the considerations just outlined, it is therefore possible, by redefining the functions of the switch positions, to adapt the differential equations of the full-bridge inverter to the half-bridge. The new functions of the switch positions are:

P_1 to simulate the conduction of S1 or S4 and D1

P_2 to simulate the conduction of S2 or S4 and D2

P_3 to simulate the conduction of S3 or S4 and D3

(4.13)

whereas P_o corresponds to the nonconducting state of all circuit semiconductors.

For the sake of clarity, the digital simulation of the cycloinverter based on the transient analysis developed here is presented in Chapter 6.

4.2.2 Steady State Harmonic Analysis

Although the steady-state performance of a cycloinverter can be more rapidly and easily investigated via a harmonic analysis[81,82] than through a full computer study, application of the harmonic analysis is unfortunately restricted to those modes of operation which produce a continuous output current. When the output current is discontinuous, none of the circuit quantities can readily be expressed by a Fourier series.

The harmonic content of the power circuit voltages and currents depends on:

1. the frequency conversion ratio.
2. the power control angle θ.
3. the commutating component values.
4. the tuning conditions and the selectivity of the tank load.

Unfortunately, when studying the effect of the above parameters on the circuit performance, the harmonic analysis is only partly useful, since some values within the range of the possible para-

meter variations will produce a discontinuous output current.

In this section, the harmonic analysis is pursued by first establishing a harmonic model for the cycloinverter output circuit. The Fourier series expansion of the driving function is subsequently evaluated, and the relation between the output quantities and the driving function for a given harmonic is derived. In the final part, a more complete harmonic model of the cycloinverter is developed.

4.2.2.1 Equivalent circuit

In the simplified power circuit diagram of Figure 4.5, the potential of point A with respect to the neutral v_{na}, has the waveform shown in Figure 4.7a. By applying Thevenin's theorem, the output circuit can be further simplified, without affecting any of the output quantities, to the equivalent form shown in Figure 4.7b.

Obviously, if a Fourier series expansion of the driving voltage v_{na} is available, it is a relatively easy task to calculate the output voltage and current.

4.2.2.2 Fourier series expansion of the driving voltage, v_{na}

The driving (input) voltage v_{na} of the equivalent output circuit exhibits the characteristics of a time-dependent source voltage, with a *beat frequency* related to the input and output

frequencies. Although at some non-multiple output frequencies the beat period may be equal to a large number of input cycles, for multiple output frequencies v_{na} can be fully described through a single input cycle. For triplen output frequencies, at which balanced conditions of operation occur, the period of v_{na} further reduces to one third that of the input cycle (i.e. $T_I/3$).

Besides the difficulty of establishing the periodicity, a further problem encountered in employing a harmonic analysis with a non-multiple output frequency is that some inaccuracies are unavoidably introduced into the analysis. As mentioned earlier, the harmonic analysis holds for continuous (or approximately continuous) output current, but at non-multiple frequencies the output current of the inverter is never entirely continuous. As is explained more explicitly later, because the waveform of v_{na} depends on the power control angle θ, the harmonic content of the output current and hence its damped resonant frequency also depend on θ. However θ is not constant for non-multiple output frequencies, so that some discontinuities in the output current are unavoidable, and the accuracy of the analysis is related to the duration of these discontinuities. In fact, the difference in the actual* and the assumed value of v_{na} during these intervals of zero output current is the cause of

---

* When the output current is zero, v_{na} is given by:

$$v_{na} = v_1 + (v_{c1} - v_o)$$

where both v_{c1} and v_o are unknown.

the error illustrated in Figure 4.8. Evidently, a high output circuit selectivity accentuates the deterioration in the accuracy of the analysis, because it causes a high v_{c1}. Briefly, the error introduced by a discontinuous output current increases with both the duration of the discontinuity and the selectivity of the commutation circuit.

For the sake of convenience in establishing the periodicity, and in achieving a satisfactory accuracy, and also because it is a commonly-encountered output frequency, the harmonic analysis of v_{na} is performed at $f_o = 3\ f_I$. The variation of the harmonic content of v_{na} with θ is shown in Figure 4.9. As expected, the fundamental component at the output frequency is a maximum when $\theta = 60^o$, corresponding to the maximum output power, and since an increased θ produces a discontinuous output current, θ is fixed at this value in the following analysis.

Clearly, the differences in employing the harmonic analysis for the half- and the full-bridge inverters stem from the different driving voltage waveforms they experience. However, at the particular operating condition of $f_o = 3\ f_I$ and $\theta = 60^o$ the waveform of v_{na} is the same for both versions.

4.2.2.3 Analysis of the harmonic equivalent circuit

Since the harmonic equivalent circuit of the cycloinverter output circuit is similar to that of the sine-wave inverter circuit analysed in Chapter 3 (as both employ series commutation),

the analysis can be performed in a analogous manner.

The Fourier series expansion of v_{na} is:

$$v_{na} = \sum_{n=1,3,5}^{\infty} \sqrt{2}\, V_{na} \mathrm{Sin}\,(n\, w_o\, t + \alpha_n) \qquad (4.14)$$

and since the total input impedance of the equivalent circuit at a frequency nf_o can be expressed as:

$$Z_n = |Z_n|\, e^{j\sigma_n}$$

the output current i_L is:

$$i_L = \sum_{n=1,3,5}^{\infty} \sqrt{2}\, I_{Ln} \mathrm{Sin}\,(n\, w_o\, t + \beta_n) \qquad (4.15)$$

where:

$$I_{Ln} = \frac{V_{na}}{|Z_n|}$$

and

$$\beta_n = \alpha_n - \sigma_n$$

The tank-load voltage v_{co} is:

$$v_{co} = \sum_{n=1,3,5}^{\infty} \sqrt{2}\, V_{con} \sin\,(n\, w_o\, t + \rho_n) \qquad (4.16)$$

where

$$V_{co_n} = I_{Ln} \quad |Z_{Ln}|$$

and

$$\rho_n = \beta_n - \phi_n$$

Z_{Ln} = impedance of the tank load circuit

$$= |Z_{Ln}| \; e^{j\phi_n}$$

The heating-coil current i_{Lo} is:

$$i_{Lo} = \sum_{n=1,3,5}^{\infty} \sqrt{2} \; I_{Lon} \; \text{Sin} \; (n \; w_o \; t + \zeta_n) \qquad (4.17)$$

where

$$I_{Lon} = \frac{V_{con}}{R_o \sqrt{1 + Q_L^2 \; n^2}}$$

and

$$\zeta_n = \rho_n - \tan^{-1} Q_L$$

The harmonic equivalent circuit used in this analysis is confined to the cycloinverter output circuit and cannot be employed to investigate the input conditions of the inverter.

4.2.2.4 Harmonic model of the cycloinverter

The harmonic equivalent circuit of Figure 4.7. although very useful in evaluating the harmonic content of the output quantities, does not provide information on the input conditions of the cycloinverter. For instance, with this model the distortion components of the input current cannot be calculated, although this information is needed in any optimisation considerations of the inverter performance and in designing a suitable input filter. Nevertheless, from a knowledge of the harmonic content of the output current, it is possible to develop a complete model of the cycloinverter power circuit.

It has been stated[83] that any converter operating from a 3-phase or a single-phase a.c. source, drawing or supplying balanced currents, can be represented by harmonic models. The generalised input frequency model of a converter, shown in Figure 4.10a, consists of a generated voltage $E_1 \angle \gamma_1$ in series with an impedance at fundamental frequency Z_1. (The generated voltage is present only when the load is active, e.g. a motor load). The source can be represented by the line-to-neutral voltage $V_1 \angle 0.$, in series with the source reactance X_{s_1} at the source frequency.

For the harmonic currents generated in the converter system, the source presents a reactance X_{sh} which is a function of the harmonic frequency. Thus a harmonic model comprising a harmonic current source I_{1h} and a source reactance X_{sh} (Figure 4.10b) is

valid only at that single frequency, and separate models (with different values of I_{1h} and X_{sh}) must be used for each harmonic frequency. Therefore for a complete harmonic model of the cycloinverter, the parameters Z_1 and I_{1h} (since E = 0) of the inverter need to be known.

The cycloinverter equivalent circuit at the source frequency is shown in Figure 4.11, in which X_s is neglected. Clearly, knowing the fundamental or source frequency component of the line thyristor currents I_{s11}, I_{s21}, I_{s31} (for I_{skn} is the nth-harmonic current in line k), the input line currents can be calculated from:

$$I_{k1}\angle\psi_{k1} = I_{sk1}\angle\delta_{sk1} - V_1 w_I C\angle\pi/2 \qquad (4.18)$$

where k = 1, 2, 3, to give I_{11}, I_{21} and I_{31} respectively. Thus the per phase cycloinverter input impedance at the source frequency (i.e. Z_{I1}, Z_{I2}, Z_{I3}) is given by:

$$|Z_{Ik}|\angle\lambda_k = \frac{V_1}{I_{k1}\angle\psi_{k1}} \qquad k = 1, 2, 3 \qquad (4.19)$$

and the source frequency harmonic model of the cycloinverter may be redrawn as in Figure 4.12a. When the cycloinverter is operating at balanced operating conditions (i.e. $f_o = 3f_i$, $9f_i$ etc), the equivalent circuit can be reduced to the single phase model of Figure 4.12b, since for this case

$$I_{11} = I_{21} = I_{31}$$

The harmonic model of the cycloinverter at frequencies other than the input frequency can be developed, by applying the concept illustrated above in the generalised case of Figure 4.10. In so doing, the harmonic model of the cycloinverter is assumed of the form shown in Figure 4.13. The distortion components of the input line current I_{kh} are calculated by considering the line thyristors (i.e. S1 and S4; S3 and S6; S2 and S5) as sources of distortion currents, and the cycloinverter harmonic equivalent circuits are hence redrawn as in Figure 4.14, where the source reactance X_{sh} at a distortion frequency w_h is neglected. Examination of Figure 4.14 indicates that:

- The distortion components of the thyristor currents which do not flow through the output circuit (i.e. S1 is open circuit at these frequencies) appear fully in the input lines, hence

$$I_{kh'} \angle \psi_{kh'} = I_{skh'} \angle \delta_{skh'} \qquad (4.20)$$

since

$$I_{ckh} = 0.$$

where: k = 1, 2, 3 and subscript h' denotes distortion harmonics which do not appear at the output.

- At output frequency harmonics (i.e. at triple input frequencies, since $f_o = 3\ f_I$), S1 is closed, and assuming balanced operating conditions there is no current circulation around the input loops. Hence, at these frequencies,

$$I_{kh} = 0.$$

In the considerations outlined above, the harmonic content of the thyristor currents are assumed known. In fact, knowing the sequence of thyristor conduction and the harmonic content of the output current, the harmonics of the thyristor currents can be calculated as described in Section* 5.2.3.

Nevertheless, calculating the harmonic content of the input line current by first determining the harmonic content of the thyristor currents, is not the easiest way of tackling the problem. A preferable technique is first to calculate the instantaneous variation of the output current i_L, via a harmonic analysis. The relations derived during the transient analysis are then employed to find the instantaneous input line current, and a subsequent numerical analysis is conducted to determine the harmonic content.

However, one significant advantage of the former method is that its application is not limited to the assumptions of the harmonic analysis, so that it can be employed for all operating

---

* In Section 5.2.3, the method is described for high frequency operation; nevertheless it is also fully applicable at the frequencies concerned here.

conditions for which the output current harmonics are available.

4.2.2.5 Performing the harmonic analysis

Examination of the variation of the harmonic content of v_{na} with θ shown in Figure 4.9 indicates that to achieve a sufficiently close approximation to the time-domain waveform, at least the first 11 harmonics need to be considered. On the other hand, the analysis may be required to be performed several times, to enable a full study to be made of the effect of differing design values on the inverter performance. Application of the analysis therefore necessitates use of a computer.

The flow chart of a computer program prepared for this purpose is given in Figure 4.15, where after calculating the Fourier components of v_{na} for a given θ and f_o, the tank load impedance Z_{Ln}, the equivalent circuit input impedance Z_n and output current I_{Ln}, together with the tank-load voltage V_{con} and current I_{Lon}, are calculated for each harmonic, as described by equations (4.14 - 4.17). Subsequently, harmonics of the input line current are obtained by first calculating their instantaneous values and then performing a numerical Fourier analysis. In the final part of the program, various performance parameters of the cycloinverter (described in the following section) are calculated, and the circuit quantities

of interest are plotted via a graph-plotting routine and obtained numerically through the line printer. The program is prepared to enable the design parameters to be easily varied at will.

The computation time of the program for a single set of design variables is extremely short in comparison with that of the digital simulation program, being only about 15 mill units instead of 200 mill units. This illustrates well the prime advantage of the harmonic analysis over the transient analysis.

4.2.2.6 Comparison of the results of the harmonic and transient analysis

The computed waveforms of the various circuit quantities, obtained by both a harmonic and a transient analysis of the same cycloinverter power circuit are given in Figure 4.16a and 4.16b respectively. The close agreement between the two sets of results partly justifies the simplifying assumptions made in the two theoretical approaches to the cycloinverter and confirms also the accuracy of the computer programs produced.

4.3 Performance Parameters

4.3.1 Full-bridge cycloinverter

Output power

The total cycloinverter output power is given by:

$$P_T = \sum_{n=1,3,5}^{\infty} I_{Ln} V_{con} \cos \phi_n \qquad (4.22)$$

whereas the useful power is:

$$P_o = I_{L_1}^2 R_{eq} \qquad (4.23)$$

Input power factor

The input power factor is:

$$PF_I = \frac{P_I}{VA_I}$$

while for balanced operation

$$VA_I = 3 V I_1 \qquad (4.24)$$

where I_1 is the r.m.s. input current in line 1. As the inverter losses are neglected

$$P_I = P_T$$

The total input power to the cycloinverter P_I, can also be calculated from:

$$P_I = 3\, I_{11}\, V_1 \cos\psi_1 \qquad (4.25)$$

where I_{11} is the source frequency component of the input current.

On the other hand, when assessing the proportion of the input volt amperes converted into useful output power, the following definition of PF_I is more useful

$$PF_I = \frac{P_o}{VA_I} \qquad (4.26)$$

VA Ratings of the commutating components

The volt ampere rating of the commutating inductor is

$$VA_L = \sum_{n=1,2,3}^{\infty} I_{Ln}^2\, X_L\, n \qquad (4.27)$$

while for the commutating capacitors

$$VA_C' = \sum_{n=1,2,3}^{\infty} I_{Ln}^2\, X_C/n$$

Since the commutating capacitors also carry a component of current at the source frequency, their total VA rating is:

$$VA_C = VA'_C + \frac{V_{LN}^2}{3X_C} \qquad (4.28)$$

Assuming the inductor and the capacitor ratings to be weighted equally, the total commutating component VA rating is:

$$VA_T = \sum_{n=1,2,3}^{\infty} I_{Ln} \left(X_L n + \frac{X_C}{n}\right) + \frac{1}{3X_C} \qquad (4.29)$$

Thyristor derating

As defined in equation (3.12), the thyristor derating is

$$DS = \frac{V_S \times I_S}{P_o} \times \text{number of thyristors} \qquad (4.30)$$

Under balanced operating conditions each thyristor has a duty cycle of 1 in 6, or 1/6. Hence the r.m.s. thyristor current I_S is:

$$I_S = \frac{I_L}{\sqrt{6}} \qquad (4.31)$$

The peak thyristor voltage V_S (at forward or reverse bias conditions, whichever is the greater), occurs just before a thyristor is fired (while the output current is still zero), hence:

$$V_S = v_{c_1}(t_s) - v_{co}(t_s) \tag{4.32}$$

where the instantaneous commutating capacitance voltage is approximately

$$v_{c_1} = \sum_{n=1,3,}^{\infty} \sqrt{2}\, I_{Ln} \frac{X_C}{n} \cos(n w_o t + \beta_n) \tag{4.33}$$

Substituting v_{co} and v_{c1} from equation (4.16) and (4.33) in equation (4.32) results in

$$V_S = \sum_{n=1,3,}^{\infty} \sqrt{2}\, I_{Ln}\left(\frac{X_C}{n} \cos\beta_n - Z_{Ln} \sin\rho_n\right) \tag{4.34}$$

so that with all the quantities involved in equation (4.30) now known, DS can be calculated.

4.3.2 Half-bridge cycloinverter

The definitions of the performance parameters of the half-bridge cycloinverter are the same as for the full-bridge inverter, with the exception of the rectifier derating which must be considered as follows.

Rectifier derating

Due to modifications made to the power circuit in forming the half-bridge version, both the number and the rating of the thyristors are changed. Clearly, thyristor S4 now has a duty cycle of $\frac{1}{2}$, while that of the remaining thyristors is $\frac{1}{6}$. The new thyristor rating is therefore:

$$DS = \frac{V_S}{P_o} \left[\frac{I_L}{\sqrt{6}} \times 3 + \frac{I_L}{\sqrt{2}} \times 1 \right]$$

or

$$DS = 1.93 \frac{V_S}{P_o} I_L \qquad (4.35)$$

As the diodes have a duty cycle of $\frac{1}{6}$, and encounter a peak voltage equal to that of the thyristors, the total diode derating is:

$$DD = \frac{V_S}{P_o} \times \frac{I_L}{\sqrt{6}} \times 3 \qquad (4.36)$$

and the total rectifier derating is:

$$DR = DS + DD$$

$$DR = 3.15 \frac{V_S \times I_L}{P_o} \qquad (4.37)$$

Per unit base values

For convenience, the cycloinverter performance parameters are all expressed in per unit terms, with base values:

R_{eq} - equivalent tank load resistance (at f_o) = 1 p.u.

w_o - per unit angular frequency base = 1 p.u.

X_L - inductive reactance $= \frac{w_o L}{R_{eq}}$

X_C - capacitive reactance

$$= \frac{1}{3 R_{eq} w_o C}$$

V_{LN} - r.m.s. line to neutral voltage = 1 p.u.

Hence p.u. current and power bases are:

$\frac{V_{LN}}{R_{eq}}$ - current base = 1 p.u.

$\frac{V_{LN}^2}{R_{eq}}$ - power base = 1 p.u.

4.4 Output Power and Frequency Control

This section examines briefly some important aspects of the cycloinverter performance, when undergoing output power and frequency control.

4.4.1 Output power control

4.4.1.1 Variation of X_L and X_C with θ

The dependence of the *ringing* frequency of the output current on θ has already been mentioned, and it may be demonstrated indirectly* by considering the variation of X_L and X_C with θ, for a continuous output current (i.e. $f_r = f_o$). For this purpose, the flow chart of the computer program for the harmonic analysis needs to be modified to the form shown in Figure 4.17. Here, for a given θ and X_L, X_C is made to vary around an initial value** and by monitoring its effect on the output current, the precise value for which $f_r = f_o$ is calculated.

---

* To enable the harmonic analysis to be employed

** Calculated by approximating the driving voltage v_{na} to a square waveform and by replacing the tank load by its equivalent resistor R_{eq}.

Figure 4.18 shows a series of curves obtained as a result of such computations performed for a 150 Hz full-bridge cycloinverter. These curves define the lowest value of X_C (i.e. the boundary values X_{CB}) which ensures a successful commutation for a given value of θ and X_L. Thus:

$$X_C > X_{CB} \rightarrow f_r > f_o \rightarrow \text{high circuit turn off time}$$

$$X_C = X_{CB} \rightarrow f_r = f_o \rightarrow t_{off} = 0$$

$$X_C < X_{CB} \rightarrow f_r < f_o \rightarrow \text{commutation failure} \qquad (4.38)$$

The curves in Figure 4.18 indicate that, for any given X_L and X_C, f_r decreases with decreasing θ. It follows that, if the design values of X_L and X_C are selected on the curve corresponding to θ_{min}, values of $\theta < \theta_{min}$ are not permitted, as these produce commutation failure during operation. In other words, in a 150 Hz full-bridge cycloinverter, θ cannot be varied arbitrarily to a value lower than θ_{min}, which is fixed by the design variables.

It should be emphasised that the curves in Figure 4.18 depend upon the operating frequency. As this increases, it is found that the curves approach the single curve shown dashed in Figure 4.18 which corresponds to a square-wave driving function. This arises since, although at low frequencies the

variation of the driving voltage waveform during a single commutation is considerable, at high frequencies it may be regarded as constant throughout the corresponding interval.

So far, the half-bridge cycloinverter has not been considered. Unfortunately, at low operational frequencies the cycloinverter performance is not satisfactory and (due to reasons explained in the following section) high values of θ produce short-circuit conditions. However, at high frequencies, the full-bridge considerations presented above are equally applicable to the half-bridge version.

4.4.2 Power control at multiple operation frequencies

When examining the cycloinverter performance during a power control mode of operation, the output current becomes discontinuous and the transient analysis needs to be employed.

Figures 4.19 to 4.21 show various circuit waveforms for a 150 Hz full-bridge cycloinverter, when delivering a reduced output power corresponding to values of θ of 90^{o}, 120^{o} and 150^{o}. These steady-state waveforms, which are obtained via the digital simulation, indicate that at this particular output frequency, and because of the balanced operating conditions, a smooth output power control can be achieved. As can be seen from these figures, the load voltage remains free of distortion components, for a wide range of output power variation, and

retains a reasonably good sine waveform. In this respect, θ can also be regarded as a load voltage control angle.

Variations of the harmonic content of the input line current, and the output current obtained from a numerical Fourier analysis of the steady-state digital simulation waveforms, are shown in Figures 4.22 and 4.23 respectively. As predicted in Section (4.2.2.4), the input line currents do not contain any harmonics at the output frequency or its triple multiples (i.e. 3 f_I and 9 f_I).

Variations of the output power P_o and the input power factor PF_I with θ are shown in Figures 4.23 and 4.24 respectively. The output power P_o drops sharply for values of θ between 90^o and 120^o, becoming only about 4% of its maximum at around 150^o (compared with condition (4.1), which predicts $P_o \rightarrow 0$ when $\theta \rightarrow 180^o$)

The occurrence of short-circuit conditions at high θ, when controlling the output power of the half-bridge cycloinverter was mentioned previously, and the reason for this is apparent when the circuit waveforms for $\theta = 90^o$ and 150^o (Figure 4.25a and 4.25b) are examined. Although when $\theta = 90^o$, the circuit waveforms closely resemble those of the full-bridge, for $\theta = 150^o$ the negative group thyristor S4 cannot turn off, and on firing a positive group thyristor short circuit conditions exist. The corresponding driving voltage v_{na} waveforms are also shown in the figure (with, for simplicity, v_{na} drawn for

a continuous output current) and these indicate that for values of $\theta > 90^{o}$, v_{na} loses its odd symmetry, resulting in the changes in the output current waveform which ultimately lead to the short-circuit condition. Although the permissible range of θ (and hence the power control range) can be extended up to a certain limit, by increasing the selectivity of the output circuit, this is not an acceptable alternative since it is at the expense of the circuit power rating.

Figure 4.26 shows the full-bridge cycloinverter waveforms for an output frequency $f_o = 6\ f_I$, under both full and reduced power operation ($\theta = 60^{o}$ and 90^{o}). As shown for $\theta = 90^{o}$, due to the varying voltages available for commutation of the positive and the negative group thyristors, the output current waveform is modulated*. However, due to the adequate separation of the sideband harmonics from the tuned *carrier* or output frequency, the filtering function of the tank load circuit becomes effective, and the distortion components of the output current do not appear at the load circuit.

---

* A quantitative analysis of this modulation is presented in the next chapter, for even higher operational frequencies.

It is significant to note that at this operational frequency a wide range of output power control is achieved within a narrower range of variation of θ, as distinct from the 150 Hz operation. (At $\theta = 90^{o}$, P_o is reduced to about 48% P_{omax}, whereas in the 150 Hz inverter the fall is to around 80% P_{omax}). This convincingly demonstrates that, in a low-frequency cycloinverter, the variation of output power with θ depends critically on the output frequency.

Half-bridge cycloinverter waveforms for the same operating conditions of $f_o = 6\ f_I$ and $\theta = 90^{o}$ are shown in Figure 4.27. At these frequencies, the dependence of the damped resonant frequency of the output current on the power control angle θ progressively diminishes, and thus enables the power control scheme to recover from the shortcomings experienced at 150 Hz operation.

For the sake of convenience, power control at non-multiple output frequency operation is examined after the following section.

4.4.3 Frequency control

Clearly, the output frequency of a cycloinverter can be made to vary by simply varying the firing frequency of the circuit thyristors. However, this significantly affects the device performance, since this is a function of the operational frequency.

When controlling the output frequency, non-multiple output frequencies inevitably occur. The static heating load model developed in Chapter 2 suggests that a typical operational frequency range is about 0.9 - 1.1 p.u. Figures 4.28a and 4.28b show some of the circuit waveforms of a 150 Hz cycloinverter for operational frequencies of 1.6, 1.25 and 0.8 p.u. As seen the output current is highly modulated and the *modulation depth* increases as the frequency conversion ratio decreases.

Clearly, for a non-multiple operational frequency, the value of θ is not constant but drifts. The value of θ which is referred to at these frequencies is, in fact, the minimum permissible value that it can take, i.e. θ_{min}. Examination of Figure 4.28 reveals that the actual value of θ lies within the range

$$\theta_{min} < \theta < \theta_{min} + 2\pi \frac{f_I}{f_o} \qquad (4.39)$$

which indicates the reason for a high modulation depth when f_o/f_r is low. Obviously, when the envelope frequency is low, which means the sidebands are close to the output frequency, the filtering function of the load circuit becomes less effective and the distortion components appear at the heating coil. The results in Figure 4.28 also indicate that -

- at non-multiple operational frequencies the overall inverter performance deteriorates, due to high distortion currents (sideband harmonic currents) circulating through the power circuit.

- as the output frequency departs from the base frequency (3 f_I) the maximum output power capability of the inverter drops.

- as a consequence of the two items above, the maximum input power factorof the cycloinverter is obtained with balanced operating conditions.

4.4.4 Power control at non-multiple operation frequencies

An investigation of the power control characteristics of the inverter at operational frequencies which are not a multiple of the input frequency is merely of academic interest, since the poor inverter performance at these frequencies is not sufficiently attractive for practical exploitation.

Figure 4.29 shows the variation of some of the full-bridge circuit waveforms with $\theta = 90^o$ and 120^o, for an output frequency of 1.25 p.u. Although for multiple output frequencies the maximum cycloinverter output power corresponds to a particular value of θ (for 3 f_I, 6 f_I and 9f_I to 60^o, 60^o and 40^o respectively), for all non-multiple output frequencies the maximum

output power occurs at $\theta = 30^{o}$.

4.5 Optimisation of the Cycloinverter Performance

In this section a criteria is established for selection of the commutating component values of a 150 Hz, full-bridge cycloinverter, to produce an optimum performance when supplying an induction heating load. Since the inverter is likely to be employed as a fixed frequency source, a load with stable characteristics (i.e. a continuous heating load) is assumed.

In selecting the design variables X_L and X_C, the following requirements are considered:

i) minimum possible output current harmonics,

ii) minimum circuit losses

iii) maximum possible input power factor

iv) minimum possible rectifier derating

v) minimum possible ratings for the commutating components

The parameters related to each of these items, with the exception of (ii), have already been presented. For a measure of this requirement the parameter

$$\frac{1}{(\text{output current distortion factor, } DF_{iL})^2}$$

is used, as suggested by equation (3.21).

The weighting of the different items was discussed in Section 3.5.1 in relation to the sine-wave inverter. In accordance with these considerations, items (ii), (iii), and (v) carry more weight for a low frequency, high power application than do the remaining items.

As was also mentioned previously, when designing a high frequency series commutation circuit an unnecessarily high circuit turn off time causes inefficient operation. The design values of X_L and X_C should therefore be searched for among those which make the damped resonant frequency of the output current pulse equal to the operational frequency. This,conveniently, permits the use of the harmonic analysis technique during the design.

The series of curves corresponding to the variation of X_C with X_L at different firing angles θ and presented in Figure 4.18, indicates that (as explained in Section 4.4.1.1) a set of design values selected for X_L and X_C when $\theta = \theta_{min}$, readily satisfy the successful commutation condition when $\theta > \theta_{min}$ In the following procedure θ_{min} is set to 60^o, to ensure optimim inverter performance when it is most needed, i.e. when the inverter is delivering maximum output power.

Variations of the output current waveform and its harmonic content with X_L (for $\theta = 60^o$) are shown in Figures 4.30 and 4.31,

respectively. As expected, the harmonic content of the load current improves considerably as X_L is increased, with the amplitude of the fundamental component increasing but that of the higher harmonics reducing.

Variations of the output power and the ratio $1/DF_{iL}^2$ (proportional to conduction losses per useful output power) with X_L are shown in Figure 4.32. Becuase of the low harmonic content of the output current and the low resistive impedance presented at the higher harmonic frequencies, it is found that

$$P_o \simeq P_T \qquad \text{for} \qquad X_L > 0.6 \text{ p.u.}$$

The variation of both the input and output power factors with X_L are shown in Figure 4.33. The high output power factor is again obviously due to a high tank load selectivity and a small harmonic content in i_L.

As X_L increases, the commutating circuit becomes increasingly underdamped, which, of course, causes high commutating component and thyristor ratings. Figure 4.34 shows the variations of P_o/VA_T and of 1/DS with X_L, and from these the values of X_L to produce the maximum output power per commutating component and thyristor rating respectively can be evaluated. The figure shows that

Max $[\frac{P_o}{VA_T}]$ occurs at around X_L = 0.5 p.u.

and

Max $[\frac{1}{DS}]$ occurs at around $X_L \simeq 0.6$ p.u.

By combining the information in the cycloinverter performance curves described above, it can be suggested that the best inverter performance corresponds to a compromise X_L of about 0.9 p.u. The corresponding X_c from Figure 4.18 is 1.03 p.u., although a slightly higher value of X_c = 1.08 p.u. is recommended for an increased commutation reliability to produce a slightly increased circuit turn off time. Some of the inverter performance parameters for the selected design are:

f_o = 150 Hz, $\theta = 60^o$, Q_L = 10

X_L (p.u)	X_c (p.u)	PF_I	P_o (p.u)	VA_T (p.u)	DS	PF_o
0.9	1.03	0.80	1.46	3.24	4.6	0.98

and the harmonics of the input line current and the output current are:

Harmonics (p.u) / Currents	1st[50 Hz for i_1 / 150 Hz for i_L]	3rd	5th	7th	9th	rms
i_1	0.52	0.0	0.28	0.14	0.0	0.6
i_L	1.21	0.16	0.05	0.03	0.01	1.22

As the 5th and 7th harmonics of the input current are respectively 46% and 22% of the fundamental amplitude, input filtering is required for most applications. A suitable filter and an appropriate design procedure are described in Chapter 7.

3-Ø MAINS

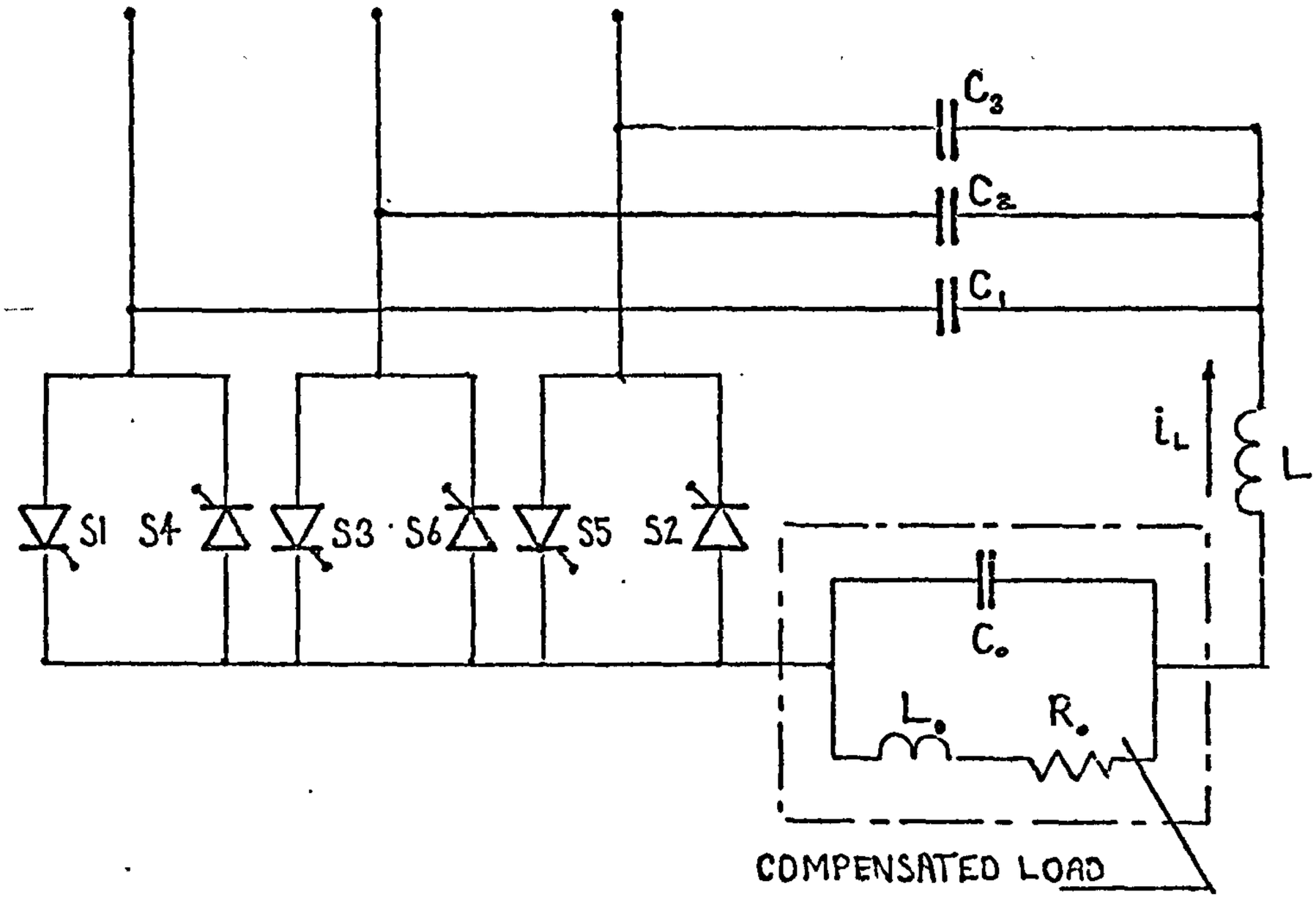

Figure 4.1 3-phase to single-phase, series commutated, full-bridge cycloinverter

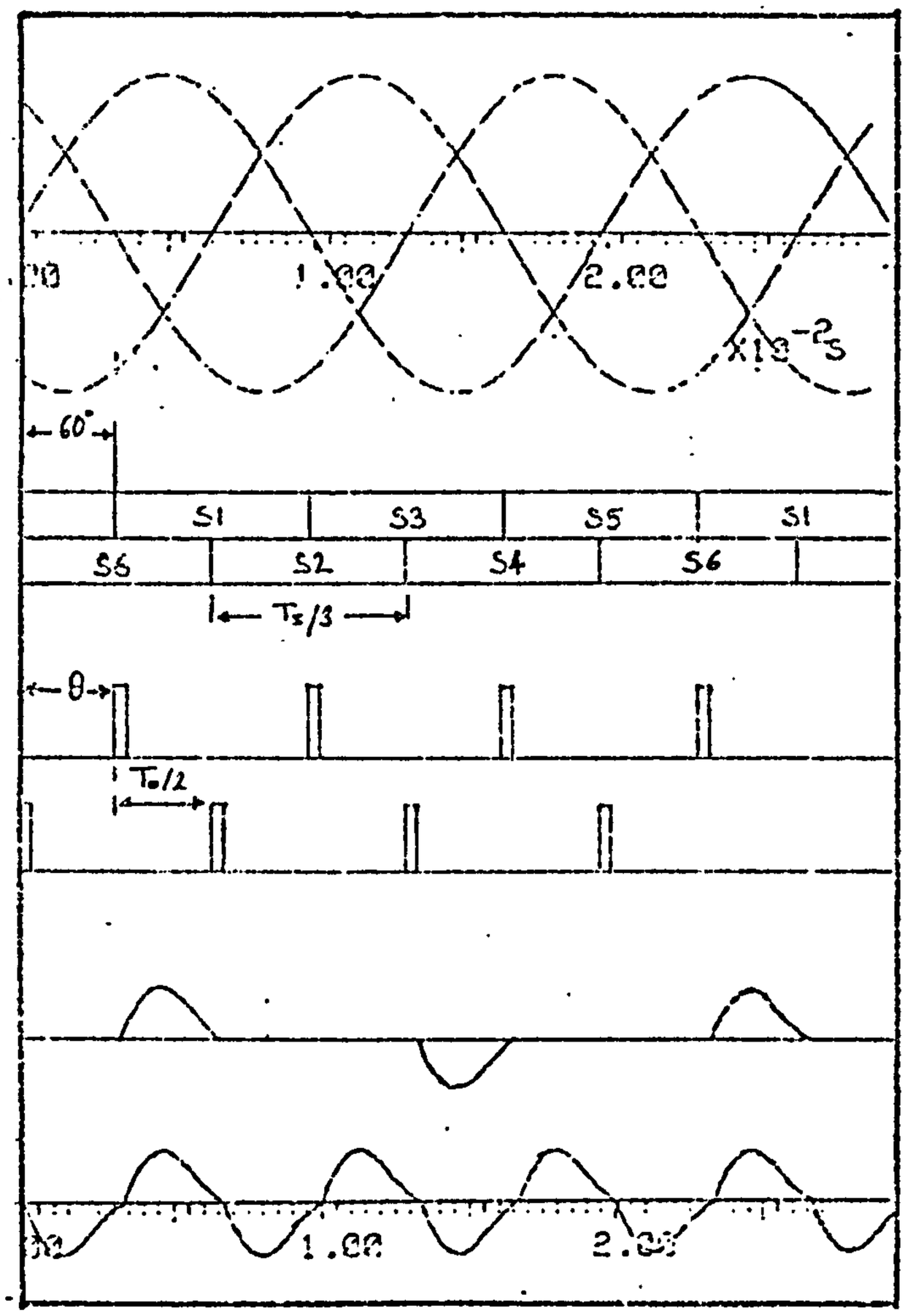

Figure 4.2 Firing sequence of the cycloinverter thyristors ($f_o = 3 f_I$)

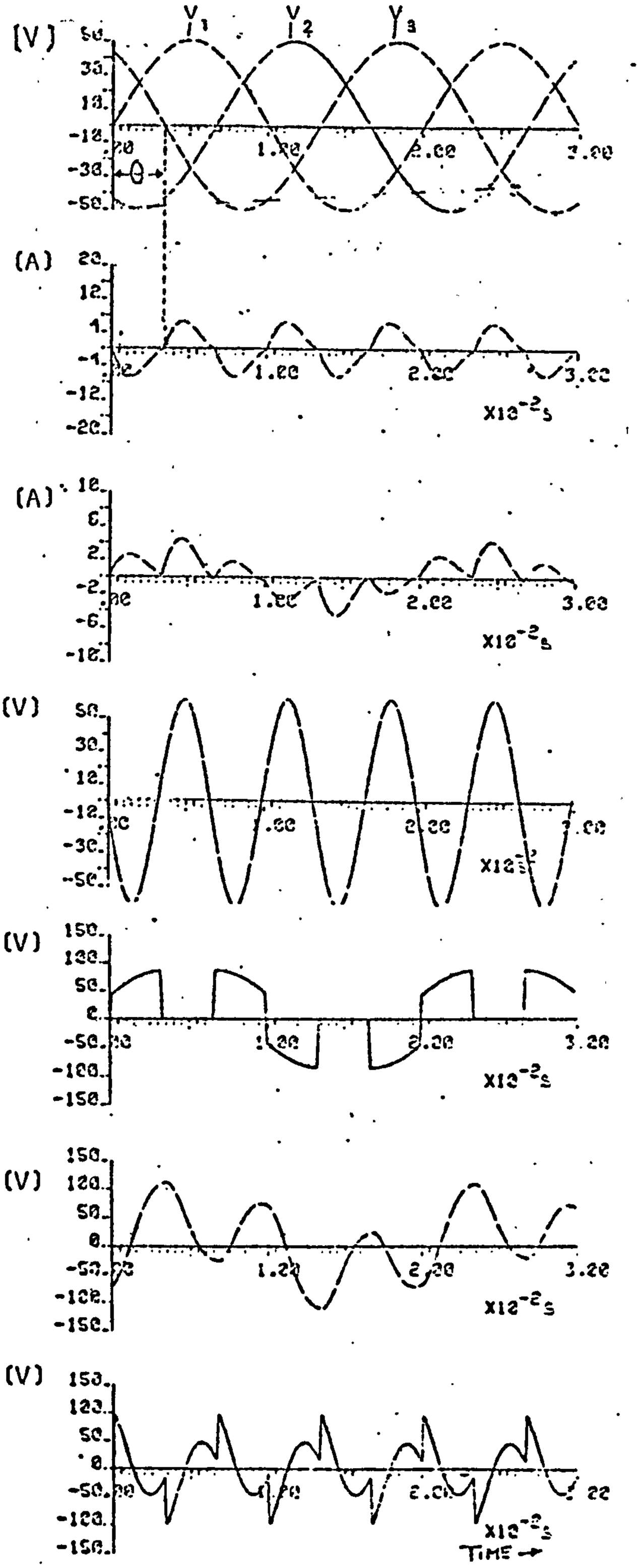

3-phase input

output current, i_L

input line current, i_1

tank-load voltage, v_{co}

thyristor voltage, v_{s1}

commutating capacitor voltage, v_{c1}

commutating inductor voltage, v_L

Figure 4.3 Full-bridge cycloinverter waveforms for full output power (f_o = 150 Hz, Q_L = 5)

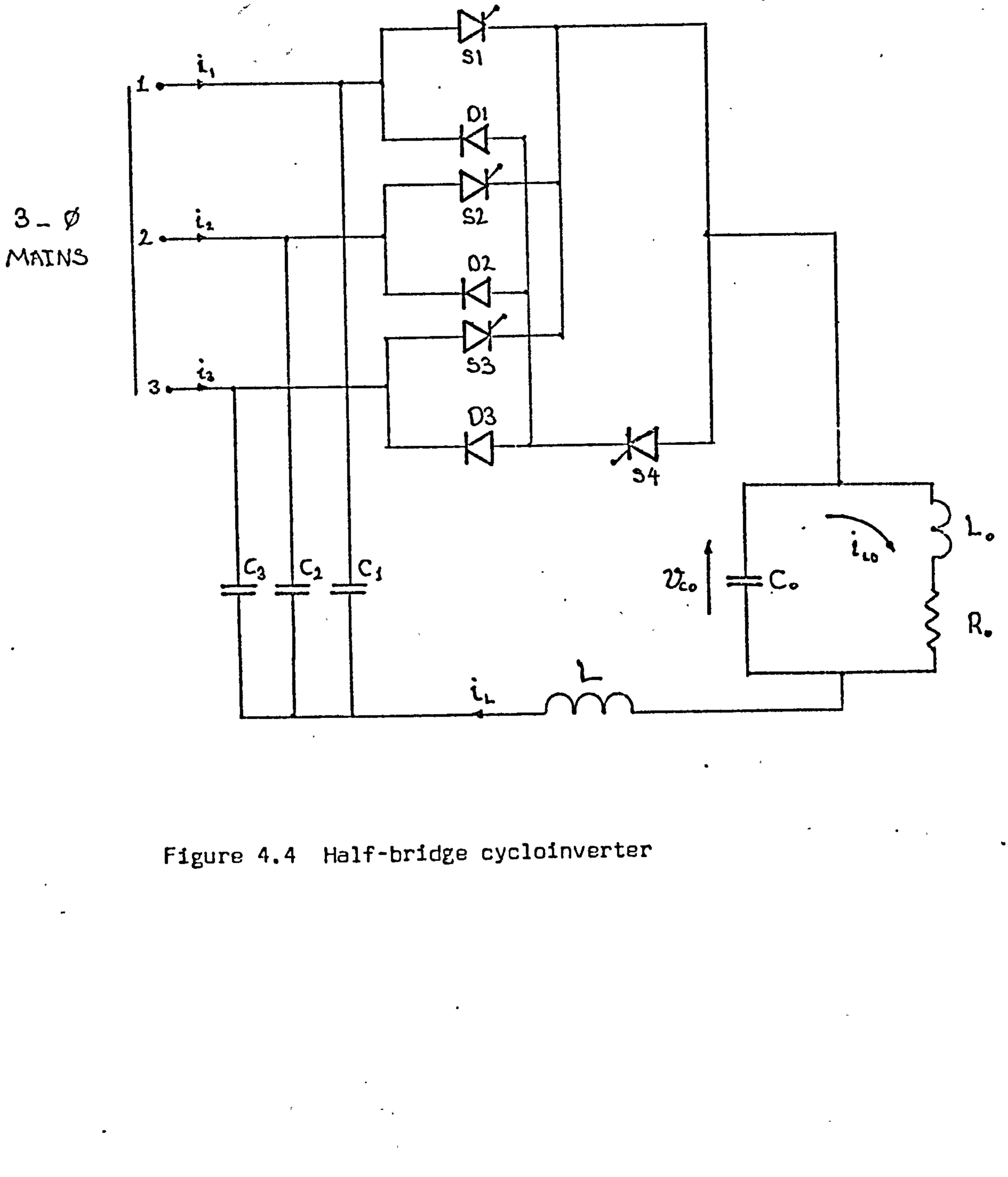

Figure 4.4 Half-bridge cycloinverter

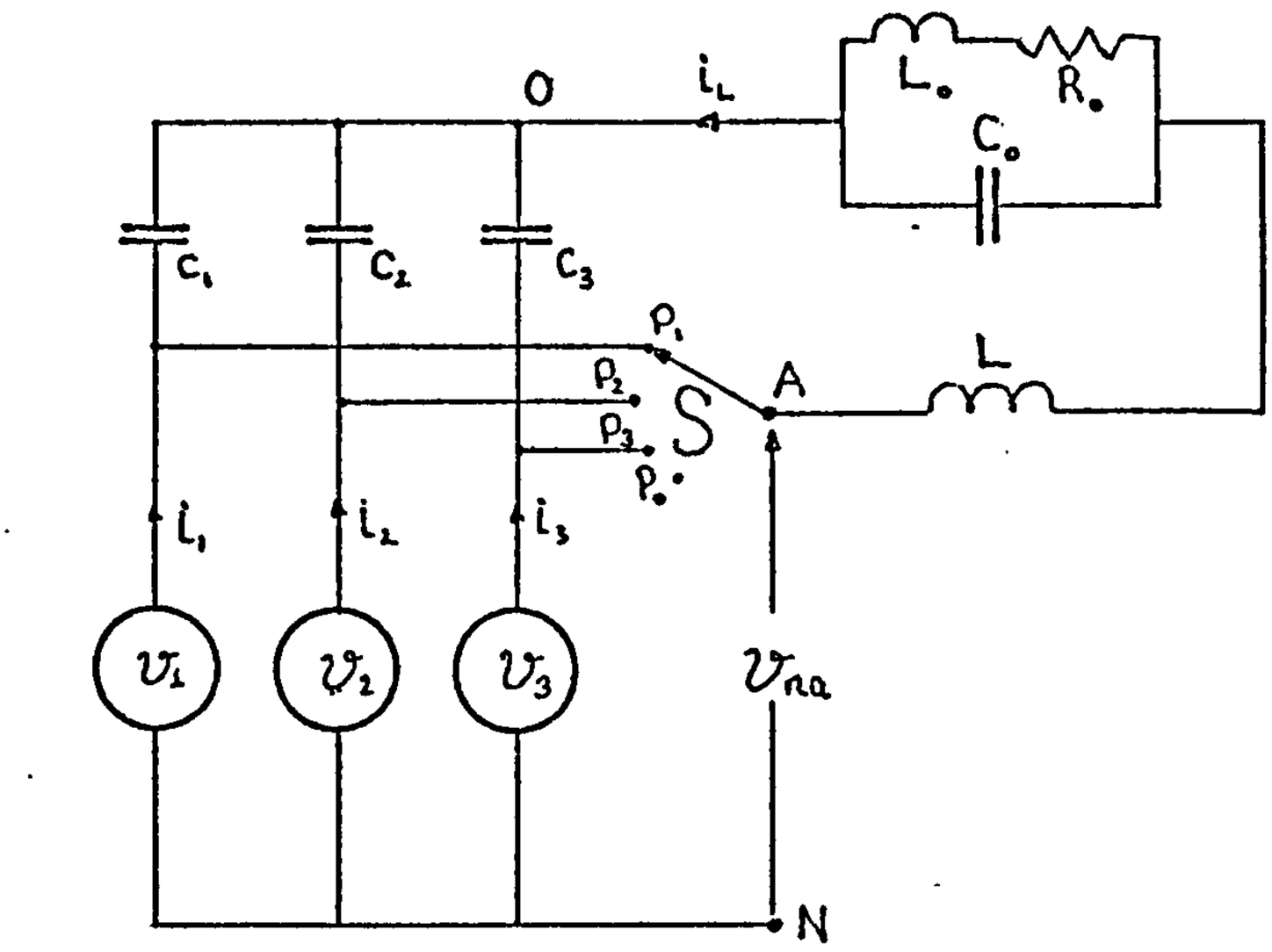

Figure 4.5 Simplified power circuit diagram of the cycloinverter

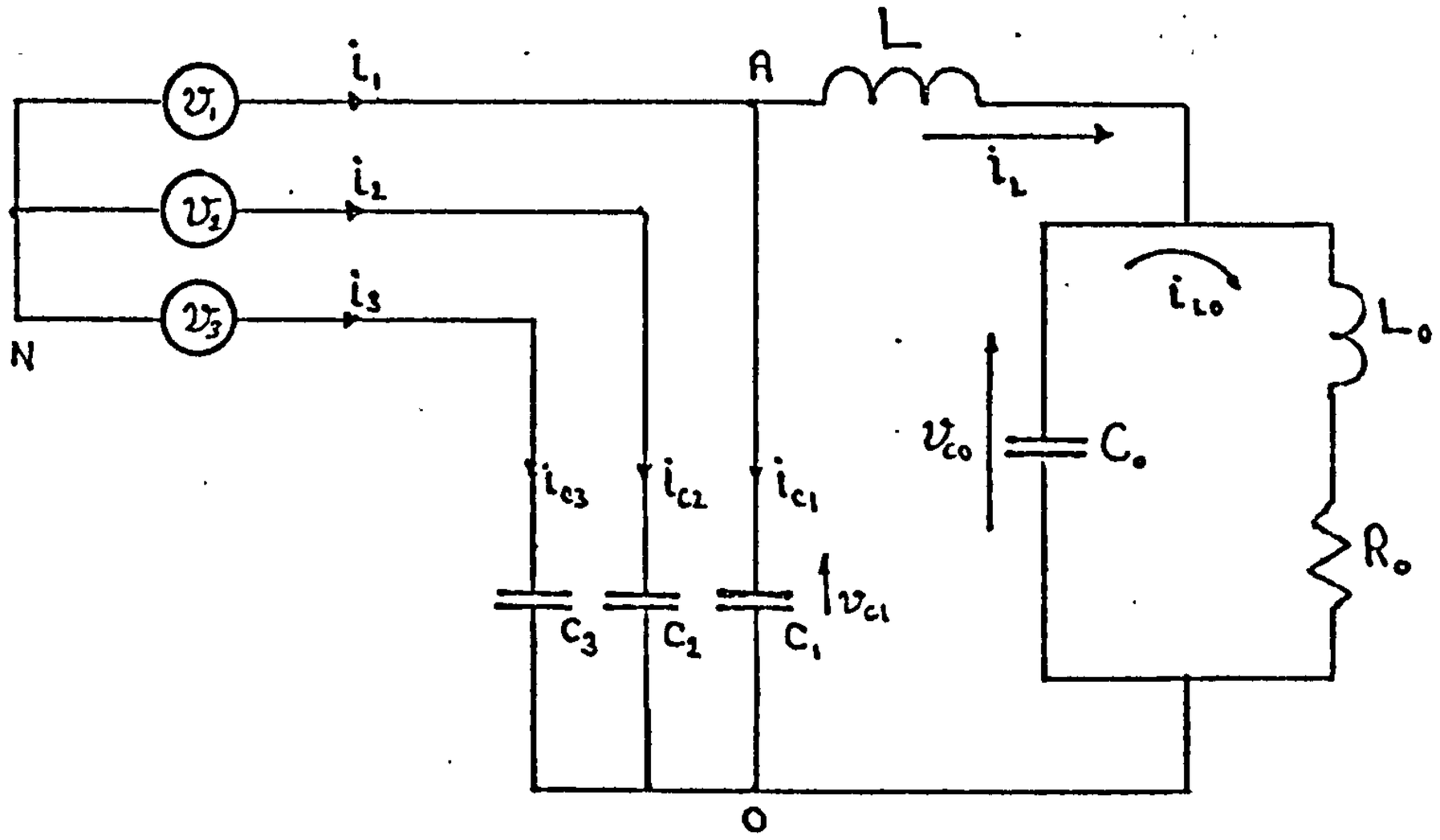

Figure 4.6 Equivalent circuit of the cycloinverter when thyristor S1 or S4 is conducting

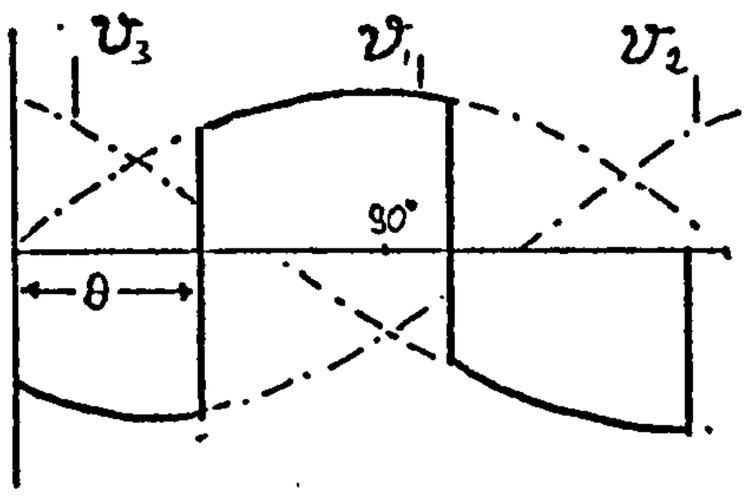

(a)

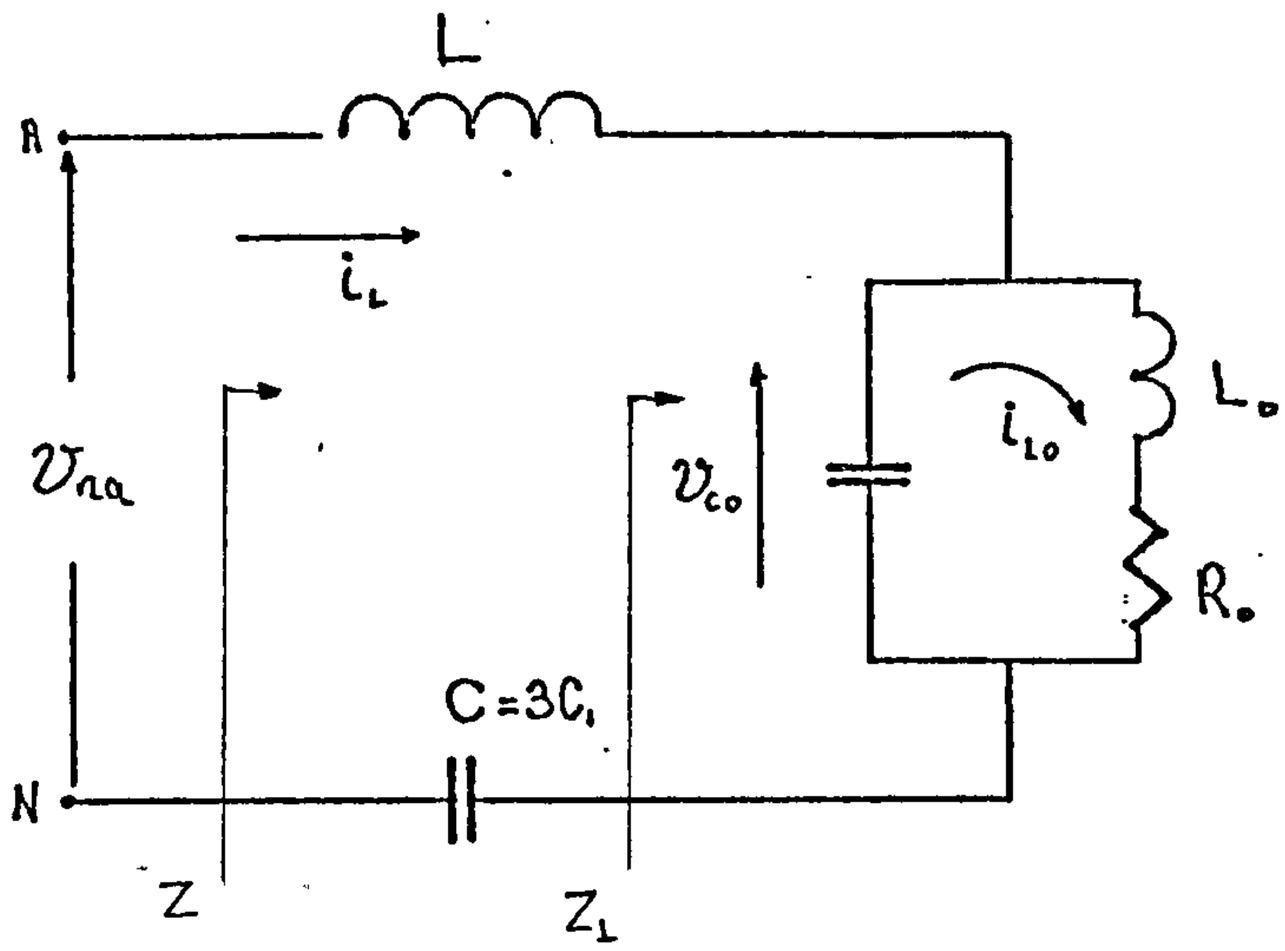

(b)

Figure 4.7 Equivalent circuit of the cycloinverter output circuit

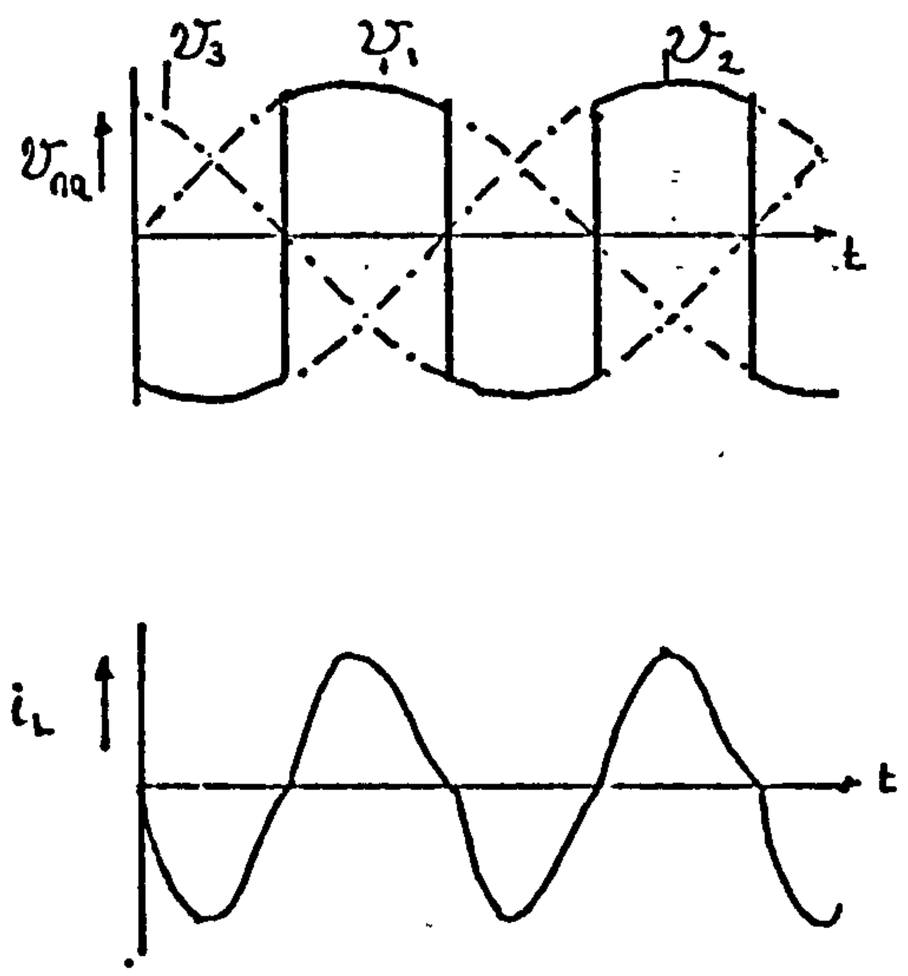

(a)

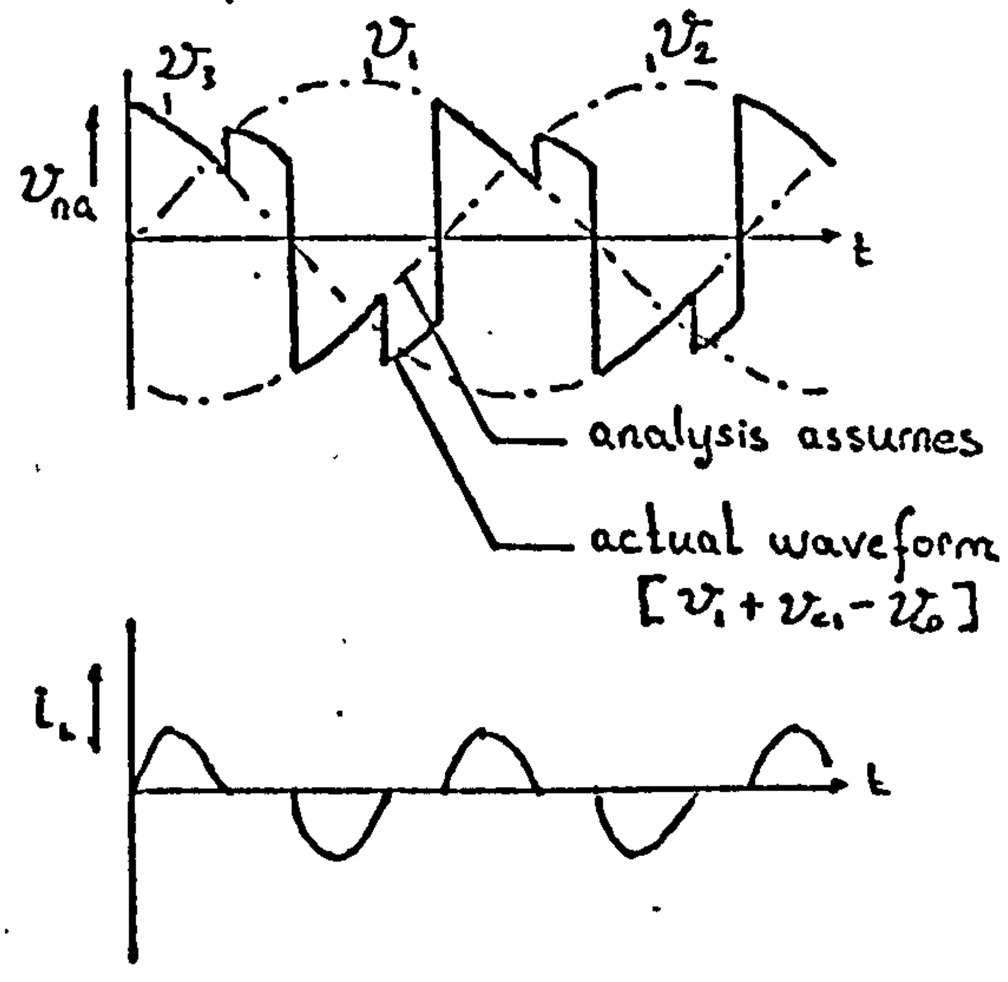

(b)

Figure 4.8 Driving voltage v_{na} for a:

a) continuous,
b) discontinuous

output current.

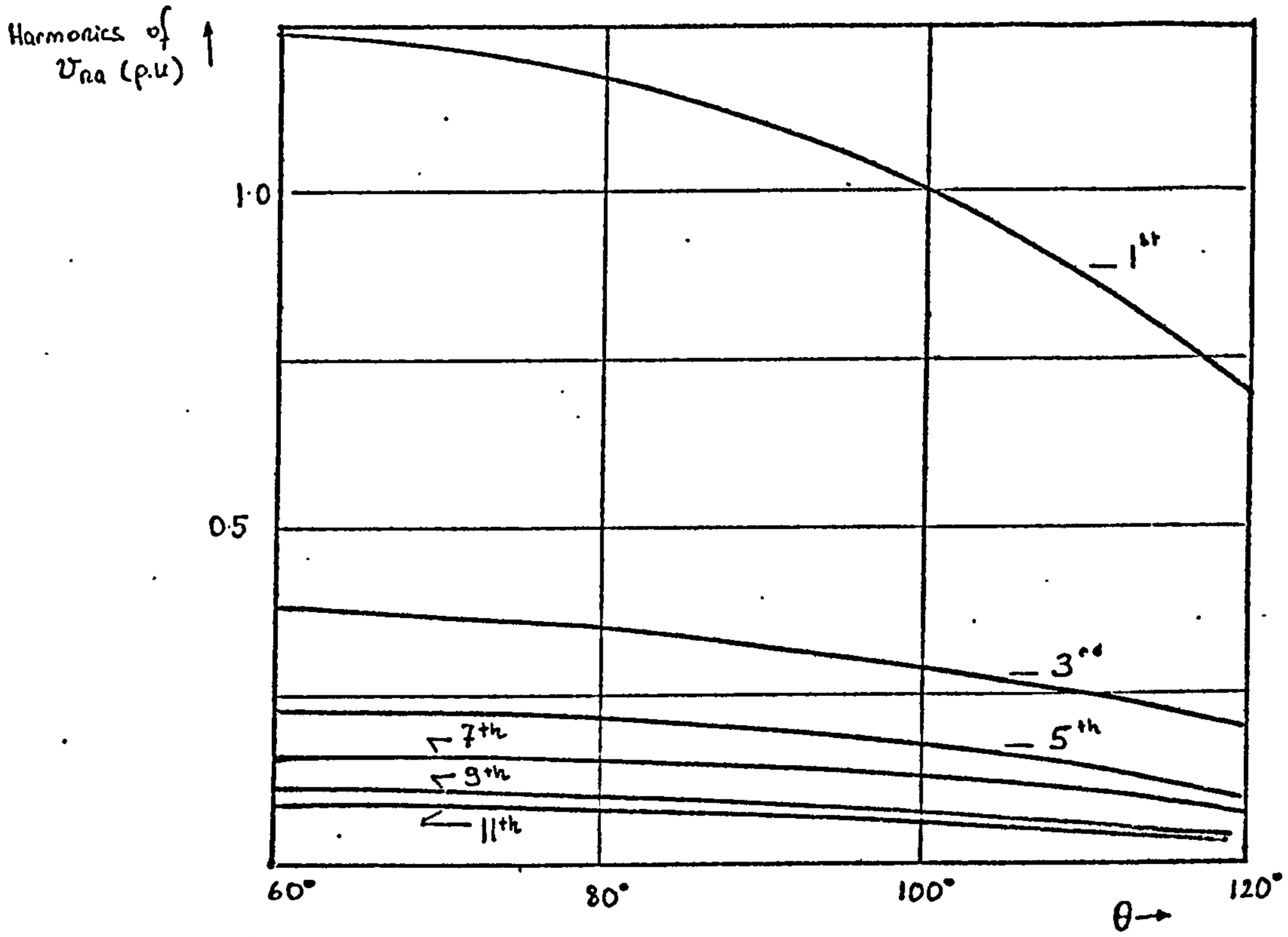

Figure 4.9 Variation of the harmonic content of the driving voltage v_{na} with the power control angle θ

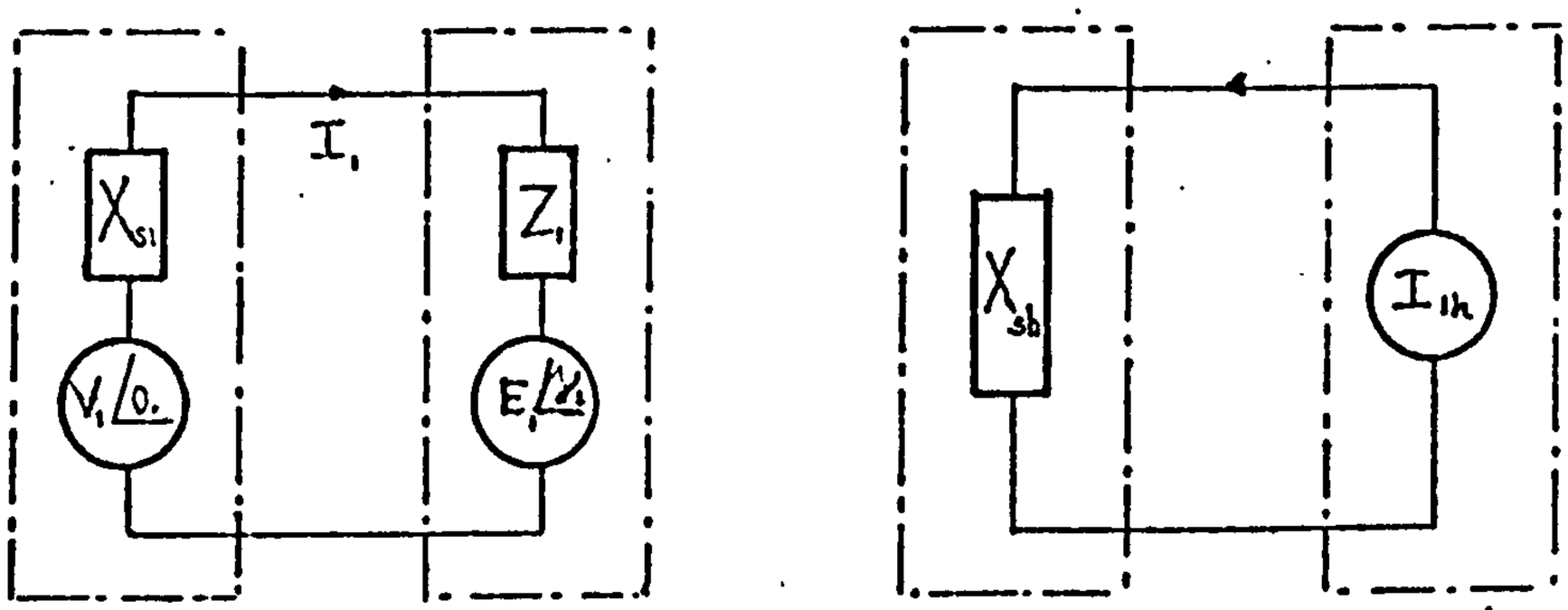

(a) (b)

Figure 4.10 General model of a converter:

a) at source frequency

b) at any frequency except source frequency

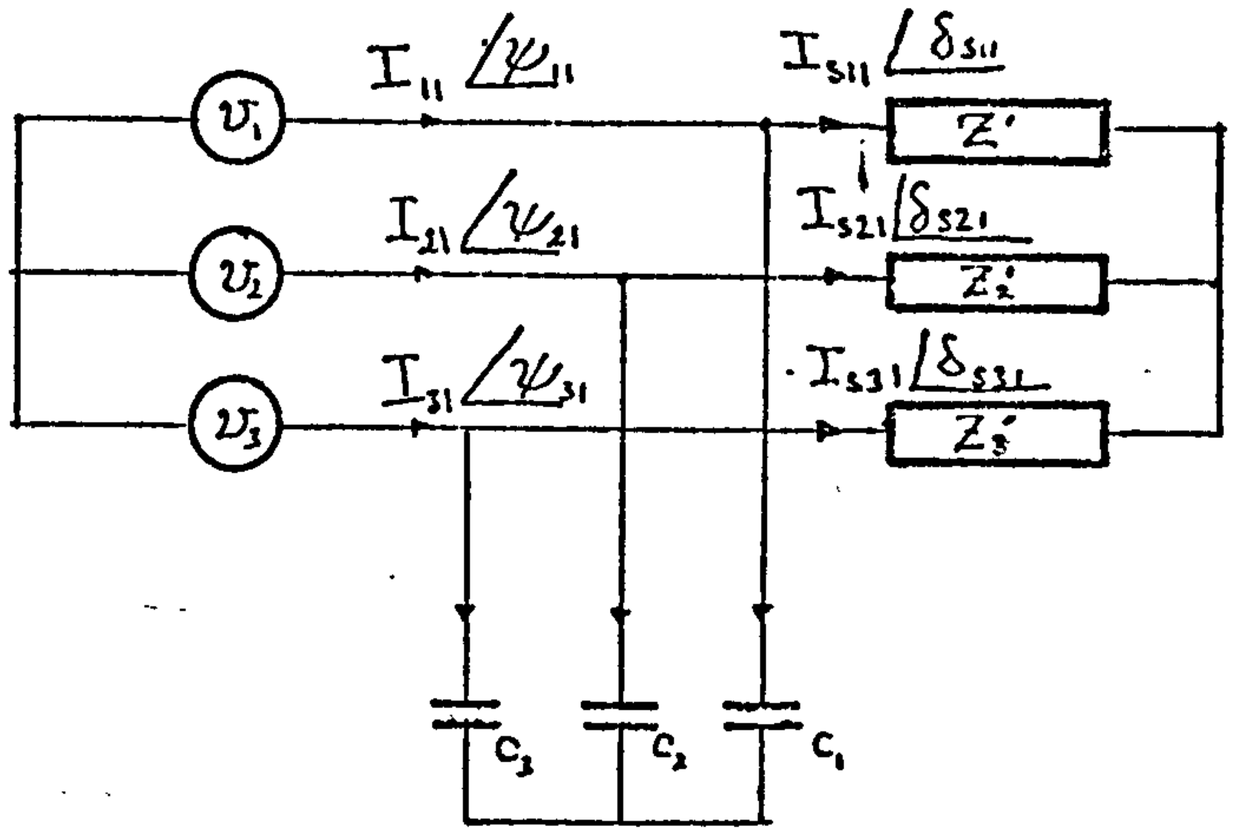

Figure 4.11 Cycloinverter power circuit at source

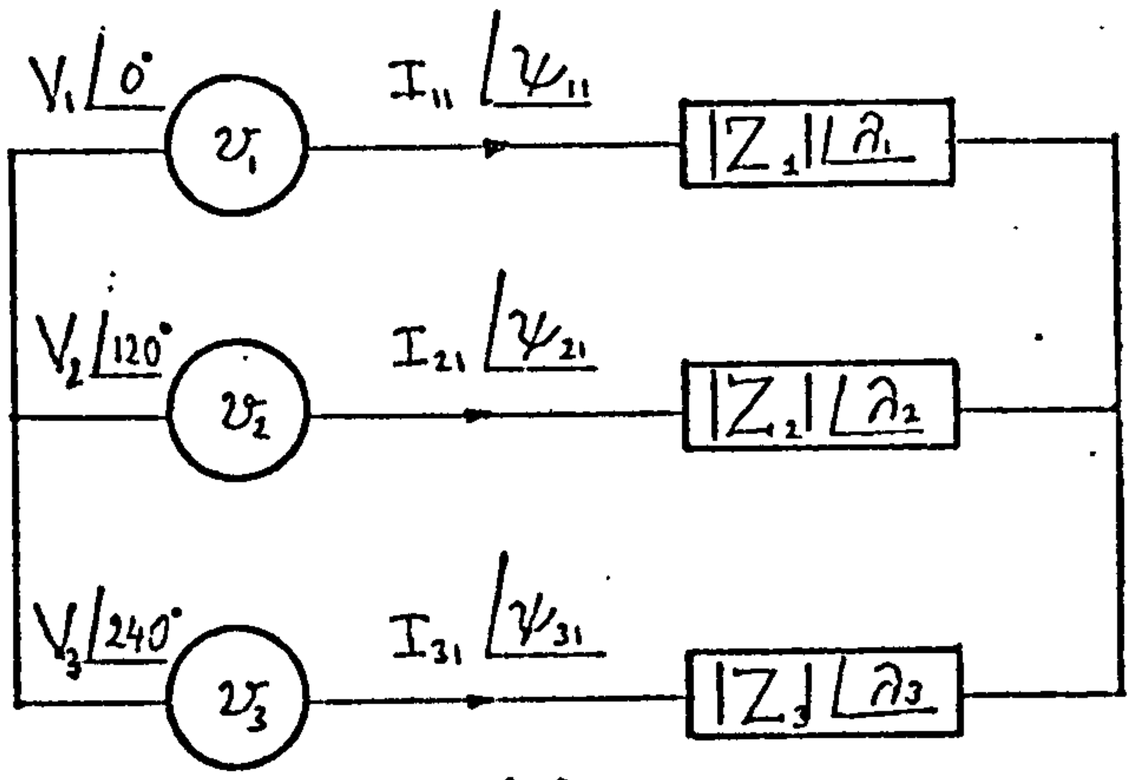

Figure 4.12 Cycloinverter model at source frequency

a) unbalanced operating conditions

b) balanced operating conditions

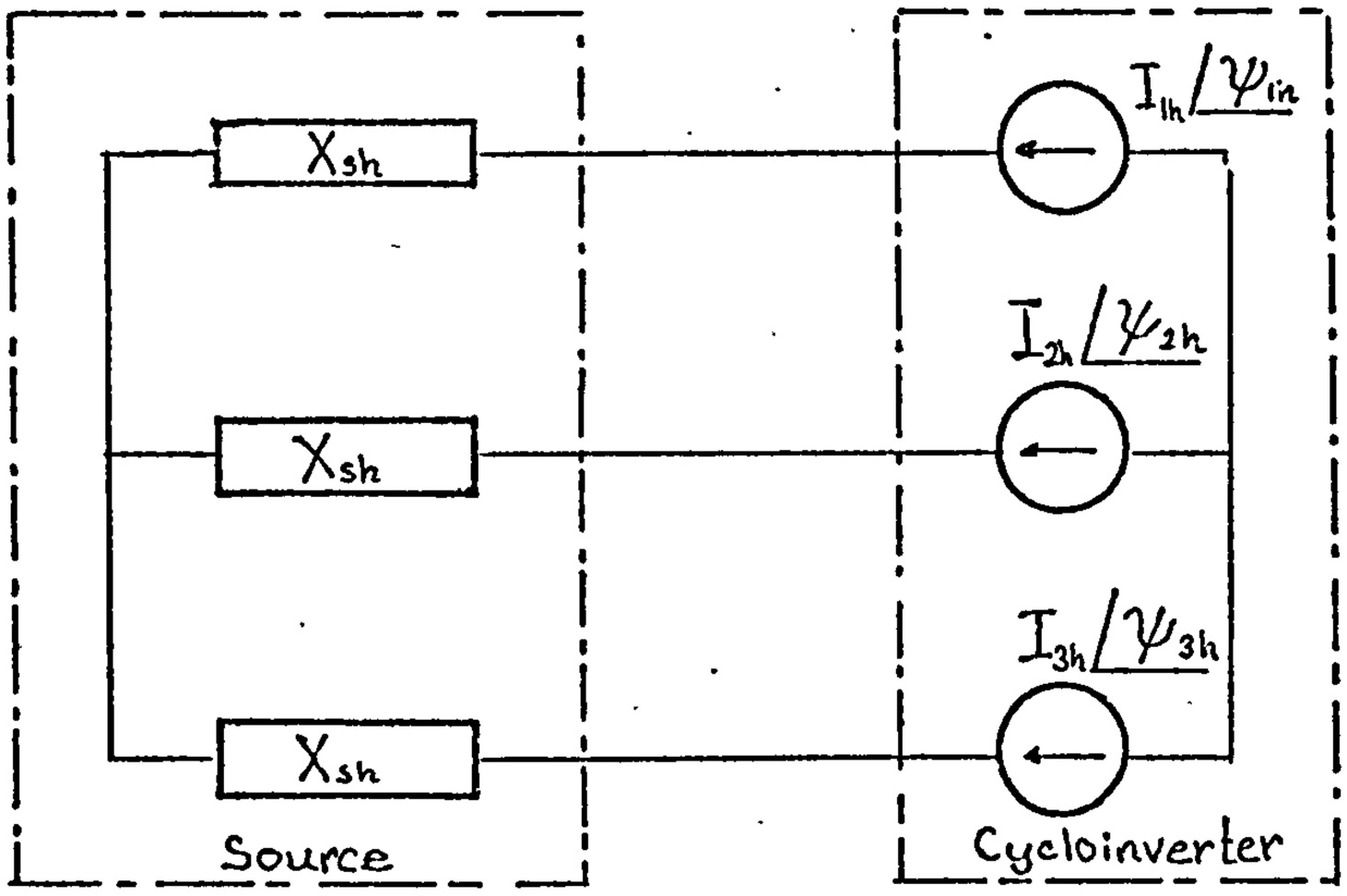

Figure 4.13 Input harmonic model of the cycloinverter

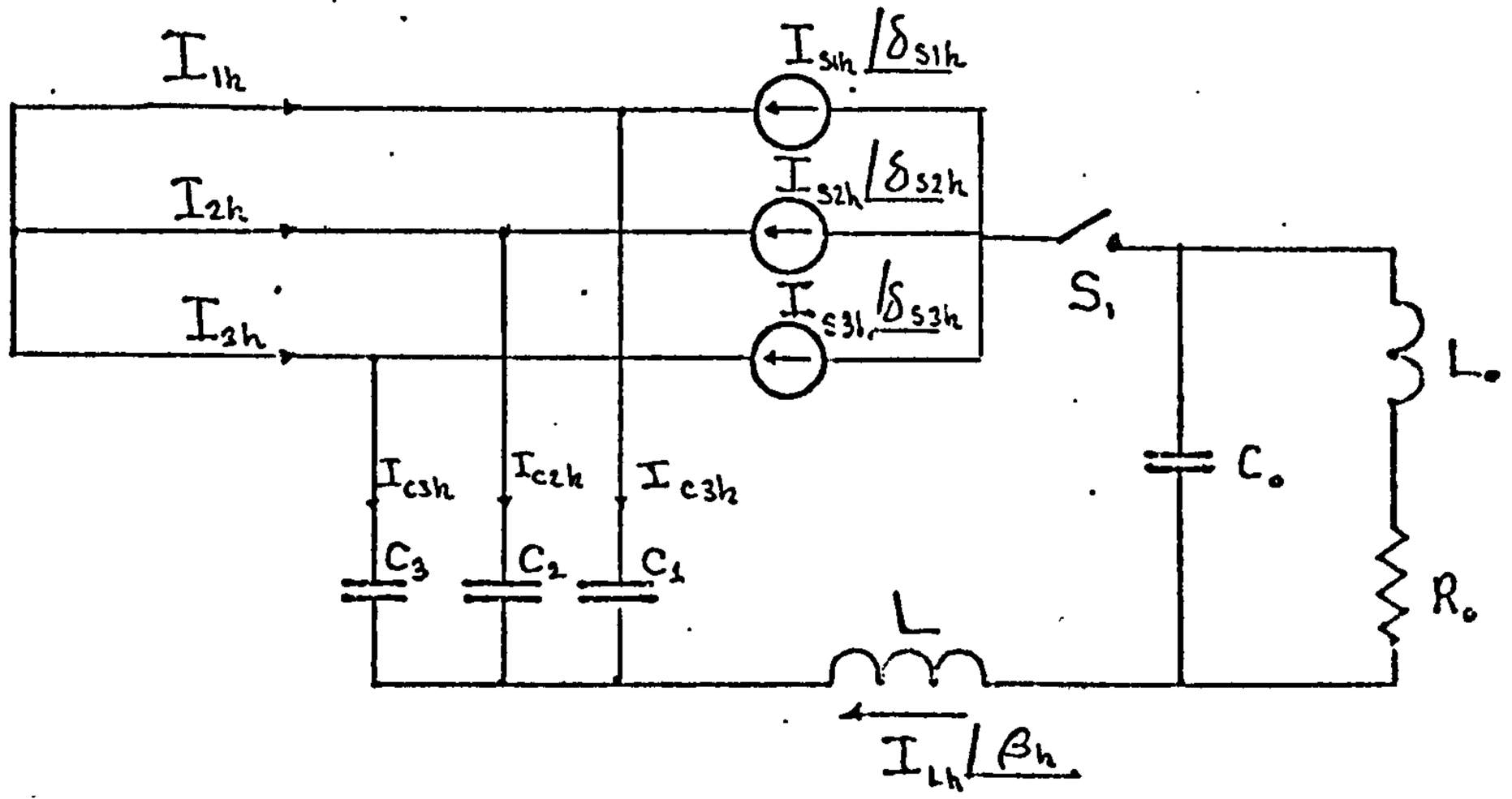

Figure 4.14 Cycloinverter power circuit at harmonic frequencies

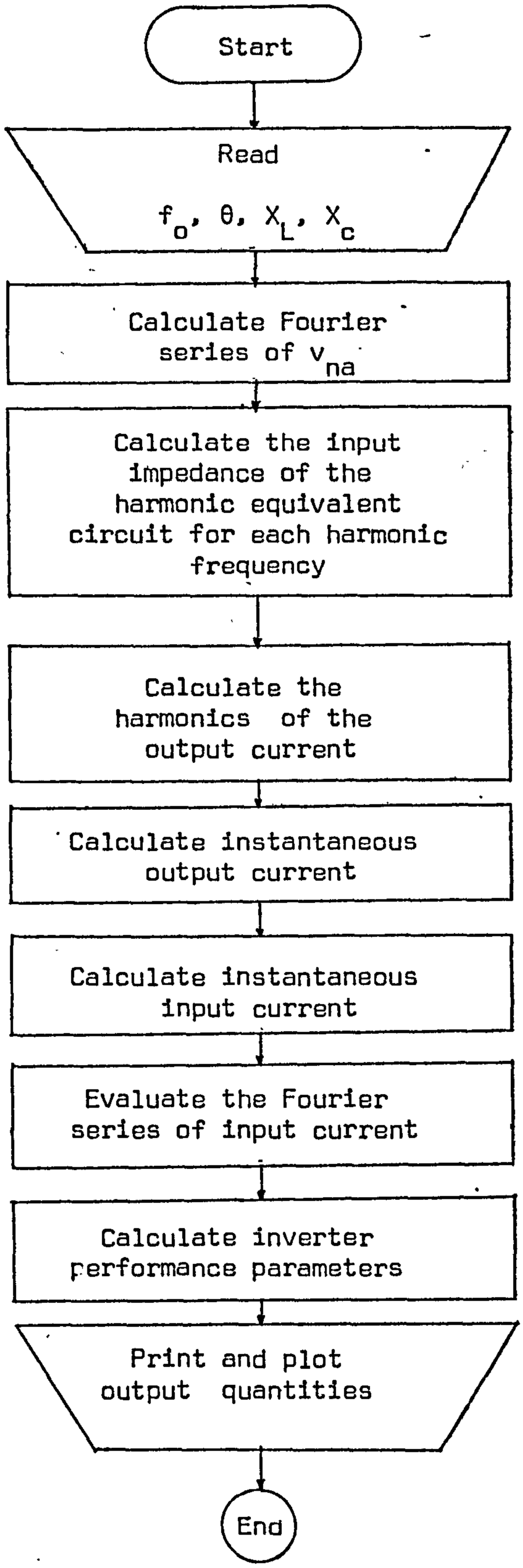

Figure 4.15 Flow chart of the computer program which evaluates cycloinverter performance using harmonic analysis

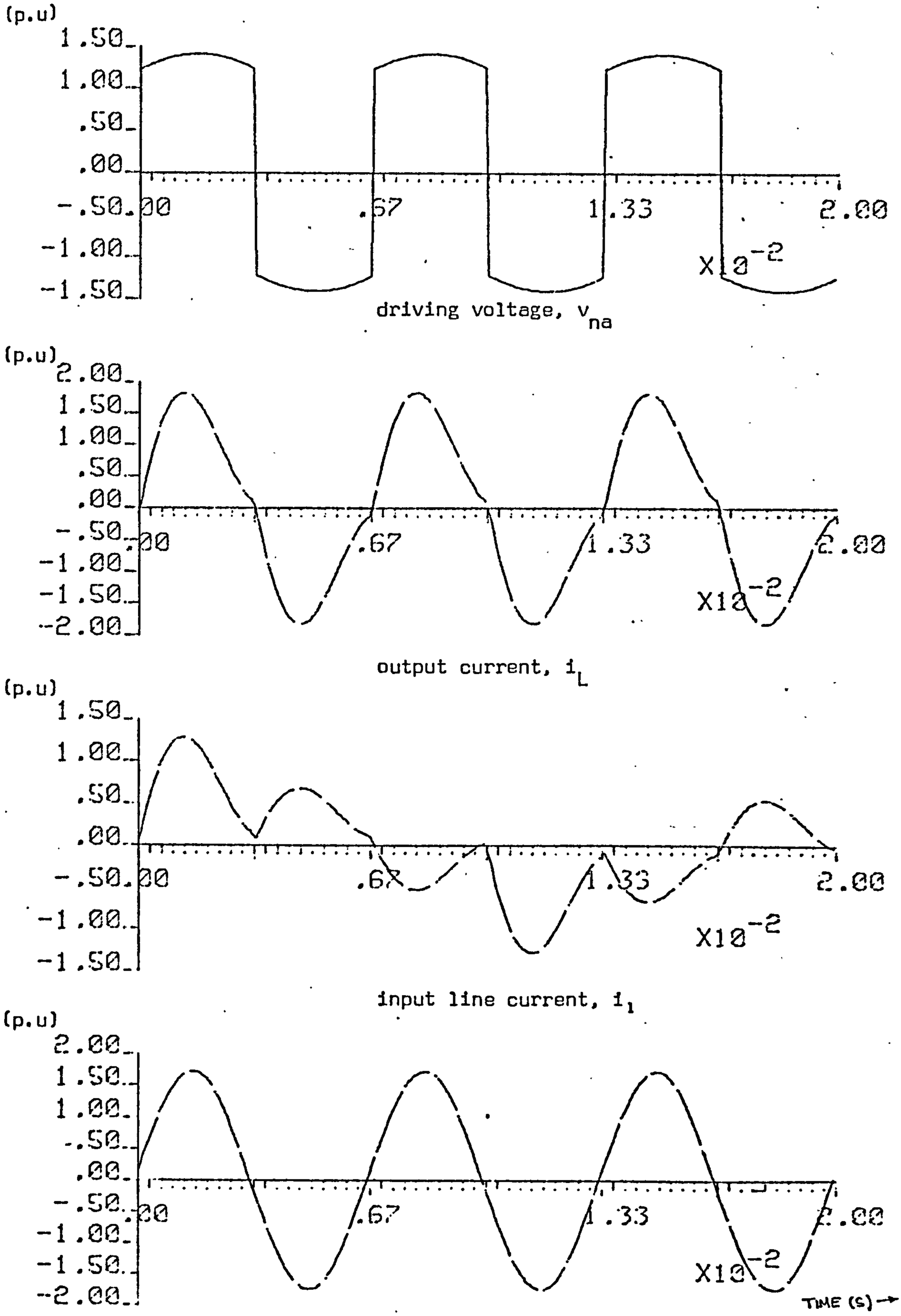

Figure 4.16a Comparison of various circuit waveforms obtained from a) harmonic analysis, (b) transient analysis

(X_L = 0.9 p.u, X_c = 1.03 p.u, $\theta = 60^o$, Q_L = 10, f_o = 15CHz

(Continued)

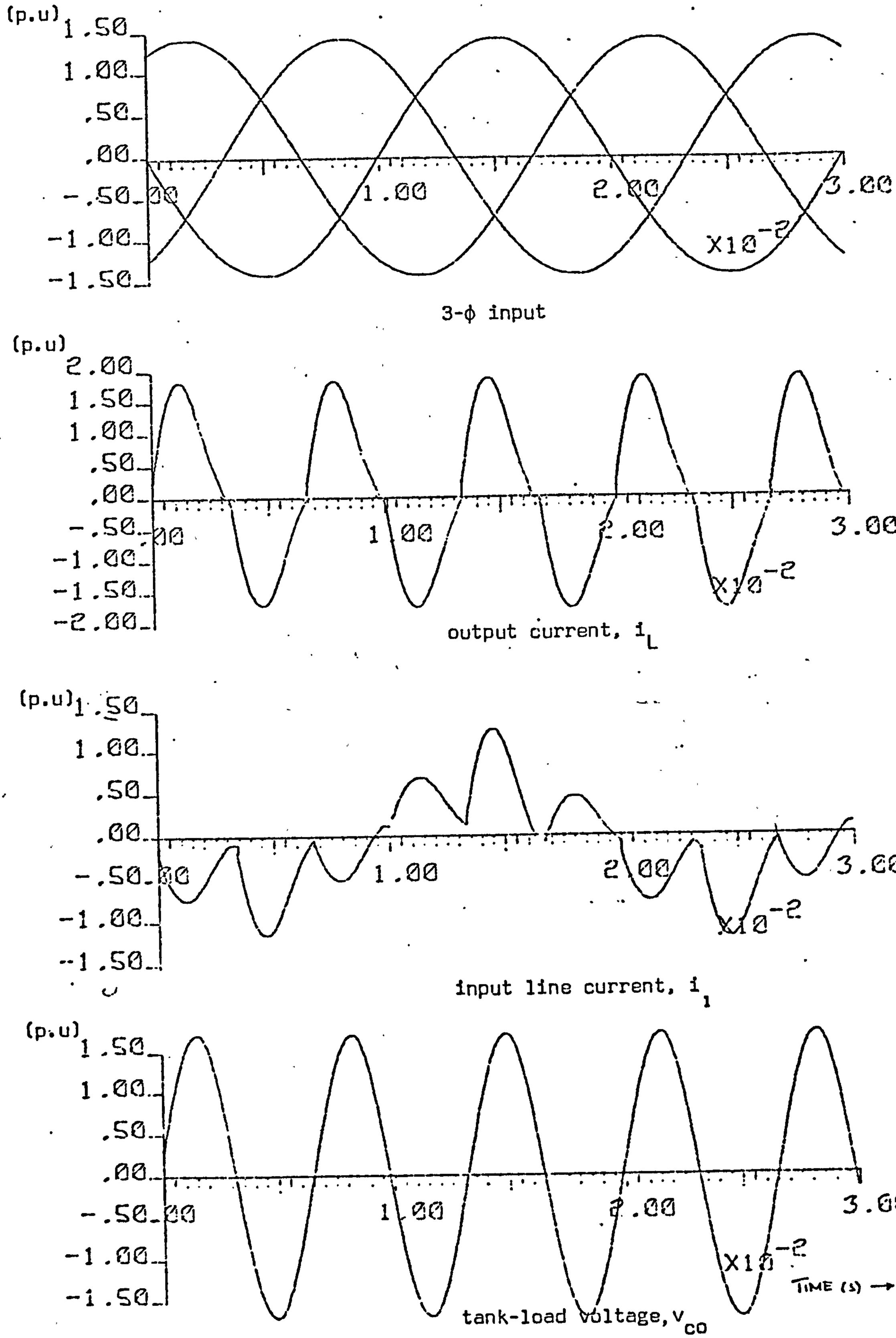
(p.u)
1.50
1.00
.50
.00
-.50
-1.00
-1.50
.00
1.00
2.00
3.00
X10-2
3-ϕ input
(p.u)
2.00
1.50
1.00
.50
.00
-.50
-1.00
-1.50
-2.00
.00
1.00
2.00
3.00
X10-2
output current, iL
(p.u)
1.50
1.00
.50
.00
-.50
-1.00
-1.50
.00
1.00
2.00
3.00
X10-2
input line current, i1
(p.u)
1.50
1.00
.50
.00
-.50
-1.00
-1.50
.00
1.00
2.00
3.00
X10-2
TIME (s) →
tank-load voltage, Vco

Figure 4.16b

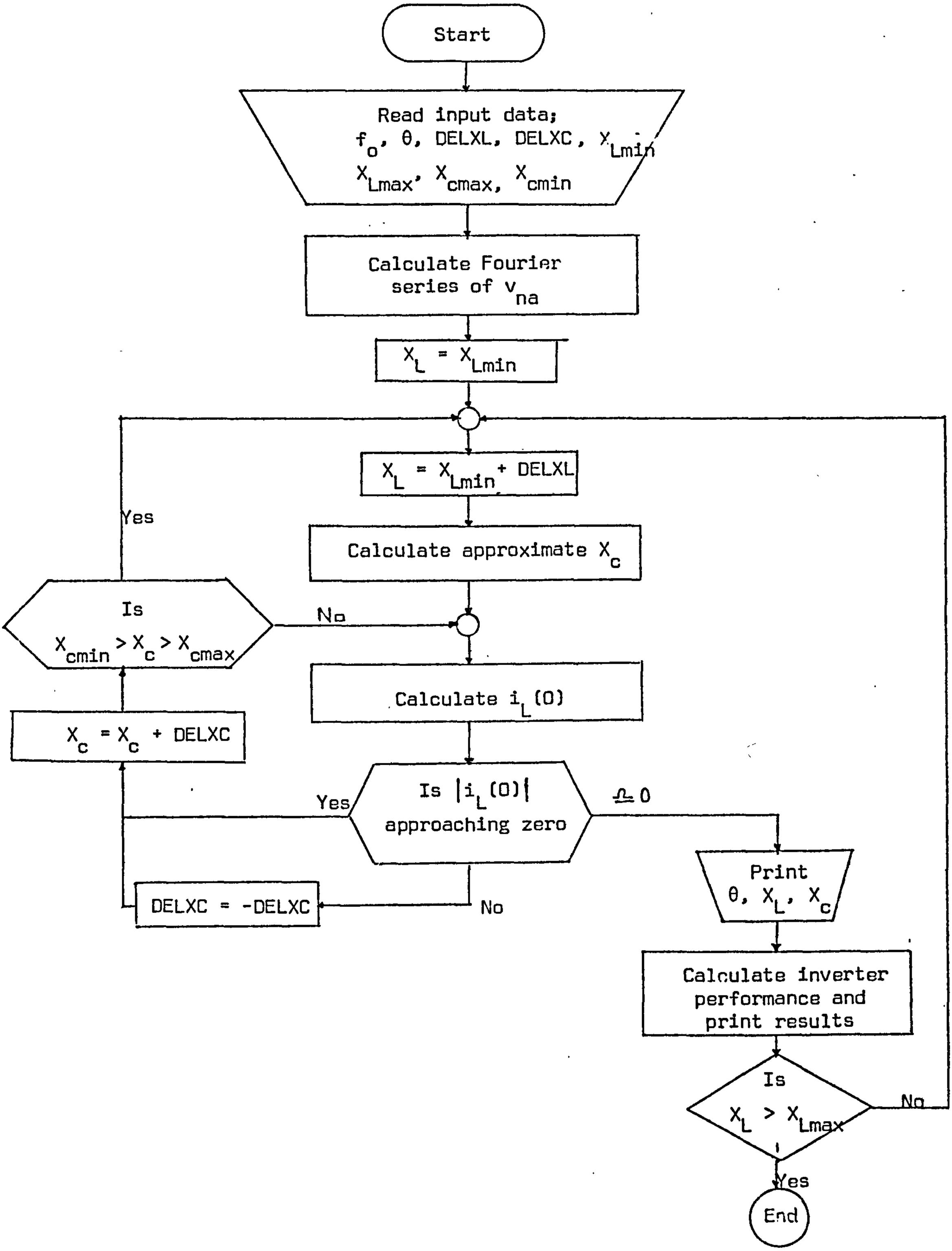

Figure 4.17 Flow chart of the computer program which calculates X_c for a given X_L and θ to produce continuous output current. The inverter performance is calculated in accordance with the flow chart of Figure 4.15

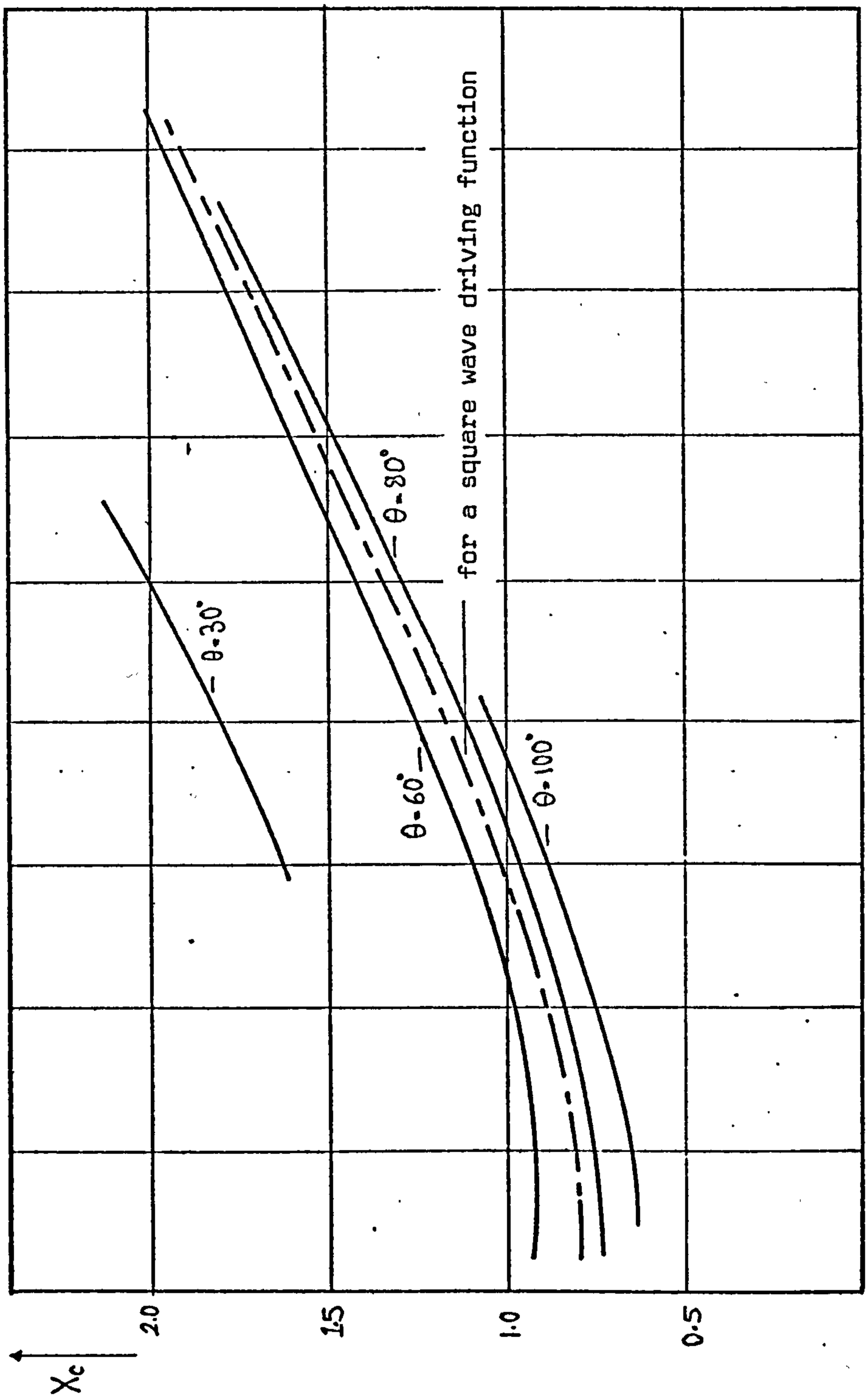
Variation of X_c with X_L for continuous output current, at difference firing angles
for a square wave driving function
θ-30°
θ-60°
θ-80°
θ-100°
2.0
1.0
X_L
2.0
1.5
1.0
0.5
X_c

Figure 4.18

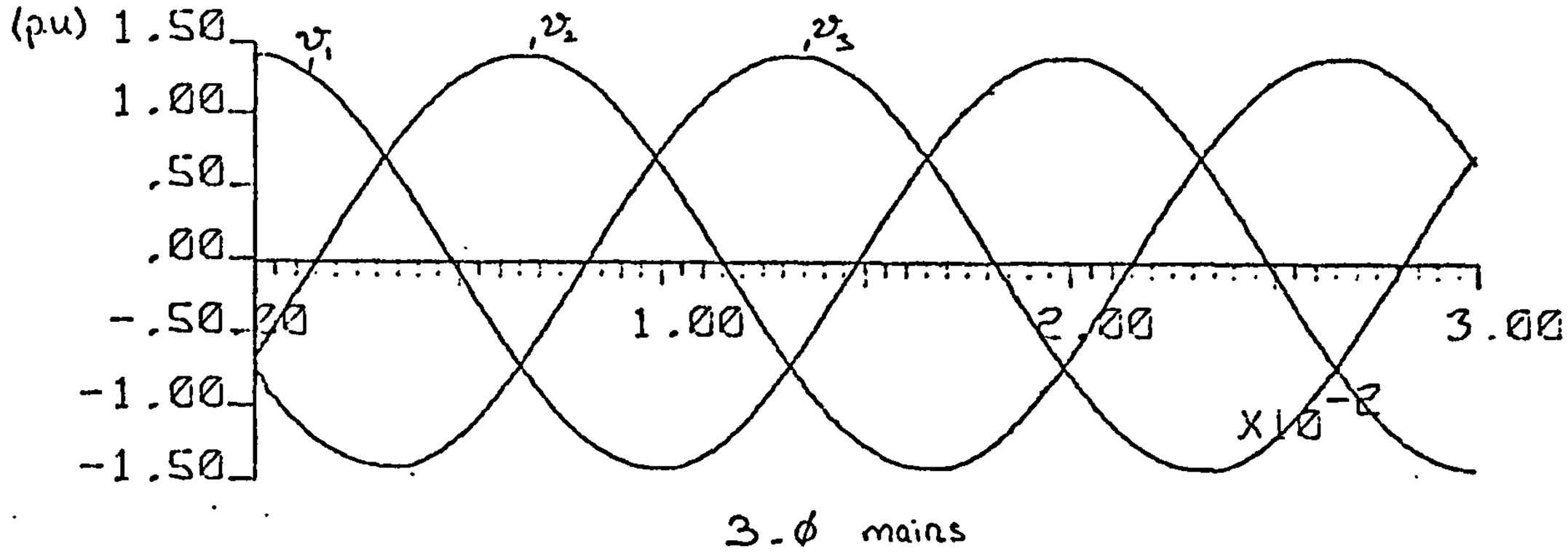

Figure 4.19 Power control in a full-bridge 150 Hz cycloinverter ($\theta = 90^{o}$)

(continued)

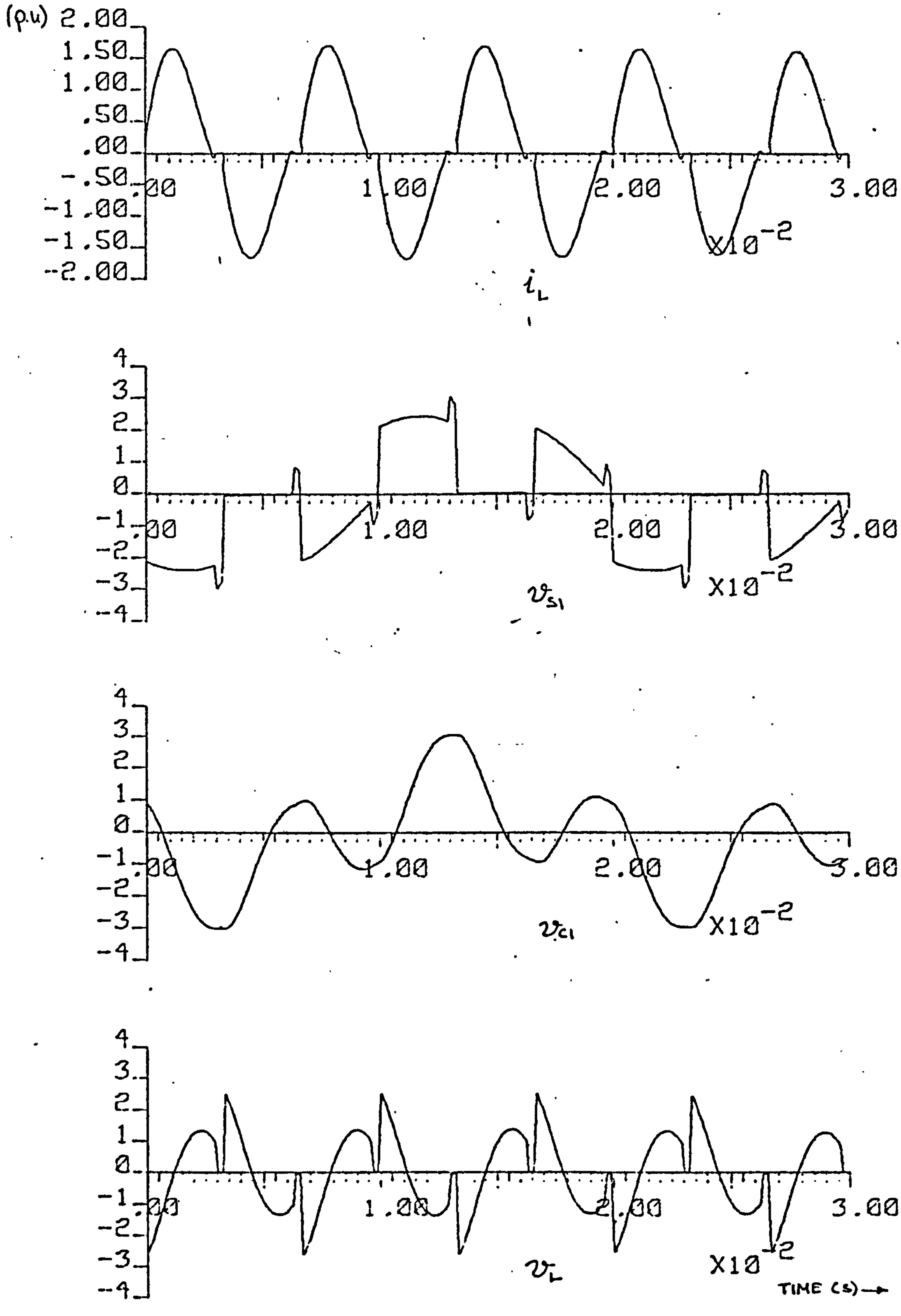
(p.u) 2.00
1.50
1.00
.50
.00
-.50
-1.00
-1.50
-2.00
1.00
2.00
3.00
X10-2
iL
4
3
2
1
0
-1
-2
-3
-4
1.00
2.00
3.00
X10-2
vs1
4
3
2
1
0
-1
-2
-3
-4
1.00
2.00
3.00
X10-2
vc1
4
3
2
1
0
-1
-2
-3
-4
1.00
2.00
3.00
X10-2
vL
TIME (s)

Figure 4.19

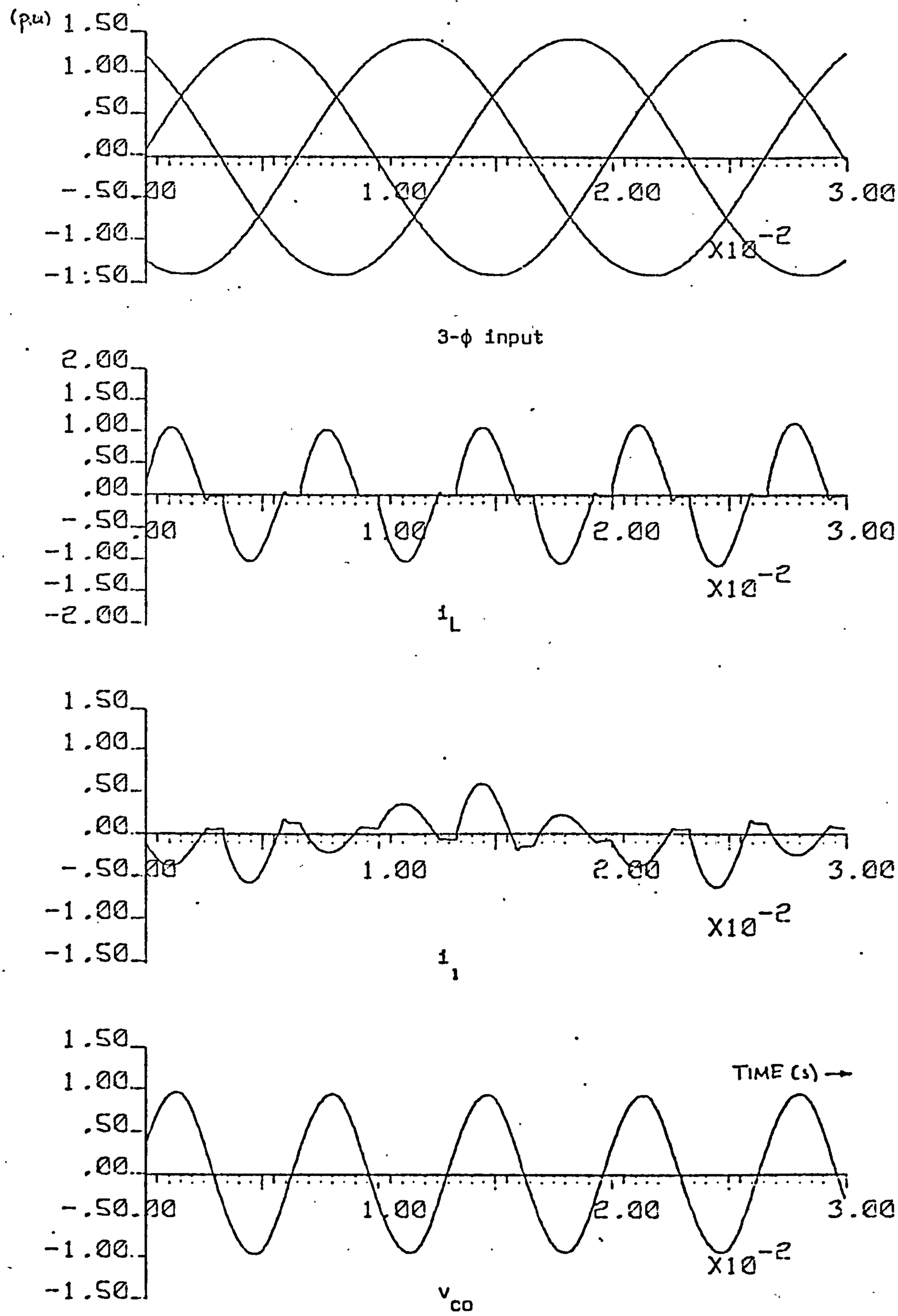

Figure 4.20 Power control in a full-bridge, 150 Hz cycloinverter ($\theta = 120^{o}$)

(continue

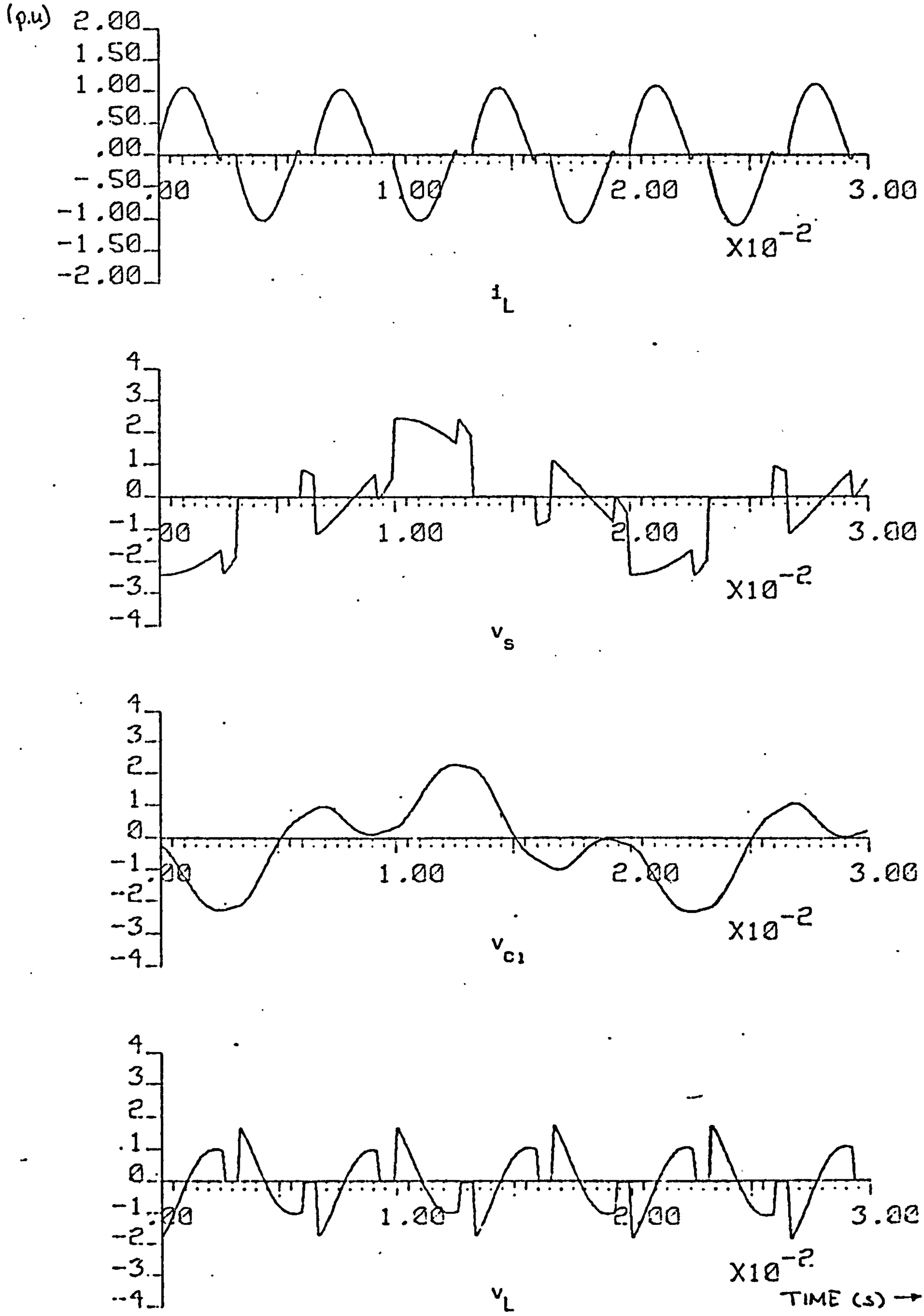
(p.u)
2.00
1.50
1.00
.50
.00
-.50
-1.00
-1.50
-2.00
1.00
2.00
3.00
X10^-2
i_L
4
3
2
1
0
-1
-2
-3
-4
1.00
2.00
3.00
X10^-2
v_s
v_c1
v_L
TIME (s) →

Figure 4.20

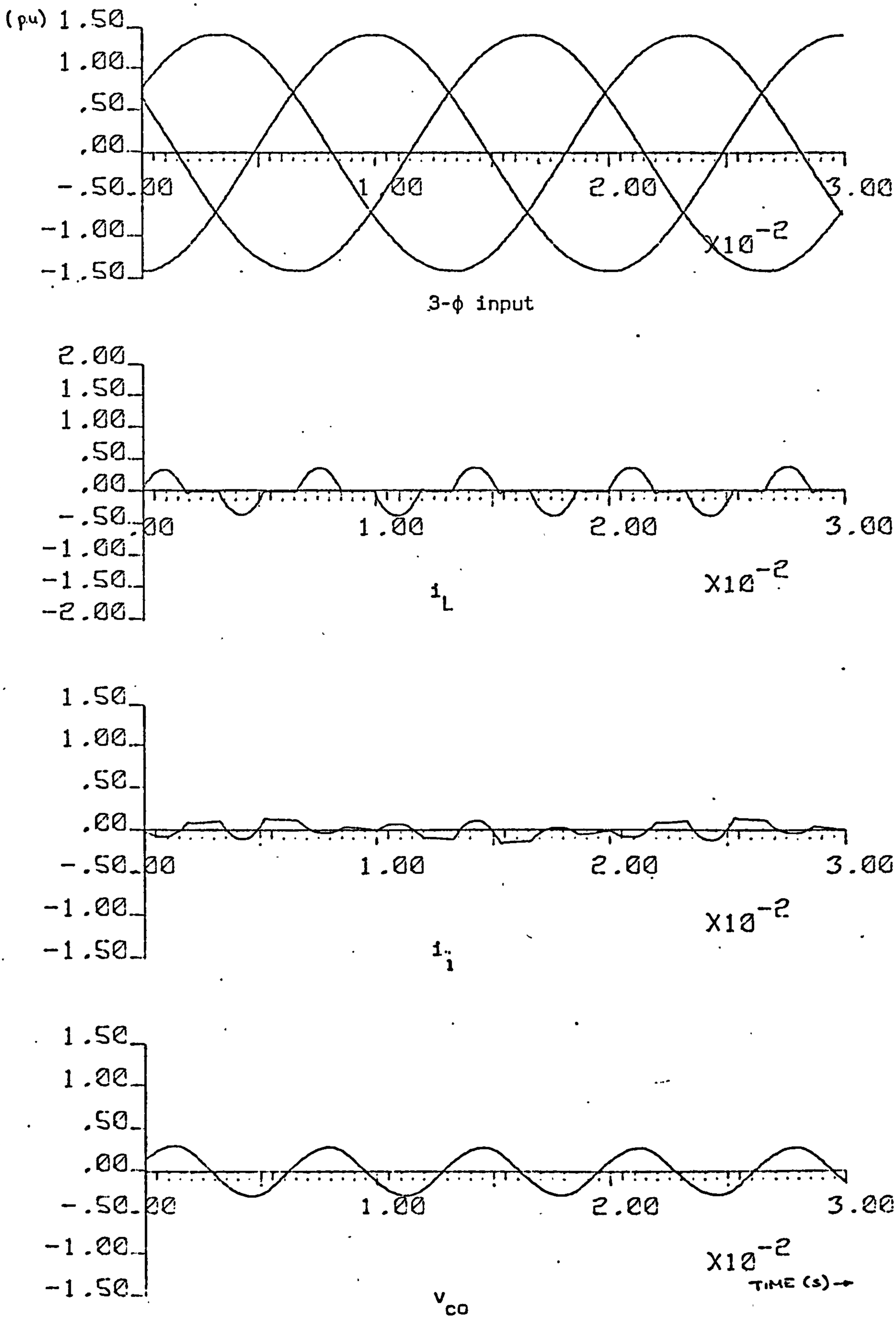

Figure 4.21 Power control in a full-bridge 150 Hz cycloinverter ($\theta = 150°$)

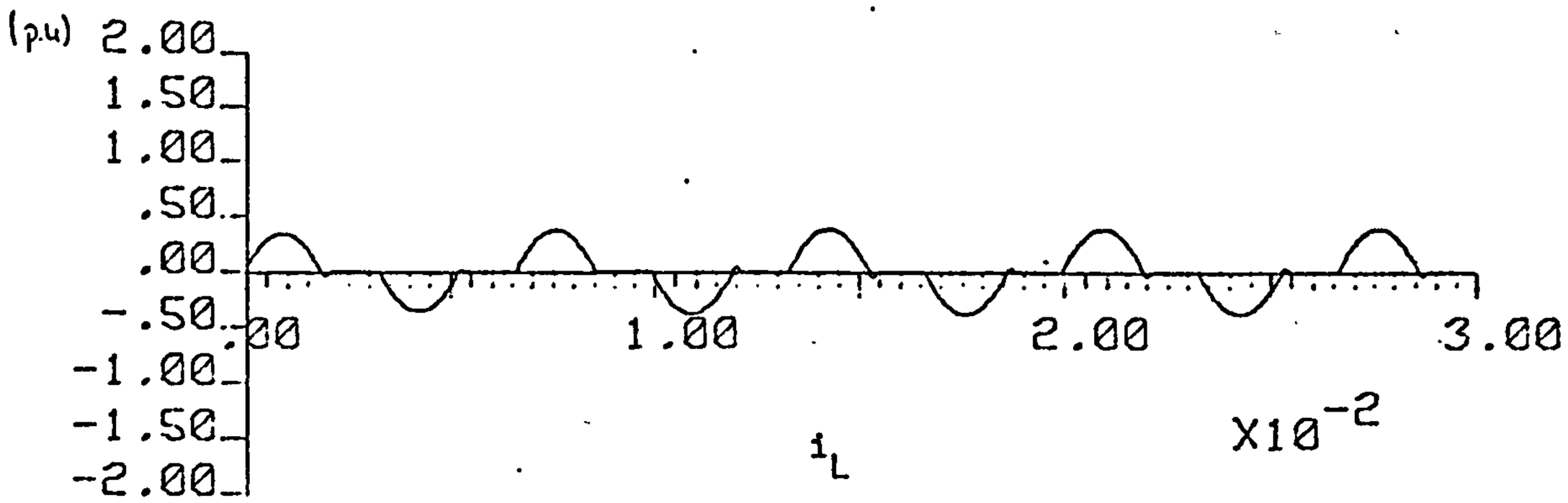

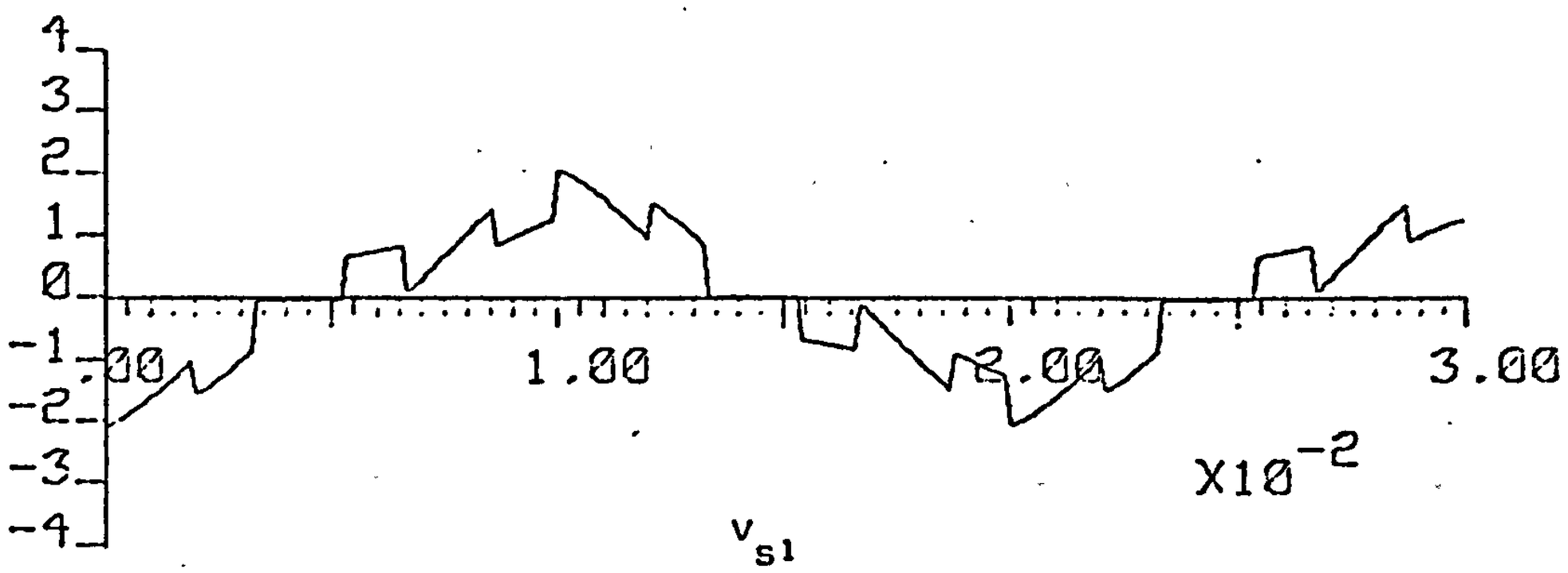

Figure 4.21b $\theta = 150^{o}$

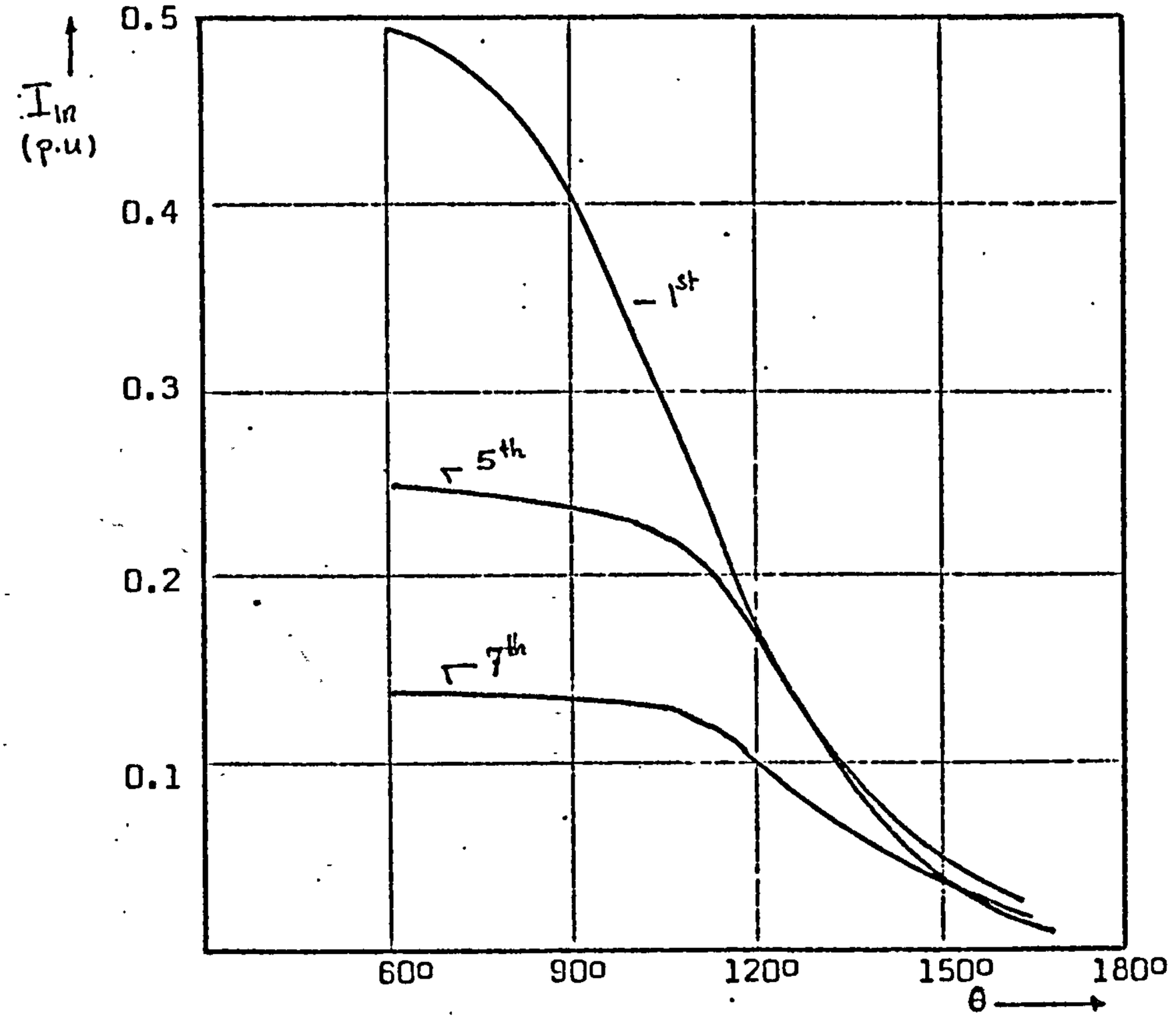

Figure 4.22 Variation of input line current harmonics I_{in} with θ in a 150 Hz full-bridge cycloinverter

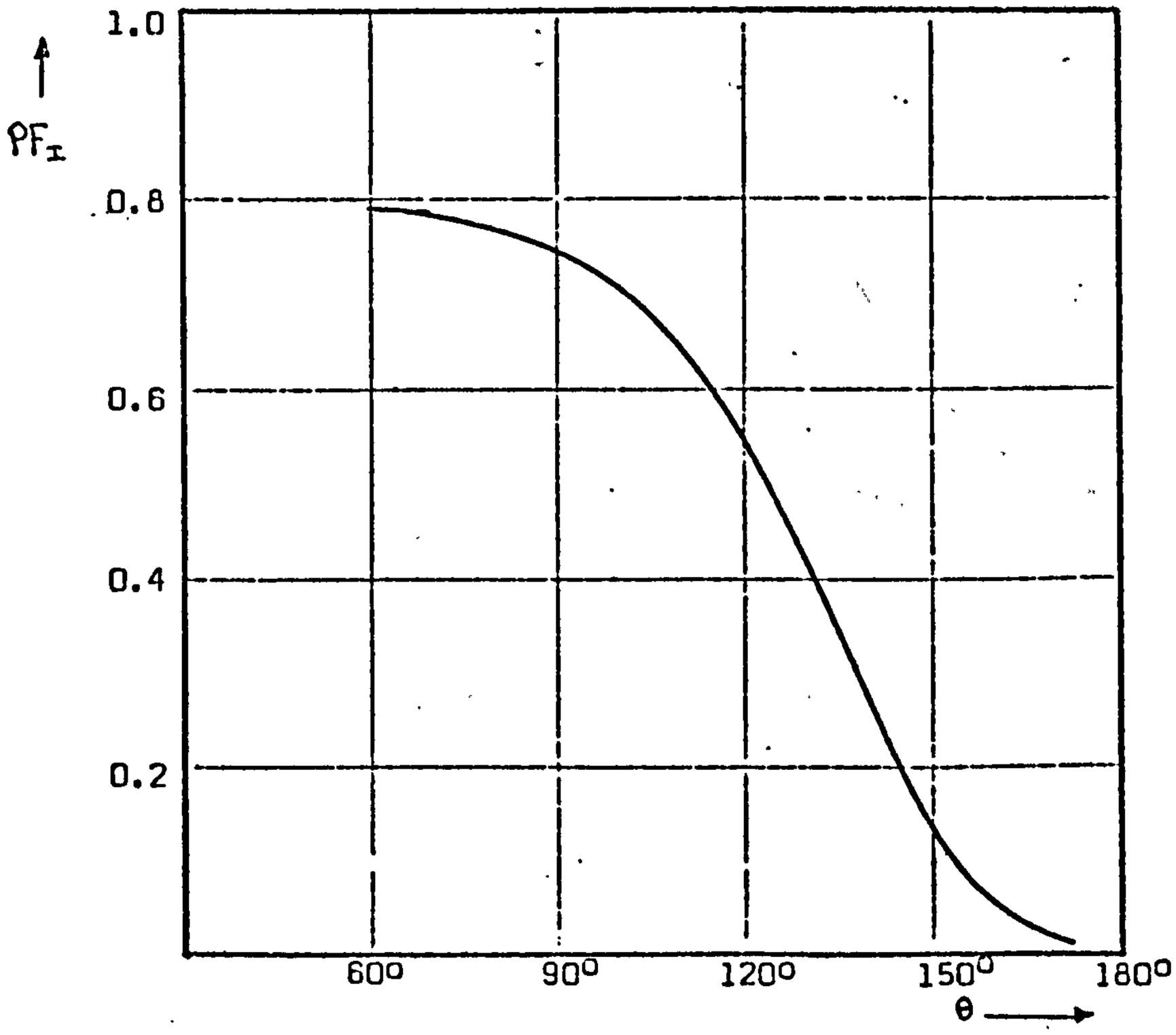

Figure 4.24 Variation of input power factor PF_I with θ in a 150 Hz full-bridge cycloinverter

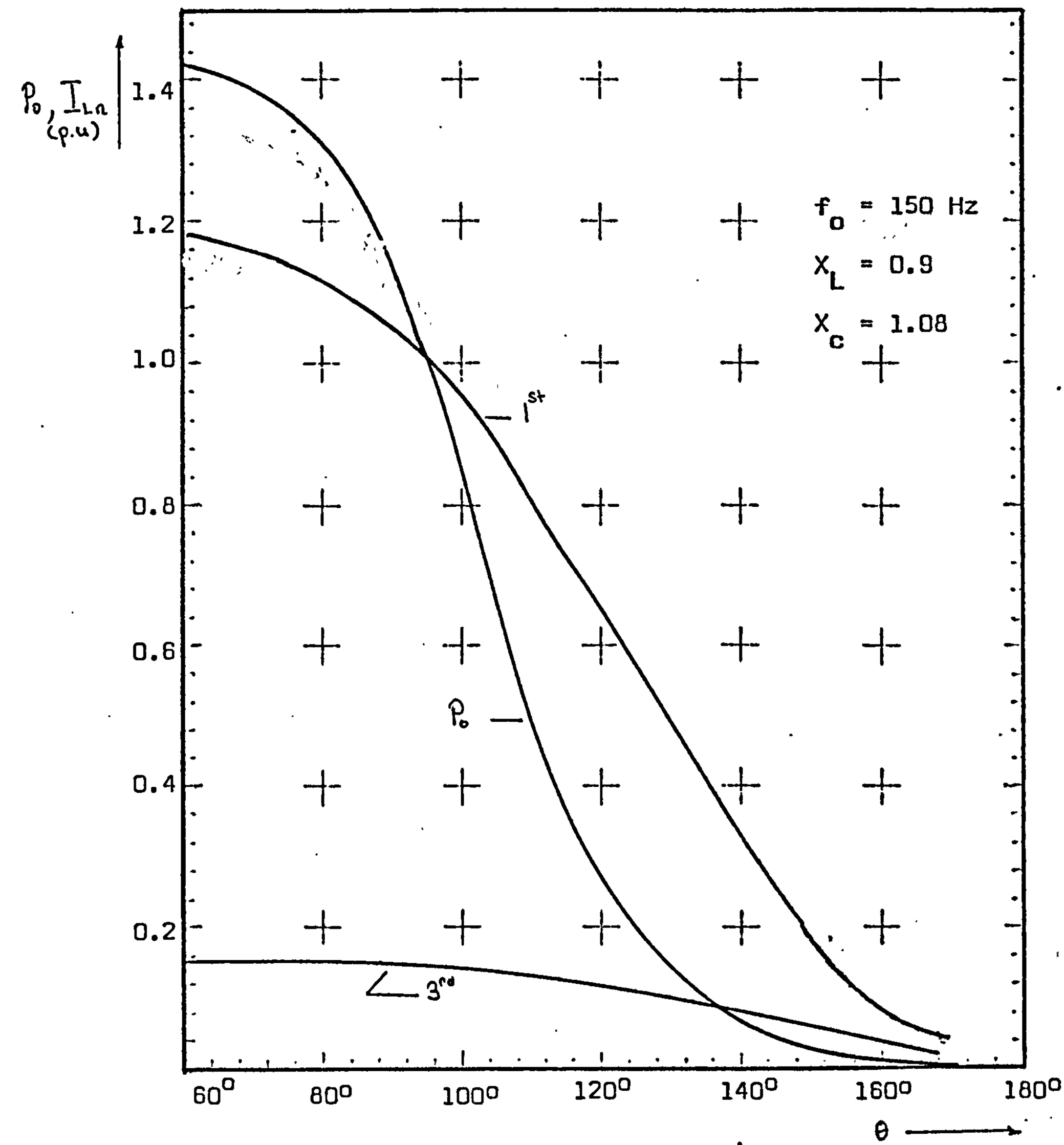

Figure 4.23 Variation of output current harmonics I_{Ln} and output power P_o with θ in a 150 Hz full-bridge cycloinverter

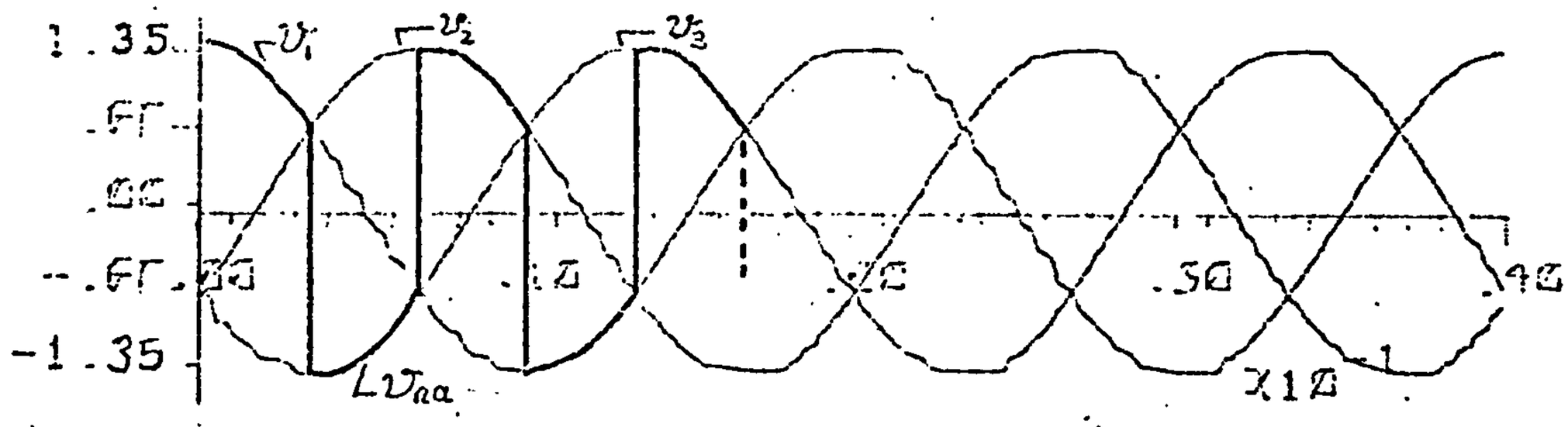

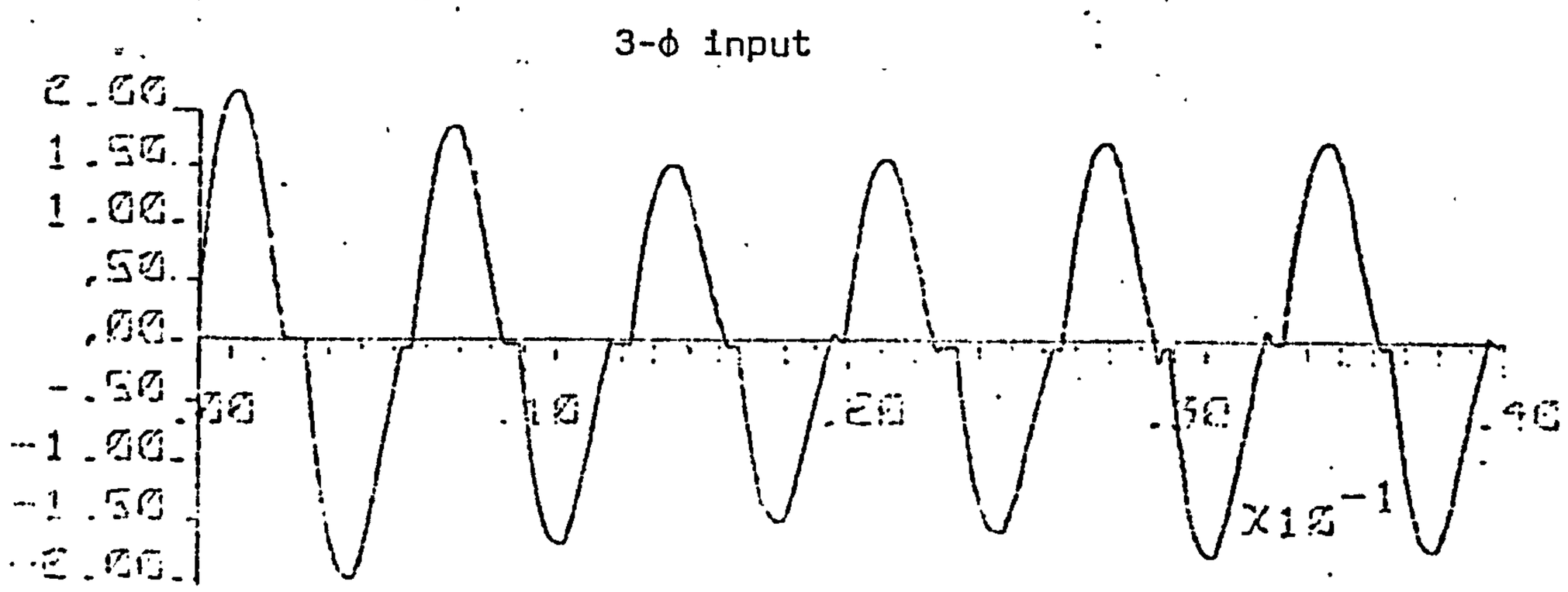

(a)

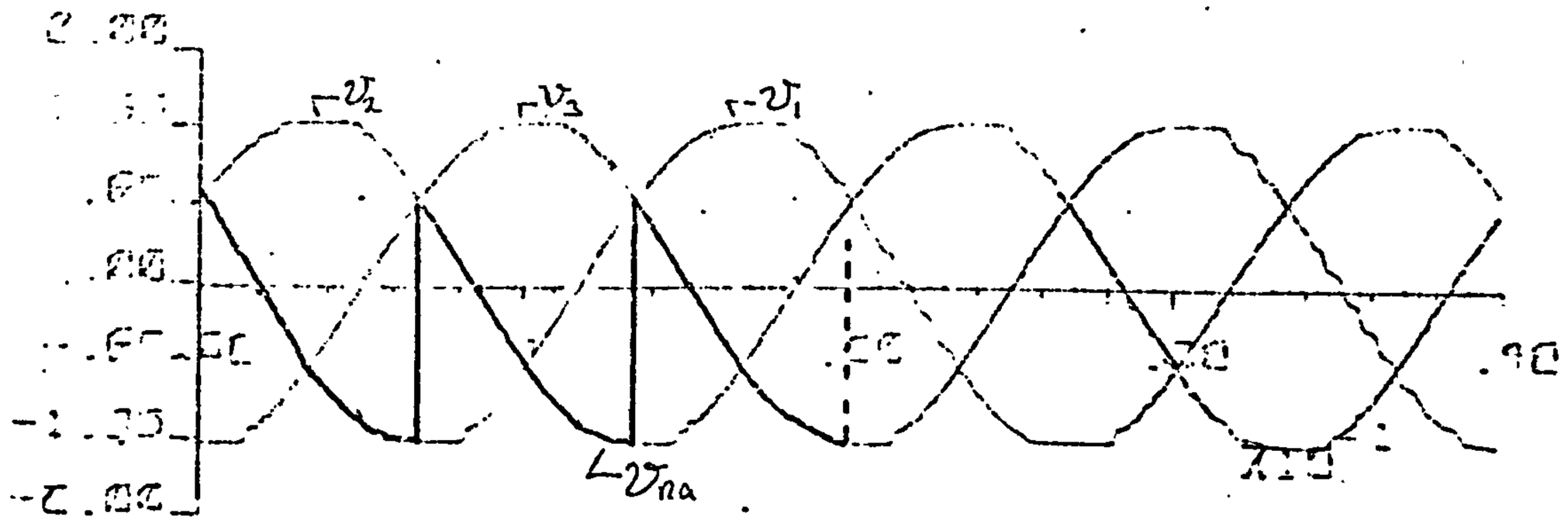

(b)

Figure 4.25 Power control in a half-bridge, 150 Hz inverter

a) $\theta = 90^{o}$ b) $\theta = 150^{o}$

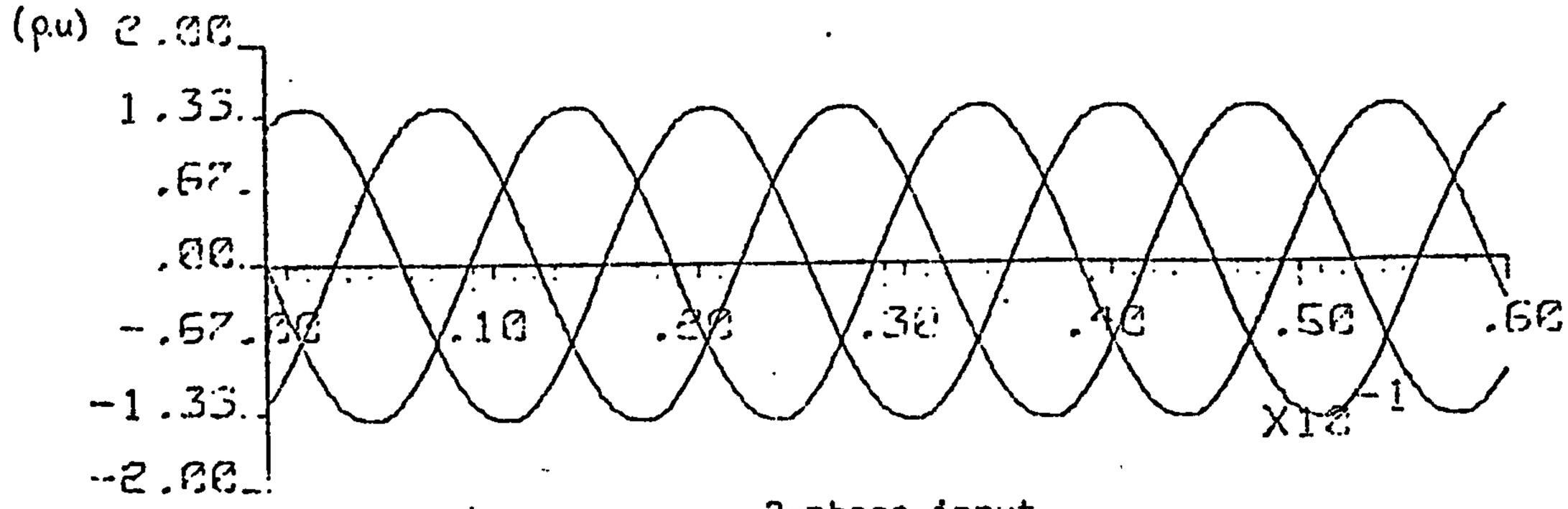

(a)

Figure 4.26 Circuit waveforms in a full-bridge cycloinverter when operating at $f_o = 6\ f_I$ ($Q_L = 5$)

a) $\theta = 60^0$

/Continued

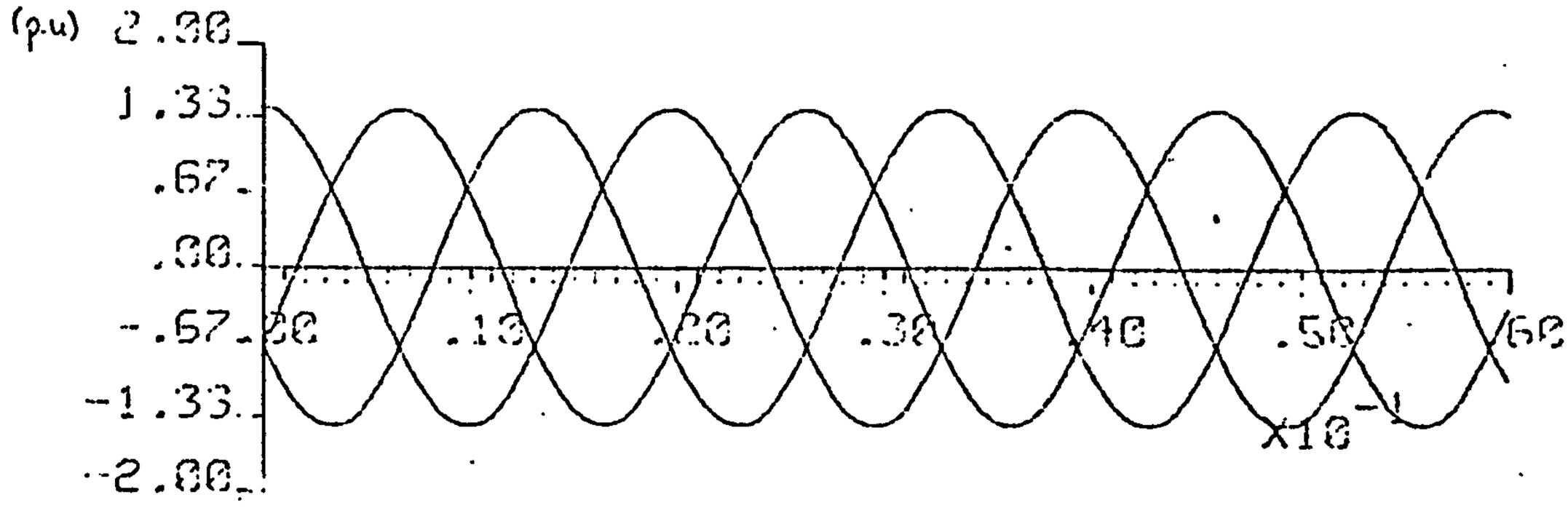

Figure 4.26b $\theta = 90^0$

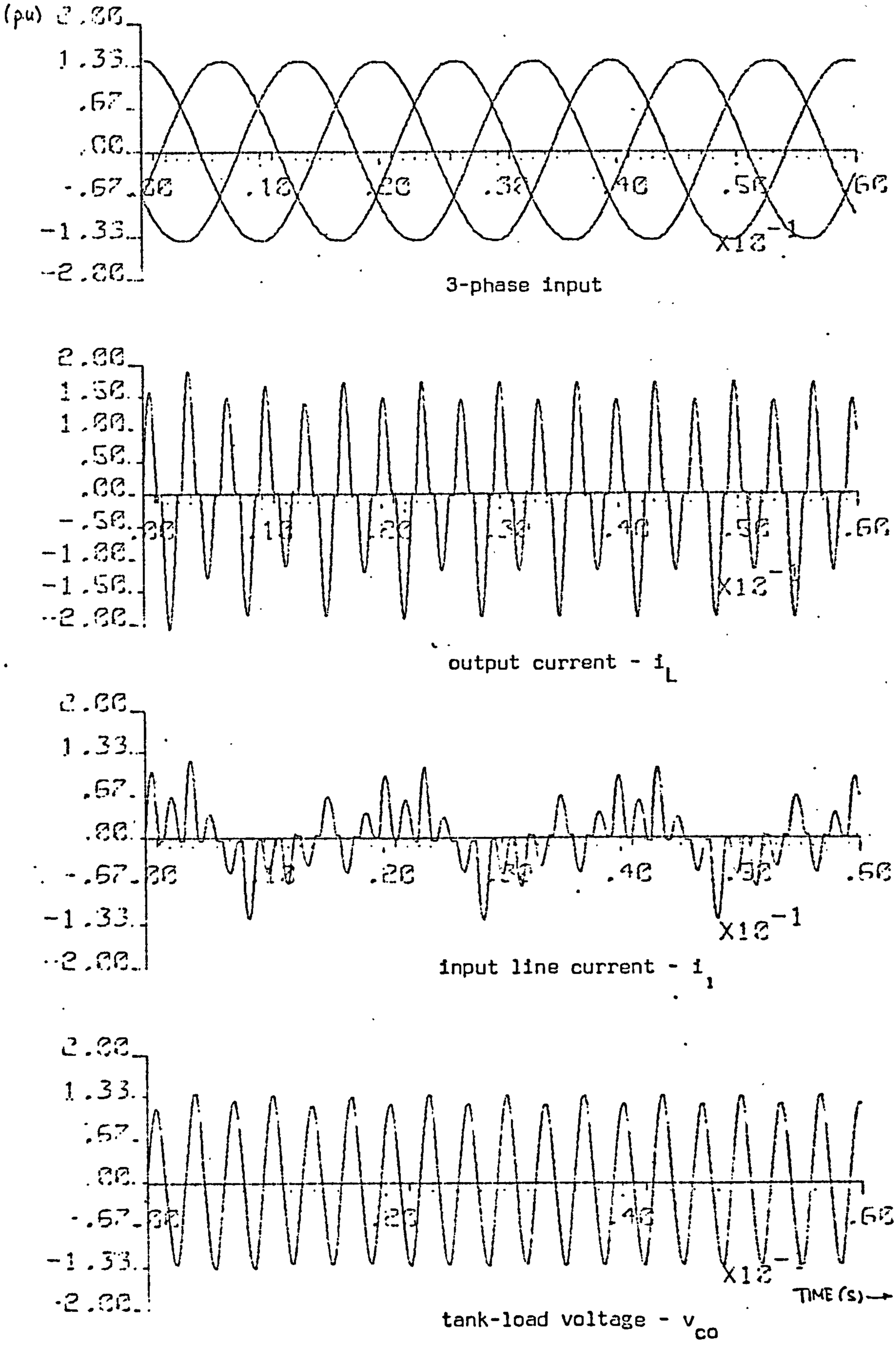

Figure 4.27 Circuit waveforms in a half-bridge cycloinverter when $\theta = 90^0$ and operating at $f_o = 6\ f_I$

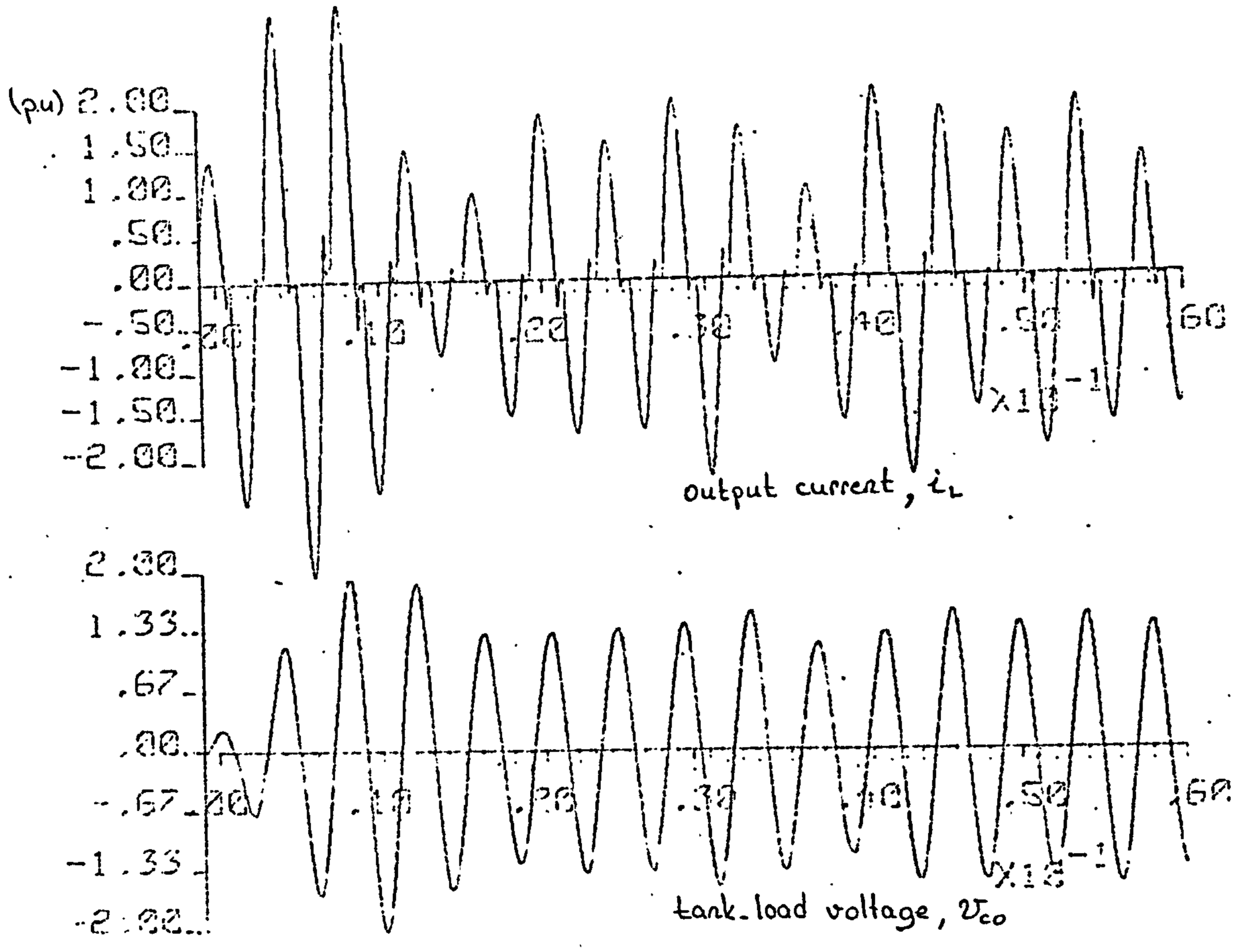

Figure 4.28 Cycloinverter operation at non-multiple output frequencies (150 Hz = 1 p.u; $Q_L = 5$, $\theta = 30^0$)

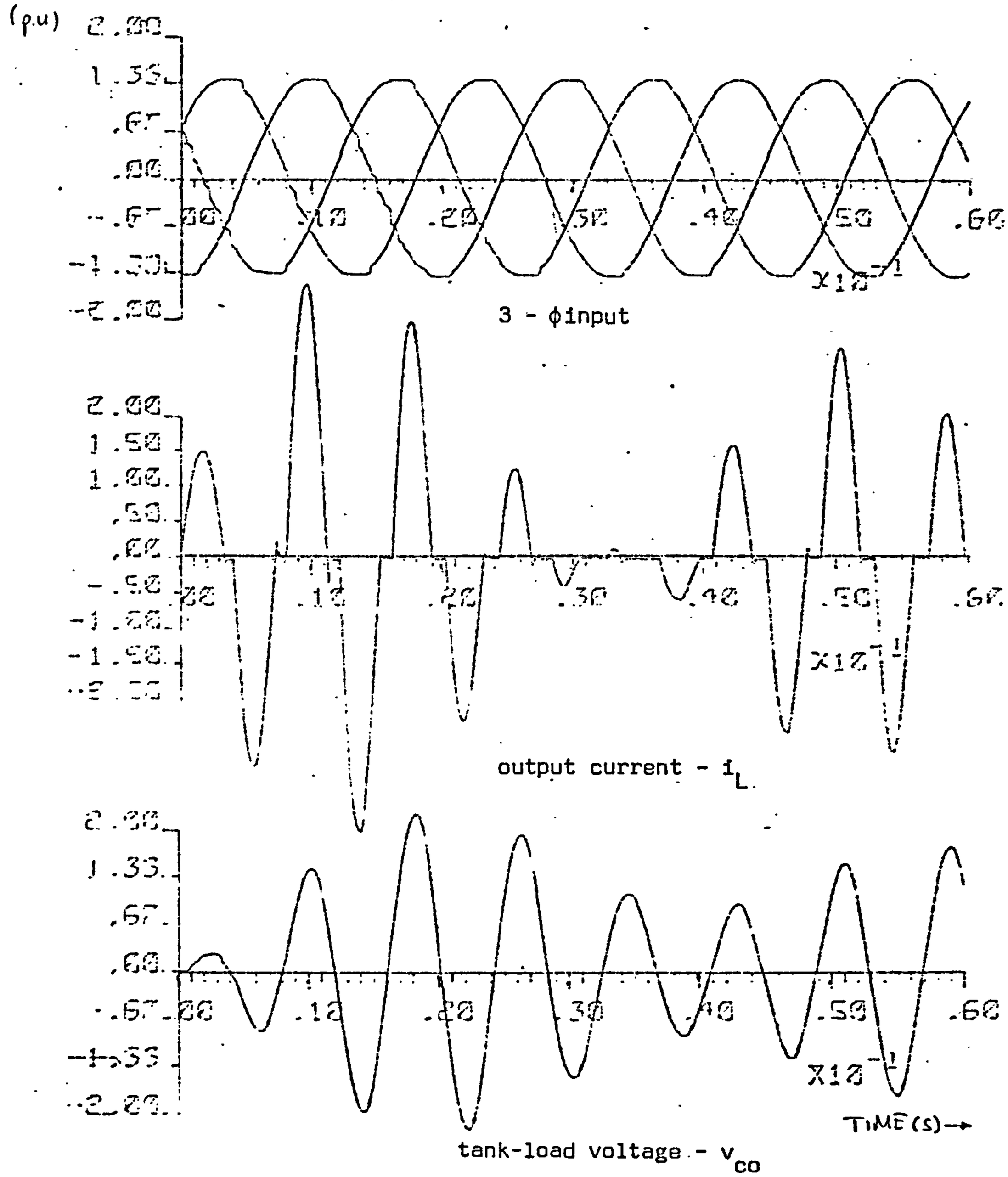

Figure 4.28c f_o = 0.8 p.u.

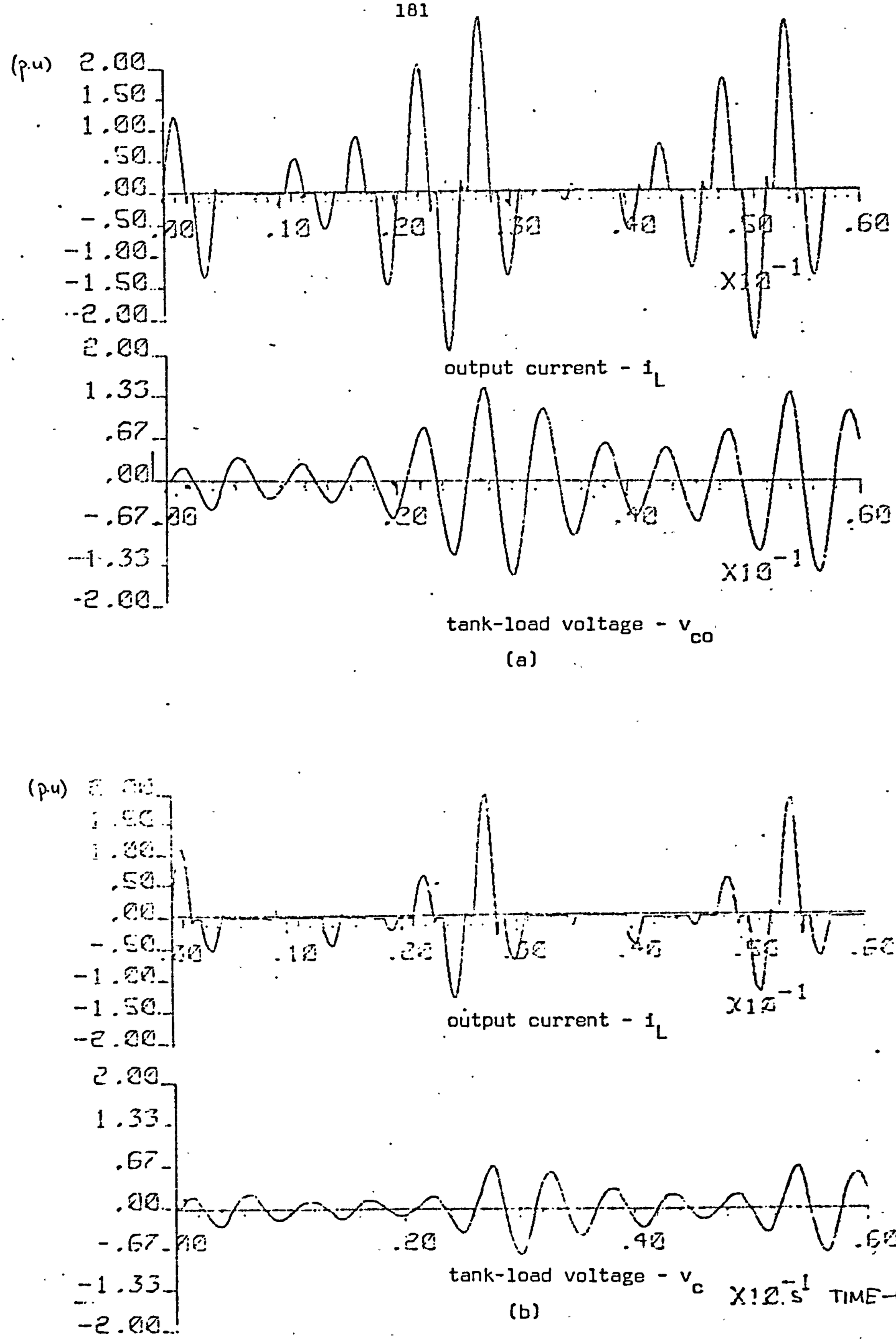

Figure 4.29 Output power control at a non-multiple output frequency (f_o = 1.25 p.u., Q_L = 5).
a) $\theta = 90^0$
b) $\theta = 120^0$

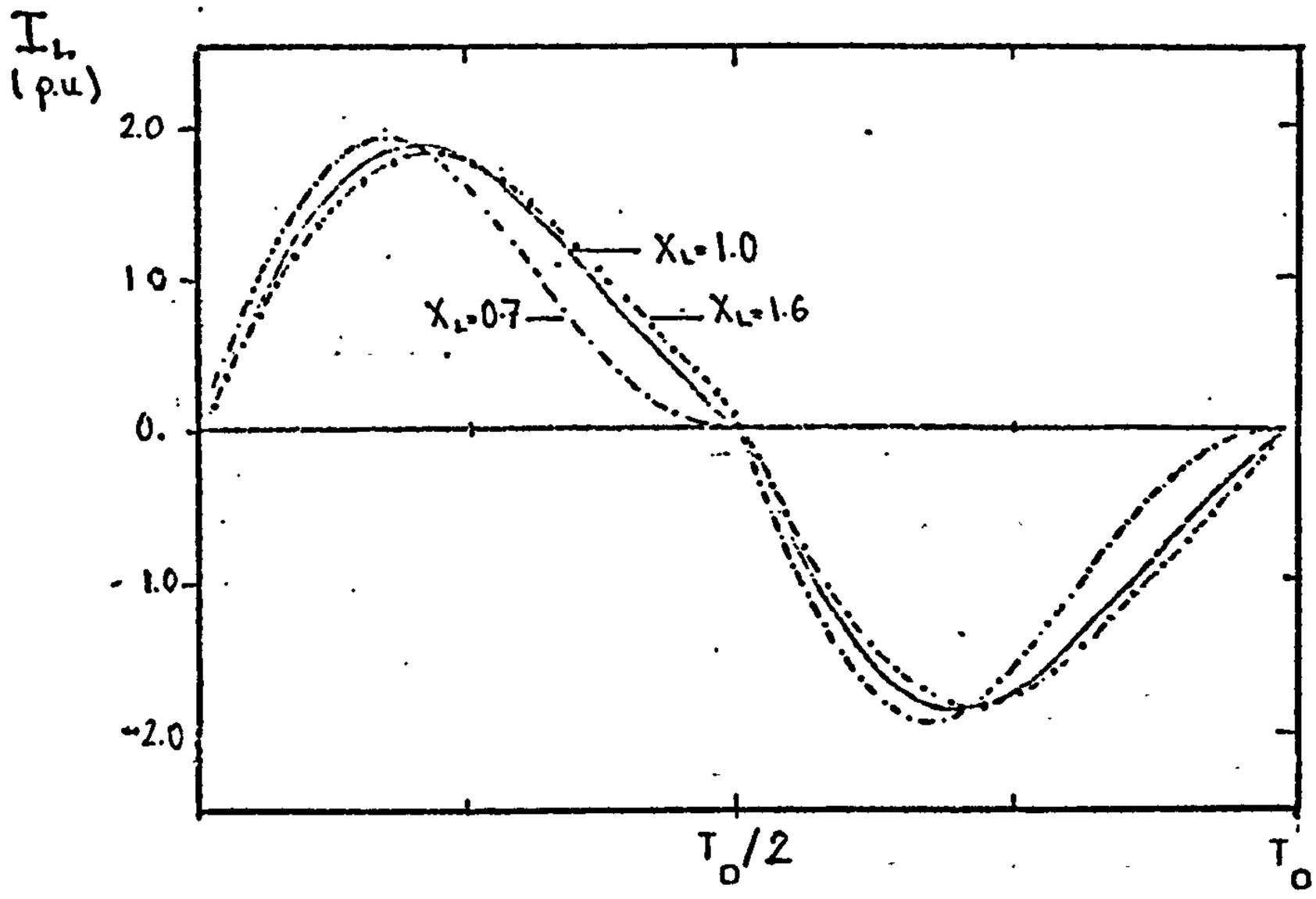

Figure 4.30 Variation of the output current waveform with X_L (for a continuous output current)

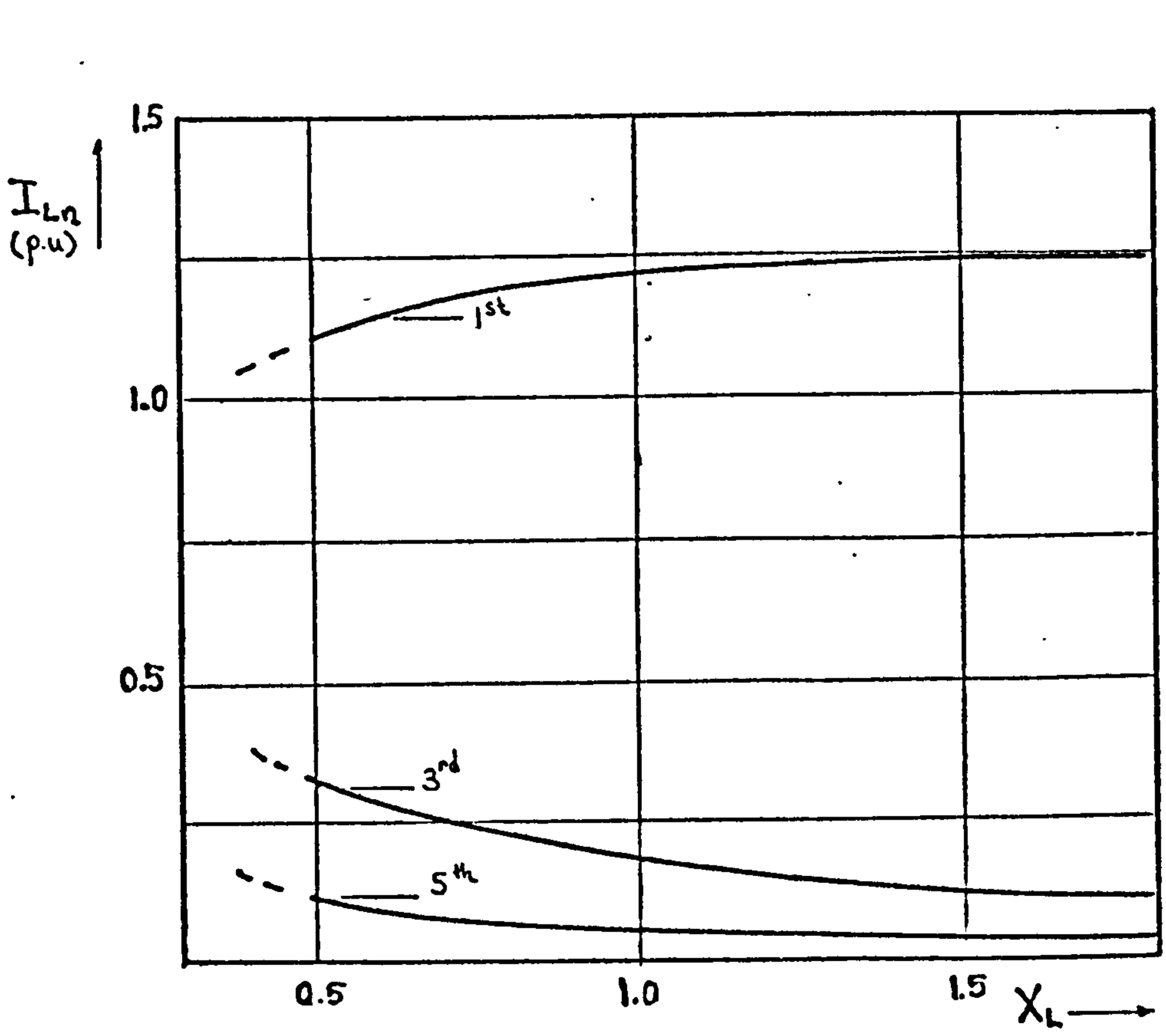

Figure 4.31 Variation of output current harmonics with X_L

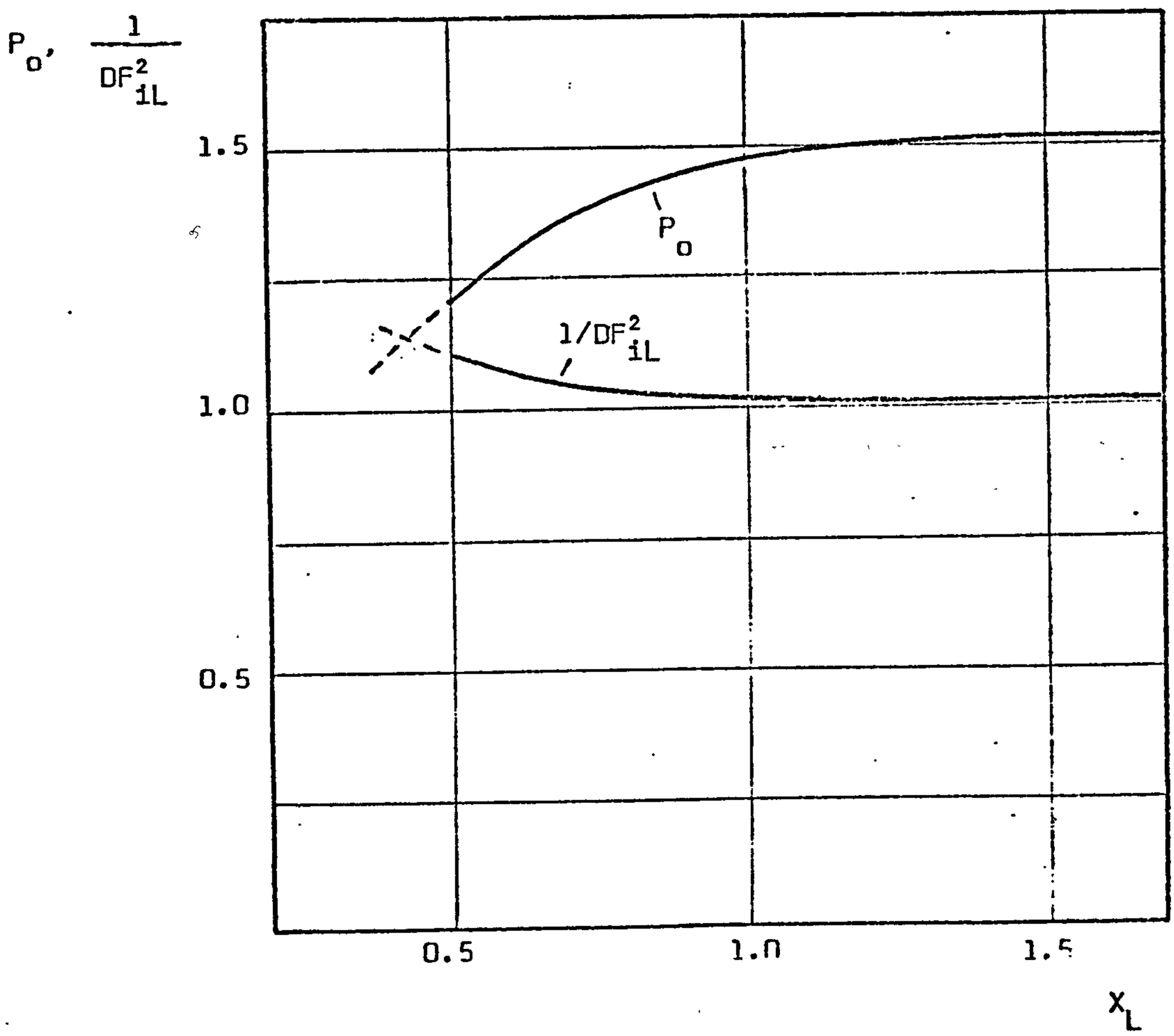

Figure 4.32 Variations with X_L of output power and relative conduction losses (i.e. $1/DF_{iL}^2$)

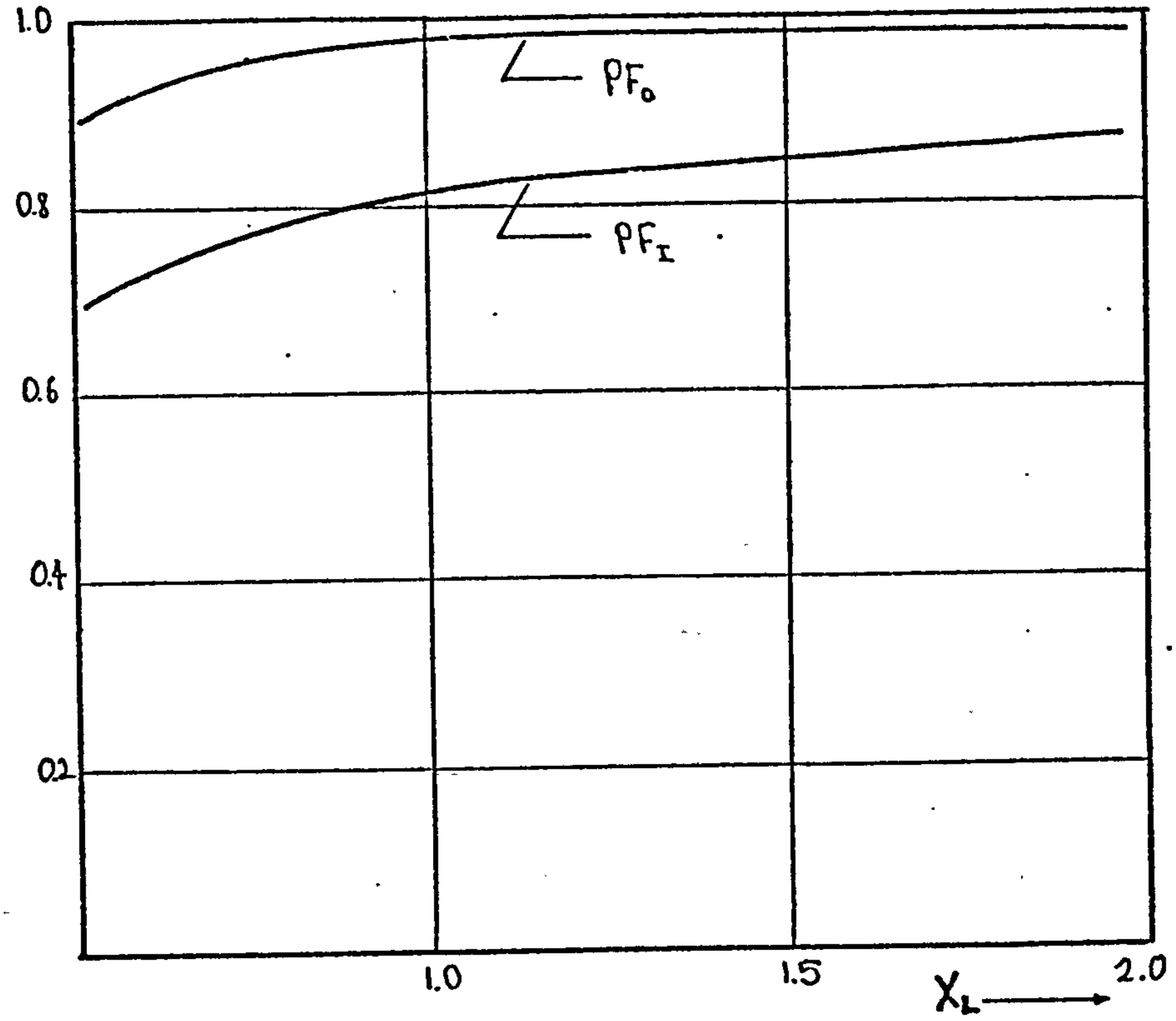

Figure 4.33 Variation of input and output power factors with X_L

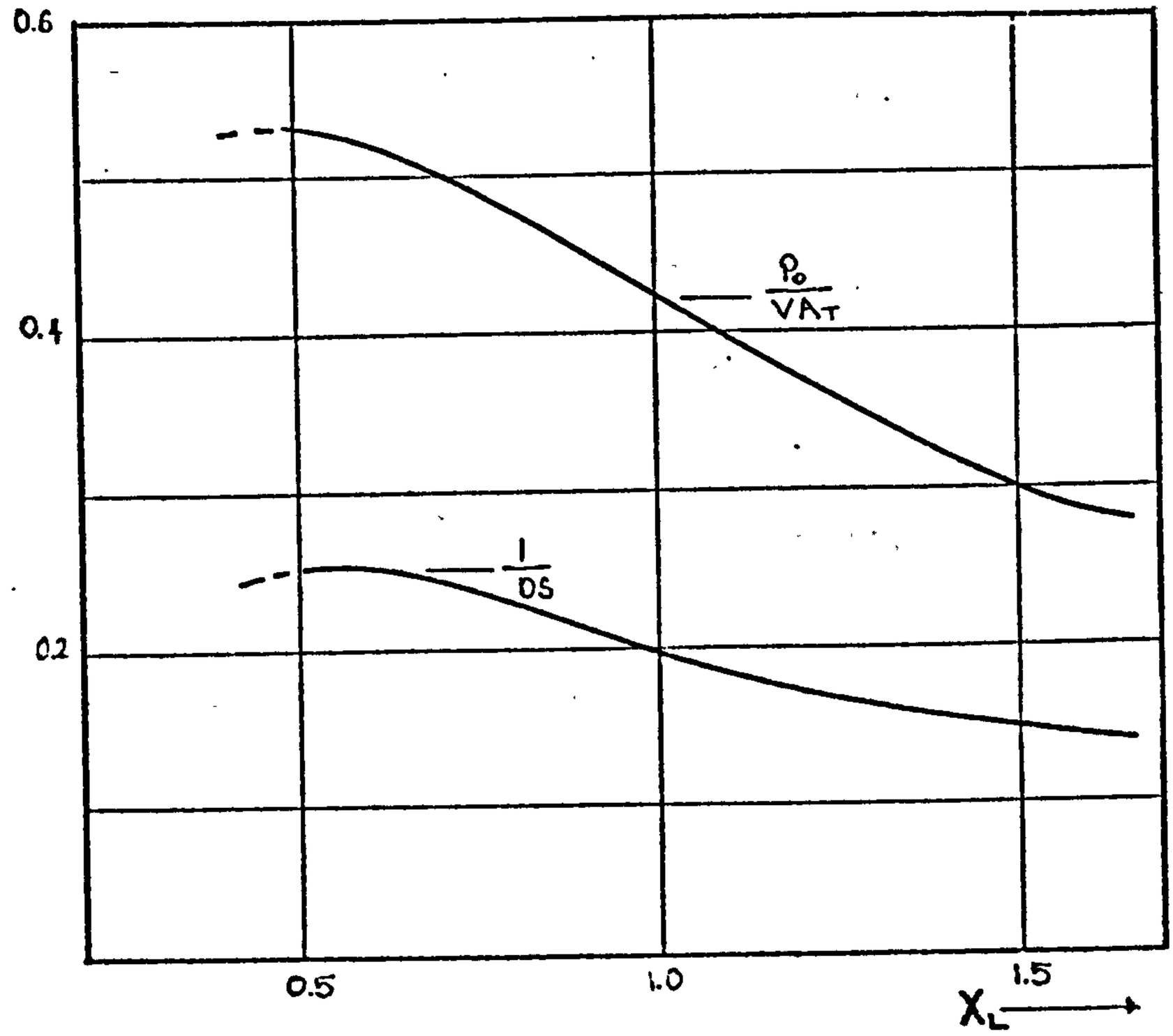

Figure 4.34 Variation of P_o/VA_T and $1/DS$ with X_L

CHAPTER 5

THE HIGH-FREQUENCY CYCLOINVERTER

The cycloinverter produces its best performance when used as a high-frequency power source (at around or above 1 kHz), for induction heating and melting applications. The improvement in the inverter performance stems from the fact that, in high-frequency applications, the controlled rectification and inversion performed simultaneously by the switching elements are more clearly distinguished, so that it is possible to control separately both the inversion frequency and the output power of the cycloinverter.

At high operational frequencies, the undesirable effects of source voltage variation on the damped resonant frequency of the output current are substantially reduced. This enables some of the shortcomings of the half-bridge cycloinverter to be overcome, and permits its wider application.

This chapter aims to study and to optimise the performance of both the half- and full-bridge versions of the cycloinverter, as applied to induction heating at these frequencies. In so doing, the analyses of the inverters are performed basically by adapting and developing the methods used for the low-frequency cycloinverter in the previous chapter. The cycloinverter performance is analysed at steady-state full output power, at reduced output power levels and under varying load conditions.

To achieve a satisfactory inverter performance at different operating modes, the distortion components generated within the inverter during these modes are given full consideration. For this purpose both the numerical and the Boolean techniques of Fourier analyses are extensively used.

5.1 Principles of Operation

The basic principles of cycloinverter operation remain unchanged at high output frequencies. The theoretical waveforms of the envelope of the input line voltage available for conversion, the input line and output currents, and the commutating circuit voltages of the inverter when delivering full output power, are as shown in Figure 5.1a and 5.1b respectively. Evidently, the input line current waveform contains a component at the input frequency, which is responsible for the per phase input power. As shown in the figure, the envelope of the output current is modulated by the input line voltage waveform. A more detailed and quantitative description of these waveforms is provided in the following sections.

The cycloinverter performs the duty of both a controlled rectifier and an inverter, and for the sake of simplicity, it may be regarded therefore as a half- (or full-) controlled bridge rectifier in cascade with a series inverter, without any intermediate filtering, as shown in Figure 5.2. Obviously, in

this case, the a.c. to d.c. converter does not have problems associated with overlap interference, since the output current is in the form of high-frequency current pulses. The model of Figure 5.2 is helpful in demonstrating the power control mechanism within the cycloinverter. Clearly, the output voltage of the half-bridge rectifier (for the case of the half-bridge cycloinverter) can be fully controlled from a maximum to zero, simply by varying the firing angle θ over the range

$$30^{o} < \theta < 210^{o} \qquad (5.1)$$

Accordingly, because the inverter output current is modulated by the input line* voltage, the output power can be controlled from a maximum to zero, within the same range of θ. In an analogous manner, it can be argued that, for the full-bridge inverter, the range of θ to achieve full output power control is:

$$30^{o} < \theta < 150^{o}$$

---

* The input line voltage of the cycloinverter may be defined as the output voltage of a rectifier with a similar configuration. Although this cannot be monitored anywhere in the cycloinverter power circuit, it nevertheless is a useful concept when describing the behaviour of the device.

However, both practical work on a prototype and the computer simulation of the full-bridge inverter presented in the following chapter, show that the upper limit of θ extends approximately to 180°, i.e.

$$30^{o} < \theta < 180^{o} \qquad (5.2)$$

The reason for this can be explained with the help of Figure 5.3. When $\theta = 150^{o}$ phase crossover occurs, and the positive and negative group thyristors which are to be fired successively (say the positive group thyristor S1 of phase 1 and the negative group thyristor S6 of phase 2) become reverse biased with respect to the line voltage between the phases. On the other hand, for $150^{o} < \theta < 180^{o}$, thyristor S1 is still forward biased with respect to the neutral and it can therefore commutate with the next negative group thyristor, which also has a forward bias condition. Within this range of power control, the output current will have a duty cycle

$$DC_{iL} = \frac{6\ T_r}{T_I} \quad \text{for } 150^{o} < \theta < 180^{o}$$

where T_r is the period of the damped resonant output current; or assuming $f_f \simeq f_o$

$$DC_{iL} = \frac{6\ f_I}{f_o} \quad \text{for } 150^{o} < \theta < 180^{o} \qquad (5.3)$$

Based on these considerations, the input line voltage available for the commutation has, in fact, the form shown in Figure 5.3(b).

In the previous chapter, power control at low operational frequencies was considered, and the minimum permissible value of θ (i.e. θ_{min}) was shown to be dependent on the output frequency. However, at high operational frequencies θ_{min} is always equal to approximately 30^{o}, as given both by conditions (5.1) and (5.2).

5.2 Theory of Operation

The methods of analysis employed in investigating high-frequency operation of a cycloinverter are:

1. Transient analysis.
2. Steady-state harmonic analysis.

Application of both of these methods to the cycloinverter power circuit was described in the previous chapter, when the low-frequency operation was studied. However, different requirements in the analysis of high frequency operation necessitate separate considerations and these are presented below.

The assumptions made in developing the methods of analysis in Section 4.2 are also required for the following considerations.

5.2.1 Transient analysis

In a cycloinverter, the number of possible operational modes of the circuit thyristors (i.e. 7), and the equivalent circuit in a particular mode, do not depend upon the operational frequency. The differential equations which describe the low-frequency operation can therefore also be used to analyse the high-frequency operation. However, since the sequence of modes through which the inverter operates is dependent on the output frequency, this is changed, and modifications are required to the digital simulation program of the cycloinverter described in Chapter 6.

For high-frequency operation, application of the digital simulation program presents some problems. As indicated by forward reference to the flow-chart diagram of Figure 6.10 steady-state conditions during the digital computation are checked by comparing the values of certain circuit quantities at two consecutive points in time, differing by the input period. If these quantities are sufficiently close, the steady-state is achieved. However, since the output frequency may not be a multiple of the input frequency, the steady-state can only be checked after:

$$n = k \frac{f_I}{f_o} \qquad (5.4)$$

complete cycles, where k is the least possible integer for which n is also an integer. If the frequency conversion ratio

is such that the value of n is high, the search for the steady-state clearly demands a substantial computation time. Use of this method of analysis in optimisation process which investigates the variation of the circuit performance with several design parameters is therefore quite impracticable.

Various circuit waveforms of a 1 kHz cycloinverter obtained via the digital simulation program have already been presented in Figure 5.1. When developing full output power (i.e. $\theta = 30^{o}$) the input line voltage seen by the cycloinverter is approximately the same for both the half- and full-bridge versions, and the waveforms are therefore common to both. Further circuit waveforms computed for different power control levels and operational frequencies will be presented in the following sections.

5.2.2 The steady-state harmonic analysis

It was seen in the previous chapter that, when applied to low-frequency operation, harmonic analysis offers a comparatively simple and rapid technique for studying the cycloinverter power circuit. However, since its application is restricted to situations which produce a continuous or an approximately continuous output current, it cannot be used in studying the inverter behaviour during power control.

When the cycloinverter is operating at full power, the switching sequence of the circuit thyristors results in the equivalent circuit seeing the input voltage waveform shown in

Figure 5.4. The Fourier series expansion of this rather complicated waveform can best be obtained by resolving it into the simpler waveforms, with known Fourier series expansions, shown in Figure 5.5. (In some publications[82] this technique is termed the *Boolean technique for Fourier analysis*). The component waveforms r(t), s(t) and u(t), z(t) in fact correspond respectively to the rectifying and the switching functions of the power circuit. As Figure 5.5 indicates, the Fourier series expansion of the input voltage (which actually appears between the neutral and the point A in Figure 4.5 can be obtained from the expansion:

$$v_{na}(t) = F[R] * F[U] + F[S] * F[Z] \qquad (5.5)$$

where F[G] indicates the Fourier series of the function g(t).

The waveform r(t) closely resembles the output voltage of a 3-phase half-bridge rectifier, so that its Fourier expansion is[79]

$$F[R] = \frac{3\sqrt{3}}{\sqrt{2}\pi} V_{LN} \left\{1 + \sum_{n=1}^{n=\infty} \left(\frac{1}{3n-1} - \frac{1}{3n+1}\right) \text{Sin} \left[3\theta_I n + (1-n)\frac{\pi}{2}\right]\right. \qquad (5.6)$$

where $\theta_I = w_I t$. Since waveforms r(t) and s(t) are mutually displaced by 60°, the Fourier expansion for s(t) is obtained by

substituting $(\theta_I + \frac{\pi}{3})$ for θ_I in expression (5.6). Thus

$$F[S] = \frac{3\sqrt{3}}{\sqrt{2}\pi} V_{LN} \{1 + \sum_{n=1}^{n=\infty} (\frac{1}{3n-1} - \frac{1}{3n+1}) \text{Sin} [3n \theta_I + n\pi + (1-n) \frac{\pi}{2}]$$

(5.7)

The Fourier series for u(t) and z(t) in terms of $\theta_o = w_o t$ are

$$F[U] = \frac{1}{2} + \frac{2}{\pi} \sum_{r=1,3}^{r=\infty} \frac{1}{r} \text{Sin } r \theta_o$$

$$F[Z] = -\frac{1}{2} + \frac{2}{\pi} \sum_{r=1,3}^{r=\infty} \frac{1}{r} \text{Sin } r \theta_o \qquad (5.8)$$

and substituting for F[R], F[S], F[U] and F[Z] in equation (5.5) yields:

$$v_{na}(t) = \frac{3\sqrt{6}}{\pi} \{[1 + \sum_{n=1,2,3}^{n=\infty} (\frac{1}{6n-1} - \frac{1}{6n+1}) \text{Sin } [6n \theta_I + (1-2n) \frac{\pi}{2}]$$

$$* \frac{2}{\pi} \sum_{r=1,3}^{r=\infty} \frac{1}{r} \text{Sin } r \theta_o$$

$$+ \frac{1}{2} \sum_{n=1,3,5}^{n=\infty} (\frac{1}{3n-1} - \frac{1}{3n+1}) \text{Sin } [3n \theta_I + (1-n) \frac{\pi}{2}]\} \text{ p.u.}$$

(5.9)

or

$$v_{na}(t) = \frac{6\sqrt{6}}{\pi^2}\{\text{Sin } w_o t - \frac{1}{35}\,[\text{Sin } (w_o - 6\,w_I)t + \text{Sin } (w_o + 6\,w_I)t]$$

$$+ \frac{1}{153.8}\,[\text{Sin } (w_o + 12\,w_I)t + \text{Sin } (w_o - 12\,w_I)t] + \ldots$$

$$+ \frac{1}{3}\,\text{Sin } 3\,w_o t - \frac{1}{105}\,[\text{Sin } (3\,w_o - 6\,w_I)t + \text{Sin } (3\,w_o + 6\,w_I)t]$$

$$+ \ldots\ldots \qquad + \frac{1}{5}\,\text{Sin } 5\,w_o t + \ldots.$$

$$+ \frac{3\sqrt{6}}{2\pi}\,[\frac{1}{4}\,\text{Sin } 3\,w_I t - \frac{1}{40}\,\text{Sin } 9\,w_I t + \ldots.]\} \quad \text{p.u.}$$

(5.10)

On this basis, the harmonic content of the output current, tank-load voltage and the heating coil current can be calculated, as described in Section 4.2.2.3.When pursuing the analysis further, it can be shown that the output current expression has the form:

$$i_L(t) = \frac{6\sqrt{6}}{\pi^2}\left\{\frac{1}{|Z_{wx}|}\ \mathrm{Sin}\ (w_o t + \beta_x) - \frac{1}{35}\left(\frac{1}{|Z_{wx}|}\ \mathrm{Sin}[(w_o - 6w_I)t + \beta_x]\right.\right.$$

$$+ \frac{1}{|Z_{wx}|}\ \mathrm{Sin}\ [(w_o + 6\,w_I)t + \beta_x]) + \cdots$$

$$+\frac{1}{3|Z_{wx}|}\ \mathrm{Sin}\ (3\,w_o t + \beta_x) + \cdots\cdots$$

$$+\ \frac{3\sqrt{6}}{8\pi}\ \left[\frac{1}{|Z_{wx}|}\ \mathrm{Sin}\ (3\,w_I t + \beta_x)\right] + \cdots\cdots\cdots\ \Big\}\ \text{p.u.}$$

(5.11)

where Z_{wx} and β_x are respectively the impedance and the phase delay of the output circuit at the frequency involved.

Expression (5.11) represents basically a waveform with output frequency harmonics of nw_o and sidebands at frequencies $\pm$ 6 kw_I. Calculations for a range of values of X_L and X_C which produced successful commutation, showed that the second and higher sidebands (i.e. those greater than $w_o \pm 12\ w_I$) and components at triple multiples of the input frequency ($3nw_I$) could be ignored without introducing any appreciable error. In addition to its restricted application, a major weakness of the harmonic analysis

approach is that it cannot directly provide information on the input conditions of the cycloinverter. Fortunately, the harmonic analysis developed for the input line current in the next section fulfils this requirement.

5.2.3 Harmonic analysis of the input line current

The harmonic models of the cycloinverter developed for low operational frequencies in Chapter 4 remain fully applicable for inverter operation at high frequencies. However, calculation of the harmonic content of the input line current from these models requires a knowledge of the harmonic content of the thyristor currents, and this is not readily available. A different technique needs therefore to be adapted for this purpose.

The waveform of the input current shown in Figure 5.1 indicates clearly that in obtaining the harmonic content of the input line current, the conventional technique of separately integrating each and every segment to find the Fourier constants is both time consuming and tedious. This process may, however, be avoided by calculating the Fourier series of this current from a knowledge of the harmonic content of the output current.

Figure 5.6 illustrates the formation* of the input current

---

* This is based on equation (4.11). For the sake of clarity in Figure 5.6, the commutating capacitor current due to the input phase voltage (i.e. $C\dot{v}_1$ in equation (4.11)) is omitted. This component is, nevertheless, considered in the input current equation (5.12).

in line 1, i_1, for a known output current, by use of the Boolean functions $u(\phi_o)$, $z(\phi_o)$, $g(\phi_I)$ and $h(\phi_I)$. The functions $u(\phi_o)$ and $z(\phi_o)$ define the intervals of positive and negative output current flow respectively, whereas $g(\phi_I)$ and $h(\phi_I)$ correspond to the times at which line 1 is delivering the output power. As shown, the Boolean expression for i_1 is obtained in the form

$$i_1 = \left\{ -\frac{1}{3} + F[U] * F[G] * F[Z] * F[H] \right\} * F[I] + \sqrt{2}\ \frac{1}{X_c}\ \frac{w_I}{w_o}\ \text{Cos}\ w_I t \qquad (5.12)$$

The Fourier series of a general rectangular waveform of unit amplitude, and with a delay γ_1 and width γ_2 (Figure 5.7) is:

$$q(\phi) = F[Q] = \frac{\gamma_2}{2\pi} + \sum_{r=1,3,5}^{r=\infty} \left\{ \frac{2}{r\pi}\ \text{Sin}\ \frac{\gamma}{2}\ \text{Cos}\ (\gamma_1 + \frac{\gamma_2}{2} - \phi)n \right\} \qquad (5.13)$$

On substituting the appropriate quantities in the above equation, the Fourier representationsof the Boolean functions are obtained as:

$$F[U] = \frac{1}{2} + \sum_{r=1,3,5}^{\infty} \frac{2}{r\pi} \text{Sin } r\,\phi_o$$

Since $z(\phi) = 1 - u(\phi)$

$$F[Z] = \frac{1}{2} - \sum_{r=1,3,5}^{\infty} \frac{2}{r\pi} \text{Sin } r\,\phi_o$$

and

$$F[G] = \frac{1}{3} + \sum_{n=1,2}^{\infty} \frac{2}{n\pi} \text{Sin } \frac{n\pi}{3} \text{Cos } (\phi_I - \theta - \frac{\pi}{3})n \qquad (5.14)$$

$$F[H] = \frac{1}{3} + \sum_{n=1,2,3}^{\infty} \frac{2}{n\pi} \text{Sin } \frac{n\pi}{3} \text{Cos } (\phi_I - \theta - \frac{4\pi}{3})n \qquad (5.15)$$

In the half-bridge inverter, only the most negative phase supplies the negative load current pulse, and the position of $h(\phi_I)$ does not change with reference to v_1 for varying power control angle, θ. On the other hand, the interval that the thyristor in phase 1 (thyristor S1) is active (corresponding to $g(\phi_I)$) shifts in position relative to v_1, until its negative-

going edge coincides with 210^{o}, which is the limit of the conduction interval of thyristor S1. When this limit is reached, there is no need to reduce further the width of $g(\phi_I)$ for higher values of θ, since with the variation in the wave shape of the output current, this is performed automatically and simultaneously within the multiplication. Clearly, the Boolean function corresponding to the positions of the positive and the negative current pulses $u(\phi_o)$ and $z(\phi_o)$ remains unchanged throughout power control.

If the cycloinverter has the full bridge configuration, the positions of both $g(\phi_I)$ and $h(\phi_I)$ shift with θ, in a manner similar to the variation of $g(\phi_I)$ in the half-bridge inverter, but only until their negative-going edge coincides respectively with the end of the positive and negative cycles of phase 1. This difference of behaviour between the two inverters during their power control modes is reflected in equation (5.15), so that although for the half-bridge inverter θ is replaced by $\frac{\pi}{6}$, for the full-bridge it remains unaltered.

With the Boolean functions shown in Figure 5.6, it is also possible to synthesise the thyristor current waveforms. Since $g(\phi_I)$ defines the active interval of thyristor S1, the current flowing through it is:

$$i_{s1} = F[U] * F[G] * F[I] \qquad (5.16)$$

Similarly, the current flowing in the reverse direction (through thyristor S4 for the case of the full-bridge, and thyristor S4 and diode D1 for the case of the half-bridge), is:

$$i_{s4} = F[Z] * F[H] * F[I_L] \qquad (5.17)$$

Hence the current at the input for whichever device is in line 1 is:

$$i_{1s} = \{F[U] * F[G] + F[Z] * F[H]\} * F[I_L] \qquad (5.18)$$

It is interesting to note, from equations (5.12) and (5.18), that:

$$i_{1s} = i_1 + \frac{1}{3} i_L - \sqrt{2} \frac{1}{X_c} \frac{w_I}{w_o} \text{Cos } w_I t \qquad (5.19)$$

The harmonic content of the input line current can be obtained by introducing the Fourier representations of the Boolean functions into equation (5.12). On so doing and on applying familiar trigonometric relationships:

$$i_{1H\text{-}B} = \{ \sum_{n=1,2,3}^{\infty} \frac{2}{\pi n} \text{Sin} \frac{\pi n}{3} .\text{Cos} \left(\frac{7\pi}{12} - \frac{\theta}{2}\right).\text{Cos} \left(\phi_I - \frac{\theta}{2} - \frac{11\pi}{12}\right)n$$

$$+ \sum_{r=1,3,5}^{\infty} \frac{2}{\pi r} \text{Sin}\ r\phi_o \sum_{n=1,2,4,5}^{\infty} \frac{4}{\pi n} \text{Sin}\left(\phi_I - \frac{\theta}{2} - \frac{11\pi}{12}\right)n.\text{Sin} \frac{n\pi}{3} .\text{Sin}\left(\frac{\theta}{2} - \frac{7\pi}{12}\right)n\}*F[I_L]$$

$$+ \sqrt{2}\, \frac{1}{X_c} \frac{w_I}{w_o} \text{Cos}\ w_I t \qquad (5.20)$$

for the half-bridge inverter, and

$$i_{1F\text{-}B} = \{ \sum_{n=2,4,6}^{\infty} \frac{2}{\pi n} \text{Sin} \frac{\pi n}{3} . \text{Cos} \frac{\pi n}{2} . \text{Cos} \left(\phi_I - \theta - \frac{5\pi}{6}\right)n$$

$$- \sum_{r=1,3,5}^{\infty} \frac{2}{\pi r} \text{Sin}\ r\phi_o \sum_{n=1,5,7,11}^{\infty} \frac{4}{\pi n} \text{Sin} \frac{\pi n}{3} .\text{Sin} \frac{\pi n}{2} .\text{Sin}\left(\phi_I - \theta - \frac{5\pi}{6}\right)n\}*\ F[I_L]$$

$$+ \sqrt{2}\, \frac{1}{X_c} \frac{w_I}{w_o} \text{Cos}\ w_I t \qquad (5.21)$$

for the full-bridge inverter. Using these equations, the input line currents of both types of cycloinverter can be calculated

for a given $F[I_L]$.

If only the dominant harmonics are included, the Fourier expansion of the output current for both cycloinverters at full power may be approximated to (see equation (5.11)):

$$F[I_L] = A_{11}\mathrm{Sin}(\phi_o + \psi_{11}) + A_{16}\mathrm{Sin}(\phi_o + 6\phi_I + \psi_{16}) + A'_{16}\mathrm{Sin}(\phi_o - 6\phi_I - \psi'_{16})$$

$$+ A_{31}\mathrm{Sin}(3\phi_o + \psi_{31}) \qquad (5.22)$$

On substituting $F[I_L]$ in equations (5.20) and (5.21), the power component of the input line current (i.e. the source frequency component) is obtained as approximately:

$$i_{11H\_B} = 0.247\ [A_{11}\mathrm{Cos}\,\psi_{11}.\mathrm{Sin}\,(\frac{7\pi}{12} - \frac{\theta}{12}).\mathrm{Sin}\,(w_I t - \frac{\theta}{2} + \frac{\pi}{12})$$

$$+ \frac{A_{13}}{4}\,\mathrm{Sin}\,2(\frac{7\pi}{12} - \frac{\theta}{2}).\mathrm{Sin}(w_I t - \psi_{13} + \theta + \frac{11\pi}{6})$$

$$+ \frac{A'_{13}}{4}\,\mathrm{Sin}\,2(\frac{7\pi}{12} - \frac{\theta}{2}).\mathrm{Sin}(w_I t + \psi'_{13} + \theta + \frac{11\pi}{6})]$$

$$+ \sqrt{2}\ \frac{1}{X_c}\ \frac{w_I}{w_o}\,\mathrm{Cos}\ w_I t \quad \text{p.u.} \qquad (5.23)$$

for the half-bridge inverter, and as:

$$i_{11F-B} = 0.247\ [A_{11} \text{Cos}\ \psi_{11} \text{Sin}(w_I t - \theta + \frac{\pi}{6})]$$

$$+ \sqrt{2}\ \frac{1}{X_c}\ \frac{w_I}{w_o} \text{Cos}\ w_I t \qquad \text{p.u.} \qquad (5.24)$$

for the full-bridge inverter.

Considering the general form of the input power expression:

$$P_I = 3\ I_{11}\ V_{LN} \text{Cos}\ \delta \qquad (5.25)$$

the above equations indicate* that:

- the cycloinverter input power is a maximum when $\theta = 30^o$, and the maximum input power is identical for both inverters.
- at full output power the input displacement factor Cos δ (for the assumed tuned load conditions) is approximately equal to 1. This conclusion confirms the results of the digital simulation shown in Figure 5.1.

---

* Calculations show that Cos $\psi_{11} \simeq 0.96$, and since Cw_I is numerically small, the term $\sqrt{2}\ \frac{1}{X_c}\ \frac{w_I}{w_o}$ Cos $w_I t$ may be neglected.

- at reduced output power levels, i.e. $\theta > 30^{\circ}$, the input displacement factor is lagging.

- equations (5.20) and (5.21) indicate that at full output power, the predominant input distortion harmonics are

$$w_o \pm 2\, w_I, \qquad w_o \pm 4\, w_I, \qquad 5\, w_I$$

In order to obtain further information on the harmonic content of the input line current at reduced output power levels, the increasing amplitudes of the sideband harmonics of the output current must be taken into account, by expanding equation (5.22).

Figure 5.8 shows the variation with θ of the harmonic spectrum of the input current of the full-bridge cycloinverter. The spectrum is obtained from a numerical Fourier analysis performed in the computer simulation program, immediately after steady-state conditions are established. The frequency spectrum of the input line current given here is in close agreement with the input current harmonics predicted by equation (5.21). The harmonics at frequencies $5\, f_I$ and $7\, f_I$ are caused mainly by the increasing output current sidebands at lower output power levels. Clearly, when the amplitudes A_{16} and A'_{16} in the output current expression (5.22) becomes significant, the $5\, f_I$ and $7\, f_I$ frequencies are primarily generated by multiplication of the terms:

$$\text{Sin } (\phi_o \pm 6\ \phi_I) \quad \text{and} \quad \text{Cos } [\phi_o \pm (\phi_I - \theta - \frac{5\pi}{6})]$$

5.2.4 Comparison of the results of the harmonic and transient analyses

Figure 5.9 shows the waveform and the harmonic spectrum of the output current, obtained from the transient analysis, for a 1050 Hz cycloinverter with design values of X_L = 1.2 p.u. and X_c = 1.3 p.u. and operating at full output power. The spectrum is in close agreement with the analytical output current expression (5.11) derived for the harmonic analysis. The output current waveform which this expression produces for the same values of X_L and X_c, is shown later in Figure 5.32, together with the dominant harmonics of the waveform. The consistency of these results indicates the correctness of both analyses, and justifies the assumptions made in their development.

The harmonic spectrum of Figure 5.9 is obtained via a numerical analysis, performed immediately after steady-state conditions are achieved in the digital simulation. The accuracy of the numerical Fourier analysis is confirmed later, by reversing the procedure and reproducing a time-domain output by feeding in a sufficient number of calculated Fourier components.

Selection of an output frequency of 1050 Hz is not arbitrary, but serves to simplify application of the numerical

Fourier analysis which requires an accurate description of the waveform throughout its period. Because the output current contains distortion terms,which are related to both input and output frequencies, these constitute beat frequency components of high period, and cause application of the analysis for a non-multiple output frequency to require an excessive computation time. On the other hand, the periods of the beat frequencies drops considerably for multiple output frequencies, enabling appreciable savings in the computation time to be achieved, especially at triplen output frequencies, and a balanced loading of the 3-phase source. The frequency of 1050 Hz was therefore selected for the investigation, since it is the triplen output frequency nearest to 1 kHz.

5.3 Output Power Control and Output Harmonics

The basic principles of power control in the cycloinverter have already been mentioned. Although the power control scheme, being inherent in the configuration, offers significant advantages, it does unfortunately have one important problem. The high-frequency output waveform has a low-frequency source waveform as an amplitude-modulated envelope, and the depth of the modulation progressively increases at reduced output power levels. For some heat treatment applications, the distortion

currents in the heating coil must be removed, or reduced to acceptably low levels, since they may otherwise cause faults in the process (such as deviations from the intended penetration depth etc), as various load parameters are highly dependent on the frequency of the heating coil current. Nevertheless, for most induction heating applications such as metal melting, reasonably low level distortion harmonics may be tolerated.

Owing to its well-suited load characteristics, the power control capacity of the cycloinverter can be exploited to a considerable extent in induction heating applications, without any additional circuitry. As is quantitatively supported later in this section, the filtering action of the tuned load circuit of an induction heating load is generally sufficient to exercise a wide range of output power control.

In a high-frequency cycloinverter with an induction heating load, the harmonic content of the load voltage depends mainly on:

1. The number of phases involved in the power conversion,
2. The firing or power control angle, θ,
3. The selectivity and the tuning conditions of the tank-load circuit,
4. The commutating components.

Among these factors, the effect on the load voltage waveform of the varying commutating components which produces a sensible inverter performance is of secondary importance. However, they are the principal parameters determining the overall cycloinverter performance and therefore, and for the sake of clarity, they are investigated separately in Section 5.4.1. The remaining items are investigated below.

5.3.1 The multi-phase cycloinverter

It has been established that in a high-frequency cycloinversion process with series commutation, the envelope of the input line voltage is reflected to the output, as the envelope of the output current pulses. Since this is in fact a result of the direct energy conversion in a cycloinverter, whereby the source directly *sees* the load, it is possible to obtain a smoother output current by including more phases into the cycloinversion.

Before the introduction of multi-phase cycloinverters, the output distortion of single-phase cycloinverters presented a serious problem. A typical single-phase cycloinverter with a synchronous tap changer (Figure 1.8) was introduced in Chapter 1.

As mentioned, the synchronous tap changer operates by synchronously changing the number of primary turns so as to

reduce the harmonic content of the secondary voltage. Although this filtering scheme is conceptually simple, its design and optimisation are rather complex. Moreoever, a high number of switching elements is required, in comparison with a multi-phase cycloinverter in which the output smoothing is done within the inverter by changing the output voltage successively from one line to another.

The advantage of the multi-phase cycloinversion may be more explicitly demonstrated by using the output current expression (5.11). When deriving this equation, the input voltage to the harmonic equivalent circuit is assumed to have the form shown in Figure 5.5. If, however, the cycloinverter consists of (say) 6-phases, the rectifier voltage waveforms r(t) and s(t) contain harmonics at frequencies $\pm 12\ nw_I$, giving rise to sidebands at $w_o \pm 12\ nw_I$ in the output current equation. Eliminating harmonics at frequencies $w_o \pm 6\ nw_I$ in equation (5.11) gives the amplitudes of the first sidebands as:

$$\frac{1}{153.8}\ \frac{1}{|Z_{wx}|}$$

As the example above indicates, increasing the number of phases in the cycloinversion is advantageous in two ways, as it causes:

1. an increase in the amplitude of the sideband.

2. an increase in the separation of the sidebands from the carrier,

leading to a more effective filtering action for a given tank-load selectivity.

5.3.2 Effect of power control on the output harmonics

Because the application of the harmonic analysis approach is restricted to full output power operation, the power control mode of the inverter operation is investigated by means of a transient study via a digital simulation.

The computation time limitation of the transient analysis clearly imposes some restraints on its application. In general, the numerical analysis produces accurate results for any particular set of conditions in a given system, but these are of limited use in demonstrating how the results are related to the system parameters. To generalise the analysis, it is necessary therefore to repeat the computation with varying parameter values. Considering these, the following analysis is performed with fixed values of X_L and X_c, with the operational frequency selected as 1050 Hz. The values X_L and X_c (1.0 and 1.05 p.u. respectively) are chosen from among those which ensure successful commutation of the circuit thyristors, and produce a sensible inverter performance. The effect of varying both X_L and X_c is investigated later in Section 5.4.

To determine the effect of the output power control on the harmonic content of the load voltage of the cycloinverter, the steady-state output current waveforms at various power control angles θ were obtained from the digital simulation of the inverter. A Fourier analysis of these waveforms was subsequently performed within the same computer program, so that the variation in the frequency spectrum of the output current with θ was obtained. This also enables the variations of both the useful output power and the input power factor with the control angle to be investigated.

As the power developed in the induction heating load is assumed to be an I^2R relation, the distortion factor of the heating coil current DF_{iLo} becomes an important parameter, when used as a measure of the output power developed by the sidebands. This component of the output power is undesirable, and it may be regarded as a wasted power P_w which is:

$$\frac{P_w}{P_o} = \frac{P_{CT} - P_o}{P_o} = \frac{R_o I_{Lo}^2 - R_o I_{Lo1}^2}{R_o I_{Lo1}^2} \qquad (5.26)$$

$$P_w = \frac{1}{DF_{iLo}^2} - 1 \quad \text{per useful output power} \qquad (5.27)$$

When performing the above calculations, there is no need to repeat the Fourier analysis for i_{Lo}, once the harmonic content

of i_L is obtained, since its harmonic content can be calculated from the known harmonics of i_L, as described in Section 4.2.2.3.

5.3.2.1 Power control in the half-bridge cycloinverter

Figures 5.10 and 5.11 show various steady-state circuit waveforms in a half-bridge cycloinverter, for power control angles of 30°, 90°, 120° and 150°. These theoretical waveforms, obtained via a digital simulation, clearly indicate the progressive worsening in the harmonic content of the output current and the tank-load voltage with reducing output power.

Figures 5.12 to 5.14 show frequency spectra of the output current and the heating coil current for the same control angles, and Figure 5.15 combines information from Figures 5.12 to 5.14 to show explicitly the variation of the frequency spectrum of the output current with θ.

The variation of the useful output power P_o with θ was evaluated from the variation of the fundamental (1050 Hz) component of the output current, and is given in Figure 5.16. It will be noted that, although the full range of θ was given in Section 5.1 as 30° to 210°, the output power has already fallen to well below 10% of its maximum at an angle of 180°.

The variations of the distortion factor of the heating coil current and the wasted power per useful output power are shown in Figure 5.17, which indicates that the useful output power can be reduced to 65% of its maximum at the cost of wasting 20% of the power delivered to the load (in Figure 5.17 the ratio $\frac{P_w}{P_o} = 0.25$, which gives $\frac{P_w}{P_{CT}} = \frac{1}{5}$).

Results obtained so far indicate that, for an induction heating load of coil selectivity 5, the power control characteristic of the half-bridge cycloinverter is not altogether satisfactory. The power wasted can, of course, be reduced by additional filtering at the output. On the other hand, for applications where a power control facility is vital, preference may be given to the full-bridge cycloinverter to be investigated next.

5.3.2.2 Power control in the full-bridge inverter

It has been seen that the first sideband harmonics $w_o \pm 3\ w_I$ of the output current of the half-bridge inverter are mainly responsible for the deteriorating performance of the inverter during the power control mode of operation. The full-bridge configuration enables these harmonics to be eliminated and hence produces a more efficient performance at reduced output power levels.

Figures 5.18 and 5.19 show digitally-computed variations of the input line current i_1, the output current i_L, and the

load voltage v_{co}, for power control angles of 90° and 120°. To obtain further information from these waveforms, the harmonics of the output current were analysed numerically (as for the half-bridge inverter). The results of this analysis, giving the harmonic spectra of the output current and of the coil current are shown, together with their waveforms, in Figures 5.20 and 5.21.

The output current spectra for various control angles presented in Figure 5.22 shows an improvement in its harmonic content when compared with Figure 5.15. The variation of the useful output power with θ, together with that for the half-bridge inverter, was given previously in Figure 5.16 which showed that the output power falls to 10% of the maximum when θ is around 135°. The distortion factor of the coil current DF_{ILo}, and the power lost in the heating coil in achieving the power control, were also given in Figure 5.17, together with the same quantities for the half-bridge inverter.

5.3.3 Effect of the heating coil selectivity on the output harmonics

Obviously, the harmonic content of the tank-load voltage depends to a great extent on the selectivity of the second-order LC-filter formed by the tuned tank circuit. The filtering action of the load naturally becomes more effective as the sidebands depart from the output frequency.

For example, to attenuate the power in the sidebands adjacent to the output frequency $w_o \mp w_s$ by a factor of 2, would require the tuned tank-load circuit to have a selectivity of[84]

$$Q_L = \frac{w_o}{4\, w_s}$$

For attenuation by a factor of 10, Q_L becomes:

$$Q_L = \frac{w_o}{w_s}$$

so that if the ratio w_o/w_s is high, effective filtering requires quite impractical values of Q_L (whereas, for an induction heating coil Q_L is usually within the range 5 to 20).

Fortunately, however, the formulae above do not cover all aspects of sideband attenuation in cycloinverter power circuits. As is shown later in Section 5.5, at high output frequencies, which produce high w_o/w_s for a given configuration, the cycloinverter output circuit has a high impedance at the sideband frequencies, and these components are therefore considerably attenuated prior to filtering.

In order to show the effect of varying Q_L on the performance of both the full- and the half-bridge cycloinverters, this was varied over the likely range for a heating coil, and the corresponding cycloinverter output quantities were computed.

Figures 5.23 to 5.24 show some of the results obtained, for Q_L = 5, 10 and 20 and for various modes of operation of both types of inverter. These figures demonstrate clearly the improvement obtained in the tank circuit voltage waveform with an increase in Q_L. The output current waveforms shown in Figures 5.25 and 5.26 indicate that the variation of Q_L does not cause any significant change in the output current waveform of the full-bridge inverter, whereas it does produce a slight improvement in the harmonic content of that of the half-bridge inverter.

The variation of the wasted power P_W with useful output power for both cycloinverter configurations is shown in Figures 5.27 and 5.28. Figure 5.27 indicates that the power control performance of the half-bridge inverter significantly improves with Q_L, so that with a coil selectivity of 10, for example, the useful output power can be halved at a cost of wasting about 7.5% of the power delivered to the load. Clearly, for higher values of Q_L, the power control range increases further. On the other hand the power control performance of the full-bridge inverter with increased Q_L is quite satisfactory for most high power induction heating applications.

5.3.4 Variation of input power factor with power control

The input power factor of a cycloinverter is given by

$$PF_I = \frac{V_{LN} \cdot I_{11}}{V_{LN} \cdot I_1} \text{ Cos } \delta \qquad (5.28)$$

or:

$$PF_I = \text{(Displacement factor)} \times \text{(Input current distortion factor)} \tag{5.29}$$

and since the harmonic content of the input current is known, from equations (5.20) and (5.21), these quantities can be calculated. Alternatively, by ignoring the cycloinverter power losses and the power dissipated in the heating coil due to the distortion components (i.e. P_W), the input power expression (5.28) may be converted to a more useful form of:

$$PF_I = \frac{P_o}{V_{LN} \cdot I_1}$$

which also helps to simplify the calculations.

Because of the complexity of the input line current expression, the calculation of its r.m.s. value I_1 is difficult. Nevertheless, the selection of the output frequency as an integral multiple of the input frequency clearly produces beat frequencies at multiples of the input frequency, and permits the calculation of I_1 from[85]:

$$I_1 = \sqrt{\sum_{n=1}^{\infty} I_{1n}^2} \tag{5.31}$$

so that all quantities in the input power factor equation are known.

Figure 5.29 shows the variation of PF_I with the power control angle θ, for both the half-bridge and the full-bridge cycloinverters. As expected, the input power factor of the full-bridge inverter is considerably better than that of the half-bridge inverter, although it is still low, particularly for power control greater than 50% (i.e. at 50%, $PF_I = 0.6$). This inferior power factor is unfortunately inherent in the basic power control mechanism of the cycloinverter, and, in this respect, shows similarities with the power factor performance of the cycloconverters.

In fact, without resorting to detailed mathematics, it can be shown that the maximum input power factor of a cyclo-inverter (which corresponds to full output power) is limited to a value lower than the maximum input power factor of a rectifier with a similar configuration. To do this, the maximum output power developed in the cycloinverter and the a.c. to d.c. converter are compared for a fixed input VA rating as follows (see Figures 5.30a and 5.30b).

The output power of (say) a 3-phase full-bridge rectifier is:

$$[P_o]_R = E_{d.c}\ I_{d.c.}$$

and the input line current has a square waveform with a duty cycle of $\sqrt{\frac{2}{3}}$ and an amplitude equal to that of the steady direct

output current $I_{d.c}$ [79]. Thus, if the r.m.s. input line current is I_1,

$$[P_o]_R = E_{d.c.} \sqrt{\frac{3}{2}} I_1 \qquad (5.32)$$

Now, considering the equivalent output circuit of the cyclo-inverter of Figure 5.30b at ideal operating conditions*, the maximum load voltage that can be achieved is

$$v_o = \frac{2 E_{d.c}}{\pi} \text{Sin } (w_o t + \beta) \qquad (5.33)$$

It can be shown that, for a given input current I_1, the r.m.s. output current is, approximately, (see Appendix 5)

$$I_o = \frac{3 I_1}{\sqrt{2}} \qquad (5.34)$$

---

* i.e. with a distortion free output current. This cannot, of course, be realised practically, but it can be approached if the driving voltage to the output circuit has a square waveform of amplitude $\frac{E_{d.c}}{2}$ (hence no sideband distortion) and if the output circuit has a high X_L (hence small output-frequency-harmonic distortion).

and if the phase lead* of the output current i_o with respect to v_o is ignored, the output power is:

$$[P_o]_{C\text{-}I} = \frac{2\,E_{d.c}}{\pi\sqrt{2}} \cdot \frac{3\,I_1}{\sqrt{2}} = \frac{3}{\pi}\,E_{d.c}\,I_1 \qquad (5.35)$$

Comparison of equations (5.32) and (5.35) indicates that with a given input current the cycloinverter produces a maximum output power only 0.77 of that obtainable from a bridge rectifier, and it follows that the maximum input power factor of the cycloinverter is 0.77 as compared with 1.0 for the rectifier. However, because the maximum input power of the bridge rectifier is 0.95[79], the best input power factor for a cycloinverter circuit is 0.73, and in fact, as shown in Figure 5.29, the maximum input power factor obtained with the cycloinverter is about 0.7. The small discrepancy is, of course, due to the non-ideal operating conditions.

Before changing the topic, it may be noted that the effect of the variation of the heating coil selectivity Q_L on the input power factor is negligible, as this is not an important parameter in determining the harmonic components of the output current.

---

* Necessary to provide thyristor turn-off conditions.

5.4 Optimisation of the Cycloinverter Performance

An attempt is made in this section to establish criteria for deciding the design values of the commutating components X_L and X_c of the cycloinverter power circuit, in order to optimise the inverter performance when supplying induction heating loads with both stable and with varying characteristics, i.e. continuous heating and static heating loads respectively.

Optimisation of the inverter is performed for full output power operation, which is justified in applications where the cycloinverter is fully rated during most of the heating cycle. On the other hand, since the optimisation considerations involve minimisation of the effects of the sideband harmonics, it can be argued that the criteria derived also produces a comparably better inverter performance when the inverter is subjected to power control.

In selecting a value for X_L and X_c, the following requirements are considered:

1. Minimum possible output current harmonics.
2. Maximum possible input power factor.
3. Minimum possible ratings for the commutating components.
4. Minimum possible rectifier derating.
5. Maximum possible adaptation and tolerance to varying load conditions.

6. Minimum circuit losses.

A brief discussion on the weighting of these items was presented previously in Section 3.5.1. Due to the reasons outlined there, and considering high power applications at around 1 kHz (1050 Hz for continuous heating and 908-1050 Hz for static heating applications) items 1, 2 and 6 in the list are given higher weighting than the rest. It may be restated here that the conduction losses (included in item 3) are related to the harmonic content of the output current (item 1) via the distortion factor as shown in equation (3.21).

Due to the very close similarity between the full output power operating conditions, the following considerations are applicable to both the half-bridge and full-bridge cycloinverters.

5.4.1 Optimisation for a continuous heating load

In a cycloinverter commutating circuit, the thyristor turn-off time is not constant but varies from cycle to cycle. This is caused mainly by the sidebands of the output frequency harmonics in the input line voltage, which unfortunately create further difficulties in both the circuit analysis and design. Nevertheless, for the sake of simplicity, and assuming for the moment that the varying turn-off time is a negligible part of the output period, the output current may be considered as continuous. This assumption permits the use of harmonic analysis,

and may be justified on the grounds that the prevention of an unnecessarily high turn-off time is a fundamental design objective, as this would adversely affect the overall circuit performance. Additionally, the minimum required turn-off time of the thyristors constitutes only 4% of the output period, at an operational frequency of 1 kHz, and this can certainly be neglected without introducing any significant error. Before proceeding further, it should however be emphasised that the application of harmonic analysis to output circuits producing high and widely varying turn-off time will result in erroneous solutions.

To achieve a reasonable accuracy in calculating the parameters for an optimum cycloinverter performance (with a continuous heating load), the harmonic analysis performed includes the first 9 output harmonics,together with the first sidebands of the fundamental component (i.e. $w_o \mp 6\ w_I$) of the driving voltage waveform. Clearly, this requires a digital computation, and the flow chart of a program prepared for this purpose is obtained by modifying and expanding the computer program developed previously for the harmonic analysis of the low-frequency cycloinverter (Figure 4.15). Modifications are required to include the sideband harmonics in the driving voltage equation, and extensions for this purpose are necessary to assess the validity of the assumptions made in neglecting the effect of circuit turn-off time for all design values of X_L and X_c considered. This check is performed by calculating and printing

out the waveforms of the output current pulses at various parts of the operational cycle of the cycloinverter. Design values of X_L and X_c which produce highly distorted and inconsistent current pulses are assumed to violate the assumptions of the harmonic analysis and are disregarded.

Figure 5.31 shows the variation of X_c with X_L required for a continuous output current. This curve is very similar to that obtained with a square input driving voltage waveform which, for comparison, is plotted on the same graph. The similarity was predicted earlier in Section 4.4.1.1, and clearly indicates the small effect of the sideband harmonics on the full power output current waveform. However, this is not the case when X_L is around 0.8 p.u., where the harmonic analysis does not produce sensible results.

Figures 5.32 and 5.33 present results from the computer program for the harmonic analysis,where the output current i_L and the load voltage v_{co} waveforms are synthesised from their Fourier components. Figure 5.32 is obtained for X_L = 1.2 p.u, and since the value of X_c used satisfies the curve of Figure 5.31, the output current is continuous and well behaved.

Figure 5.33 shows the output current waveform for X_L = 0.8 p.u and X_c = 0.97 p.u, from which it can be seen that the number of output current pulses cannot fall to zero before the start of the next commutation current pulse in the opposite direction. This obviously results in a short-circuit condition which

will occur periodically. Somewhat surprisingly, the commutation recovers at lower values of X_L around 0.6 p.u., as shown in Figure 5.34. The reason for the commutation failure at around X_L = 0.8 p.u. becomes apparent when the variation of the output current harmonics with X_L, shown in Figure 5.35 is examined. The amplitude of the upper sideband for these values of X_L rises sharply, in a way which causes a high distortion in the output current sufficient to result in a commutation failure. For lower values of X_L the distortion harmonic falls again, and the commutation may again be successful.

The increase in the upper-sideband harmonics at around 0.8 p.u. is due mainly to an unfortunate coincidence. Figure 5.36 shows the variation of the modulus of the output circuit impedance with frequency, for X_L = 1.4, 0.8 and 0.6 p.u. As the figure indicates, in order to retain a damped frequency of w_o, for values of X_L decreasing from 1.4 p.u, the natural resonant frequency of the commutating components must be increased. As a result, the overall series resonant frequency w_s of the output circuit shifts towards the upper-sideband frequency for these values of X_L, with the actual coincidence occurring for X_L around 0.8 p.u. Thus, if X_L is close to 0.8 p.u, the output circuit presents a low impedance at the upper-sideband frequency of the input line voltage and it causes, therefore, a high distortion current. If X_L is reduced even further, the series resonant frequency shifts away from the

upper sideband, and the circuit again returns to the stable operation mode.

The instability in the cycloinverter operation described above (i.e. inverter operation with widely and periodically varying turn-off time and commutation failures for X_L around 0.8) obviously requires some modifications to the familiar graph of X_c versus X_L for series commutation. Clearly, for an ordinary series inverter, this graph defines the boundary of a successful operation, as it corresponds to the variation of the minimum value of X_c to ensure safe commutation with X_L. However, this is not completely true for the cycloinverter power circuit, because for values of $X_L > 0.8$ p.u. there are always corresponding values of X_c which, although within the safe operational region, cause an unstable inverter operation by shifting nearer to the sideband frequency. The exact value of X_c' at which the series resonant frequency of the output circuit coincides with the upper sideband frequency can be calculated from

$$X_L\,(w_o + 6\,w_I) - \frac{X_c'}{(w_o + 6\,w_I)} + \left|\mathfrak{I}\,[Z_L]\right|_{w=w_o + 6\,w_I} = 0 \qquad (5.36)$$

where $\left|\mathfrak{I}\,[Z_L]\right|_{w= w_o + 6\,w_I}$ is the imaginary part of the tank load impedance at the upper sideband frequency. Substituting

w_o = 1.0 p.u. and Q_L = 5 in equation (5.36) yields:

$$X'_c = 1.3^2 X_L - 0.452$$

When this variation of X'_c with X_L is plotted in Figure 5.37 it crosses, as predicted, the boundary line, at approximately X_L = 0.8 p.u. Since values of X_c close to X'_c also cause instability, the region around the line defining X'_c is restricted for the circuit designer. As shown in the figure, this region of instability narrows for increasing values of X_L, since with it X'_c departs from the boundary line resulting in an increase in higher order output current harmonics i.e. 3 f_o, 5 f_o etc. which partly compensates for the adverse effects of a high upper-sideband. Before progressing further, it is useful to note that this region of unstable operation varies with the output frequency f_o and the tank-load selectivity Q_L, in accordance with the equation (5.36).

The optimisation considerations may be summarised on Figure 5.37 as follows. The design values of X_L and X_c on the boundary line produce successful commutation with a minimum turn-off time, and hence produce a higher fundamental content of the output current. Values of X_c for a given X_L higher than the boundary value and outside the region of instability, produce a more reliable but less efficient operation, with an unnecessarily high turn-off time. For values of X_L around 0.6 p.u., the amplitude of the third harmonic of the output frequency becomes high

(see Figure 5.35), leading to a deterioration in the inverter performance. The best method to follow for optimisation with a stable load is therefore to search for the design values of X_L and X_c on that part of the boundary line where $X_L > 1.0$ p.u. After selecting the best design values, the corresponding value of X_c should be increased slightly, so as to have some safety margin on the circuit turn-off time against the complex duty that the thyristors face.

Figures 5.35 and 5.38 to 5.40 show the variation of various inverter performance parameters with X_L, and indicate that the harmonic content of the output current, the input power factor and the circuit conduction losses do not significantly vary for $X_L > 1.2$ p.u. However, the commutating capacitor voltage rises sharply, causing a high rectifier derating (see Figure 5.39). For these values of X_L, the variation of commutating component rating and the total component rating per useful output power (i.e. VA_T/P_o) is shown in Figure 5.40, and these performance curves (together with those presented previously) suggest that for a high-power application X_L = 1.2 p.u. and X_c = 1.3 p.u. may be regarded as the best compromise between the circuit power losses, the input power factor requirements and the power circuit component ratings.

It is pertinent to consider briefly the effect of an optimum selection of design parameters on the circuit performance

during power control. As outlined in section 5.3, during the power control mode the harmonic content of the input line voltage increases sharply. In the full-bridge cyclo-inverter, the ratio of the sideband harmonic amplitudes to the fundamental increases, whereas in the half-bridge inverter extra sideband harmonics, of high amplitude, appear at frequencies $w_o \mp 3\ n\ w_I$. In the former case, as the sideband harmonic frequencies are basically unaltered, the behaviour of the prospective design should be acceptable. However, in the half-bridge inverter, the appearance of sideband harmonics at $w_o + 3\ w_I$, and close to the operational frequency, requires some attention, as it poses the danger of a coincidence with the series resonant frequency of the output circuit. For this purpose a further check is performed, which shows that the selected values of X_L and X_c do not shift the output circuit series resonant frequency towards the newly generated sideband harmonics (see Figure 5.37). It may be stated, therefore, that the design values X_L = 1.2 p.u. and X_c = 1.3 p.u. are also suitable for the power control modes of the inverter operation.

Investigations made with the digital simulation program indicate that some power control modes require peak voltage component ratings substantially higher than the full output ratings given in Figure 5.39. Figure 5.41 shows the instantaneous commutating capacitor and thyristor voltage in a half-bridge inverter, for firing angles of 30^o, 90^o and 150^o, and indicates that the peak capacitor and thyristor voltages at $\theta = 90^o$ are

approximately 1.6 times higher than their full load values. This increase in the commutating circuit voltage naturally stems from the transient nature of power control in a cycloinverter. Accordingly, in a full-bridge inverter, the ratio of the maximum commutating capacitor voltage to its full load value of 1.2, is lower than the same ratio in a full-bridge inverter, since the full-bridge inverter exhibits a more stable operation during power control - due to the higher (doubled) number of output current *bunches* in a given input mains cycle (or in other words due to the higher duty cycle of the output current).

Clearly, this increase in the commutating circuit component rating requirement for output power control must be taken into account in any design. By so doing, the following parameters are obtained for the optimum design (assuming $Q_L = 5$),

$X_L = 1.2$ p.u. $\qquad X_C = 1.3$ p.u.

Input power factor $PF_I = 0.7$ (at full output power)

Full output power = 1.06 p.u.

Peak commutating capacitor voltage V_{cip}

= 4.8 p.u. (half-bridge)

= 3.5 p.u. (full-bridge)

Thyristor derating DS = 9.2 (full-bridge)

= 8.5 (half-bridge)

Rectifier derating DR = 13.8 (half-bridge)

Tank-load voltage V_{co} (r.m.s) = 1.03 p.u. (at full output power)

Input line current I_1 (r.m.s) = 0.5 p.u. (at full output power)

Output current I_L (r.m.s) = 1.05 p.u. (at full output power)

5.4.2 Optimisation with static heating and melting loads

Clearly, the selection of optimum values of X_L and X_c for static heating and melting applications requires investigation of the inverter performance throughout the varying load conditions of the particular application. In so doing, the procedure required (in accordance with the guidelines given in Chapter 1) is to calculate the inverter performance parameters at some characteristic load conditions, for varying design values of X_L and X_c. By comparing the variation of the performance parameters of each design through the heat cycle, the values of X_L and X_c which produce the best inverter performance can be selected on the basis of the design criteria. A similar process was performed previously in Chapter 3, in conjunction with the sine-wave inverter. When investigating the inverter performance at varying load conditions, the presence of the unstable operational region introduced in the previous section must be given particular attention. Suppose that, when operating at the optimum operational conditions selected for the continuous heating application, i.e. X_L = 1.2 p.u. and X_c = 1.3 p.u.; the equivalent tank load resistance R_{eq} somehow starts to decrease.

The corresponding values of X_L and X_c will then increase in proportion to $\frac{1}{R_{eq}}$ (since R_{eq} is defined as the per unit resistance base) which eventually will cause a short circuit as the operational point (corresponding to the new values of X_L and X_c) enters the unstable operation region.

The example above illustrates some of the difficulties encountered when the load is varied. In a static heating or melting application, the design procedure is further complicated by the changing output frequency and the tank-load selectivity, as well as by the equivalent load resistance.

Based on the findings of Chapter 2, the variations of X_L, X_c, w_o, R_{eq}, Q_L for a typical static heating load during a complete heat cycle are given in Table 5.1. For the sake of simplicity, the values of these parameters are referred to the load conditions at the end of the heating cycle (i.e. at E), which was shown previously to correspond to the worst operating conditions for a series commutated inverter, during a complete heating cycle. This table clearly show substantial variations in both X_L and X_c through these load conditions (which, as they correspond to a particular set of values of w_o, Q_L, R_{eq} etc. may also be called operational points). For a successful design, the values of X_L and X_c at E must be selected in such a way that when they are varied in accordance with the Table 5.1, they never enter the unstable operation region. For this purpose, it is necessary to evaluate the relative positions of the operational

line defined by the varying values of X_L and X_c, and the region of instability, in a form similar to that of Figure 5.37 (clearly, the operational line cannot be shown in Figure 5.37, which is defined for fixed w_o and Q_L i.e. 1 p.u. and 5 respectively). Although the variations in the boundary line may be ignored* for varying values of w_o and Q_L, the

---

* The boundary line shifts upwards slightly for lower values of w_o. As shown in Figure 4.18 for 150 Hz operation, to offset the adverse effects of the input voltage variation on the commutation current for $\theta = 30^o$, the natural resonant frequency of the commutation circuit must be increased, resulting in an increase in X_c for a given X_L. However, due to the high operational frequencies considered, the effect of varying w_o on the boundary line can easily be neglected. The variation of the boundary line with Q_L stems mainly from the varying capacitive impedance at the output frequency of the tank-load circuit (i.e. $-\frac{j}{Q_L}$ p.u. from equation 2.6). Hence the change in the new boundary line value of X_c is, approximately,

$$\frac{1}{Q_{L_{old}}} - \frac{1}{Q_{L_{new}}}$$

On the other hand, Table 5.1 shows that during a heating cycle, increased values of w_o occurs simultaneously with decreased Q_L, suggesting that the effect of one on the boundary lines is offset partly by the effect of the other.

region of instability varies significantly in accordance with the equation (5.36). The 3-dimensional plot in Figure 5.42 shows, approximately, the variation of this forbidden region with the load conditions of the static heating applications described in Table 5.1. It is also possible to plot on this graph the variation of X_L and X_c (the operational line) throughout the heating cycle, as shown for the design values X_L = 0.7 p.u. and X_c = 1.35 p.u. corresponding to the load condition E.

Now, the design task may be summarised by the following question. How should the operational line be placed on Figure 5.42, so that a safe and efficient operation is achieved throughout the heating cycle? When searching for an answer, it helps to consider the design values of X_L and X_c at the worst load condition, i.e. the E plane in Figure 5.42, since this safeguards crossing the boundary line during the heating cycle. In fact, the answer to the design question can be found without resorting to detailed inverter performance analysis, by examining Figure 5.42 closely. Clearly, the design values of X_L and X_c in the safe operational region beneath the unstable operational region cannot be considered, as they inevitably cause short-circuit conditions during the early stages of the heating cycle. On the other hand, the high values of X_L and X_c in the safe operation region above the region of instability, which are further magnified during the cycle of operation in

accordance with Table 5.1, produce long zero intervals in the output current waveform. This results in a deterioration in the inverter performance, and requires high commutating component ratings. Therefore the search for the optimum design values should be made around values of X_L and X_C in the upper safe operational region, close to the boundary line. Because this region has an approximate 'V' shape near the boundary line, the choice is narrowed, suggesting X_L = 0.7 p.u. and X_C = 1.35 p.u. as providing, approximately, an optimum.

The performance of the inverter with selected design values throughout the heating cycle can be evaluated with good accuracy, by using the digital simulation readily available. However, preliminary simulations unfortunately revealed that the cycloinverter performance is not particularly satisfactory around the Curie temperature i.e. at the load condition C, where the commutating capacitor voltage rises to 5.5 p.u. and the input power factor falls to 0.47. High commutating circuit voltage at high load (i.e. low equivalent tank load resistance), as discussed previously, is inherent in series commutation and is caused mainly by the increased selectivity of the commutating circuit. As this mode also corresponds to the lowest operational frequency, and to a value of X_C well above the boundary line, the circuit turn-off time becomes excessive, causing a deterioration in the harmonic content of the output current (and hence of the input current), which results

in a low input power factor. Although with such a performance the cycloinverter is not well suited to high power applications, it will nevertheless be demonstrated in Chapter 7 that a substantial improvement in the inverter performance can be achieved (both the excessive rise of the commutating capacitor voltage and the low input power factor can be prevented to a certain extent), by the addition of a suitable filter circuit at the input to the cycloinverter.

5.5 Cycloinverter Operation at Higher Frequencies (w_o > 3 kHz)

Clearly, many of the problems introduced in the previous sections in relation to the optimum design of the commutation circuit and an efficient inverter operation are characteristic of the operational frequencies concerned. When the operational frequency of the cycloinverter increases, the sideband harmonics become closer to it (and hence further from the series resonant frequency of the output circuit) which suggests that (assuming Figure 5.36 is applicable to a high-frequency operation) their amplitudes in the frequency spectrum of the output current are considerably reduced (roughly, four-fold for 3 kHz operation and seven-fold for 6 kHz). Therefore, at high frequencies, and in the absence of any significant sideband distortion components in the output current, the cycloinverter operation does not suffer from operational instabilities.

One shortcoming of the high-frequency application is, however, that the output filtering function of the tank load becomes ineffective as the sidebands approach the tuned tank-load frequency, and distortion harmonics appear in the load circuit. This can be observed clearly in the circuit waveforms of Figure 5.43,which are obtained from a digital simulation of a 3 kHz cycloinverter.delivering full output power. Alternatively, it can be argued that for many induction heating applications the distortion currents, which flow in the heating coil and have frequencies differing by less than 5% from the desired output frequency, are quite tolerable, and in fact contribute to the useful output power.

Load Condition	$\frac{w_o}{[w_o]_E}$	$\frac{L_o}{[L_o]_E}$	$\frac{R_o}{[R_o]_E}$	$\frac{R_{eq}}{[R_{eq}]_E}$	Q_L	$\frac{X_L}{[X_L]_E}$	$\frac{X_c}{[X_c]_E}$
E	1.0	1.0	1.0	1.0	10	1.0	1.0
A,D	0.95	1.11	1.42	0.77	7.38	1.22	1.35
B	0.89	1.26	2.5	0.5	4.47	1.78	2.47
C	0.86	1.33	3.21	0.41	3.59	2.1	2.81

Table 5.1 Variation of load conditions throughout a cycle of operation in a typical static heating application

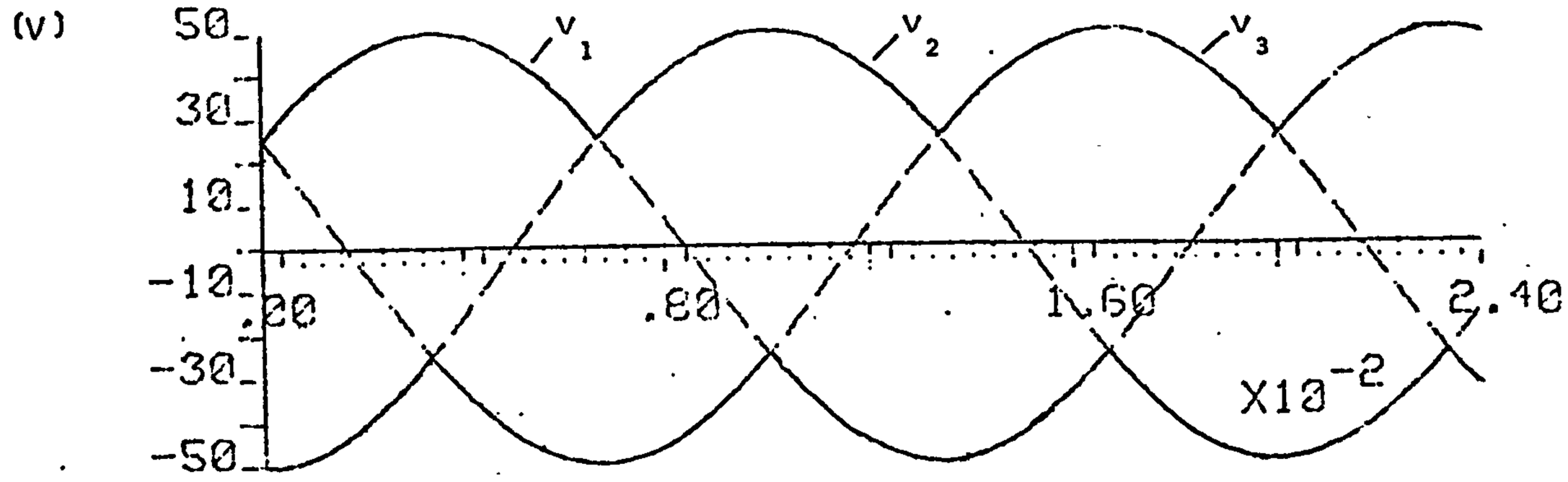

3-ϕ input

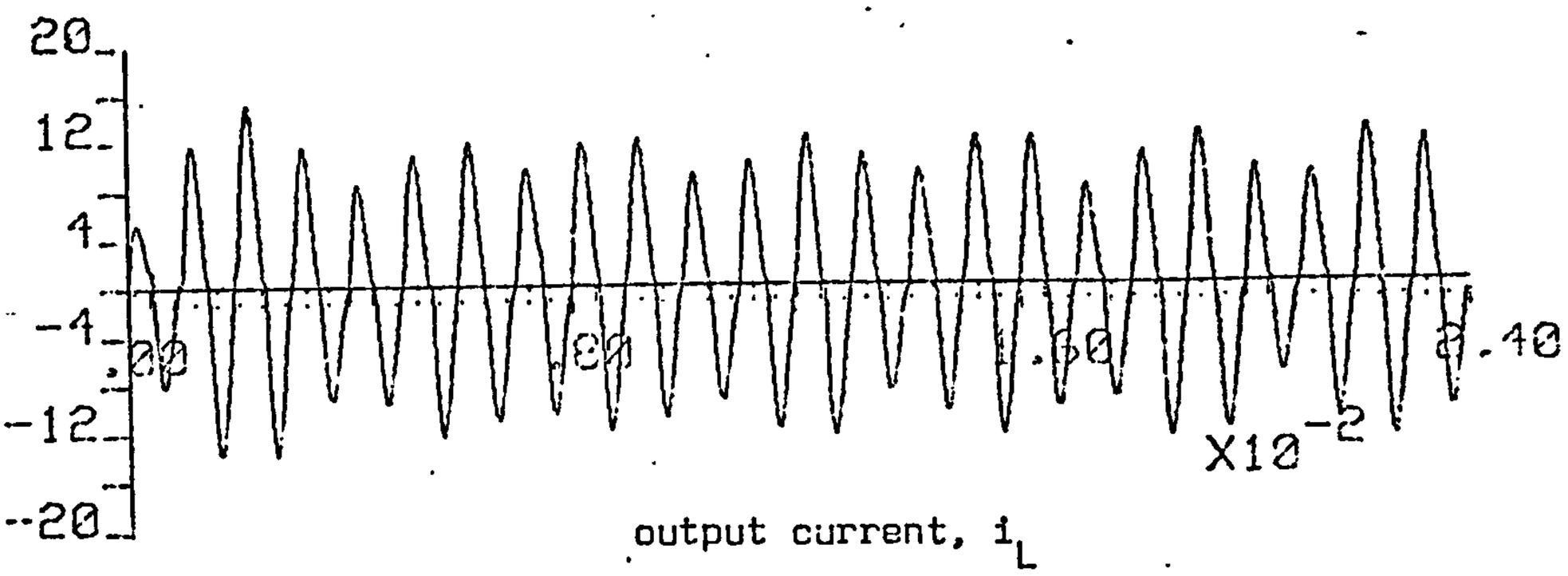

output current, i_L

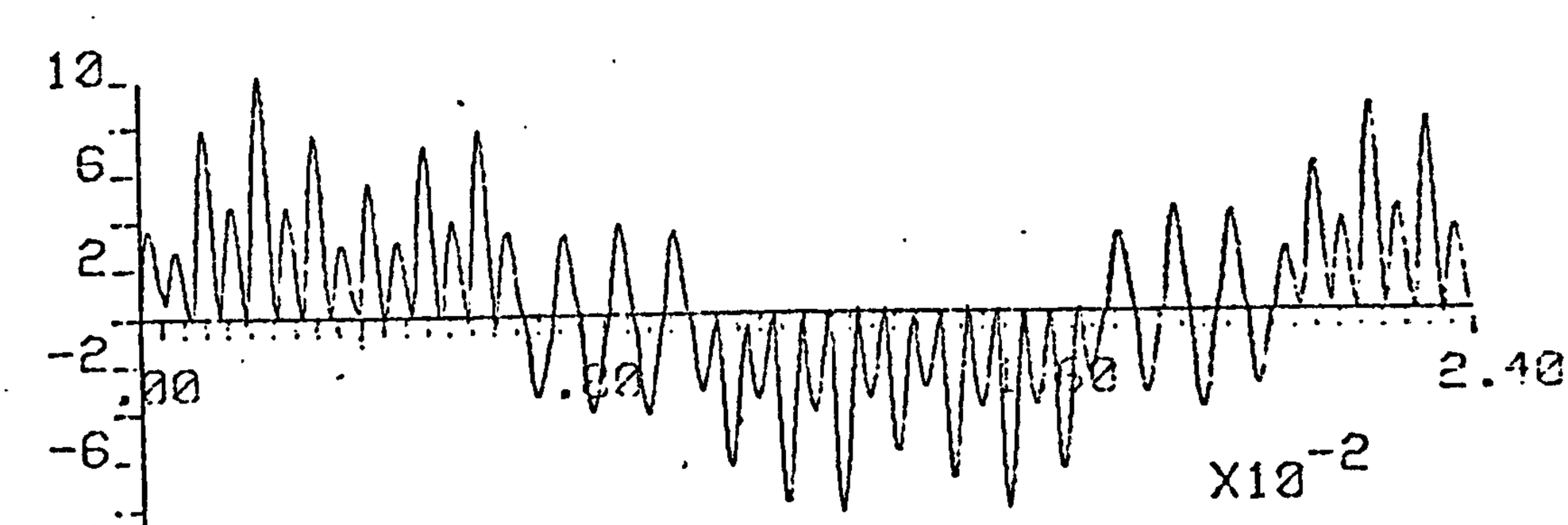

input line current, i_1

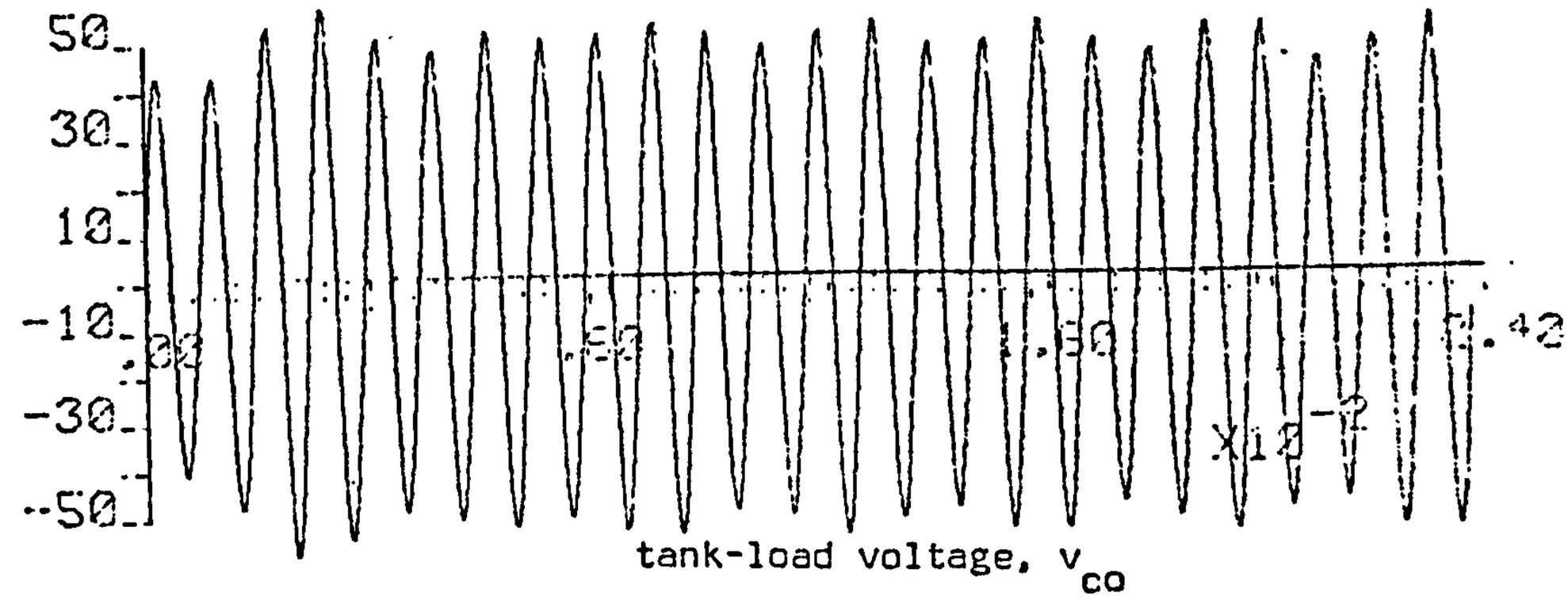

tank-load voltage, v_{co}

Figure 5.1a Circuit waveforms for the full-bridge cycloinverter when operating at 1 kHz and delivering full output power

/Continued

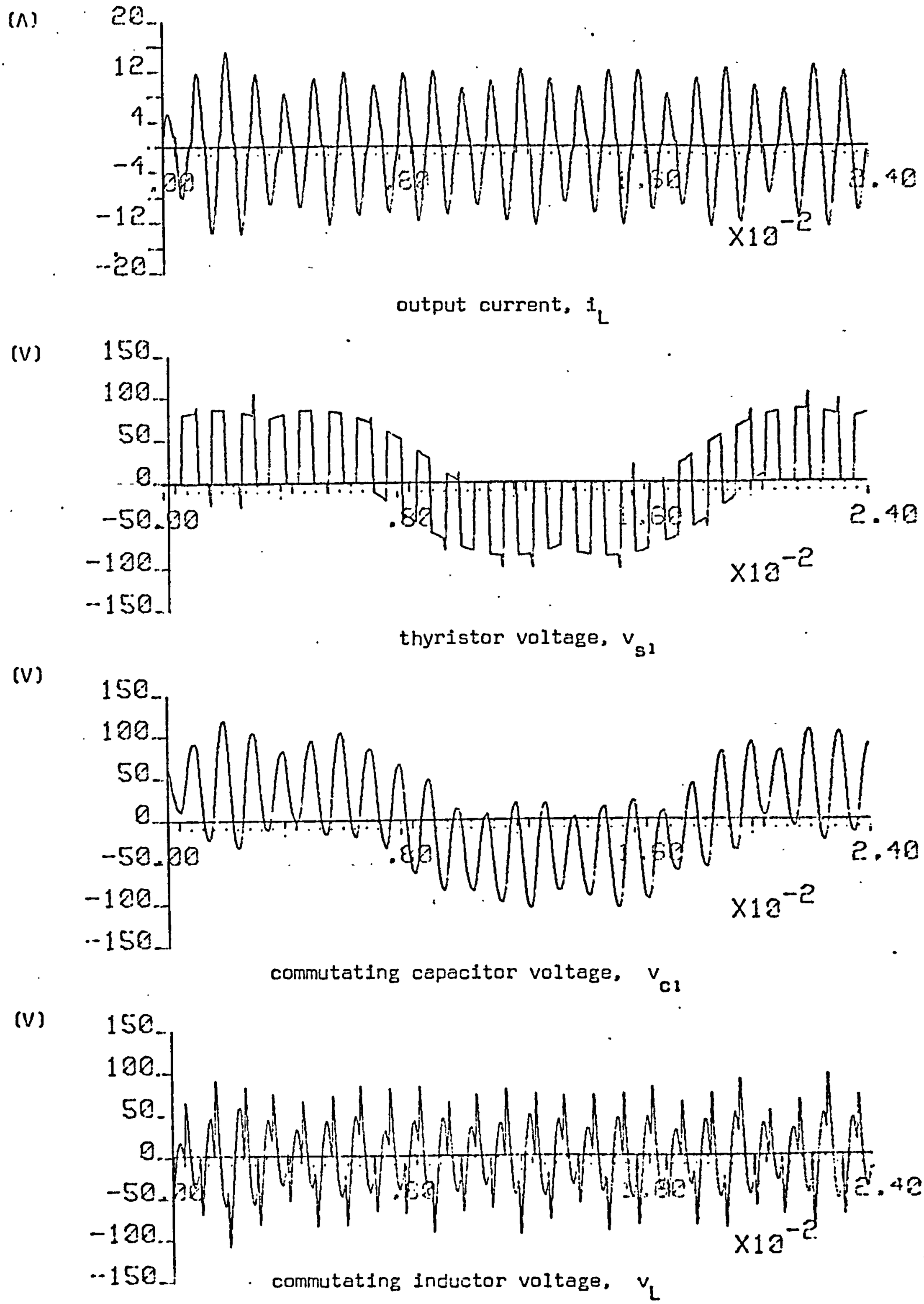
(A)
20
12
4
-4
-12
-20
.00
.80
1.60
2.40
X10-2
output current, iL
(V)
150
100
50
0
-50
-100
-150
.00
.80
1.60
2.40
X10-2
thyristor voltage, vs1
(V)
150
100
50
0
-50
-100
-150
.00
.80
1.60
2.40
X10-2
commutating capacitor voltage, vc1
(V)
150
100
50
0
-50
-100
-150
.00
.80
1.60
2.40
X10-2
commutating inductor voltage, vL

Figure 5.1b

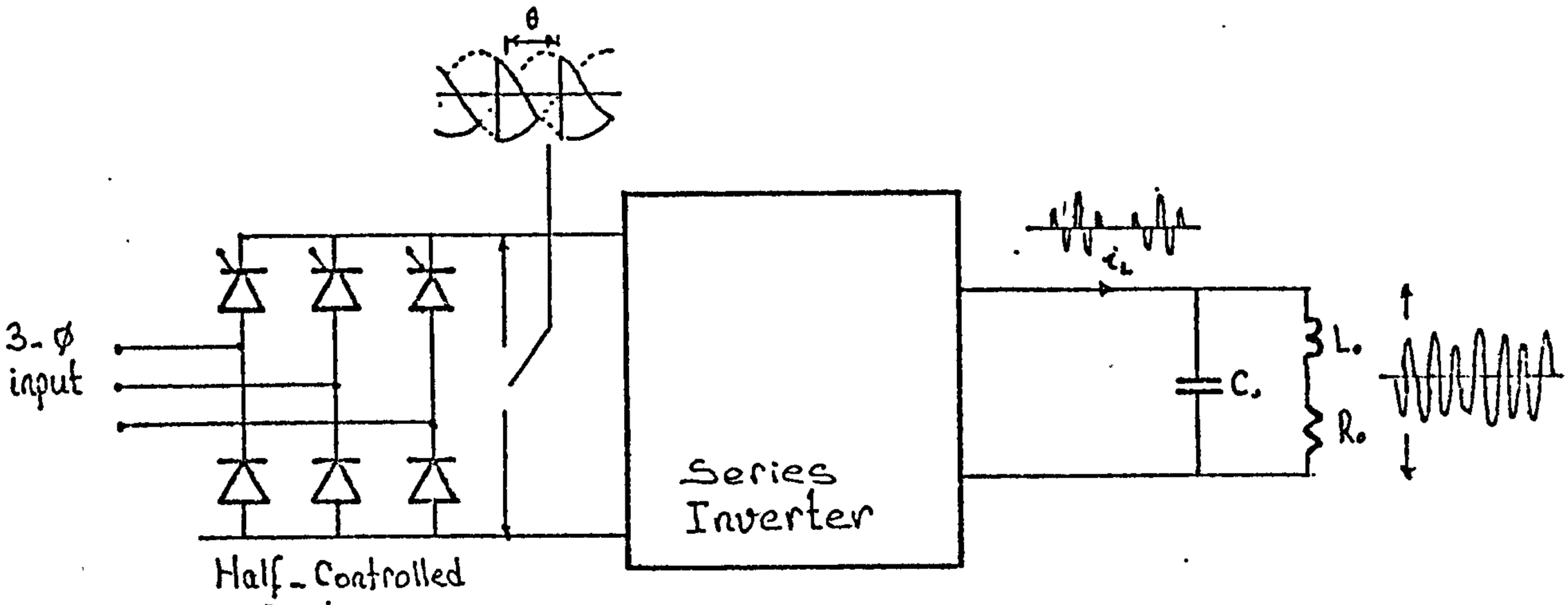

Figure 5.2 A series inverter in cascade with a half-controlled bridge rectifier is functionally analagous to a half-bridge cycloinverter

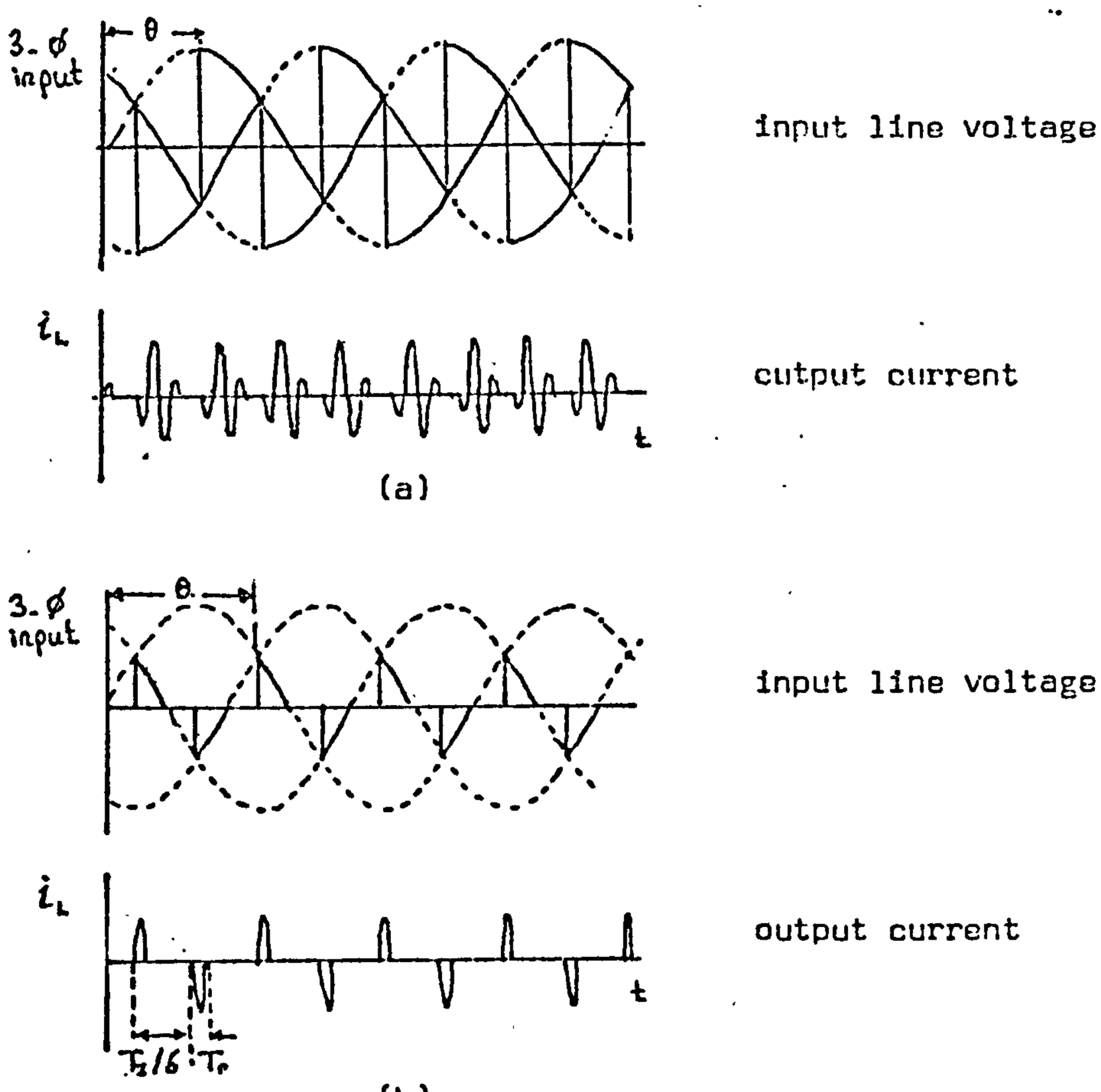

Figure 5.3 Power control in a full-bridge inverter:

a) for a control angle $\theta < 150^{o}$

b) for a control angle $\theta > 150^{o}$

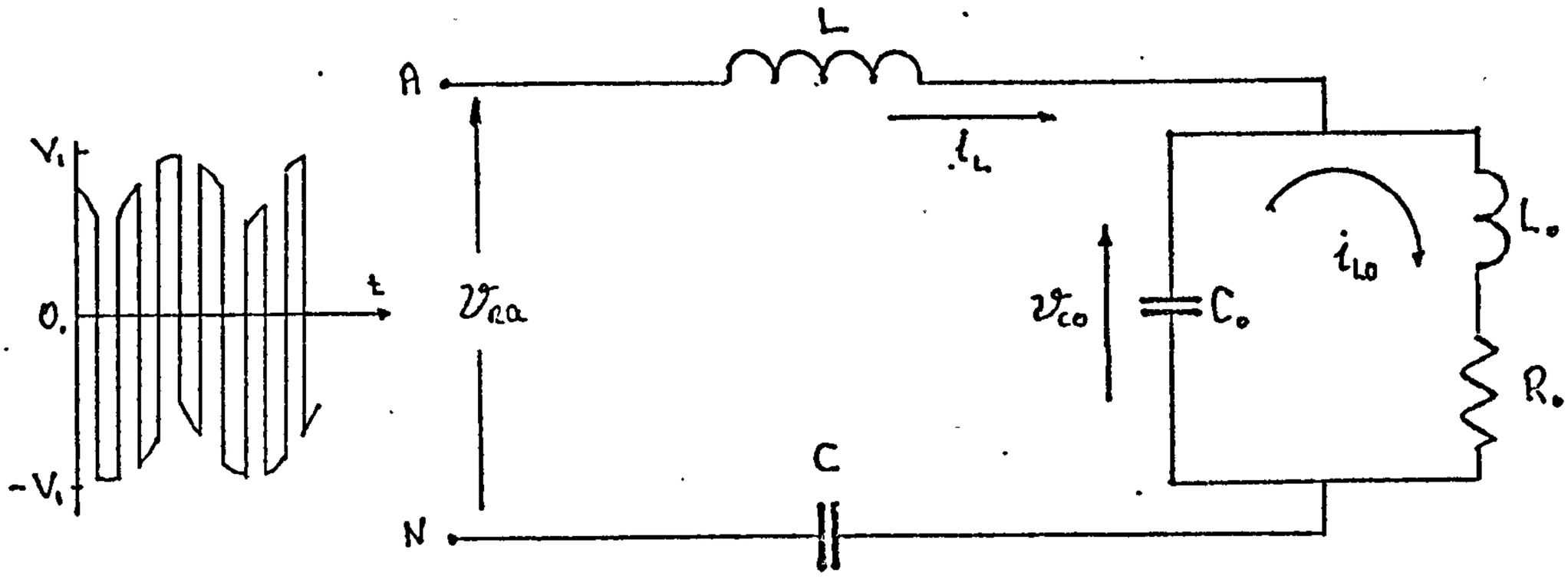

Figure 5.4 Equivalent circuit diagram of the output circuit of the cycloinverter

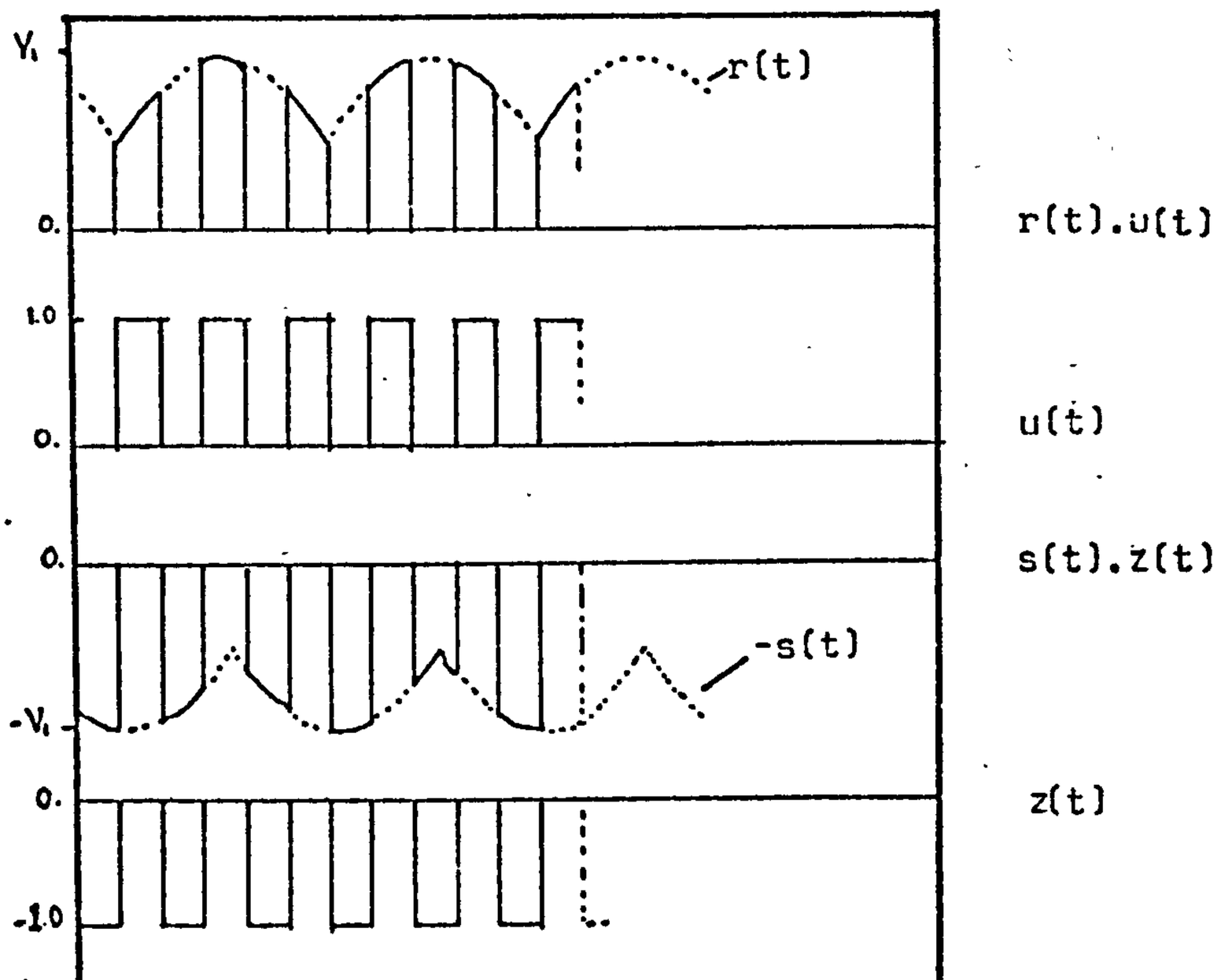

Figure 5.5 The synthesis of the driving voltage v_{na}

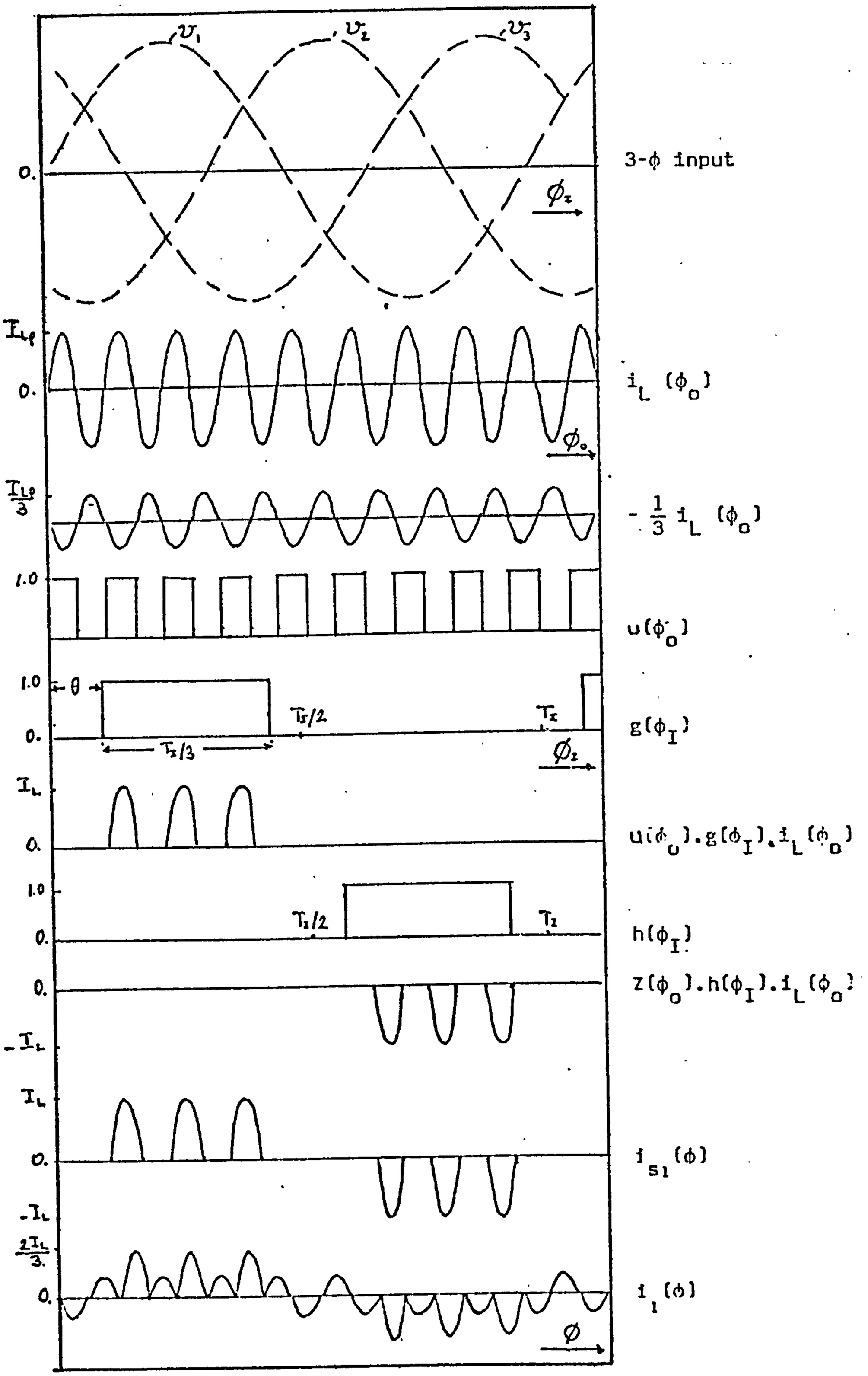

Figure 5.6 Synthesis of the input current waveform for the harmonic analysis

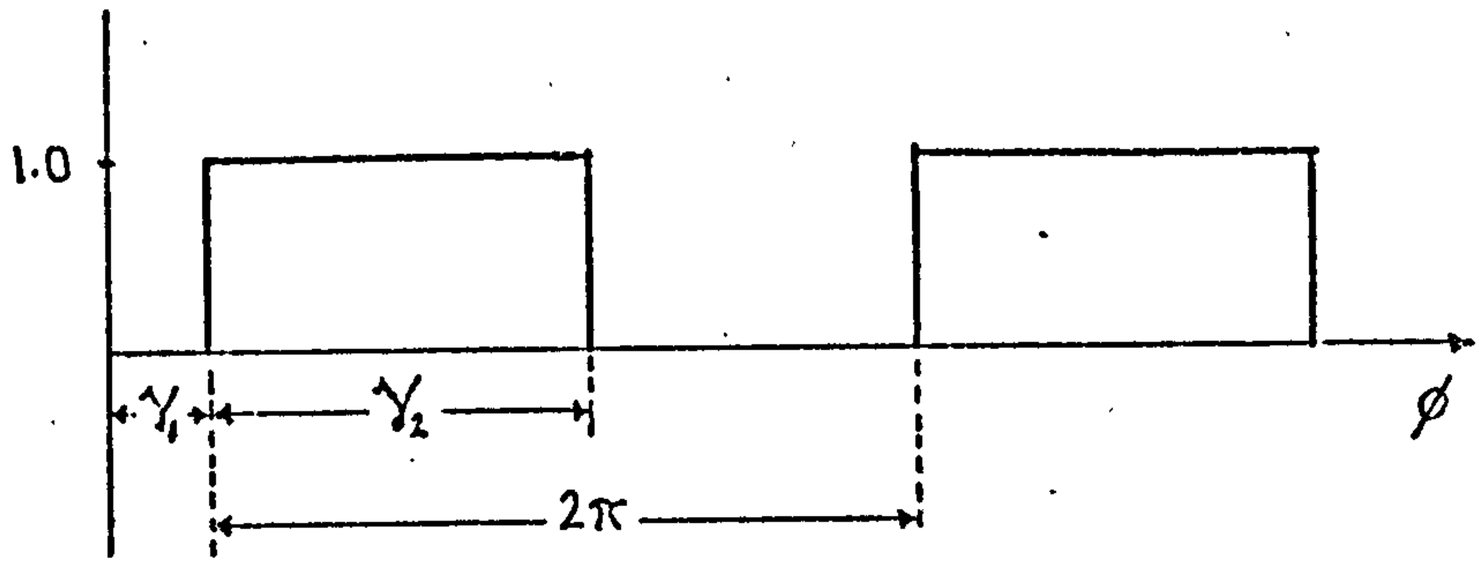

Figure 5.7 General rectangular waveform

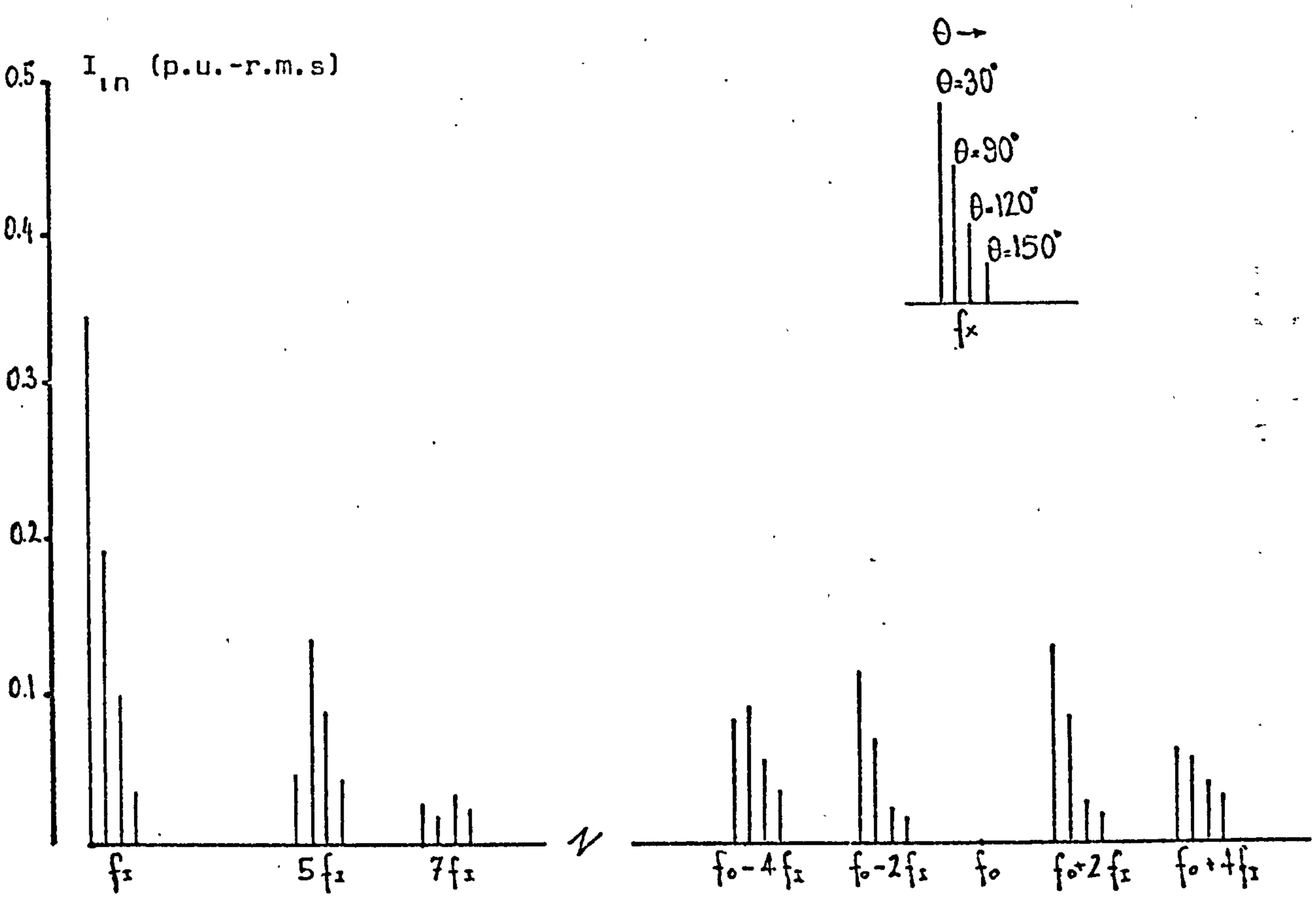

Figure 5.8 Variation of harmonic spectra of the input line current i_1 of the full-bridge cycloinverter with θ

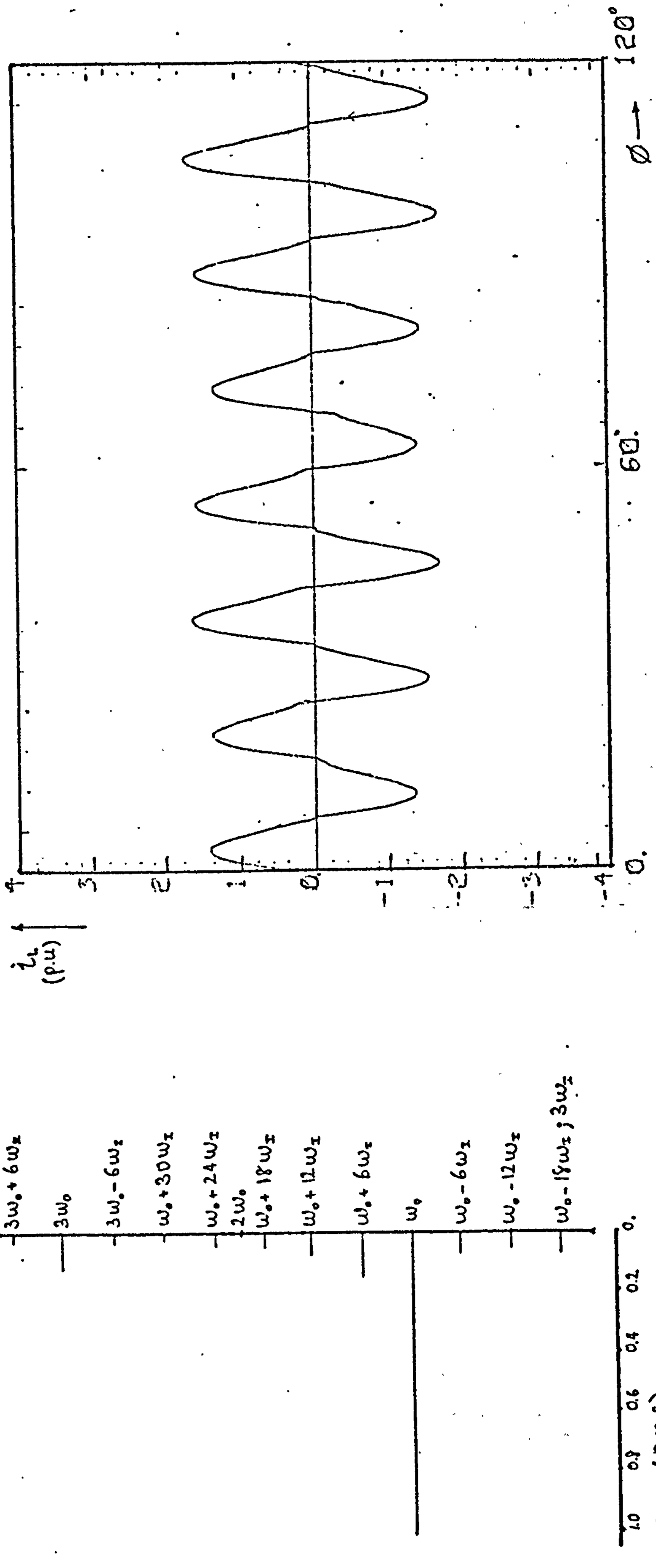

Figure 5.9 Waveforms for harmonic spectrum of the cycloinverter output current obtained from the digital simulation (X_L = 1.2 p.u, X_c = 1.3 p.u, θ = 30°, f_o = 1050 Hz, f_I = 50 Hz, i.e. f_o = 21 f_I)

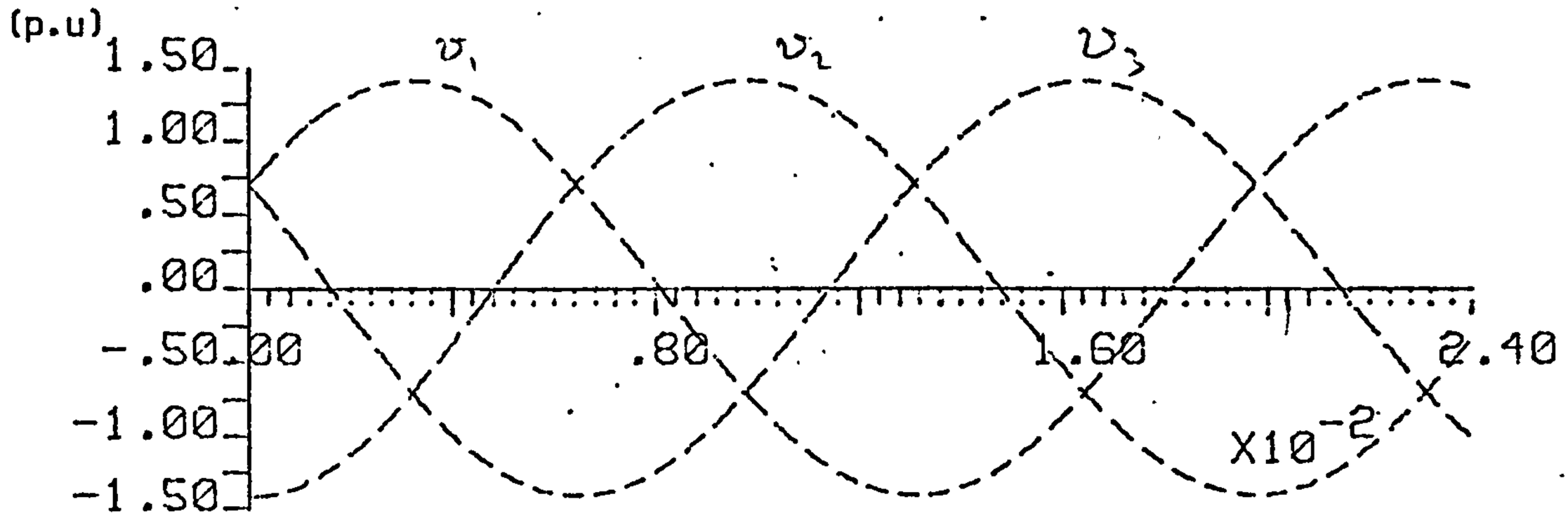

3-ϕ input

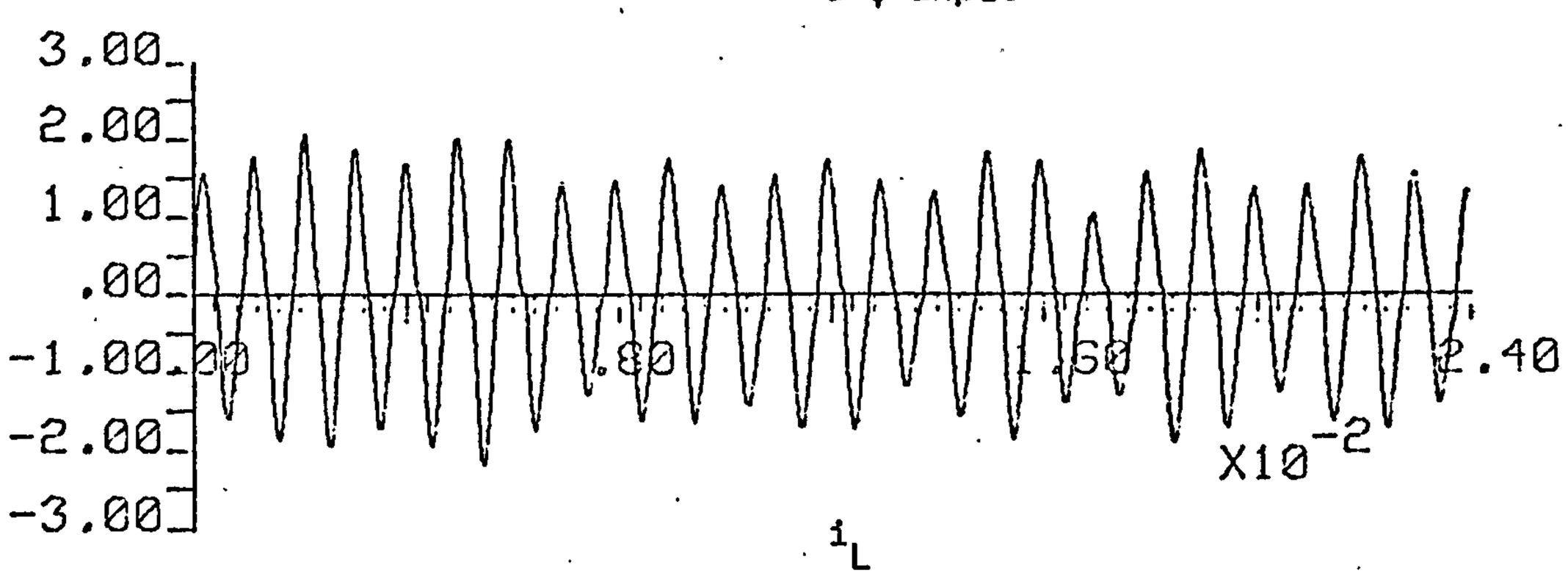

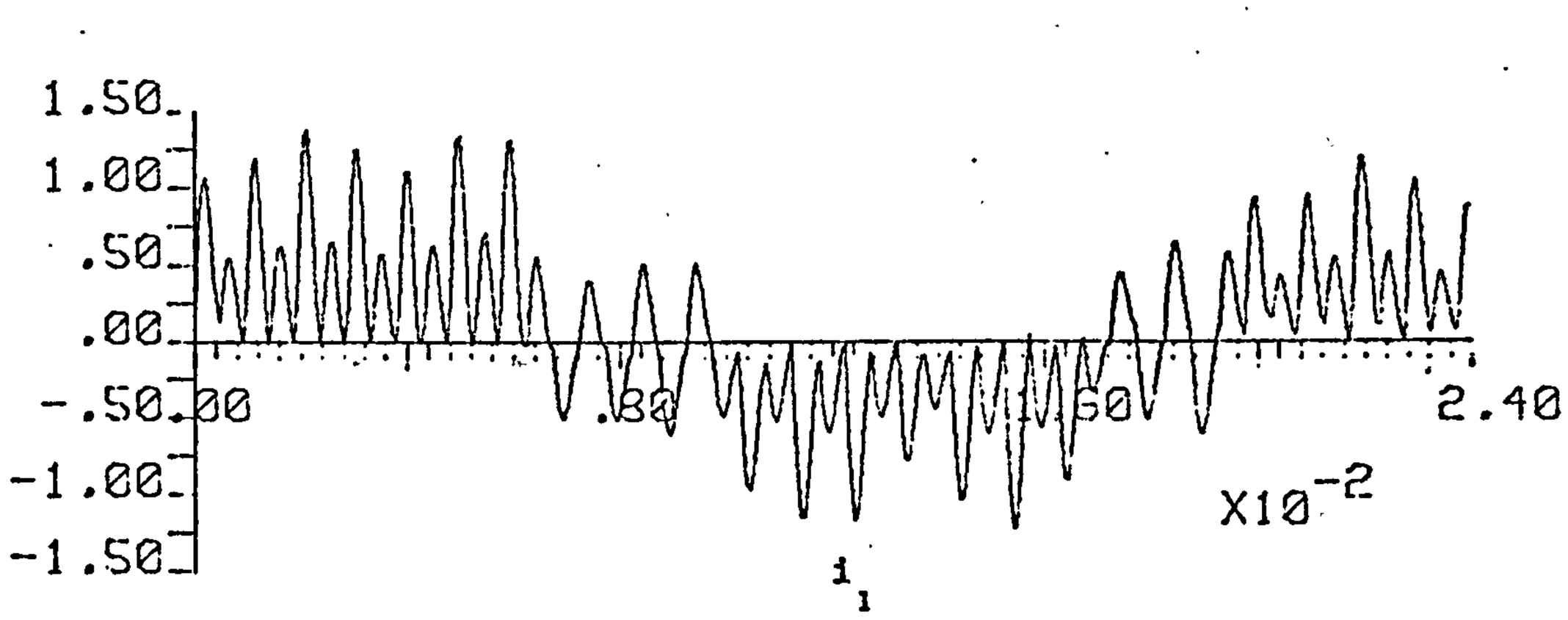

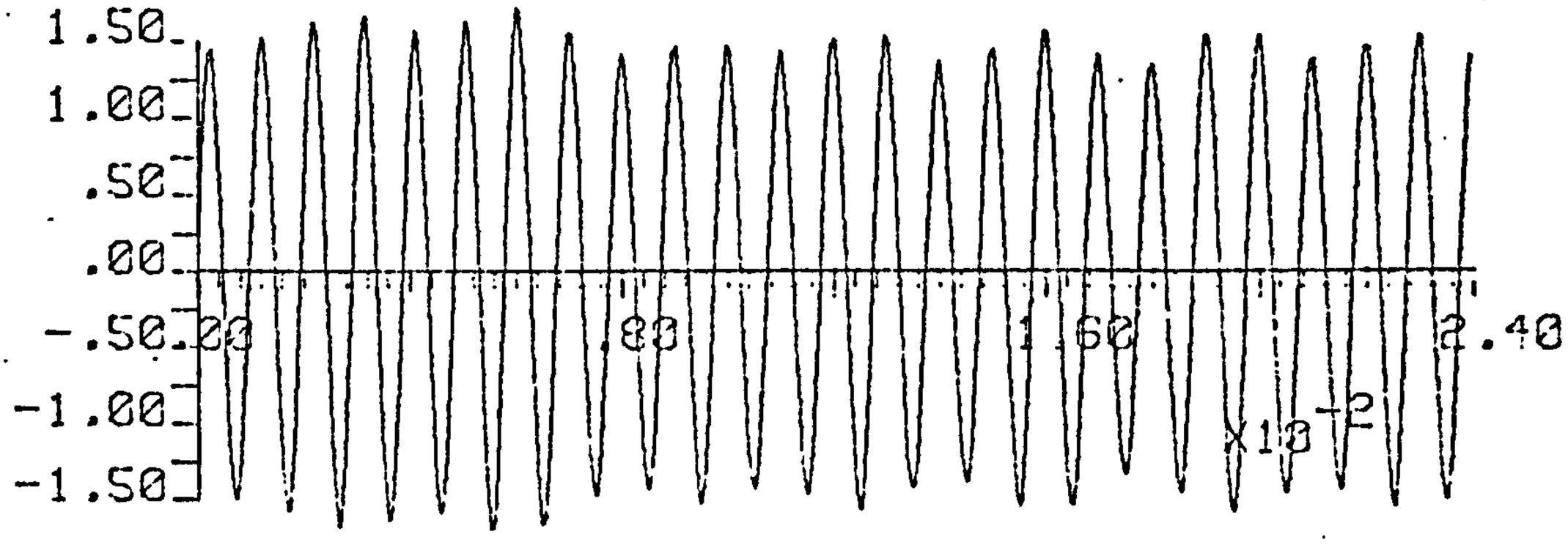

Figure 5.10 Computer waveforms for a 1 kHz half-bridge cycloinverter during power control. (θ = 30°, full output power)

/Continued.

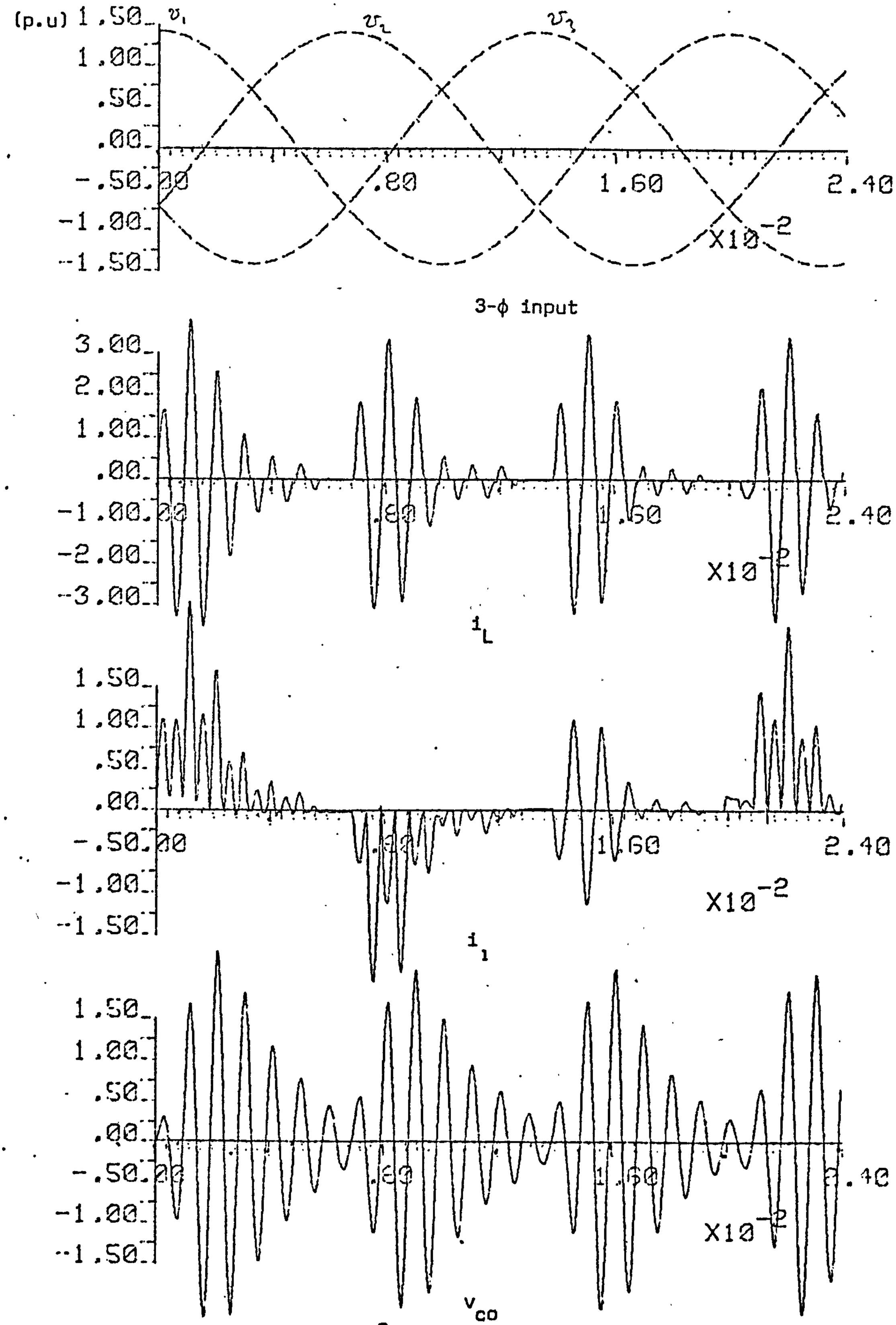

Figure 5.10 $\theta = 90^{o}$

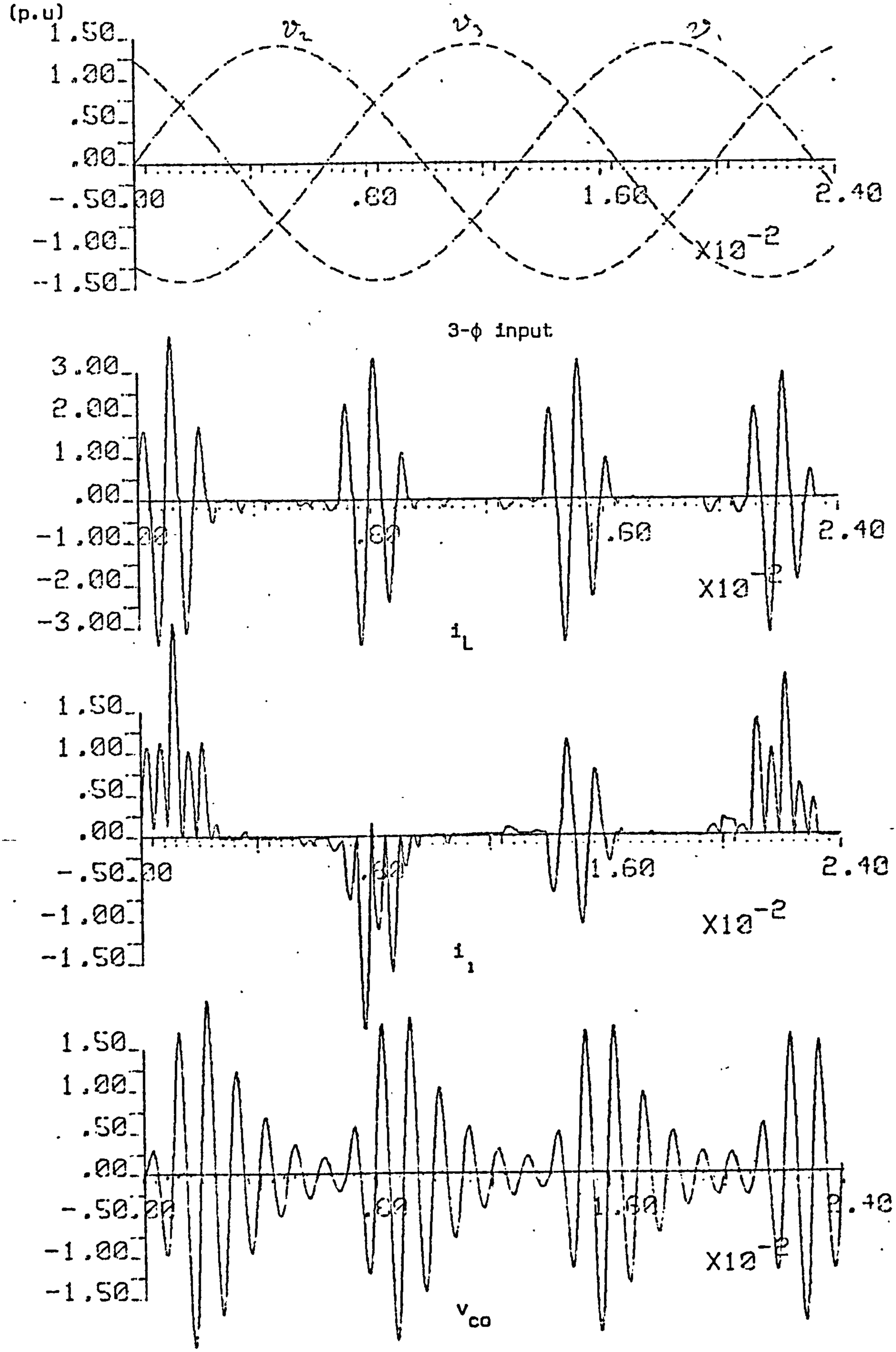

Figure 5.11 Computed waveforms for a 1 kHz half-bridge cycloinverter during power control (θ = 110°)

/Continued

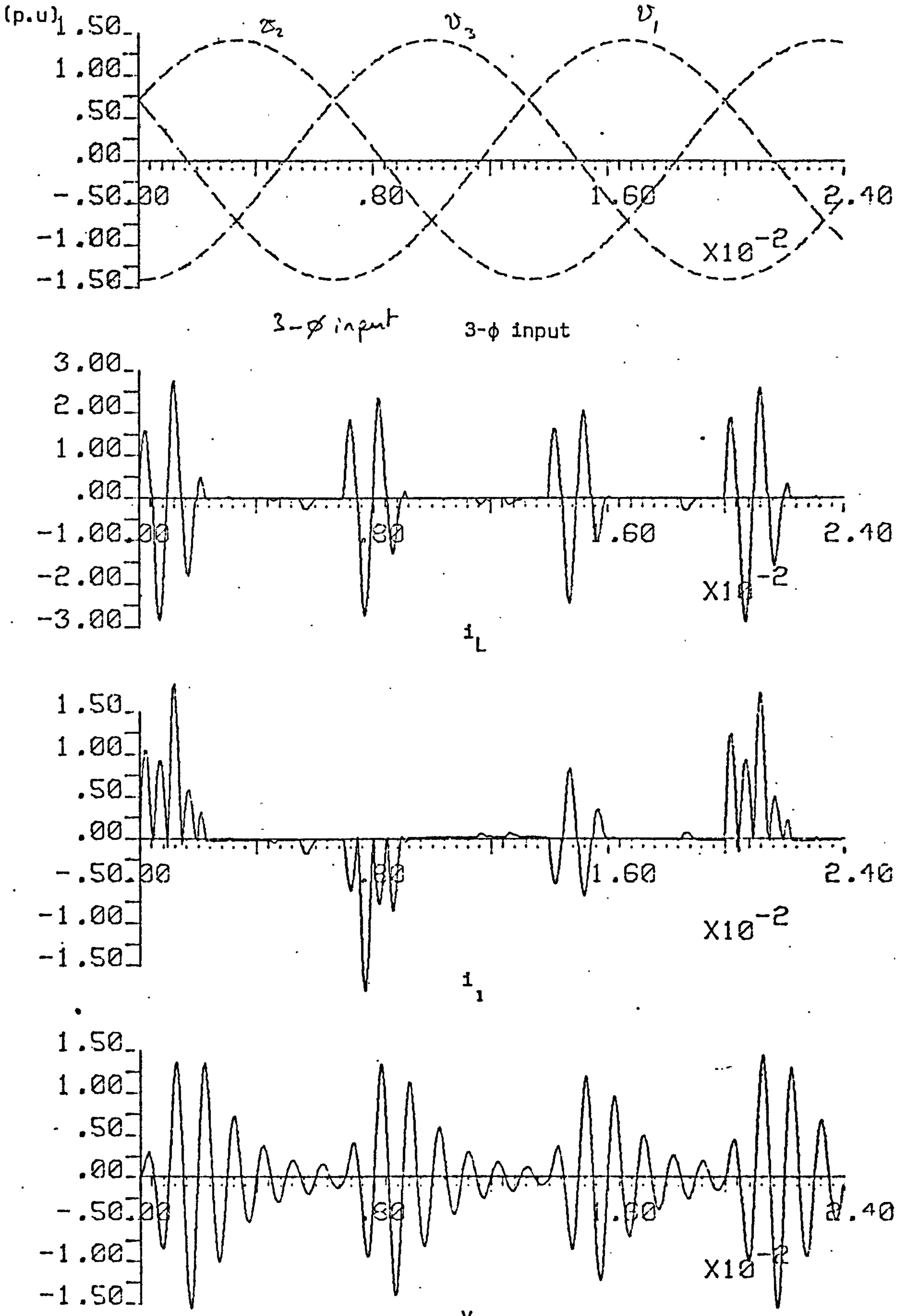

Figure 5.11 $\theta = 150^{o}$

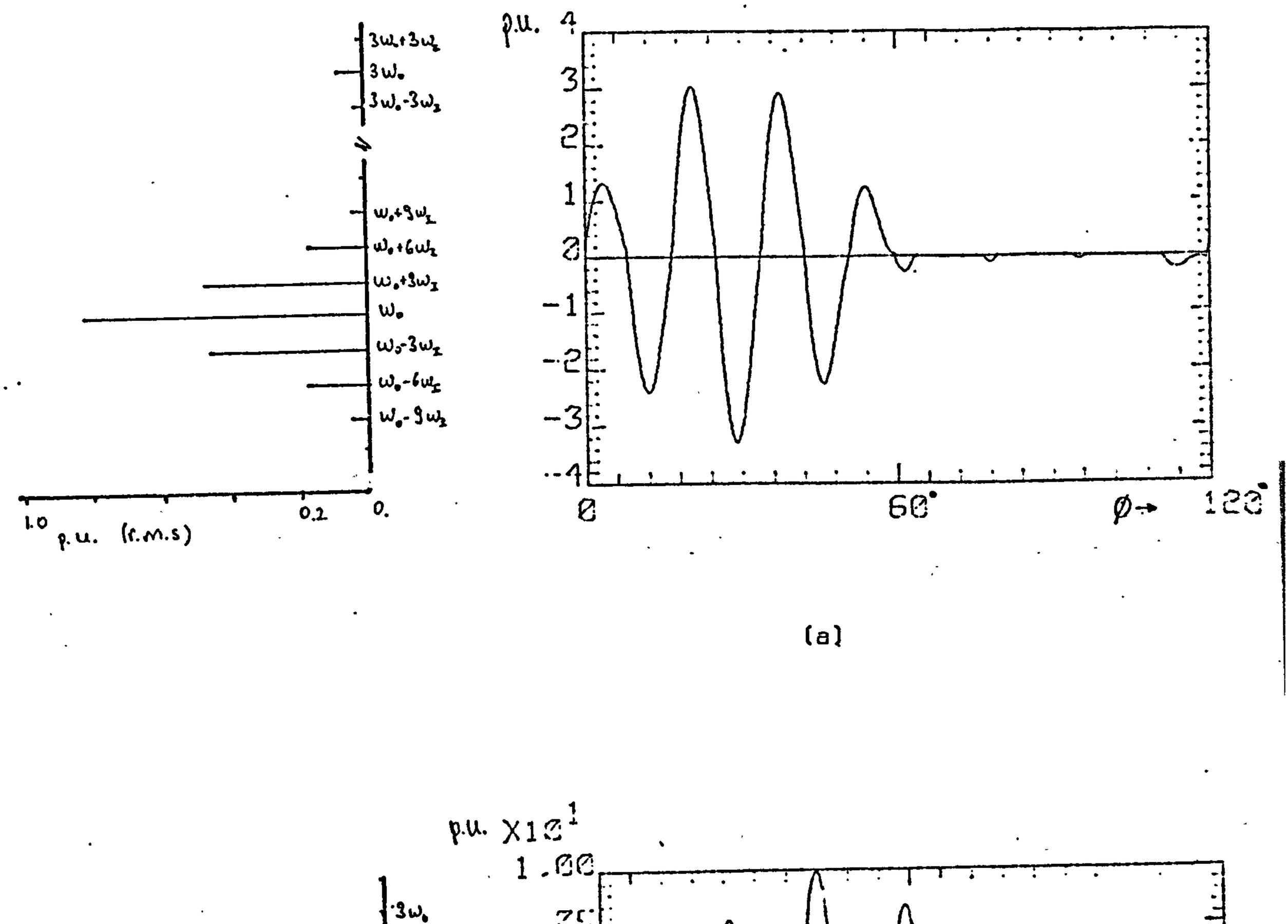

Figure 5.12 Waveform and harmonic spectrum of the:

a) output current, i_L

b) tank-load current, i_{Lo}

in a half-bridge cycloinverter when the power control angle $\theta = 90^o$

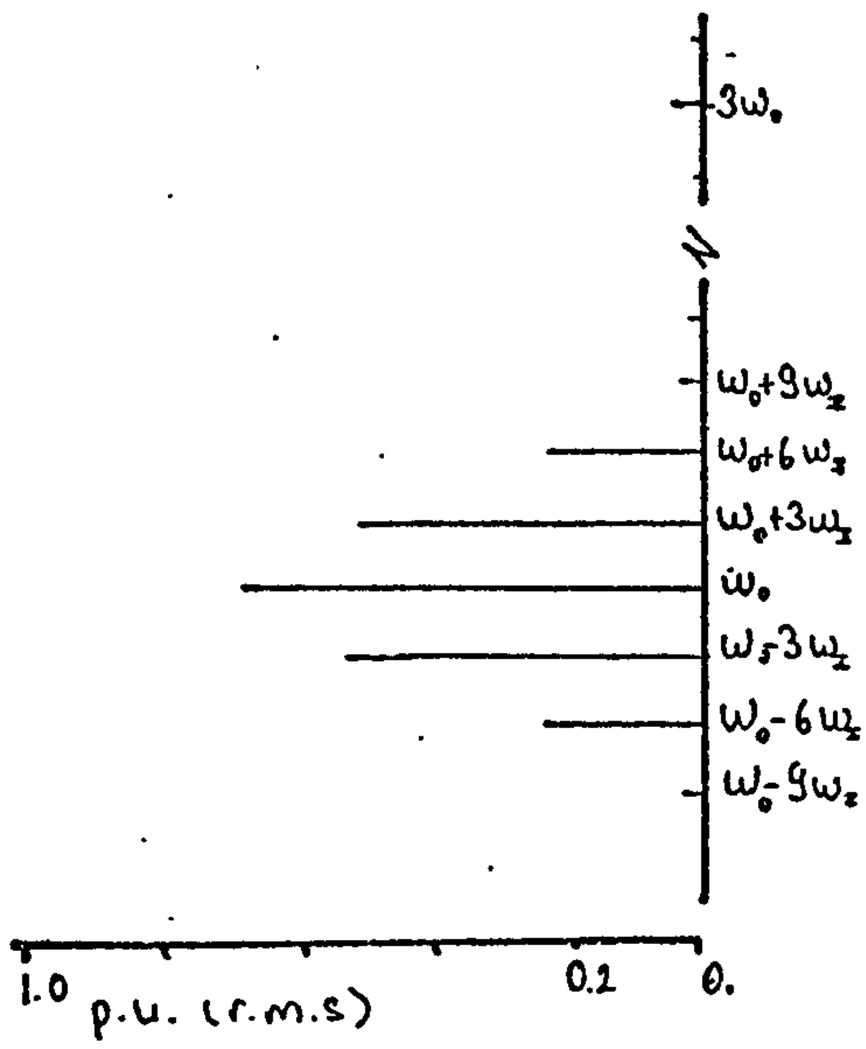

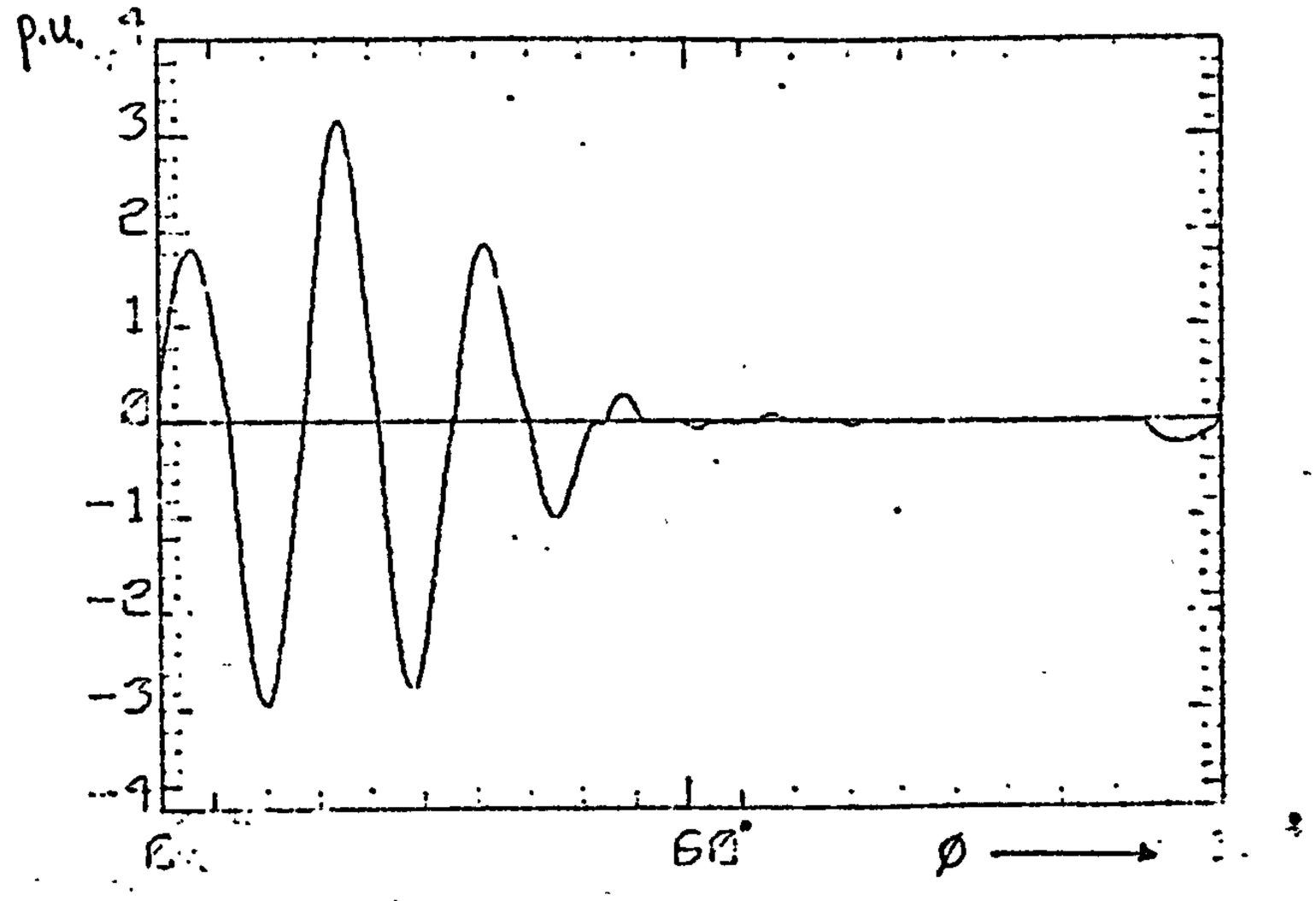

(a)

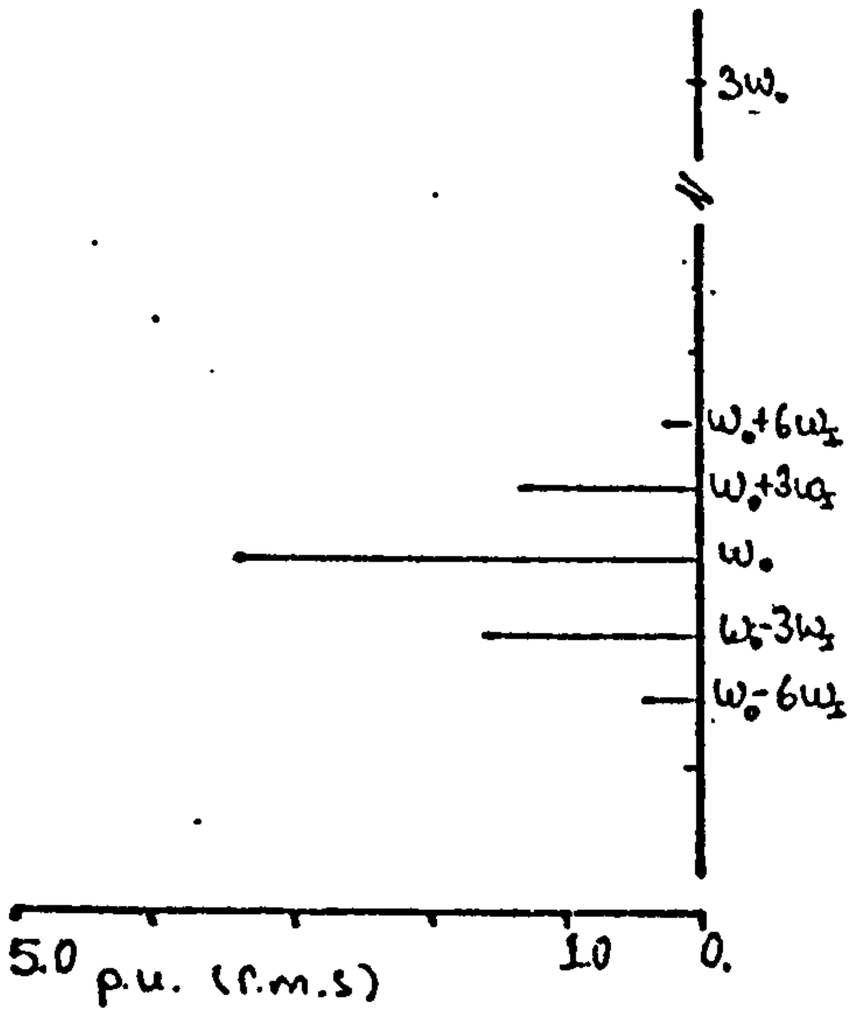

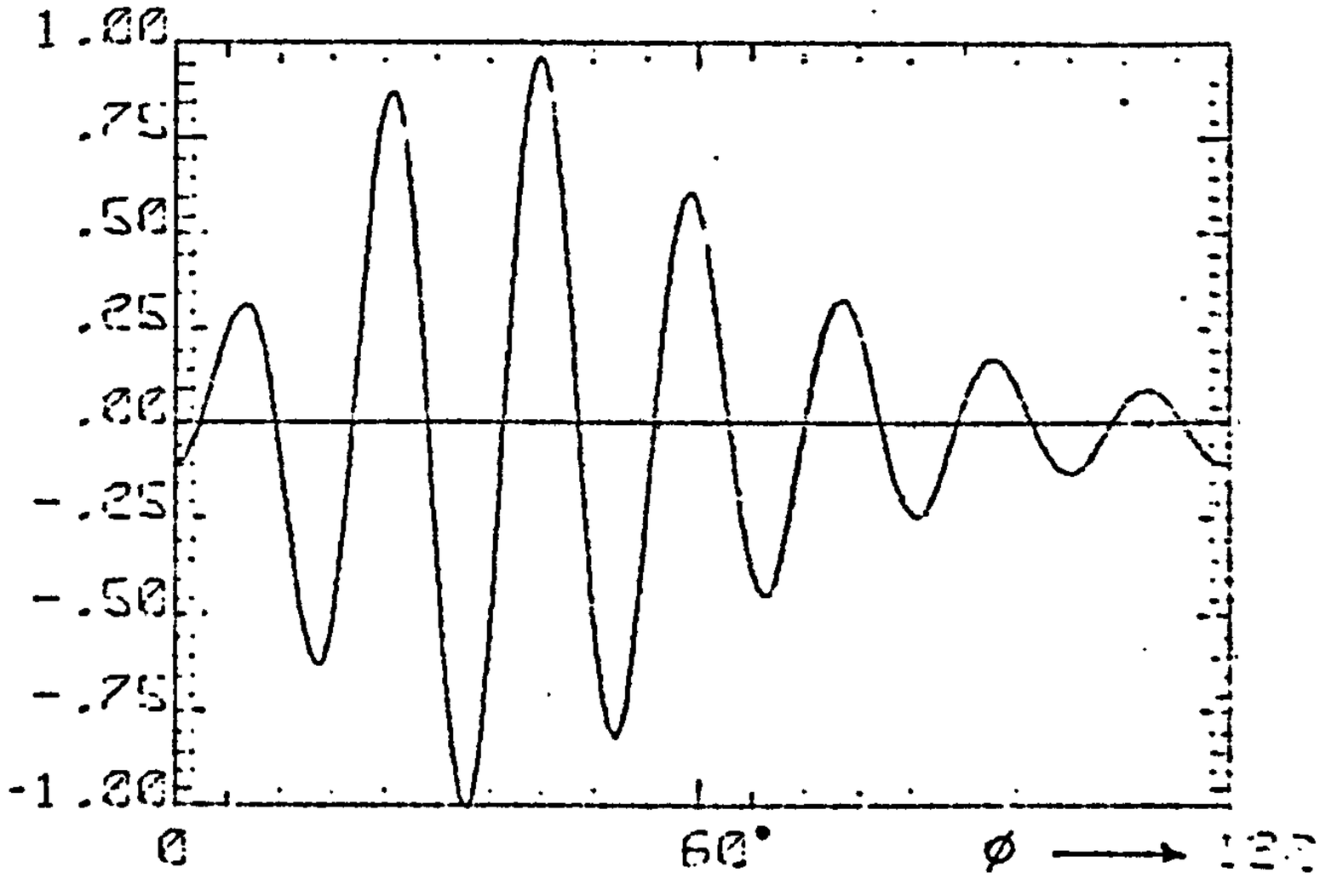

(b)

Figure 5.13 Waveform and harmonic spectrum of the

a) output current, i_L

b) tank-load current, i_{Lo}

in a half-bridge cycloinverter when the power control angle $\theta = 120^{o}$

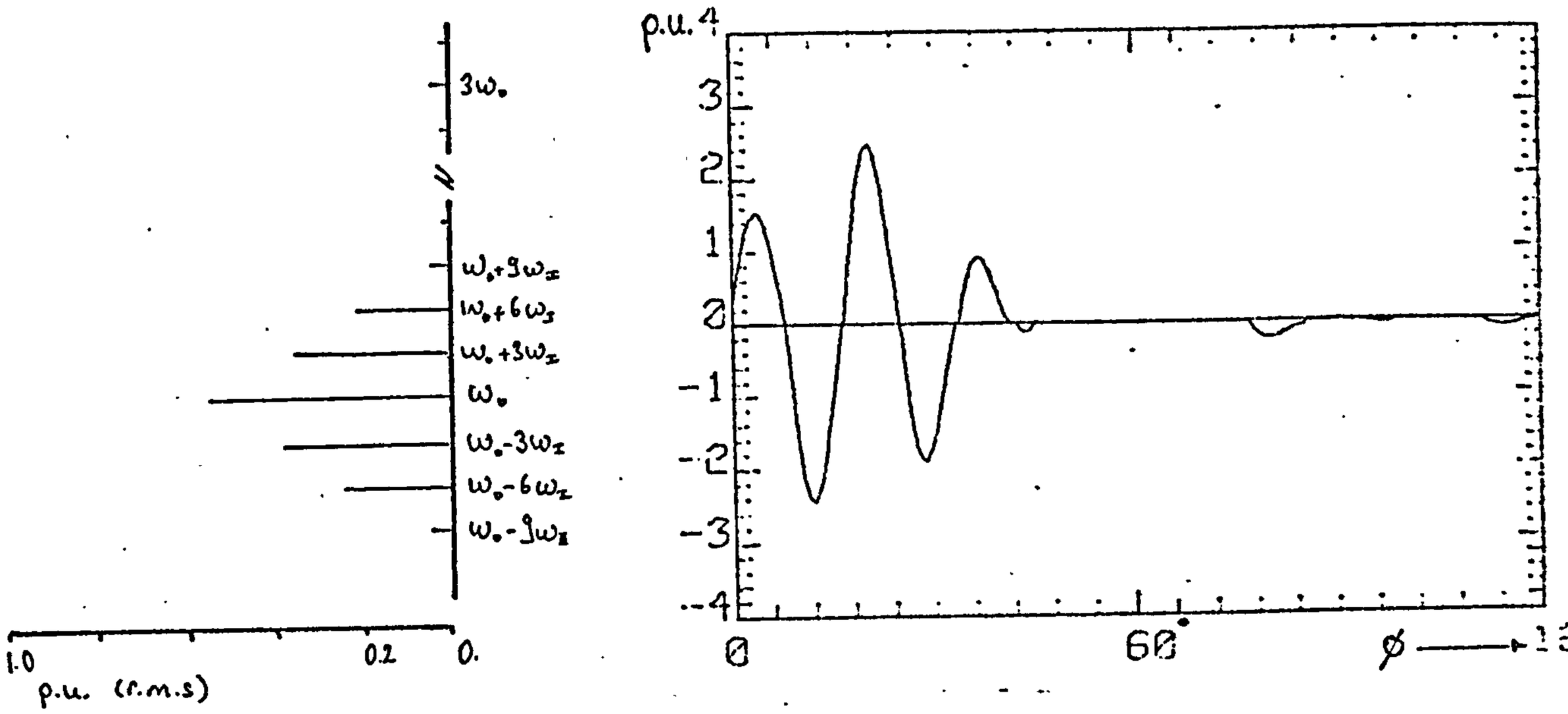

(a)

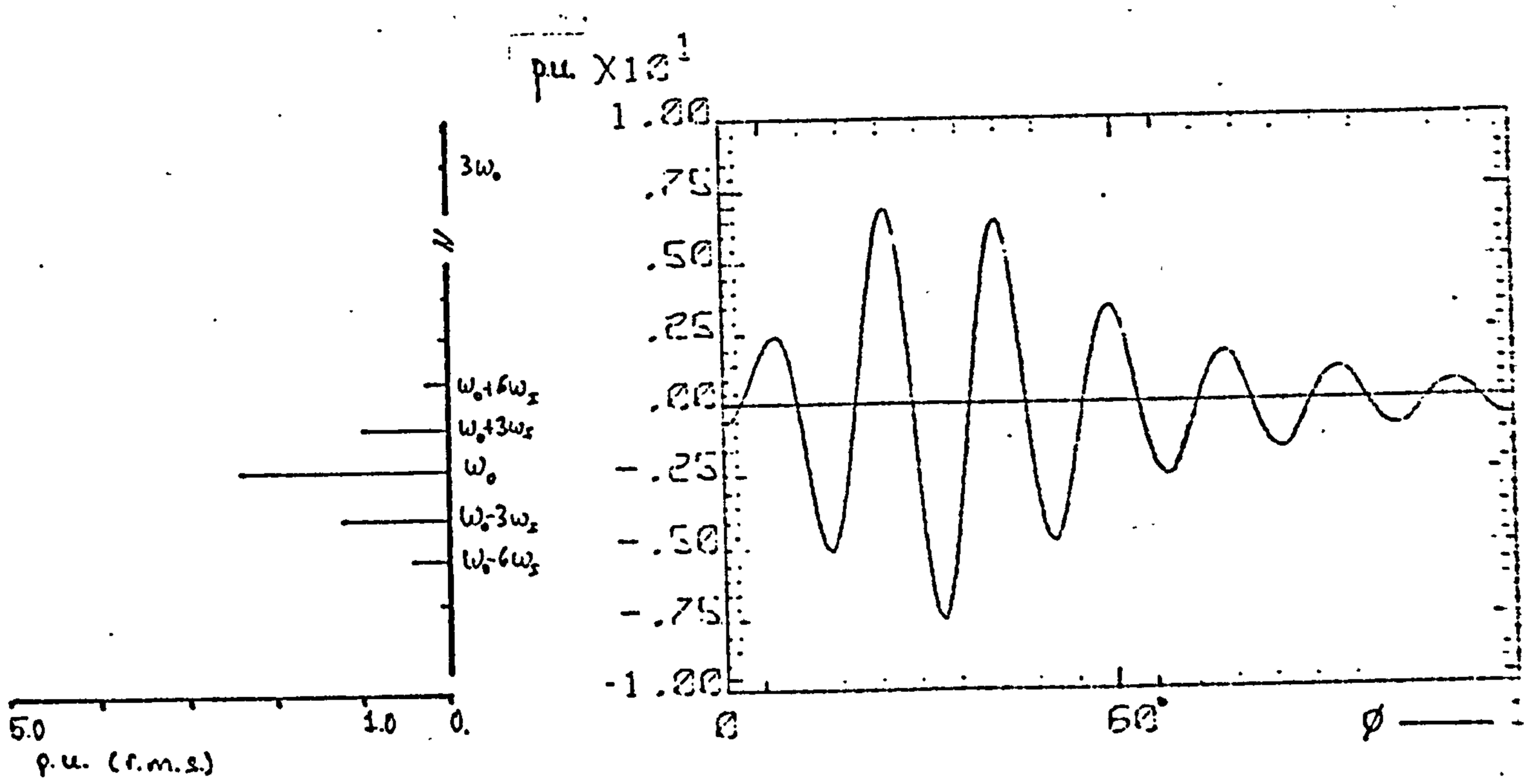

(b)

Figure 5.14 Waveform and harmonic spectrum of the

a) output current, i_L

b) tank-load current, i_{Lo}

in a half-bridge cycloinverter when the power control angle $\theta = 150^o$

Figure 5.15 Variation of frequency spectrum of the output current with the power control angle θ in a half-bridge inverter (f_o = 1050 Hz, f_I = 50 Hz, X_l = 1.0 p.u, X_c = 1.1 p.u)

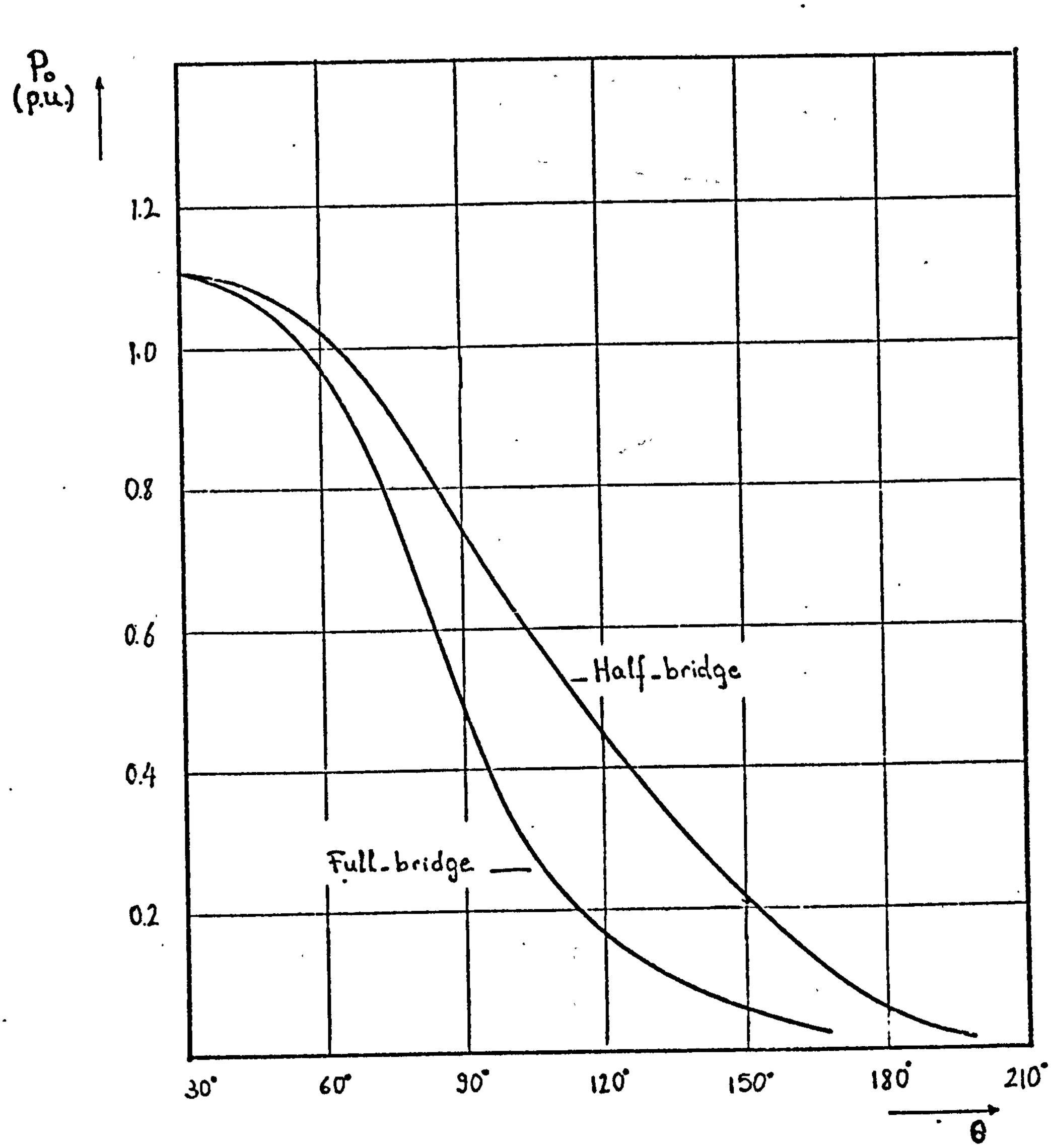

Figure 5.16 Variation of the useful cycloinverter output power, P_o with θ (f_o = 1050 Hz)

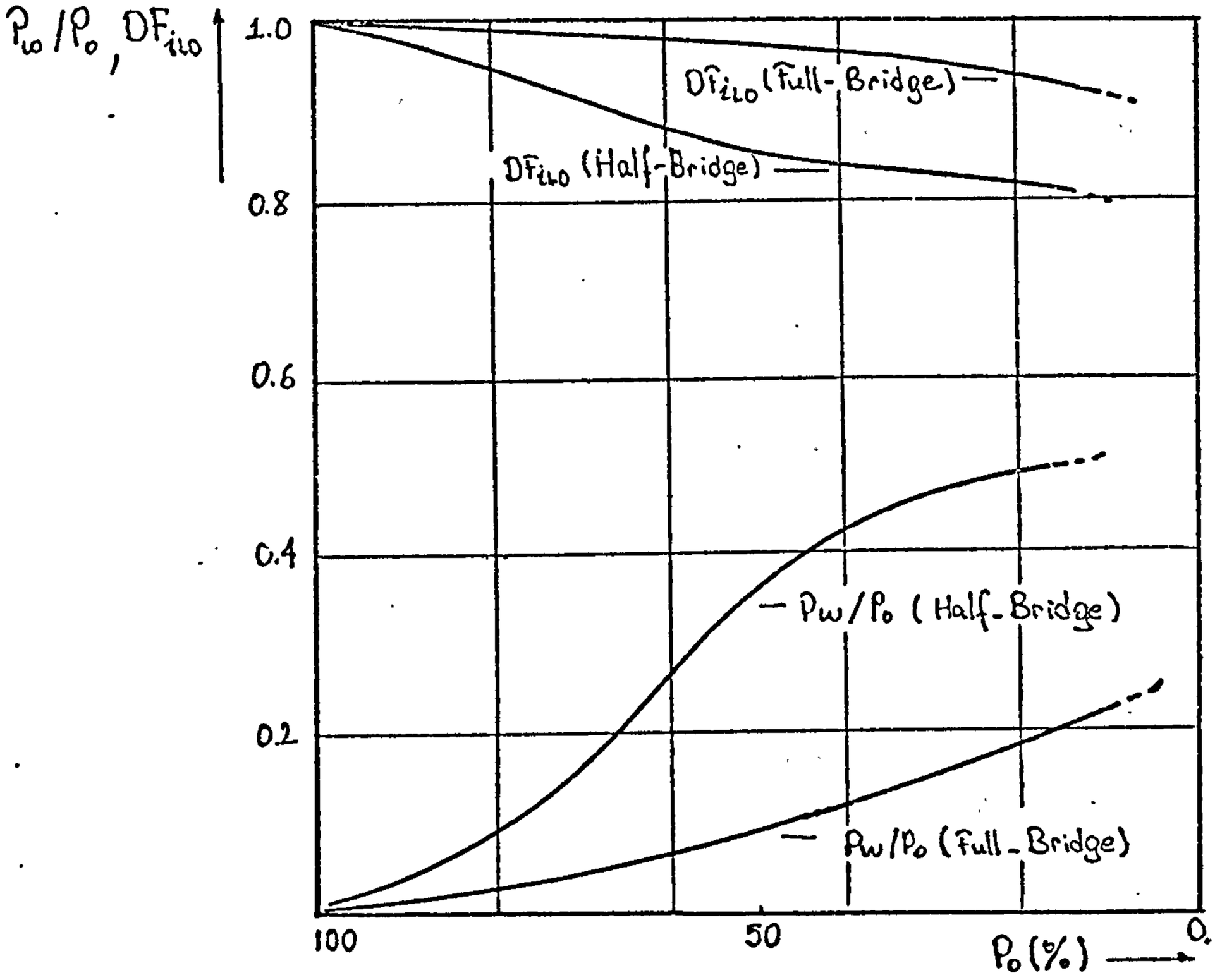

Figure 5.17 Variation, with the output power P_o, of the heating coil distortion factor DF_{iLo}, and the wasted output power per useful output power P_w/P_o in the full- and half-bridge cycloinverter

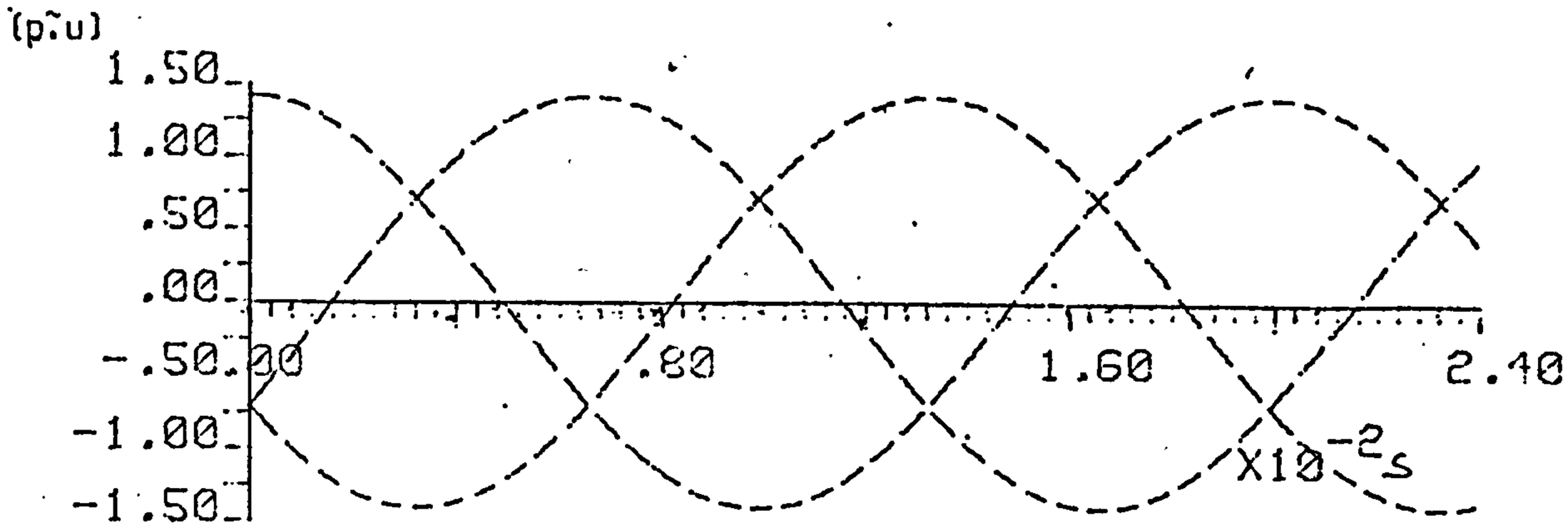

3-ϕ input

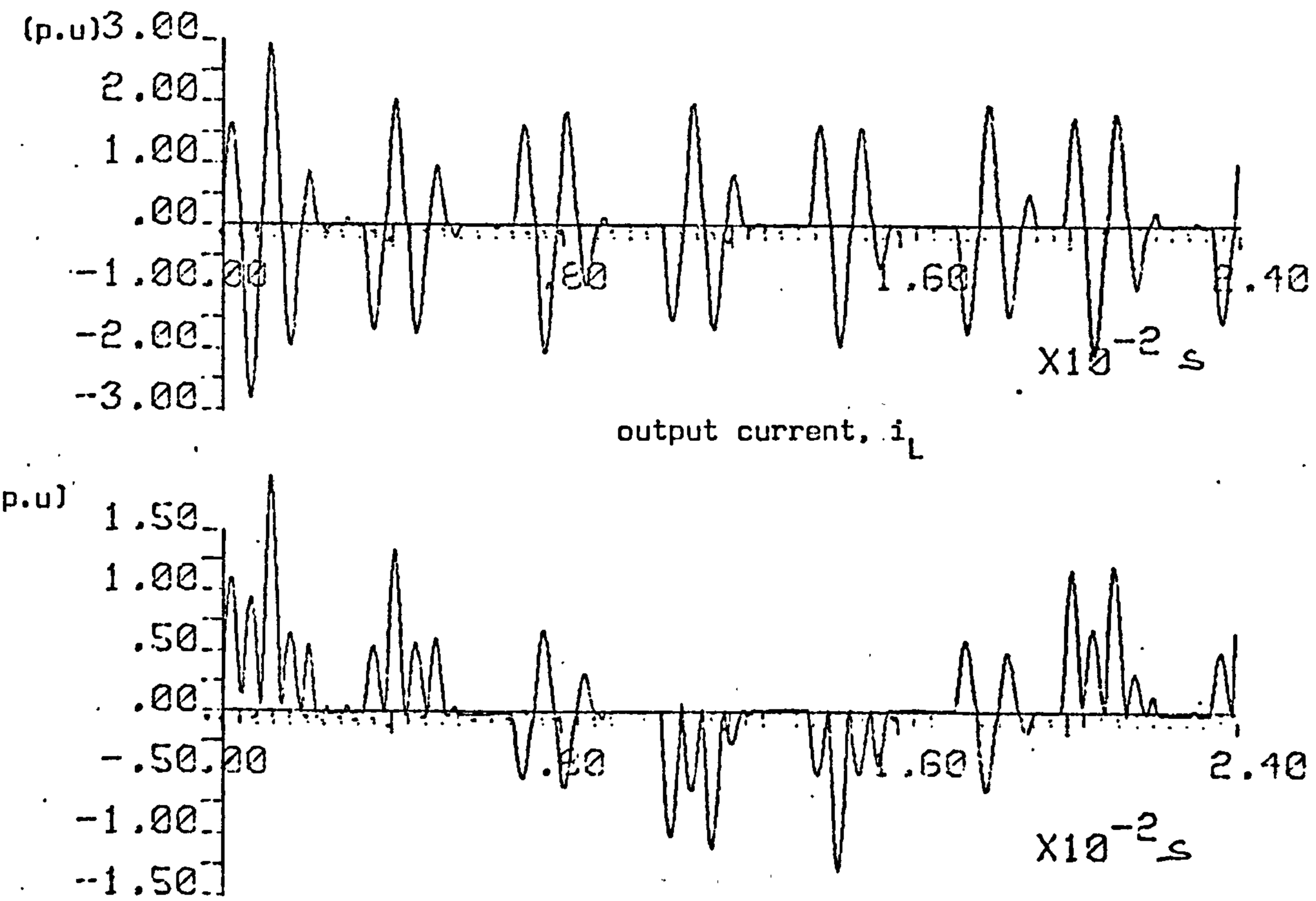

output current, i_L

input line current, i_1

tank-load voltage , v_{co}

Figure 5.18 Full-bridge cycloinverter waveforms computed for $\theta = 90^o$ (f_o = 1050 Hz, Q_L = 5)

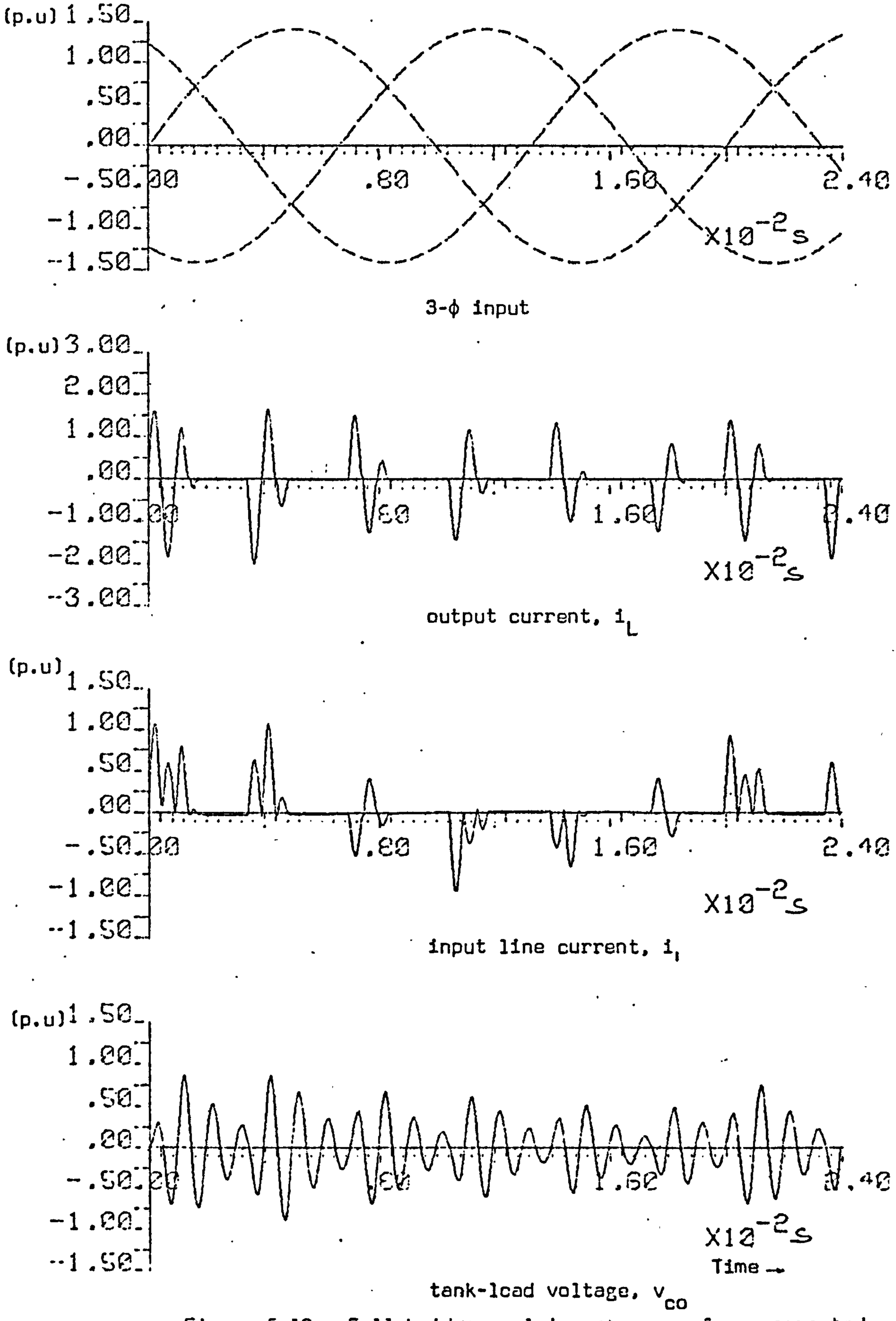

Figure 5.19 Full-bridge cycloinverter waveforms computed for $\theta = 120^{o}$ (f_o = 1050 Hz, Q_L = 5)

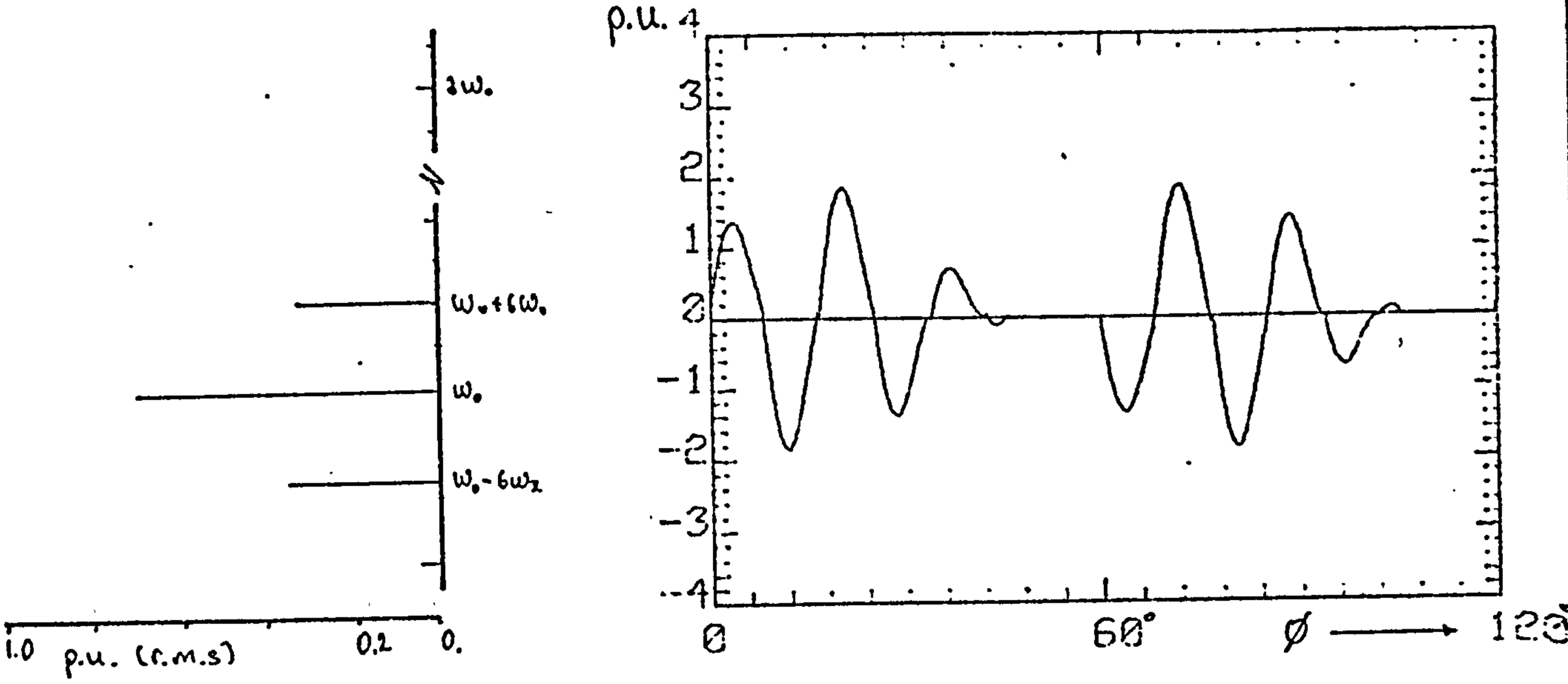

Figure 5.20 Waveform and harmonic spectrum of the:

a) output current, i_L b) tank-load current, i_{Lo}.

in a full-bridge cycloinverter, when the power control angle $\theta = 90^o$

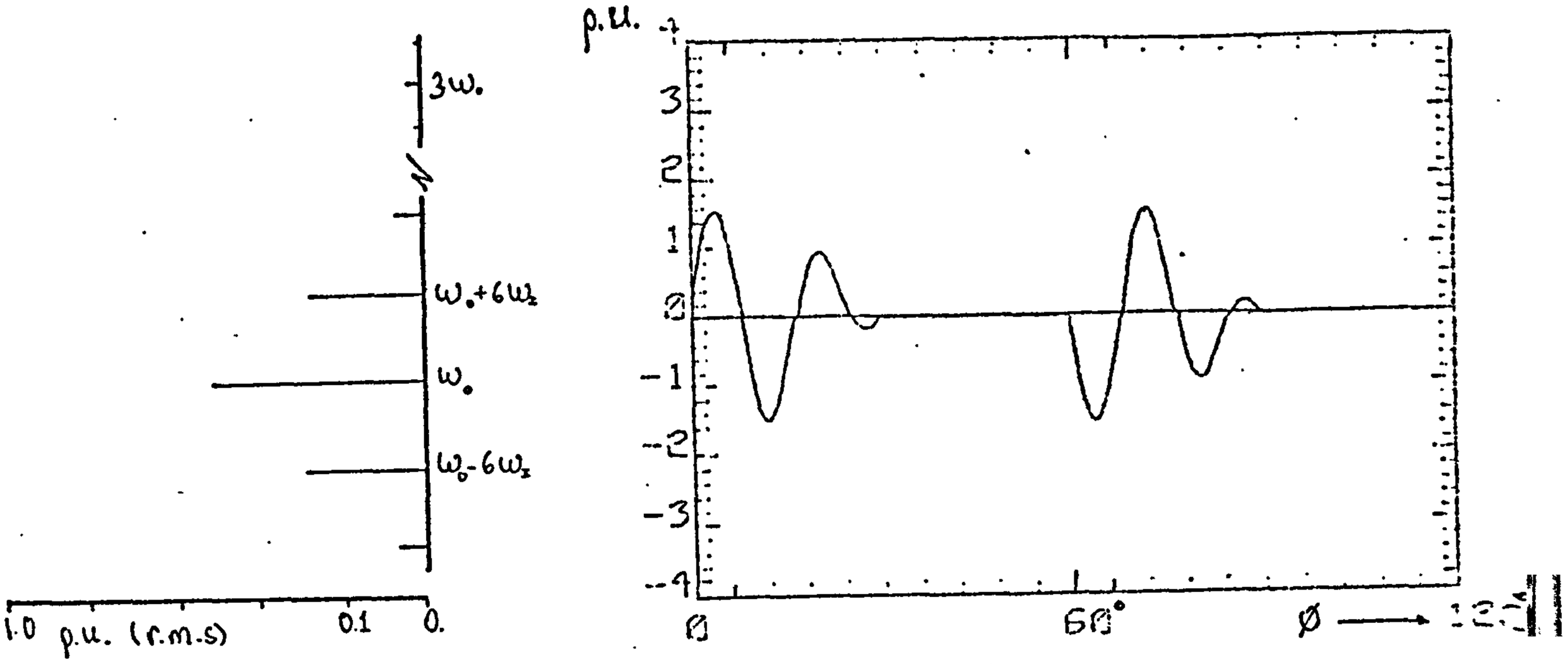

(a)

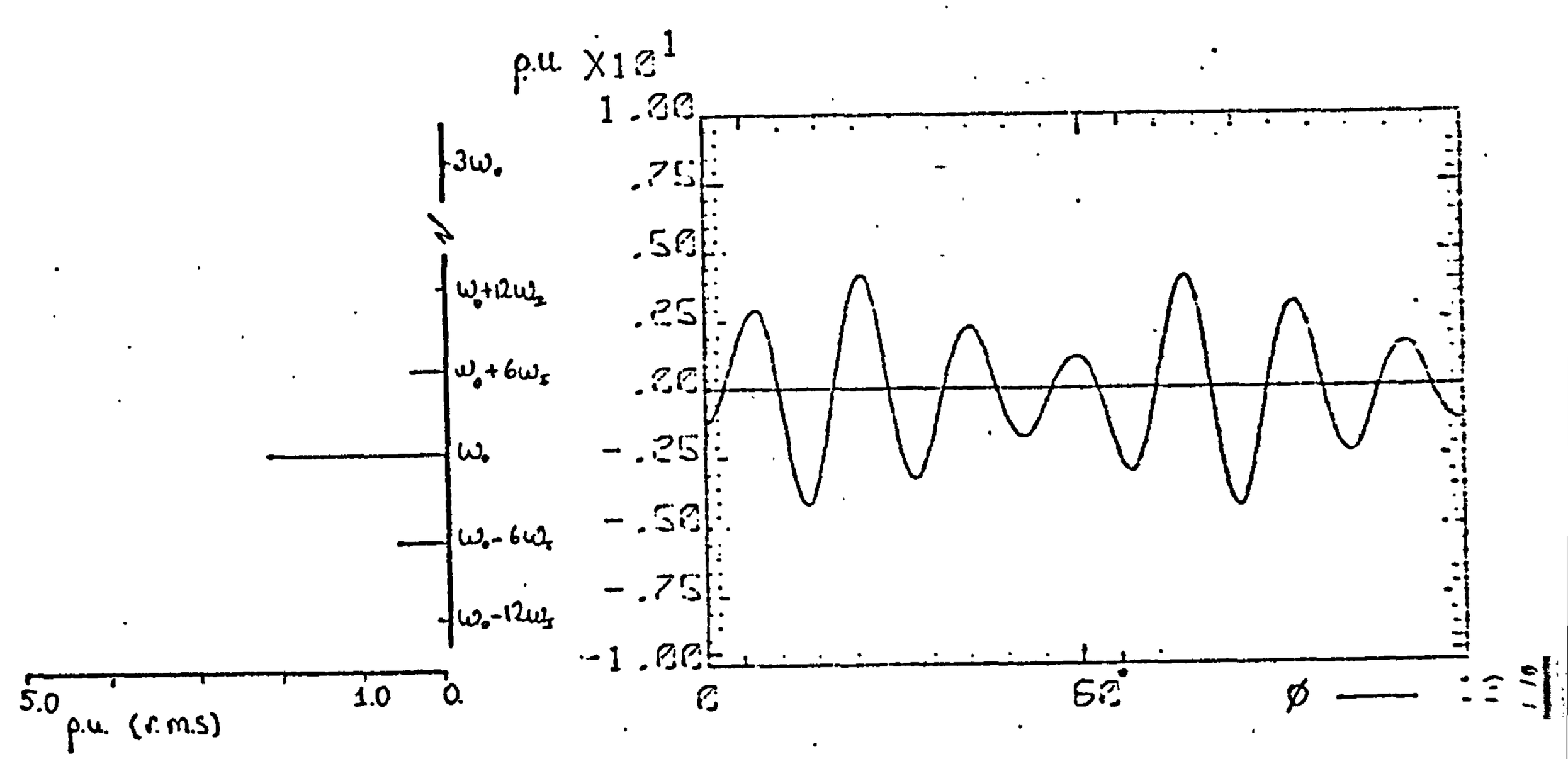

(b)

Figure 5.21 Waveform and harmonic spectrum of the:

a) output current, i_L b) tank-load current, i_{Lo}

in a full-bridge cycloinverter, when the power control angle $\theta = 120^o$

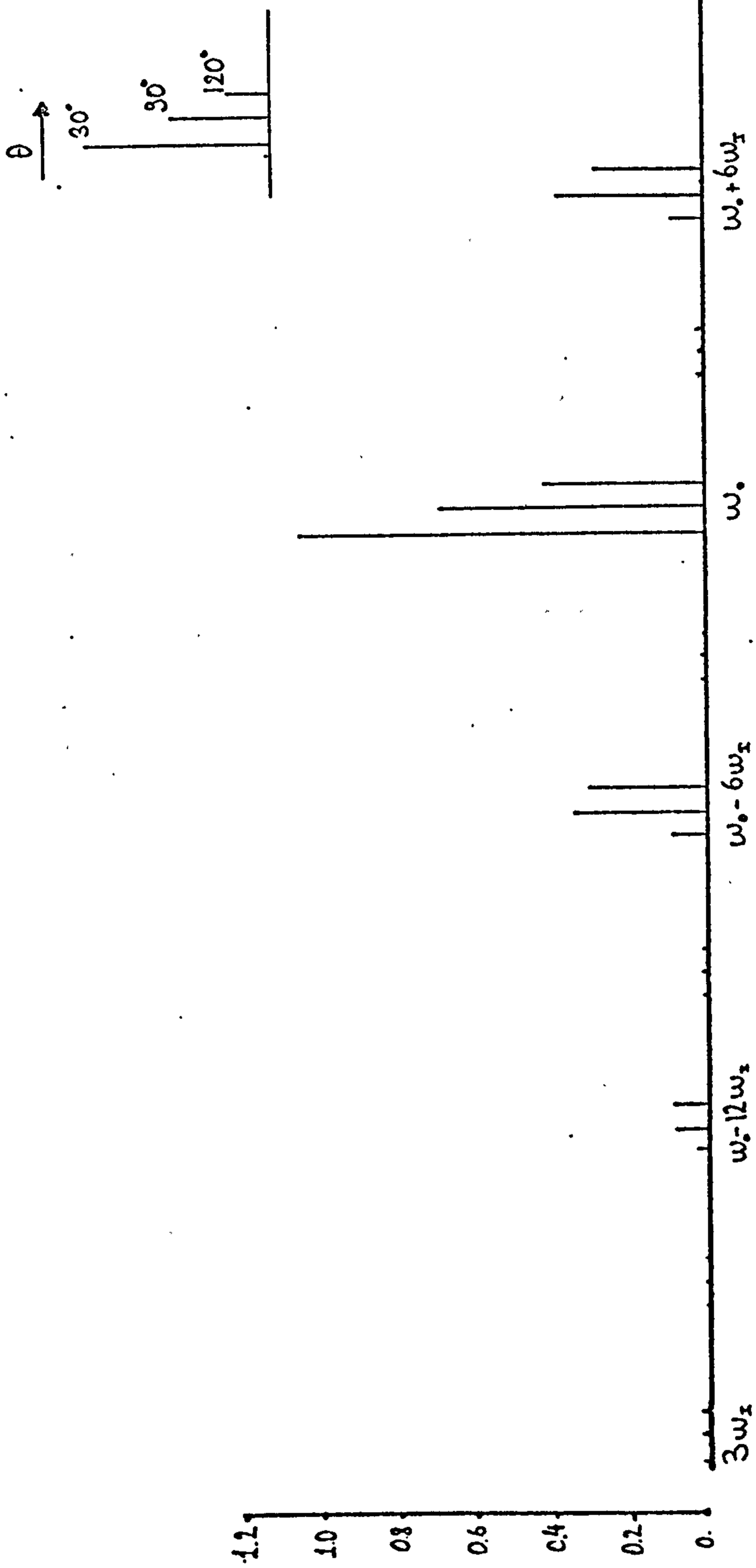

Figure 5.22 Variation of frequency spectrum of the output current with power control angle θ in the full-bridge inverter (f_o = 1050 Hz, f_I = 50 Hz)

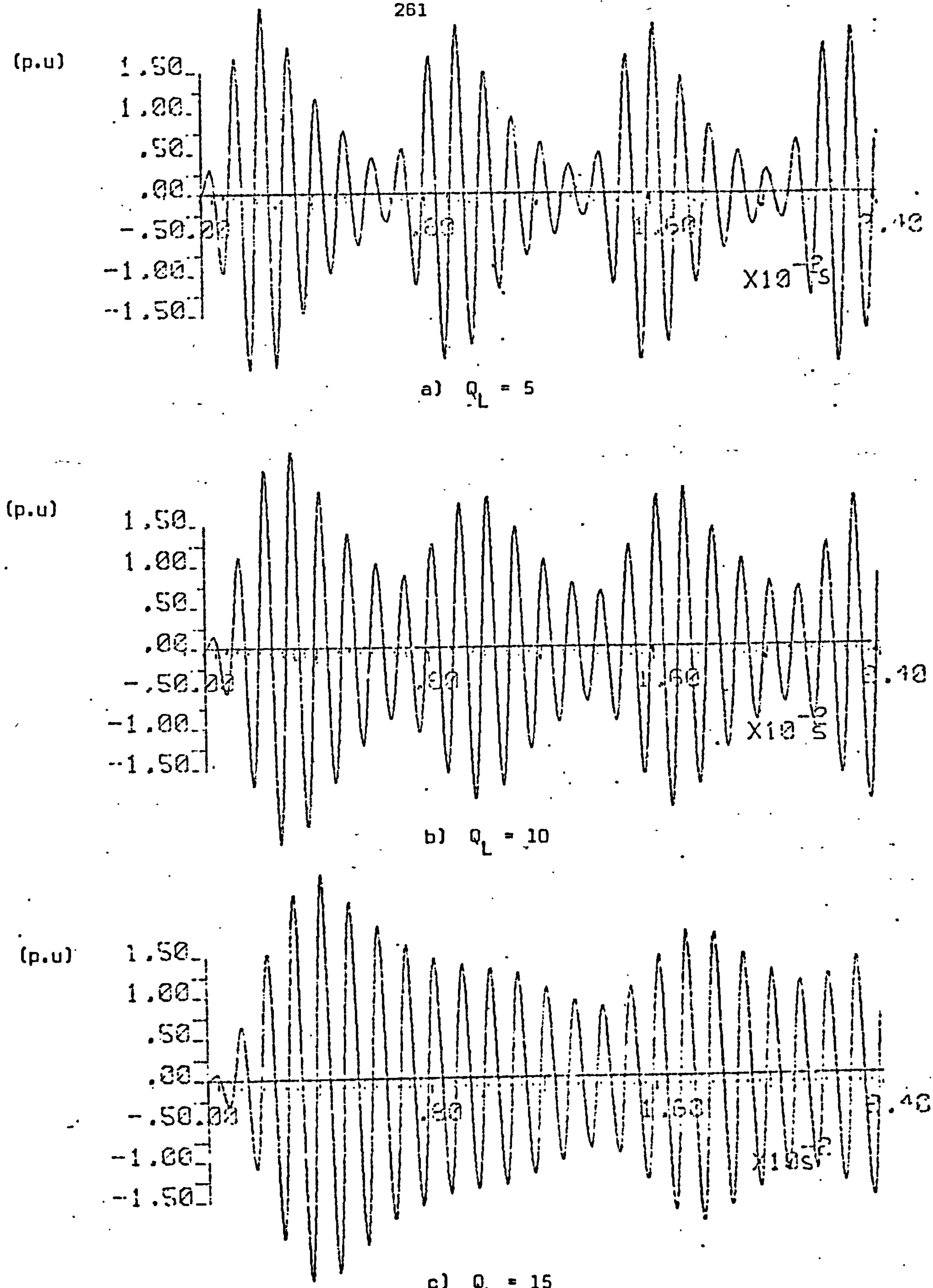

Figure 5.23 Variation of tank-load voltege v_{co} with Q_L in a half-bridge cycloinverter

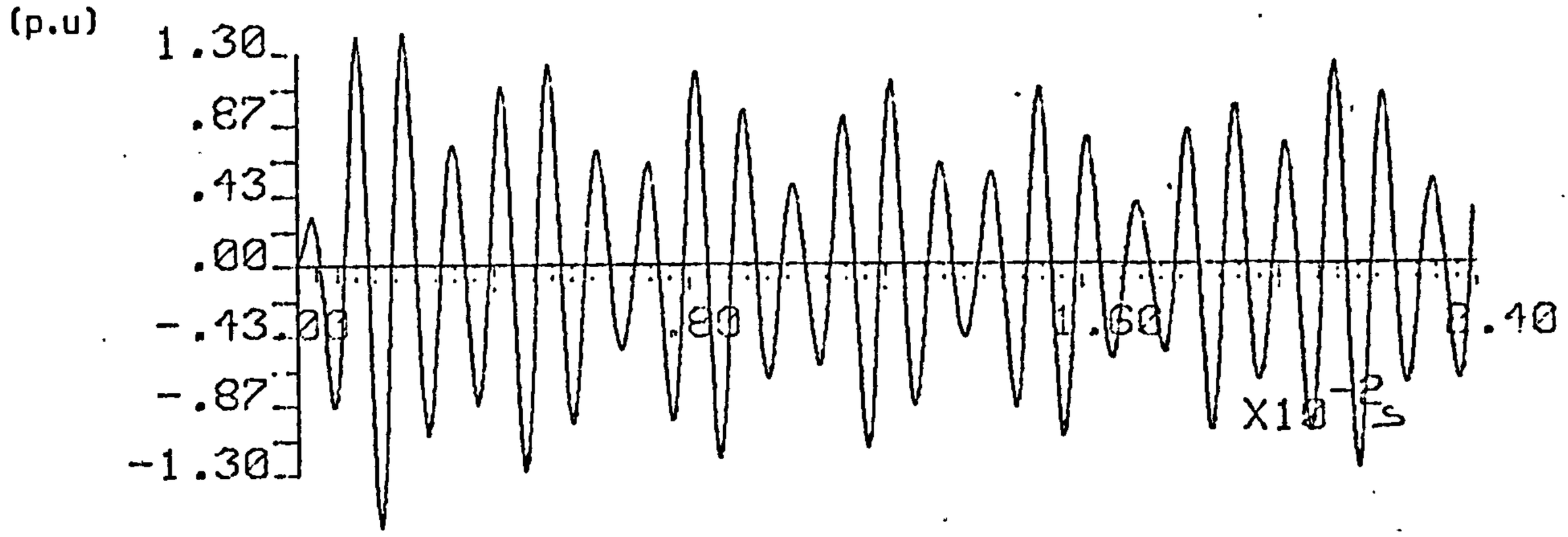

a) $Q_L = 5$

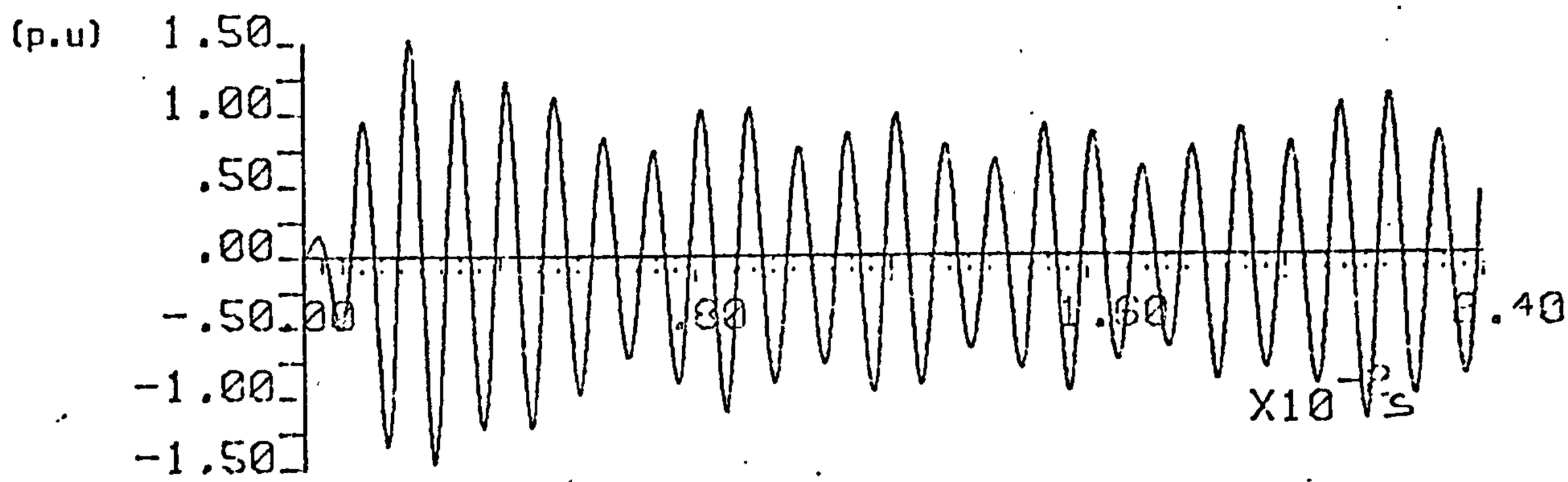

b) $Q_L = 10$

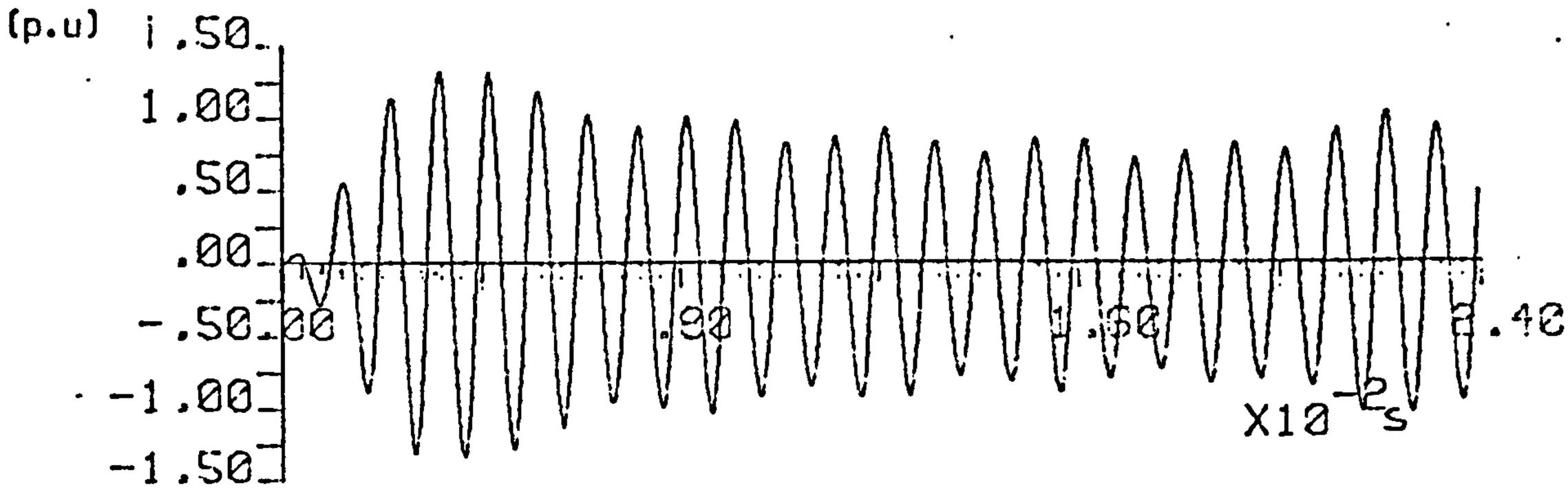

c) $Q_L = 20$

Figure 5.24 Variation of tank-load voltage v_{co} with Q_L in a full-bridge cycloinverter

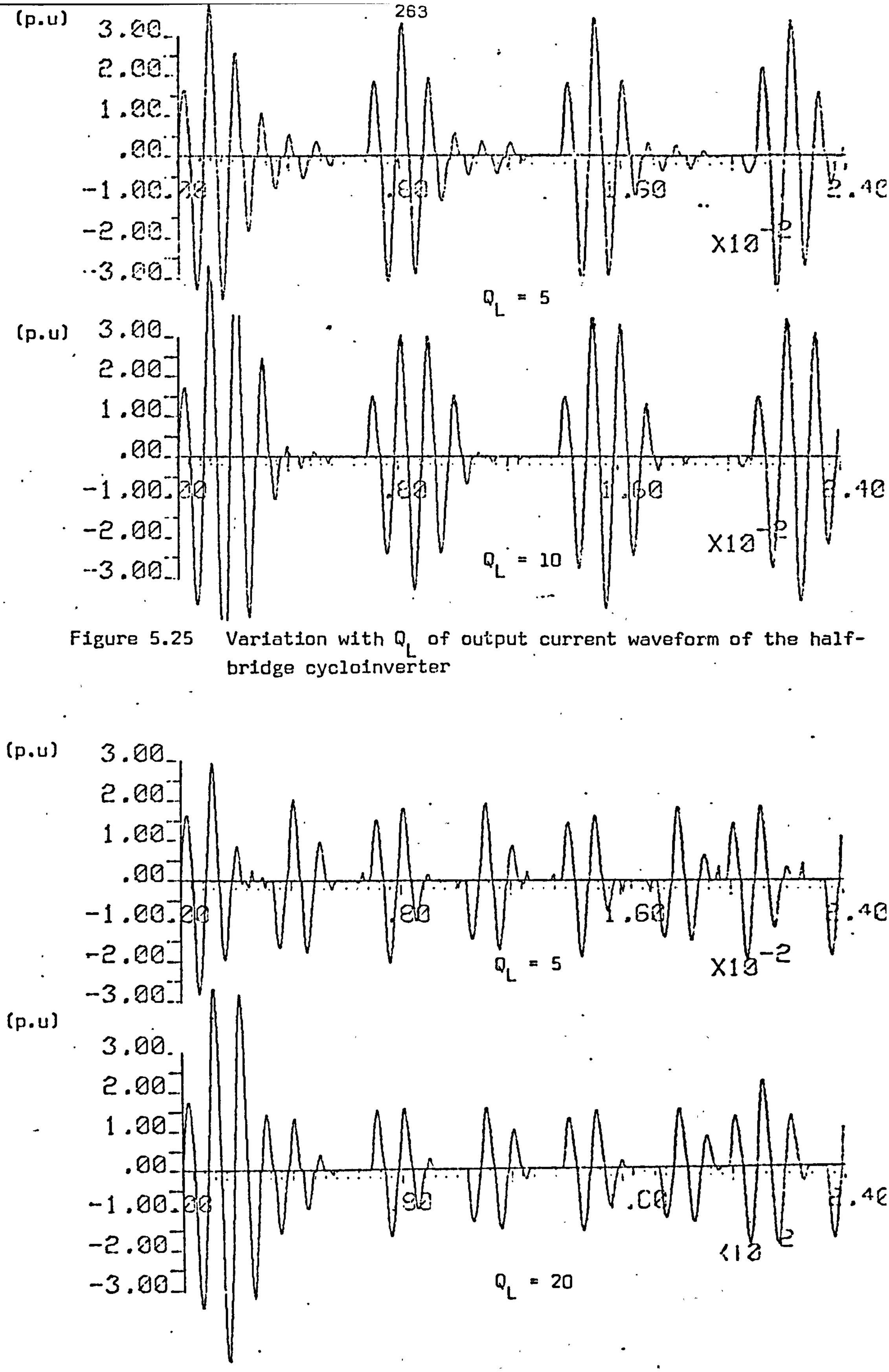

Figure 5.25 Variation with Q_L of output current waveform of the half-bridge cycloinverter

Figure 5.26 Variation with Q_L of output current waveform of the full-bridge cycloinverter

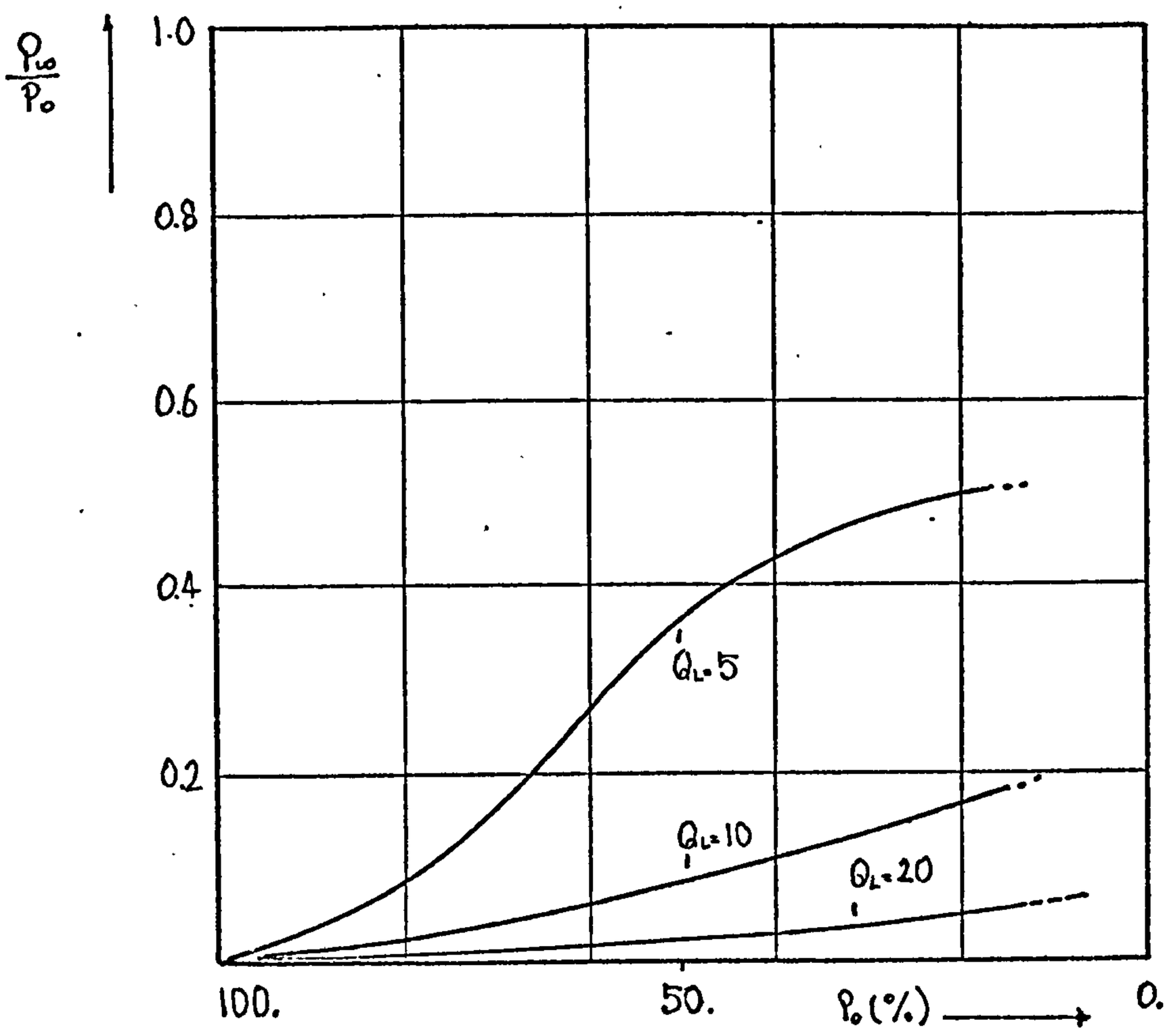

Figure 5.27 Variation of wasted power per useful output power with output power in a half-bridge cycloinverter

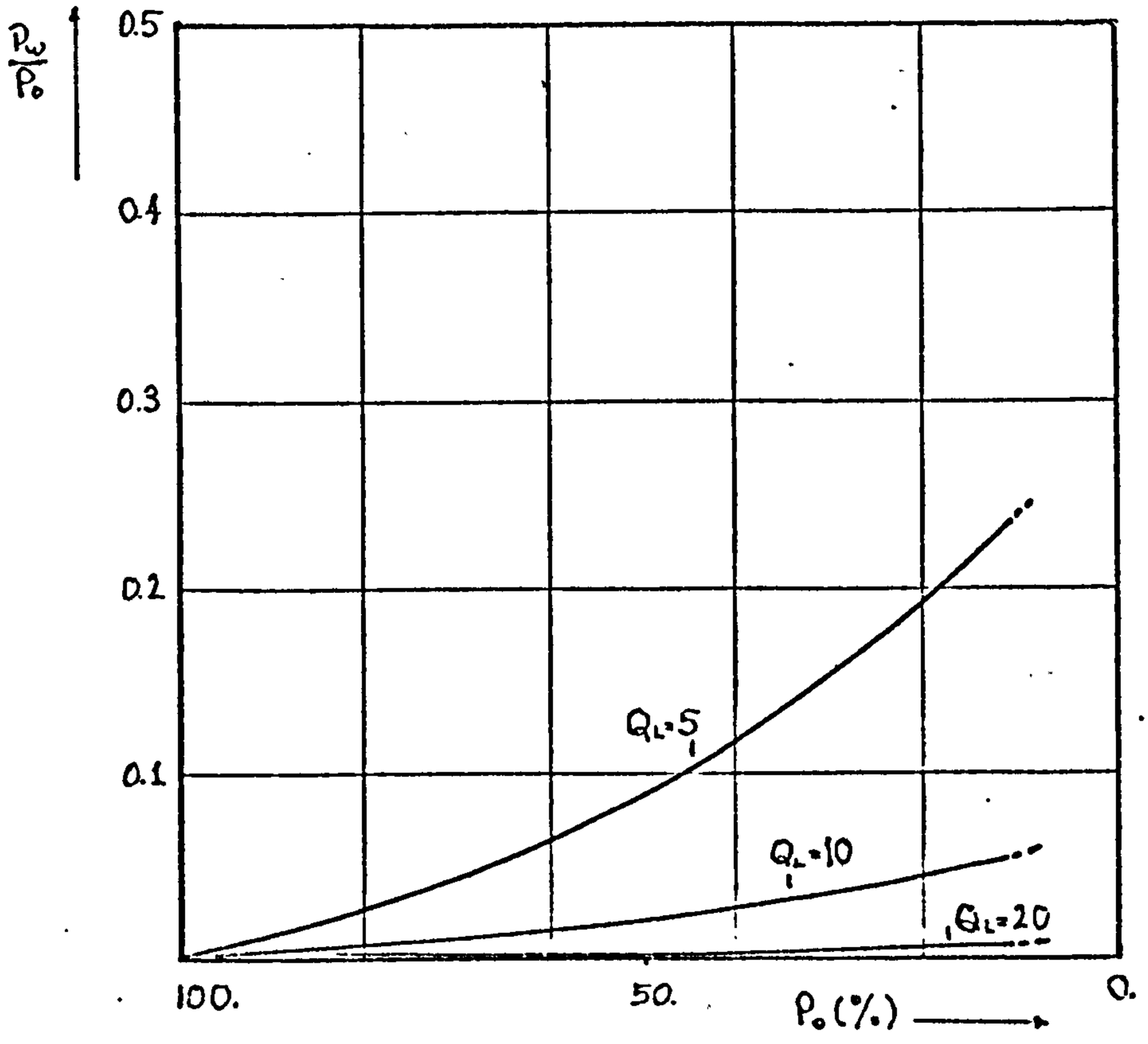

Figure 5.28 Variation of wasted power per useful output power with output power in a full-bridge cycloinverter

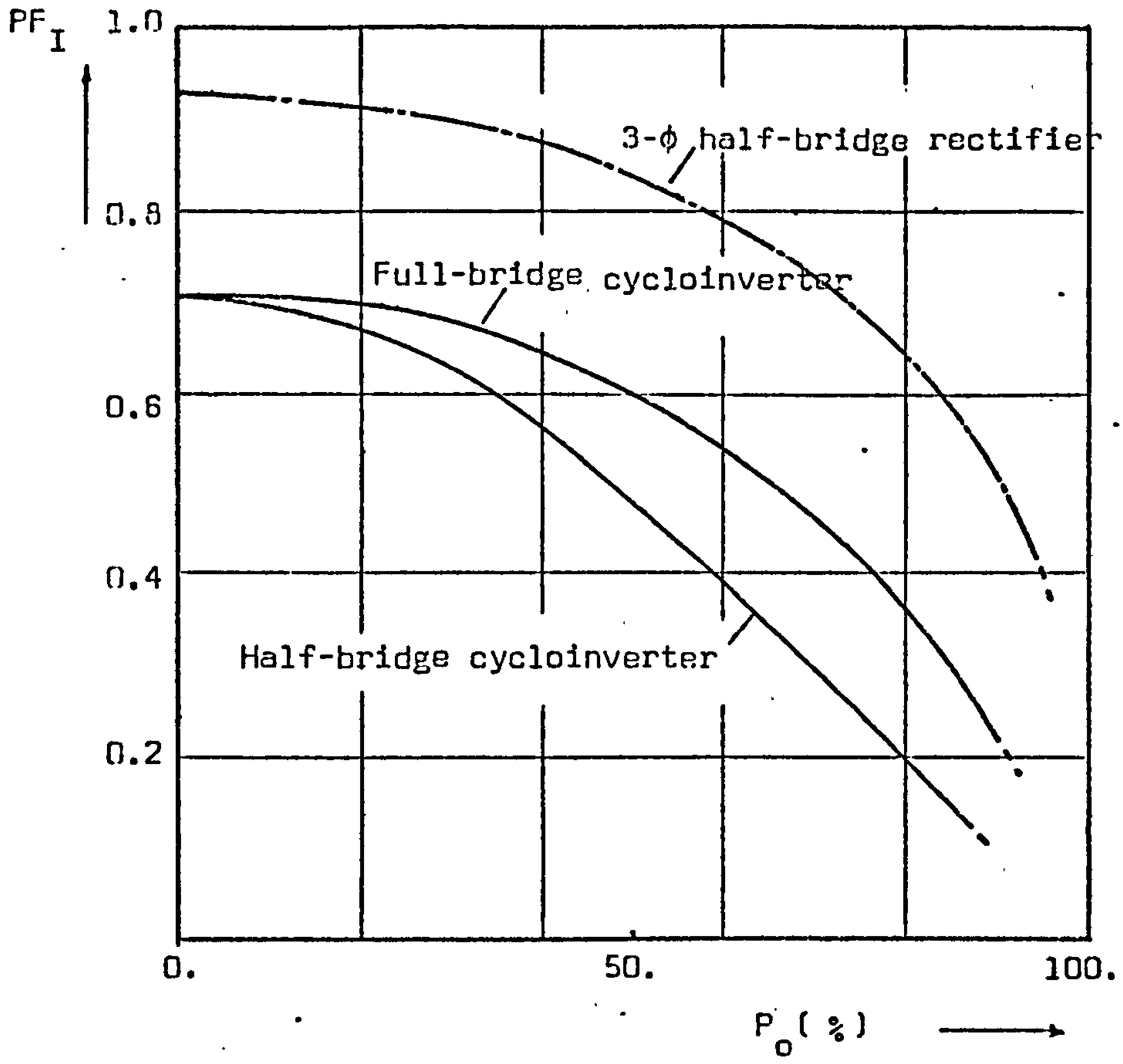

Figure 5.29 Variation of input power factor with output power control

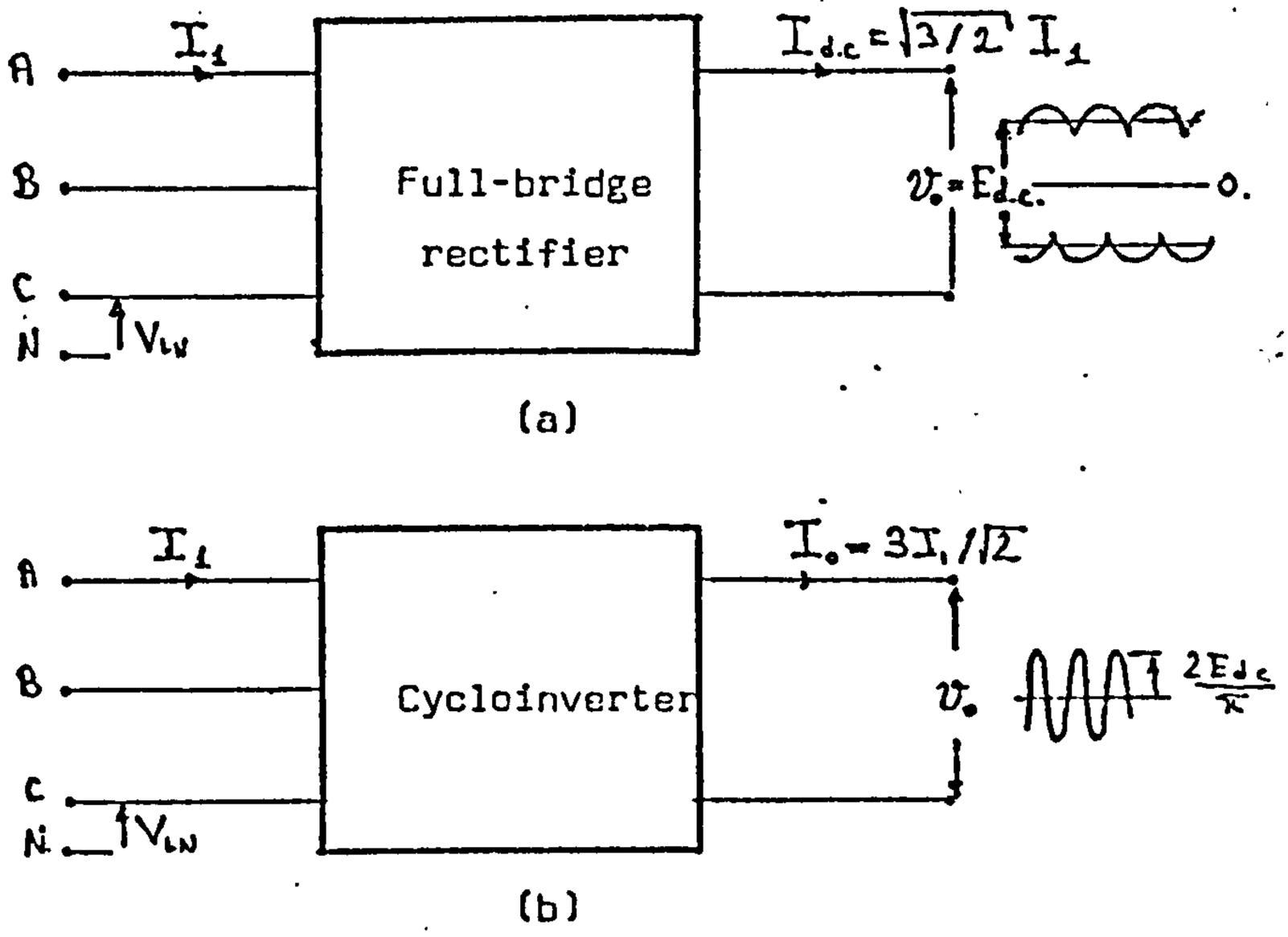

Figure 5.30 Comparison of the output power developed for a given input line current I_1

a) full-bridge rectifier

b) cycloinverter

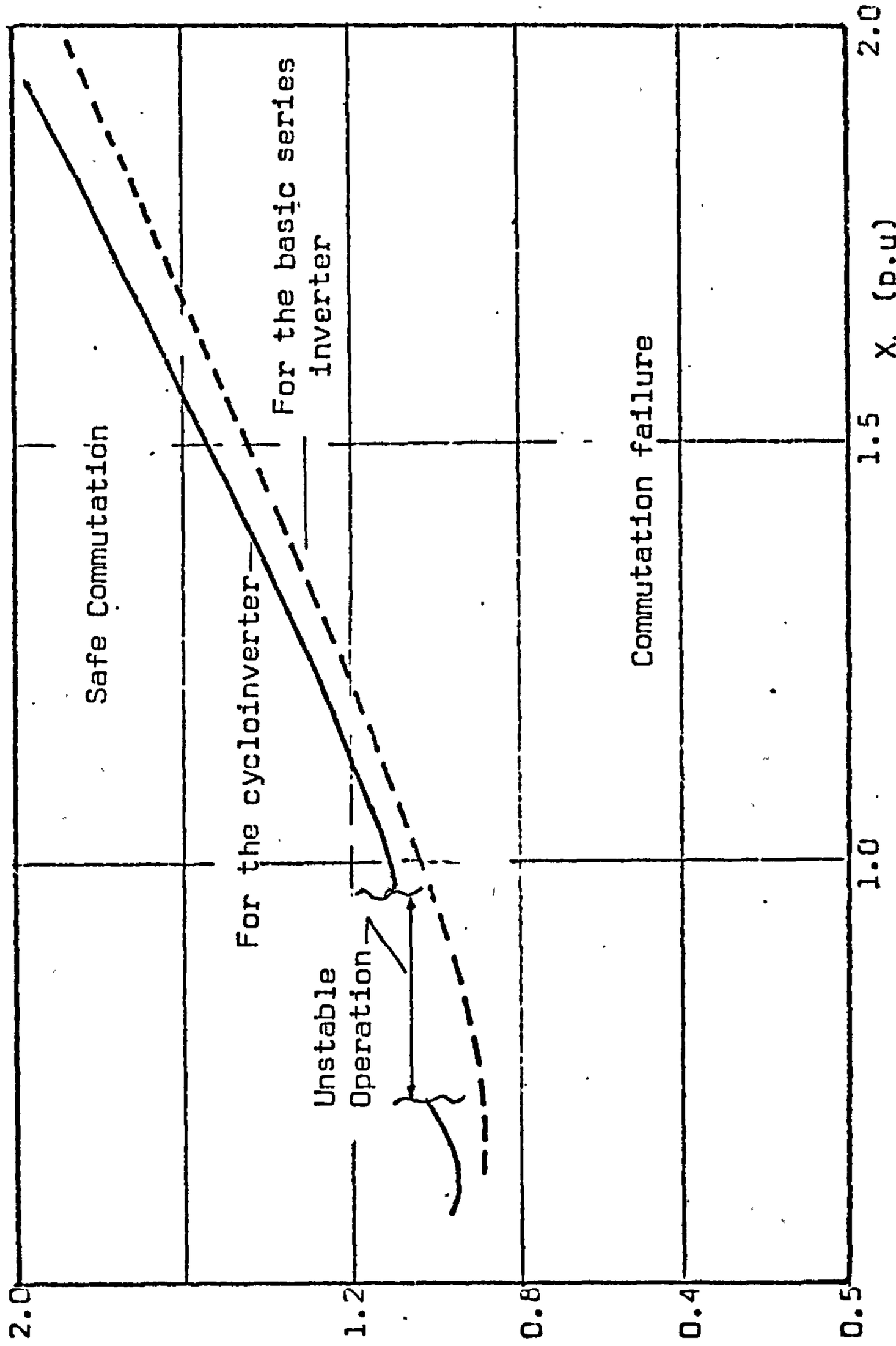

Figure 5.31 Variation of X_c with X_L for a continuous output current (i.e. $f_r \simeq f_o$)

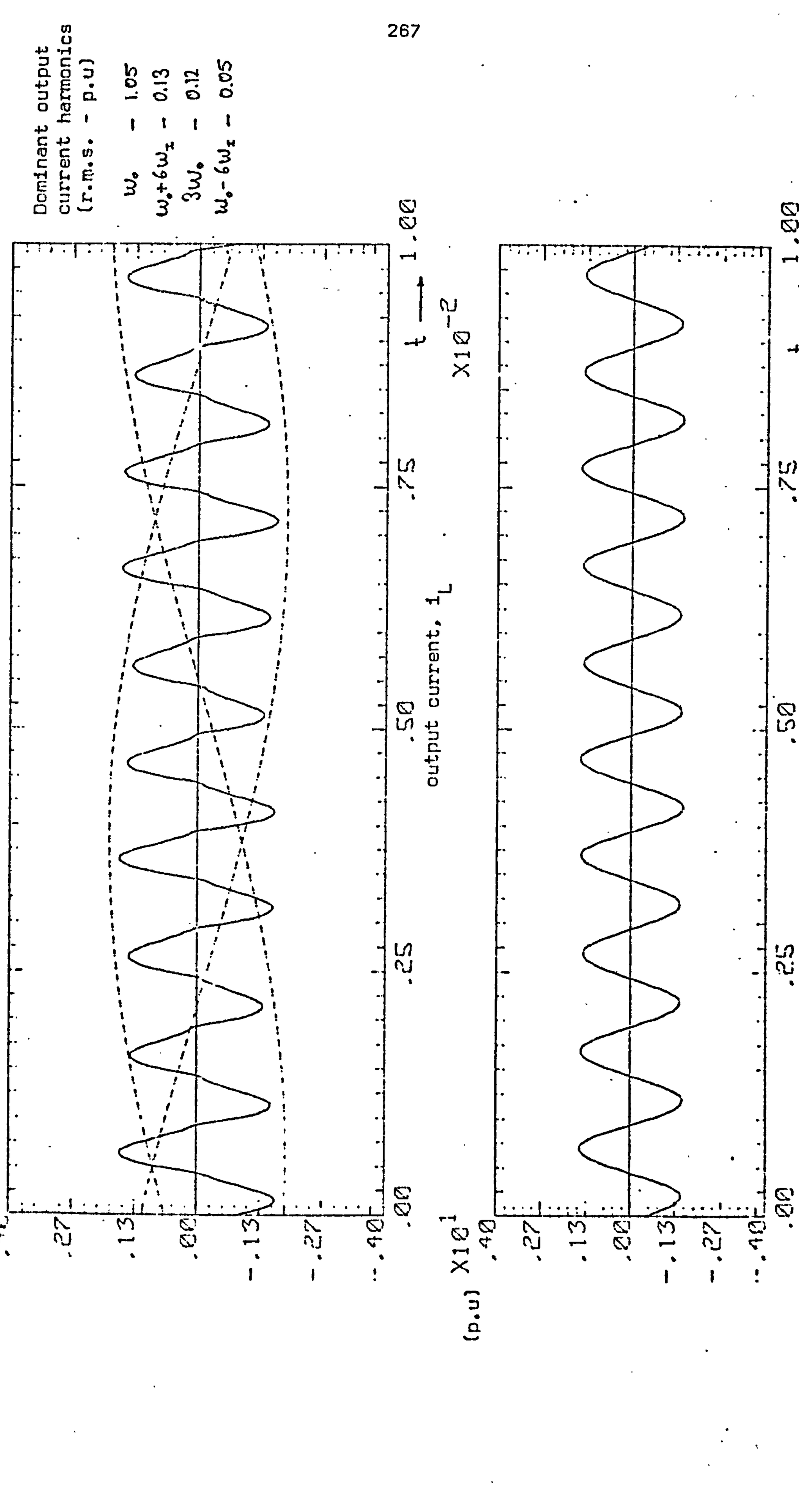

Figure 5.32 Harmonic analysis results for X_L = 1.2 p.u (f_o = 1050 Hz, Q_L = 5)

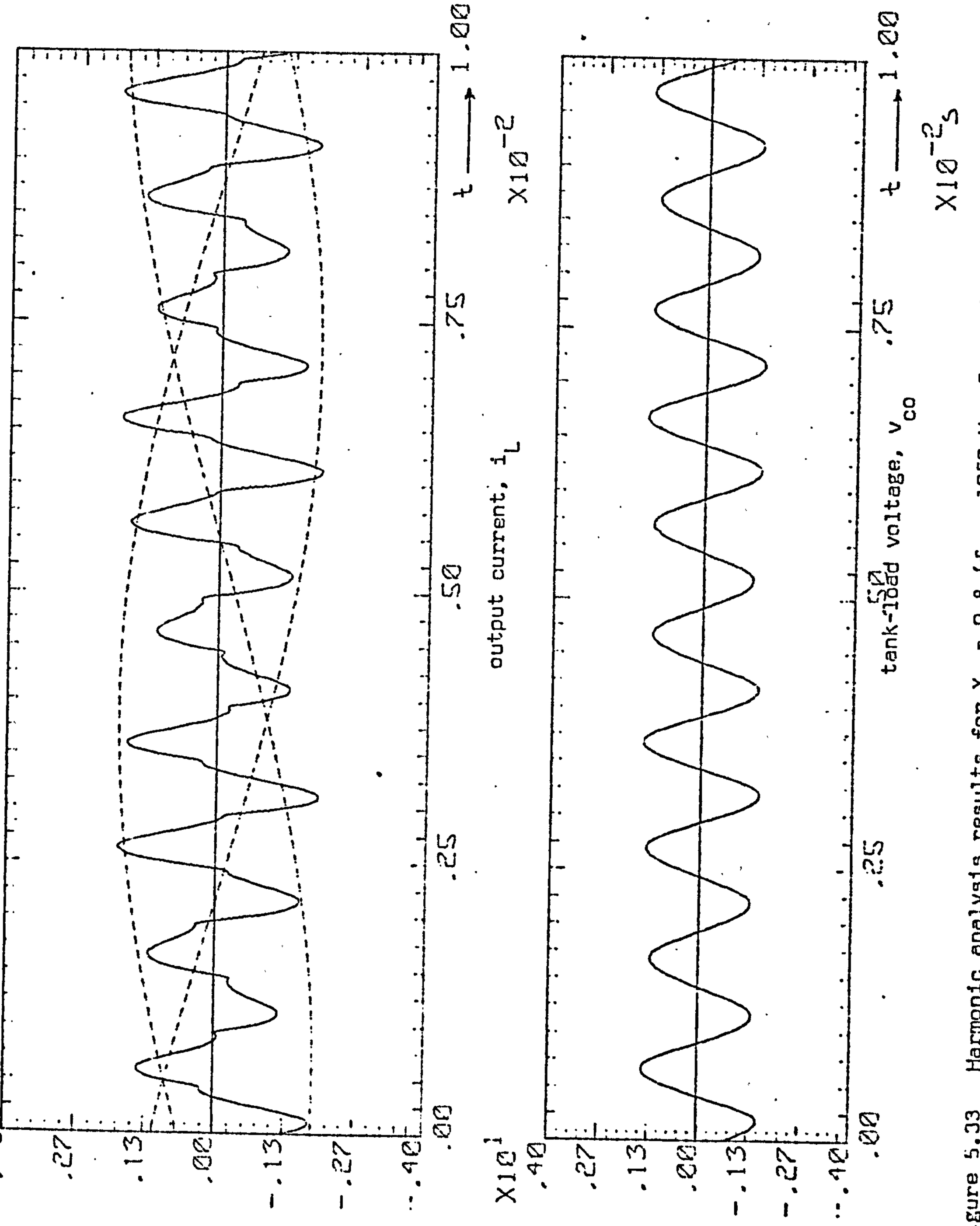

Figure 5.33 Harmonic analysis results for X_L = 0.8 (f_o = 1050 Hz, Q_L = 5)

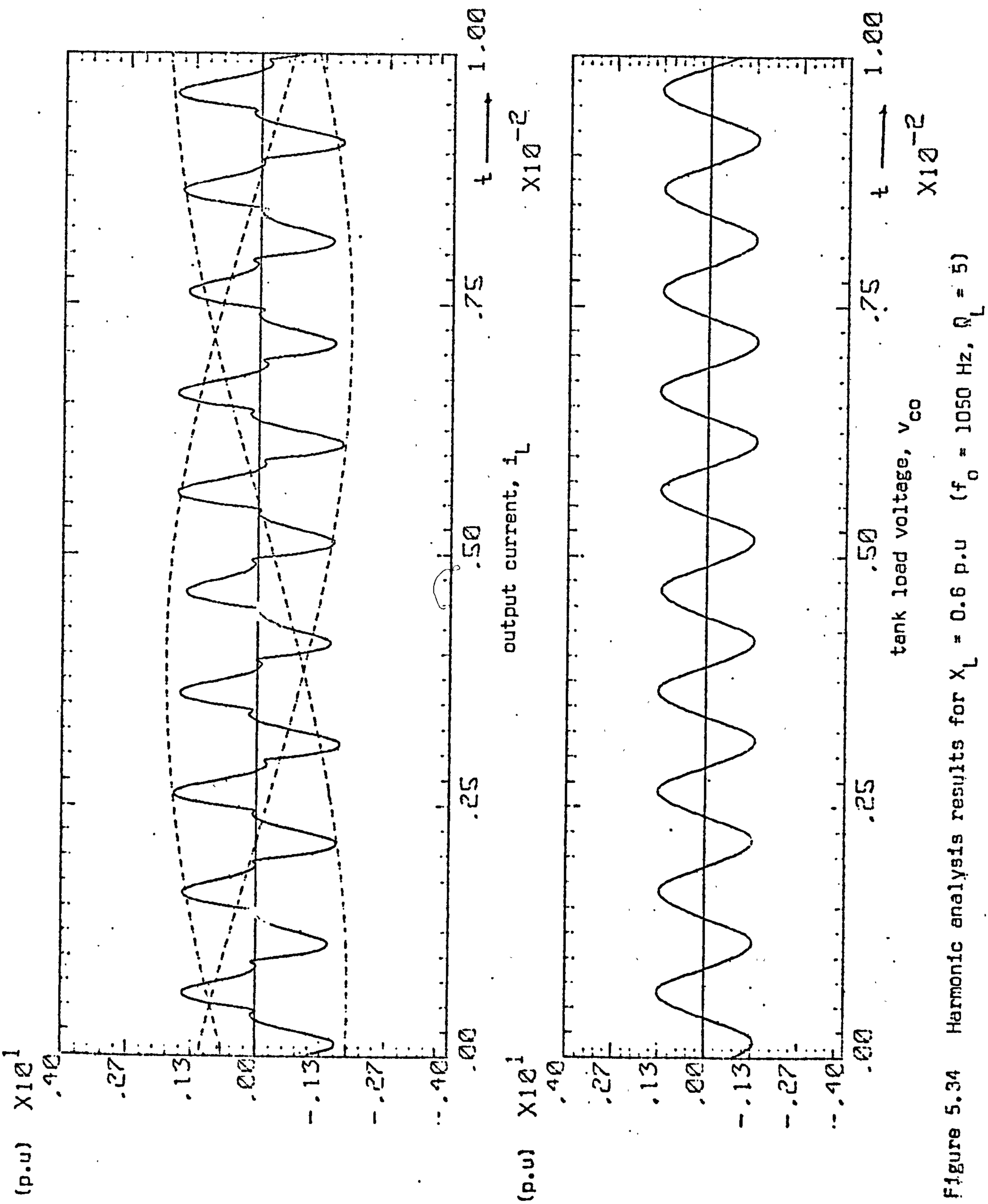

Figure 5.34 Harmonic analysis results for X_L = 0.6 p.u

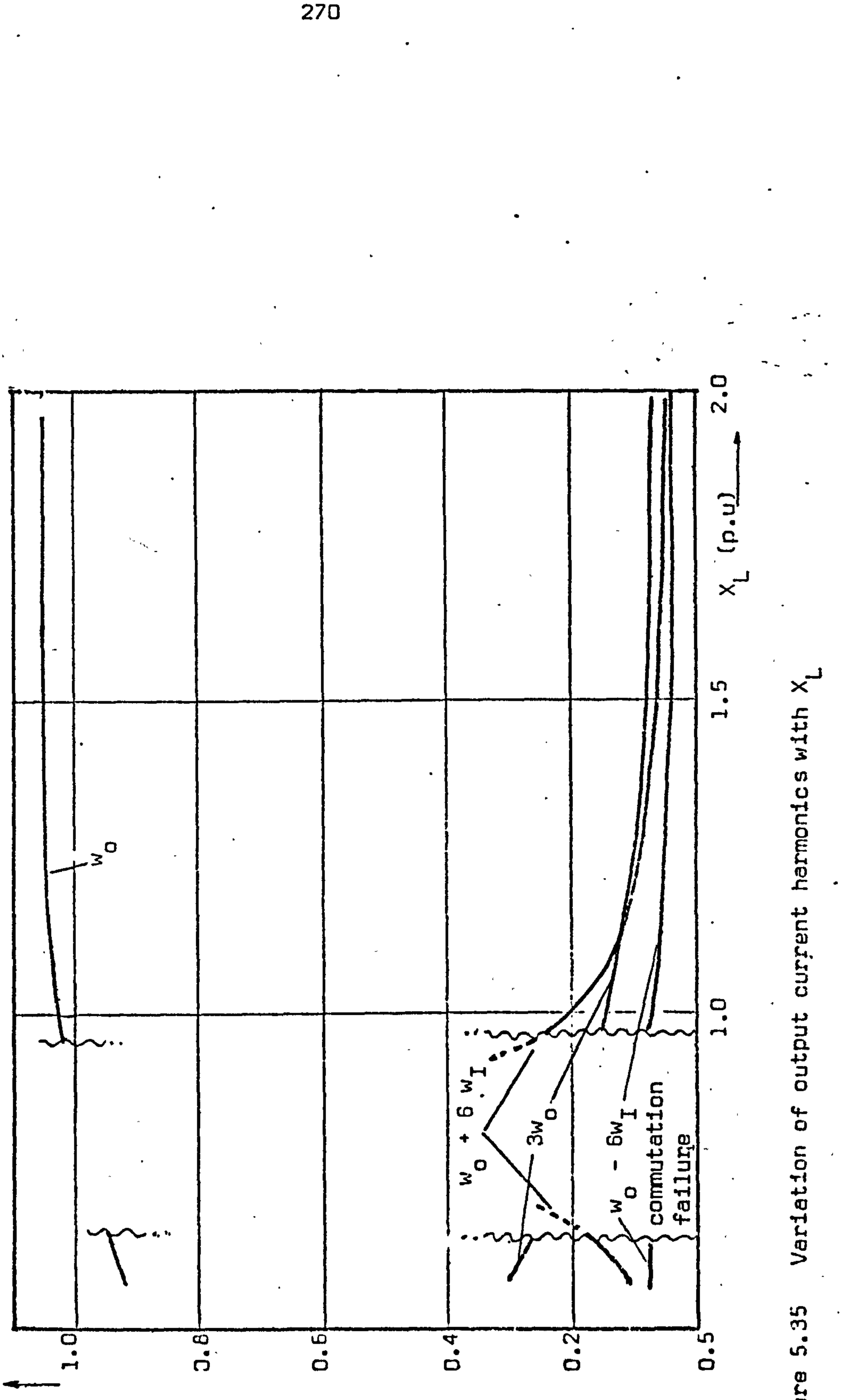

Figure 5.35 Variation of output current harmonics with X_L

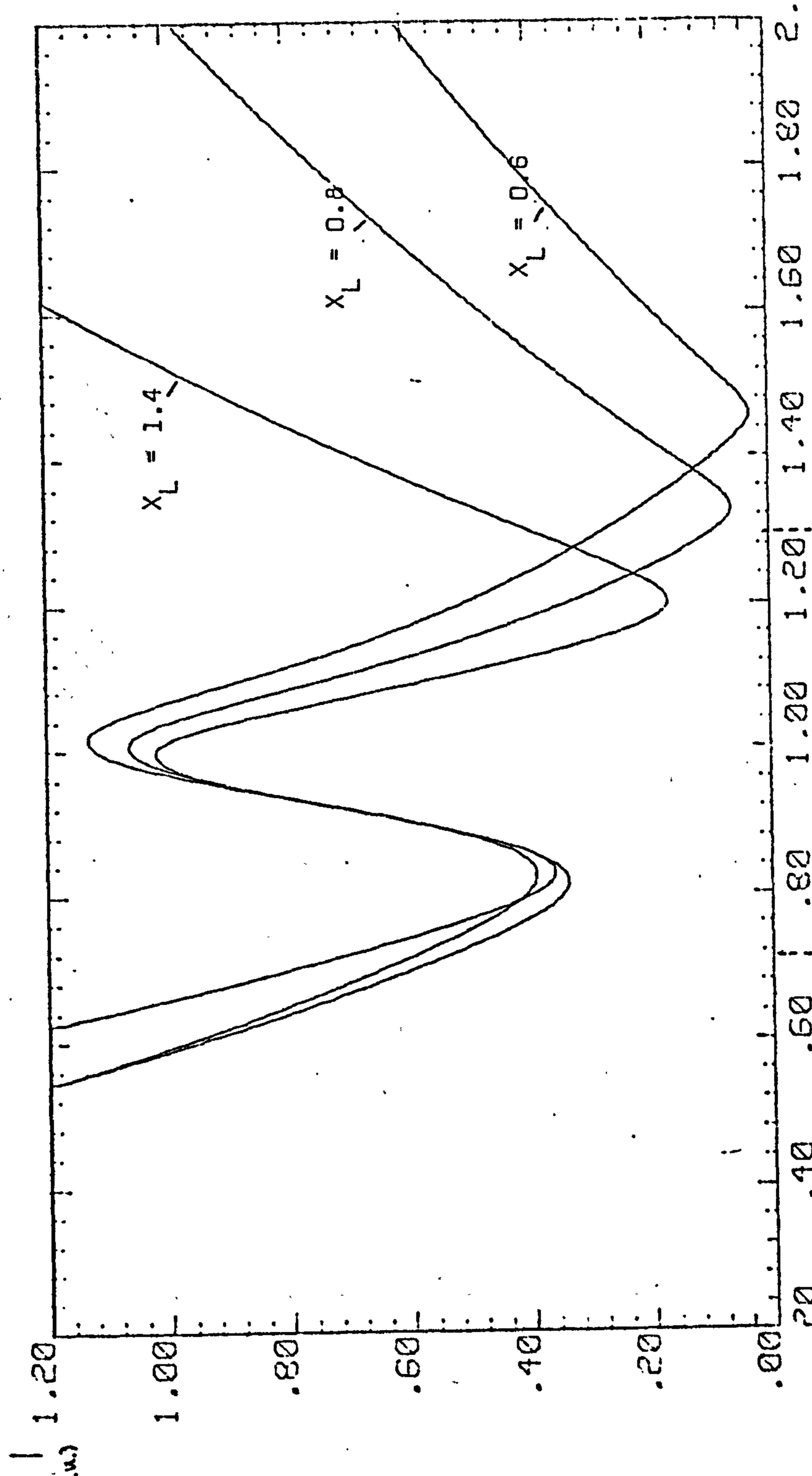

Figure 5.36 Variation of the output circuit impedance|Z | with frequency for different values of X_L cycloinverter

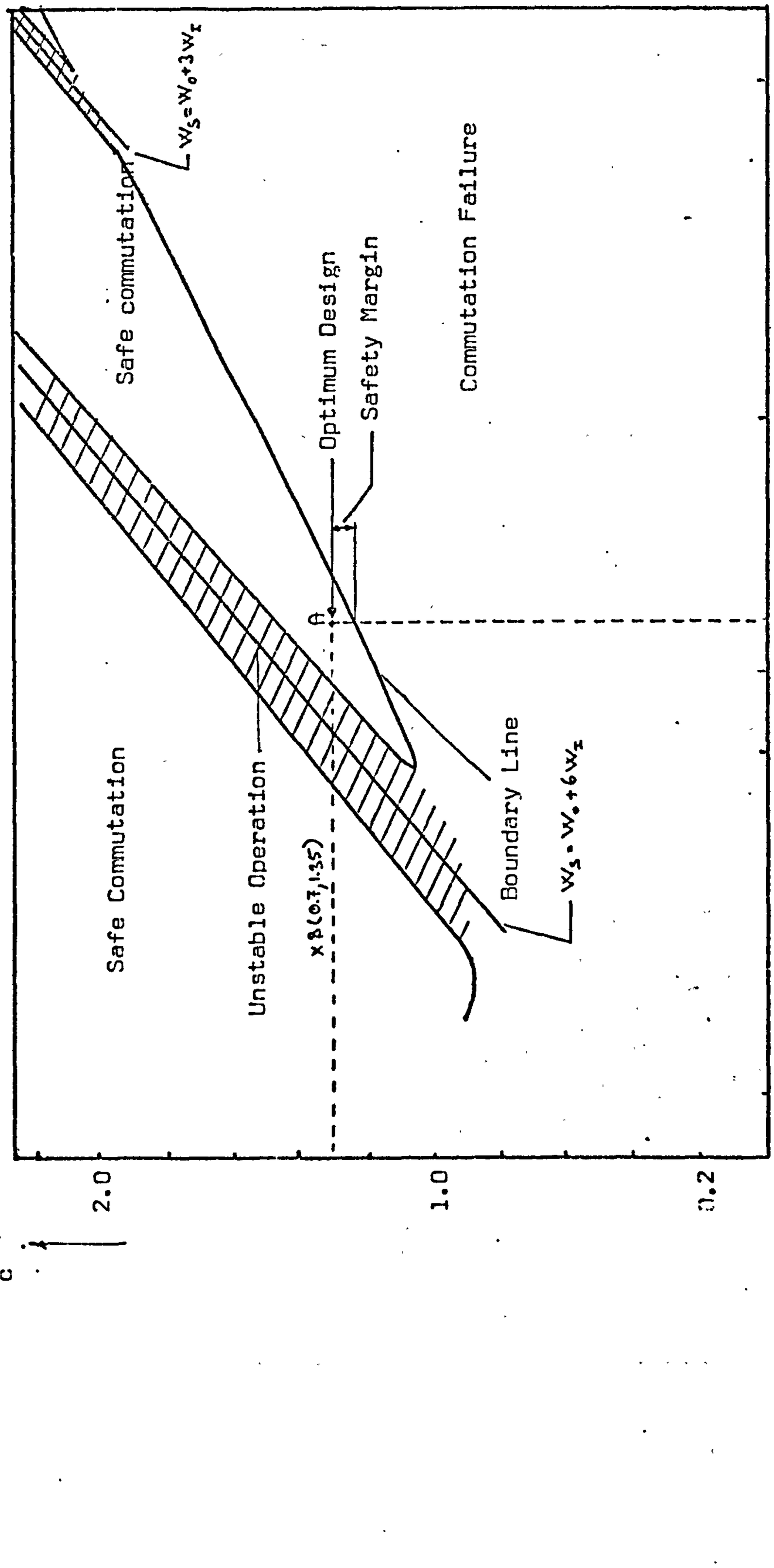

Figure 5.37 Variation of X_c with X_L for a safe commutation

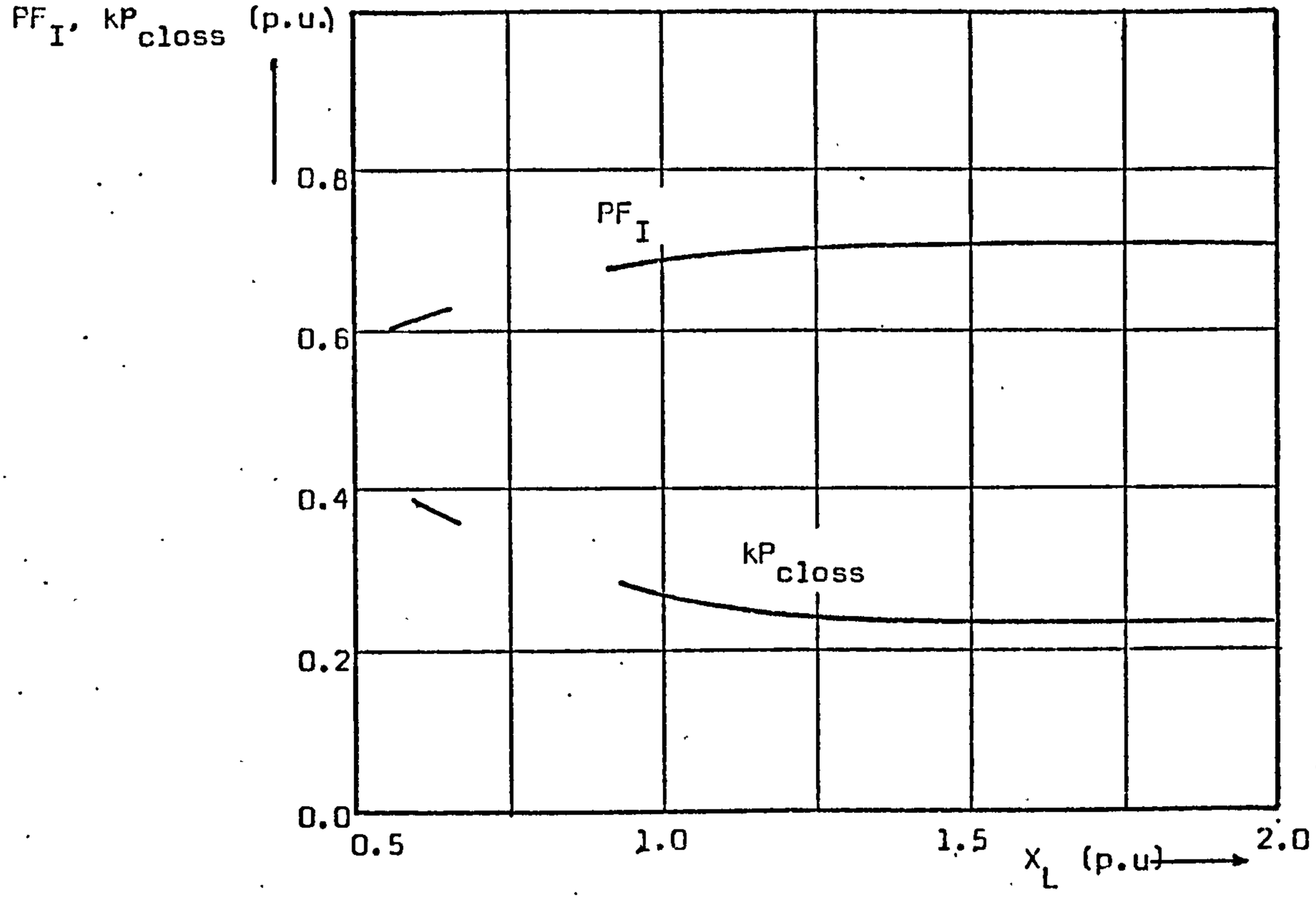

Figure 5.38 Variation of input power factor PF_I and relative conduction losses kP_{closs} with X_L

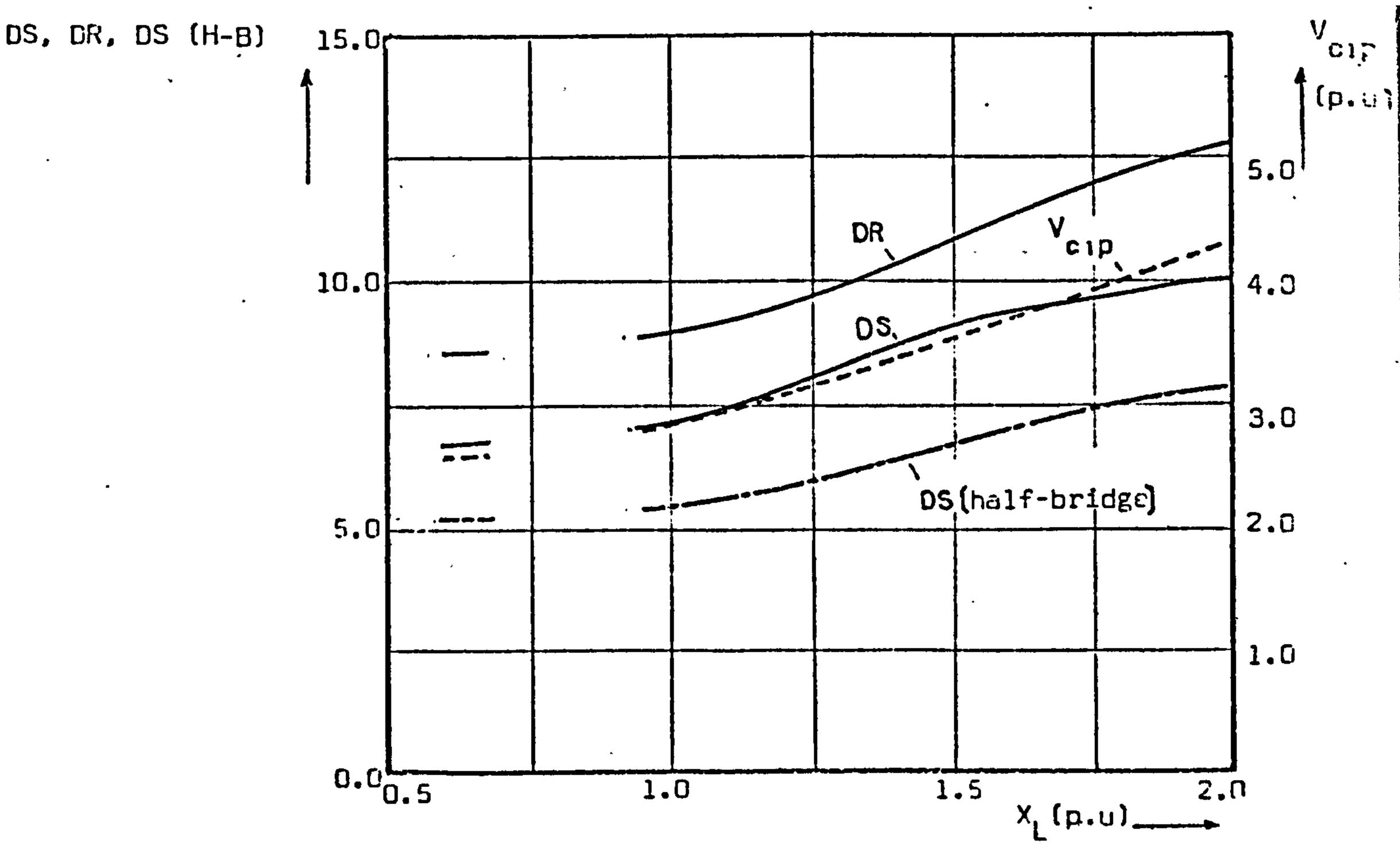

Figure 5.39 Variation of peak commutating capacitor voltage and solid-state device derating with X_L

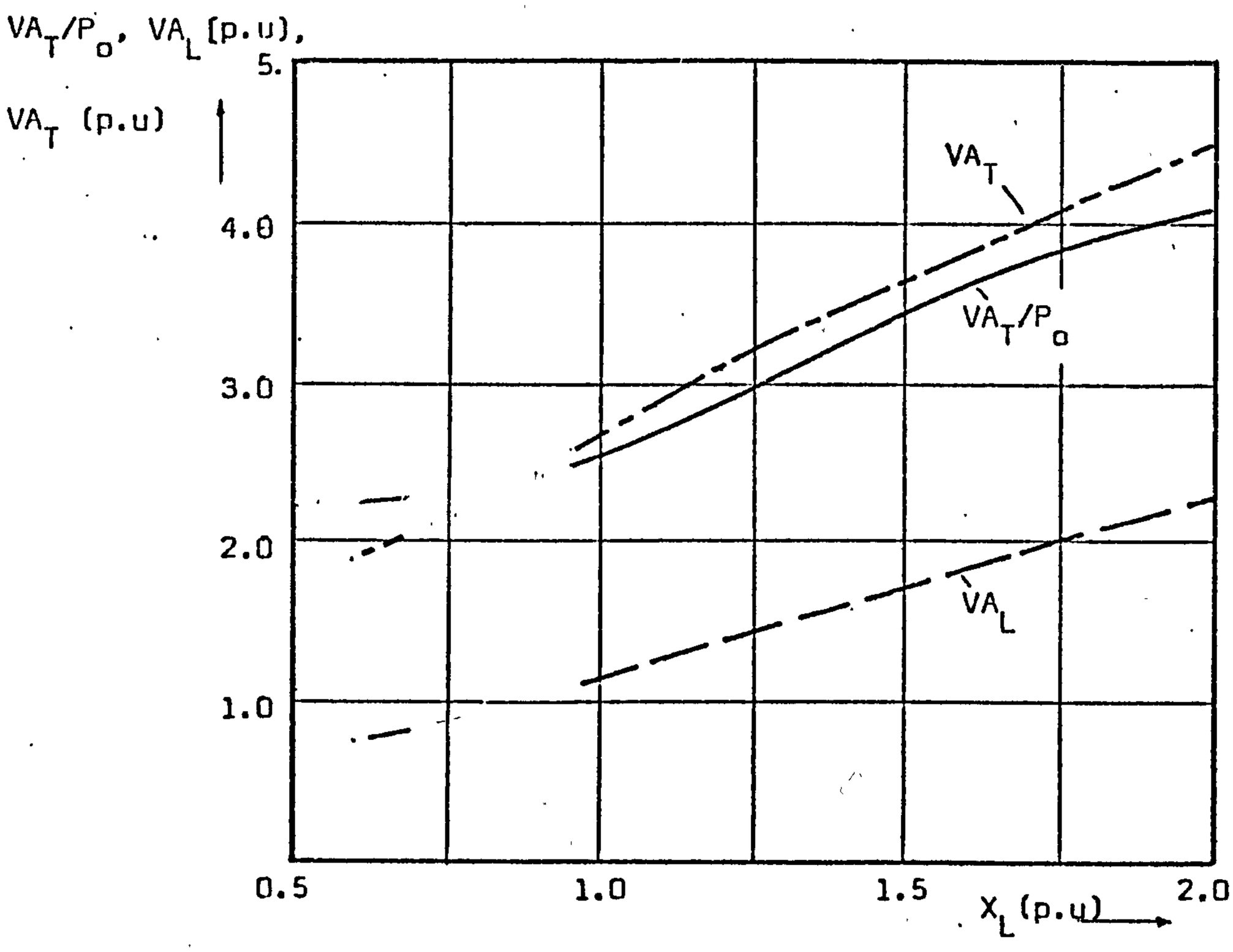

Figure 5.40 Variation of commutating circuit component rating with X_L

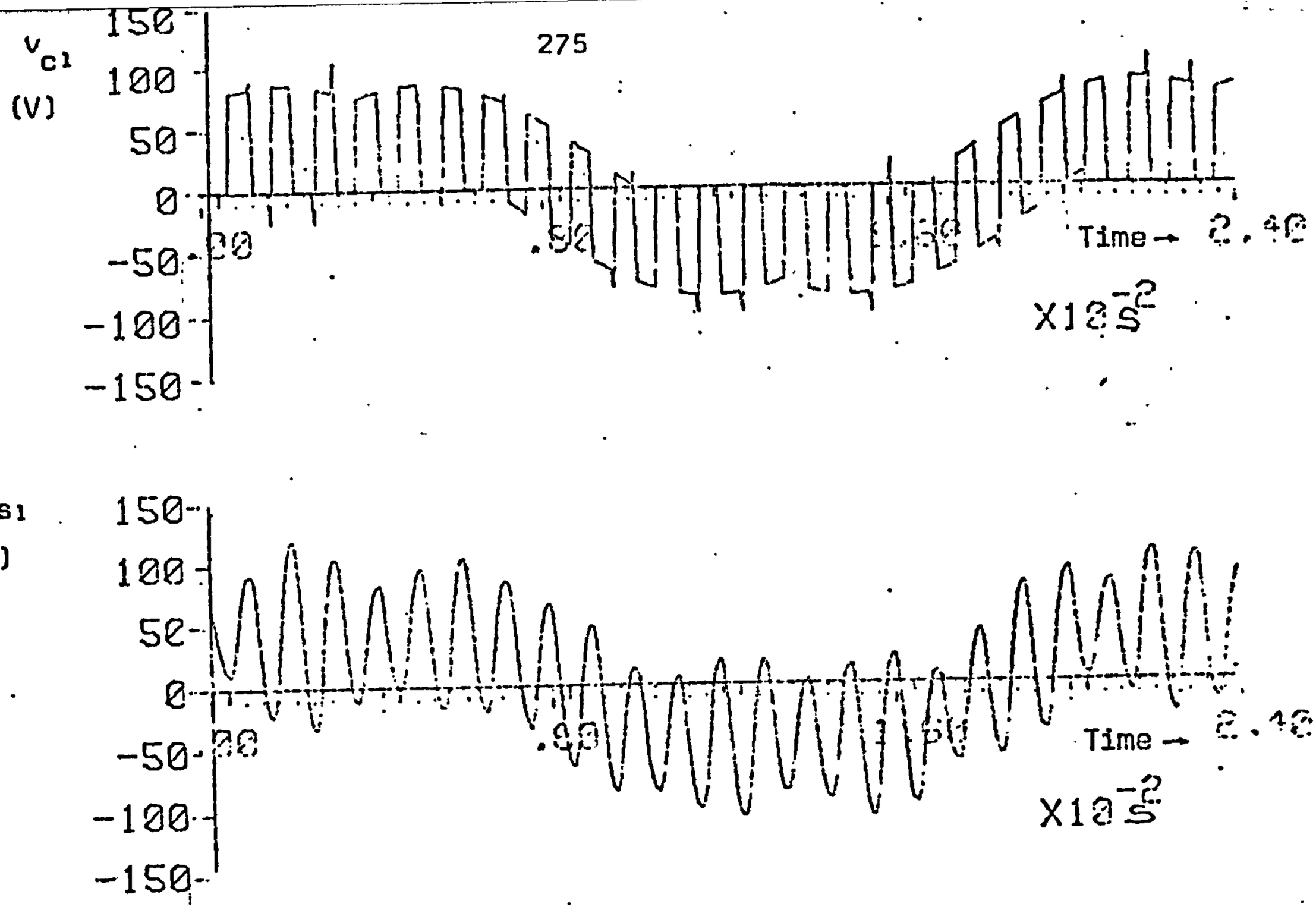

(a)

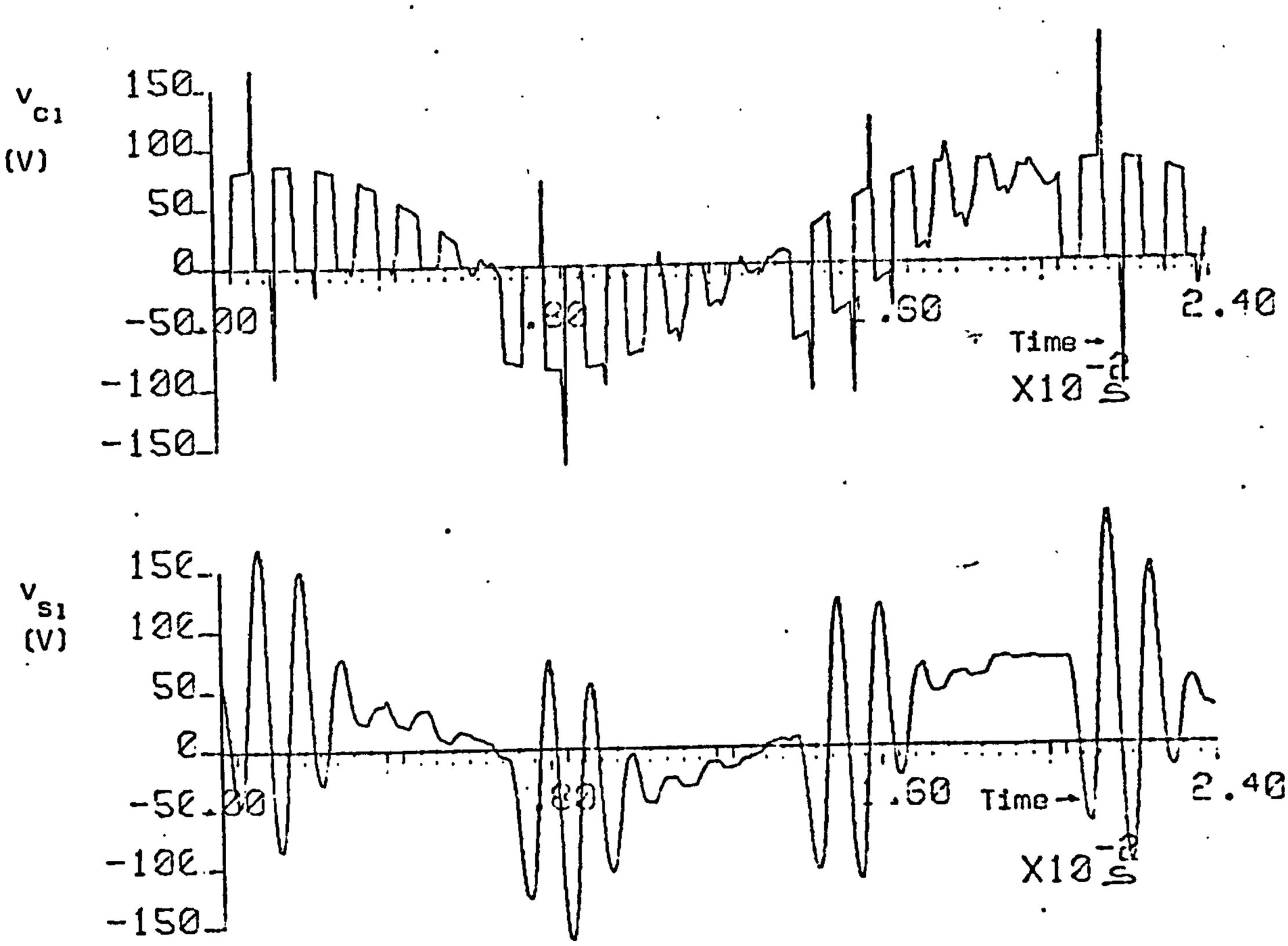

(b)

Figure 5.41 Computed waveforms of commutating capacitor and thyristor voltage during power control (a) $\theta = 30^{o}$ and (b) $\theta = 90^{o}$ (V_{in} = 50V, X_l = 1.2 p.u., X_c = 1.35 p.u., R_{ext} = 5Ω) (contd)

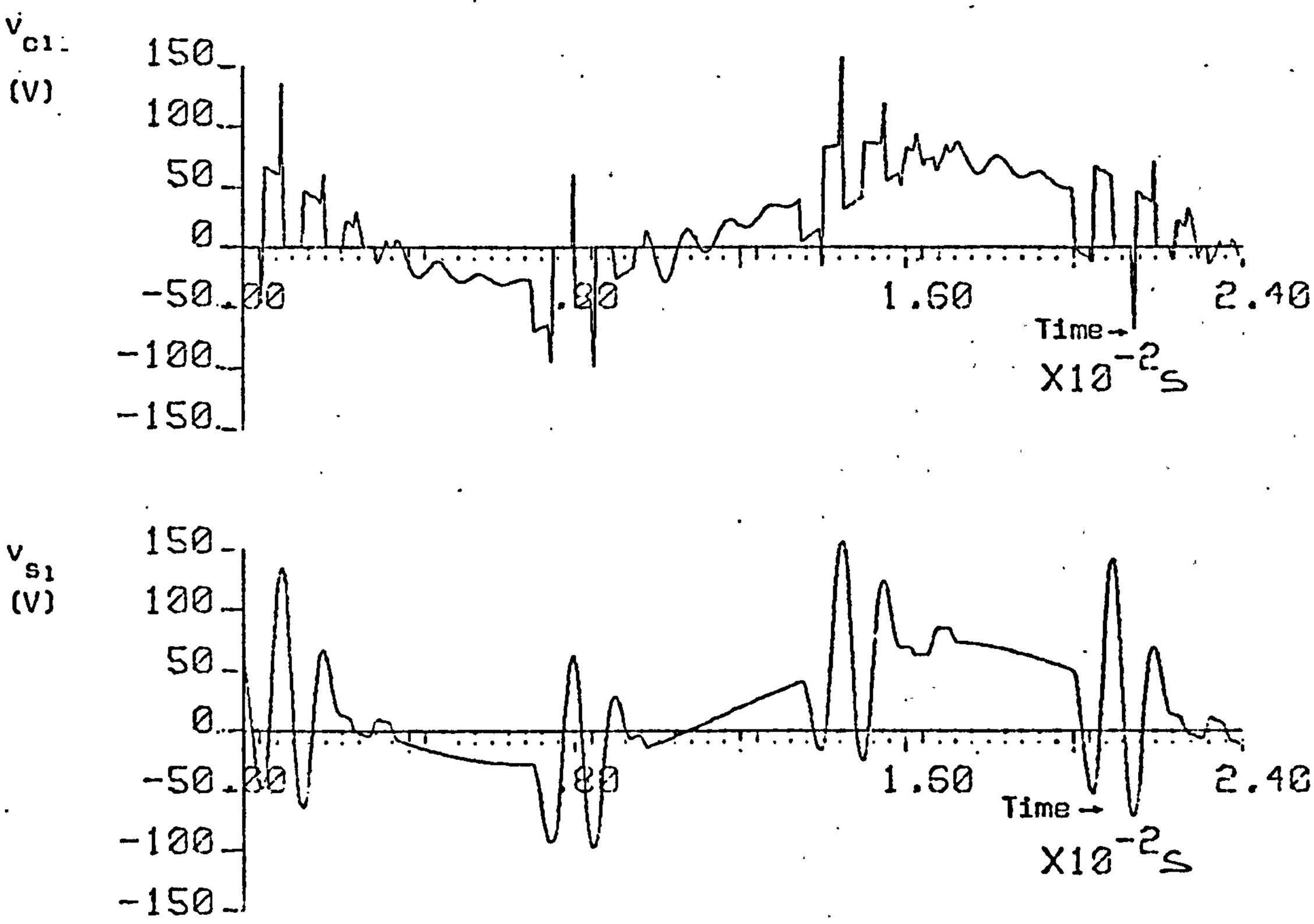

Figure 5.41c $\theta = 150^{o}$

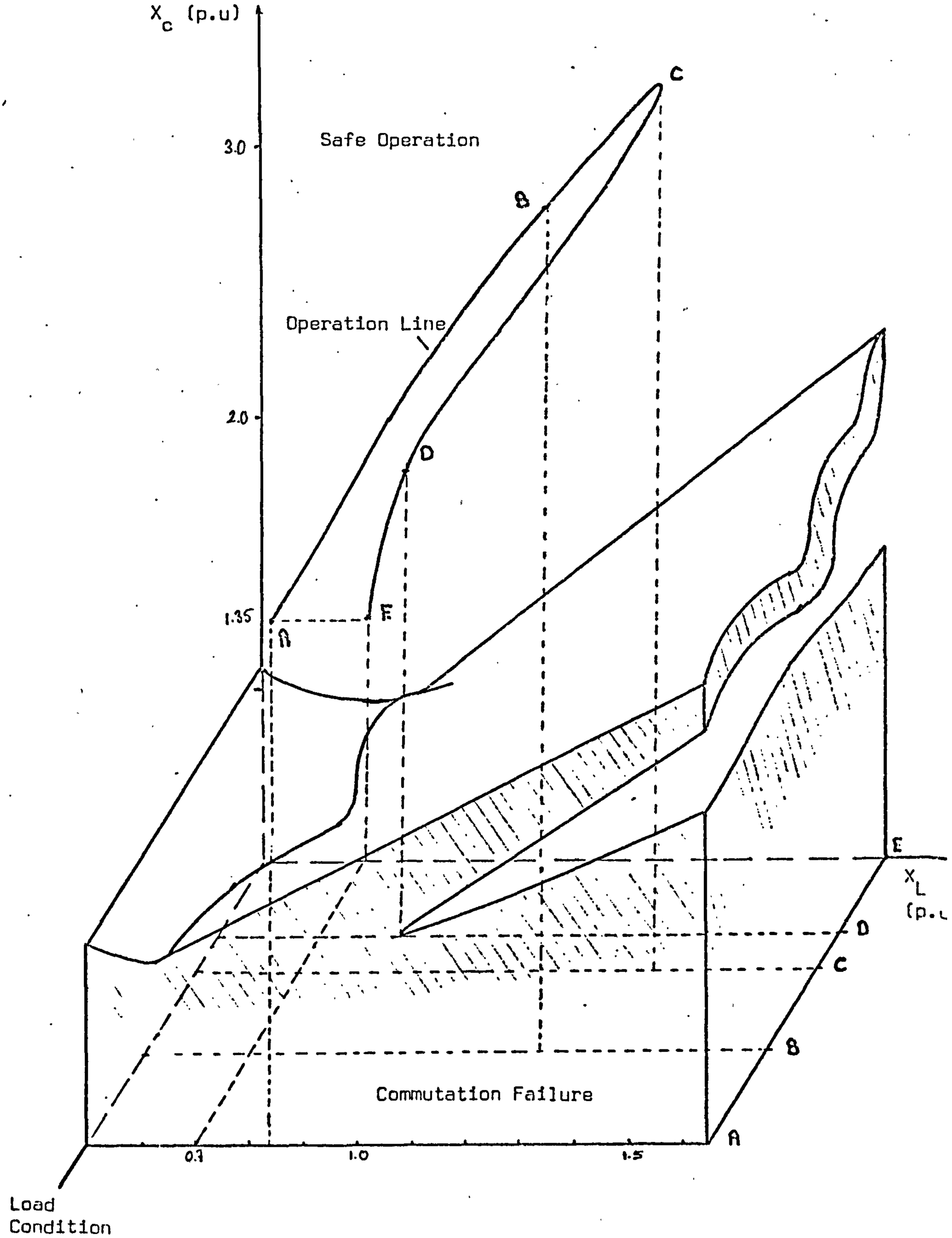

Figure 5.42 Variation of optimum design values of X_c and X_L throughout the heating cycle

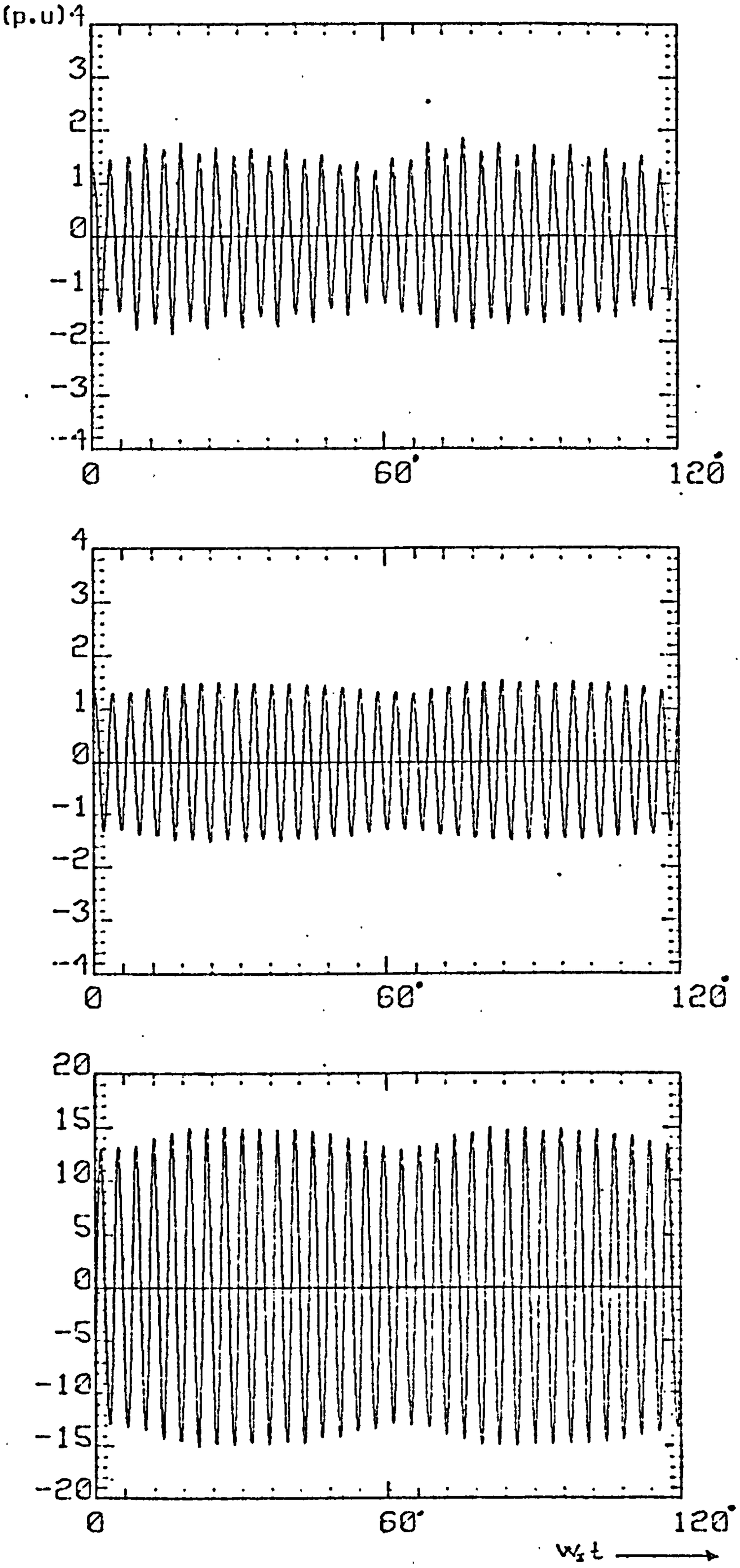

Figure 5.43 Computed output waveforms for the 3 kHz, full-bridge cycloinverter when delivering full output power (X_L = 1.2 p.u, X_c = 1.35 p.u, Q_L = 10)

CHAPTER 6

DIGITAL SIMULATION OF THE CYCLOINVERTER CIRCUITS

A computer-based study of system performance allows the parameters of the system studied to be varied at will, and so provides a relatively quick, accurate and inexpensive way of investigating the optimum system performance. In the past, the analogue computer has often been preferred to the digital computer when simulating thyristor circuits, since it has an intrinsically higher computation speed. Many valuable contributions[86,88] have been produced in this field, in which the thyristor simulation is accomplished by using conventional amplifiers and reed relays in a polarity-sensitive switch.

However, the use of analogue computers involves several serious disadvantages. For example, in a complicated simulation, which includes a number of thyristor and diode models, the computation will tend to suffer from drift, noise and stability problems. Furthermore, to process the results provided into the form of the system performance parameters generally requires digital computation. It is therefore perhaps not surprising that with the availability of fast digital computers, and the development of readily available and compact subprograms, preference in recent times has been given to the digital investigation of the system performance.

This chapter establishes the digital simulation of both the full- and the half-bridge versions of the cycloinverter.

The simulations are obtained in a generalised form, so as to make them independent of the operational frequency. This is possible, since the state equations of the corresponding modes for both high- and low-frequency operation are the same, and the differences appear principally in the mode sequencing. In achieving the simulation, an improved numerical method, simpler but more powerful and versatile than the operational method (as used in Chapter 3 in conjunction with the sine-wave inverter) is employed. Previously, when simulating the sine-wave inverter, the different equivalent circuits for the different modes of inverter operation were considered, with the differential equations corresponding to each mode being set up and solved by means of Laplace and inverse Laplace transformations. However, in the method described in this chapter, a single set of differential equations, valid for all modes of the cycloinverter operation, is derived and solved by numerical analysis. This is accomplished by introducing *logic variables* obtained on the basis of the mode equivalent circuits.

In the following section of this chapter,the method used for the digital simulation is introduced in detail. The subsequent section presents a discussion on the available numerical integration techniques, to enable a selection to be made of which is most suitable for the present application. The final sections establish numerical simulation for both versions of the cycloinverter.

6.1 Digital Simulation of Thyristor Circuits

There are a number of methods available[89-96] for the digital computation of complicated thyristor circuits, which enable the circuit differential equations to be assembled and solved in a systematic and efficient manner. The usefulness of these techniques naturally depends on the availability of accurate models for the description of the circuit elements.

6.1.1 Mathematical model for a thyristor and a diode

In most analytical solutions, the thyristors and diodes are assumed as ideal switches. However, when using numerical analysis, a more accurate representation of the device characteristics is possible. In some commercial programs available for the analysis of networks (ECAP, SCEPTRE, etc), these devices are represented by models based on piecewise-linear approximations of the device characteristics[95].

Figure 6.1 shows a piecewise-linear approximation to the diode characteristics, where the cut-off and conducting regions are both represented by single straight lines. The voltage/current characteristic of a thyristor and its piecewise-linear representation are depicted in Figure 6.2a and 6.2b. The coordinates of point P correspond to the holding current and the corresponding forward voltage of the thyristor, and the slopes of the linear parts to the on- and the off-state resistances of the device (typically $R_s \simeq 0.01\Omega$ and $R_c \simeq 300\ k\Omega$ respectively). Neglecting the holding current, an equivalent

circuit can be obtained with idealised elements only as shown in Figure 6.3, where the switches S and S' determine whether the thyristor is on or off. Clearly, when employing this type of mathematical model in a digital simulation the network topology remains unaltered throughout the computation. If, however, numerical integration techniques are employed in the programming for a time-domain analysis, the problem of instability may arise, because of the widely differing time constants associated with the different on and off resistances of the devices.

Another suggestion for accommodating the semiconductor devices characteristics in a circuit computation, is to devise a method of allowing for the open or closed state of a switching element in terms of the voltage across it. Such a technique involves the compensation theorem, which states that an element can be replaced by a voltage generator of zero internal impedance, provided that this has the same value as the voltage which would exist across the real element. Hence, if the voltages across the switches can be calculated, these can be replaced by equivalent voltages, by effectively introducing extra voltage sources into the network. However, it is obvious that the switch voltage expression involves a substantial number of terms, which makes their evolution within a computer program unacceptably long.

In recent publications on the digital simulation of switching networks, the modelling problem has been overcome ,

with a slight sacrifice in the modelling accuracy, by regarding them as open circuits when in the non-conducting state, and representing them by their on resistances at all other times. By thus omitting the off-state resistance from the differential equations the instability problems previously encountered are avoided.

It is possible to simplify this representation still further, without any deterioration in the accuracy of the analysis, by representing the voltage across the device in its on state by the staircase approximation shown in Figure 6.4. With this approximation, only one parameter, the on-state forward voltage, is required to represent the device characteristic. Once the integration step is performed, and the state variables and the thyristor current are calculated, the forward voltage can be modified to correspond to the voltage/current characteristic for the next iteration. This, in fact is the model adopted for the devices in the simulations described in the following sections.

6.1.2 Systematic analysis of thyristor circuits

The adoption of an open-circuit representation of an off-state semi-conductor device obviously requires a change in the topology of the original network from mode to mode. Hence, the number of possible network configurations increases dramatically as the circuit complexity increases. There is thus a need for

an automatic formulation of the network equations at the mode changeover points. This task was first successfully implemented by Htsui and Shepherd,[89] who showed that it is possible to establish a single set of differential equations valid for all modes of operation of a 3-phase bridge rectifier circuit. By using proper forcing functions, this common network equation is automatically modified to the form required for the mode concerned.

This method of formulation of the generalised state equations was subsequently generalised by Revankar,[90-92,94] for the digital computation of diode-thyristor circuits. The method makes use of *binary logic variables*, determined by the thyristor and the diode logic modules in accordance with the devices conduction state, to transform successively and in the correct sequence the generalised state equations for the different modes of the circuit operation. An important advantage of this method is that the state equations can be set up without an exact knowledge of the circuit operation, since the mode identification is performed automatically within the program.

At present there are more sophisticated methods available[92,94] for the computer analysis of switching networks, which rely principally on topological considerations of the network investigated. When employing these methods only the overall network topology is required and the state equations for the different conduction modes are formulated by the computer,

depending on the corresponding network topology and the conducting or non-conducting mode of the circuit components. In the analysis, all the switches are tested for their on and off states, and all off branches are subsequently removed from the circuit, together with all other branches (hanging branches) which are open-circuited because of the off-switch branches. The thyristors on branches switched on are represented by their forward resistance. In doing this, a matrix, called the incidence matrix, is used to describe the state of the network topology which exists at each iteration step. Hence, with an updated knowledge of the circuit topology, the state equations are solved, and the output quantities of interest may be calculated. An algorithm for this purpose is fully described in references 92, 94.

A topological approach to thyristor-circuit analysis is only efficient in comparison with previous methods if the network topology includes a high number of branches with switching elements. Otherwise the programming is unnecessarily complicated, since the same simulation can be performed more easily with generalised state equations, which also provide more insight to the problem. On a computational time basis, the topological approach, with its set algorithm, does not offer any significant advantage over the generalised equations method when it is used for relatively simple switching networks, while the latter may be faster since it can be made more flexible to suit the particulars of any given application. Because of

these considerations it was decided to adopt the generalised state equation method for the simulation of the cycloinverter configurations and the details of this are presented below.

6.1.3 Formulation of the generalised state equations

As previously mentioned, the automatic formulation of the state equations is based principally on a parameter introduced to define the state of the semi-conducting devices. This parameter[89-90] is called a logic binary variable, with the logic states 1 and 0 corresponding respectively to the conducting and non-conducting modes of the switching devices.

The binary variables for thyristors and diodes, denoted by S_j and D_j respectively, are used to force the device current and the device voltage, together with their derivatives, to the values demanded by the device conditions. At each iterative integration step of the circuit equations, the logic states of the devices are checked, and the device currents and voltages updated.

The prime task of the logic variables is, however, in performing the duty of a forcing function to modify the network equations. When a device is off, its current and the derivative of this have both to be forced to zero. If a state variable can be identified with a device current, the necessary conditions for the state equation can be satisfied by multiplying the corresponding state variable and its

derivative expression by the appropriate S_j and D_j. If a state variable cannot be directly identified with the device current, it is necessary to develop a proper forcing function to account for the changes to be made in the state equations and the state variables. Fortunately this is a rare case, since it is generally possible to choose the state variables in terms of the device currents.

When a particular device is on, the voltage across it is forced to the on-state level and the derivative of the voltage is made zero (in accordance with the step approximation to the device characteristic). When a device is off, the voltage across it has to be calculated from information obtained from the remaining circuit components.

On the basis of the information given above, the state equations can be derived in a generalised form to cover all operational modes, in terms of circuit parameters, state variables, device voltages and logic parameters, i.e.

$$\dot{Z}_j = f\,(Z_j,\ V_s,\ V_D,\ S_n,\ D_n,\ R,\ L,\ C,\ t,\ v_I) \qquad (6.1)$$

where $n = 1, 2, \ldots, N$ and

N is the total number of semiconductor devices and Z_j are the state variables.

Recognition of the correct logic variables for the incoming iteration is made by employing logic modules

developed for the particular semiconductor device, as described below.

6.1.4 Logic modules

Flow charts of the logic modules for the automatic recognition of the state of logic variable (1 or 0) of a thyristor and a diode are shown respectively in Figures 6.5 and 6.6. When determining the logic variable of a thyristor, the items considered are:

1) the presence of a firing signal at the gate
2) the instantaneous thyristor current, i_s
3) the instantaneous anode-cathode voltage of the thyristor v_s.

It is also suggested[96] that, for calculation of the next state logic variable of a thyristor S_j, further binary logic variables (S_{gj}, S_{ij}, S_{uj}) corresponding to each of these items may be introduced, instead of using logic modules, so as to enable S_j to be calculated from the Boolean expression;

$$S_j = S_{uj} (S_{gj} + S_{ij}) \tag{6.2}$$

It similarly follows for a diode that,

$$D_j = D_{uj} \tag{6.3}$$

and both these Boolean expressions are clearly the formulisation of the processes performed by the logic modules of Figures 6.5 and 6.6.

Alternatively, if sufficient knowledge is available on the circuit operation, the logic module approach can be simplified by using a pre-prepared logic state (mode) sequence table, with a suitable table for a low-frequency cycloinverter being given in Figure 6.7.

In a simulation program, with an updated knowledge of the logic states of the circuit semiconductor obtained as described above, the generalised state equations can be accordingly transformed to the correct mode equations.

6.2 Numerical Analysis Methods

This section discusses the numerical methods available for the solution of a set of differential equations and for a Fourier analysis.

6.2.1 Numerical integration

It is well established that, by using a proper integration scheme and error criterion, a digital computation can give a circuit response almost identical with that obtained in practice. Careful attention must therefore be given to the selection of both the numerical method and the error criterion.

A comparative study of the different numerical methods available for the solution of differential equations showed that Runge-Kutta methods[97] are most suitable for the present purpose, since:

1) They do not use information from previously calculated points, and are therefore self starting.

2) Being self-starting, they readily permit a change in the step length.

3) Apart from the inherent instability (when the solution of the equation contains time constants of greatly differing magnitudes), any instability due to spurious solutions is not present. Any possibility of instability is due mainly to partial instability, which can be controlled by step length variations.

However, Runge-Kutta methods generally suffer from the disadvantage that, in order to determine the accuracy of the solution and to make any step length changes necessary, they normally provide no information on the local truncation error (although a fourth-order Runge-Kutta can do this in a very lengthy way[97]).

The truncation error is introduced in a numerical integration process, since the differential system is approximated

by an algebraic one, to enable calculations to be performed at that step. This error is thus caused by the replacement of a finite process by an approximate one.

All Runge-Kutta methods rely on the Taylor's series expansion of a function y(x) at the point $x = x_i + h$, so that

$$y_{i+1}(x_i + h) = y_i + \dot{y}_i h + \frac{1}{2!}\ddot{y}_i h^2 + \ldots \qquad (6.4)$$

where h is the increment of the independent variable X, and i = 1, 2, 3 ....n.

Because computation of the higher derivatives of y(x) is very difficult, the overall computation of the expansion is stopped after a certain number of terms and this inevitably introduces a truncation error. The cumulative effect of the truncation error in the subsequent steps can lead to serious total errors in the final solution. Equation (6.4) clearly indicates that the per-step truncation error is a function of the step size h, and as such it is obvious that the only means of reducing the per-step truncation error and its associated overall error, is by a reduction in the step size.

A useful method for estimating the truncation error is to halve the step-size and to perform the integration process twice[98] (thus reaching the same position in x as formerly), to obtain a second and comparative result. However, it will be realised that such a process is extremely time consuming.

This problem has been overcome by Merson[99] who produced formulae which, although requiring one more evaluation of the function f(x,y) at each step, give an estimate of the local truncation error with a reasonable accuracy. Hence, in order to produce a solution both numerically stable and accurate, while economic in computation time, the Runge-Kutta-Merson method was selected.

6.2.2 Kutta-Merson method

There is a computer subprogram[97] (NAG LIBRARY SUBROUTINE D02AAF) available which advances the solution of a system of first-order ordinary differential equations,

$$\dot{Z}_i = f_i\ (t,\ Z_1,\ Z_2 \ldots\ Z_N), \quad i = 1,\ 2,\ 3 \ldots N \tag{6.5}$$

from t to t + Δt.

In the solution, the initial values of the state variables are supplied to the program, and the equations are defined by a subroutine (DERIV) which evaluates the derivatives f_i in terms of t and Z_1, Z_2 ... Z_N. The subroutine also gives an estimate of the truncation error in each of the variables.

There is a further subprogram available[97] (SUBROUTINE D02ABF), which solves the system of differential equations

throughout an interval t_o, and in so doing varies the step length automatically to keep the estimated local truncation error below an error bound specified by the user.

However, because the numerical analyses (such as Fourier analysis) performed in the later parts of the simulation program require a constant step size, the former subroutine (D02AAF) is most suitable for the present purpose.

Selection of step-size

The intention in selecting the step-size is to ensure stability of the analysis (i.e. a small propagated error) while keeping the accuracy of the method high. Nevertheless, determination of the optimum step-size is a very complex process. In reducing the per-step truncation error, by decreasing the step size, a limit is reached at which any further decrease increases the total number of steps, to a point where the round-off error (the error which results from replacing a number having more than N digits by one of only N digits) becomes dominant, and the total error will increase with any further reduction in step-size. Obviously, an unnecessarily small step-size also has an adverse effect on the computation time.

In the digital simulation program developed, the selection of the step-size is based on considerations of system stability, accuracy, computation time and the particular form of the solution required for the subsequent stages. The accuracy

of the solution (in the subroutine employed the truncation error per step is of the order of h^5 for a sufficiently small h) is further checked by repeating the whole calculation with the step-length halved. In so doing, the error estimates provided by the program are assumed to be reliable.

6.2.3 Numerical Fourier analysis

After obtaining the steady-state solution of the state variables in the programs, the harmonic compounds of various circuit quantities are obtained, with the aid of the subprogram NAG LIBRARY SUBROUTINE C06AAF, which uses the Cooley-Tukey[100] algorithm to calculate the finite Fourier transforms of $2n = 2^{M1/2}$ real data values (X_0, X_1 ..... X_{2n-1}). The Fourier cosine and sine coefficient a_k and b_k are calculated from the relations

$$a_k = \frac{1}{n} * \sum_{j=o}^{2n-1} X_j \text{ Cos } (\pi\, jk/n) \qquad k = 0, 1 \ldots n$$

$$b_k = \frac{1}{n} * \sum_{j=o}^{2n-1} X_j \text{ Sin } (\pi\, jk/n) \qquad k = 0, 1 \ldots n$$

Although the subroutine does not provide any error indicators, it nevertheless offers inverse transformation facilities. These are exploited in the program to generate the original time domain input data from the calculated sine and cosine coefficients, to provide an estimate of the accuracy of the method.

6.3 Simulation of the Full-Bridge Cycloinverter

6.3.1 Generalised state equations

The state equations of the cycloinverter circuit for all modes of operation were given in Chapter 4 . Based on the same assumptions on which those equations were formulated, they can be converted into generalised state equations in the following way.

Rewriting and identifying the state equations with the thyristor logic variable yields:

$$\dot{Z}_1 = \dot{v}_1 - \frac{Z_2}{3C} \qquad (6.6)$$

$$\dot{Z}_2 = \begin{cases} Z_1 - V_S - Z_3 & \text{when } S(1) = 1 \\ v_3 - v_1 + Z_1 + V_S - Z_3 & S(2) = 1 \\ v_2 - v_1 + Z_1 - V_S - Z_3 & S(3) = 1 \\ Z_1 + V_S - Z_3 & S(4) = 1 \\ v_3 - v_1 + Z_1 - V_S - Z_3 & S(5) = 1 \\ v_2 - v_1 + Z_1 + V_S - Z_3 & S(6) = 1 \\ 0. & \text{when } S(1), S(2), S(3), S(4), S(5), S(6) = 0 \end{cases}$$

Therefore:

$$\dot{Z}_2 = \frac{1}{L} \{S(1)\ [Z_1 - V_S] + S(2)\ [v_3 - v_1 + Z_1 + V_S]$$

$$+ S(3)\ [v_2 - v_1 + Z_1 - V_S] + S(4)\ [Z_1 + V_S]$$

$$+ S(5)\ [v_3 - v_1 + Z_1 - V_S] + S(6)\ [v_2 - v_1 + Z_1 + V_S]$$

$$- A\ Z_3\} \qquad (6.7)$$

where:

$$A = S(1) + S(2) + S(3) + S(4) + S(5) + S(6)$$

$$\dot{Z}_3 = \frac{1}{C_o}\ (Z_2 - Z_4) \qquad (6.8)$$

$$\dot{Z}_4 = \frac{1}{L_o}\ (Z_3 - R_o\ Z_4) \qquad (6.9)$$

The thyristor voltage and current equations are required for the evaluation of the binary logic variable S(j). The thyristor voltages are given by (where $\overline{A}$ is the inverse of A):

$$V_{S1} = S(1)\ V_S - S(4)\ V_S + S(3)\ [v_1 - \dot{v}_2 + V_S]$$

$$+ S(6)\ [v_1 - v_2 - V_S] + S(5)\ [V_1 - V_3 - V_S]$$

$$+ S(2)\ [v_1 - v_3 - V_S] + \overline{A}\ [Z_1 - Z_3 - L\ \dot{Z}_2]$$

$$V_{S3} = S(1)\ [v_2 - v_1 + V_S] + S(4)\ [v_2 - v_1 - V_S]$$

$$+ S(3)\ V_S - S(6)\ V_S + S(5)\ [v_2 - v_3 + V_S]$$

$$+ S(2)\ [v_2 - v_3 - V_S] + \overline{A}\ [v_2 - v_1 + Z_1 - Z_3 - L\ \dot{Z}_2]$$

$$V_{S5} = S(1)\ [v_3 - v_1 + V_S] + S(4)\ [v_2 - v_1 - V_S]$$

$$+ S(3)\ [v_3 - v_2 + V_S] + S(6)\ [v_3 - v_2 - V_S]$$

$$+ S(5)\ V_S - S(2)\ V_S + \overline{A}\ [v_3 - v_1 + Z_1 - Z_3 - L\ \dot{Z}_2]$$

$$V_{S2} = -V_{S5}$$

$$V_{S4} = -V_{S1}$$

$$V_{S6} = -V_{S3} \qquad (6.10)$$

In accordance with the step-by-step approximation to the *piecewise linear* thyristor characteristics, the on state voltage V_s is

$$V_s = R_s |i_s| \tag{6.11}$$

The thyristor currents are given by:

$$\begin{aligned} i_{s1} &= S(1)\, Z_2 \\ i_{s2} &= -S(2)\, Z_2 \\ i_{s3} &= S(3)\, Z_2 \\ i_{s4} &= -S(4)\, Z_2 \\ i_{s5} &= S(5)\, Z_2 \\ i_{s6} &= -S(6)\, Z_2 \end{aligned} \tag{6.12}$$

and the input line currents by:

$$i_1 = \{2\,[S(1) + S(4)] - S(2) + S(3) + S(5) + S(6)]\} \frac{Z_2}{3} + C\dot{v}_1$$

$$i_2 = \{2\,[S(3) + S(6)] - [S(1) + S(2) + S(4) + S(5)]\} \frac{Z_2}{3} + C\dot{v}_2$$

$$i_3 = \{2\,[S(2) + S(5)] - [S(1) + S(3) + S(4) + S(6)]\}\,\frac{Z_2}{3} + c\,\dot{V}_3 \qquad (6.13)$$

6.3.2 Mode sequencing

As mentioned previously, the modal sequence throughout a cycle of operation of a cycloinverter can be decided either by logic modules or by set tables, with the mode sequence table for a 150 Hz cycloinverter operation being given in Figure 6.7. One serious weakness of mode identification from a table is that it does not allow operational flexibility, since it demands different sequence tables for different output frequencies and power levels. Clearly, these disadvantages become more serious at high operational frequencies.

In the simulation program developed, mode recognition is therefore performed via logic modules, with the correct firing pulses for the thyristor logic module obtained by simulating the actual logic of the cycloinverter control circuit.

The flow chart for the simulation of the thyristor firing pulses is shown in Figure 6.8, where the logic variables LJPOZ

and LJNEG define the sequence of the positive and the negative group thyristors. Once the group of the incoming thyristor has been fixed, with the help of the logic variable LSJ corresponding to the permissible firing interval of the Jth thyristor (see Figure 6.9), a precise identification is made. Following this, the conduction state of the fired thyristor (i.e. whether it can turn on) is decided by the logic module, and the binary logic variable for this thyristor is accordingly determined. With this model, power control is readily achieved by shifting the position of the permissible firing interval of the thyristors, in accordance with the power control angle θ. In the actual program, further facilities are included so that, if required, the incoming firing pulses can be suppressed by forcing J to 0. Clearly mode identification in this manner is independent of the output frequency, and is equally applicable to the simulation of both low- and high-frequency cycloinverters.

On the other hand, for 150 Hz output frequency operation this process can be significantly simplified, by considering the firing pulse for the Jth thyristor to correspond to the Jth output of a conventional 6 bit shift register, with a mathematical model

```
S(K) = 0                                    K = 1, 2, ..., 6

IF(J.EQ.6) J = 1

J = J + 1

S(J) = 1
```

(6.14)

Flow chart

The flow chart for simulation of the cycloinverter operation is shown in Figure 6.10with the actual program presented in Appendix 4. Although the flow chart is largely self explanatory, nevertheless some important steps in the program are explained below:

a) Clearly, when using generalised state equations, there is no need to calculate the initial conditions for each mode, as this is performed automatically during the computation. Hence the flow diagram omits this process.

b) Steady-state conditions are checked at each starting instant of a arbitrarily chosen steady-state decision mode (i.e. J = JSSDM). For this purpose, the initial values of the variables v_{c1}, v_{c0}, i_{L0} at the beginning of the control mode are compared with their prestored values at the corresponding instant of the previous cycle of operation. If an approximation is established within the bounds of the preset steady-state decision margin (0.005 p.u), a positive decision is taken. Trial computations established that the occurrence of the steady-state condition can be predicted as described in section 5.2.1. This obviously provides the advantage of enabling an estimate to be made of the computation time required for each run.

c) To save on computation time, a search is made for the presence of the firing signal, not iteratively, as suggested by the original logic module flow diagram, but only when its presence is expected, that is at times when

$$t = k\, T_o/2$$

where k is the commutation count.

d) If a thyristor when fired does not turn-on, a warning is provided.

e) The program includes a short-circuit detection facility. If any two of the positive- and the negative-group thyristors are simultaneously on, a short circuit decision is taken (at output frequencies less than about 1 kHz, minimum thyristor turn-off time considerations are neglected).

f) Once, steady state conditions are established, the computation proceeds to the Fourier analysis of the output current i_L and the input line current i_1. Subsequently, the system performance parameters are calculated in accordance with the formulae given in previous chapters.

g) With the help of the compact plotting subprograms (GINO LIBRARY) the output quantities are plotted graphically.

h) During computation, the truncation errors of the state variables are constantly checked and, with a proper selection of Δt, are made to be less than 10^{-4}.

6.4 Simulation of the Half-Bridge Cycloinverter

6.4.1 Generalised state equations

Based on the considerations outlined in section 4.2.1.2, the generalised state equations for the half-bridge cycloinverter are:

$$\dot{Z}_2 = \frac{1}{L} \{S(1)\,(Z_1 - V_s) + S(2)\,(v_2 - v_1 + Z_1 - V_s)$$

$$+ S(3)\,(v_3 - v_1 + Z_1 - V_s) + S(4)\,[D(1) + D(2)\,(v_2 - v_1)$$

$$+ D(3)\,(v_3 - v_1) + Z_1 + V_s + V_D]$$

$$- [S(1) + S(2) + S(3) + S(4)]\; Z_3\} \qquad (6.15)$$

Since $S(4)\,[D(1) + D(2) + D(3)] = S(4)$.

Because they are applicable to all modes of operation, the state equations defining $\dot{Z}_1$, $\dot{Z}_3$, $\dot{Z}_4$ remain unchanged. The generalised equations for the input line currents are:

$$i_1 = \{2\,[S(1) + S(4) * D(1)]$$

$$- [S(2) + S(3) + S(4)\,(D(2) + D(3))]\}\,\frac{Z_2}{3} - C\,\dot{v}_1$$

$$i_2 = \{2\,[S(2) + S(4) * D(2)]$$

$$- [S(1) + S(3) + S(4)\,(D(1) + D(3))]\}\,\frac{Z_2}{3} - C\,\dot{v}_2$$

$$i_3 = \{2\,[S(3) + S(4) * D(3)]$$

$$- [S(1) + S(2) + S(4)\,(D(1) + D(2))]\}\,\frac{Z_2}{3} - C\,\dot{v}_2 \qquad (6.16)$$

and those for the thyristor voltages are:

$$v_{s1} = S(1)\,V_s - S(4)\,D(1)\,(V_s + V_D) + S(2)\,[v_1 - v_2 + V_s]$$

$$+ S(3)\,[v_1 - v_3 + V_s] + S(4) * D(2)\,[v_1 - v_2 - V_s - V_D]$$

$$+ S(4) * D(3)\,[v_1 - v_3 - V_s - V_D] + \bar{A}\,[Z_1 - Z_3 - L\,\dot{Z}_2]$$

$$v_{s_2} = S(2)\, V_s - S(4)\, D(2)\, [V_s + V_D] + S(1)\, [v_2 - v_1 + V_s]$$

$$+ S(3)\, [v_2 - v_3 + V_s] + S(4)\, D(3)\, [v_2 - v_3 - v_s]$$

$$+ S(4)\, D(1)\, [v_2 - v_1 - V_s - V_D] + \bar{A}\, [v_2 - v_1 + Z_1 - Z_3 - L\, \dot{Z}_2]$$

$$v_{s_3} = S(3)\, v_s - S(4)\, D(3)\, [V_s + V_D] + S(1)\, [v_3 - v_1 + V_s]$$

$$+ S(2)\, [v_3 - v_2 + V_s] + S(4)\, D(2)\, [v_3 - v_2 - V_s - V_D]$$

$$+ S(4)\, D(1)\, [v_3 - v_1 - V_s - V_D] + \bar{A}\, [v_3 - v_1 + Z_1 - Z_3 - L\, \dot{Z}_2] \qquad (6.17)$$

and

$$v_{s_4} + v_{D_1} = - S(1)$$

$$v_{s_4} + v_{D_2} = - S(2)$$

$$v_{s_4} + v_{D_3} = - S(3) \qquad (6.18)$$

The thyristor currents are:

$$i_{sj} = S(J)\, Z_2 \qquad J = 1, 2, 3$$

$$i_{s_4} = -S(4)\, Z_2 \qquad (6.19)$$

6.4.2 Mode sequencing

It is possible to adapt the simulation program of the full-bridge inverter for the half-bridge, by modifying only the computation logic used to determine the firing instants of the negative group thyristors. This becomes possible because the principal difference between the operational characteristics of these two types of cycloinverter circuits is the sequence of the operational modes, whereas the state equations for the corresponding modes are basically the same. In modifying the logic, the binary variables LS4, LS6, LS2 defining the firing interval of the negative group thyristor of the full-bridge S4, S6 and S2 must be evaluated from the Boolean expressions:

$$LS4 = LS4' * LD1$$

$$LS6 = LS4' * LD2$$

$$LS2 = LS4' * LD3 \qquad (6.20)$$

Obviously, in these equations the binary variable of thyristor S4 of the half-bridge circuit LS4' is always 1, as it can be turned-on any time during the cycle of operation. On the other hand, the permissible active interval of the circuit diodes are naturally fixed being the duration when the corresponding phase voltage is most negative.

6.4.3 Flow chart

On applying the modifications described to the mode identification process, the flow chart of the full-bridge inverter can be used directly* for the simulation of the high frequency half-bridge inverter. In so doing, however, the inner iteration loop of the flow diagram must be broken at point X in Figure 6.10 and an additional step must be inserted. This enables the logic variables D(1), D(2), and D(3) to be updated iteratively within the loop, in order to include the transfer of the output current between the diodes, in case a phase crossover occurs when S4 is conducting.

---

* Clearly, in adapting the program for the half-bridge inverter, some of the computational steps require further modifications (since these are differences in the establishment of the periodicity of the output current for the numerical Fourier analysis, the definitions of some of the system performance parameters, etc). Nevertheless, as these points have already been outlined in the previous chapter, they are not restated here.

6.5 Discussion

Detailed comments on the results of the simulation have already been presented in the relevant sections of the previous chapters. Generally speaking, these are in close agreement with the results of the harmonic analysis (comparisons can be made only for full output power operation), which is not unexpected since many of the assumptions made are common to both. Further checks with the experimental results are therefore required.

Clearly, the simulation programs presented in this chapter can be extended to include the effects of any additional component included in the cycloinverter, such as the snubber circuits of the thyristors and the source reactance. Based on the considerations outlined in this chapter, the cycloinverter simulation with a suitable input filter is presented separately in the following chapter.

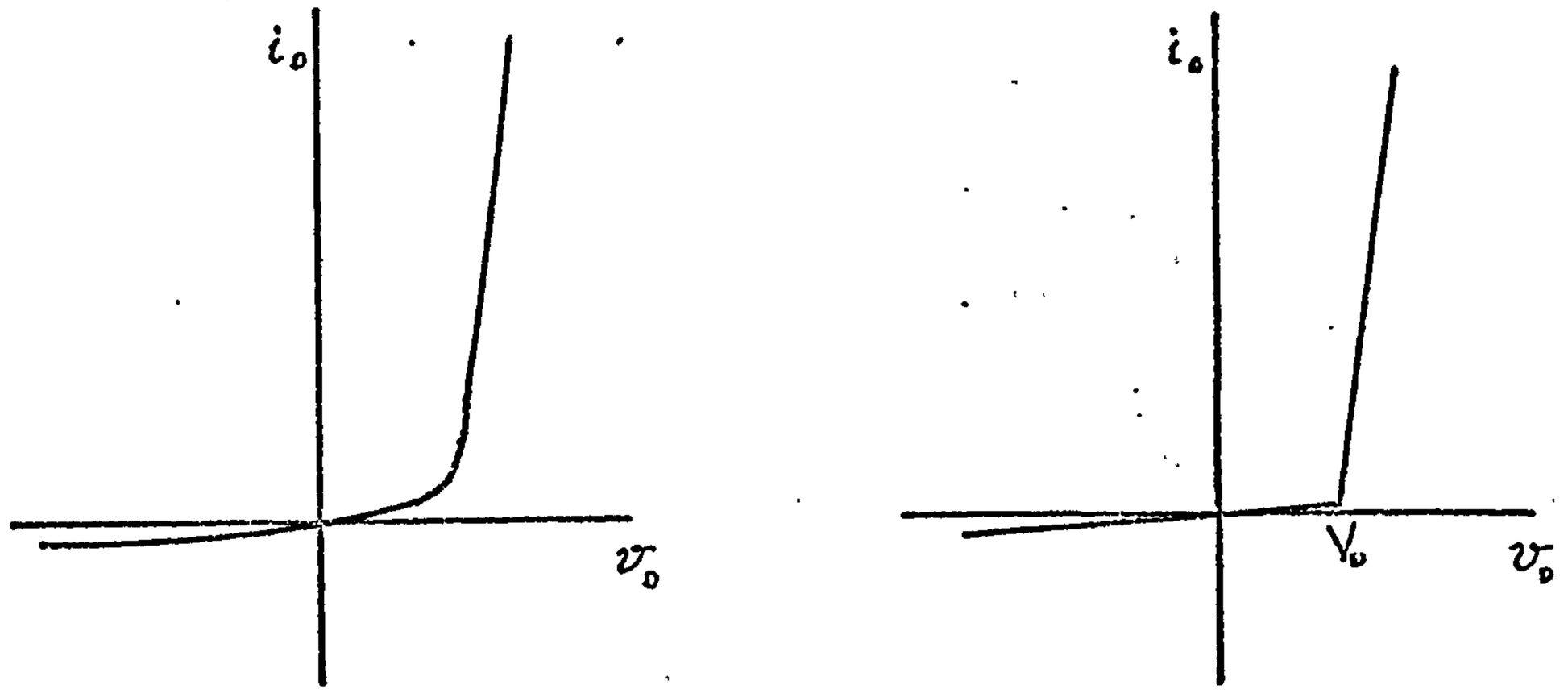

(a) (b)

Figure 6.1 a) Actual diode characteristics
b) Piecewise linear representation

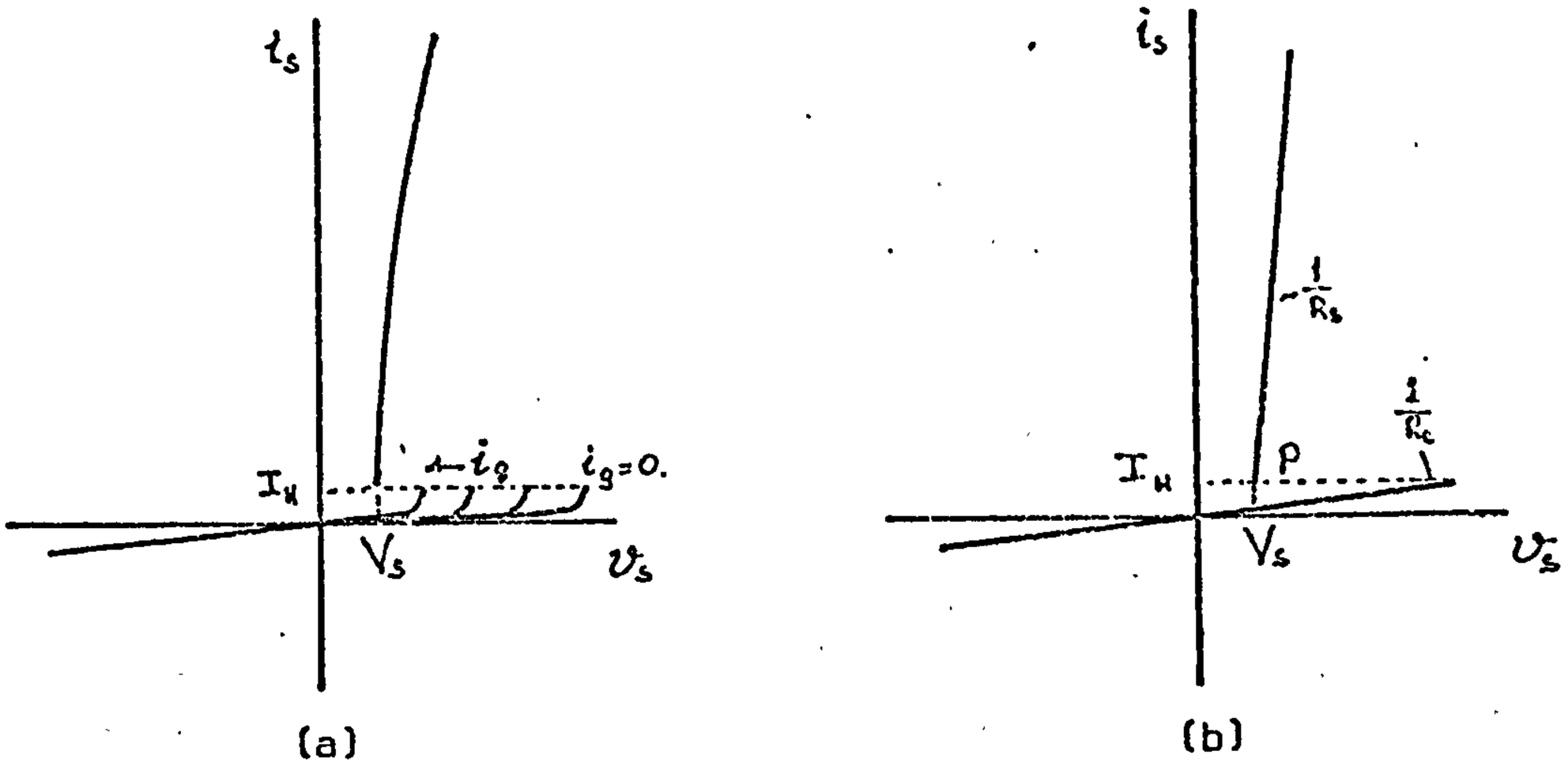

(a) (b)

Figure 6.2 a) Actual thyristor characteristics
b) Piecewise linear representation

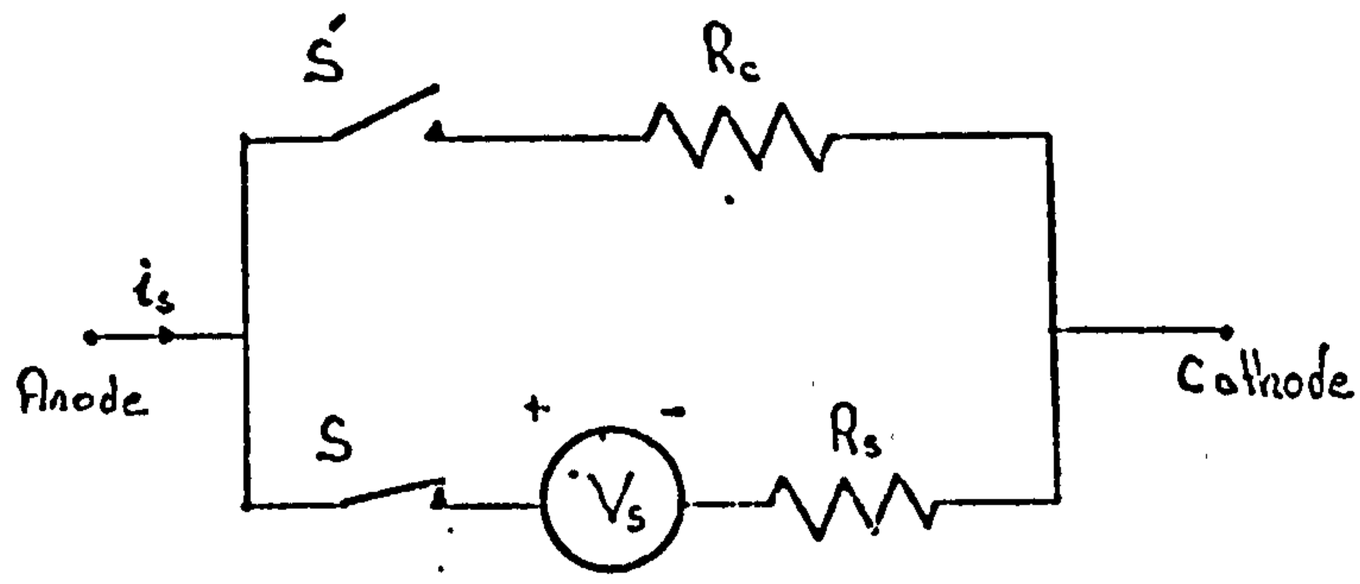

Figure 6.3 An equivalent circuit for a thyristor

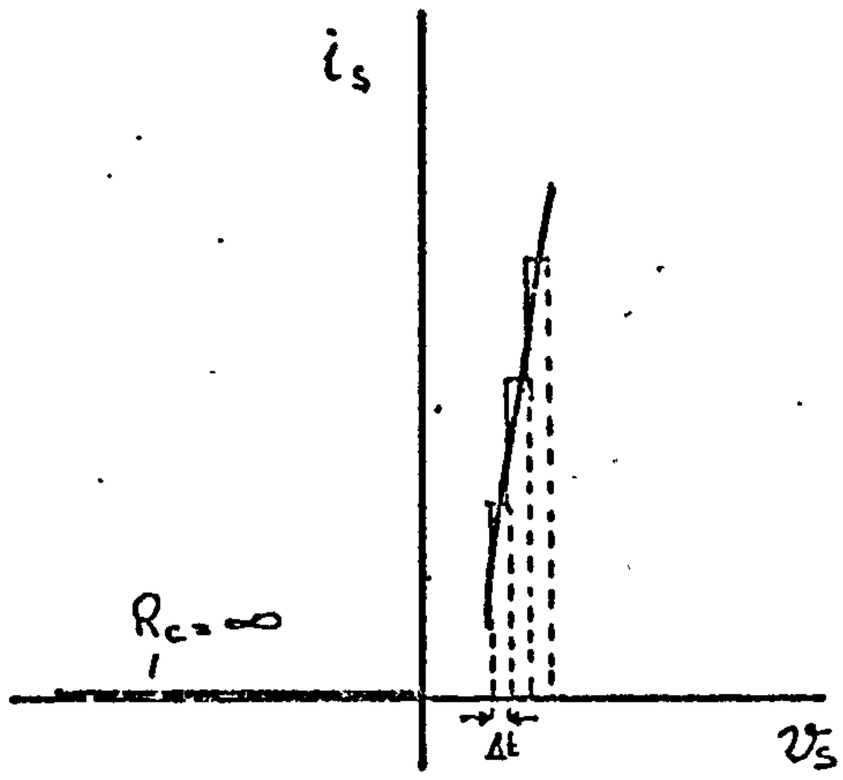

(a)

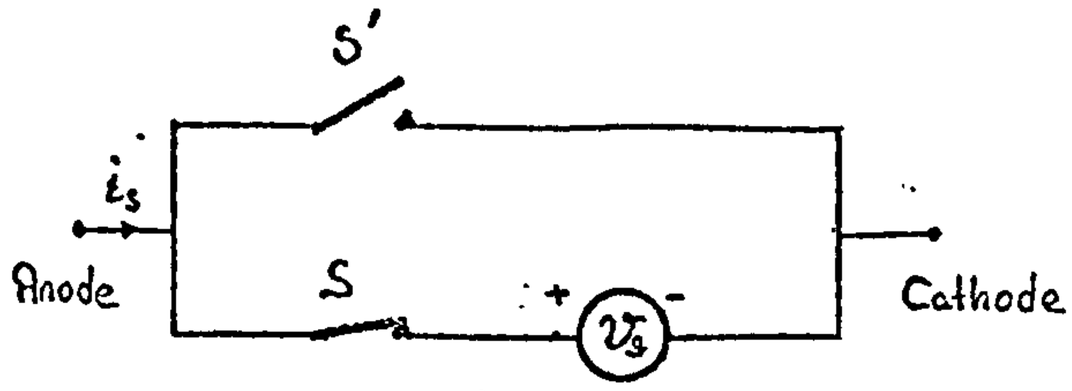

(b)

Figure 6.4 a) Step approximation of the v/i characteristic of a thyristor
b) Simplified equivalent circuit

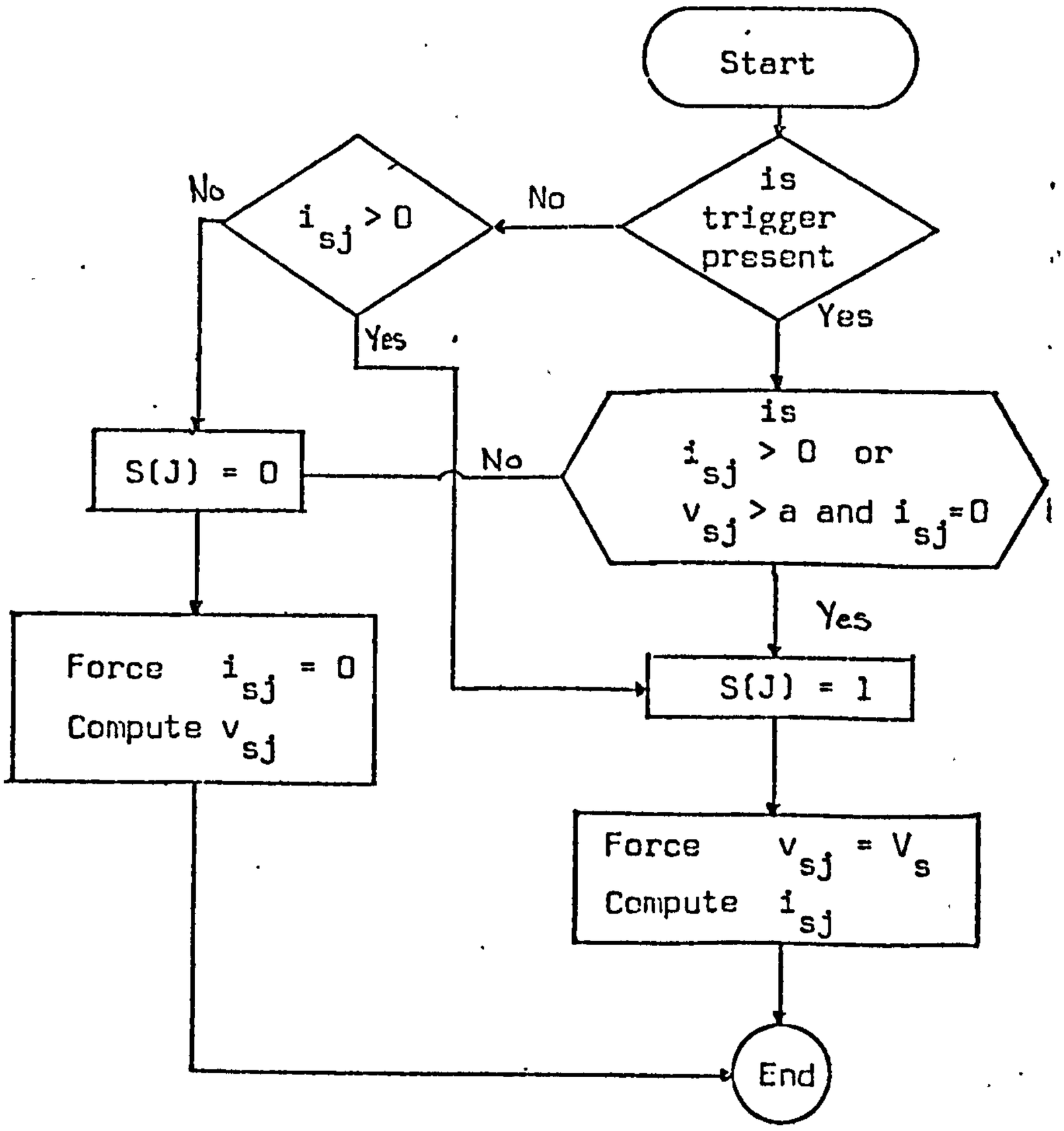

Figure 6.5 Logic module for a thyristor

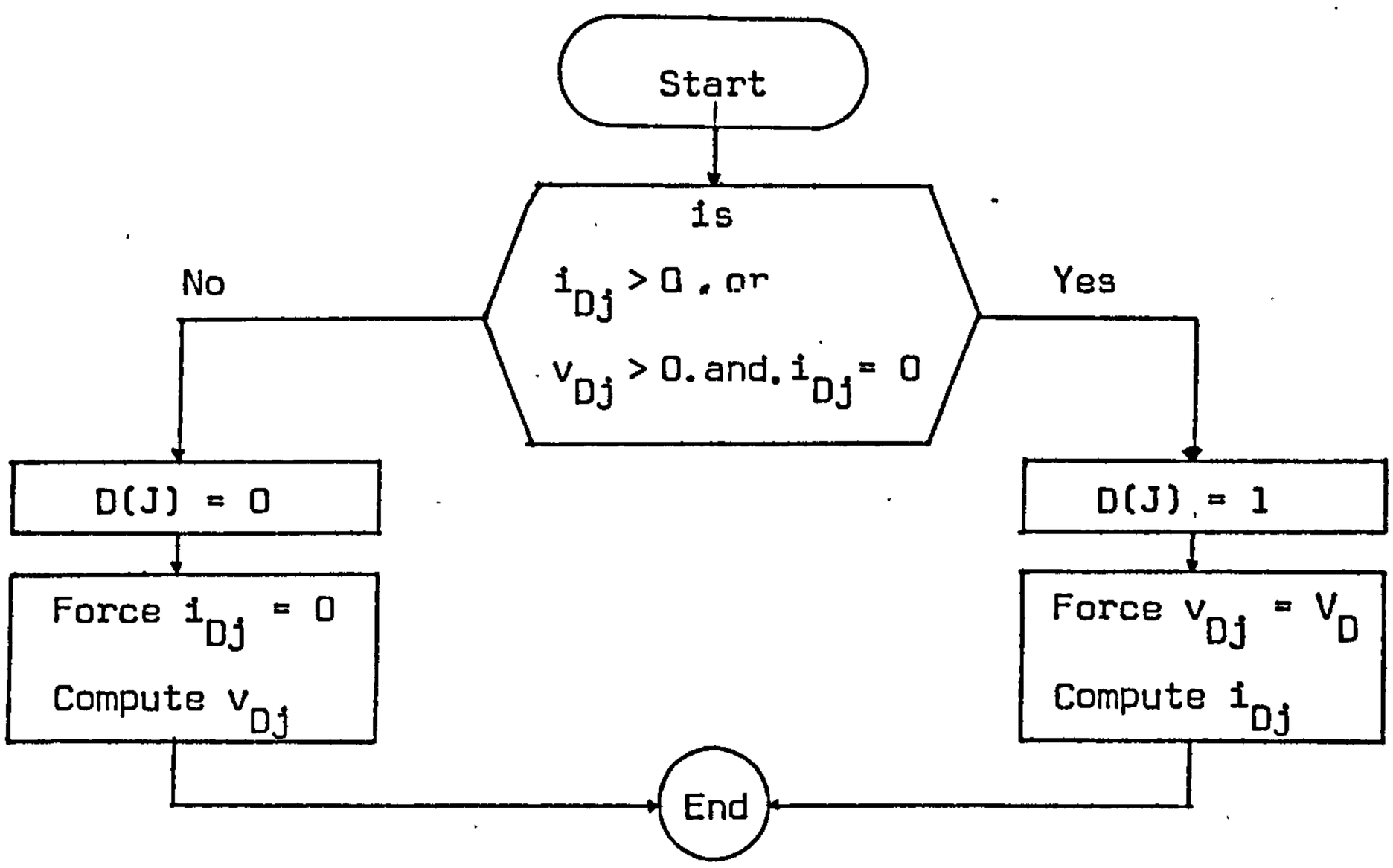

Figure 6.6 Logic module for a diode

Angle \ S(J)	S(1)	S(2)	S(3)	S(4)	S(5)	S(6)
0^o	0	0	0	0	0	1
60^o	1	0	0	0	0	0
120^o	0	1	0	0	0	0
180^o	0	0	1	0	0	0
240^o	0	0	0	1	0	0
300^o	0	0	0	0	1	0
360^o; 0^o	0	0	0	0	0	1
60^o	1	0	0	0	0	0

Figure 6.7 Mode sequence table for a 150 Hz, full power cyclo-inverter operation ($\theta = 60^o$)

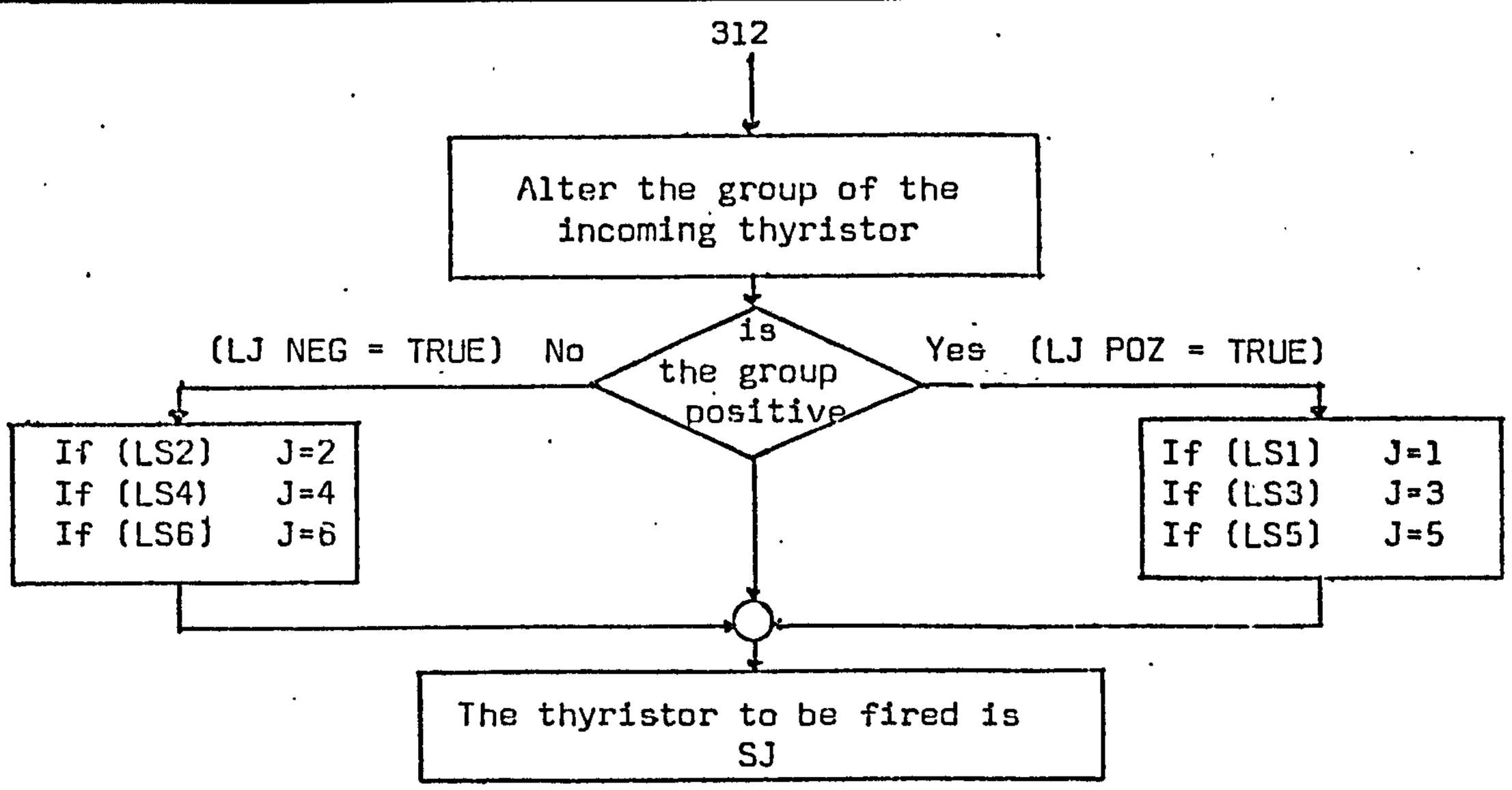

Figure 6.8 Flow chart for the computation of the thyristor firing sequence in a full-bridge cycloinverter

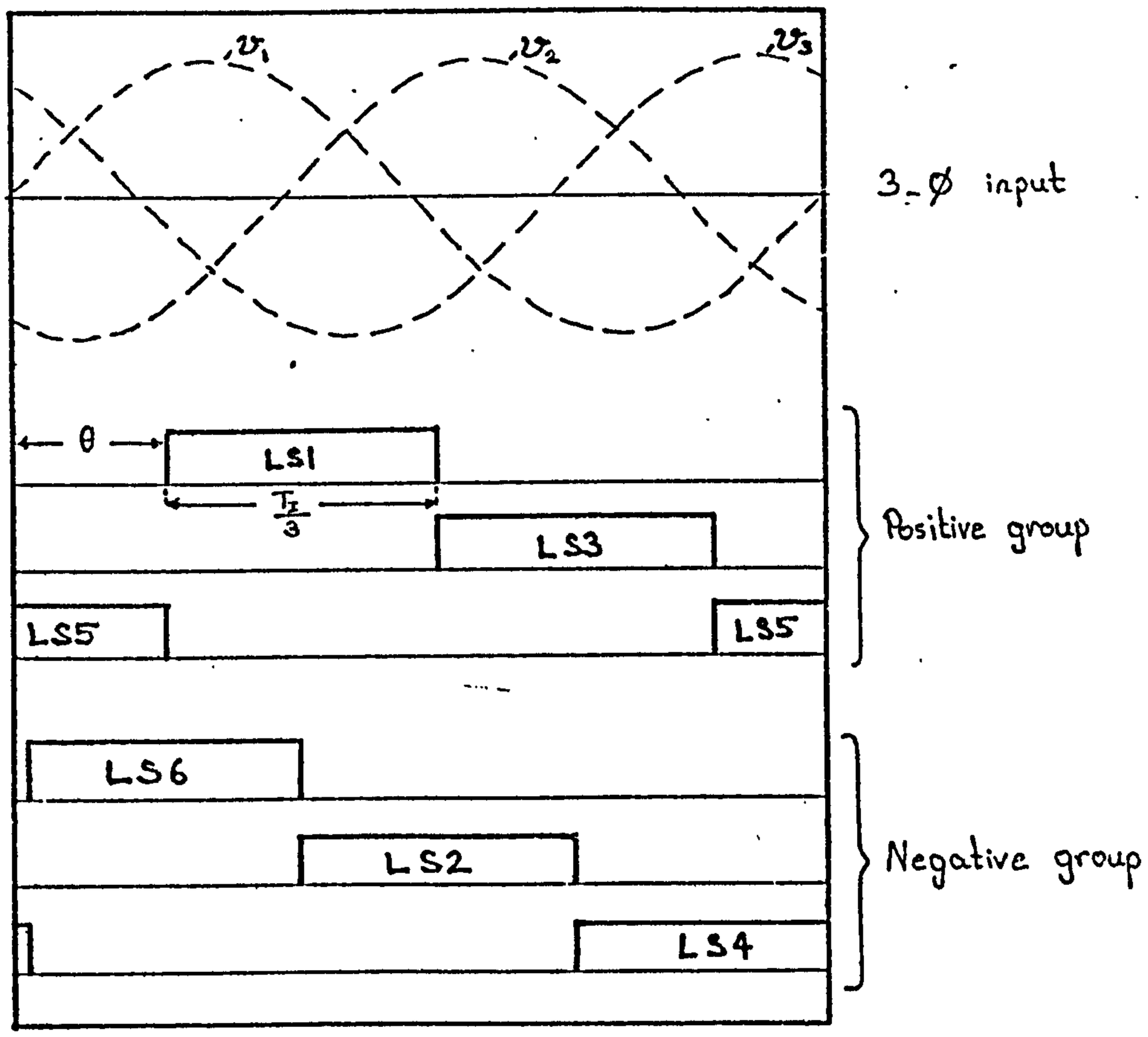

Figure 6.9 Binary logic variable LSj define the permissible firing range of the Jth thyristor

Figure 6.10 Flow chart of the digital simulation of the cycloinverter

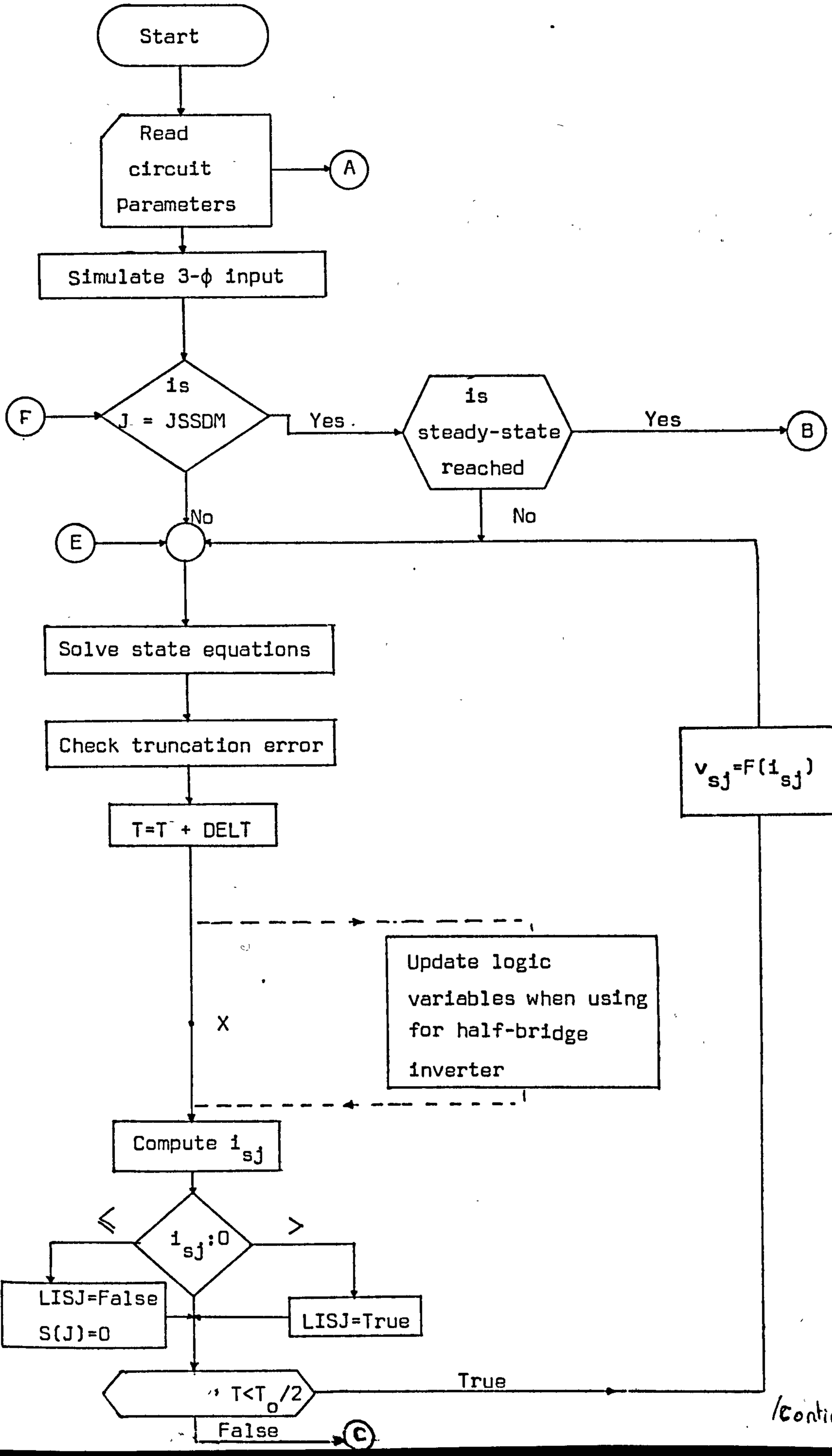

/continued

Figure 6.10

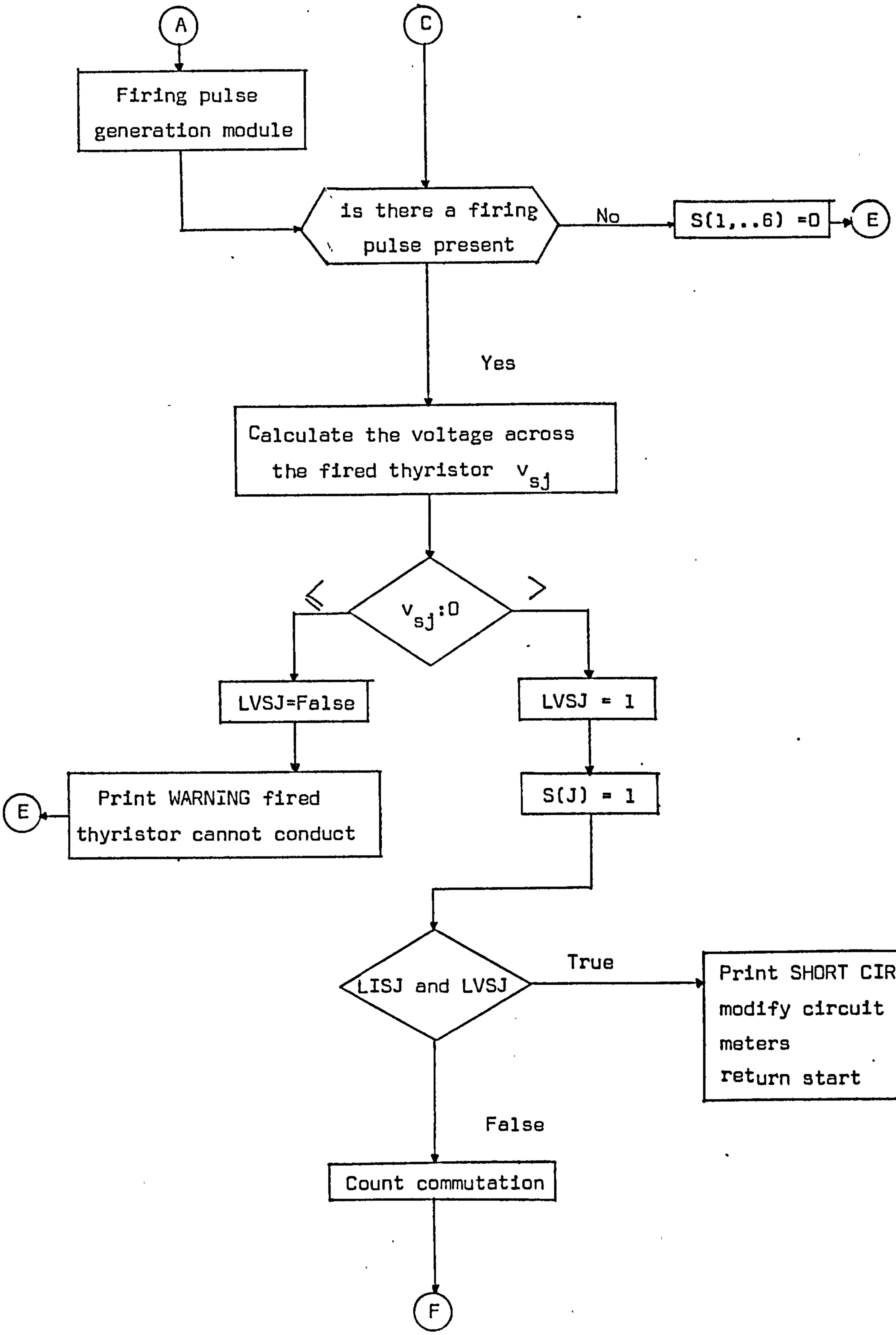

/Continued

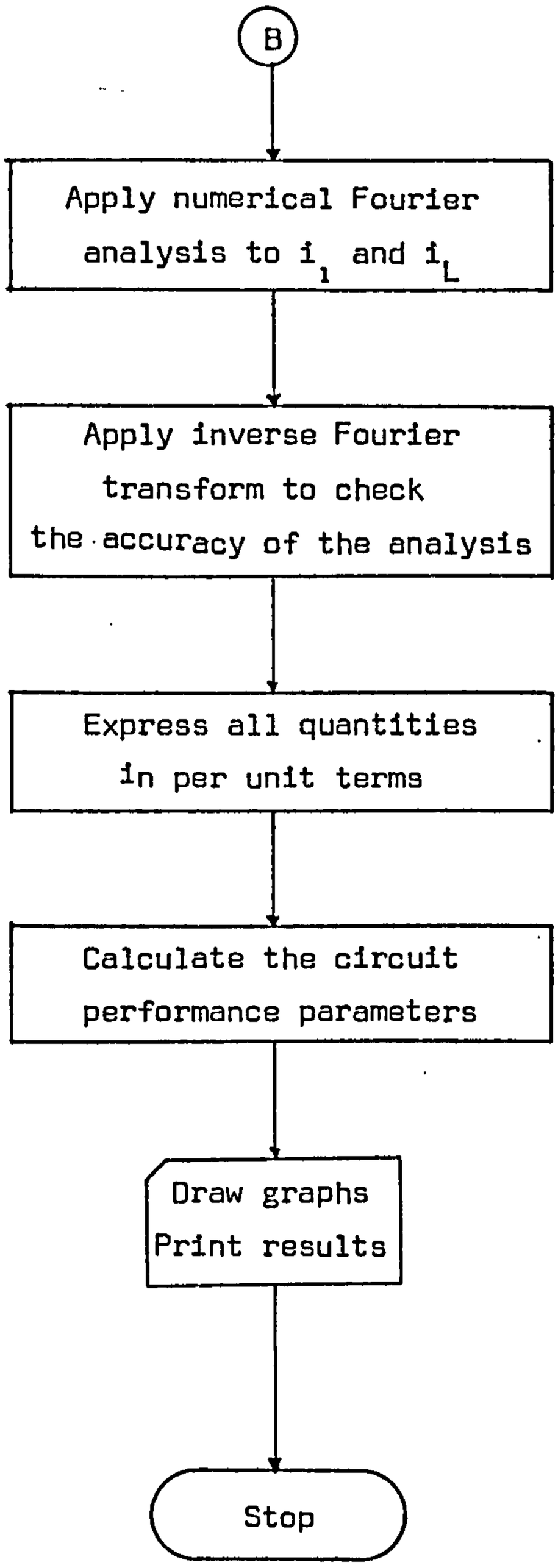
B
Apply numerical Fourier analysis to i_1 and i_L
Apply inverse Fourier transform to check the accuracy of the analysis
Express all quantities in per unit terms
Calculate the circuit performance parameters
Draw graphs
Print results
Stop

Figure 6.10

CHAPTER 7

AN INPUT FILTER FOR THE CYCLOINVERTER

The frequency spectrum of the input line current of the cycloinverter, given in Figure 5.8, indicates that during power conversion a significant number of distortion harmonics are generated, and fed back to the a.c. power supply. These harmonic currents are responsible for voltage drops in the supply impedance, and may result in excessively distorted voltage waveforms in power distribution and transmission systems. It is therefore important that they should be substantially reduced, especially in high-power applications.

The distortion components of the input current are, of course, also responsible for the low input power factor of the cycloinverter. This relation is shown explicitly when the input power factor is defined as (see equation (5.28)),

PF_I = (Input displacement factor) x (Input current distortion factor)

The concluding statements of Section 5.2.3 indicate that, when delivering full output power, the input displacement factor of a high-frequency cycloinverter is near unity, so that the low input power factor of about 0.7 is primarily caused by the low input current distortion factor.

One major disadvantage of the cycloinverter in induction heating applications, is the excessive rise of commutating

capacitor and thyristor voltages at high loads which is inherent in series commutation. The study presented in Section 5.4.2 indicated that, for a range of load variation typical of static heating applications, the peak commutating capacitor and thyristor voltages increase to 5.5 p.u. and 6.2 p.u. respectively. At high operational frequencies, certain power control modes of inverter operation also cause high capacitor and thyristor voltages, independently of the state of the load. The findings of Section 5.4.1 indicate that at 1050 Hz operation, the thyristor and commutating capacitor voltage both increase to approximately 1.6 times their full-load values. This is caused principally by the transient nature of the power control mode of the cycloinverter operation at these frequencies (i.e. the bunch of output current pulses succeeding a long zero interval). Clearly, high voltage rating requirements for the power circuit components appreciably increase the initial cost of the cycloinverter. Further, the possibility of an excessive rise of commutating capacitor voltage in hazardous situations, such as a load short circuit, presents a potential danger.

Fortunately, it is possible both to improve the input power factor of the cycloinverter by reducing the input harmonics and to partially avoid excessive voltage rises in the commutating circuit by introducing an input current regulator with a suitable input filter circuit. In this chapter such a filter is designed, and its effects on the circuit performance are

studied, as it is imperative that the addition of the filter produces minimum undesirable effects on the optimum operating conditions established for the cycloinverter. Initially, a design criteria for the input filter is outlined and, following a brief discussion, the most suitable filter arrangement is selected. Various harmonic models for the filter cycloinverter configuration are then presented and, based on these models, the possible constraints imposed on various filter design parameters by the design criteria are deduced. The effects on the overall circuit performance of varying these parameters is investigated, and from this basis the best design values are suggested. The transient analysis presented later in this chapter enables an accurate study to be made of the cycloinverter performance, with any proposed input filter design at different operating conditions.

This chapter concentrates primarily on an input filter for a 1050 Hz, full-bridge cycloinverter with the optimum design values suggested in Section 5.4. Nevertheless, the technique employed can easily be extended to both low-frequency and half-bridge cycloinverter applications.

7.1 Selection of the Input Filter

An input filter for the cycloinverter should be chosen and designed to meet the follpwing criteria,

i) Maximum input power factor

ii) Minimum undesirable (side) effects on the inverter performance

iii) Minimum rating of the filter components

iv) The input current when thyristors are not conducting should not exceed the rated line current.

Various input filter arrangements may be considered[101,102], depending on the priorities given to the criteria listed above. One approach to satisfying the requirements is to design a filter for the selective attenuation of the dominant distortion harmonic(s) at the input, and the tuned branch filter formed using the commutation capacitors and shown in Figure 7.1 may be used for this purpose. The filter inductor L_{F1} is selected such that it resonates with the commutating capacitors at the dominant distortion frequency, and by providing a short-circuit path it prevents the flow of current at this frequency back to the supply. The inductor L_{F2} is used both to present a high source impedance to the distortion currents and to improve the input displacement factor. However the use of a selective attenuation approach does have some serious disadvantages, and these are outlined below so as to indicate some of the typical problems associated with the filter design.

i) As the spectrum of the input line current in a 1050 Hz cycloinverter for different output power levels shows (Figure 5.8), the distortion harmonics are distributed through a wide range (occurring at frequencies of 250, 850, 950, 1150 Hz with a 50 Hz input). Moreover, there is no clearly dominant harmonic, as each will become significant at a different power control mode. It therefore follows that, for a satisfactory filtering performance, more than one tuned branch is necessary.

ii) Because of the wide frequency spectrum of the input line current, there is a possibility of undesirable parasitic resonances.

iii) The inclusion of L_{F1} within the cycloinverter commutation circuit severely affects the inverter performance. Further, due to the ringing frequency restrictions of a series commutation circuit, L_{F1} cannot always be allowed to take the values needed for the attenuation of the low-frequency harmonics.

The nature of the problems listed above indicates that a more satisfactory filtering performance can be obtained using an external path of small impedance for most of the distortion harmonics, and thereby reducing any interference with the operation of the commutating circuit. In this respect, the conventional LC-filter formed with a series inductor and a shunt capacitor (see Figure 7.2) offers a simple but effective solution.

With this arrangement it is also possible to achieve a resistive input impedance at the source frequency for a particular operational condition.

So far, the considerations for the prevention of an excessive voltage rise in the commutating circuit have been neglected. In fact, by analogy with the constant-current source drive suggested for the basic series inverter to prevent these excessive voltage rises at high loads (see Figure 1.13), it may be assumed that the LC-type filter configuration is also particularly suitable for a similar task in the cycloinverter power circuit. For the sake of simplicity, the filter capacitors may be regarded as a *pseudo-source* to the cycloinverter, while the input current to this source is controlled (or regulated) by the filter inductor. When the equivalent tank-load resistance drops, the input current to the cycloinverter is expected to increase accordingly. However, since such a demand cannot be met by the source capacitors, it results in a reduction in the input voltage to the cycloinverter. Hence by means of this regulating function of the input filter, the occurrence of an excessive voltage rise in the output circuit can be prevented. As a result of these considerations, the input filter arrangement of Figure 7.2 is selected for further study in the remaining sections of this chapter.

7.2 Input Filter Design

In the following considerations, the cycloinverter is assumed to supply a continuous heating load (i.e. one with stable load characteristics).

This permits the considerations associated with the excessive voltage rises in the commutating circuit under varying load conditions to be neglected. However, it is shown later that the design procedure established in this section is also suitable for varying load conditions.

7.2.1 Design constraints

Under balanced operating conditions, the source frequency model of the filter cycloinverter configuration has the form shown in Figure 7.3. The modelling is achieved by a delta-to-star transformation of the filter capacitor C_F, leading to

$$X_{CF} = \frac{1}{3\ C_F\ w_I\ R_{eq}} \quad \text{p.u.}$$

while the per unit inductive reactance is

$$X_{LF} = \frac{L_F\ w_I}{R_{eq}} \quad \text{p.u.} \qquad (7.1)$$

When a LC-filter is included at the input, the overall performance of a cycloinverter is unavoidably affected.

Nevertheless, if, for a first approximation, this effect is assumed to be negligible, the source frequency input impedance of the cycloinverter alone Z'_{I1} for a given power control angle can be calculated from the fundamental (i.e. source frequency) component of the input current, as described in Section 4.2.2.4. The variation of the fundamental input current with the control angle (as shown in the frequency spectrum of Figure 5.8) can therefore be used to obtain the variation of the source frequency input impedance of the cycloinverter with the control angle. Figure 7.4 shows the variation of Z'_{I1} with θ for a full-bridge cycloinverter operating at 1050 Hz and with a commutating circuit optimised for continuous heating application (i.e. X_L = 1.2 p.u. and X_C = 1.3 p.u., as established in Section 5.4.1).

The condition of unity input displacement factor at a given output power level (relating to the first of the input filter design criteria) requires that the total input impedance

$$Z_{I1} = X_{LF}\, j + \frac{a + bj}{a + (b - X_{CF})j} \cdot (-X_{CF}\, j) \qquad (7.2)$$

where a and b are the real and imaginary parts of the cyclo-inverter input impedance for particular operating conditions (corresponding to the output frequency w_o and an output power level P_o), must be resistive. Solution for this condition yields,

$$X_{LF} = \frac{a^2 + b^2 - X_{CF}\, b}{a^2 + (b - X_{CF})^2}\; X_{CF} \qquad (7.3)$$

so that the equivalent input impedance is

$$R_{I1} = \frac{a\ X_{CF}^2}{a^2 + (b - X_{CF})^2} \tag{7.4}$$

The source frequency input current is, therefore,

$$I_{11} = \frac{V_1}{R_{I1}} \tag{7.5}$$

and the current at the input to the cycloinverter is,

$$I'_{11} = \frac{-\ X_{CF}\ j}{a + (b - X_{CF})j}\ I_{11} \tag{7.6}$$

On the other hand, the input current when the circuit thyristors are all non-conducting is,

$$I_{11off} = \frac{V_1}{X_{CF} - X_{LF}} \angle 90^o \tag{7.7}$$

It is particulary desirable when using a cycloinverter that the highest possible input power factor is achieved when the inverter is operating at full output power. In other words, the input displacement factor should be unity at this condition. The values of a and b in the above equations should therefore correspond respectively to the real and imaginary components of the input impedance Z'_{I1} of the cycloinverter alone at $\theta = 30^o$.

The fourth of the input filter design criteria requires that, for a suitable filter,

$$|I_{11off}| < |I_{11}| \tag{7.8}$$

and substituting for I_{11off} and I_{11}, from equations (7.7) and (7.5) respectively yields,

$$\frac{1}{X_{CF} - X_{LF}} < \frac{1}{R_{I1}}$$

when X_{LF} is eliminated by substituting from equation (7.3), this condition simplifies to,

$$X_{CF} > a + b \tag{7.9}$$

The harmonic attenuation of the filter can be calculated approximately by making use of the harmonic-frequency model of Figure 7.5, which gives,

$$I_{1n} = - \frac{X_{CF}}{n^2 X_{LF} - X_{CF}} I'_{1n} \tag{7.10}$$

In order to reduce I_{1n} for the n^{th} harmonic,

$$n^2 X_{LF} > X_{CF} \tag{7.11}$$

and obviously values of X_{LF} and X_{CF} for resonance at any distortion frequency (i.e. $n^2 X_{LF} = X_{CF}$) must be particularly avoided.

When pursuing the filter design, consideration should also be given to the input voltage conditions of the cycloinverter, so as to avoid the need for quite impractical component values. When all the circuit thyristors are nonconducting, the input phase voltage of the cycloinverter is, approximately,

$$V_{a1off} = \frac{X_{CF}}{X_{CF} - X_{LF}} V_1 \qquad (7.12)$$

and when operating with an input impedance Z_I' it becomes:

$$V_{a1} = \vec{V}_1 - I_{11}^{\rightarrow} X_L \qquad (7.13)$$

The third of the design criteria requires the filter components to have minimum VA ratings. The source-frequency VA rating of the filtering inductor is

$$VA_{LF} = I^2_{LFmax} X_{LF} \qquad (7.14)$$

and that of filtering capacitor is

$$VA_{CF} = I^2_{CFmax} \quad X_{CF} \tag{7.15}$$

where I_{LFmax} and I_{CFmax} are the maximum input current and the filtering capacitor current occurring during a possible mode of operation. Clearly for an acceptable design,

I_{LFmax} = source-frequency input line current I_{11} at full output power approximately.

The total VA of the filter components is obviously

$$VA_T = VA_{LF} + VA_{CF} \tag{7.16}$$

7.3 Selection of filter components

The input filter design requirements and the associated constraints on the design values of X_{LF} and X_{CF} have already been outlined. In this section, values of X_{LF} and X_{CF} are varied within these constraints, and the corresponding circuit performance is investigated, to enable selection of the design

---

* For the sake of simplicity the VA contribution of the harmonic currents are neglected, since the distortion components of the filtering inductor current and capacitor voltage are small in comparison with the corresponding source frequency components.

values which produce a performance closest to the design requirements.

Figure 7.4 shows that for full output power the cycloinverter input impedance

$$Z'_{I1} = 2.78 + j\ 0.\ \text{p.u.}$$

is purely resistive. Substituting the values of a and b obtained from this expression in condition (7.9) gives,

$$X_{CF} > 2.78\ \text{p.u.} \qquad (7.17)$$

Figure 7.6 shows variations of X_{LF} and the input resistance R_{I1} with X_{CF}, to satisfy equation (7.3), (7.4) and condition (7.17). Figure 7.7 shows variations of the source-frequency input current I_{11} and the cycloinverter input phase voltage V_{a1}, both when all the circuit thyristors are non-conducting ($P_o = 0$) and when they are fired to give full output power. It will be seen that the input current for full power output is greater than that for zero power output for $X_{CF} > 2.78$ p.u. and equal to it when $X_{CF} = 2.78$ p.u., in accordance with condition (7.8). Figure 7.7 also indicates that, with low values of X_{CF}, the off-state cycloinverter input voltage is substantially higher than the full power input voltage and the filtering capacitor therefore requires an unnecessarily high voltage rating. Clearly, the phase of V_{a1} with respect to V_1 varies

with the load presented by the cycloinverter, and, since this variation is important when adjusting the power control angle θ, it is considered further in the following sections.

The variation with X_{CF} of the distortion harmonics in the input line can be calculated from equation (7.10), but preliminary calculations using this equation for $2.78 < X_{CF} < 5.0$ p.u. showed that at full output power the maximum harmonic amplitude, which corresponds always to the lowest-frequency component, is always well below 10% of the fundamental. Clearly,the distortion factor of the input current is very close to unity with this level of attenuation, and since filter designs with unity input displacement factor are considered, the input power factor should also be very close to this value.

Figure 7.7 indicates that maximum current in the inductor and maximum voltage across the capacitor of the filter circuit occur when the cycloinverter is operating at full and at zero output power respectively (When $P_o = 0$, all the input current flows through C_F). The corresponding currents must obviously be used in calculating the maximum VA rating of the filter components, in accordance with equations (7.14) and (7.15). By doing this, the results of Figure 7.8 are obtained where, with the per unit output power as a parameter, the variations of VA_{CF}, VA_{LF} and VA_T with X_{CF} are presented.

The variations in filter performance with X_{CF} so far investigated suggest that high design values for X_{CF} are preferable, as this enables components of lower ratings to be

employed. However, caution must be exercised when selecting such a design value since:

a) High design values for X_{CF} (i.e. low values of C_F) cannot provide the stiff input voltage characteristics required for the cycloinverter, even at low loads *. Since the envelope of the input voltage is reflected to the output current during cycloinversion, this may cause severe distortion of the output current and a deterioration in the inverter performance.

b) High design values of X_{CF} require lower values of X_{LF} (see Figure 7.6) for a resistive input impedance, but this may cause condition (7.11) of Section 7.2.1 to be violated when the distortion frequencies shift to the lower end of the spectrum at reduced output power levels (as shown in Figure 5.8).

The effects of different filter designs on the cycloinverter performance (the first of the two items above) can only be accurately investigated with a transient analysis, since the initial assumption for the harmonic modelling states that with

---

* At high loads, due to the excessive input current demand, the input voltage to the cycloinverter inevitably becomes distorted. However at low loads this can be avoided.

the addition of the input filter, the harmonic content of the input current and (therefore) the output and input voltages remain unaltered. A transient analysis of the complete circuit is presented later. Nevertheless, by continuing to rely on this assumption for the values of X_{CF} under consideration, it is possible to pursue the investigation required in the second item stated above, and for this purpose the distortion-frequency model of the configuration given in Figure 7.5 is conveniently employed. Equation (7.10) indicates that parallel resonance of L_F and C_F can occur only among the lowest distortion frequencies. The resonant frequency for the following design values are,

X_{CF}, p.u.	X_{LF}, p.u.	f_F, Hz
5	1.18	102
4	1.3	87
2.78	1.4	70

As seen for $X_{CF} > 5$ p.u. the resonant frequency increases towards the distortion frequencies (for $X_{CF} = 5$ p.u. A distortion harmonic at 100 Hz is amplified by 17 times).

Figure 7.9 shows the variation of the input displacement factor with output power, for various design values of X_{CF}, and as a consequence of the design constraint (7.3) these curves approach unity at full output power. Figure 7.9 indicates

clearly that the best displacement factor is achieved with the highest value of X_{CF} considered, i.e. X_{CF} = 5 p.u. However, it must be remembered that the curves shown do not provide full information on the variation of the input power factor with P_o since, as mentioned previously, the distortion factor of the input current deteriorates when $X_{CF} > 5$ p.u. and this causes a corresponding fall in the input power factor.

The above study of the variation of the circuit behaviour with X_{CF}, on the basis of the design criteria, indicates that for a good input power factor characteristic, with the smallest possible filter component ratings

$$X_{CF} = 4.0 \text{ p.u.} \qquad \text{and} \qquad X_{LF} = 1.3 \text{ p.u.} \qquad (7.18)$$

may be selected respectively as the design base for the filter capacitor and inductor.

Expected Performance

By using harmonic models, the following operational conditions are predicted for the selected design values of the filter components:

- Good sinusoidal input current waveform for all modes of power control, with a distortion factor of approximately unity.

- The highest distortion current amplitude at 250 Hz is about 12% of the fundamental.

- At maximum output power, the phase shift between the source and the cycloinverter input phase voltages is approximately -12^{o}. The full power firing angle with respect to the source phase voltage is therefore,

$$\theta' = 30^{o} - (-12^{o}) = 42^{o}$$

- The expected variation of input power factor with θ is shown in Figure 7.10, and since this is as high as 0.87 even at 40% of maximum output power, it can be considered quite satisfactory. The improvement in the input power factor brought about by the input filter becomes apparent when compared with the corresponding variation for a cycloinverter without an input filter.

Because of the assumptions in the harmonic modelling, the selected design values for X_{CF} and X_{LF} are only preliminary, and the findings of this section need to be confirmed by the more accurate transient analysis presented in the next section.

7.4 Transient Analysis

7.4.1 Generalised state equations

The simplified power circuit diagram of the cycloinverter with a LC-type input filter is shown in Figure 7.11. Based on this diagram, and the assumptions given in Section* 4.2, the circuit differential equations for the transient analysis of the cycloinverter may be derived as follows.

Applying Kirchhoff's law to the input voltage loops formed by the source and the filter components yields,

$$v_1 - v_2 = L_F (\dot{i}_1 - \dot{i}_2) + R_F (i_1 - i_2) + v_{ab}$$

$$v_2 - v_3 = L_F (\dot{i}_2 - \dot{i}_3) + R_F (i_2 - i_3) + v_{bc}$$

$$v_3 - v_1 = L_F (\dot{i}_3 - \dot{i}_1) + R_F (i_3 - i_1) + v_{ca} \qquad (7.19)$$

where

$$v_1 + v_2 + v_3 = 0 \qquad (7.20)$$

$$i_1 + i_2 + i_3 = 0 \qquad (7.21)$$

$$v_{ab} + v_{bc} + v_{ca} = 0 \qquad (7.22)$$

---

* Obviously assumption 2 is omitted

The nodal current equations at the junction of the filter capacitors are

$$i_1 = i'_1 + i_a - i_c$$

$$i_2 = i'_2 + i_b - i_a$$

$$i_3 = i'_3 + i_c - i_b \qquad (7.23)$$

where the filter capacitor currents are

$$i_a = C_F \dot{v}_{ab}$$

$$i_b = C_F \dot{v}_{bc}$$

$$i_c = C_F \dot{v}_{ca} \qquad (7.24)$$

From the voltage loops formed by the filter and commutating capacitors,

$$\dot{v}_{ab} = \frac{1}{C}(i_{c1} - i_{c2})$$

$$\dot{v}_{bc} = \frac{1}{C}(i_{c2} - i_{c3})$$

$$\dot{v}_{ca} = \frac{1}{C}(i_{c3} - i_{c1}) \qquad (7.25)$$

since $C_1 = C_2 = C_3 = C$

The nodal current equation at the star point of the commutating capacitors is,

$$i_{C1} + i_{C2} + i_{C3} = -i_L \tag{7.26}$$

where,

$$i_{C1} = C \dot{V}_{C1}$$

$$i_{C2} = C \dot{V}_{C2}$$

$$i_{C3} = C \dot{V}_{C3} \tag{7.27}$$

Assuming that binary logic variables P(1), P(2) and P(3) and P(0) represent, respectively, states P_1, P_2, P_3 and P_0 of switch S, the input currents to the cycloinverter are,

$$i'_1 = C \dot{V}_{C1} + P(1)\, i_L$$

$$i'_2 = C \dot{V}_{C2} + P(2)\, i_L$$

$$i'_3 = C \dot{V}_{C3} + P(3)\, i_L \tag{7.28}$$

The loop voltage equation for the output circuit gives,

$$P(1)\, v_{c1} + P(2)\, v_{c2} + P(3)\, v_{c3} = L\, \dot{i}_L + [P(1) + P(2) + P(3)]\, v_{co} \qquad (7.29)$$

while the equations for the tank-load circuit are,

$$\dot{v}_{co} = \frac{1}{C_o} (i_L - i_{Lo}) \qquad (7.30)$$

$$\dot{i}_{Lo} = \frac{1}{L_o} (v_{co} - R_o\, i_{Lo}) \qquad (7.31)$$

Circuit equations (7.19 to 7.31) indicate that operation of the filter-cycloinverter configuration can be fully described in terms of the 8 state variables

$$Z_1 = i_1 \qquad Z_2 = i_3$$

$$Z_3 = v_{ab} \qquad Z_4 = v_{ca}$$

$$Z_5 = v_{c1} \qquad Z_6 = i_L$$

$$Z_7 = v_{co} \qquad Z_8 = i_{Lo} \qquad (7.32)$$

In order to derive generalised state equations valid for all modes of operation, the remaining unknowns may be eliminated systematically as follows. Elimination of v_{bc} and i_2 from equations (7.19), by making substitutions from equations (7.20), (7.21) and (7.22), yields,

$$\dot{Z}_1 = \frac{1}{3 L_F} (3 v_1 - Z_3 + Z_4 - 3 R_F Z_1) \qquad (7.33)$$

$$\dot{Z}_2 = \frac{1}{3 L_F} (3 v_3 - Z_3 - 2 Z_4 - 3 R_F Z_2) \qquad (7.34)$$

Using equations (7.25), (7.27) and equation (7.26) it can be shown that,

$$\dot{Z}_5 = 3 (\dot{Z}_1 - \dot{Z}_2 - \frac{Z_6}{C}) \qquad (7.35)$$

By substituting first for v_{C2} and v_{C3} from (7.27) in (7.28) respectively, and then for the cycloinverter input currents i_1', i_2' and i_3' from equation (7.23) together with i_a, i_b and i_c from equation (7.24) yields,

$$Z_1 = (C_F + \frac{C}{3}) (\dot{Z}_3 - \dot{Z}_4) + [2 P(1) - P(2) - P(1)] \frac{Z_6}{3} \qquad (7.36)$$

$$Z_2 = (C_F + \frac{C}{3})\ (2\ \dot{Z}_4 + \dot{Z}_3) + [2\ P(3) - P(1) - P(2)]\ \frac{Z_6}{3} \qquad (7.37)$$

By combining equations (7.33), (7.34), (7.36) and (7.37), it can then be shown that

$$\dot{Z}_3 = \frac{1}{C + 3\ C_F}\ [2\ Z_1 + Z_2 - (P(1) - P(2)\ )\ Z_6\ ] \qquad (7.38)$$

$$\dot{Z}_4 = \frac{1}{C + 3\ C_F}\ [\ Z_2 - Z_1 - (P(3) - P(1)\ )\ Z_6\ ] \qquad (7.39)$$

The 8 generalised state equations corresponding to the 8 state variables are therefore equations (7.29, 30, 31, 33, 34, 35, 38, 39).

After obtaining functional equivalents for the logic states P(1), P(2), P(3) and P(0) in terms of the familiar thyristor state logic variables, and substituting these and the thyristor forward voltage drop V_s in the generalised state equations we obtain

$$\dot{Z}_1 = \frac{1}{3\,L_F}\,(3\,v_1 - Z_3 + Z_4 - 3\,R_F\,Z_1)$$

$$\dot{Z}_2 = \frac{1}{3\,L_F}\,(3\,v_3 - Z_3 - 2\,Z_4 - 3\,R_F\,Z_2)$$

$$\dot{Z}_3 = \frac{1}{C + 3\,C_F}\,[2\,Z_1 + Z_2 - (S(1) + S(4) - S(3) - S(6))\,Z_6]$$

$$\dot{Z}_4 = \frac{1}{C + 3\,C_F}\,[Z_2 - Z_1 - (S(2) + S(5) - S(1) - S(4))\,Z_6]$$

$$\dot{Z}_5 = \frac{1}{3}\left(\dot{Z}_3 - \dot{Z}_4 - \frac{Z_6}{C}\right)$$

$$\dot{Z}_6 = \frac{1}{L}\,[S(1)\,(Z_5 - V_s) + S(4)\,(Z_5 + V_s)$$

$$+ S(3)\,(Z_5 - Z_3 - V_s) + S(6)\,(Z_5 - Z_3 + V_s)$$

$$+ S(5)\,(Z_5 + Z_4 - V_s) + S(2)\,(Z_5 + Z_4 + V_s) + AZ_7]$$

$$\dot{Z}_7 = \frac{1}{C_o}\,(Z_6 - Z_8)$$

$$\dot{Z}_8 = \frac{1}{L_o}\,(Z_7 - R_o\,Z_8) \qquad (7.40)$$

7.4.2 Digital simulation

Despite the addition of the input filter, the basic principles used in developing the flow chart of Figure 6.10 for the digital simulation of the cycloinverter remain unchanged. However, both (i) initialisation of the state variables and (ii) the firing logic module, require further consideration.

Due to the high and low frequency currents which circulate on both sides of the input filter, the search for the steady-state conditions now poses some serious problems relating to the computation time. Evidently, the time constant of the filter circuit is dominant in setting the duration of the transient response, which in some cases may last for several supply cycles, whereas the step length of the integration is of the order of micro-seconds, as determined by the high output frequency.

Another important factor contributing to a long transient response is the continually varying firing angle θ seen by the cycloinverter. Clearly, the phase of the cycloinverter input voltage shifts with respect to the source voltage, depending upon the loading. Hence, if the firing logic module of the cycloinverter has the source phase voltage as the reference, the firing angle θ also shifts, causing even further changes in the output power. For instance, when establishing the firing sequence for full output power, the following may take place. Before switch-on (when all thyristors are non-conducting) the

cycloinverter input voltage is naturally in phase with the source voltage. Therefore on switch-on, with $\theta_F' = 30^o$ with respect to the source voltage, the cycloinverter functions with full output power, but, in so doing, it causes a change in the phase difference $\alpha_{v_1 - v_a}$ between the inverter input phase voltage v_a and the source voltage v_1. Therefore, to maintain the full output power, the firing sequence θ_F' must be varied as

$$\theta_F' = \alpha_{v_1 - v_a} + 30^o \qquad (7.41)$$

A further difficulty encountered during computing is a continuation of the above problem, and is in establishing steady-state conditions, since the steady-state value of $\alpha_{v_1 - v_a}$ for a given power control angle θ' is not known in advance. Nevertheless, equation (7.41) suggests that both the problems of a long transient response and of establishing steady-state conditions can be avoided by considering the cycloinverter as operating under closed-loop control, achieved by removing the phase reference of the firing logic module from the source voltage to the filter capacitor voltage. In so doing, the positive-going zero crossings of the filter capacitor voltages can be taken as the phase reference for full output power, since they lead the cycloinverter input phase voltages by 30^o. However, this solution necessitates further analysis, since the

filter capacitor voltages have distortion components and need to be further filtered before being fed into the firing logic module.

Alternatively, the problems stated above can, of course, be eliminated, by correctly initialling the state variables to correspond with their steady-state values. The steady-state harmonic models given in the previous sections can readily be used for this purpose, so that, for example, when initialling the state variables for $\theta = 120^{o}$ (w.r.t. cycloinverter input voltage), the steps followed are:

From Figure 7.4 the cycloinverter input impedance corresponding to $\theta = 120^{o}$ is

$$Z'_{I1} = 9.78 \angle 58^{o} \text{ p.u.}$$

and from equation (7.2) the total input impedance of the configuration is

$$Z_{I1} = 4.59 \angle -66^{o} \text{ p.u.}$$

The steady-state input current at the source frequency is

$$I_{11} = \frac{1}{Z_{I1}} = 0.21 \angle 66^{o} \text{ p.u., r.m.s.}$$

while from equation (7.13) the source frequency component of the A-phase input voltage to the cycloinverter is

$$V_{a1} = V_1 \angle 0^\circ + I_{11} \; X_L \angle 90^\circ + 66^\circ$$

$$= 1.25 \angle -5^\circ.1 \text{ p.u.}$$

The firing angle with respect to the source voltage is therefore,

$$\theta' = 120^\circ - (-5^\circ.1) = 125^\circ.1$$

and the first four state variables corresponding to the filter circuit voltages and currents are, approximately,

$$Z_1 = 0.21 \sqrt{2} \text{ Sin } \theta' = - 0.39 \text{ p.u.}$$

$$Z_2 = 0.21 \sqrt{2} \text{ Sin } (120^\circ + \theta') = -1.56 \text{ p.u.}$$

$$Z_3 = \sqrt{2} \sqrt{3} \; 1.25 \text{ Sin } (\theta + 30) = 1.53 \text{ p.u.}$$

$$Z_4 = \sqrt{2} \sqrt{3} \; 1.25 \text{ Sin } (\theta + 120^\circ + 30^\circ) = -3.02 \text{ p.u.}$$

7.5 Digital Simulation Results for the Cycloinverter Performance at Constant Load Conditions

7.5.1 Circuit performance at full output power

Figures 7.12 to 7.14 show the variations of the chosen state variables at steady-state, for a series of values of X_{CF}.

It is possible with these results to investigate to what extent the optimised cycloinverter operation conditions are affected by the addition of the input filter. This information is also important in establishing the validity of the starting assumptions for the harmonic modelling, which requires that for the range of X_{CF} and X_{LF} involved, the cycloinverter operation conditions are not significantly affected. The easiest way this can be investigated is by a comparison of the harmonic content of the cycloinverter output current with and without the input filter, for a series of values of X_{CF}. Figure 7.15 shows the variation of the harmonic content of the output current with X_{CF}. For the sake of simplicity, only the dominant output current harmonics at frequencies w_o, $w_o \pm 6\ w_I$ are considered. The figure indicates that with $X_{CF} < 6.0$ p.u., the increase in sideband harmonics are less than 13%, so that, for $2.78 < X_{CF} < 6$ p.u, predictions made from the harmonic models are quite reliable. The curves of Figure 7.15 also indicate that lower values of X_{CF} are preferable,on the basis of the output current distortion. This phenomenon is in fact predicted in Section 7.3.2, and its cause

can be seen in the computer results of the transient analysis in Figures7.12 to 7.14. As shown, for increasing values of X_{CF} (i.e. decreasing C_F) the stiff voltage characteristics at the input of the cycloinverter cannot be maintained (compare the variation of v_{ab}, v_{bc} and v_{ca} with X_{CF}) and the input voltages become progressively distorted. This is consequently reflected in the output current, causing higher sideband harmonics.

The variation of the filter input current with X_{CF} given in Figures 7.12 to 7.14 indicates that, although the input displacement factor is maintained satisfactorily high, its harmonic content deteriorates for high values of X_{CF}.

Figure 7.16 shows the variation of the input distortion currents with X_{CF}, and indicates that the 250 Hz component increases sharply with X_{CF}. The variation of the input current harmonics in this figure clearly justifies once more the selection of the design value X_{CF} = 4 p.u.

7.5.2 Circuit performance at power control modes

Some results of a graphical transient analysis showing the variation of various circuit quantities for various reduced output power levels are given in Figures 7.17 to 7.19. As predicted in Section 7.3.3, the input current waveform retains a reasonably good shape throughout the power control. When performing a numerical Fourier analysis of the input current for varying

output power levels, the variation with θ of the dominant harmonics in the input lines can be obtained, as shown in Figure 7.20, where the variation of the output power is also provided. Although the harmonic content of the input current deteriorates slightly at around $\theta = 100^{o}$, it can be seen that the ratio of the distortion harmonic to the fundamental is always less than 14%.

The variation with θ of the peak commutating capacitor voltage, which can be obtained from Figures 7.17 to 7.19, indicates that the designed filter has also been successful in preventing an excessive voltage rise in the commutating circuit. It has been demonstrated earlier that, in the cyclo-inverter without the input filter, the voltage of the commutating capacitor rises to 1.6 times the full load value when θ increases to 90^{o}. However, as seen in the computed waveforms, the commutating capacitor voltage with a filter is always less than its full load value, for all output power levels.

The variation of the input displacement factor with the output power is given in Figure 7.21. Comparison of this curve with that obtained from the harmonic modelling confirms again the consistency between the results of both methods of analysis. Clearly, because of the near unity input current distortion factor, this curve also corresponds approximately to the variation of the input power factor.

In brief, the results of the digital simulation obtained for a 1050 Hz cycloinverter operation with the continuous heating load, can be seen:

i) to be in close agreement with those of the harmonic analysis (and hence confirm the validity of the assumptions made in harmonic modelling),

ii) to justify the selection of the design values for X_{CF} and X_{LF},

for both full and reduced output power operations.

7.5.3 Results of the transient analysis of the cycloinverter performance under varying load conditions

The presence of the region of instability in the cycloinverter operation prevents the load from being varied at will for any commutating circuit. As was mentioned previously in Chapter 5, the cycloinverter designed for a continuous heating load produces a short circuit when the equivalent tank resistance drops. Due to this reason, the input filter-cycloinverter configuration considered in the previous section cannot be employed to investigate the effects of the input filter on the circuit performance under varying load condition. For this purpose, the commutating circuit optimised for the varying conditions of a static heating load in Section 5.4.2. of Chapter 5 (i.e. with

X_L = 0.7 p.u. and X_c = 1.3 p.u) is therefore employed, and the typical load conditions given in Table 5.1 are assumed.

An optimum input filter design for the cycloinverter supplying a variable load can be obtained by following the steps of the input filter design procedure established in the previous sections, for the particular load condition at which the most effective filtering is desirable. On the other hand, the excessive voltage in the commutating circuit occurs for the load conditions B, C (see Figure 2.9) which demand a high cycloinverter input line current. To effectively suppress the high commutation voltages at these load conditions (by limiting the increase in the input line current), the input filter design should therefore be performed for the load condition which produces the highest cycloinverter input impedance. Based on these considerations, preliminary investigations of the harmonic analysis of the input line current of the cycloinverter alone (and at characteristic load conditions) show that, the input filter design should be performed for the end-of-heat-cycle load condition E . The design values for the filter capacitor and inductor are hence found to be:

$$X_{CF} = 4.51 \text{ p.u.}$$

$$X_{LF} = 1.63 \text{ p.u.}$$

Figure 7.22 shows the variation of various circuit waveforms obtained from the digital simulation of the cycloinverter,

with the filter design proposed above, and when operating at the load condition E. As shown, the input filter design is quite successful, and produces approximately sinusoidal input current waveforms and near to unity input displacement factor.

Figures 7.23 and 7.24 show the variation of the computed circuit waveforms at the load conditions B and C respectively. Since the operational frequencies (934 Hz and 908 Hz) are non-multiples of the source frequency, it is difficult to perform an accurate numerical Fourier analysis. Nevertheless, a numerical analysis of the input and output currents at characteristic load conditions is performed by approximating these operational frequencies to the closest multiple source frequencies (i.e. approximating $[w_o]_A$ = 994 Hz to 1000 Hz, $[w_o]_B$ = 934 Hz to 950 Hz and $[w_o]_C$ = 908 Hz to 900 Hz) and the results obtained when examined together with the computed waveforms indicate that

i) the input line currents i_1, i_2 and i_3 have a reasonably good sinusoidal shape throughout the range of load variation. The worst case input line current distortion factor is approximately 0.98, being significantly increased from the 0.48 obtained for an unfiltered cyclo-inverter with the same commutating circuit and under the same operational conditions.

ii) the input displacement factor drops with increasing load as shown in Figure 7.25.

iii) due to the near unity input current distortion factor at all times, the variation of input power factor during the heating cycle is fully dominated by the displacement factor, and it is therefore approximately equal to the variation of displacement factor in Figure 7.25. This is in contrast with thevariation of input power factor in the unfiltered cycloinverter which, due to the large input distortion currents, is dominated by the input current distortion factor. The variation of input power factor, in the unfiltered inverter, is also given in Figure 7.25 for comparison.

iv) as the loading increases, the filter capacitors cannot meet the input current demand, which causes a reduction in the input voltage to the cycloinverter. This of course causes a consequent and substantial drop in the output power (see Figure 7.26).

v) an excessive voltage rise in the commutating circuit is substantially suppressed so that the ratio of maximum-to-minimum peak commutating capacitor voltage is about 1.22, while for an unfiltered cycloinverter with the same commutating circuit and under the same load conditions it is around 1.5 to 1.6 (see Figure 7.26).

Clearly, the input filter design has been successful in achieving its principal aims, that is, the input distortion currents are eliminated and an excessive rise of the commutating capacitor voltage at high loads is prevented. However, this is achieved at the cost of both a deterioration in the output current waveform* and a reduced output power. In a series commutation circuit, the commutating capacitor voltage cannot, of course, be suppressed without an accompanying drop in the output power. Depending on the nature of the application, a compromise between the voltage ratings of the commutating circuit components (i.e. the peak thyristor voltage and the commutating capacitor voltage) and the high-load output power requirement should therefore be reached. In the input filter design presented above, emphasis was given to the low component voltage rating for the purpose of demonstration, by performing the design at the lowest load, i.e. E. Alternatively, it is possible, by performing the design at higher loads, to allow an increase in the commutating component voltage ratings, but to prevent any substantial drop in the output power. This of course, will require filter components of higher VA ratings.

---

* Clearly, the output current distortion is partly caused by the non-multiple operational frequency.

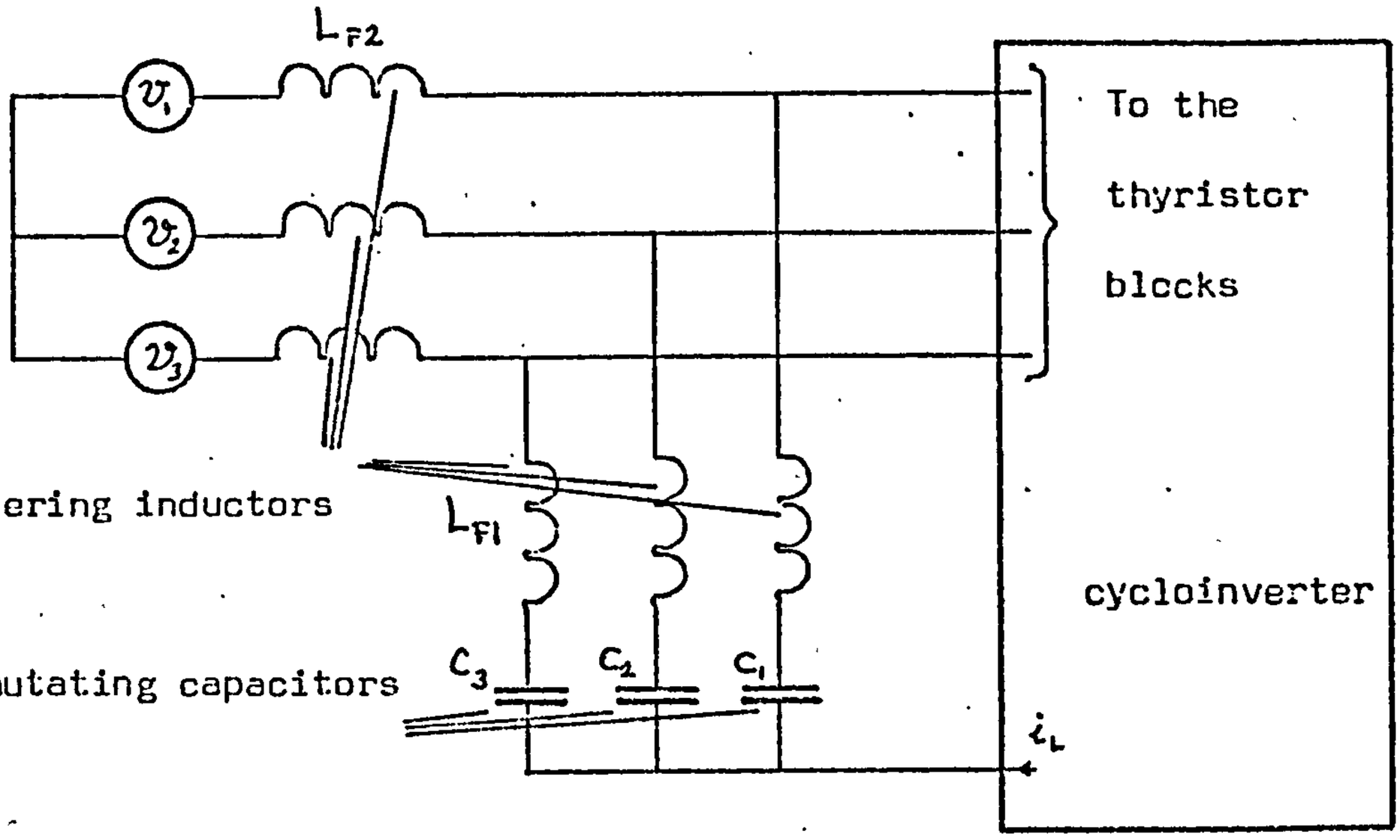

Figure 7.1 Tuned-branch input filter applied to the cycloinverter

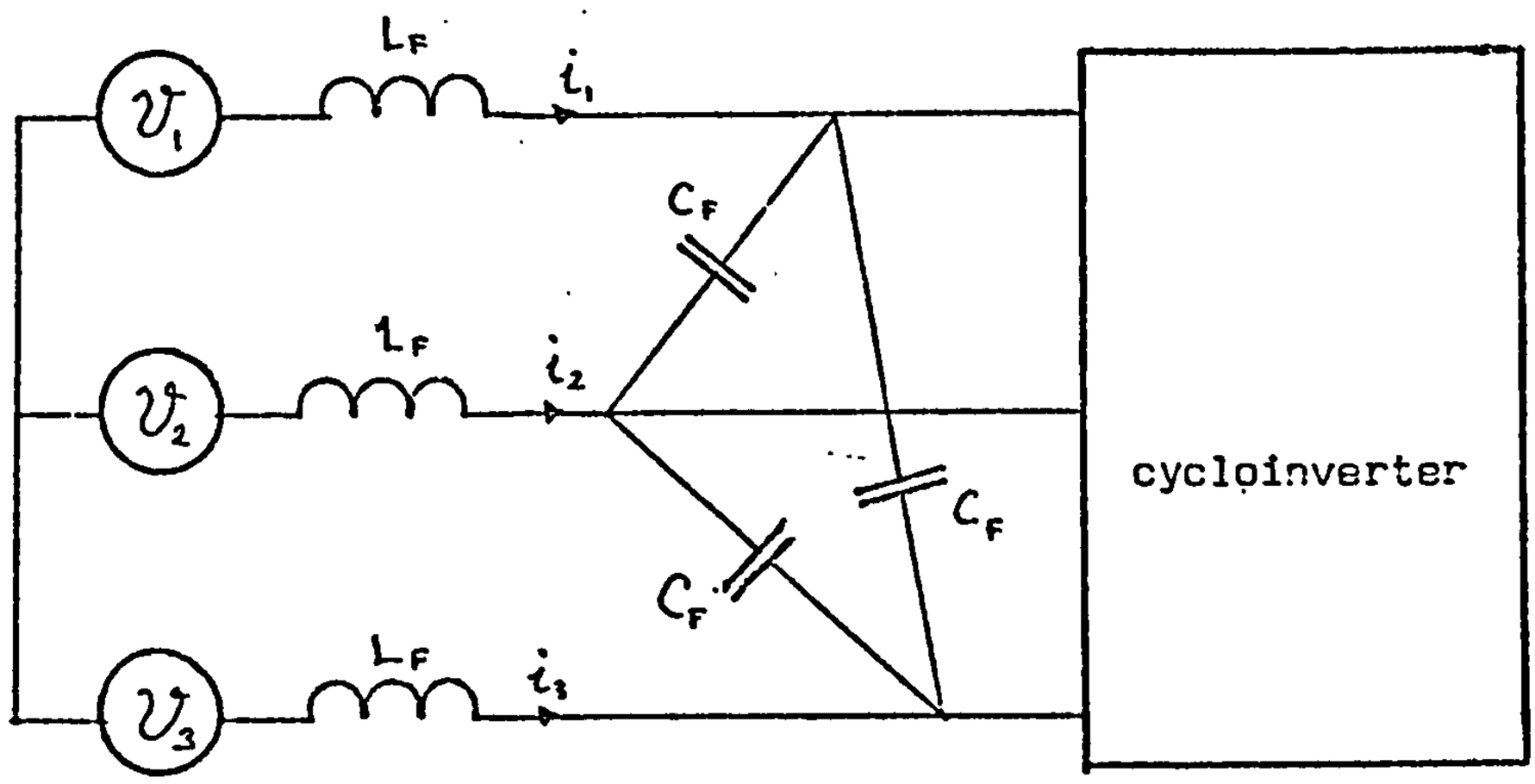

Figure 7.2 An LC-input filter for the cycloinverter

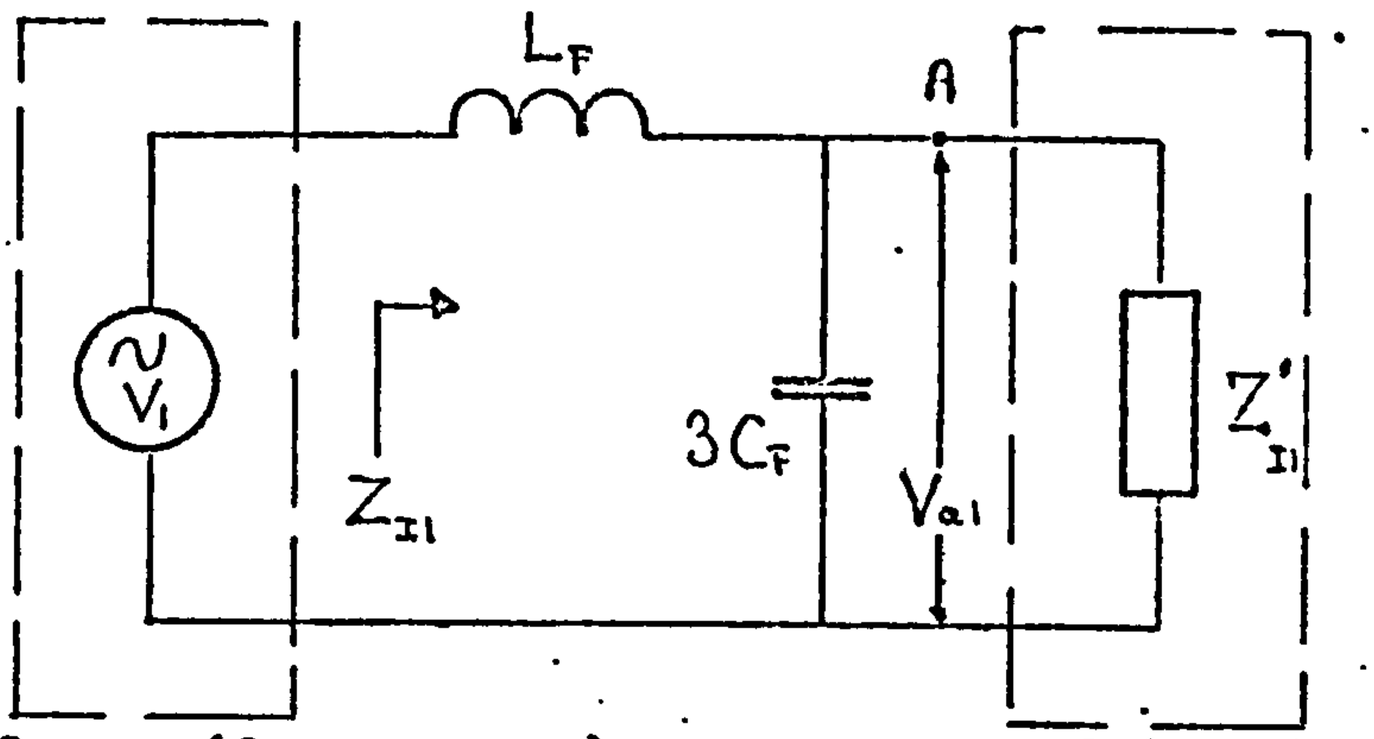

Figure 7.3 The source frequency model of the input filter-cycloinverter configuration

jb

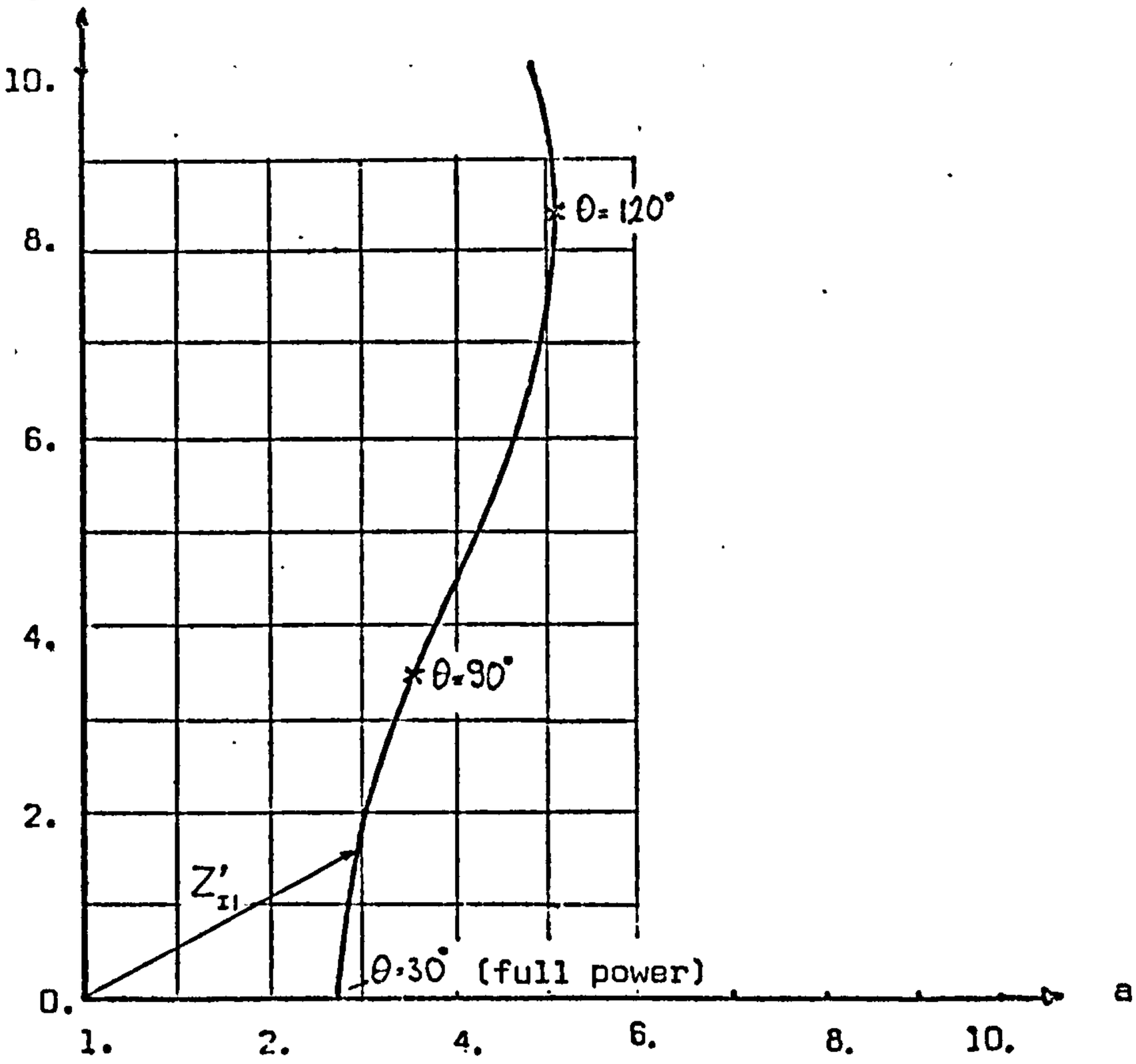

Figure 7.4 Variation of the reactive and resistive components of the cycloinverter input impedance with the power control angle θ (f_o = 1050 Hz, X_1 = 1.2 p.u, X_c = 1.3 p.u)

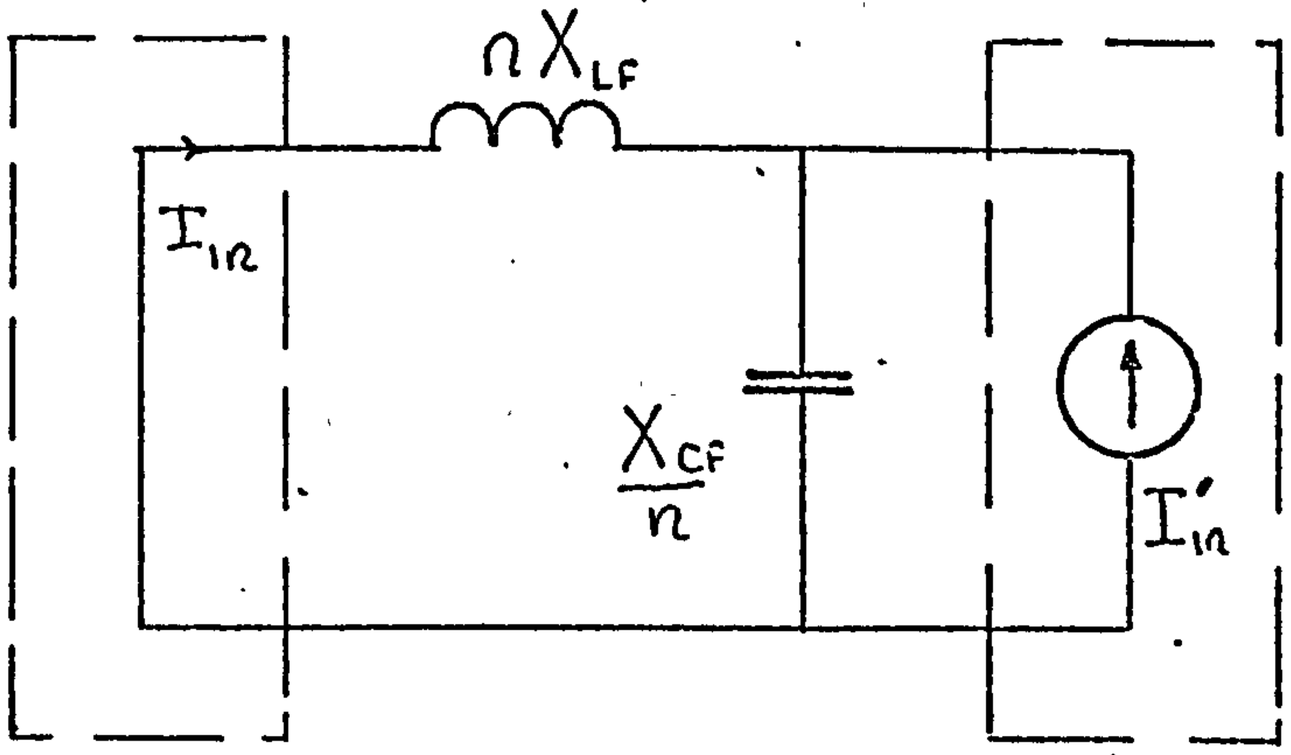

Figure 7.5 Distortion frequency model of the input filter-cycloinverter configuration

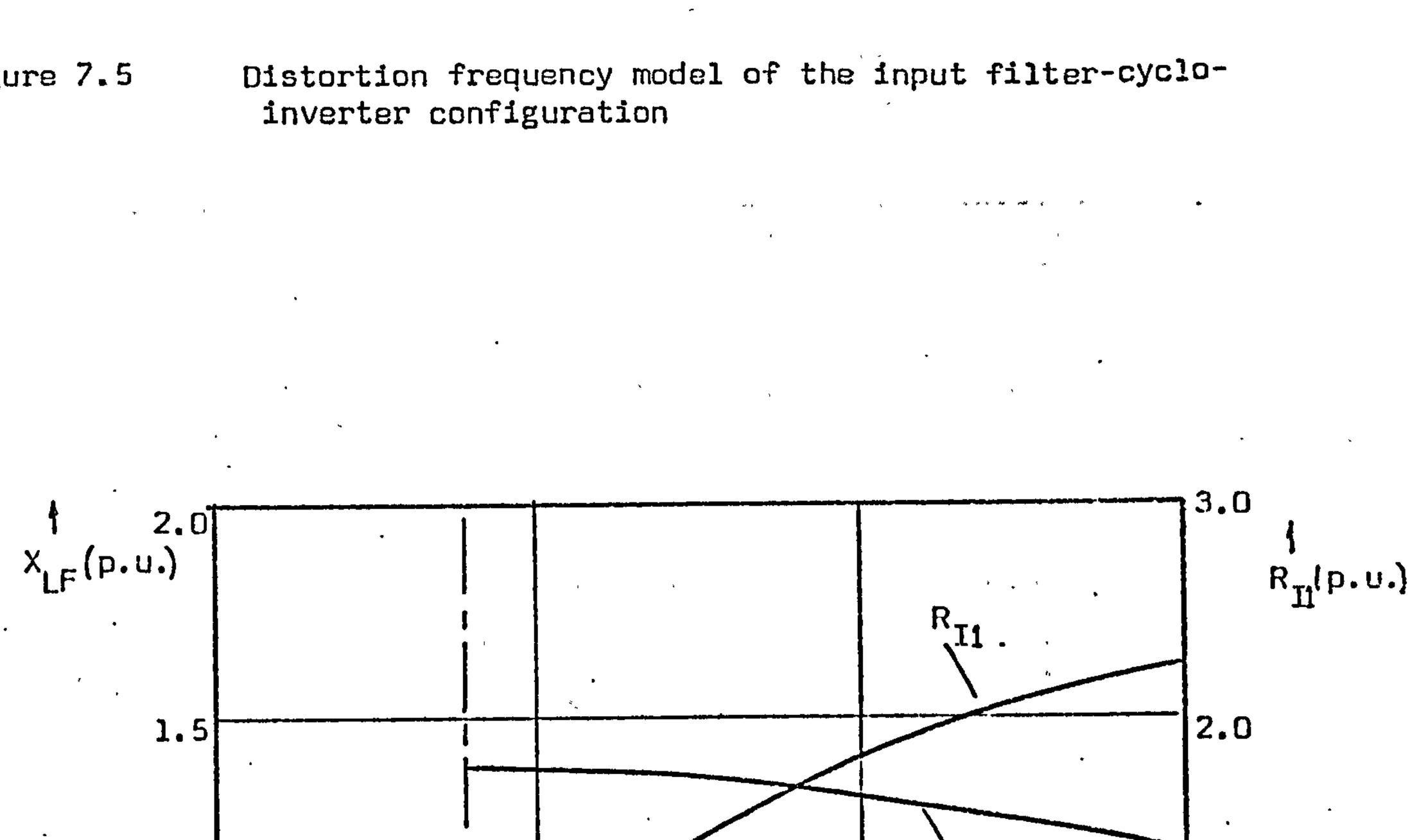

Figure 7.6 Variation with X_{CF} of R_{I1} and X_{LF} to satisfy the input filter design constraints

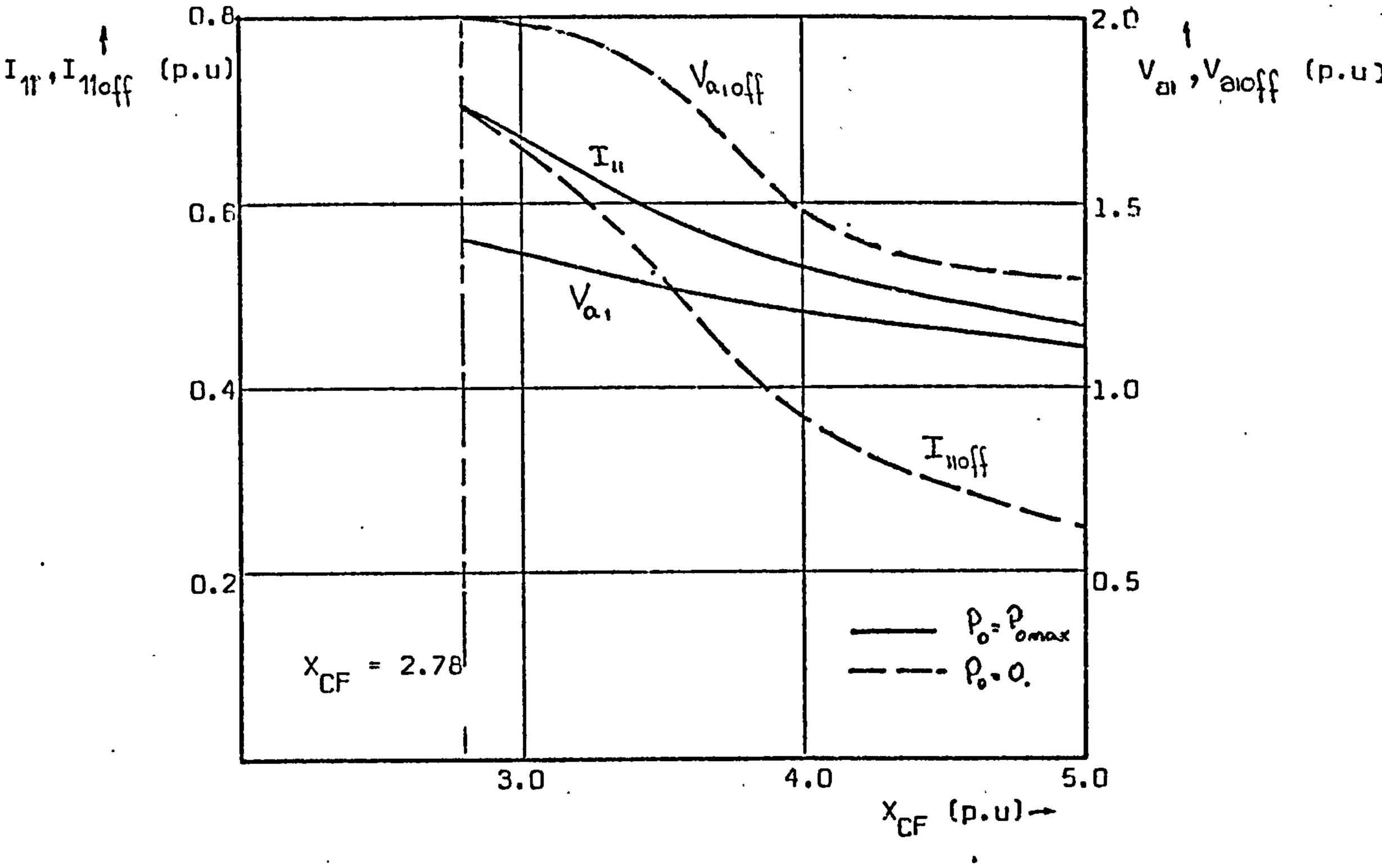

Figure 7.7 Variation with X_{CF} of various input quantities at zero and full output power

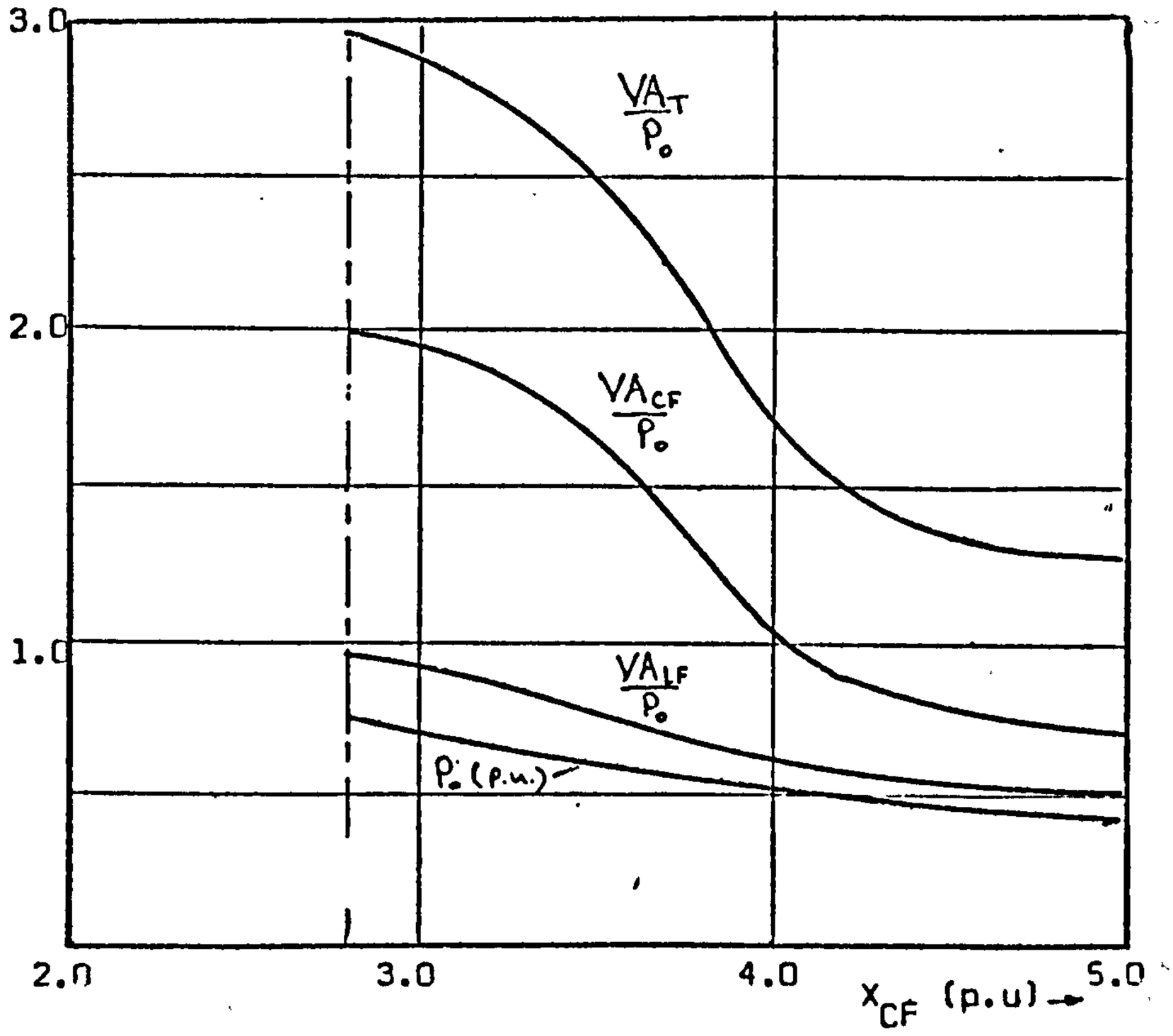

Figure 7.8 Variation of input filter component ratings and output power with X_{CF}

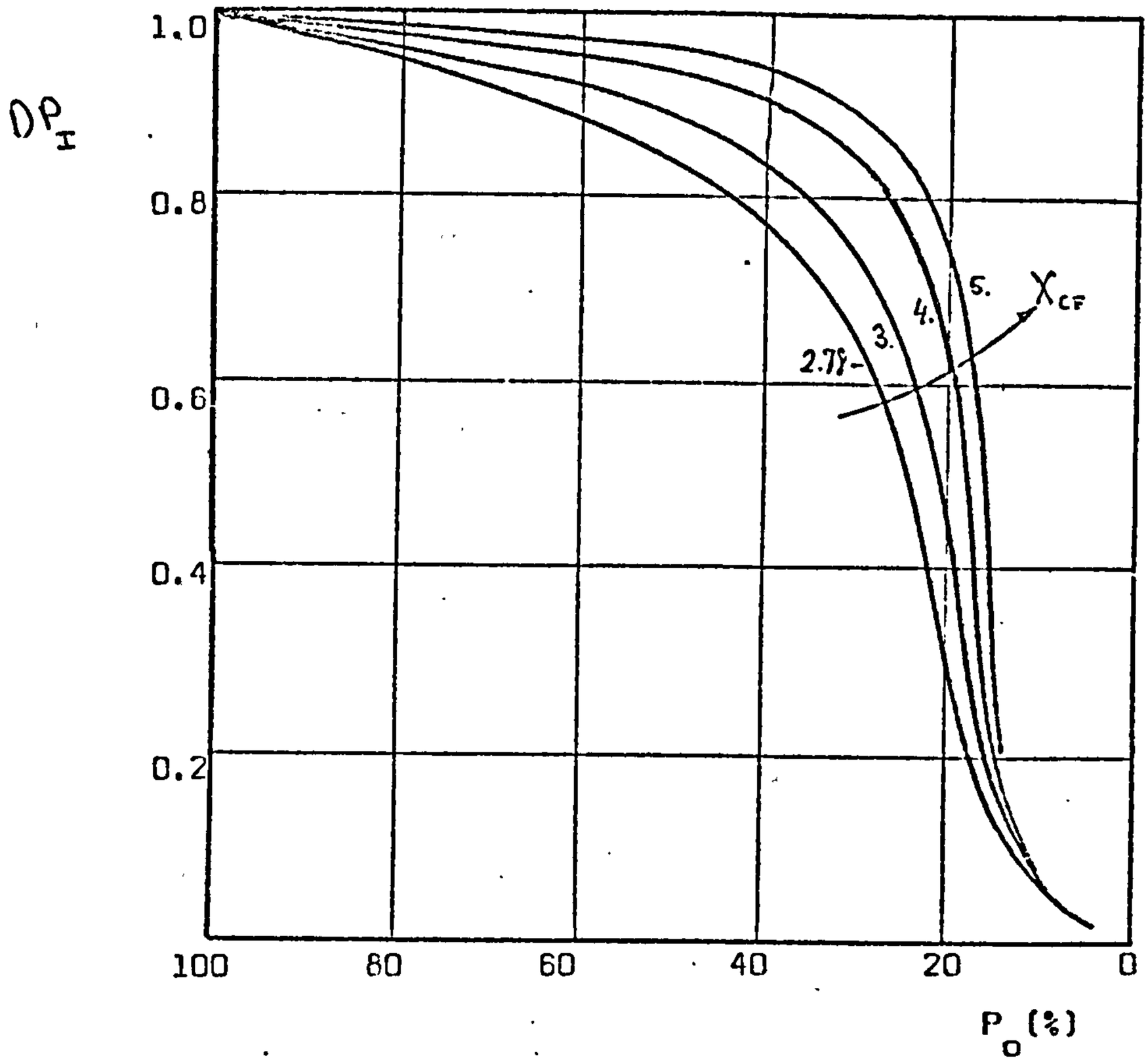

Figure 7.9 Variation of displacement factor with output power for different design values of X_{CF}

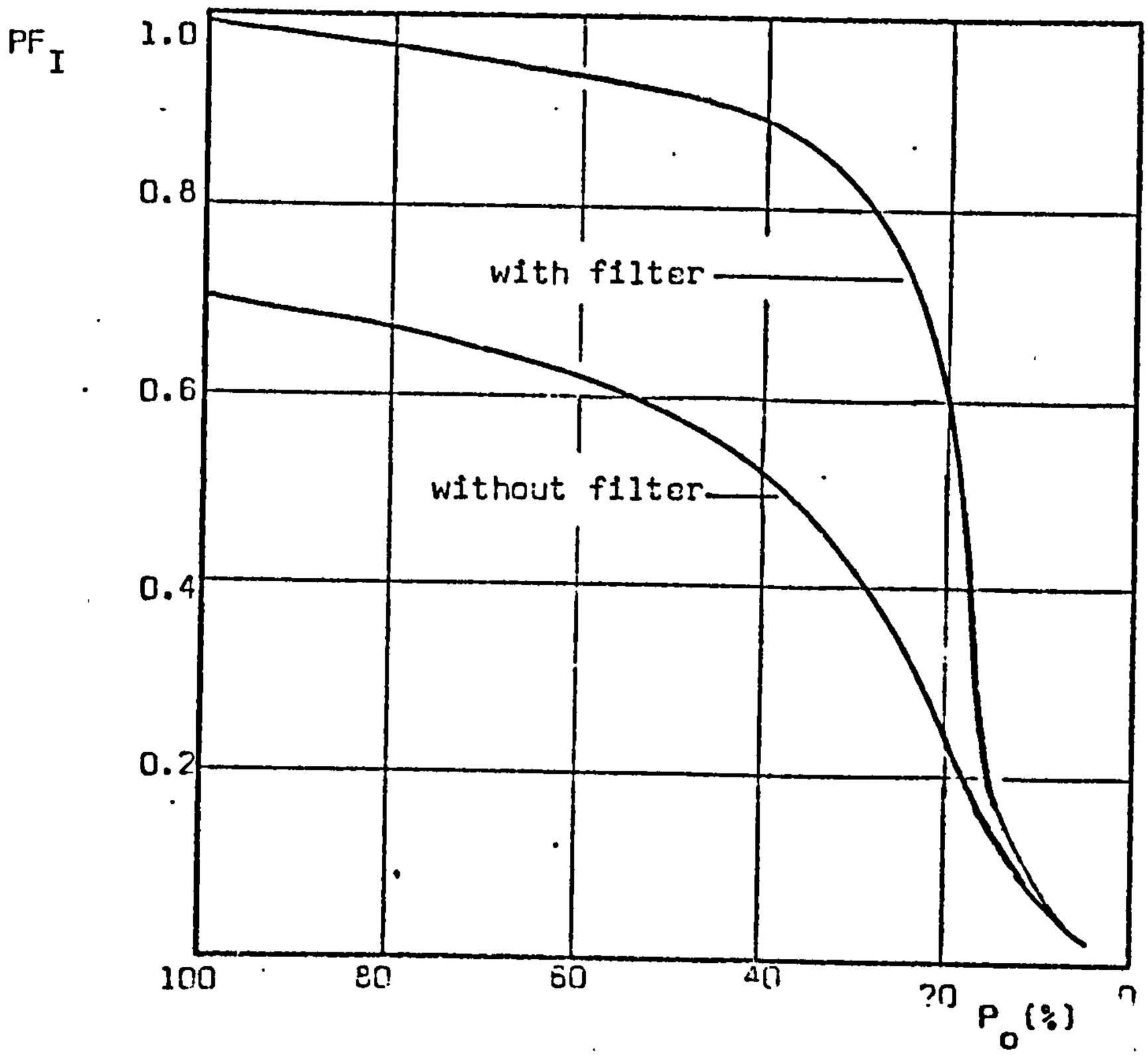

Figure 7.10 Comparison of the variation with output power of input power factor in a cycloinverter with optimum input filter and without input filter

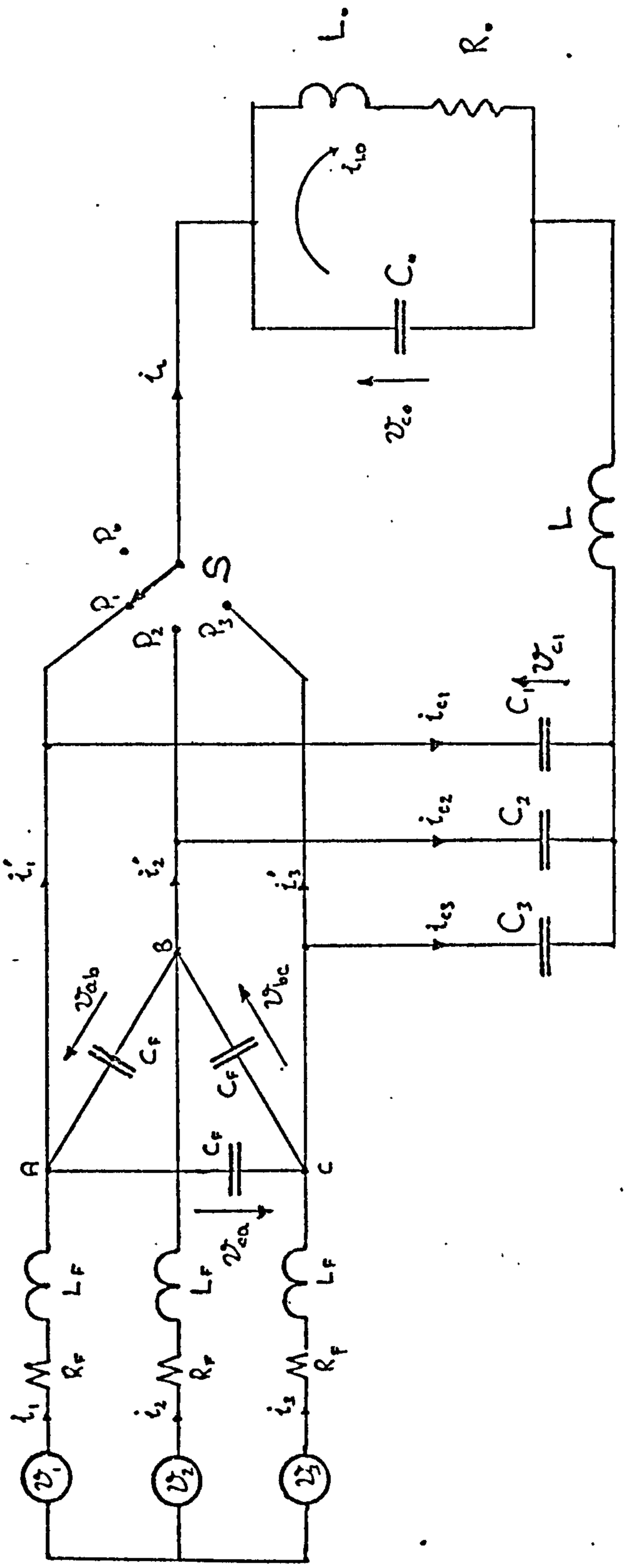

Figure 7.11 Simplified power circuit diagram of a cycloinverter with an LC-type input filter

($C_1 = C_2 = C_3 = C$)

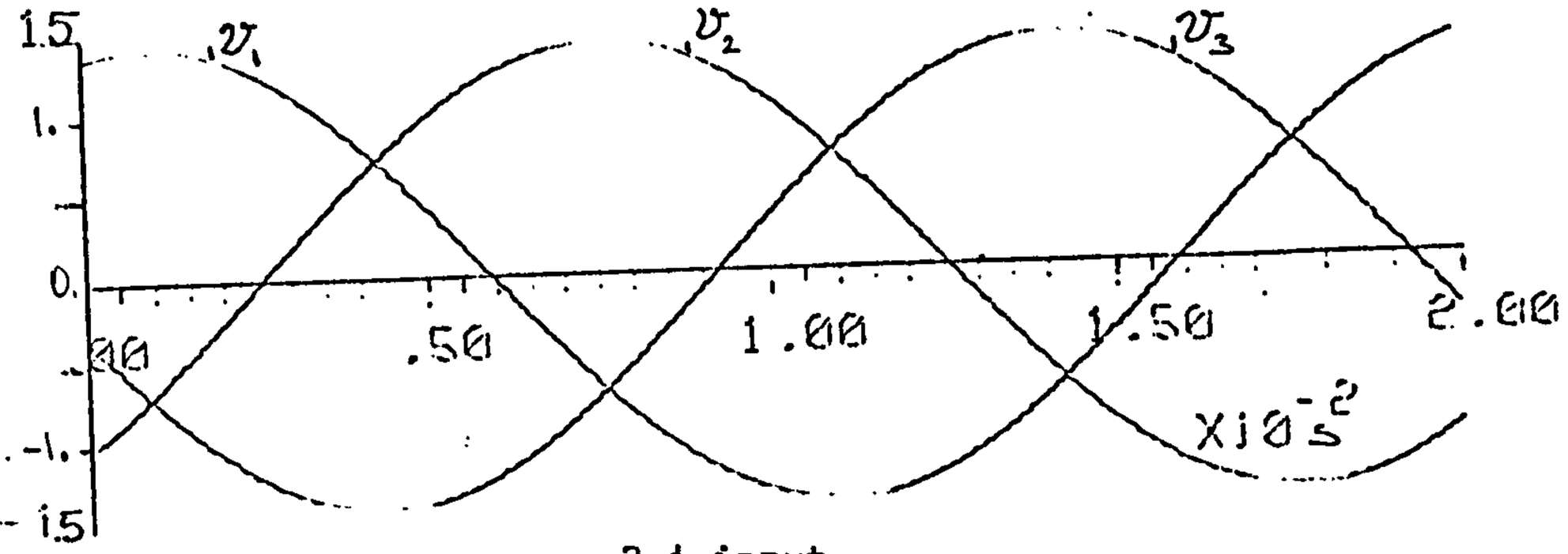

3-ϕ input

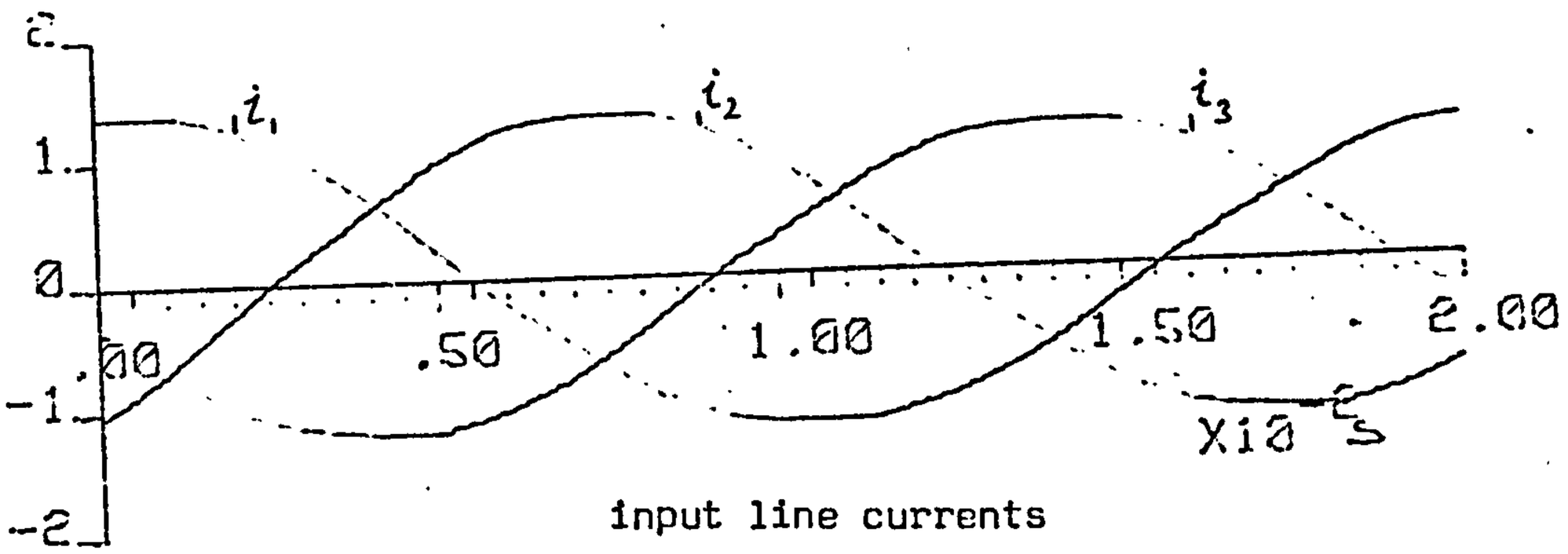

input line currents

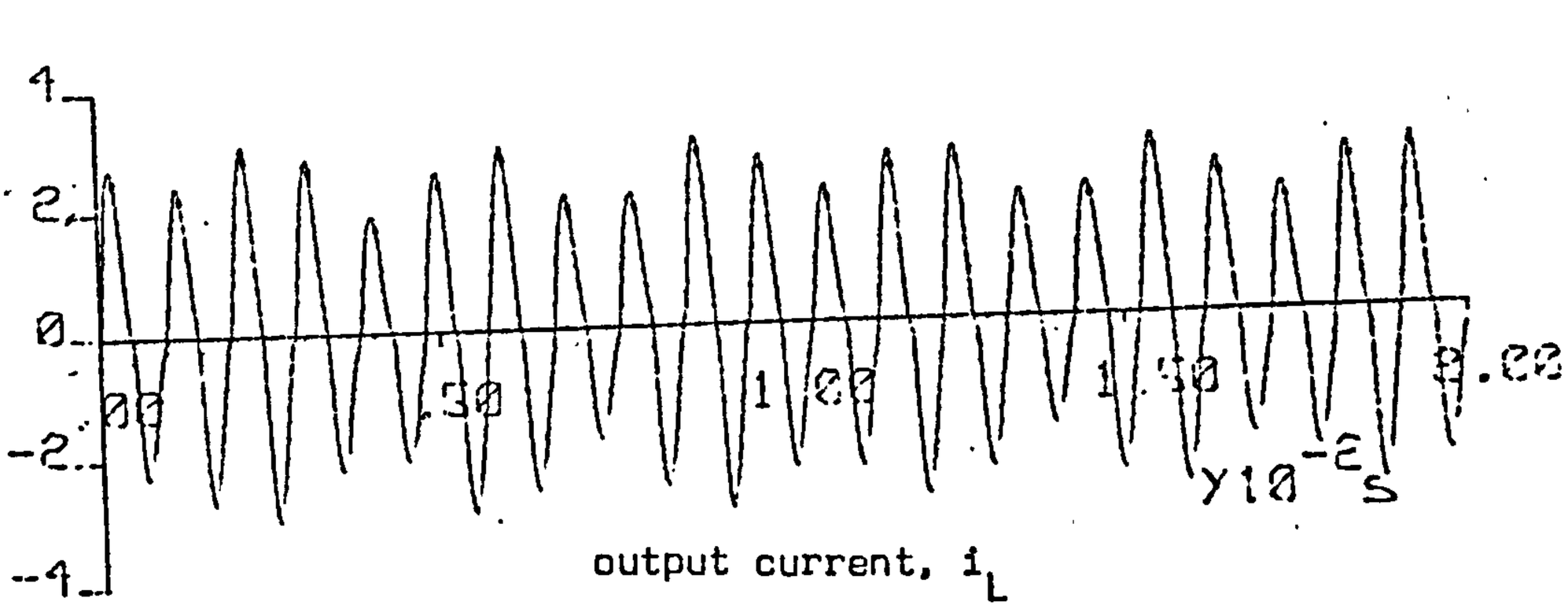

output current, i_L

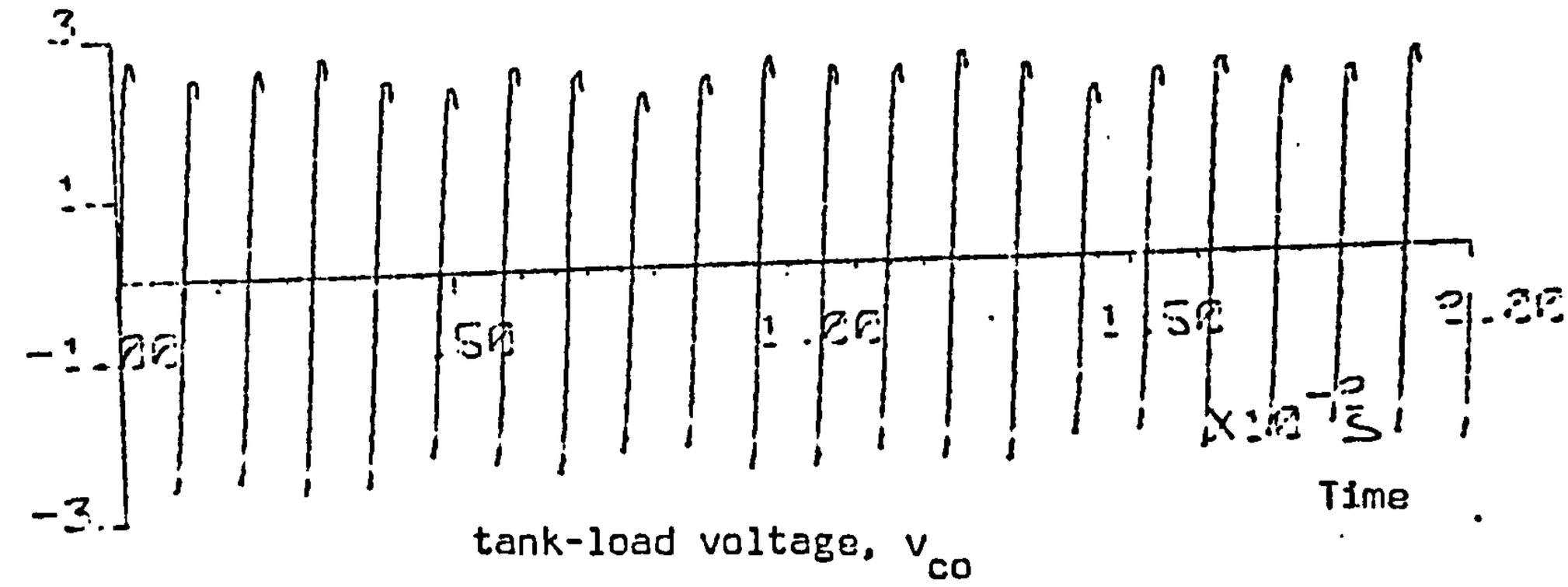

tank-load voltage, v_{co}

Figure 7.12 Computed waveforms for a cycloinverter with input filter variables X_{CF} = 2.78 p.u. and X_{LF} = 1.39 p.u. (f_o = 1050 Hz, X_L = 1.2 p.u., X_c = 1.3 p.u., $\theta = 30^o$)

/continued

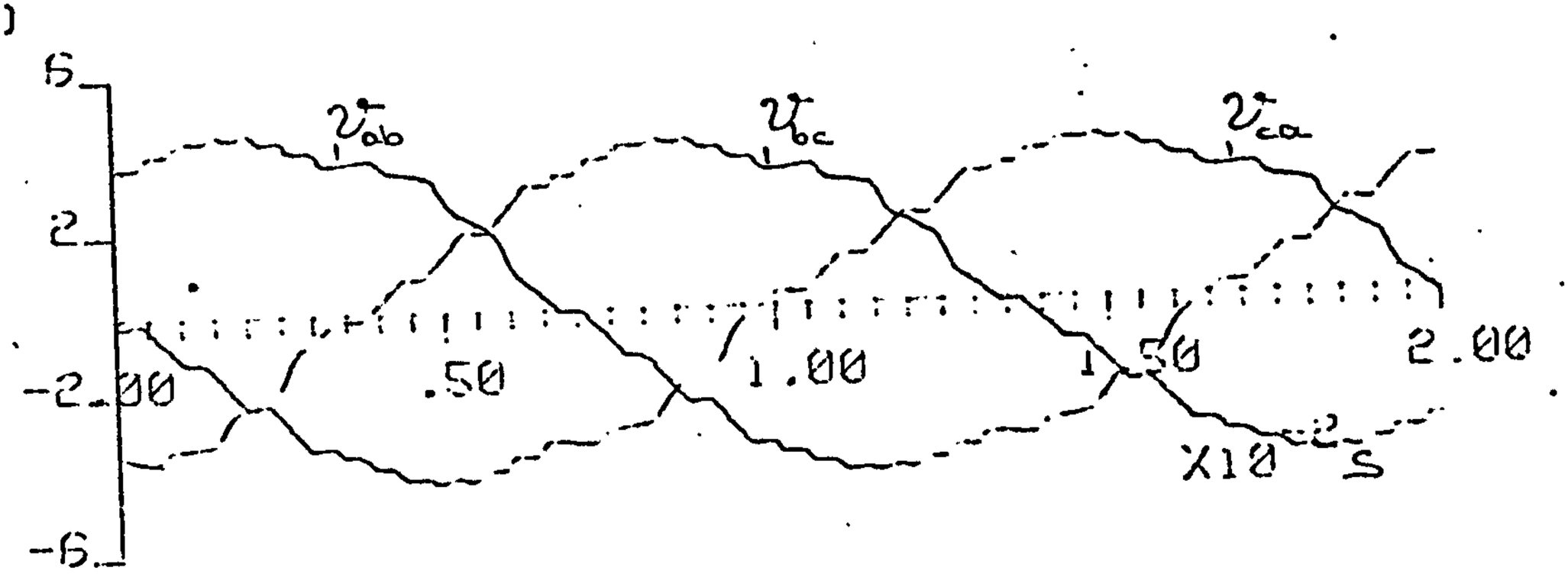

filter capacitor voltages

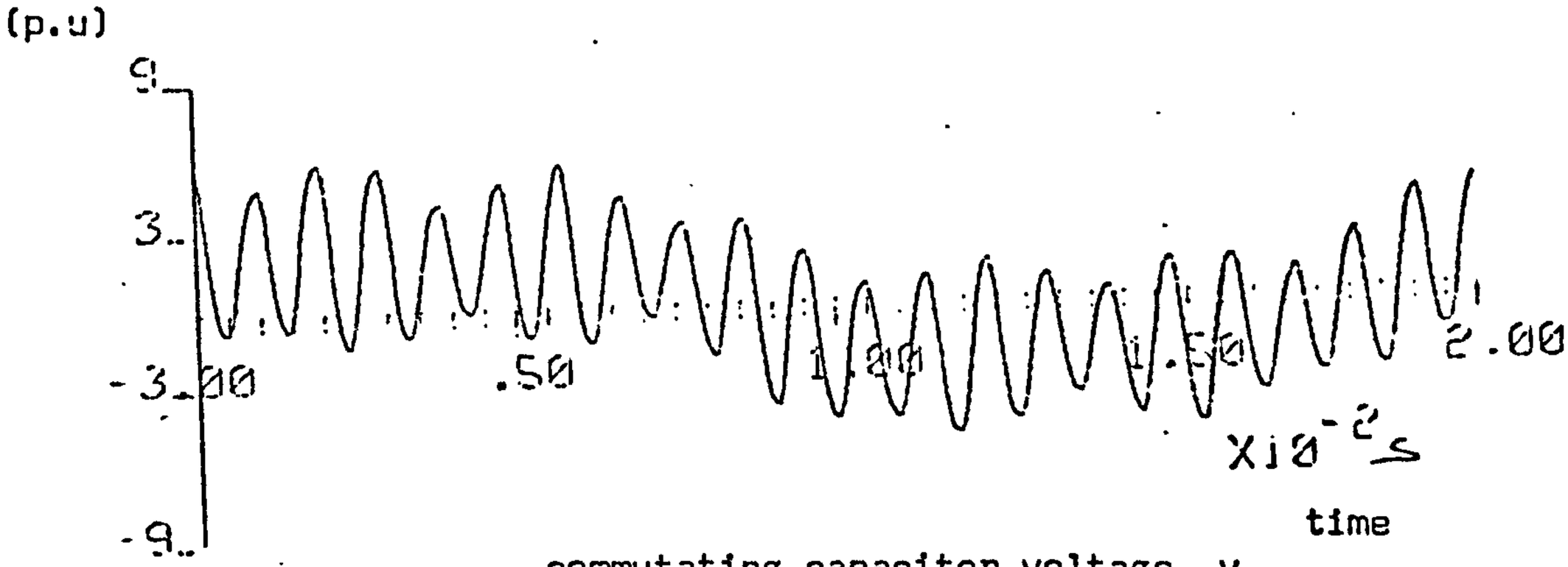

commutating capacitor voltage, v_{c1}

Figure 7.12 continuation

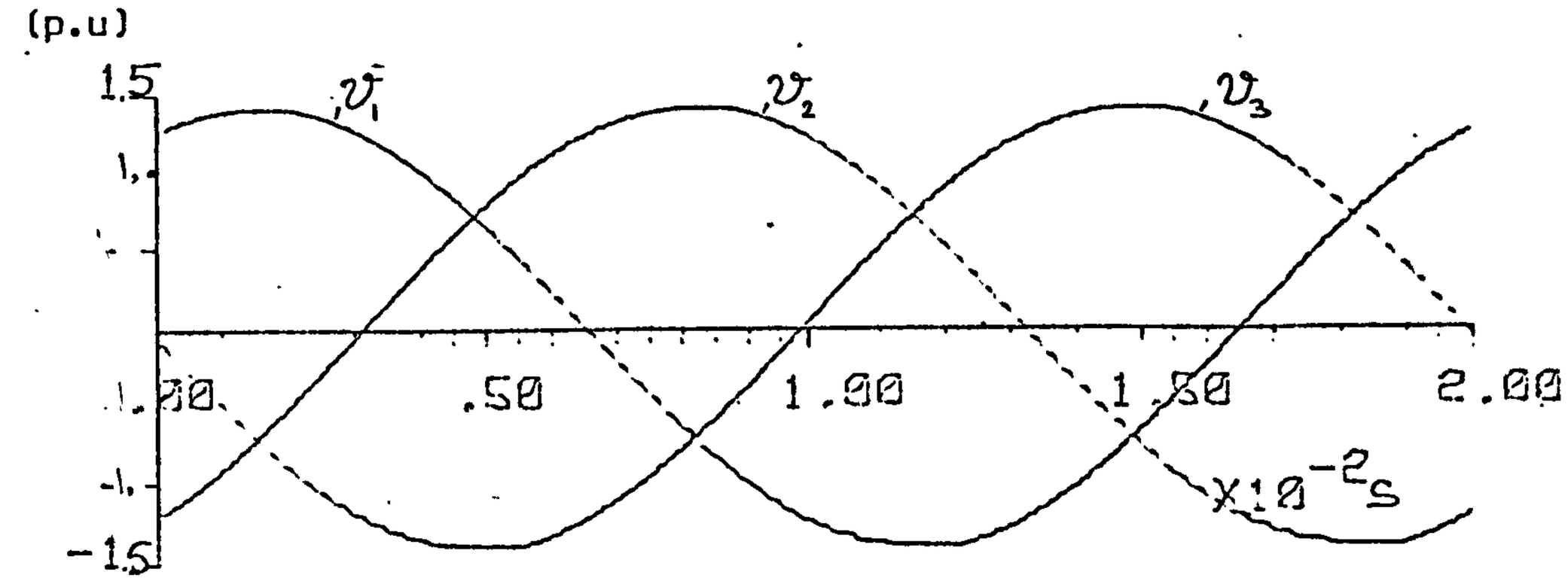

Figure 7.13 Computed waveforms for a cycloinverter with input filter variables X_{CF} = 4.0 p.u. and X_{LF} = 1.3 p.u.

(f_o = 1050 Hz, X_L = 1.2 p.u., X_c = 1.3. p.u., θ = 30o)

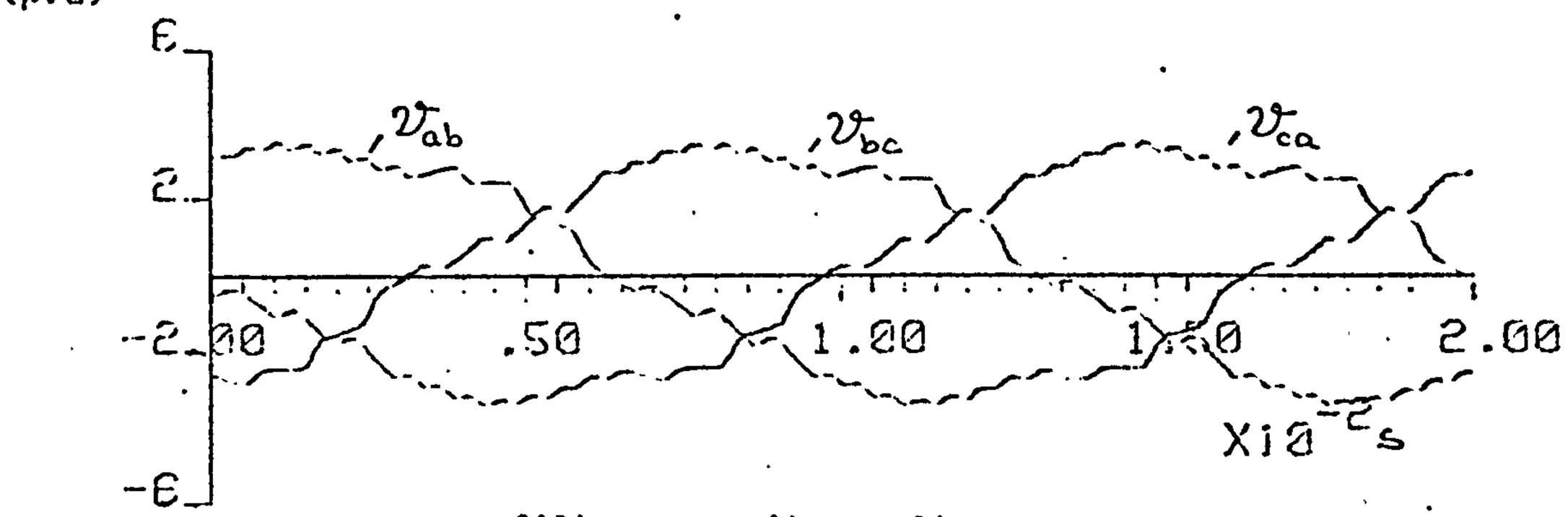

filter capacitor voltages

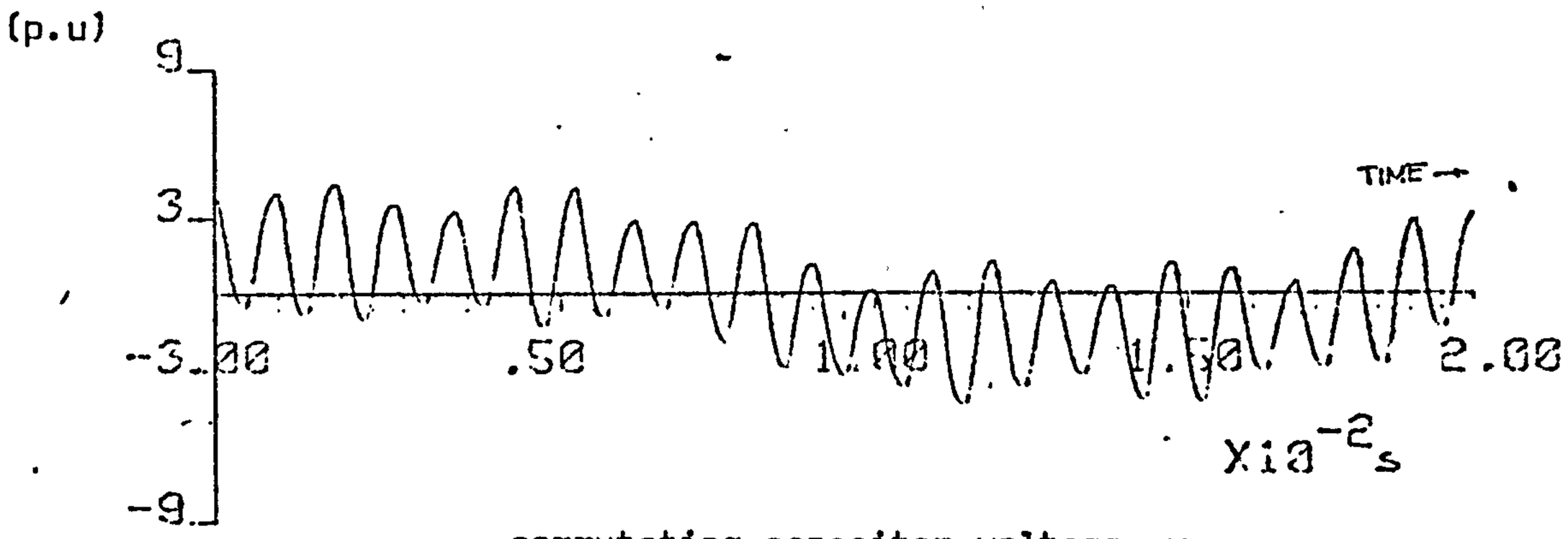

commutating capacitor voltage, v_{c1}

Figure 7.13 Continuation

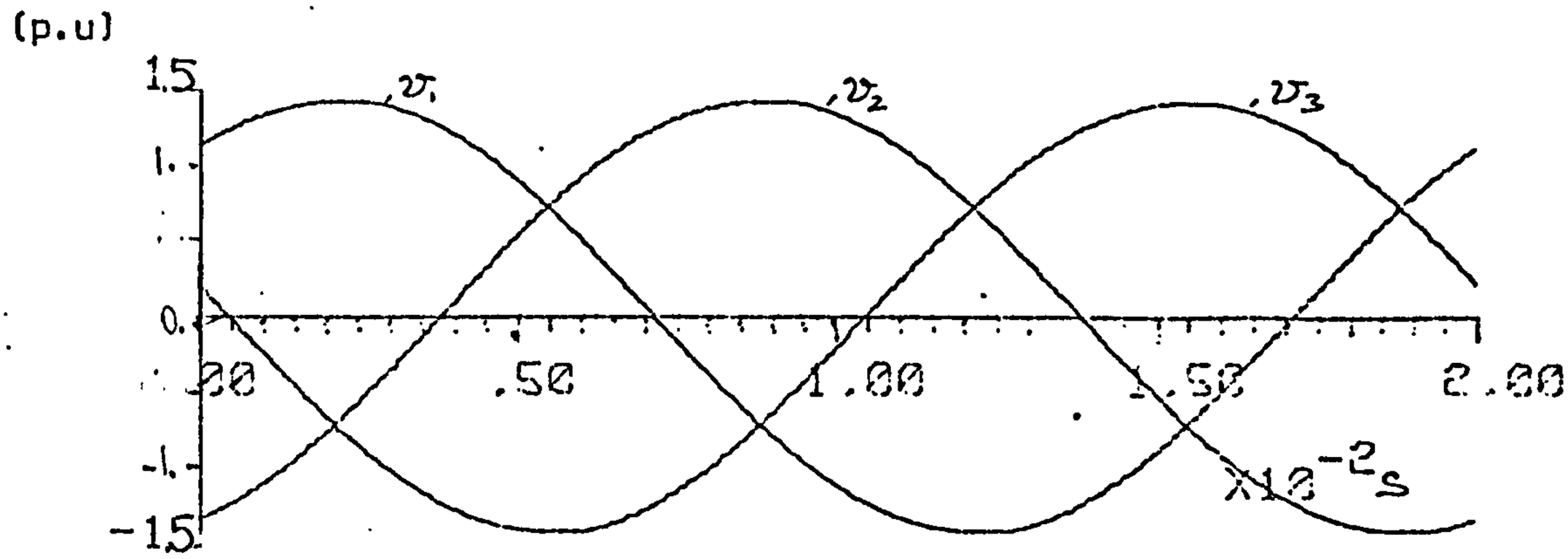

3-ϕ input

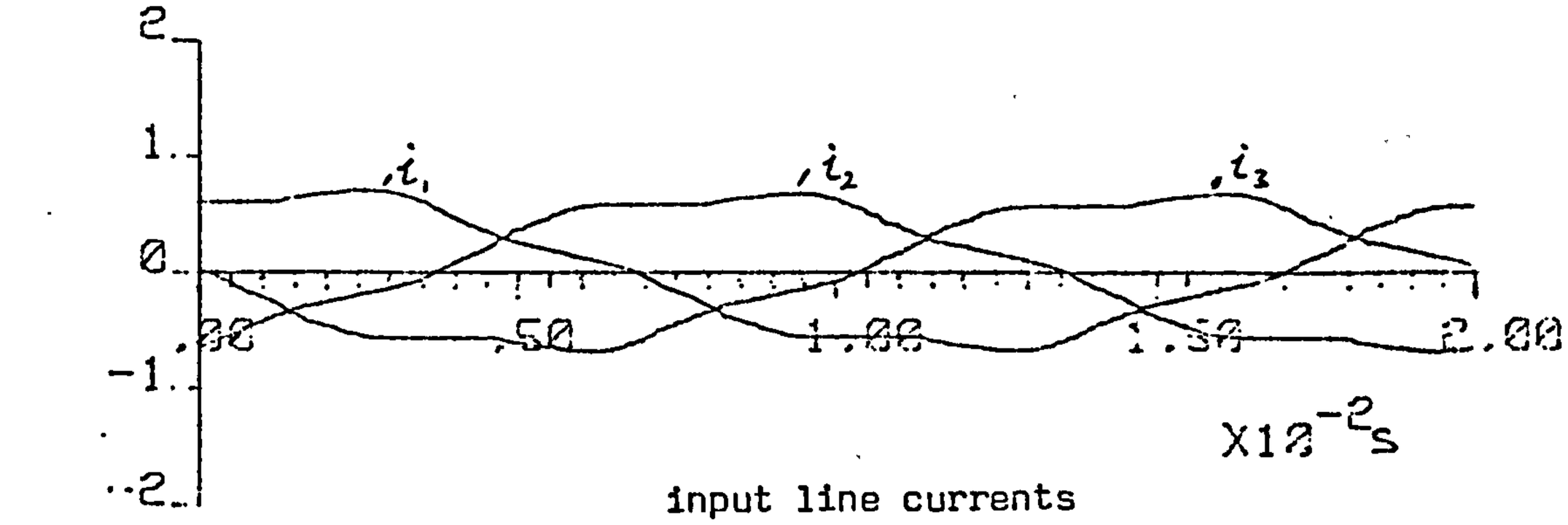

input line currents

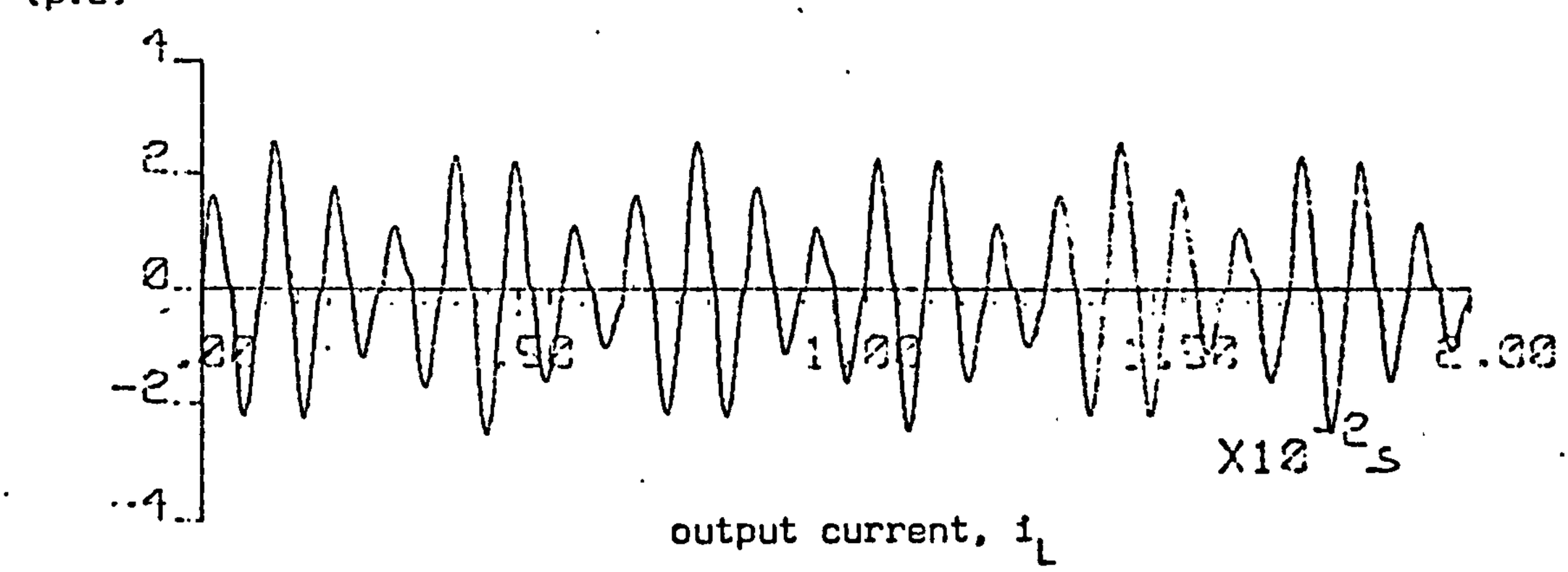

output current, i_L

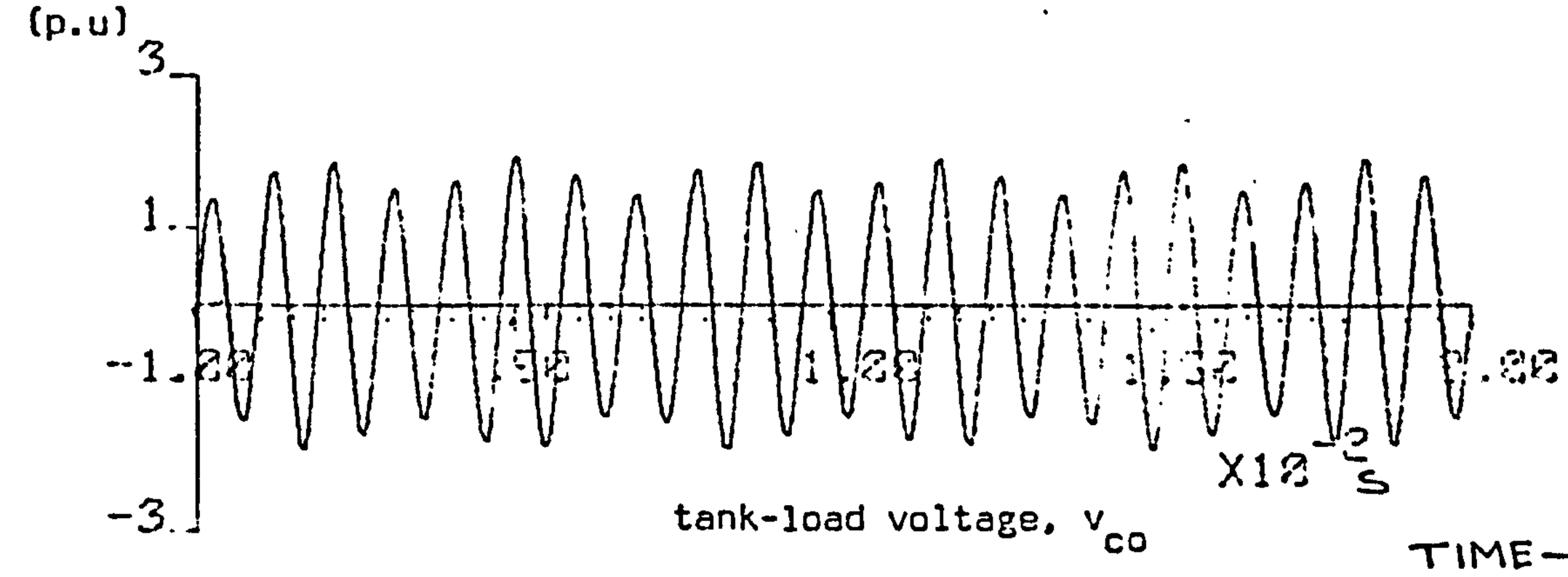

tank-load voltage, v_{co}

Figure 7.14 Computed waveforms for a cycloinverter with input filter variables X_{CF} = 6.5 p.u, X_{LF} = 1.18 p.u. (f_o = 1050 Hz, X_L = 1.2 p.u, X_c = 1.3 p.u, $\theta = 30^o$)

/Continued

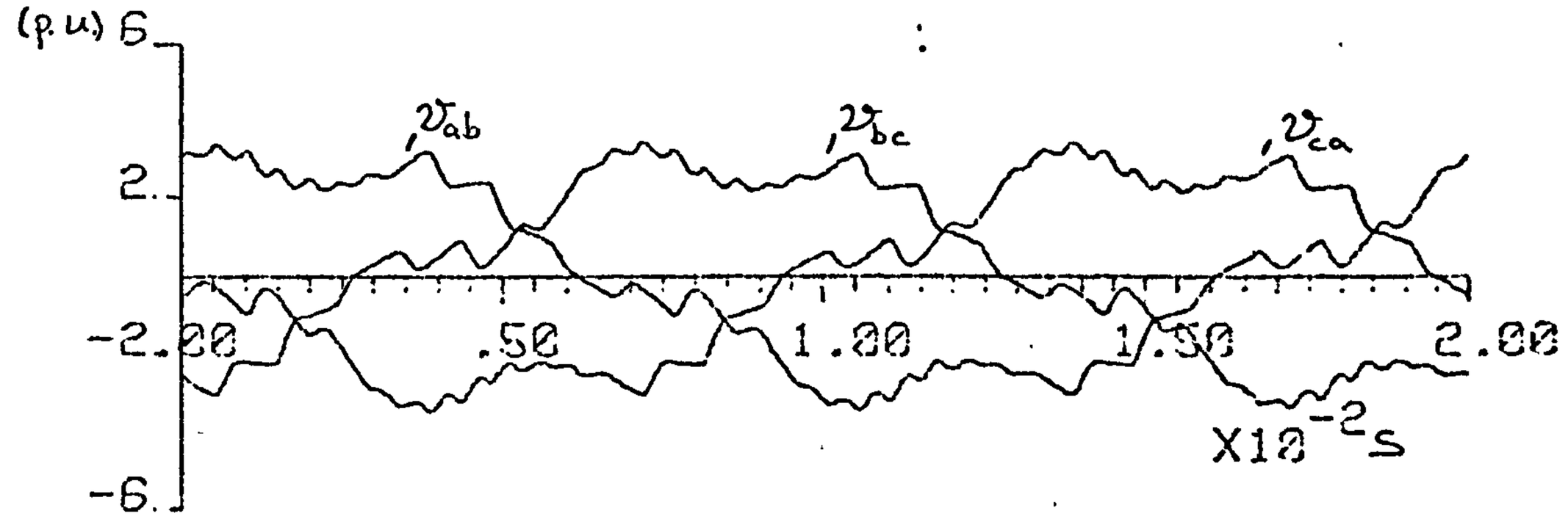

filter capacitor voltages

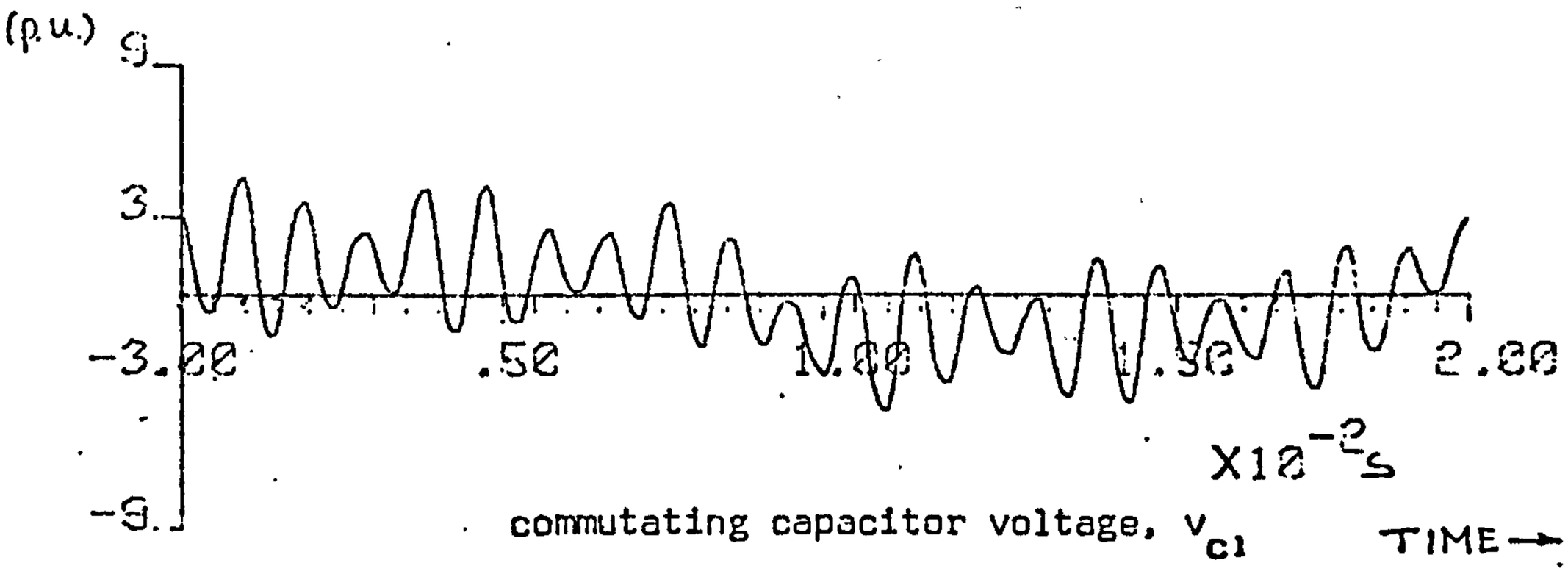

commutating capacitor voltage, v_{c1}

Figure 7.14 Continuation

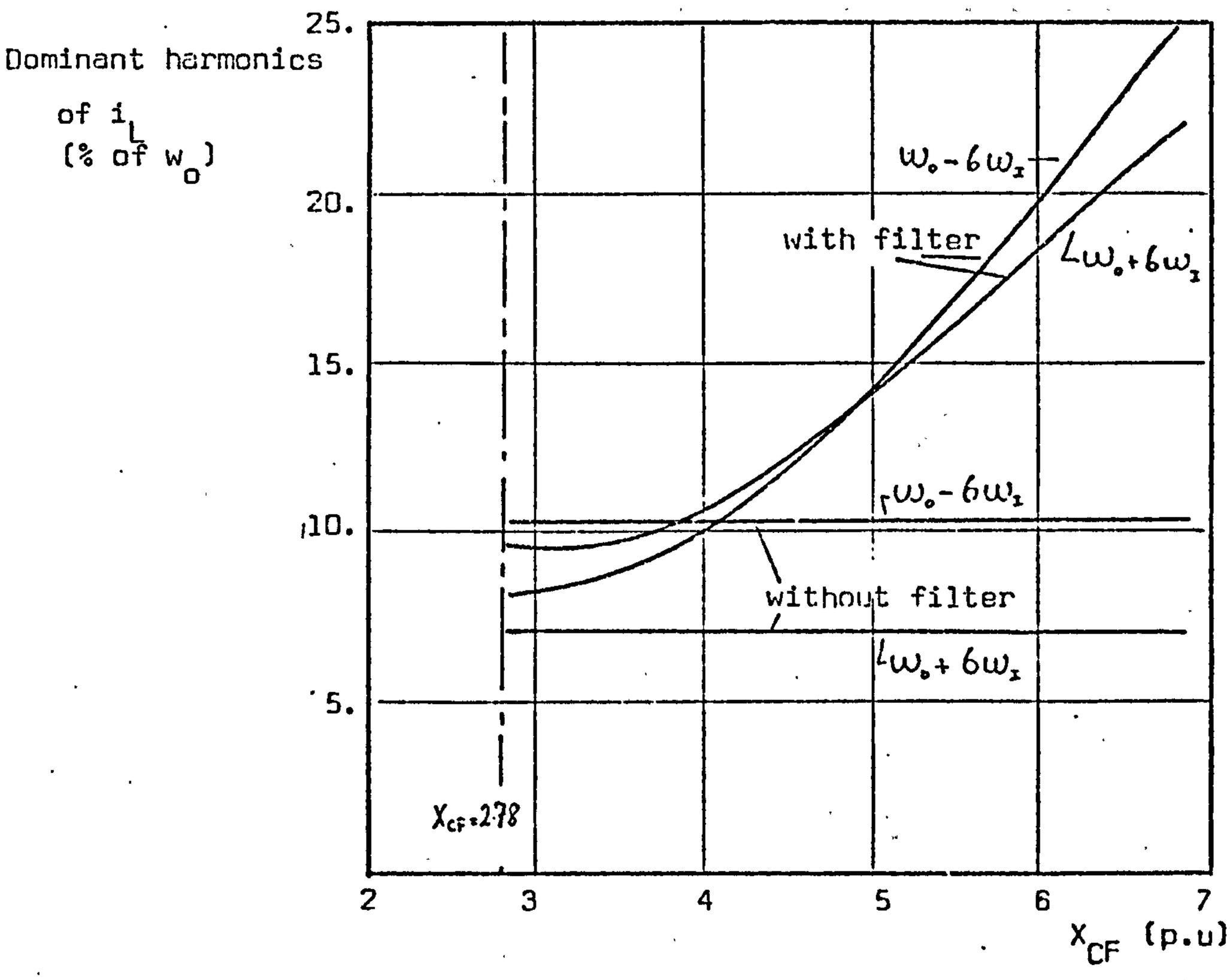

Figure 7.15 Variation of dominant harmonics of the cycloinverter output current with X_{CF}.
(Output harmonics without input shown merely for comparison)

f_o = 1050 Hz, X_L = 1.2 p.u, X_c = 1.3 p.u, $\theta = 30^o$

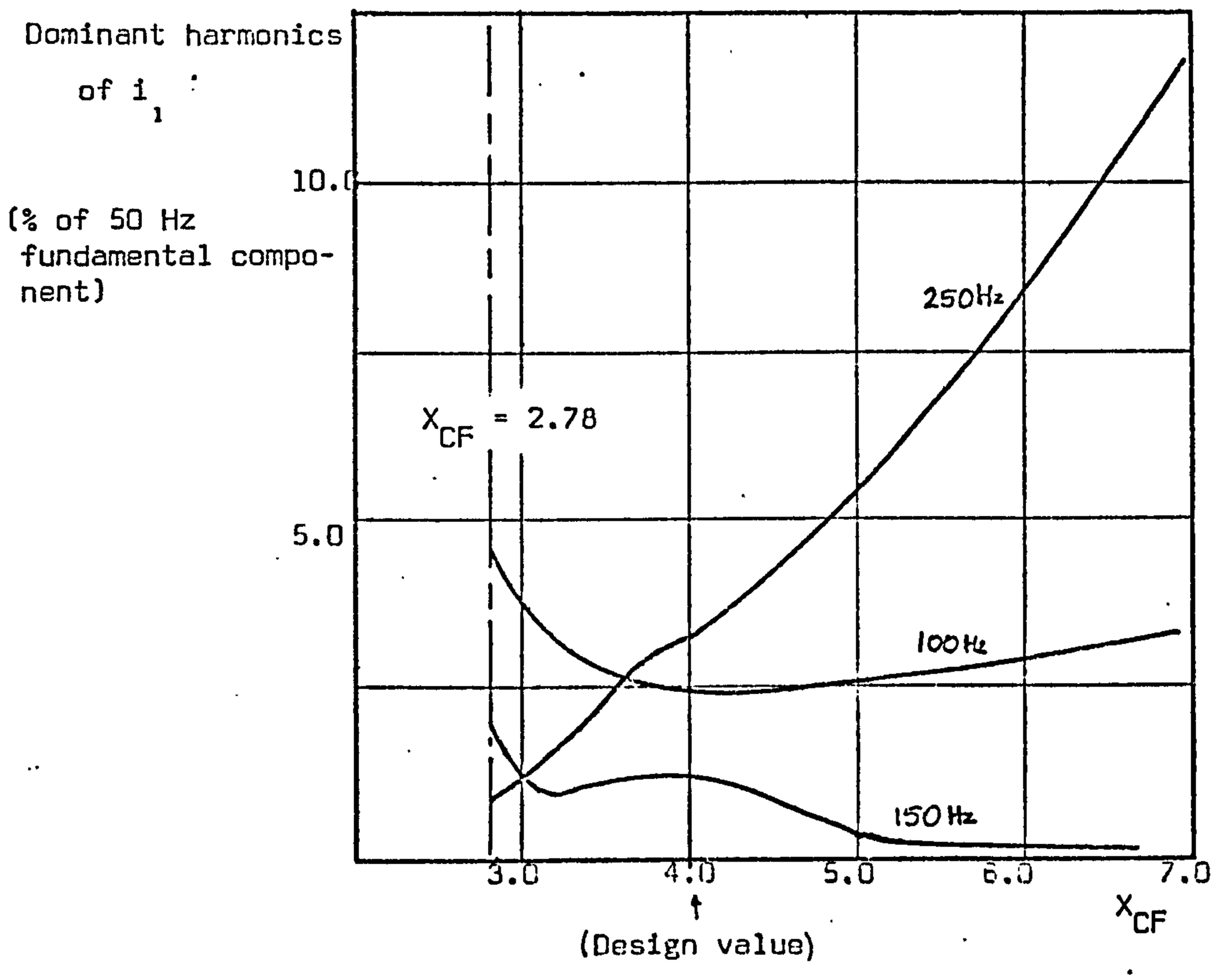

Figure 7.16 Variation of dominant harmonics of input line current with X_{CF}
(f_o = 1050 Hz, X_L = 1.2 p.u, X_c = 1.3 p.u, $\theta = 30^o$)

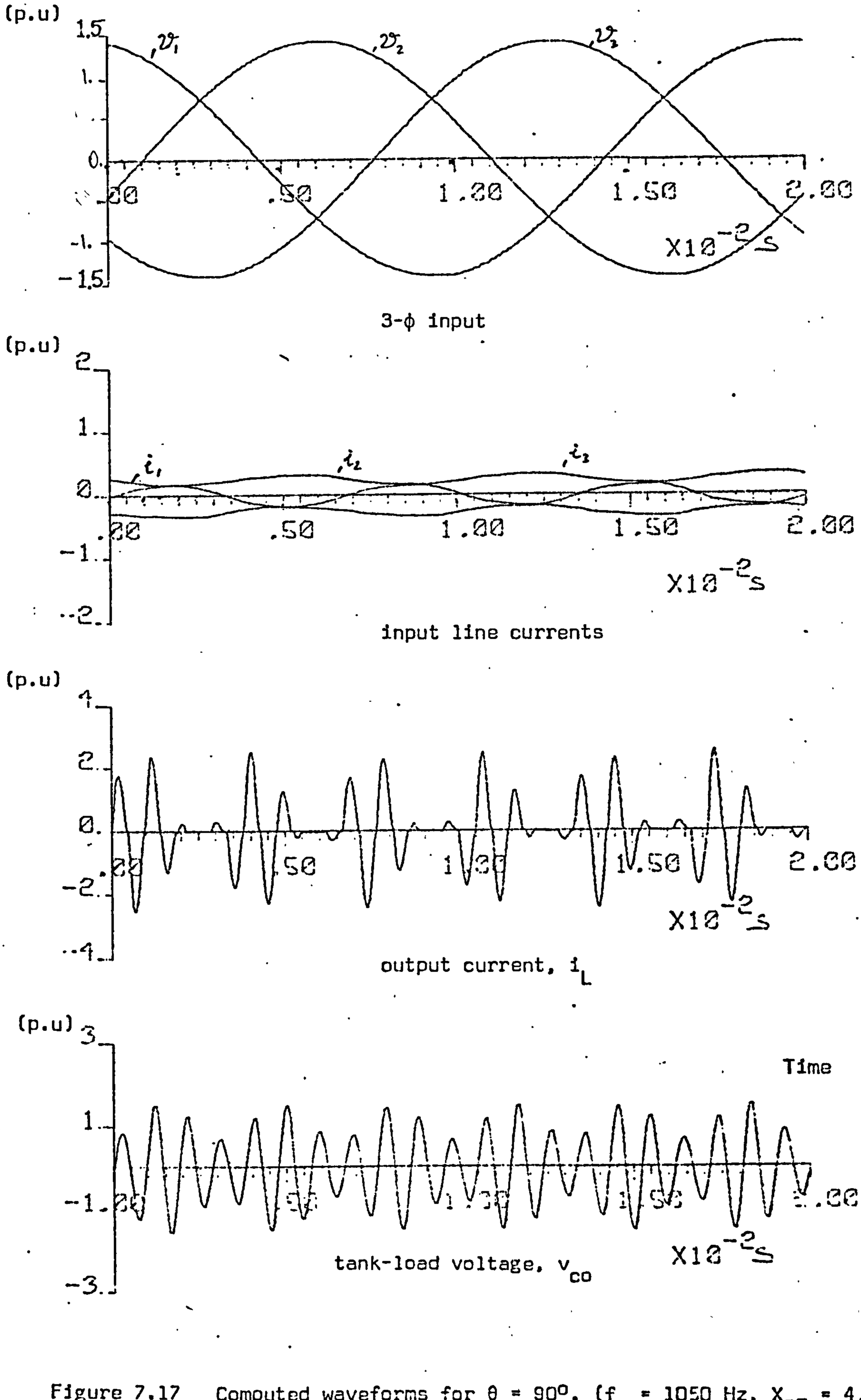

Figure 7.17 Computed waveforms for $\theta = 90^{o}$. (f_o = 1050 Hz, X_{CF} = 4, X_{LF} = 1.3, X_L = 1.2, X_c = 1.3 p.u, Q_L = 5)

/Continued.

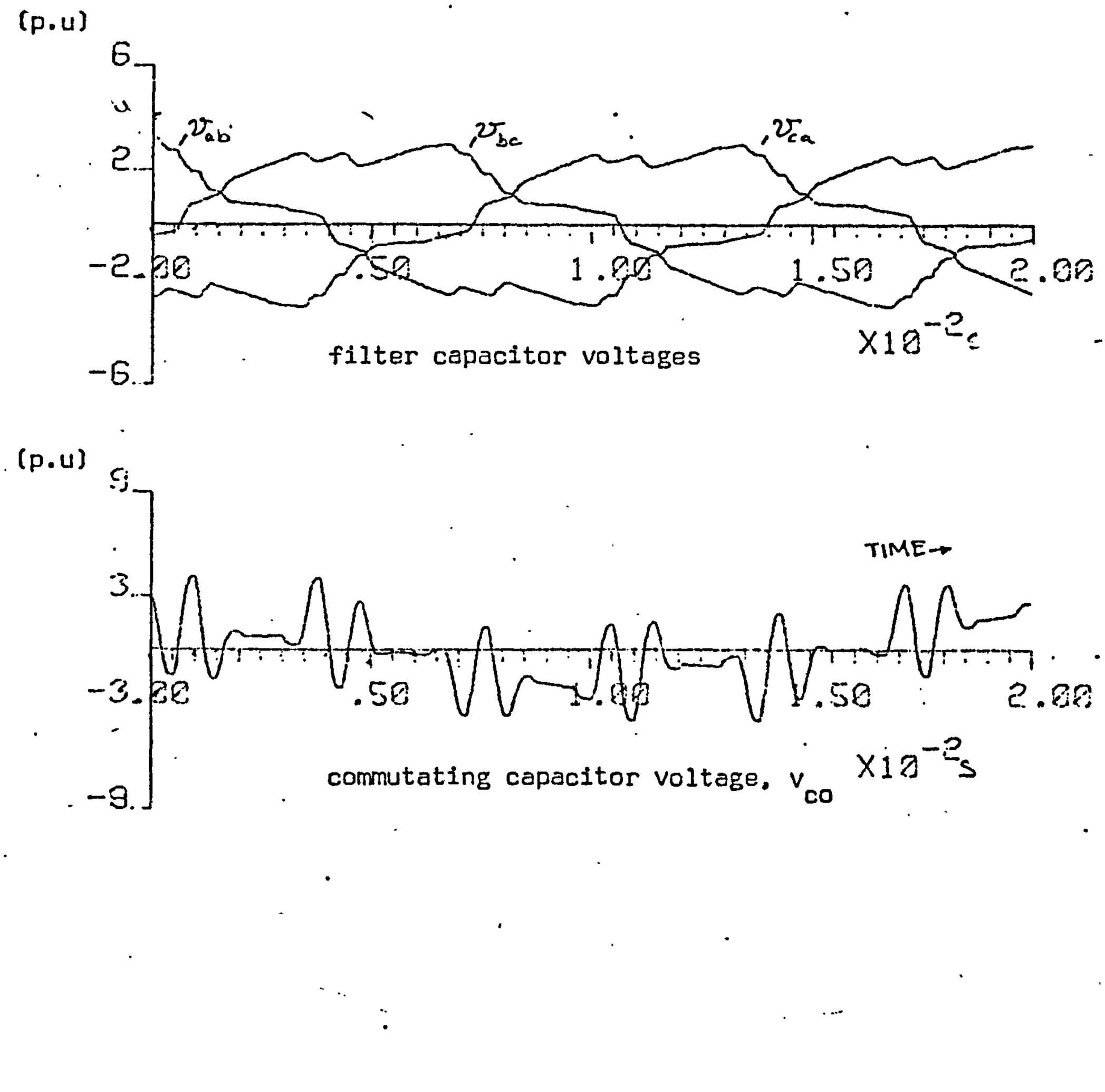

Figure 7.17 Continuation

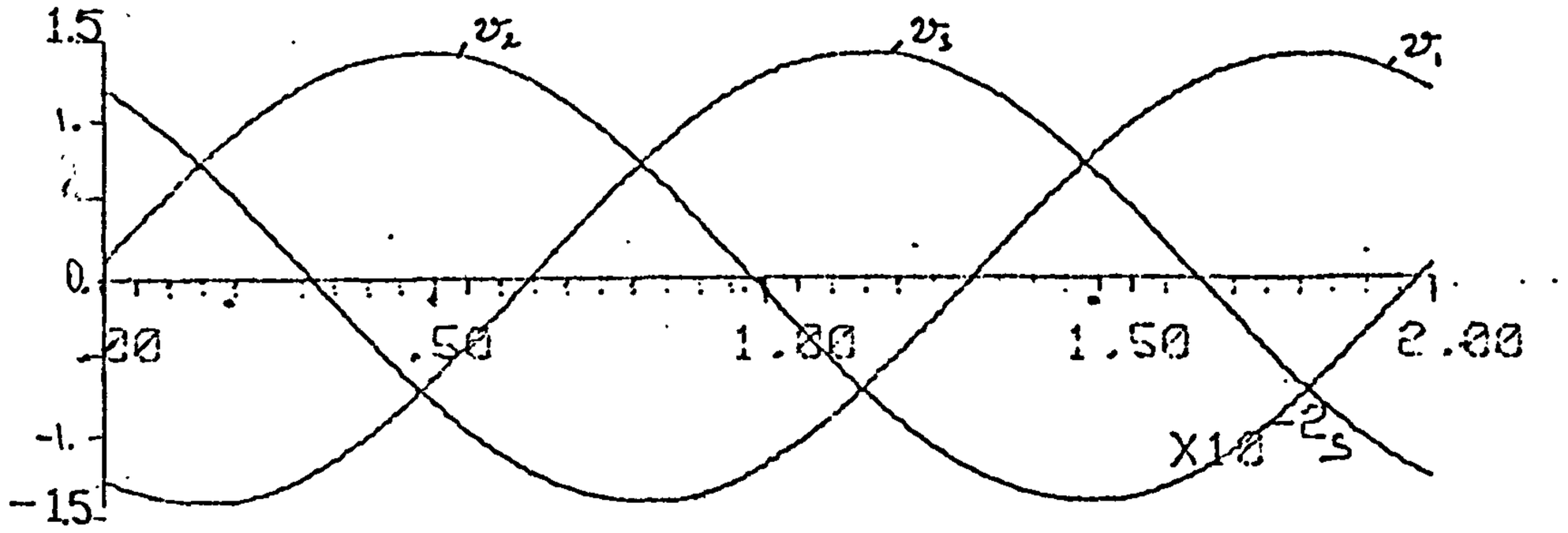

3-ϕ input

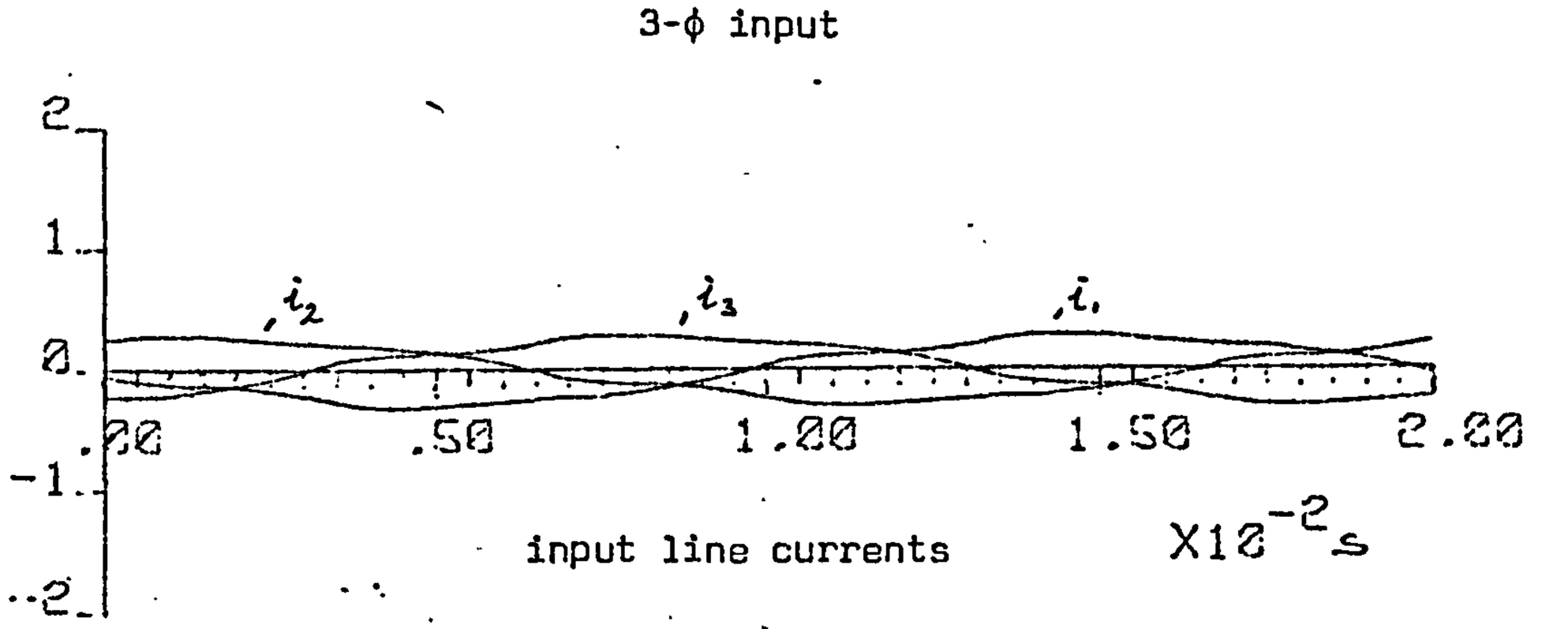

input line currents

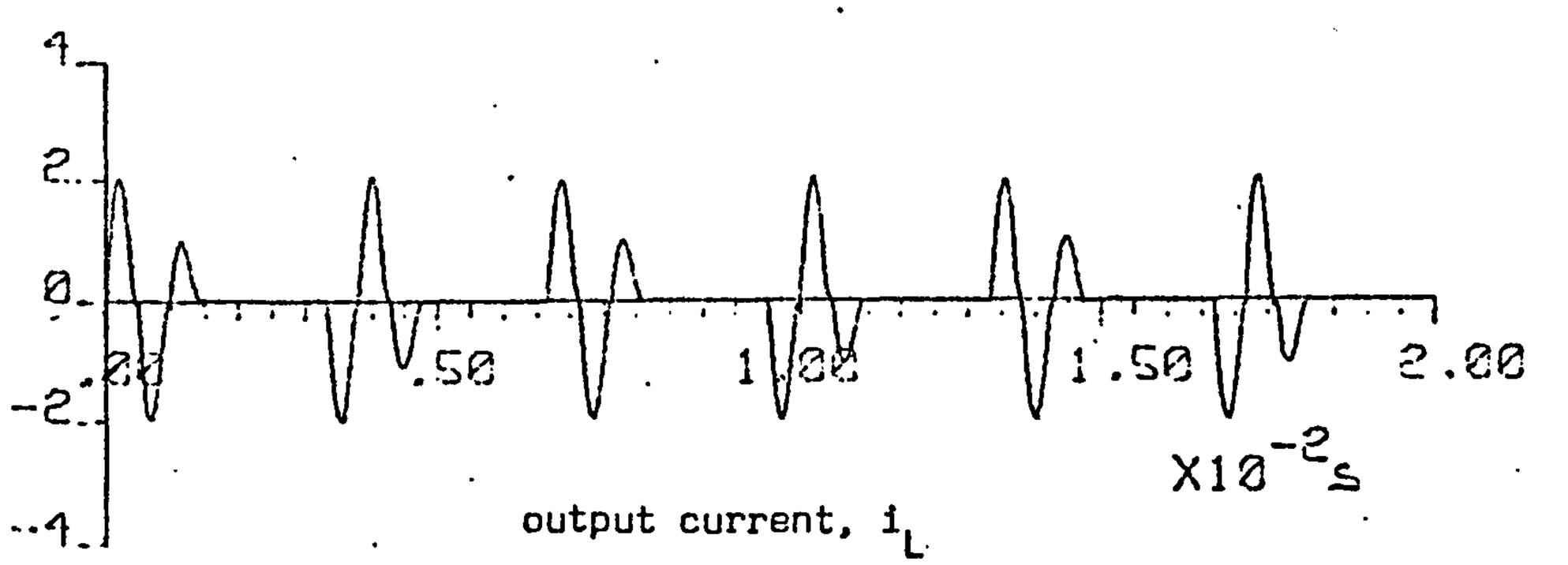

output current, i_L

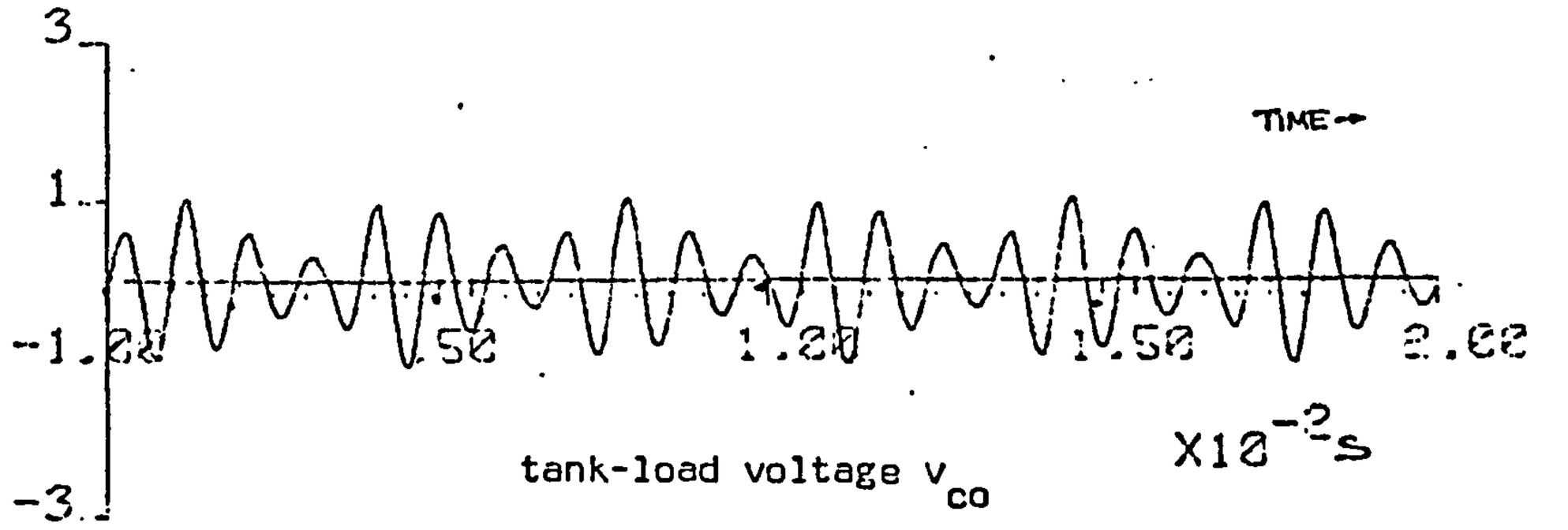

tank-load voltage v_{co}

Figure 7.18 Computed waveforms for $\theta = 120^{o}$. (f_o = 1050 Hz, X_{CF} = 4, X_{LF} = 1.3, X_L = 1.2, X_c = 1.3 p.u, Q_L = 5)

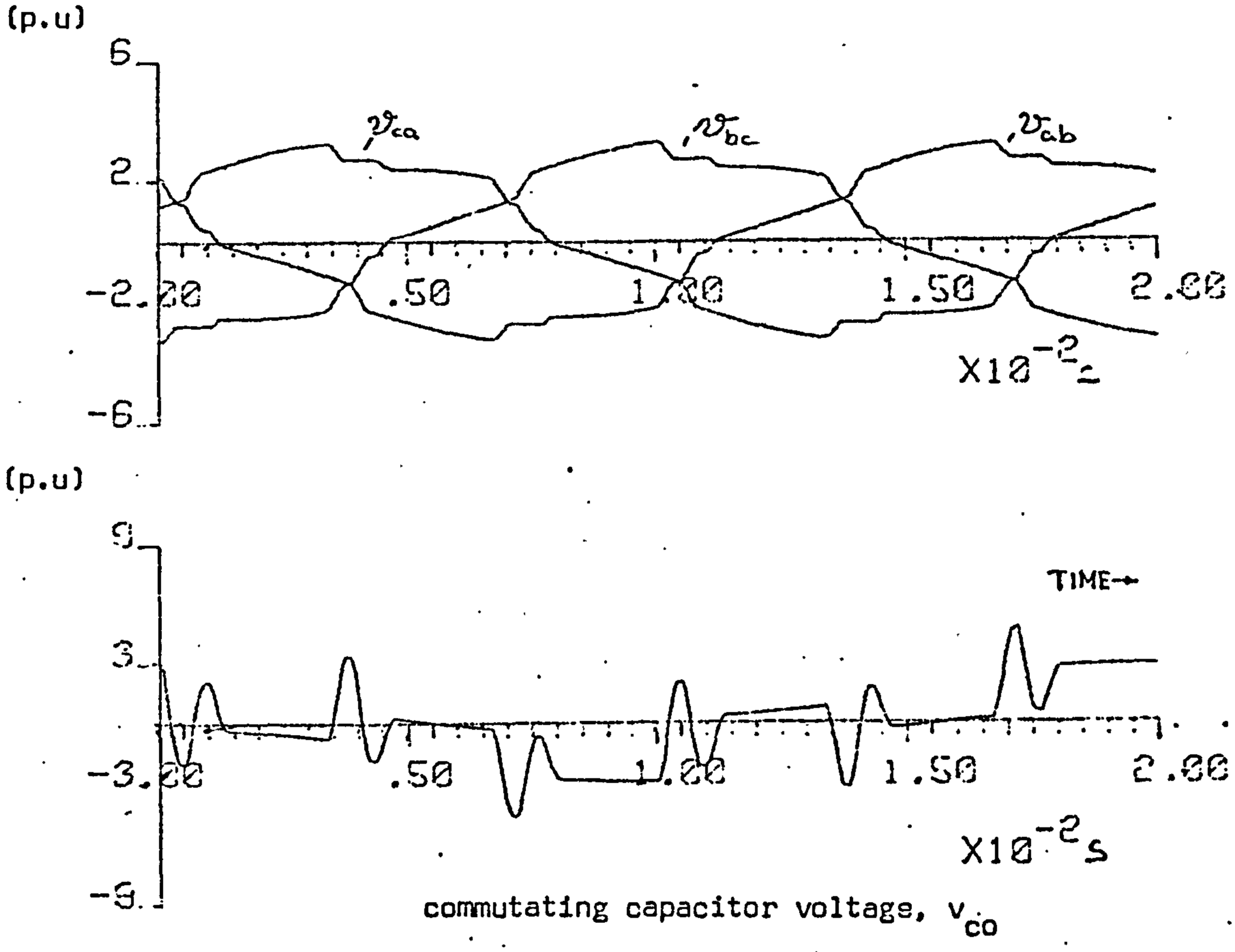

commutating capacitor voltage, v_{co}

Figure 7.18 Continuation

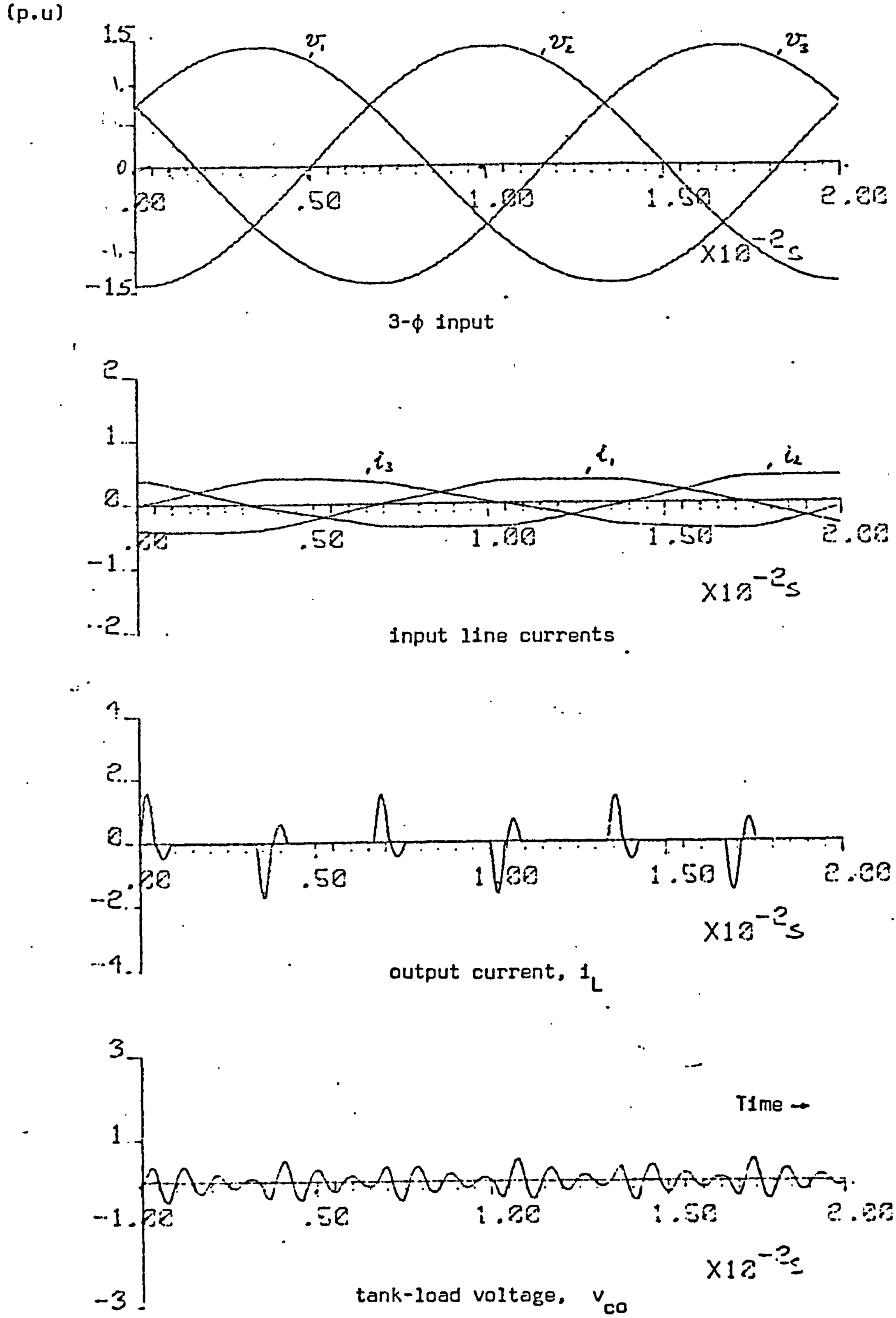

Figure 7.19 Computed waveforms for $\theta = 150^{o}$ (f_o = 1050 Hz, $X_{CF} = 4$, $X_{LF} = 1.3$, $X_L = 1.2$, $X_c = 1.3$ p.u, $Q_L = 5$)

/Continued

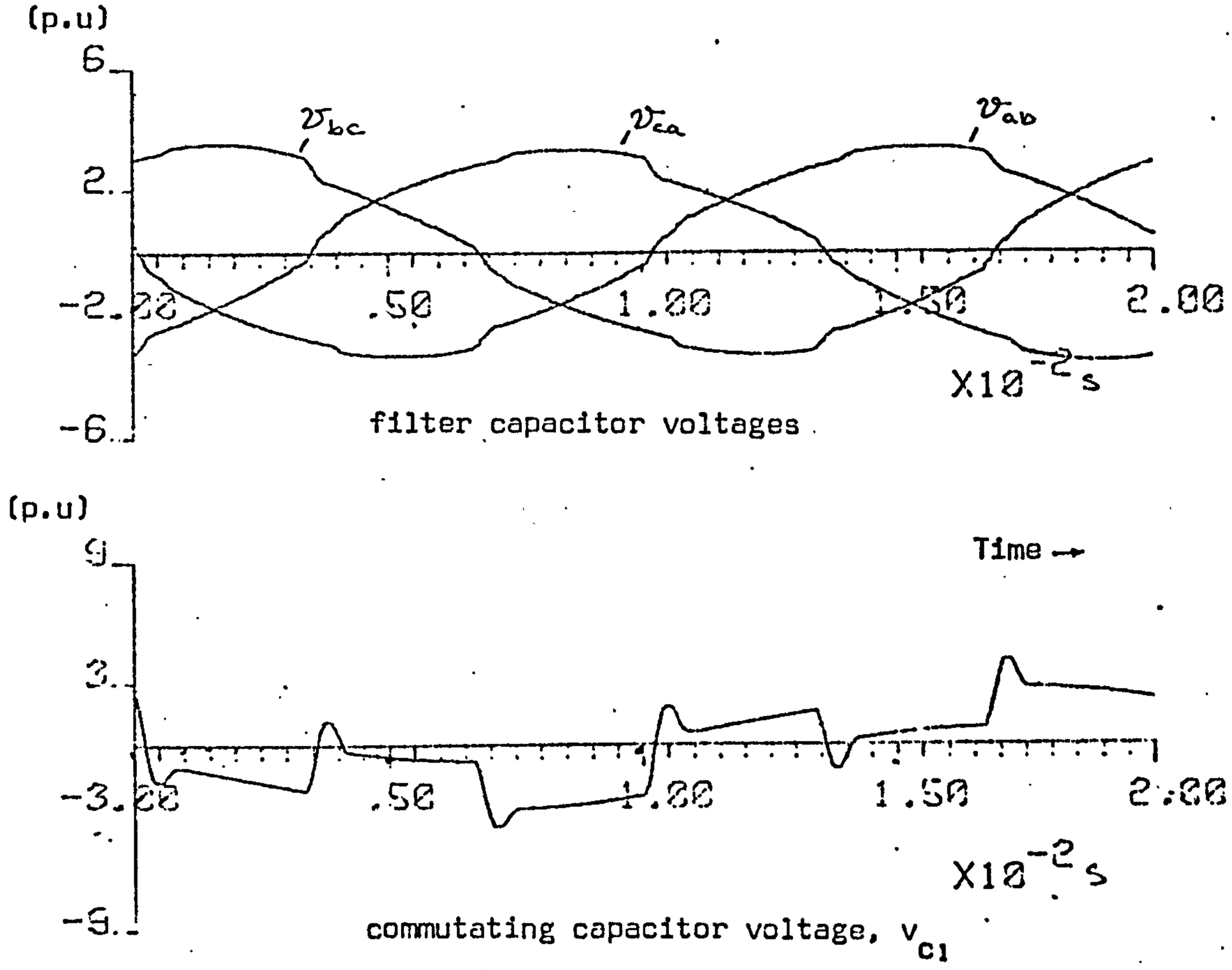

Figure 7.19 Continuation

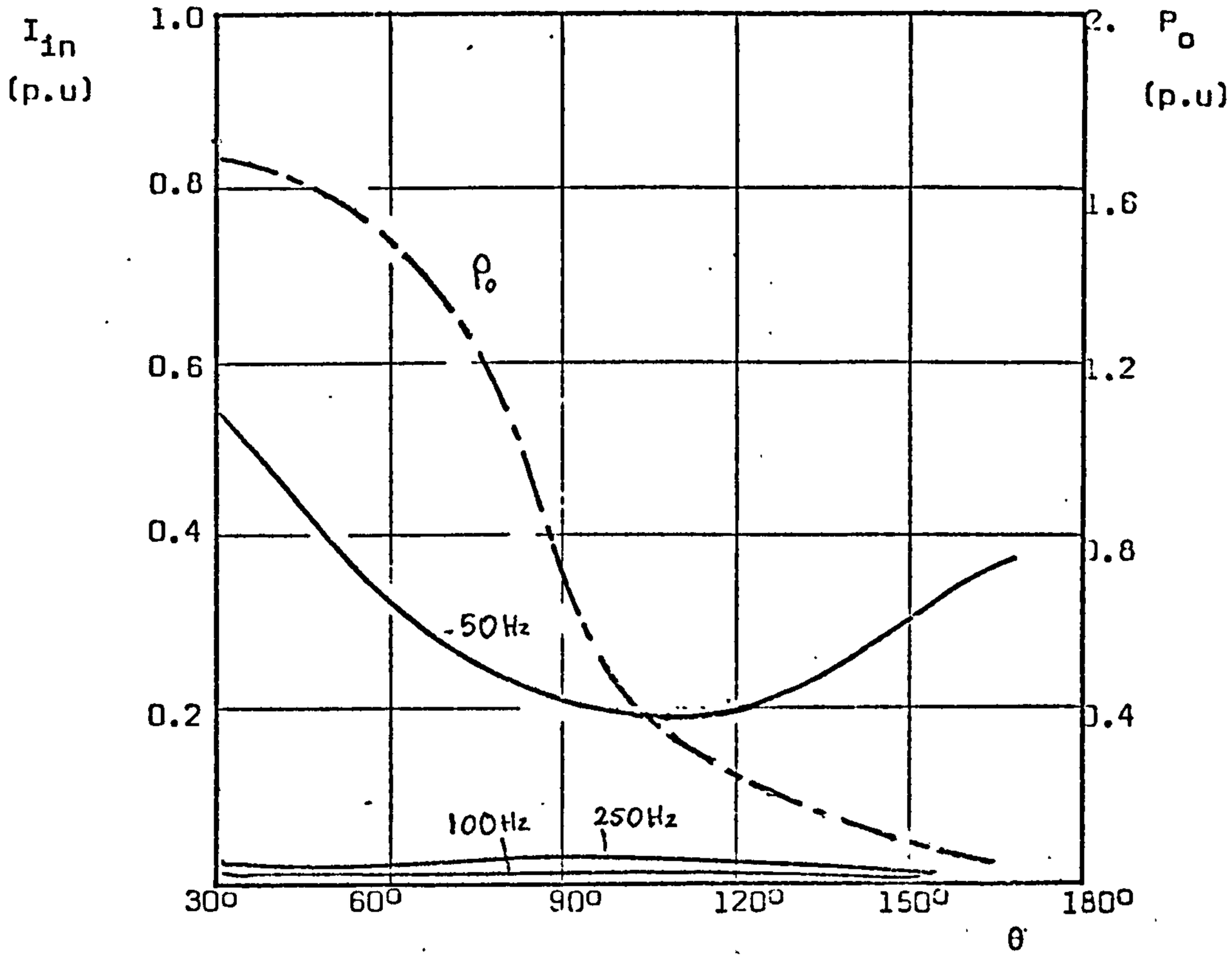

Figure 7.20 Variation of dominant input line current harmonics and output power with θ
(f_I = 50 Hz, f_o = 1050 Hz, X_{CF} = 4, X_{LF} = 1.3, X_L = 1.2, X_c = 1. p.u)

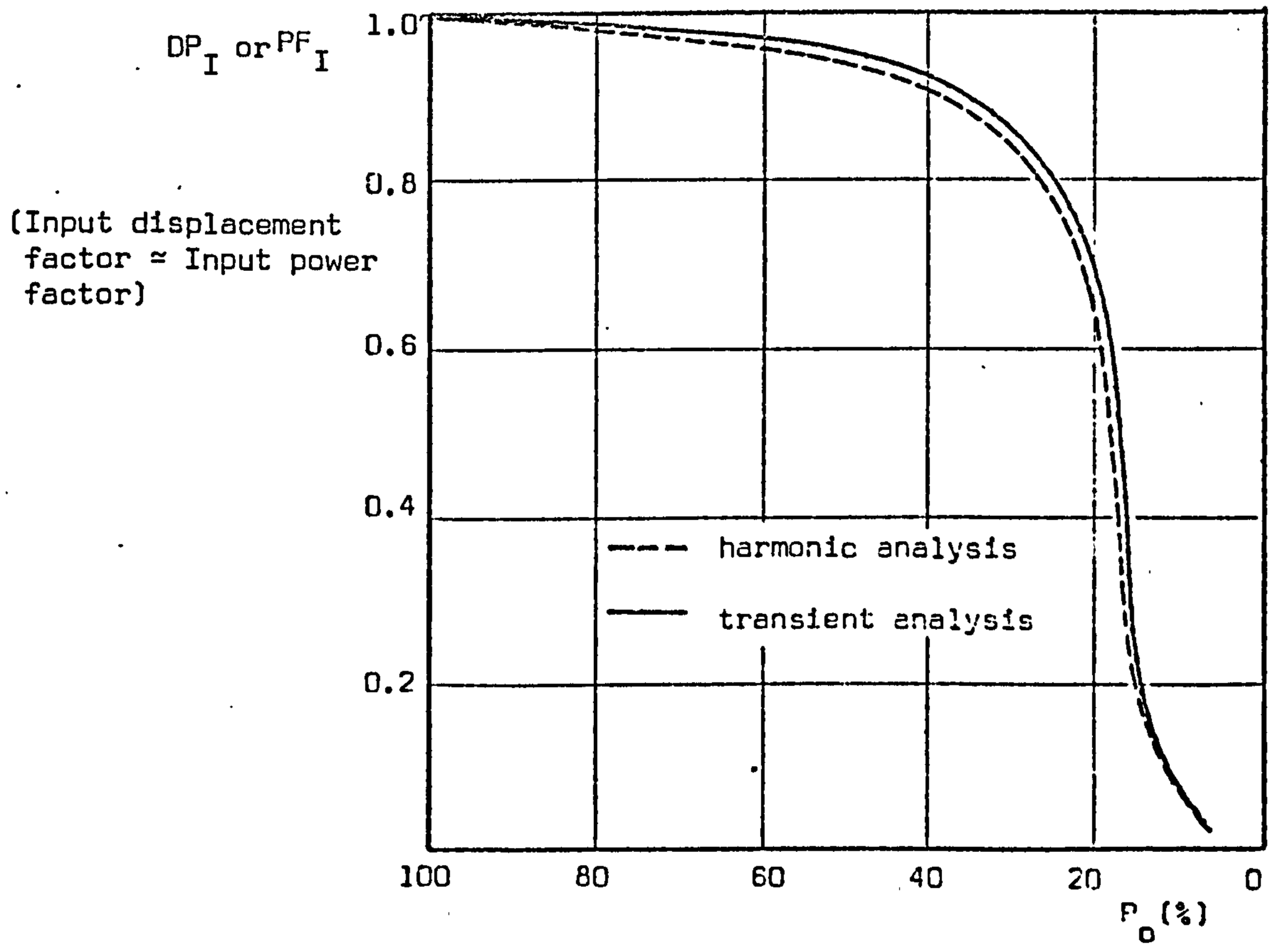

Figure 7.21 Comparison of the variation of input power factor with output power predicted by transient and harmonic analyses

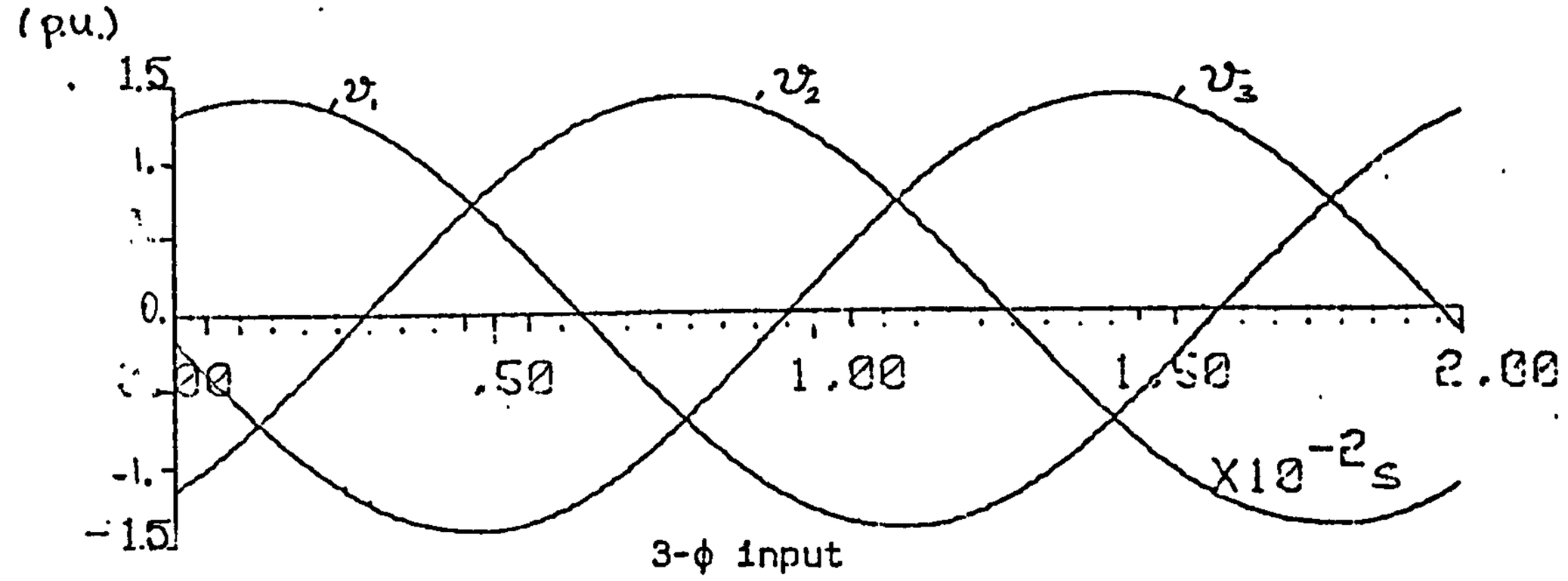

3-ϕ input

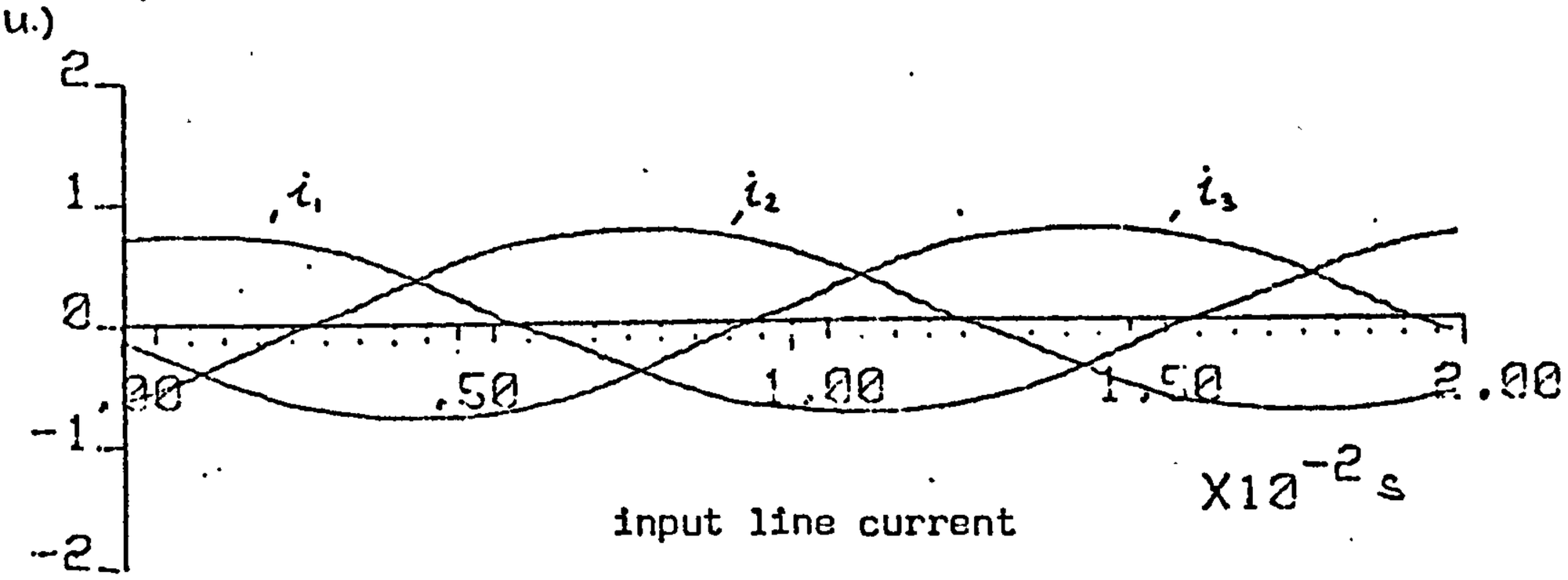

input line current

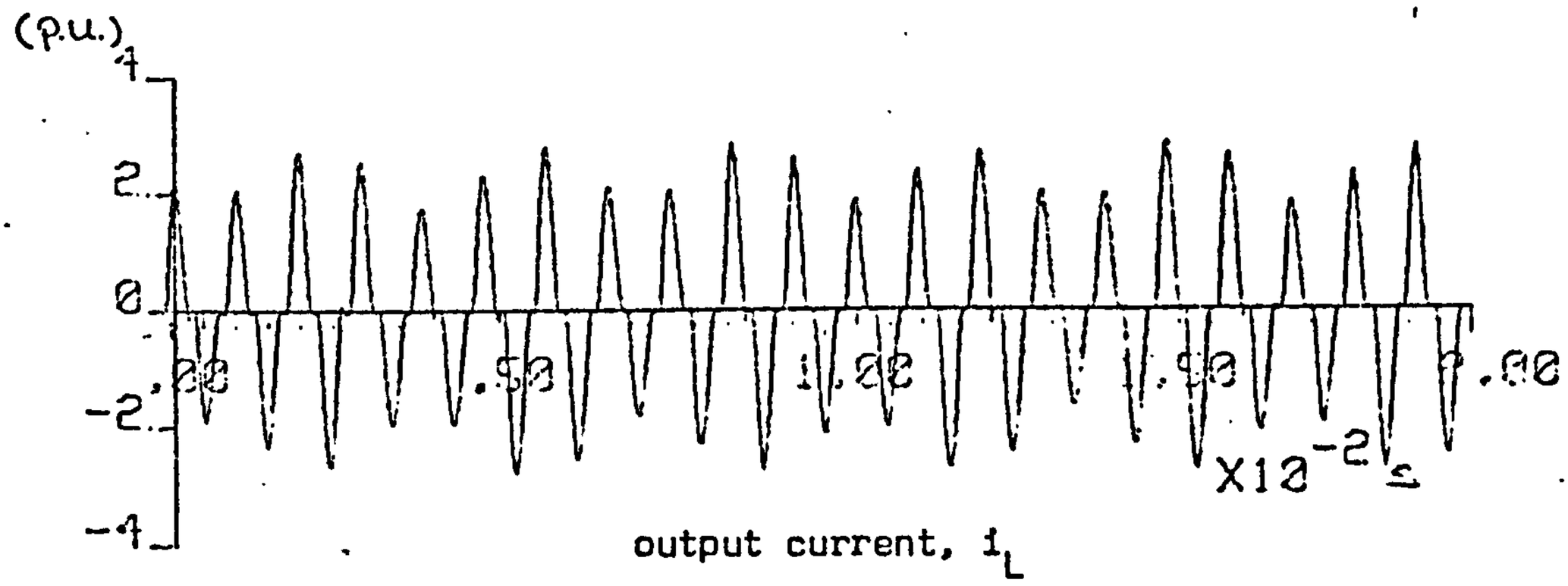

output current, i_L

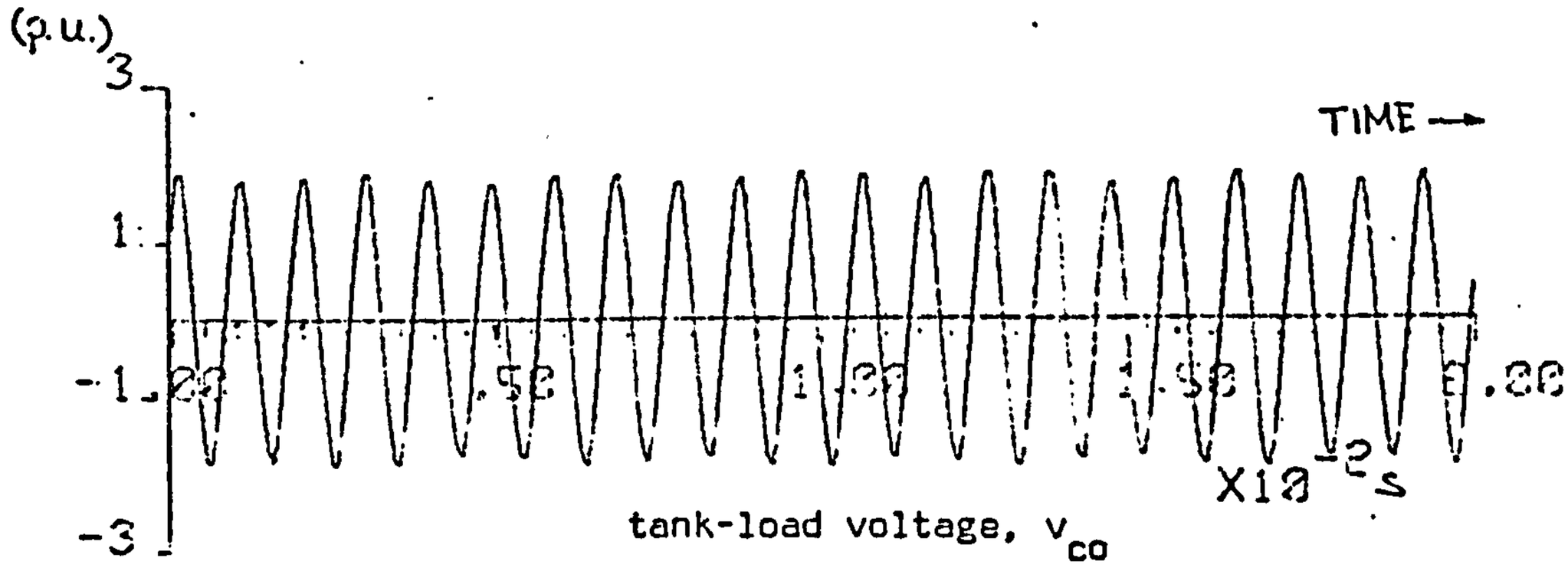

tank-load voltage, v_{co}

Figure 7.22 Computed waveforms at end-of-heating-cycle load conditions (i.e. at E)

(f_o = 1050 Hz, Q_L = 10)

/Continued

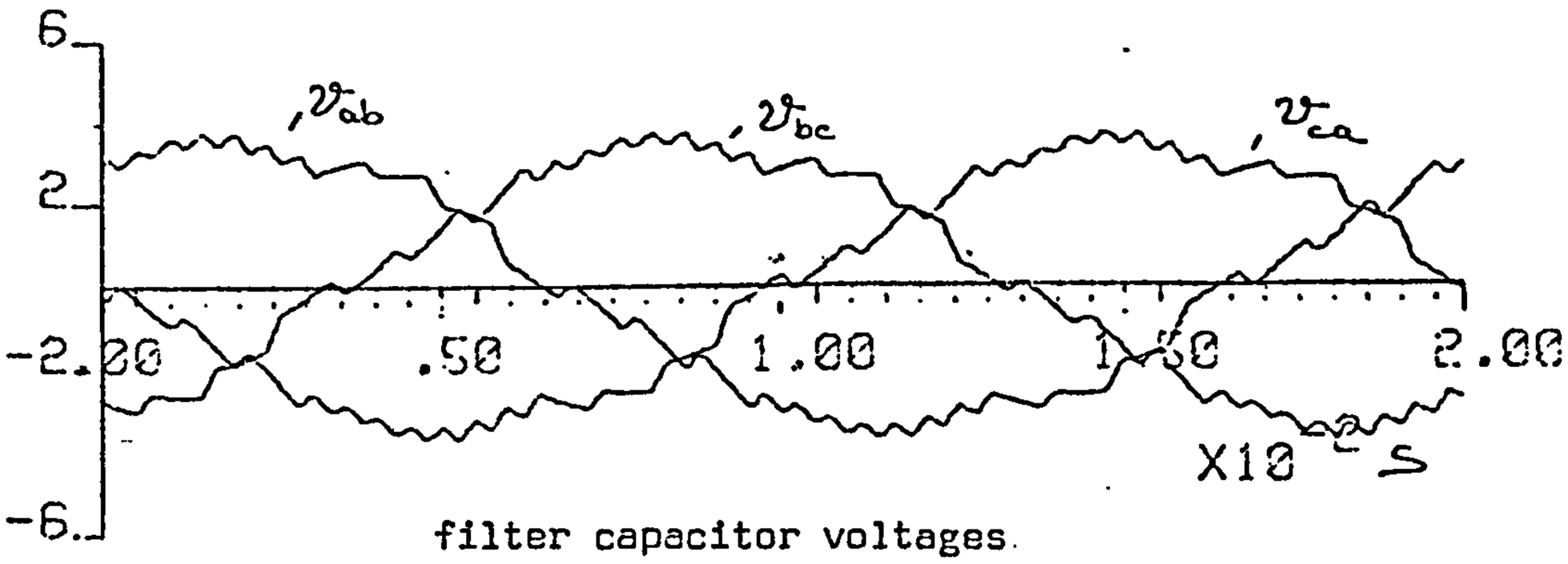

filter capacitor voltages.

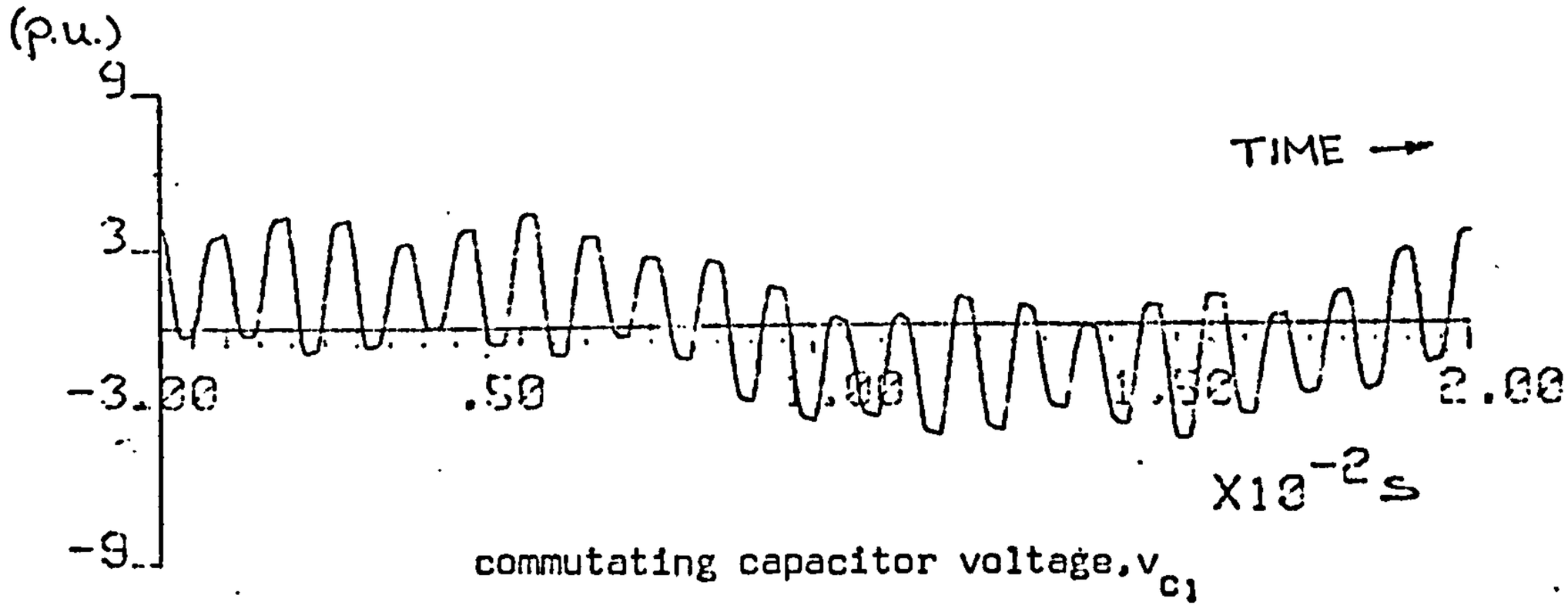

commutating capacitor voltage, v_{c_1}

Figure 7.22 Continuation

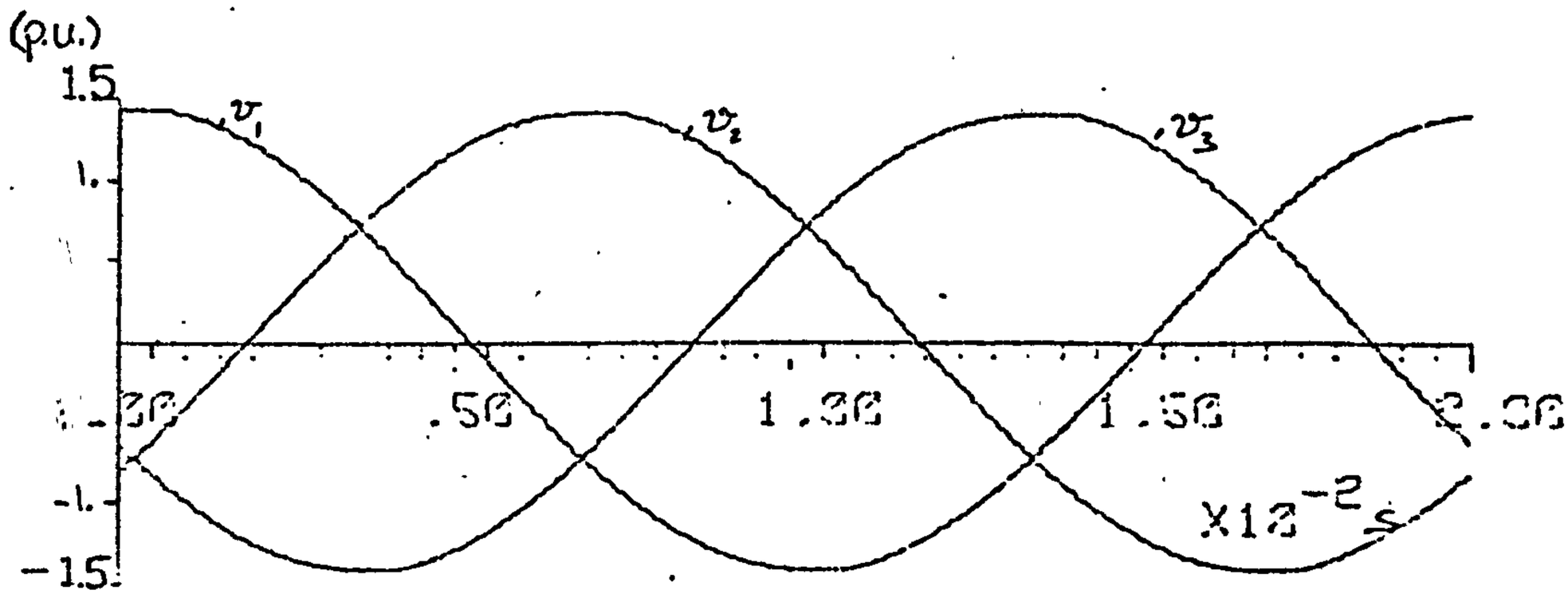

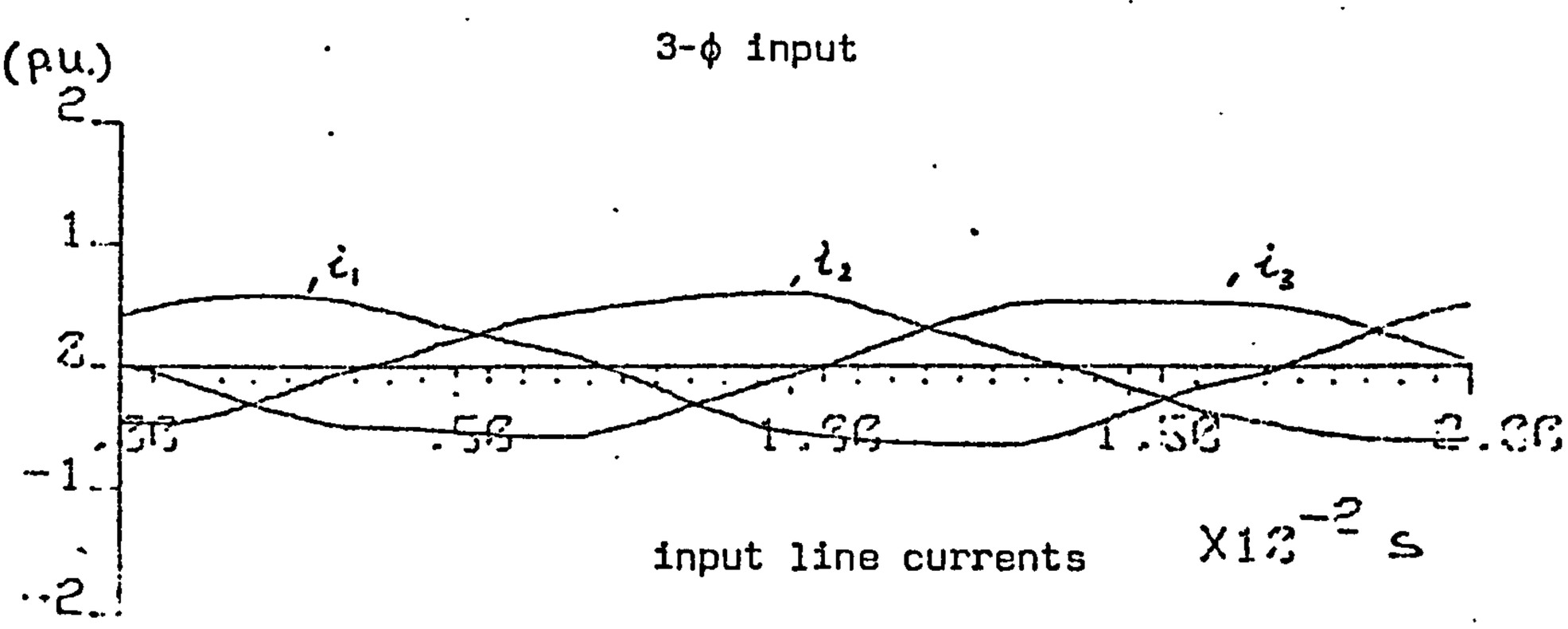

input line currents

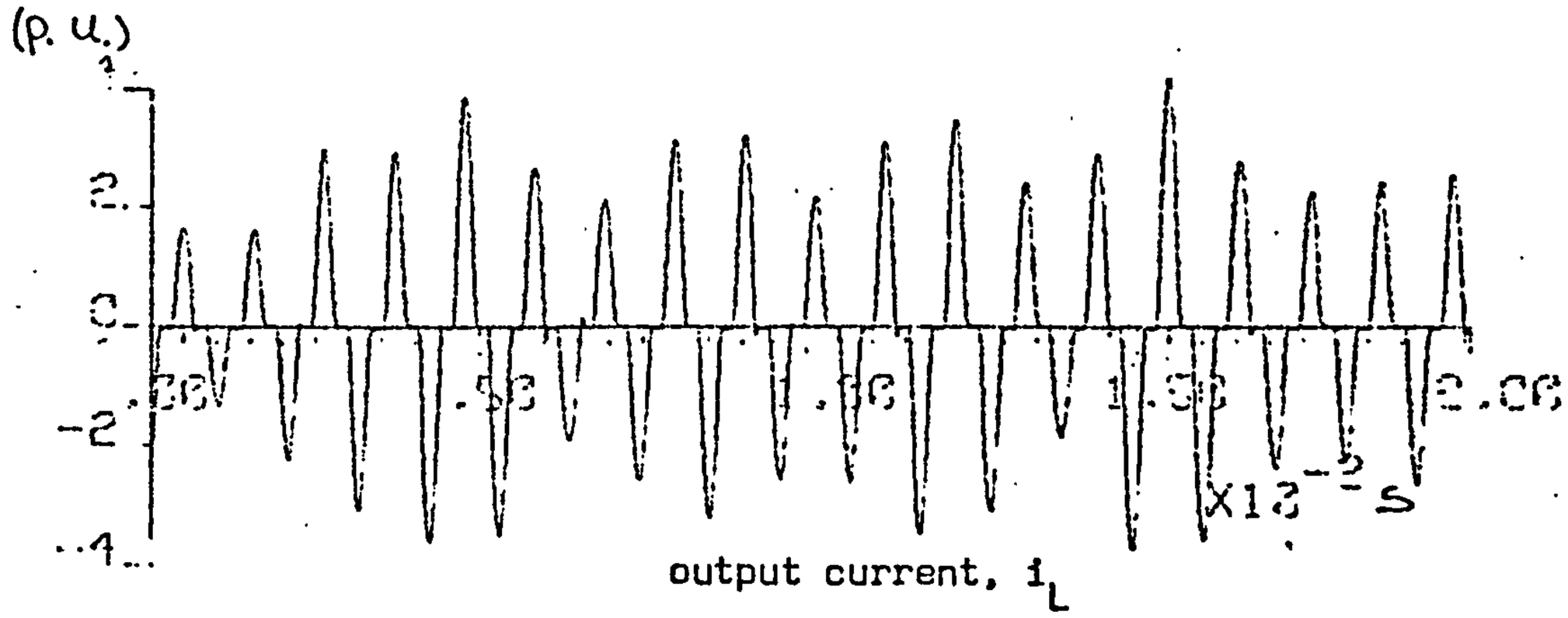

output current, i_L

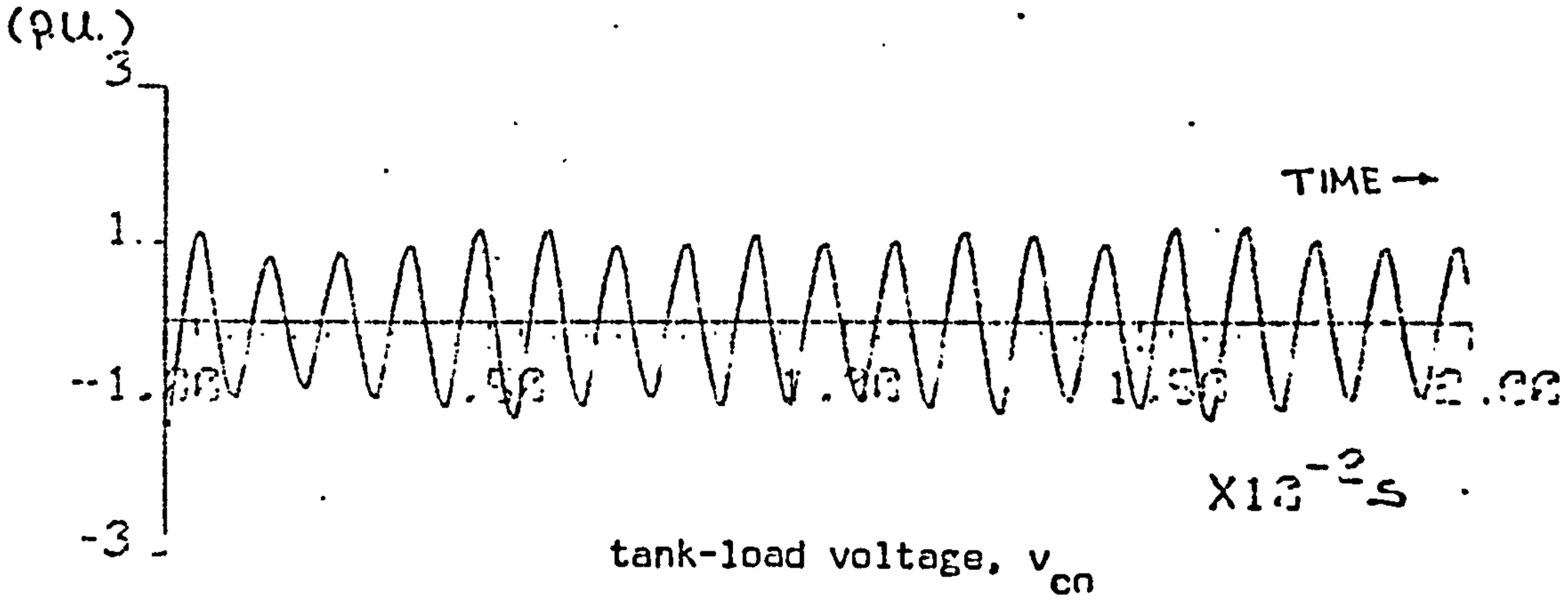

tank-load voltage, v_{cn}

Figure 7.23 Computed waveforms at the load condition B (f_o = 934.5 Hz, Q_L = 4.47)

/Continued

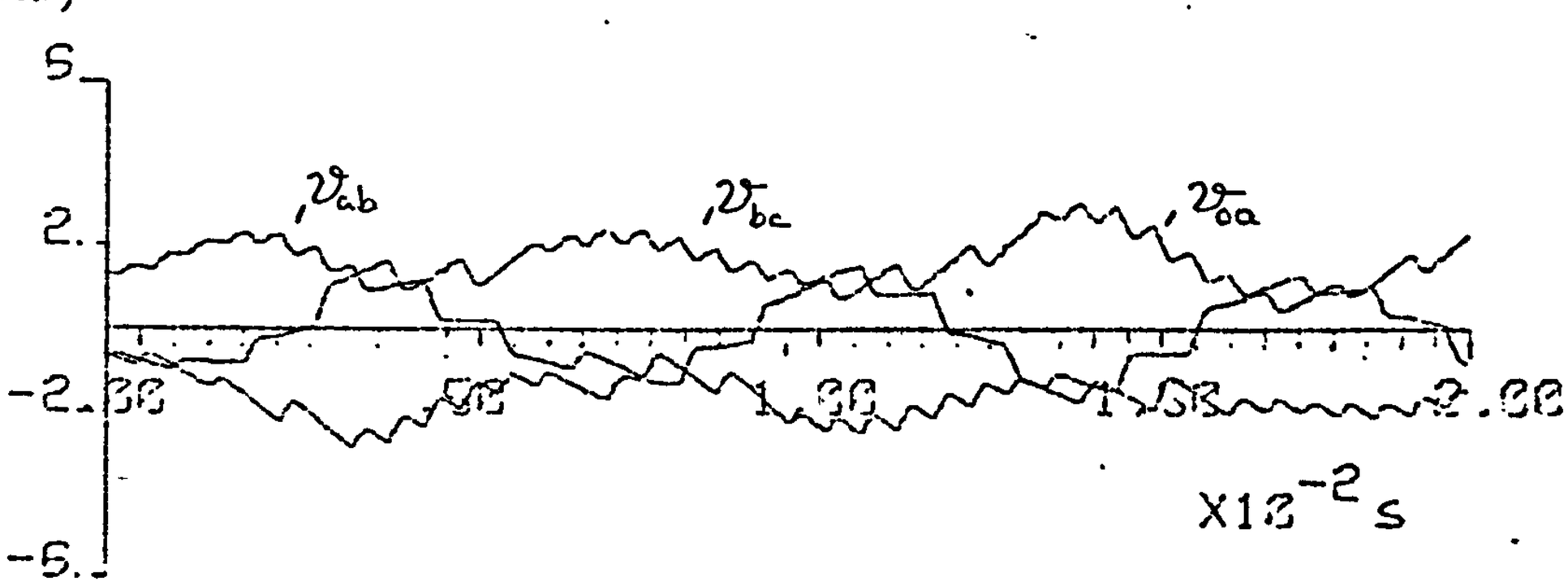

filter capacitor voltage

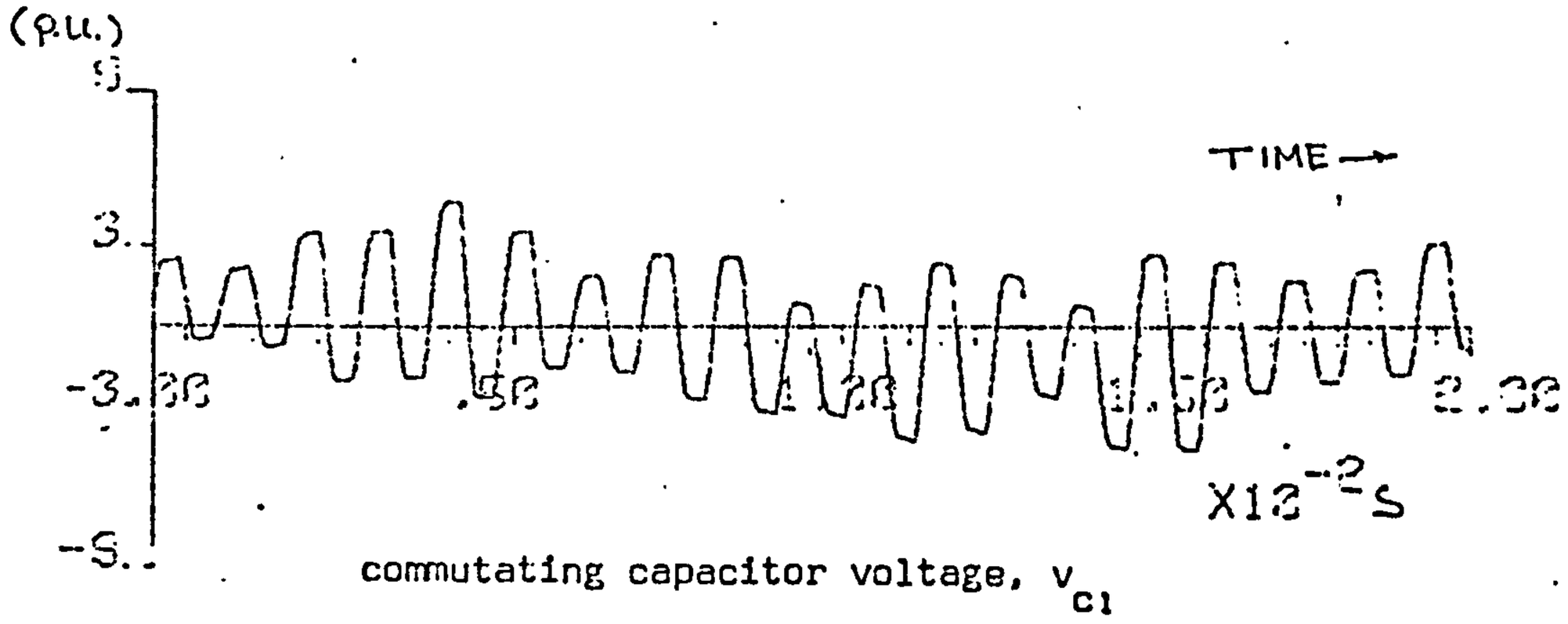

commutating capacitor voltage, v_{c1}

Figure 7.23 Continuation

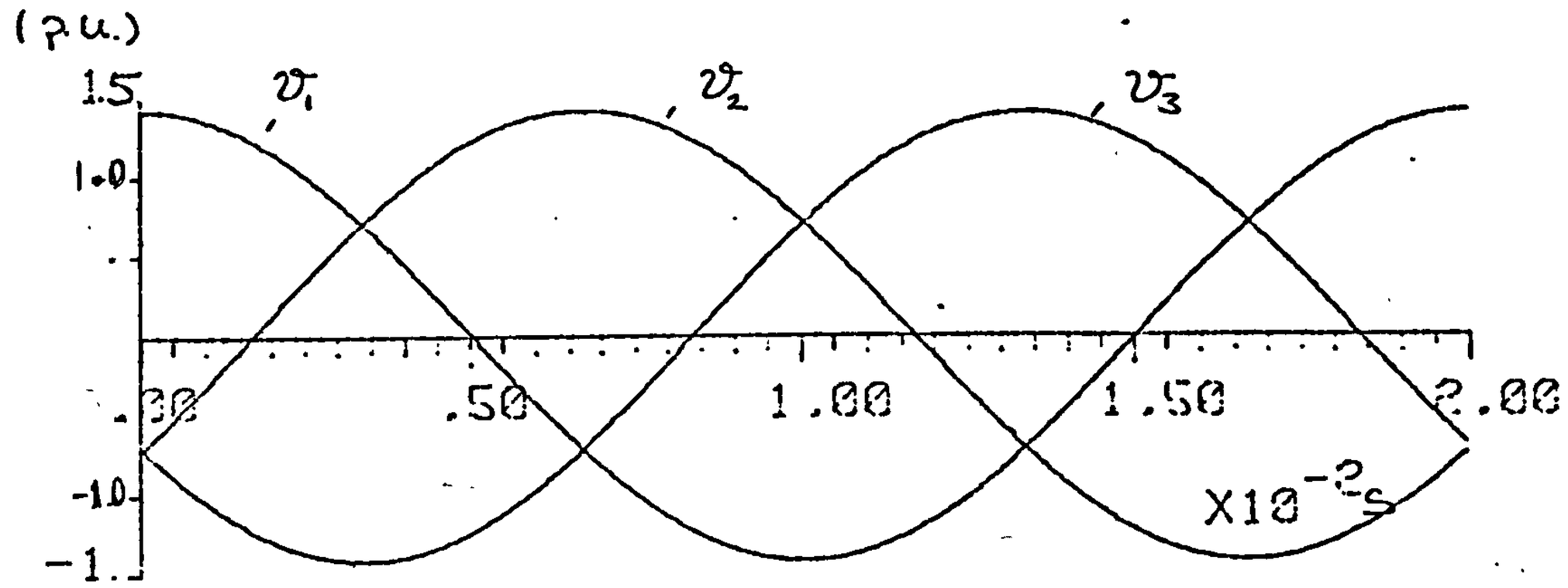

Figure 7.24 Computed waveforms when the furnace temperature is raised at around Curie temperature i.e. at the load condition C. (f_o = 908 Hz, Q_L = 3.6)

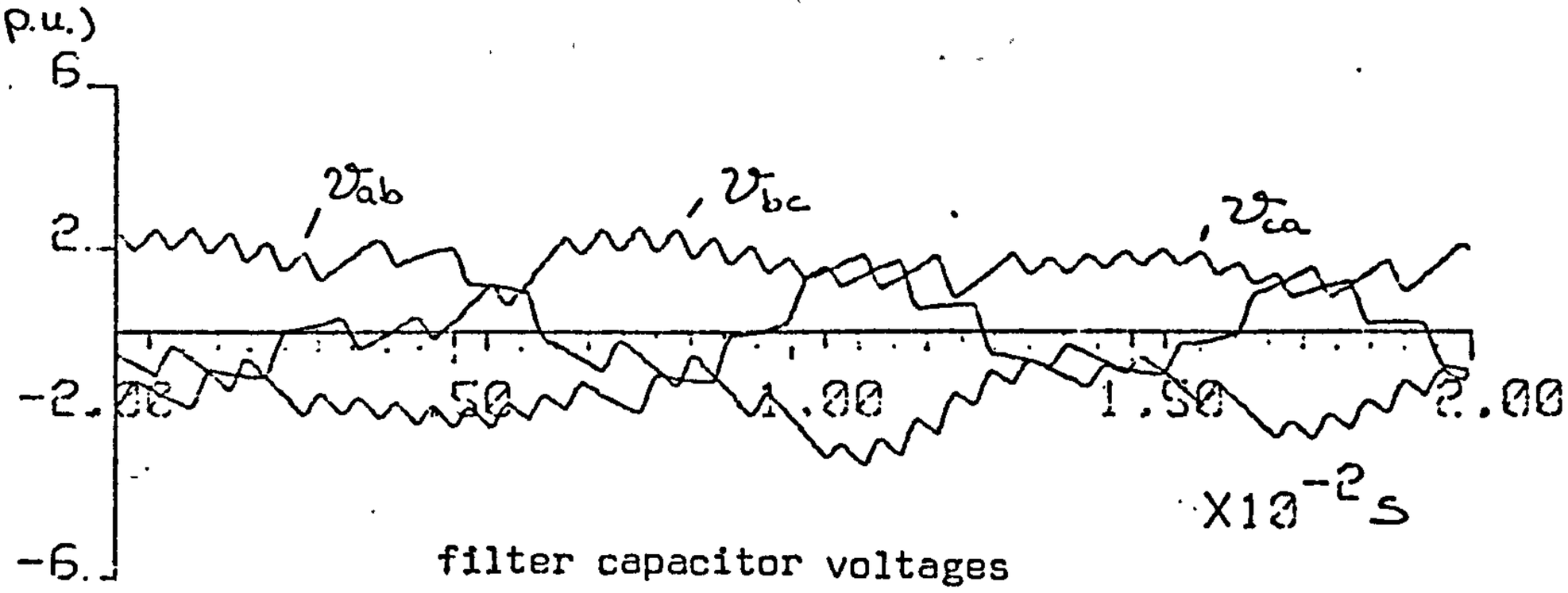

filter capacitor voltages

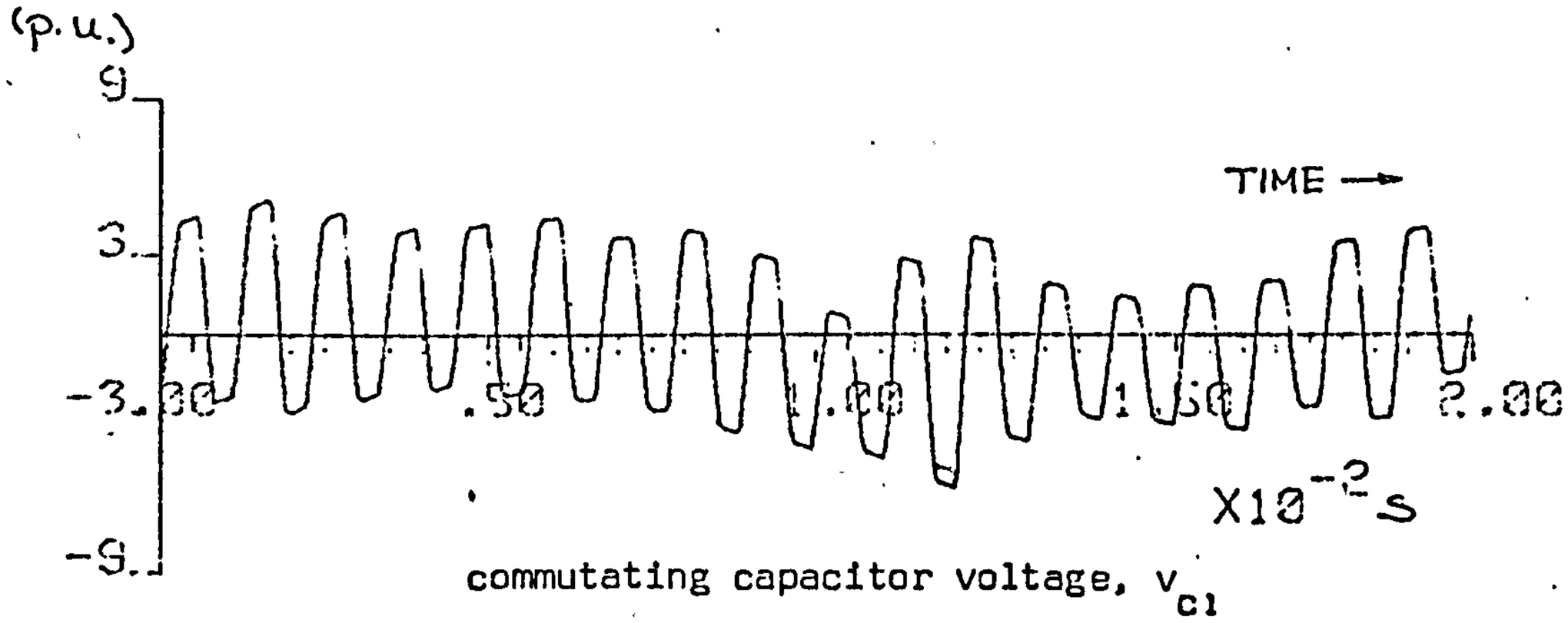

commutating capacitor voltage, v_{c1}

Figure 7.24 Continuation

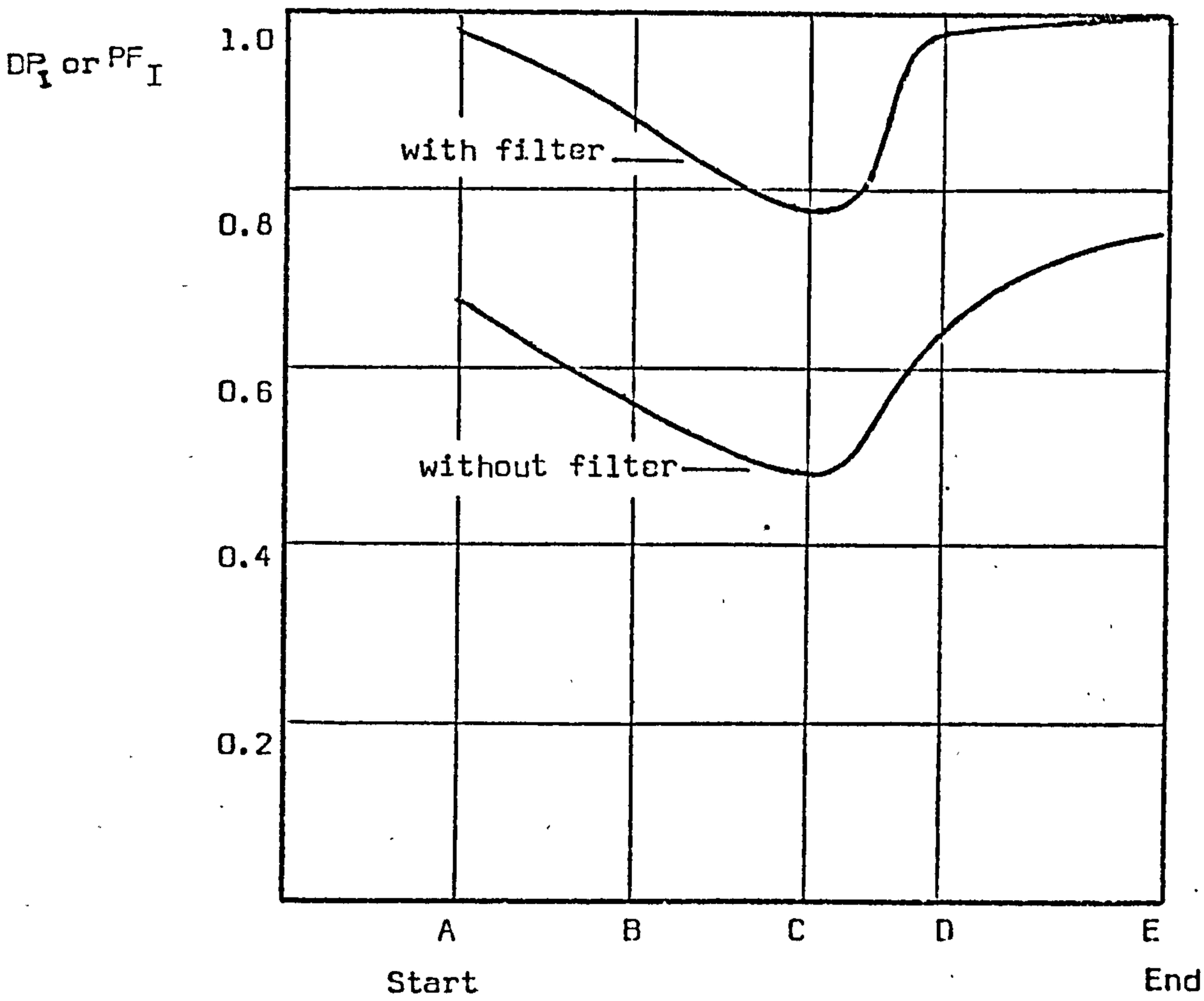

Figure 7.25 Variation of input power factor during heating cycle (X_{CF} = 4.51, X_{LF} = 1.63, X_L = 0.7, X_c = 1.35 p.u, $\theta = 30^o$)

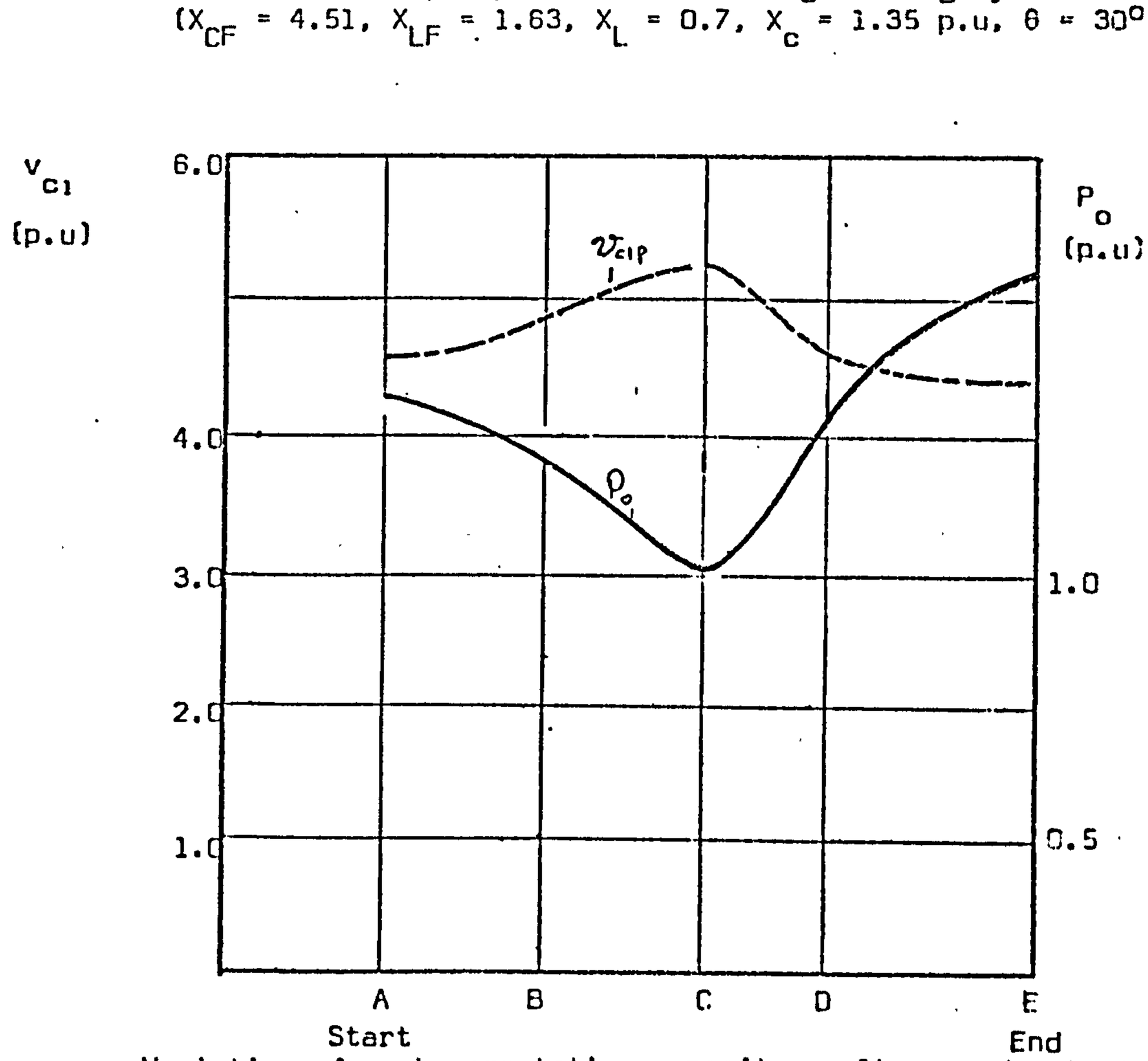

Figure 7.26 Variation of peak commutating capacitor voltage and output power during heating cycle (X_{CF} = 4.51, X_{LF} = 1.63, X_L = 0.7, X_c = 1.35 p.u, $\theta = 30^o$)

CHAPTER 8

EXPERIMENTAL INVESTIGATION

In this chapter, an experimental investigation is conducted to demonstrate the validity of the theoretical considerations and the digital simulation developed and presented previously. A complete experimental verification of the selection of optimum values for the inverter design parameters performed previously clearly presents difficulties, since it is both a costly and a lengthy procedure to design and test a cycloinverter with all possible values of design parameters and at all possible operational and load conditions. In fact, avoiding such a practice is precisely the reason for the development of the digital computer simulation. The prime aim of this chapter is therefore to show the validity of the digital simulation, for all possible operational conditions and at various load conditions. By so doing, results obtained from the digital simulation for different design parameters can be safely assumed as reliable.

The experimental work described in this chapter is confined to a 150 Hz full-bridge cycloinverter, suitable for continuous-heating applications, and a high-frequency input-filtered cycloinverter, designed for static heating applications. Both inverters were designed on the basis of the optimised design criteria established in earlier chapters, and their performances are investigated, recorded and compared with theoretical predic-

tions. A brief section is also devoted to the power control scheme of the half-bridge cycloinverter, since in this aspect it differs somewhat from the full-bridge inverter.

8.1 Control Circuits

The basic features of the control circuit for the cycloinverter are shown in block diagram form in Figure 8.1. The mains reference circuit provides synchronising pulses to the control circuit, and comprises an isolating transformer, a filter and a Schmitt trigger. The controllable delay circuit is introduced to vary the power control angle θ, manually or in a close-loop system as desired. The logic circuit decides the allowable firing range of each of the positive and negative group thyristors, and directs the clock pulses accordingly via the firing pulse circuits.

Since the cycloinverter performance is heavily dependent on the power control angle θ, it is important that the firing pulses to the thyristors of all phases are delayed accurately. For this purpose, one of the control techniques[79,103] developed for cycloinverter use (i.e. *Cosine Wave Crossing Control*, *Integral Control*, or a method based on a phase-locked-loop oscillator) can be adopted. The functional diagram of a reliable control circuit for the simultaneous and accurate delay of all three phases is shown in Figure 8.2. The phase-locked loop produces a 300 Hz square voltage waveform, synchronous with the 50 Hz

mains input and having the required delay. This voltage is fed to two 3-bit shift registers to generate control signals corresponding directly to the permissible firing range of each of the circuit thyristors, as specified in the figure. However, for the sake of simplicity, an arrangement comprising fixed and variable monostable circuits was employed for this purpose in the experimental cycloinverter. Figure 8.3 shows the voltage waveform of phase 1, together with the permissible firing interval of the positive and negative thyristors of this phase (S1 and S4 respectively).

Due to the difficulties of constructing an induction heating oven, load conditions in the following investigation are simulated by using discrete components (L and R) and the frequency and power adjustments are performed manually.

8.2 The Low-Frequency Cycloinverter

The optimum design bases of the commutation circuit components for a 150 Hz cycloinverter were established in Section 4.8 as:

$$X_L = 0.9 \text{ p.u.}$$

$$X_c = 1.08 \text{ p.u.}$$

The values of the commutating circuit components are obviously determined by the value of the equivalent load resistance (that

is, the resistance base), which itself is determined by the parameters of the working coil. In most applications, input voltage limitation in achieving a high output power may require load impedance matching, but for the sake of convenience in the prototype the load is connected directly to the output circuit and

$$R_{eq} = 8.6\Omega$$

is assumed, to assign easily obtainable values for the commutating components. Hence

$$C = \frac{1}{3\ X_c\ w_o\ R_{eq}} \simeq 40\mu\ F$$

and

$$L = \frac{X_L\ R_{eq}}{w_o} \simeq 8.2\ mH$$

A tank-load circuit of selectivity, $Q_L = 5$ was constructed to simulate the approximately constant load conditions of a continuous heating load.

8.2.1 Cycloinverter performance at full output power

In the experimental set up,the prototype cycloinverter is supplied from an autotransformer, while the source impedance is minimised by a large delta-connected capacitor bank connected

across the input terminals of the cycloinverter to provide a short-circuit path for high-order harmonics.

Figure 8.4 shows a U.V. recording of some circuit waveforms of the prototype 150 Hz cycloinverter when delivering full output power, and these are clearly similar to those obtained from the digital simulation presented in Figure 4.16b the amplitude difference between the corresponding theoretical and experimental waveforms being less than 10%. As expected, since the design values of X_L and X_c are very close to the boundary line defined in Figure 4.18, the ringing frequency of the output current is approximately equal to the output frequency (i.e. $t_{off} \simeq 0$). A comparison of the theoretical and experimental values of some of the inverter parameters is:

Inverter Parameters	P_o (p.u)	PF_I	DS (p.u)
Theoretical	1.46	0.80	6.3
Experimental	1.51	0.77	6.8

where the practical value of PF_I is calculated from the r.m.s. input voltage and current. Its somewhat lower value is due mainly to the circuit losses omitted from the theoretical considerations.

When the components of the input current are determined

using a harmonic analyser, the results obtained are:

Harmonics of i_1 (p.u)	1st	3rd	5th	7th	rms
Experimental	0.55	0.05	0.31	0.13	0.65
Theoretical	0.52	0.00	0.28	0.14	0.61

The comparison of the theoretical and experimental data presented above shows clearly that they are in close agreement, the difference being less than 10% (the maximum variation of 9.3% occurs in the 3rd harmonic of the input line current). This small discrepancy stems mainly from the following differences between the theoretical considerations and the practice:

a) Due primarily to the unequal branches of the delta-connected input capacitor bank, and partly to supply variations, the input phases are not perfectly balanced (r.m.s. input phase voltages are, in order, 25.0V, 24.7V and 25.3V).

---

* When comparing these figures, note that the per unit voltage and current bases are:

$$V_{base} = 25V \quad \text{and} \quad I_{base} = \frac{V_{base}}{R_{eq}} = 2.87A$$

b) The 3-phase supply to the cycloinverter has a source impedance, whereas an ideal voltage source is assumed in the theoretical considerations.

c) In theoretical considerations the snubber circuits are neglected.

d) In practice, there is always an error in adjusting the power control angle θ.

e) In theory, the power circuit components are assumed ideal, but they deviate from this because:

i) thyristors have reverse recovery characteristics,

ii) the commutating inductor has a resistance,

iii) the star-connected commutating capacitors are not precisely balanced,

iv) the load may not be perfectly tuned.

However, a close examination of Figure 8.4c shows that, despite the items listed above, the output current pulses have approximately equal amplitudes, indicating a satisfactorily balanced operating condition. The output current waveform also indicates that the turn-off time of the negative group thyristors is higher than that of the positive group. Further examinations established that this is caused mainly by the unequal mark-to-space ratio of the external oscillator used.*

---

* The control circuit was designed to deliver a firing pulse to the positive and negative group thyristors at the positive- and negative-going edges of the square waveform of the external oscillator.

8.2.2 Cycloinverter performance at reduced output power levels

The U.V. recordings of the cycloinverter waveforms for varying output power levels (i.e. for $\theta = 90^{o}$, 110^{o} and 150^{o}) given in Figures 8.5, 8.6 and 8.7, correspond respectively to the digital simulation results shown in Figures 4.19, 4.20 and 4.21. The close similarity in shape between the corresponding theoretical and experimental waveforms indicates, of course, that they have almost the same relative harmonic content. A comparison of the amplitudes of the waveforms (after changing the experimental results to a per unit basis) indicates that these are in close agreement, the difference being approximately 7-10%. This confirmation of the digital simulation waveforms for various output power levels clearly suggests that the theoretical results obtained by processing these waveforms are also correct. Figure 8.8 shows the variation of useful output power with the power control angle θ, based on both theoretical and experimental findings. A similar comparison is also made for the input power factor PF_I in Figure 8.9, where the experimental PF_I is lower than that predicted theoretically, due primarily to the neglect of the circuit losses (including the losses in the snubber circuits) in the theoretical considerations.

8.2.3 Inverter performance at varying output frequencies

Figure 8.10 shows various cycloinverter waveforms for operation at $f_o = 0.8$ p.u. The corresponding digitally simulated output for the same operational frequency is shown in Figure 4.28c

Investigations at various other frequencies show that the inverter operation at low non-multiple output frequencies is unsatisfactory, due to the high modulation of the output current predicted previously from the computer simulation results of Section 4.4.2.

As noted in Section 8.2.1, the 150 Hz cycloinverter with an optimised commutation circuit produces continuous output current, as designed. Although this is required for a satisfactory inverter performance, it nevertheless makes the circuit susceptible to short circuits, in applications where slight variations in the load parameters are expected. Obviously, one way to make the circuit tolerate such load variations is to increase X_c from its optimum value, although this is at the expense of a deterioration in the circuit performance (i.e. lower PF_I, higher losses, etc). Alternatively, it is possible to make the circuit more tolerant of load variations, by assisting the series load commutation of the thyristors with a forced commutation arrangement. This possibility is investigated briefly in the next section.

8.3 Use of Forced Commutation in a Low-Frequency Cycloinverter

The use of forced commutation in a cycloinverter has been mentioned previously. In a force-commutated inverter, the commutating capacitor is required to deliver twice the load current flowing at the instant of a thyristor turn-off. For

high-frequency, high-power applications, the ratings of the commutating components and the thyristors both become very large. It is suggested, however, that by using a combination of forced and series load commutation (Figure 8.11) it is possible to reduce substantially circuit ratings, and to provide more reliable commutation than with series commutation alone, without significantly increasing the cost of the device. This section aims to demonstrate experimentally the use of such a commutation circuit in a cycloinverter.

The cycloinverter configuration of Figure 8.11 operates in a similar manner to the complementary impulse-commutated McMurray-Bedford inverter. When thyristor S2 is fired to turn-off the conducting thyristor S1, the voltage across C_3 appears fully across OA, as the two halves of the commutating inductor L_1 are tightly coupled. Thyristor S1 thus experiences a reverse bias, for a duration determined approximately by the natural resonant frequency w_n of the commutating components, where, since $C_3 = C_2 = C_1$,

$$w_n = \frac{1}{\sqrt{3\ C_3\ L_1}}$$

approximately. During this interval the commutating capacitor also supplies the output current (which by this time is substantially reduced), until its polarity is reversed and the incoming thyristor S2 takes over. An approximate analysis of the circuit operation (developed by adapting the analysis of the McMurray-

Bedford inverter) has provided approximate values of L_1 and C_3 for a 150 Hz experimental prototype, and Figure 8.12 shows an U.V. recording of various voltage and current waveforms monitored in the prototype. As seen in the output current waveform, the incoming thyristor is fired just before the outgoing thyristor ceases conducting,so that there is no zero interval corresponding to the thyristor turn-off time. Apart from a small superimposed high-frequency ripple, the input line and the output currents remain basically unaltered when compared with the corresponding waveforms in Figure 8.4, obtained with a series load-commutation circuit. With each commutation, an amount of energy is trapped within the loop formed by the conducting thyristor, L_1 and C_3, and Figure 8.12c shows the decaying resonant current waveform at a frequency of approximately $1/\sqrt{3\,C_3\,L_1}$. The relatively large trapped circulating current and energy are the principal disadvantages of this circuit and present a serious problem in large power, high frequency inverter applications.

8.4 The High-Frequency Cycloinverter

The optimum design base for the commutating circuit of a high-frequency cycloinverter for static heating applications was established in Section 5.4.2 as:

$$X_L = 0.7 \text{ p.u.}$$

$$X_C = 1.35 \text{ p.u.}$$

It has also been shown that the performance of the cycloinverter is improved considerably by the addition of an LC input filter, and the optimum design base for the components of this were established in Section 7.5.2 as

$$X_{LF} = 1.63 \text{ p.u.}$$

$$X_{CF} = 4.51 \text{ p.u.}$$

for the cycloinverter with the design values given above.

Based on the findings of Chapter 2, the characteristic load conditions of a typical static heating load during a complete cycle of operation may be simulated by the following tank load components:*

Load Conditions	L_o (μH)	R_o (Ω)	C_o (μF)	w_o (Hz)	R_{eq} (Ω)	Q_L
E	121.3	0.16	189.0	1050	4	5.0
A,D	135.0	0.225	189.0	994	3.1	3.95
B	152.5	0.4	189.0	934	2	2.51
C	162.0	0.513	189.0	908	1.64	2.08

---

* For the sake of convenience in obtaining the circuit components, R_{eq} is assumed to be 4Ω at the load condition 'E'.
With V_{base} = 25V, the current base therefore is:
$I_{base} = \frac{25}{4} = 6.25\text{A}.$

Hence, the input filter and commutating circuit components of the cycloinverter are:

$$L_F = \frac{X_{LF}\ (R_{eq})_E}{W_I} = 20.7\ \text{mH}$$

$$C_F = \frac{1}{3\ X_{CF}\ W_I\ (R_{eq})_E} = 58\ \mu\text{F}$$

$$L = \frac{X_L\ (R_{eq})_E}{(w_o)_E} = 424\ \mu\text{H}$$

$$C = \frac{1}{3\ X_c\ (w_o)_E\ (R_{eq})_E} = 9.35\ \mu\text{F}$$

An experimental cycloinverter constructed using these component values worked successfully. However, during the experimental investigation it was noticed that the reliability of commutation of the circuit thyristors could be improved considerably by placing commutating inductors separately in the paths of the positive and negative thyristor groups, as shown in Figure 8.13. As described in Section 3.2, in relation to the sine-wave inverter, this arrangement reduces the dv/dt stresses on the thyristors and thus prevents misfiring. Furthermore, these inductors may be coupled to present an additional turn-off time to the outgoing thyristor.

Before pursuing an investigation of the performance of the prototype, an experiment was performed to demonstrate the

presence of the region of instability and commutation failures which must be excluded by the commutating circuit design (see Figure 5.37). For this purpose, the commutating inductor L was increased by a single turn at a time, until commutation failures in the inverter operation were observed, and the corresponding value of L was noted as 603 μH. The number of turns on the inductor was further increased until the cyclo-inverter operation recovered, when L was 740 μH. The findings of this experiment agree closely with the theory, and they may be explained with the help of Figure 5.37 as follows. In Figure 5.37, an increase in the commutating inductor corresponds to a horizontal shift in the position of the operation point B towards the region of instability, with the actual crossing occurring at X_{L1} = 0.98 p.u. This corresponds to an inductance

$$L_1' = \frac{X_L R_{eq}}{w_o} = \frac{0.98 \times 4}{2\pi \times 1050} = 594.2\ \mu H$$

which compares with the lower of the experimental inductances given above. Similarly, Figure 5.37 suggests that the inverter operation is expected to recover at around X_{L2} = 1.2 or L_2 = 727.4 μH. As the presence and the position of the region of instability is already confirmed by two different theoretical approaches (using transient and harmonic analysis techniques), this experimental evidence is regarded as sufficient to validate the design considerations outlined in the previous chapters.

8.4.1 Cycloinverter performance at a fixed load condition

Figure 8.14 shows U.V. recordings of various voltage and current waveforms in a full-bridge cycloinverter, operating at 1050 Hz and delivering full output power to a tuned tank load of selectivity Q_L = 5 (i.e. at the load condition E). The recordings show clearly that:

1. When compared with the corresponding waveforms obtained from the digital simulation (Figure 7.22) ,the correlation is satisfactory. On a per unit scaling, the amplitude of the experimental and theoretical waveforms compare as, approximately:

Quantity	Experimental (p.u)	Theoretical (p.u)
3-phase mains voltage (rms)	1.0	1.0
input line current i_1 (peak)	0.67	0.72
output current i_L (peak)	1.65-2.6	1.8-2.8
tank-load voltage v_{co} (peak)	1.6-2.12	1.85-1.95
commutating capacitor voltage v_{c_1} (peak)	4.4	4.4
filtering capacitor voltage v_{ab} (peak)	3.68	3.88

the increased ripple on the experimental tank-load voltage being due to the lower selectivity of the tank-load used (the computed waveform is obtained for Q_L = 10).

2. The output current waveform is modulated as predicted by equation (5.11). As seen, the distortion harmonics which are dominant in determining the envelope of the output current are the sideband components at $w_o \pm 6\, w_I$. The slight differences between the experimental and the theoretical output current waveforms is caused basically by a shift in the operational frequency of the external oscillator controlling the cycloinverter. A better correlation with the theoretical waveform would be obtained if the output frequency was synchronised to the input.

3. The input current is free of any significant distortion component. The effectiveness of the input filtering becomes apparent when the waveforms of the input line current to the filter i_1 and the cycloinverter input line current i'_1 are compared on Figure 8.15. Together with Figure 5.1a, this figure also demonstrates the close similarity between the experimental and computed cycloinverter input line current waveforms, which provides further evidence of the correctness of the digital simulation used.

4. The input power factor of the configuration is very satisfactory. As seen, the input line current is approximately cophased with the input phase voltage, as predicted in Section 5.2.3.

Figure 8.16 shows the input line current, i_{1off} and the filter capacitor voltage v_{aboff}, when all the circuit thyristors are non-conducting. The theoretical and experimental values of these quantities are, approximately:

Quantity	Experimental (p.u)	Theoretical (p.u)
off-state input line current i_{1off} (peak)	0.64	0.63
off-state filter capacitor voltage v_{aboff} (peak)	3.6	3.5

from which it is evident that, as intended in the design of the input filter, the off-state input line current is less than the full load value of 0.67 p.u. (see item 1 above).

Figure 8.17 shows the cycloinverter circuit waveforms, with the tank-load replaced by an equivalent resistance of 4Ω. Although the circuit waveforms in general closely resemble those obtained with the tuned tank-load (Figure 8.15), the modulation of the output current is substantially reduced. This would naturally be expected since, with a tuned tank-load, the cyclo-inverter output circuit presents a lower impedance to the dominant sideband harmonics than when the load is resistive (see Figure 5.36).

8.4.2 Cycloinverter operation at varying output power levels

Figures 8.18, 8.19 and 8.20 show U.V. recordings of some of the cycloinverter waveforms, for operation at reduced output power levels corresponding to $\theta = 90^{o}$, 120^{o} and 150^{o} respectively. These results indicate that:

1. the graphical output of the digital simulation of the cycloinverter obtained for the corresponding power control angles and presented in Figures* 7.17, 7.18 and 7.19 are in close agreement with the experimental data, the amplitude difference between any corresponding pair of experimental and computed waveforms being less than 10%. The close similarity of the pairs of output current waveforms clearly indicates that both have approximately the same harmonic content, and hence that the frequency spectrum obtained from the numerical Fourier analysis of the computed output current waveform (Figure 5.22) is quite reliable.

2. in accordance with the theoretical results given in Figure 7.16, the harmonic content of the input line current remains satisfactory throughout the full range

---

* Note that these figures are obtained for slightly differing values of commutating circuit components, as indicated.

of power control, although it deteriorates slightly for $90^{o} < \theta < 120^{o}$.

3. as the output power falls, the input displacement factor becomes more leading, and for $\theta \rightarrow 180^{o}$, it approaches zero. Comparisons of the variations of the input displacement factor (which is approximately equal to the input power factor due to the low input current distortion) with the output power* obtained from both the mathematical and the experimental models are given in Figure 8.21. As the U.V. recordings of Figures8.18 to 8.21 indicate, for $\theta < 120^{o}$ a decrease in the output power is accompanied by a drop in the input line current, hence maintaining a relatively high input power factor. However, as θ is increased above 120^{o}, the input line current begins to increase again, and the reduced output power is accompanied by a sharp decrease in the input power factor. This variation of the input line current is clearly in accordance with that predicted in Figure 7.16.

---

* During experiments the total cycloinverter output power, (i.e. total power delivered to the tank-load) was for the sake of simplicity measured, whereas in theoretical work the useful output power is considered.

4. the input filter is effective in preventing high commutating capacitor voltage rises for power control angles around 90^{o}.

8.4.3 Cycloinverter operation with a varying load

To investigate the inverter performance under the varying load conditions typical of a static heating load, the operational frequency and the tank-load components were varied as suggested on page 392. The inverter behaviour under these conditions was found to be in line with the results of the digital simulation. Figure 8.22 shows U.V. recordings of various cycloinverter waveforms, when operating at the load condition C (corresponding to the lowest w_o (908 Hz) and R_{eq} (2Ω)), and digitally obtained results for the same operating conditions were given in Figure 7.24. As shown, the envelope of the output current is distorted mainly by the non-multiple operational frequency. This distortion is also caused partly by a significant error in the setting of the power control angle θ. As the control-logic circuits received a single synchronisation pulse during a full mains cycle, the firing circuits were slow in responding to phase variations of the cycloinverter input voltages (i.e. the filter capacitor voltages), and the deviations in θ were observed to be as high as approximately $\bar{+}\ 15^{o}$. Clearly, this problem can be cured by decreasing the time delay in monitoring these phase variations. Nevertheless the experimental recordings confirm the following theoretical predictions:

1. input line voltages are free of any significant distortion component for all characteristic operational conditions (operation at the load conditions A, B, C, D, E).

2. the lowest input power factor occurs at C and is about 0.8 (estimated by comparing the phases of the input line current and the source voltage in Figure 8.23). The theoretical prediction from Figure 7.25 is approximately 0.78.

3. the input filter is effective in suppressing any excessive voltage rise in the commutating circuit elements. In line with the theoretical estimation of section 7.5.2, the ratio:

$$\frac{\text{maximum peak commutating capacitor voltage (occurs at C)}}{\text{minimum peak commutating capacitor voltage (occurs at E)}} \simeq 1.2$$

8.5 Power Control in the Half-Bridge Cycloinverter

To investigate its power control characteristics, a half-bridge cycloinverter was constructed by modifying the power circuit of the full-bridge cycloinverter. In so doing, the commutating components were unaltered. To provide reverse recovery current to the negative group thyristor S4, which is

in series with diodes D1, D2 and D3, a snubber circuit was placed across each of the diodes. The output frequency of the device was adjusted to 1050 Hz and a tuned tank-load of selectivity Q_L = 5 and equivalent resistance R_{eq} = 4Ω was employed.

Figures 8.23 and 8.24 show U.V. recordings of the output current i_L, tank-load voltage v_{co} and commutating capacitor voltage v_{c1} during power control, together with computed waveforms for the same operational conditions. The close similarity of the wave shapes and their amplitudes is clearly evidence of the correctness of the digital simulation. The reasonably good correlation of the output current waveforms also indicates that the harmonic spectrum obtained numerically from the computer is quite reliable. The variation of the output power and the input power factor with power control angle θ was measured as,

PF_I/P_o \ θ	30^o	90^o	120^o	150^o
PF_I (theoretical)	0.67 (0.70)	0.64 (0.62)	0.41 (0.38)	0.25 (0.20)
P_{CT} (p.u) (theoretical)	1.0 (1.1)	0.78 (0.74)	0.55 (0.45)	0.32 (0.22)

In the table above, the experimental value of the cyclo-inverter output power is given as the total power dissipated in the tuned tank circuit P_{CT} and it is hence higher than the theoretical estimate of the useful output power P_o, due to the contribution of the sideband harmonics of the heating coil current. As seen, the difference between P_{CT} and P_o increases as the harmonic content of the heating coil current deteriorates for increased values of θ. Nevertheless, assuming that the wasted power P_w (due to the harmonics) and the useful power P_o components of the total coil power vary as in Figure 5.17, it can be shown that the experimental results are in even closer agreement with the theoretical results than is indicated in the above table. The experimental values of the input power factor were evaluted by dividing P_{CT} by the measured r.m.s. input line current and input voltage, and are therefore slightly higher than the theoretical predictions. Clearly, this increase in the experimental PF_I (due to the inclusion of P_w in the output power) is partly compensated for the circuit losses in the device, neglected when calculating PF_I theoretically.

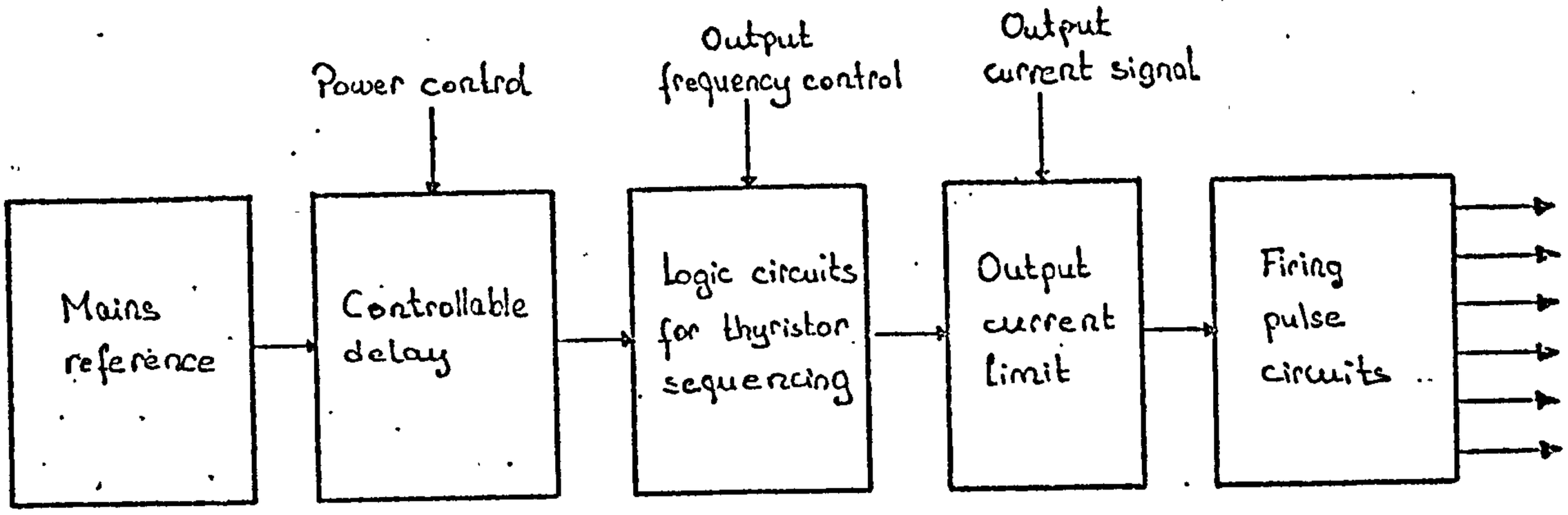

Figure 8.1 A control circuit for the cycloinverter

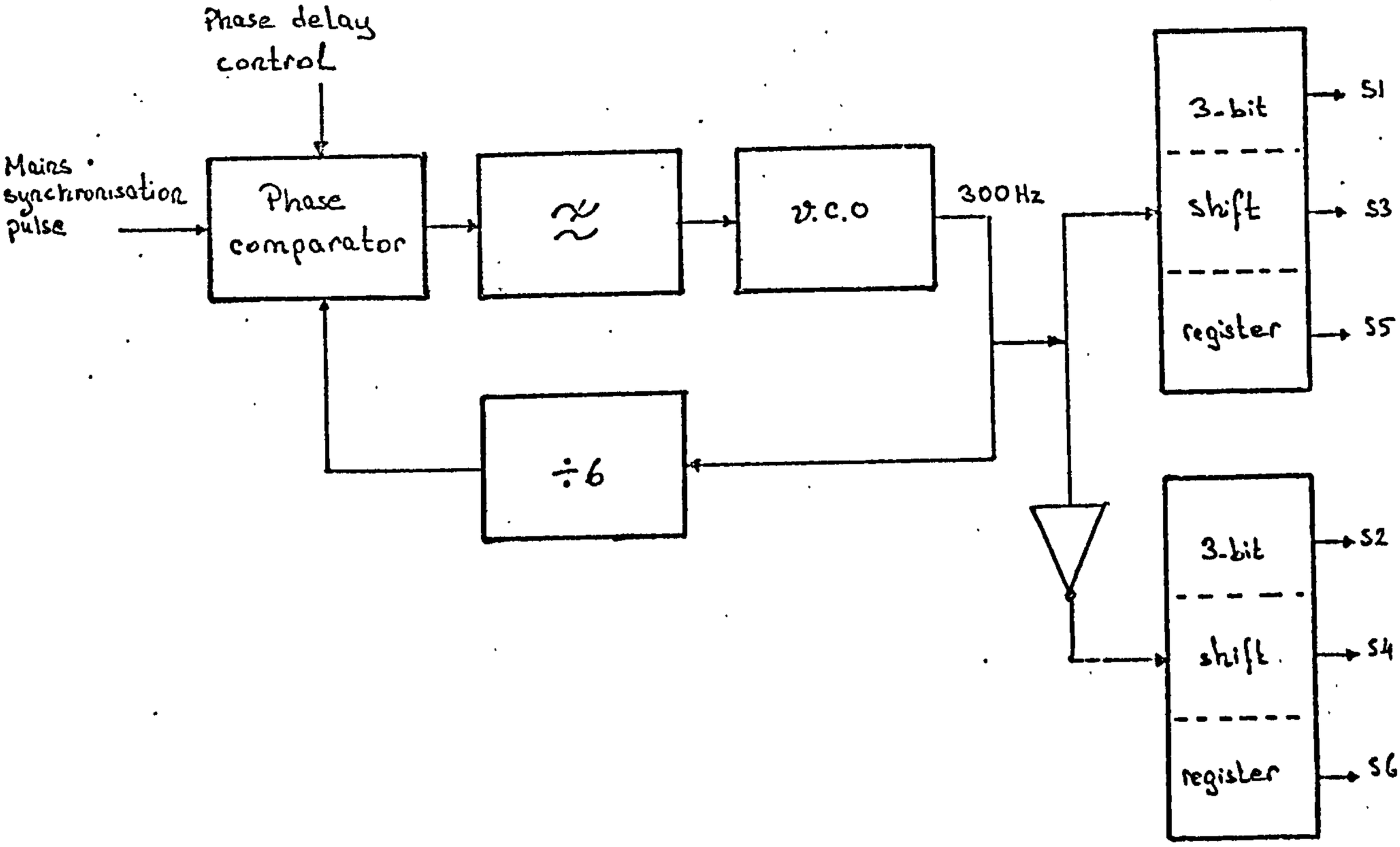

Figure 8.2 A reliable technique to obtain the permissible firing range of the cycloinverter thyristors

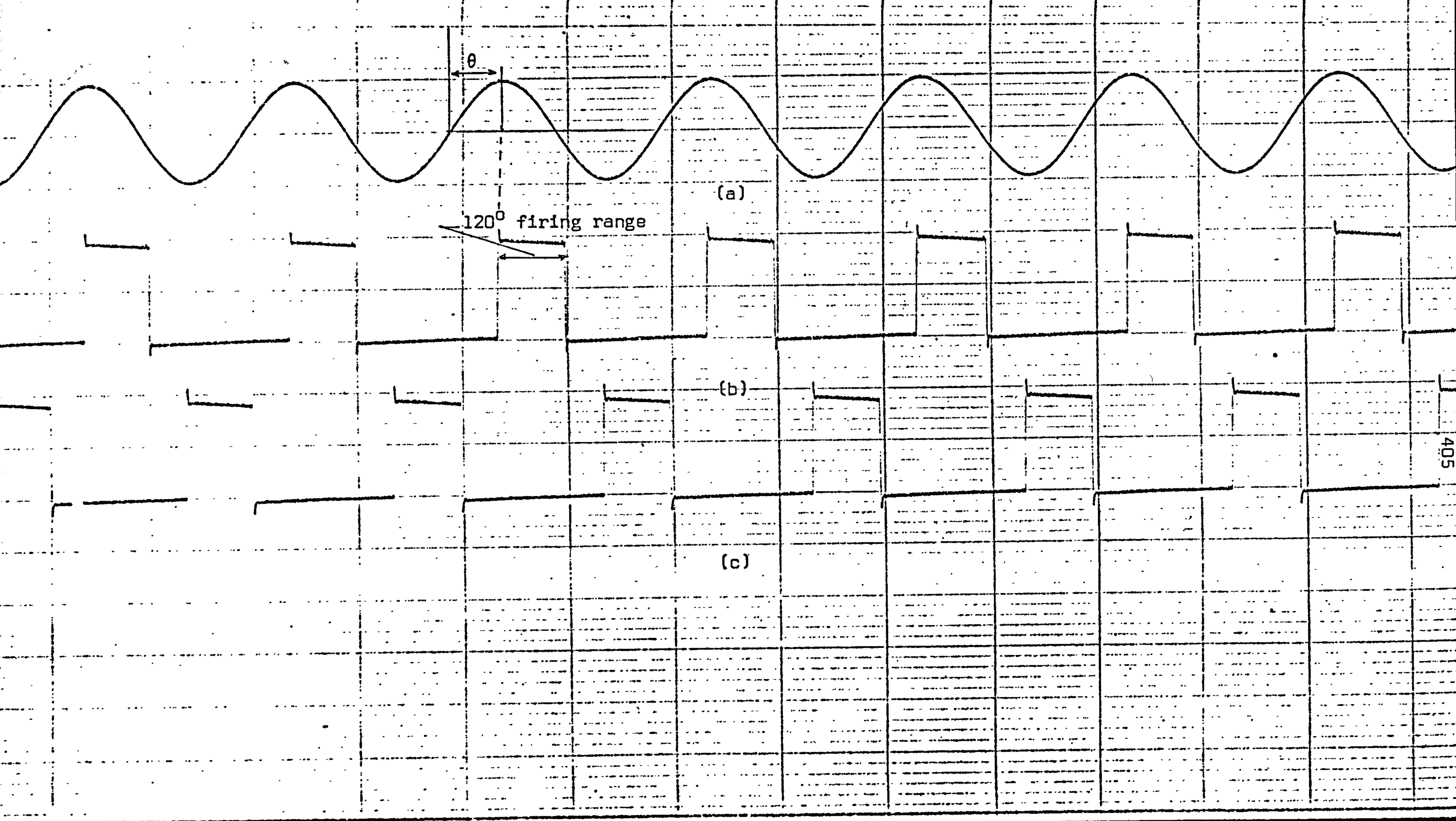

Figure 8.3 U.V. recordings of (a) the phase 1 voltage, (b) the permissible firing interval for thyristor S1, (c) the permissible firing range for thyristor S4

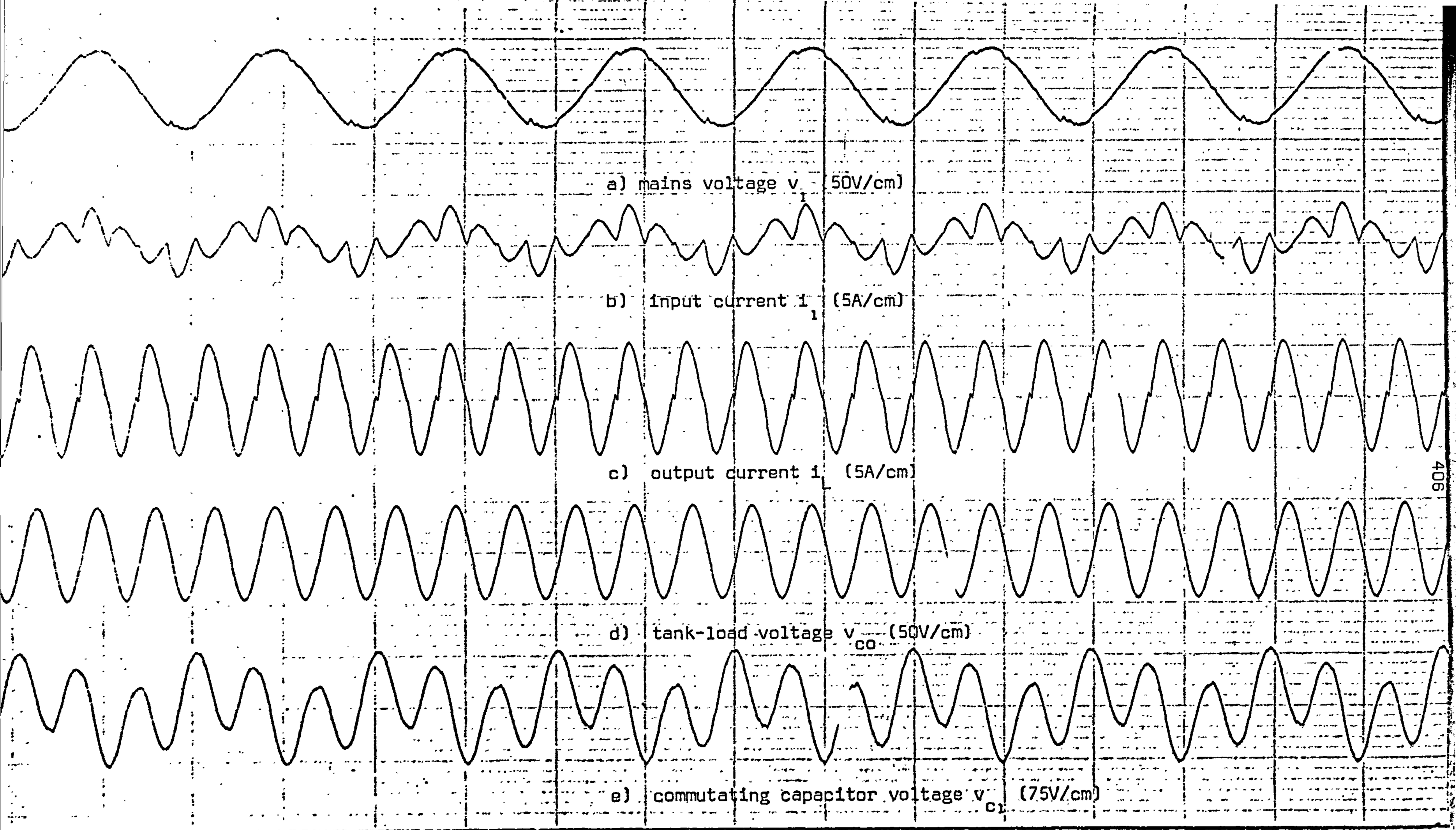

Figure 8.4 150 Hz full-bridge cycloinverter waveforms at full output power ($\theta = 30^o$, $X_L = 0.9$ p.u, $X_c = 1.08$ p.u. $Q_L = 5$)

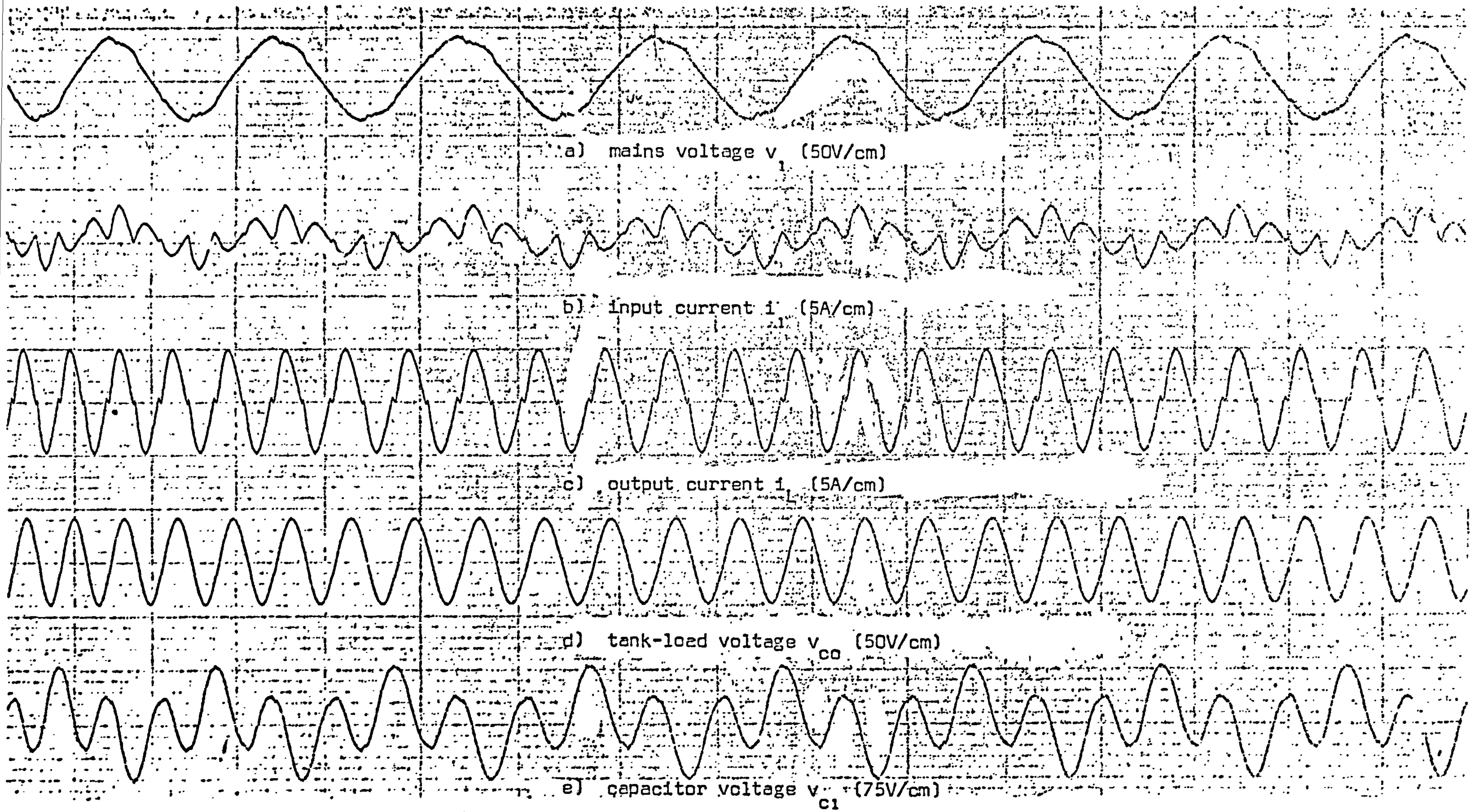

Figure 8.5 150 Hz full-bridge cycloinverter waveforms when the power control angle $\theta = 90^o$ (X_L = 0.9 p.u, X_c = 1.08 p.u, Q_L = 5)

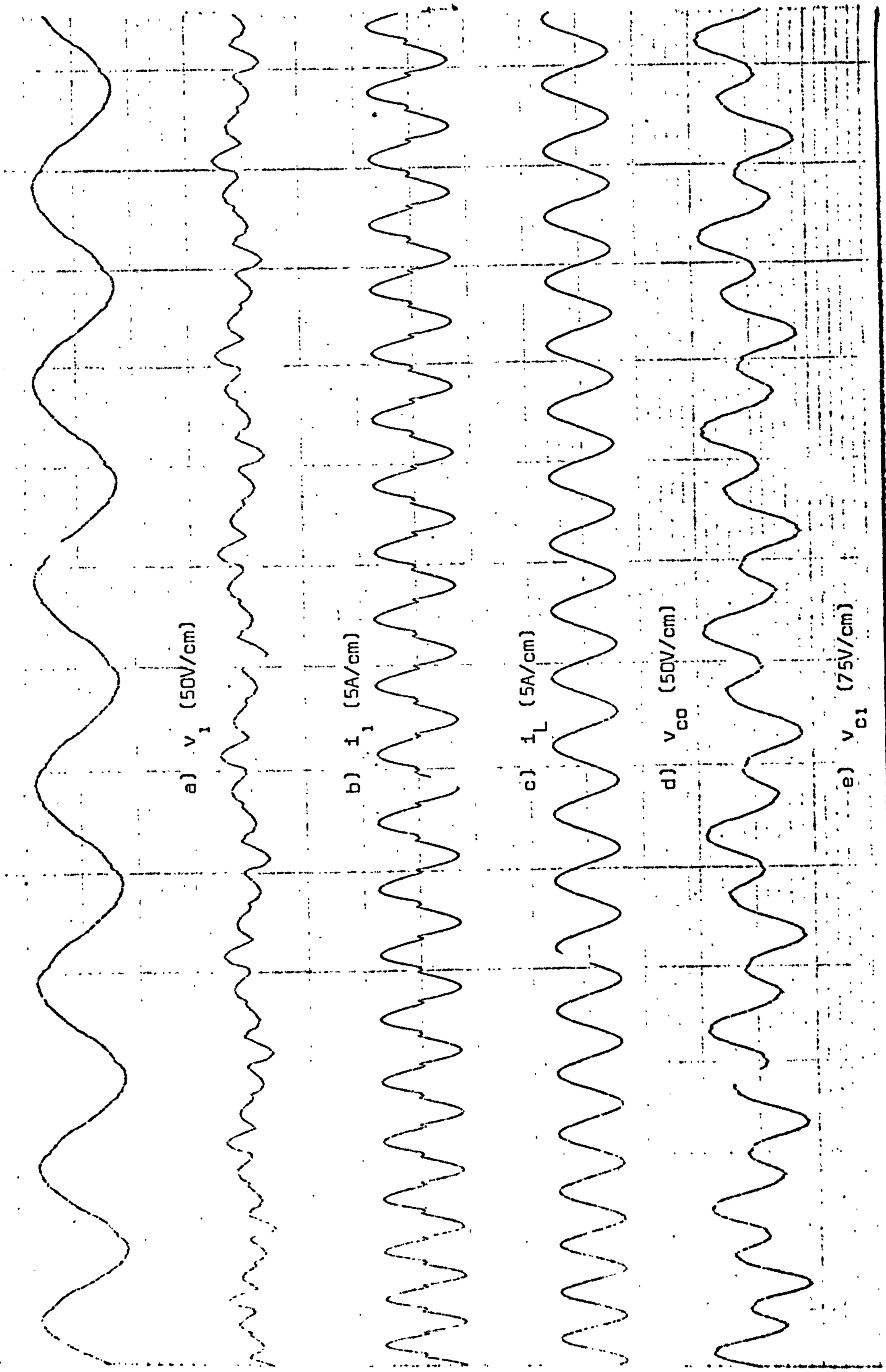

Figure 8.6 150 Hz full-bridge cycloinverter waveforms when the power control angle $\theta = 110^{o}$ ($X_L = 0.9$ p.u, $X_c = 1.08$ p.u $Q_L = 5$)

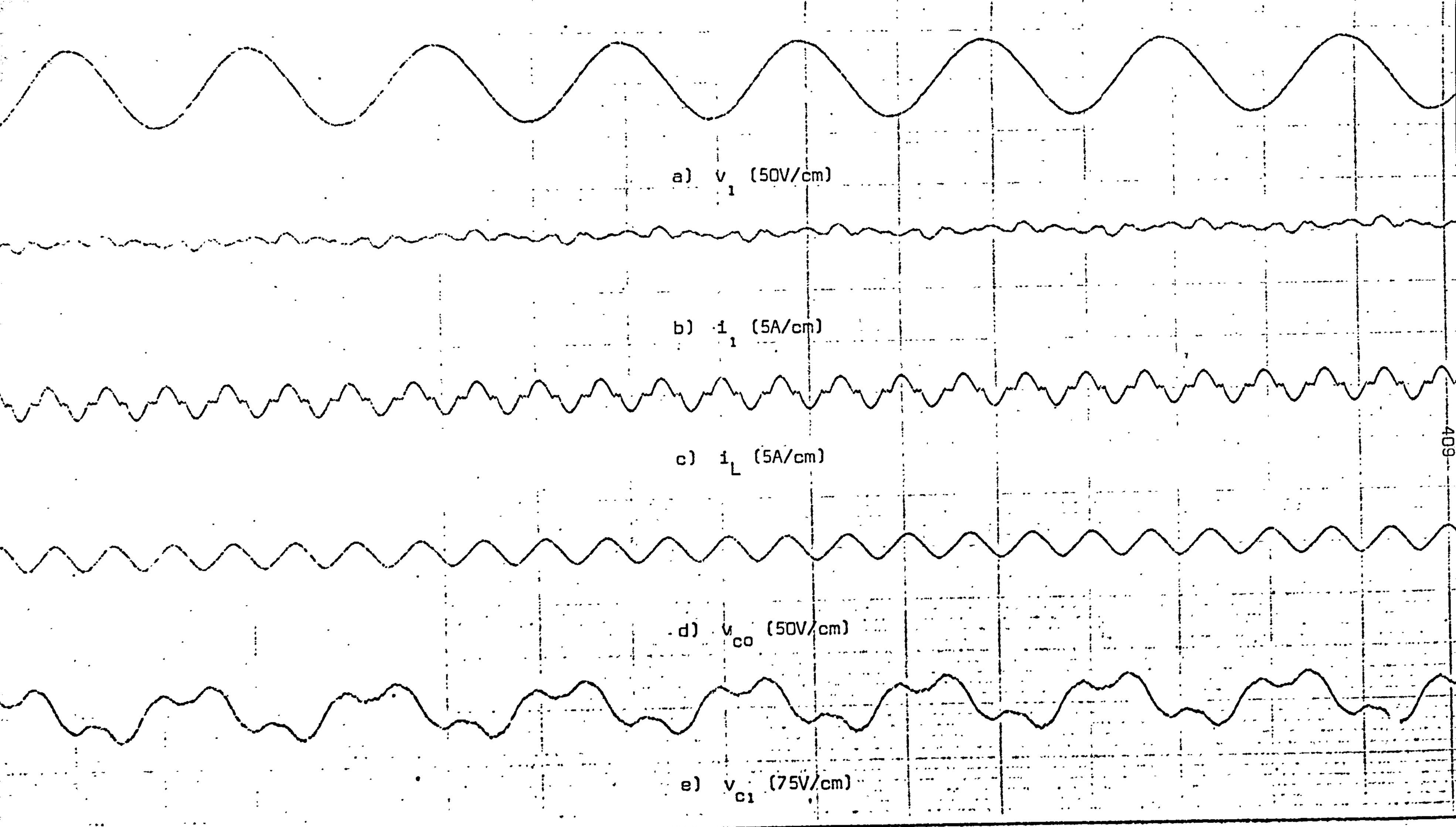

Figure 8.7 Full-bridge cycloinverter waveforms when the power control angle $\theta = 150^{o}$. (X_L = 0.9 p.u, X_c = 1.08 p.u. Q_L = 5)

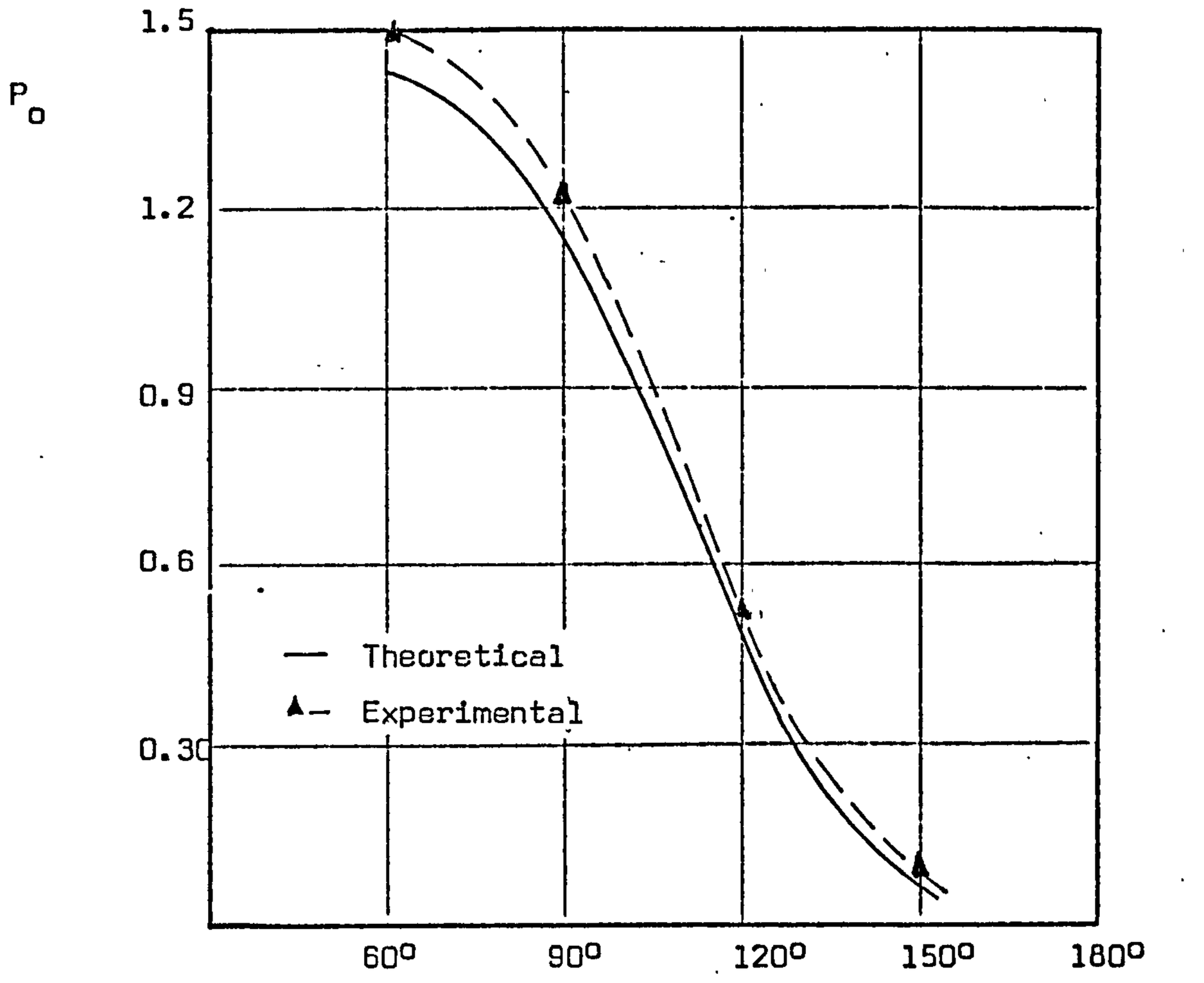

Figure 8.8 Variation with θ of output power of the 150 Hz full-bridge cycloinverter

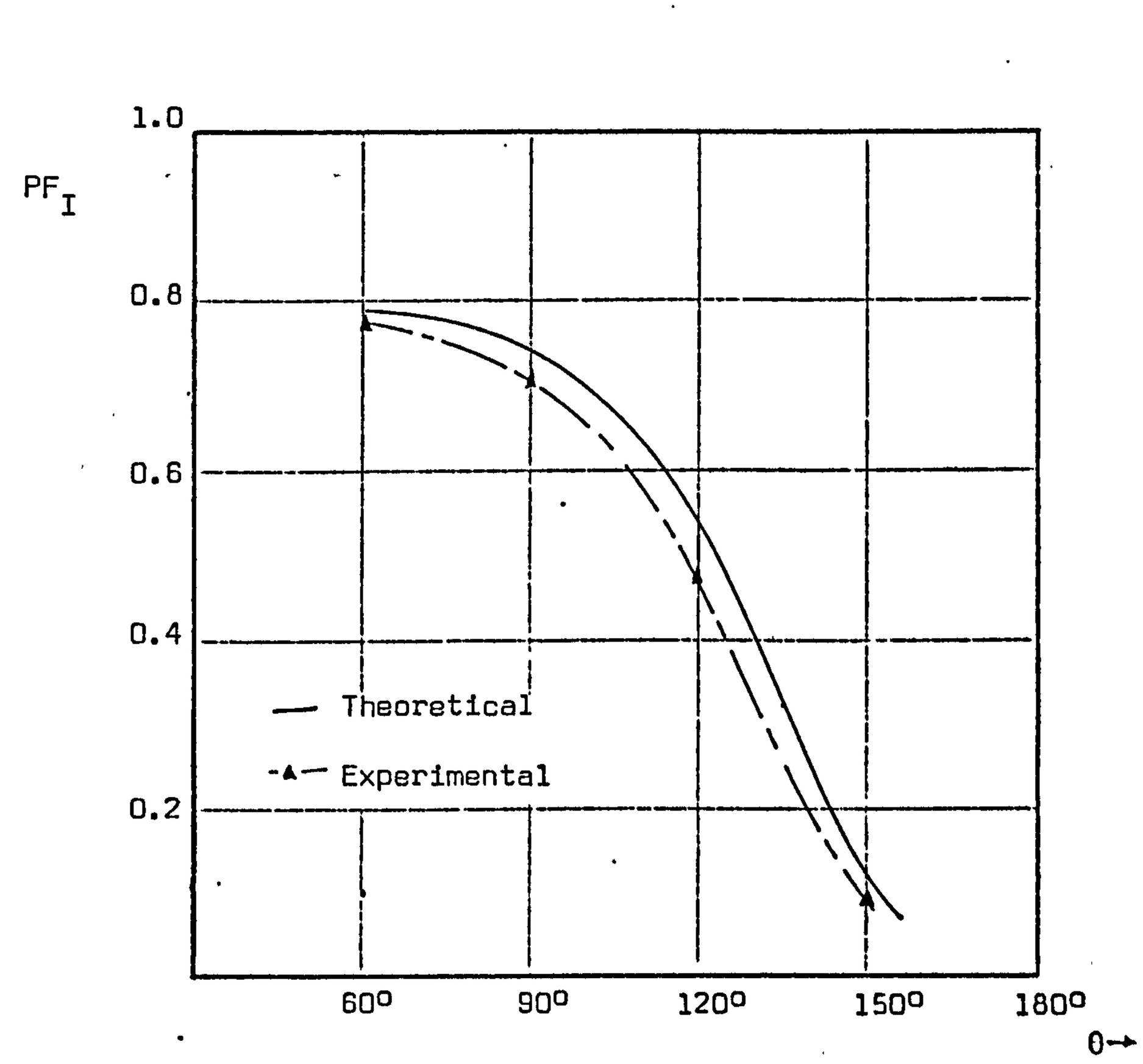

Figure 8.9 Variation with θ of input power factor of the 150 Hz full-bridge inverter

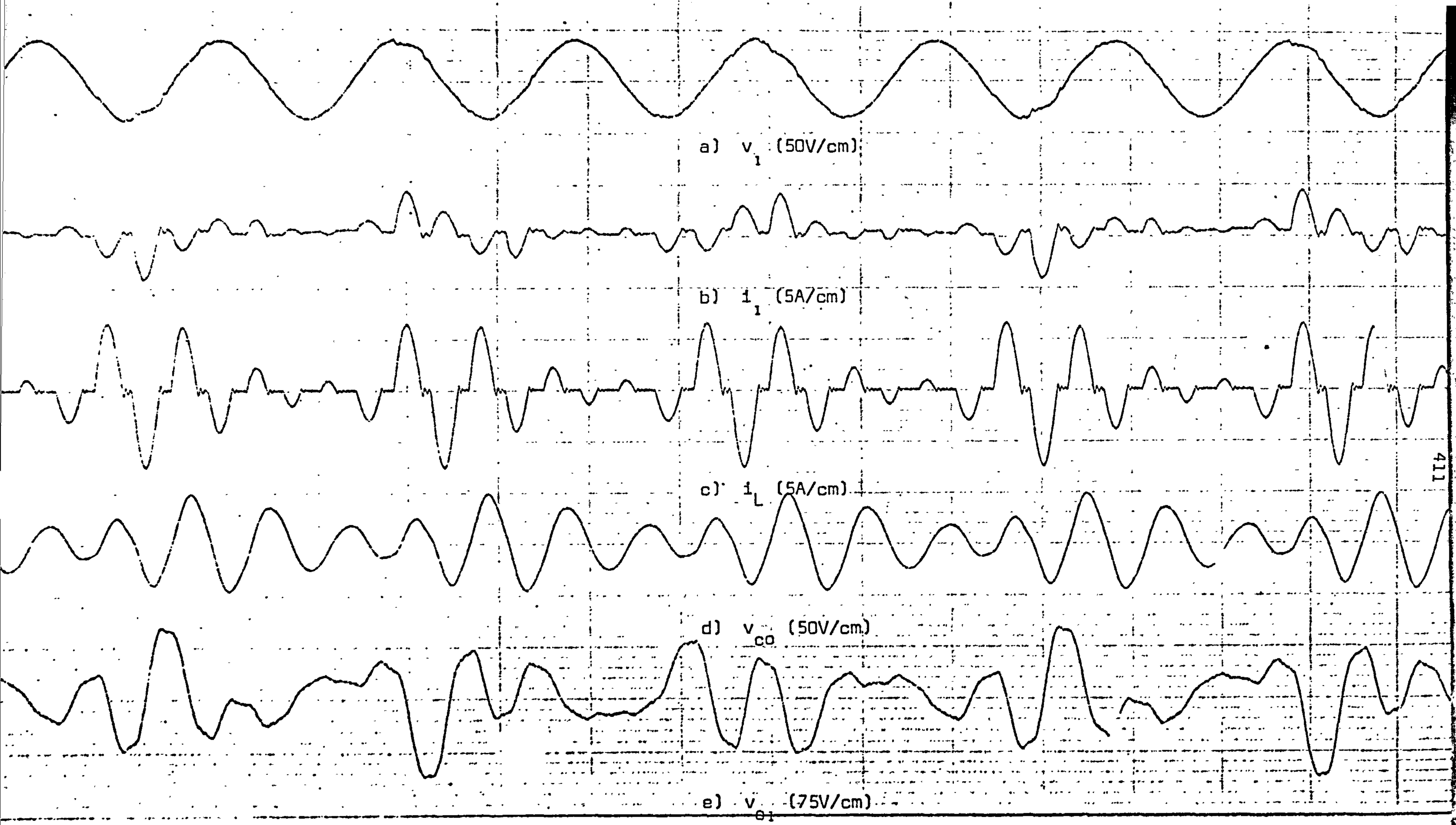

Figure 8.10 Full-bridge cycloinverter waveforms when operating at f_o = 0.8 p.u, (X_{LB} = 0.9 p.u, X_{CB} = 1.08 p.u, f_{oB} = 150Hz

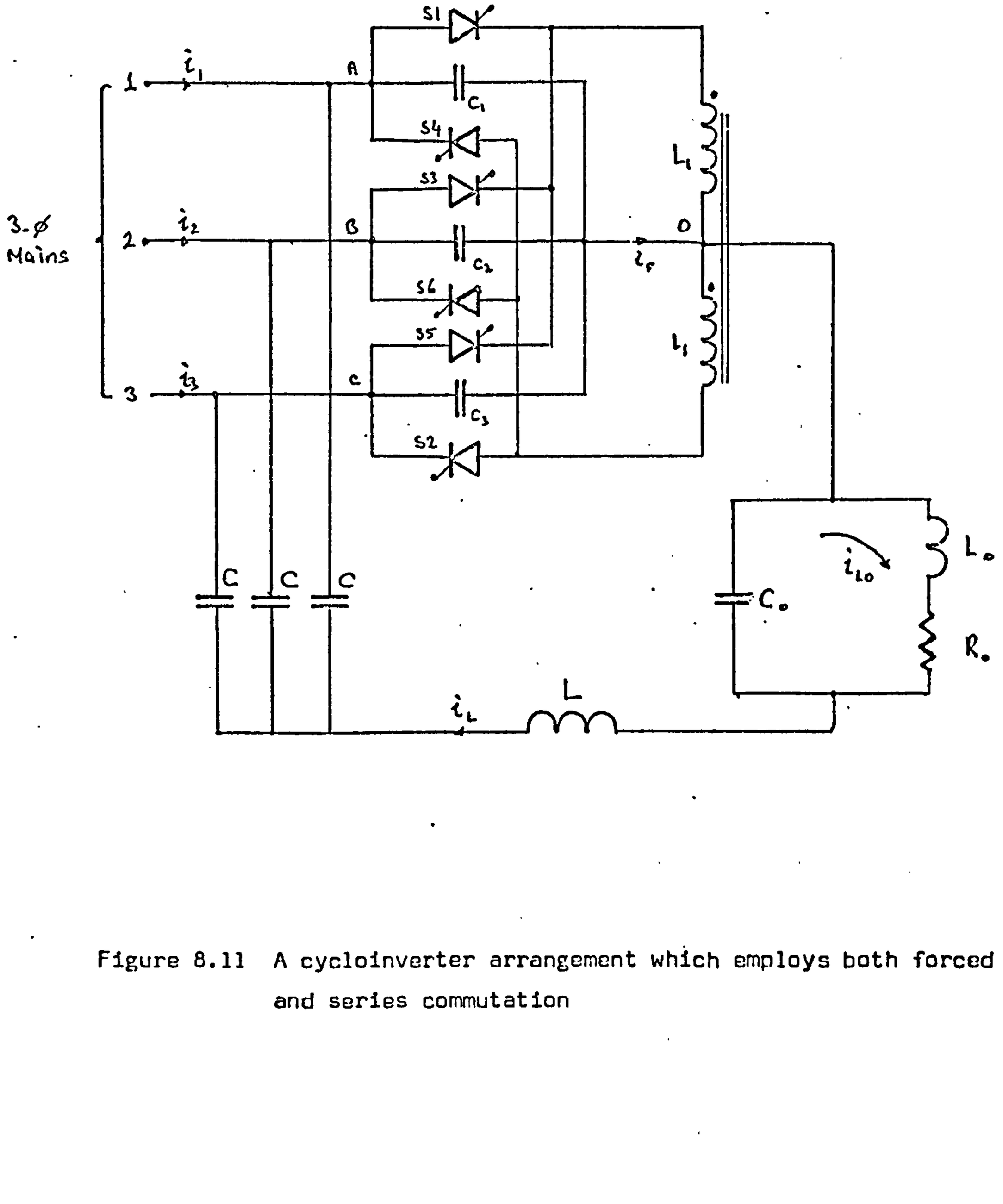

Figure 8.11 A cycloinverter arrangement which employs both forced and series commutation

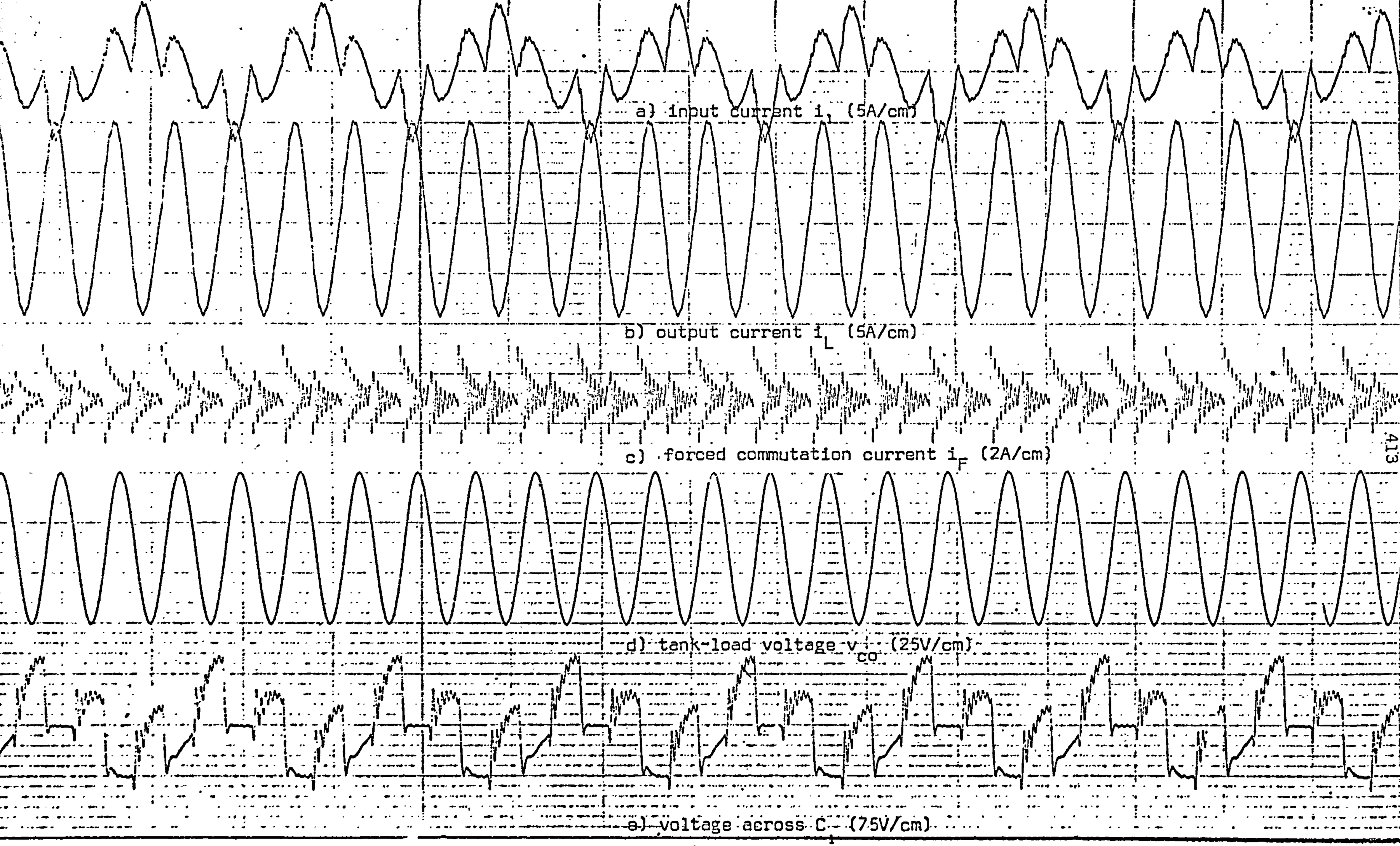

Figure 6.12 Waveforms of 150 Hz full-bridge forced and series load commutated cycloinverter

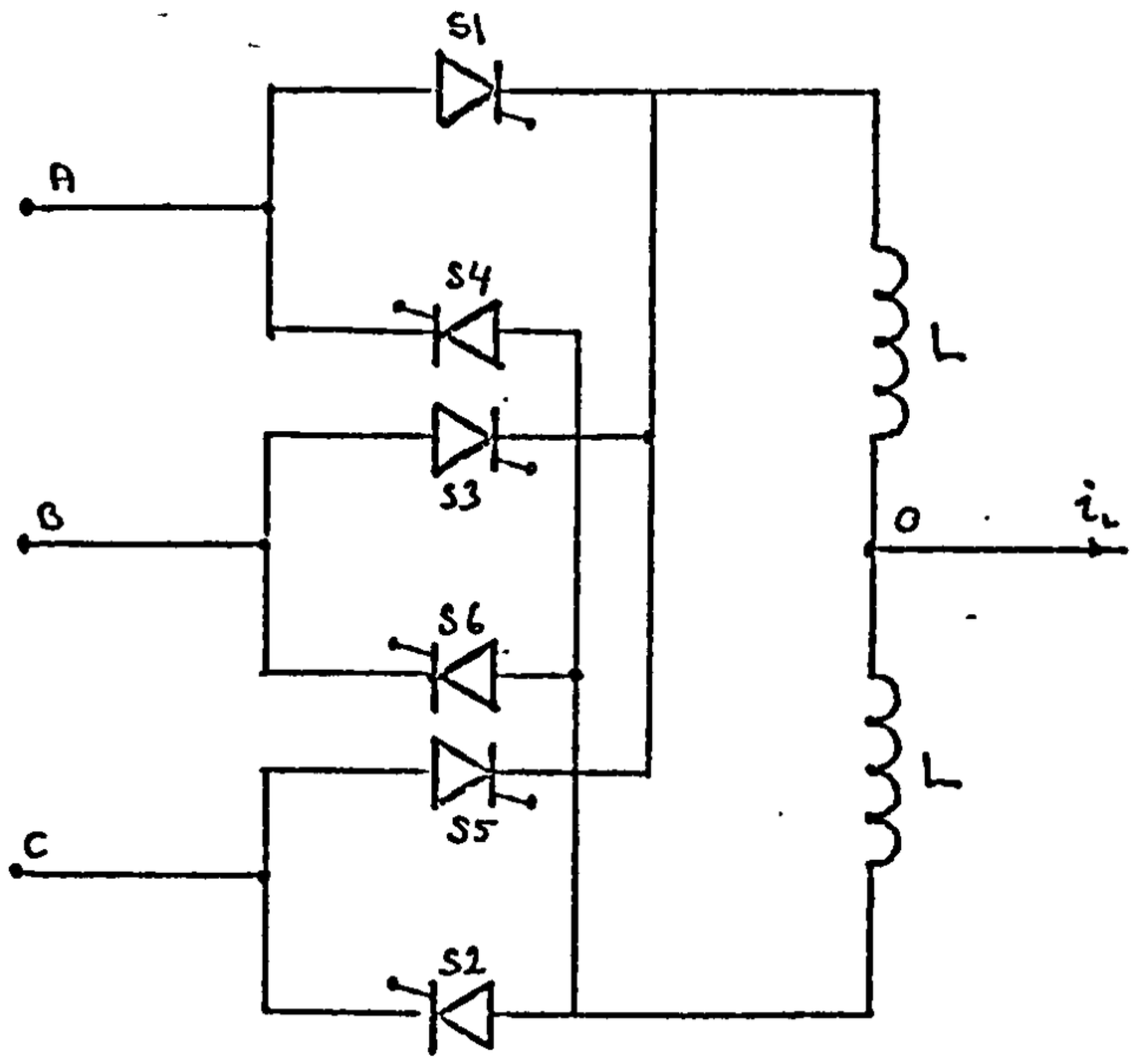

Figure 8.13 Part of a cycloinverter power circuit where separate commutating inductors are placed on the path of the positive and negative group thyristors

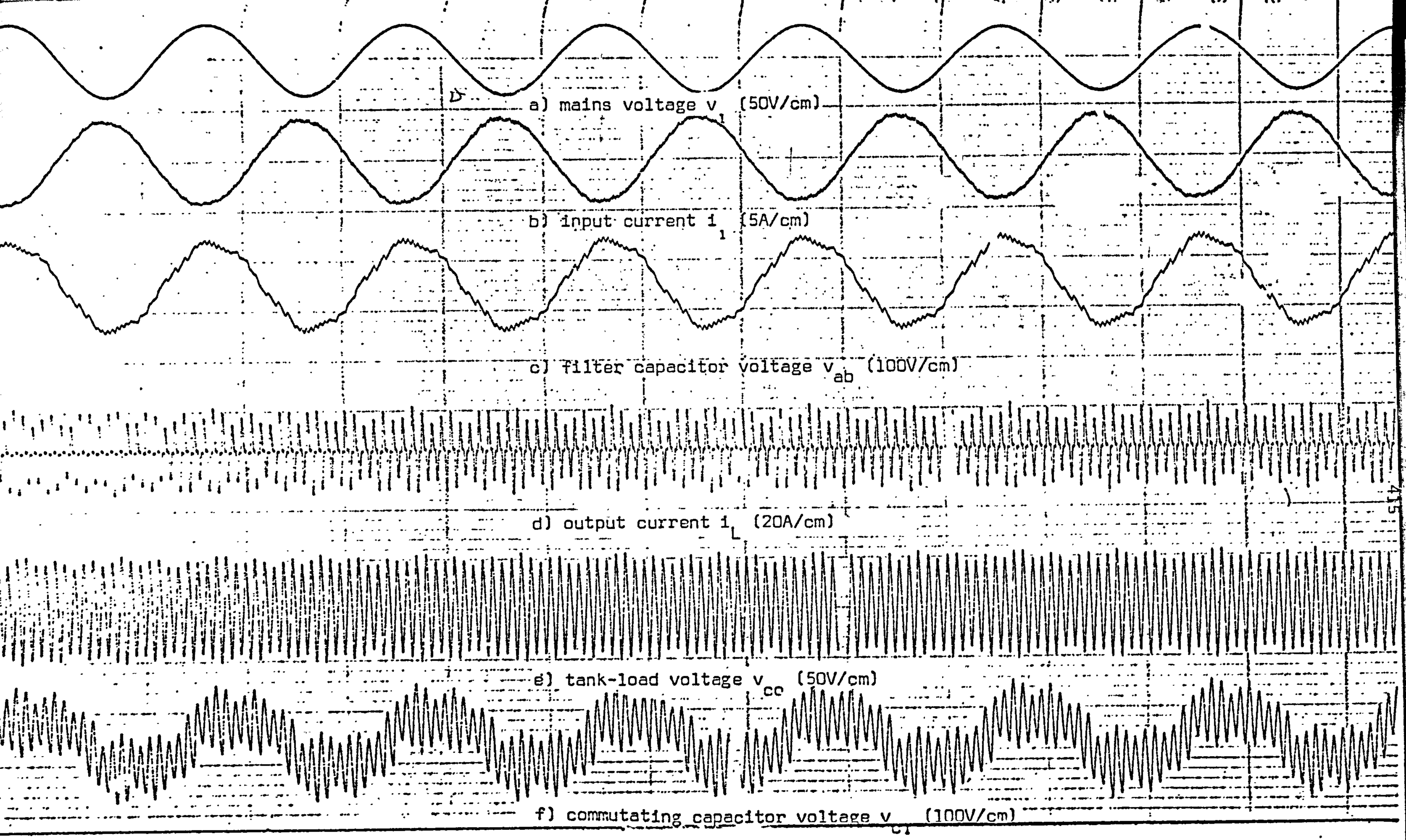

Figure 8.14 U.V. recordings for the high frequency full-bridge cycloinverter with an input filter (X_{CF} = 4.51 p.u., X_{LF} = 1.63 p.u, X_L = 0.7 p.u, X_c = 1.35 p.u, f_o = 1050 Hz, Q_L = 5, θ = 30°..

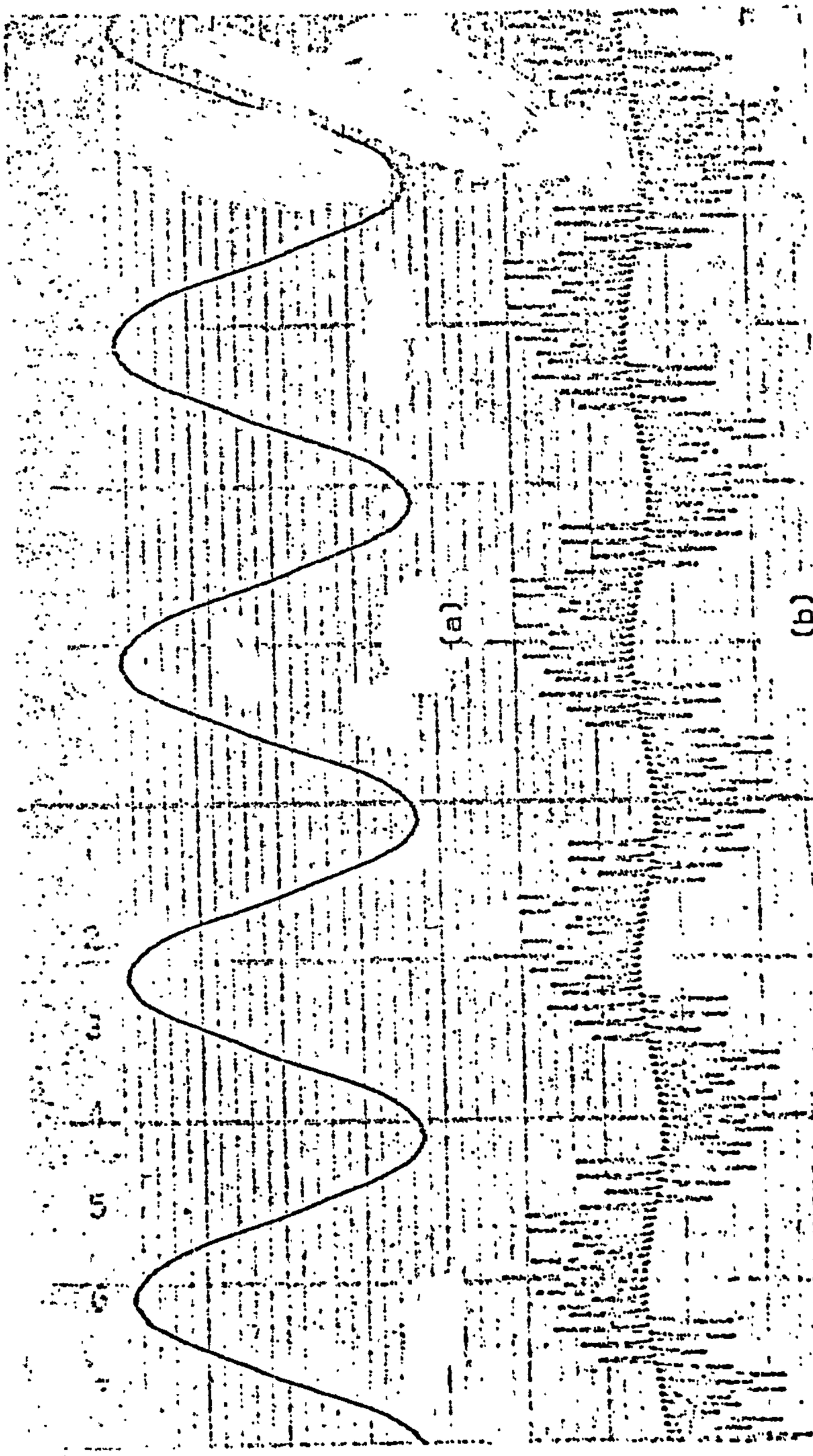

Figure 8.15 1050 Hz full-bridge cycloinverter waveforms (not scaled).
a) input current to the filter i_1,
b) input current to the cycloinverter i_1'

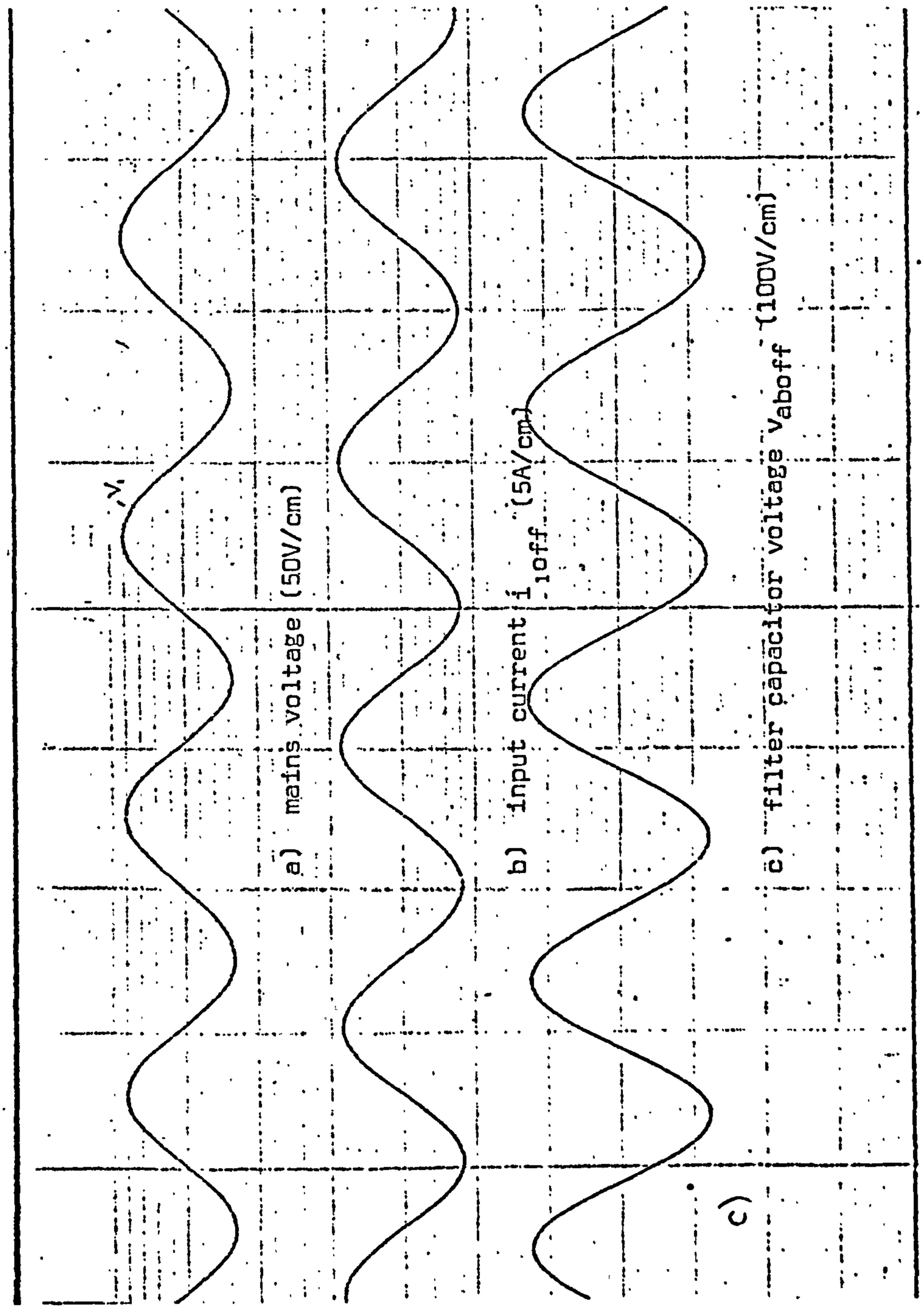

Figure 8.16 Various input filter waveforms when all the cycloinverter thyristors are nonconducting
(X_{CF} = 4.51 p.u, X_{LF} = 1.63 p.u)

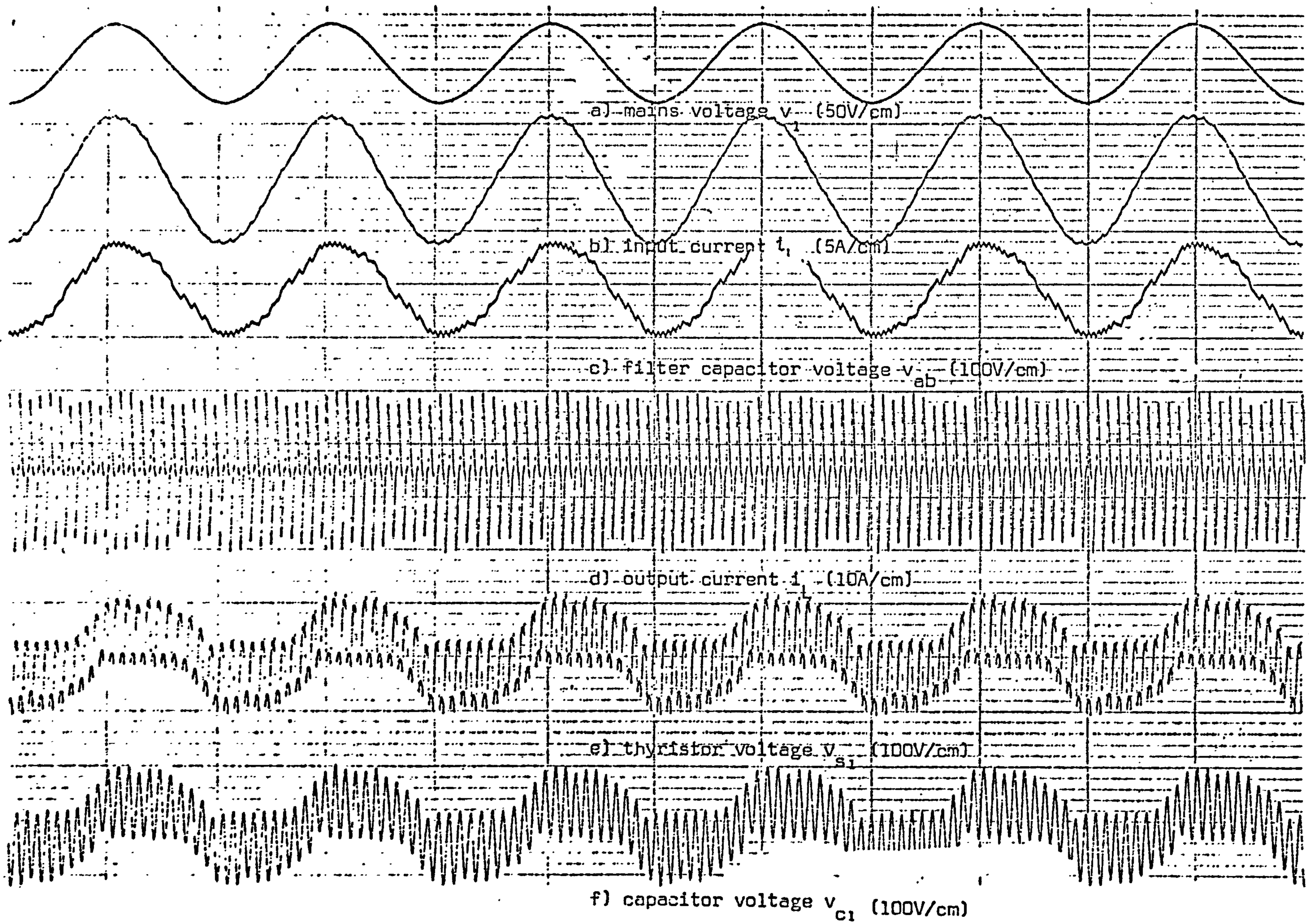

Figure 8.17 Waveforms of the 1050 Hz full-bridge cycloinverter with a resistive load (X_{CF} = 4.51 p.u, X_{LF} = 1.63 p.u. X_1 = 0.7 p.u., X_2 = 1.35 p.u)

a) mains voltage (50V/cm)

b) input current (5A/cm)

c) filter capacitor voltage v_{ab} (100V/cm)

d) output current i_L (7.5A/cm)

e) tank-load voltage v_{cb} (50V/1.5 cm)

f) commutating capacitor voltage v_{c1} (75V/cm)

Figure 8.18 1050 Hz, full-bridge cycloinverter waveforms when the power control angle $\theta = 90^o$ ($X_{CF} = 4.51$ p.u, $X_{LF} = 1.63$ p.u, $X_L = 0.7$ p.u, $X_c = 1.35$ p.u, $Q_L = 5$)

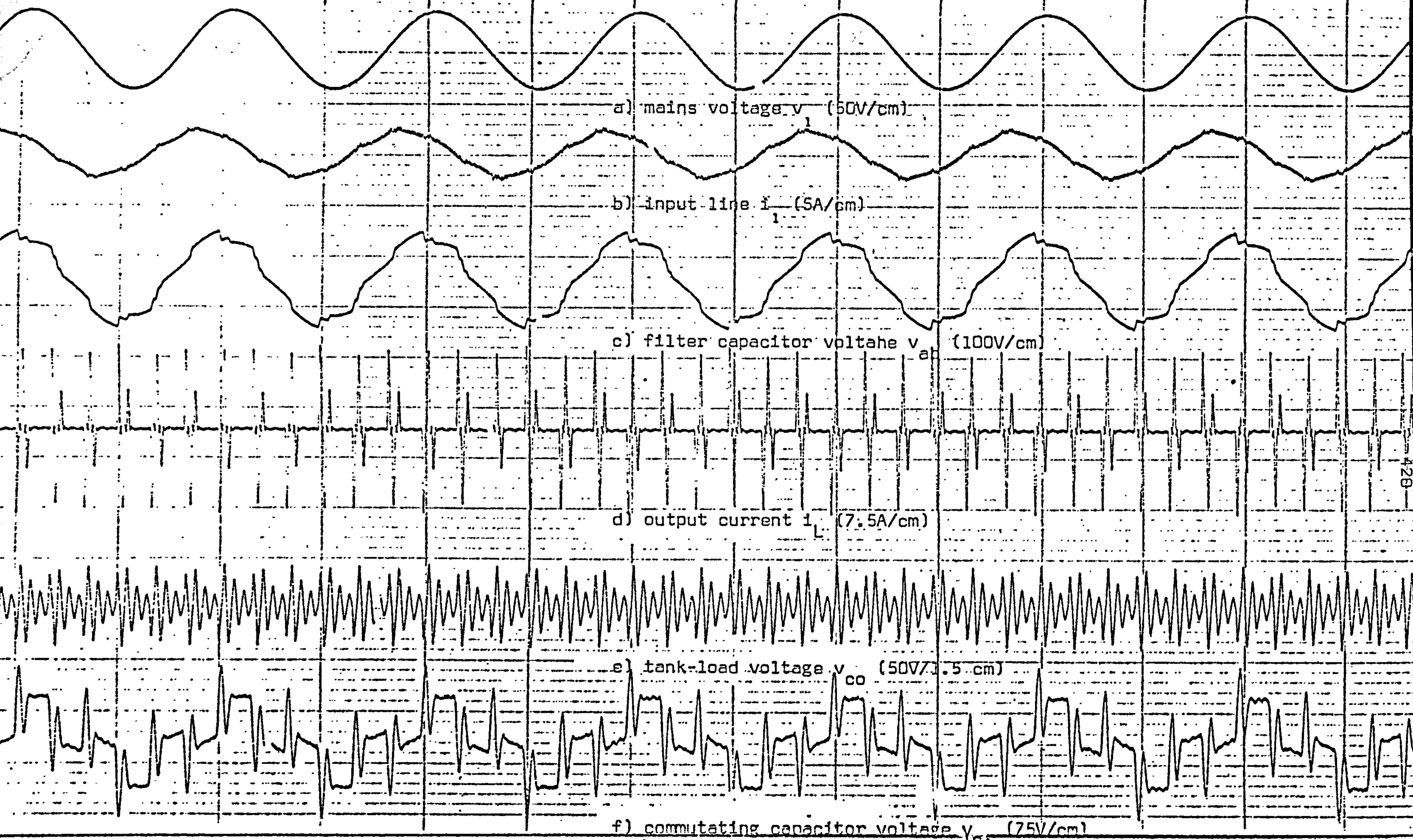

Figure 8.19 1050 Hz Full-bridge cycloinverter waveforms when the power control angle $\theta = 120^{o}$. ($X_{CF} = 4.51$ p.u., $X_{LF} = 1.63$ p.u, $X_L = 0.7$ p.u., $X_c = 1.35$ p.u., $Q_L = 5$)

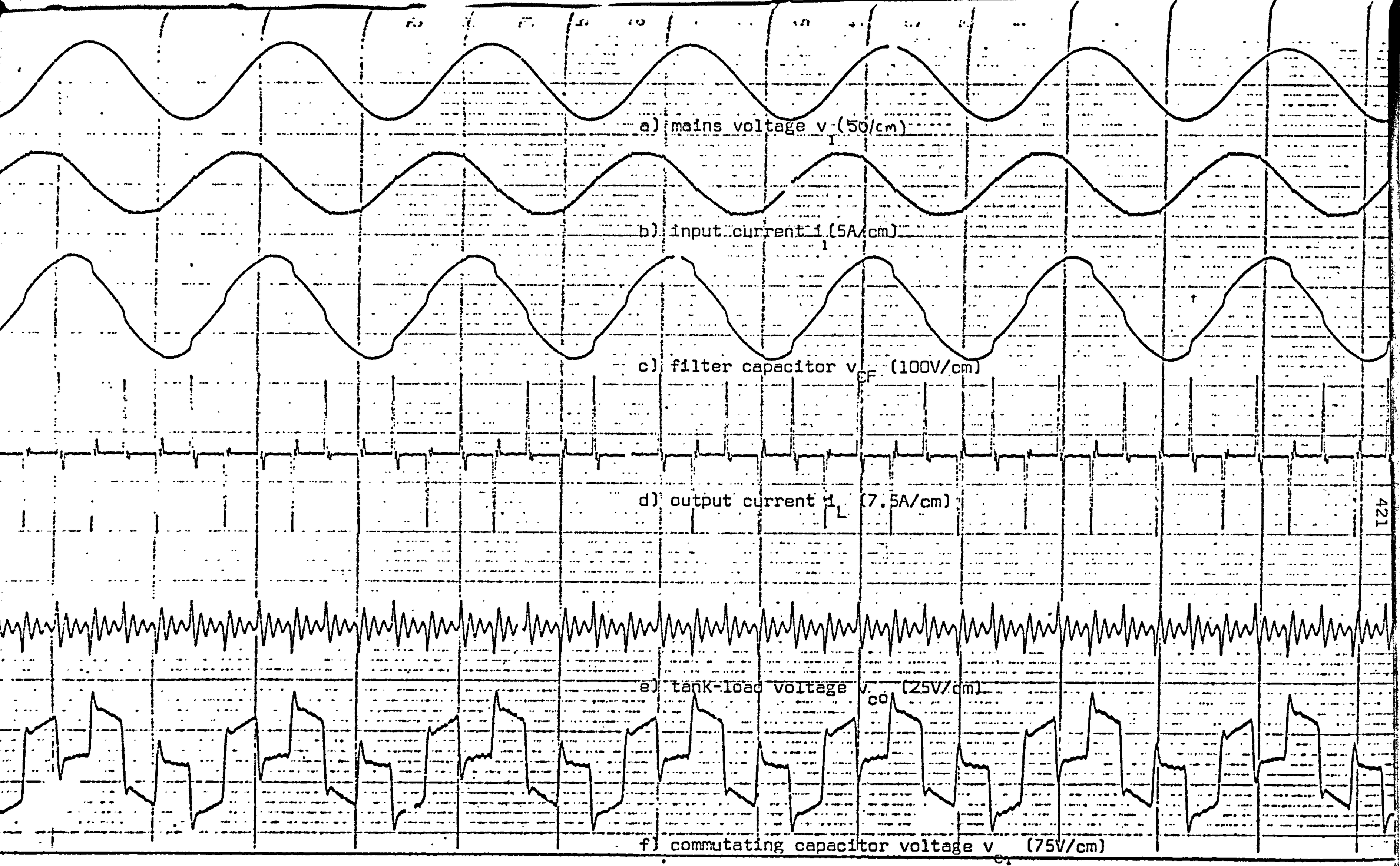

Figure 8.20 1050 Hz full-bridge cycloinverter waveforms when the power control angle $\theta = 150^{o}$. ($X_{CF} = 4.51$ p.u, $X_{LF} = 1.63$ p.u, $X_c = 1.35$ p.u, $X_L = 0.7$ p.u, $Q_L = 5$)

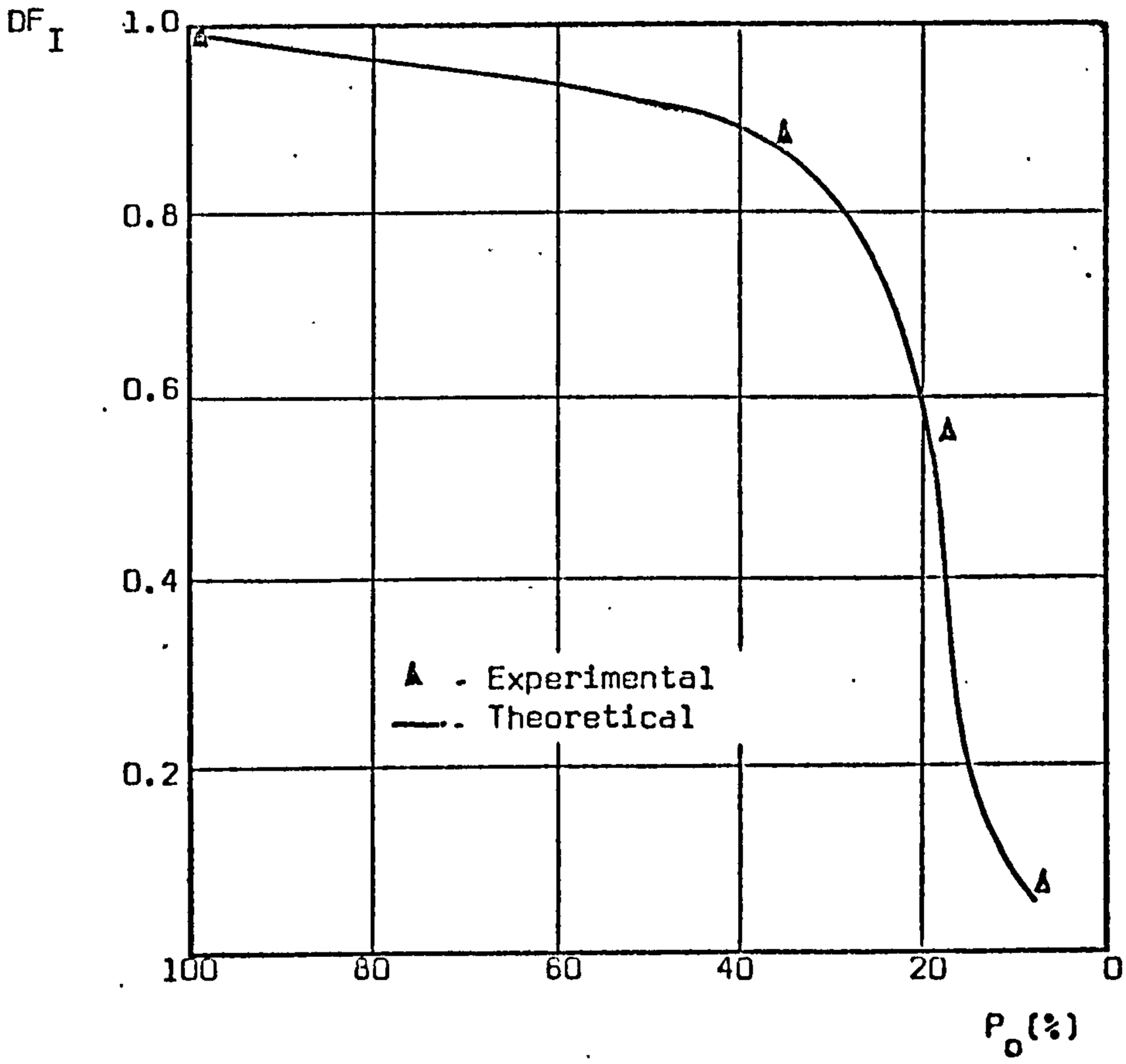

Figure 8.21 Variation of input displacement factor with output power in the input filtered full-bridge inverter (f_o = 1050 Hz, Q_L = 5).

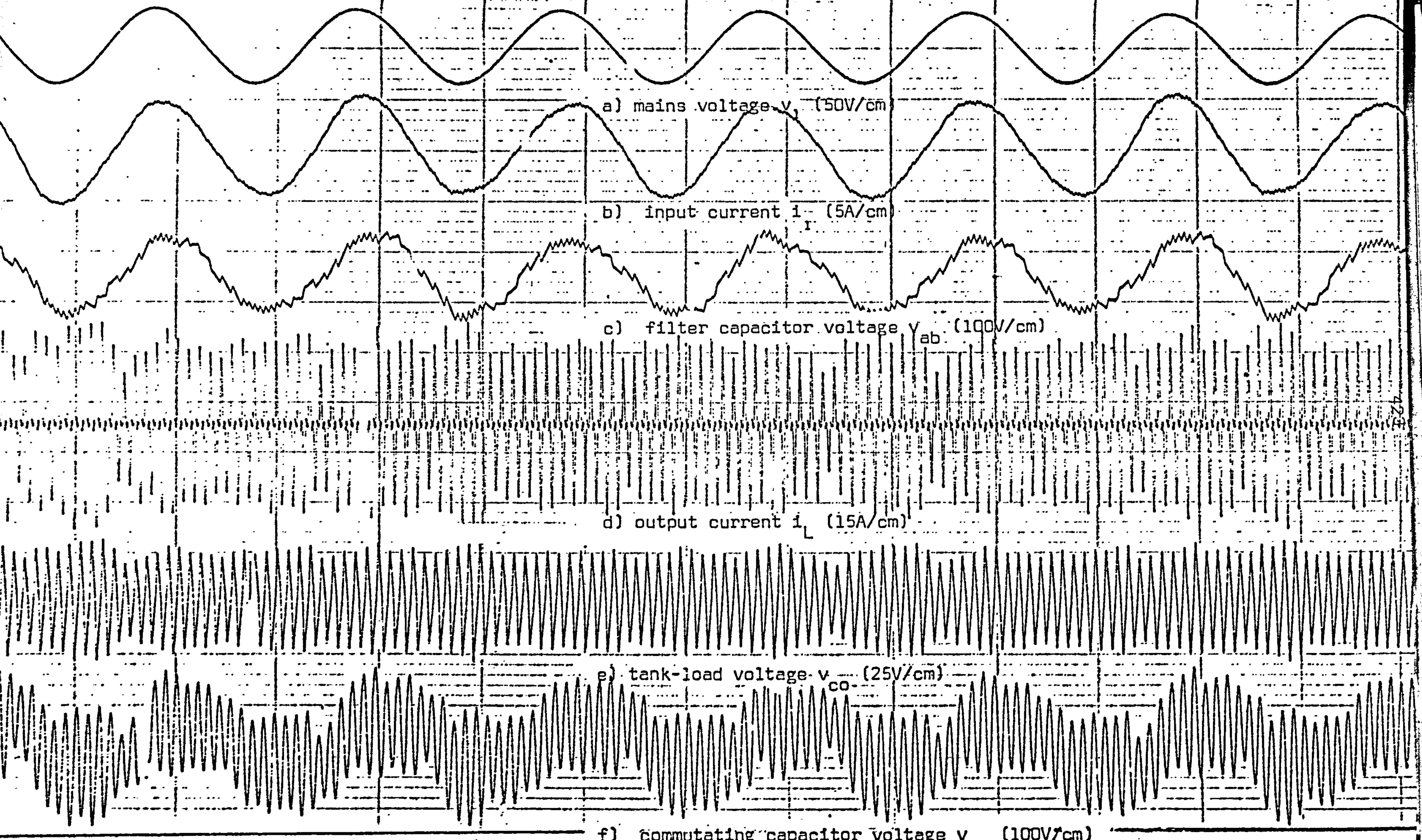

Figure 8.22 Cycloinverter waveforms corresponding to the operating condition C (f_o = 908 Hz, Q_L = 3.59)

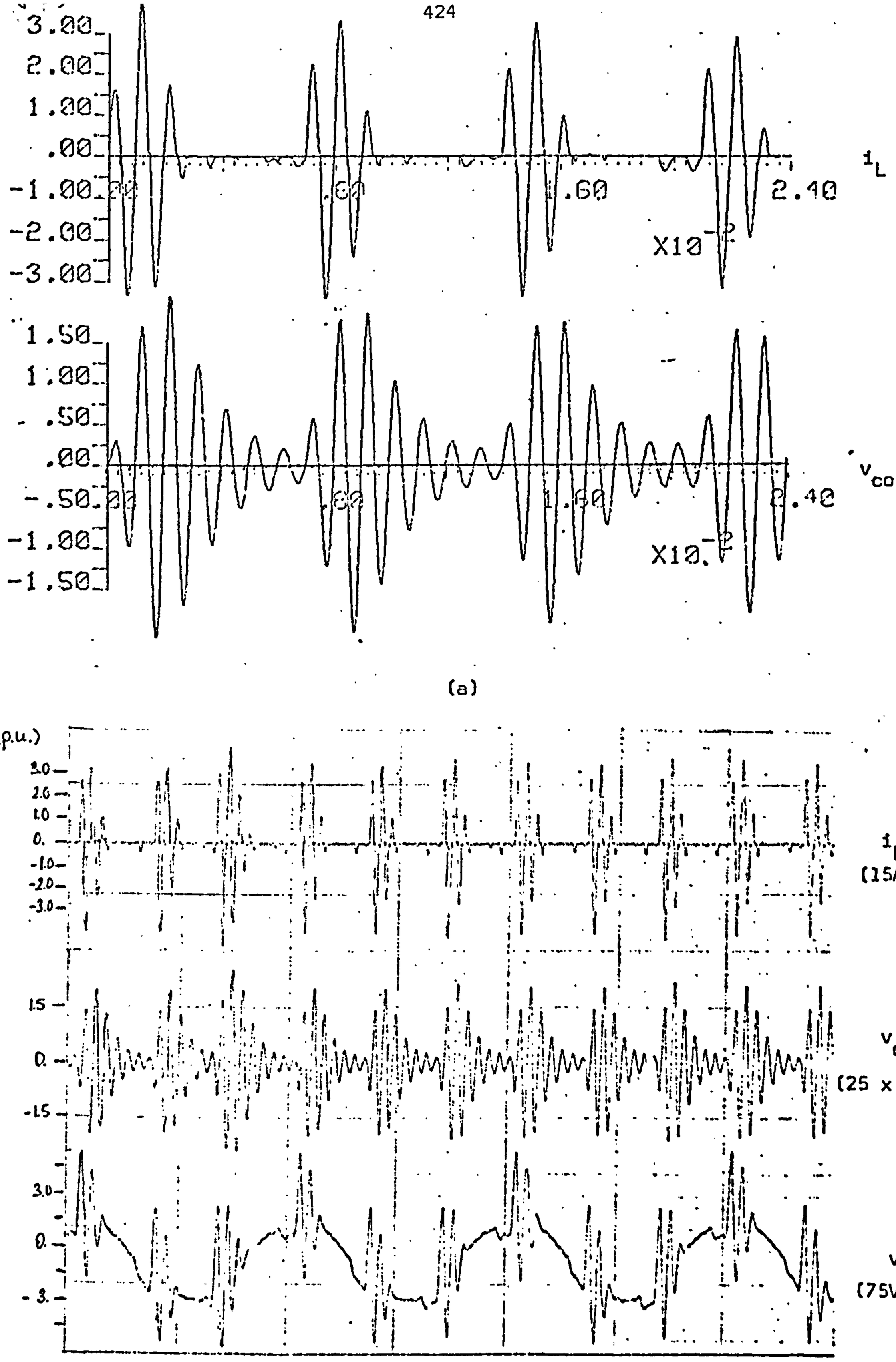

Figure 8.23 Comparison of (a) computed, and (b) experimental half-bridge cycloinverter waveforms during power control, i.e. $\theta = 120^{o}$, (f_o = 1050 Hz, Q_L = 5)

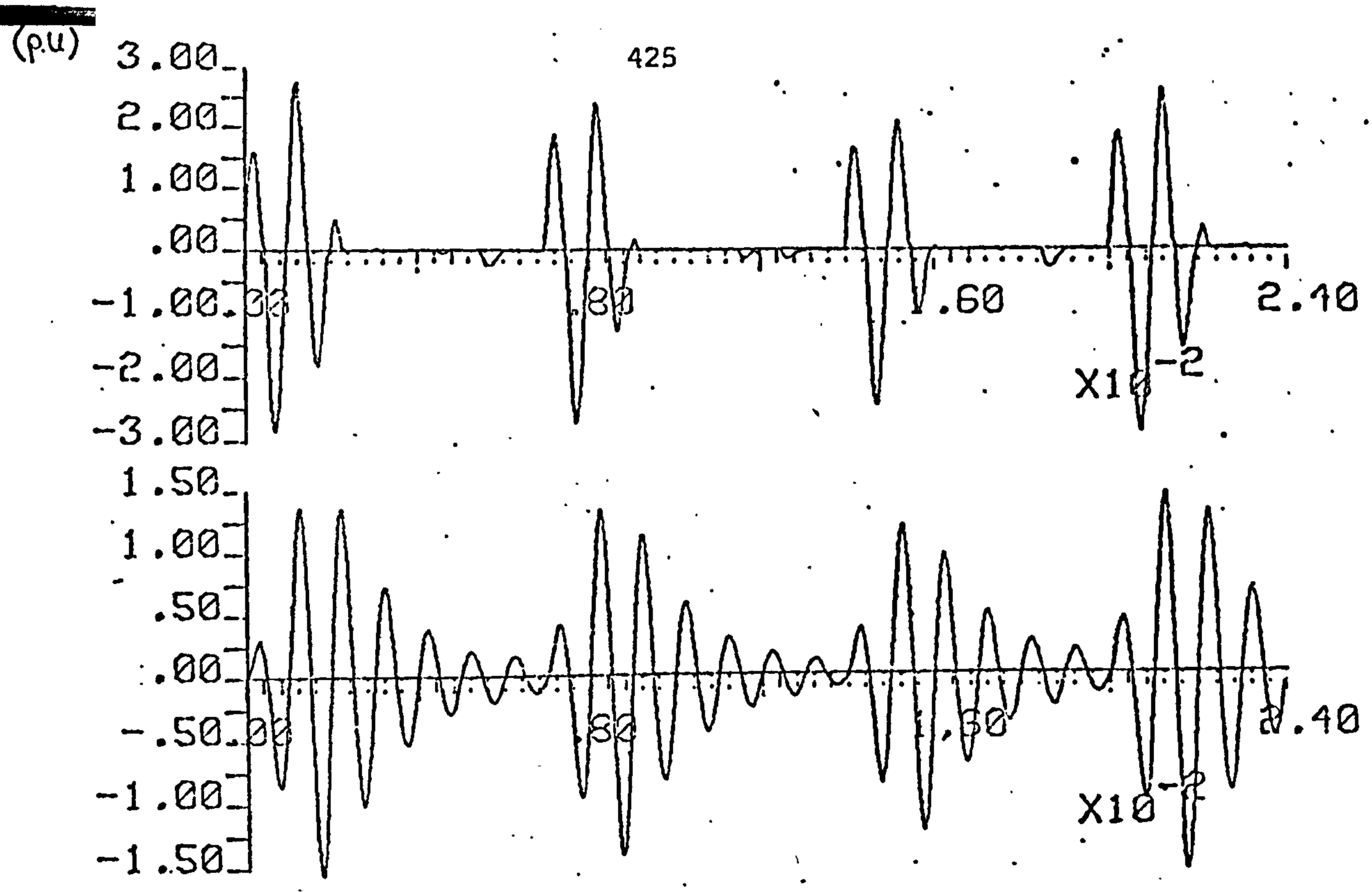

(a)

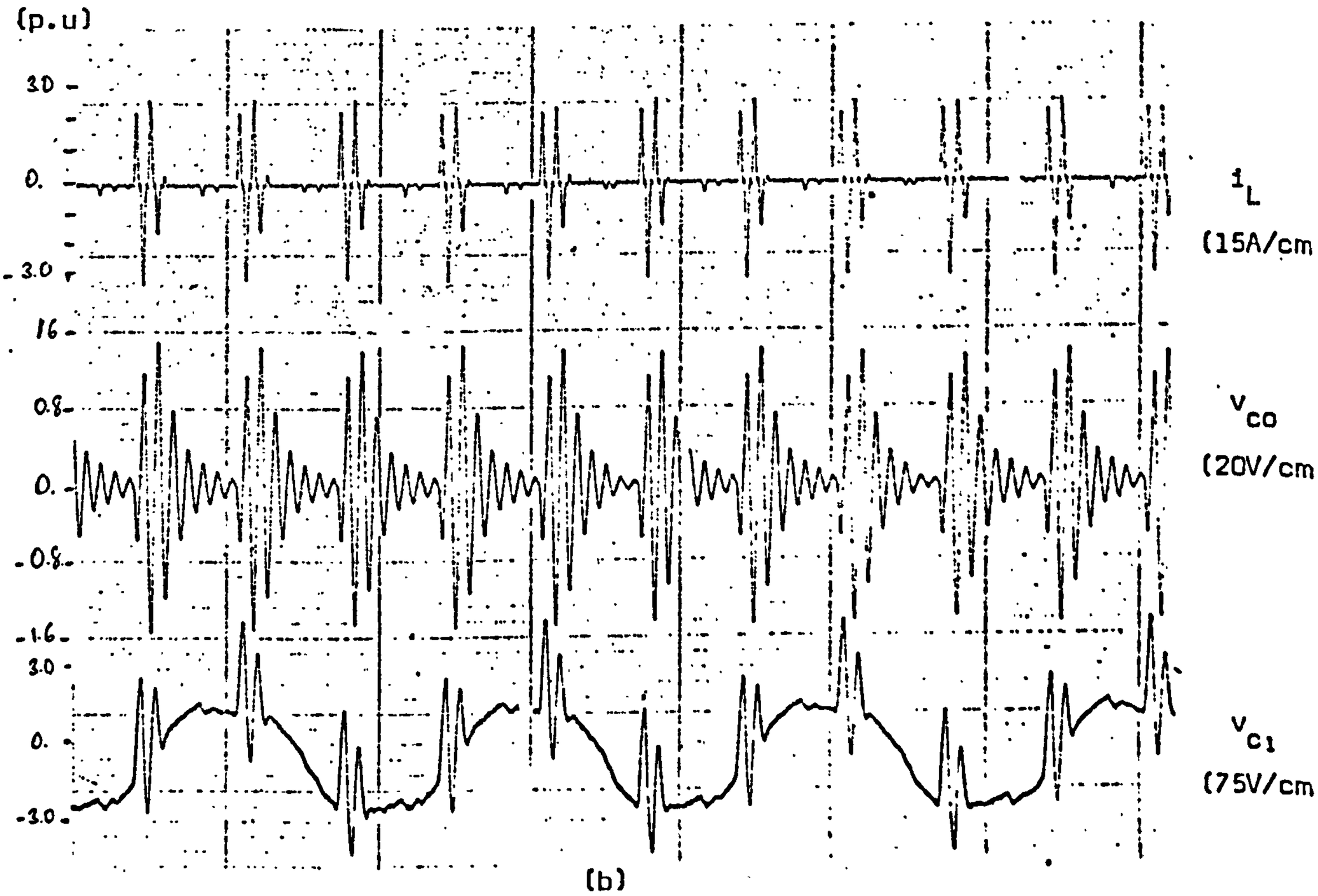

(b)

Figure 8.24 Comparison of (a) computed and (b) experimental half-bridge cycloinverter waveforms during power control, i.e. $\theta = 150^{o}$. (f_o = 1050 Hz, Q_L = 5)

CHAPTER 9

CONCLUSIONS AND SUGGESTIONS FOR FUTURE RESEARCH

9.1 Conclusions

The conclusions arising from the work described in this thesis may be summarised as follows:

1. Due to numerous difficulties encountered in developing an accurate equivalent circuit representation of the dynamic load conditions during induction heating, a method based on an approximate theory involving an evaluation of application data was employed to obtain simplified load models for different types of applications.

2. The results in Section 3.4 of the theoretical work on the sine-wave inverter assess the potential of the inverter when applied to induction heating. The performance optimisation procedure suggested in Chapter 3 leads to an efficient use of the inverter in a given situation.

3. It has been seen that the cost of eliminating an intermediate d.c. link in a.c.-to-a.c. conversion is the appearance of undesirable harmonics in the input line and output currents. The heavy dependence of these on the operational frequency of the cycloinverter necessitated a separate treatment of the inverter operation for different operational frequency ranges.

At low operational frequencies, the performance of the cycloinverter is satisfactory only at operational frequencies which are multiples of the input frequency, i.e. 3 f_I, 6 f_I, 9 f_I etc. At these frequencies, the load is equally distributed between the input phases, resulting in a balanced inverter operation. At non-multiple output frequencies, the cycloinverter output current suffers from high modulation, at beat frequencies related to both the input and the output frequencies. At low operational frequencies, the cycloinverter is therefore suited mainly to continuous heating applications, which require constant source frequencies of 150, 300, 450, 600 Hz, (with a 50 Hz mains frequency). Cycloinverter operation at 150 Hz is particularly satisfactory, for the following reasons:

i) The output has a low harmonic content.

ii) Smooth power or voltage control is available.

iii) With no output current sideband harmonics, the harmonic power dissipated in the heating coil is negligible, and since conduction and switching losses are also low, the cycloinverter has a high operational efficiency.

iv) The input power factor at full power is about 0.8 (without an input filter).

v) A simple output circuit with a well-defined behaviour results in a high operational reliability.

However, the half-bridge version of the cycloinverter is not suited to 150 Hz operation, since at this frequency the power control scheme becomes inoperative.

4. At high operational frequencies, the input line voltage seen by the cycloinverter power circuit becomes approximately independent of the output frequency, which enables simultaneous control of both output power and frequency. These desirable characteristics makes the cycloinverter an attractive power source for static heating and melting applications. Although the range of output frequency for which satisfactory inversion is possible is unfortunately limited (an inherent feature of the series load commutation technique employed), it is nevertheless sufficient for heat treatment and most melting applications. When designing a cycloinverter for operational frequencies around 1 kHz, special attention must be paid to the suppression of the upper sideband of the output current, since a faulty design can easily cause an amplification of this harmonic and lead to short circuit failure. By giving this full consideration, an optimum commutation circuit for a 1050 Hz continuous heating application and for a 900-1050 Hz static heating application (with a given set of load conditions) were suggested in Chapter 5.

At high operational frequencies, output power control is achieved at the cost of an increase in the output current

sideband harmonics. In this respect, the full-bridge inverter offers comparably better power control characteristics than the half-bridge circuit. Nevertheless, the latter can be employed successfully in applications which involve high heating coil selectivities and require moderate power control range (less than 50%). In a cycloinverter, as in a controlled rectifier, power control is always accompanied by a lagging displacement factor.

5. By the use of an LC-type input filter, the performance of the cycloinverter can be improved substantially, to provide the following features:

With a continuous heating load,

i) approximately unity input power factor,

ii) good output power control characteristics (even with a 60% output power reduction, the input power factor is still better than 0.85 leading).

iii) distortion free input line currents for all power control modes,

iv) lower power-circuit voltage ratings, due to the suppression of the commutating circuit voltage rises during power control.

While with a typical static heating load,

i) good input power factor characteristics throughout the heating cycle.

ii) low input line current distortion harmonics throughout the heating cycle,

iii) appreciable savings in the power circuit voltage rating due to a partial suppression of excessive voltage rises in the commutating circuit at high loads.

6. For the analysis of the inverters studied both transient and steady-state analysis techniques are employed. The digital simulation technique adopted led to an effective and sufficiently accurate simulation of the inverters, which was used to investigate the inverter performance at varying operational and load conditions. On the other hand, the steady-state technique provided an approximate but comparatively simple and rapid means of analysis required for the optimisation of the inverter design parameters.

7. The results of the experimental investigation obtained from prototype 150 Hz and 900-1050 Hz cycloinverters, showed good correlation with the digitally simulated results and provided sufficient evidence of the validity of the theoretical results presented.

9.2 Possible Further Investigations

The following are some of the areas where further investigation may prove fruitful:

1. To simplify the task of the circuit designers, more accurate and (perhaps) more typical load models for various induction heating applications should be established.

2. The anti-parallel thyristor connection in the cycloinverter power circuit can be used to feed back some of the reactive energy stored in the commutating capacitor following a thyristor commutation. By analogy with the duty of the feedback diode in the series inverter, the anti-parallel thyristor of the outgoing thyristor, if fired when the load current ceases, can be employed to feed some of the stored energy back to the source. This would, of course, lead to lower power thyristor and commutating capacitor ratings, and provide a good sine-wave output current. One disadvantage of such an arrangement is the increased complexity involved in the control circuitry.

3. Application of the cycloinverter in various other fields can be investigated.

4. To achieve a smoother output power control and an improved output current harmonic content, multi (>3)-phase cycloinverters can be devised and their performances investigated.

5. An optimum commutation circuit for a forced and series load commutated cycloinverter can be established.

6. The performance of the cycloinverter when employed with a multi-tap load-matching transformer can be investigated.

7. Using the analysis techniques developed, the performance of the cycloinverter at higher operational frequencies can be studied.

8. The cycloinverter can be used to obtain an isolated and regulated high voltage d.c. output from a multi-phase input, at a low cost and with high efficieny. In so doing, the employment of high operational frequencies brings about substantial savings in the power ratings of both the isolating transformer and the cycloinverter components.

REFERENCES

1. D.I. Spash and R.C.J. Ireson, *"Solid-state generators for induction heating"*, UIE Congress VII, 1972, Paper No. 707.

2. P.P. Biringer and G.R. Slemon, *"Equivalent circuit approach to the analysis of magnetic triplers"*, Proc. Special Conf. on Non-Linear Magnetics and Magnetic Amplifiers, August 1958, pp.335-347.

3. S.B. Dewan and G. Havas, *"A solid-state supply for induction heating and melting"*, IEEE Trans. on IGA, Vol. IGA-5, No. 6, 1969, pp.689-690.

4. W.W. Konas, *"New power supply - solid state converters"*, IEEE Trans. on IECI, Vol.IECI-17, 1970, pp.327-331.

5. W.E. Frank, *"Applying the induction heating static frequency converter"*, IEEE Trans. on IECI, Vol.IECI-17, 1970, pp10-17.

6. K. Tholborg, *"Frequency converters for high-frequency melting and heating plants"*, ASEA Journal, Vol. 44, No. 6, pp.185-188.

7. G.N. Revankar and S.A. Gadag, *"Analysis of high frequency inverter circuits"*, IEEE Trans. on IECI, Vol. IECI-20, No. 3, August 1973, pp.178-182.

8. A.J. Humphrey, *"Inverter commutation circuits"*, IEEE Trans. on IGA, Vol. IGA-4, No. 1, 1968, pp.104-110.

9. N.W. Mapham, *"The classification of SCR inverter circuits"*, 1964 IEEE International Conv. Rec., Vol. 12, Pt. 4, pp.99-105.

10. S.H. Jhaveri, *"Inverter for induction melting furnaces"*, IE(I) Journal-ET, Vol. 53, November 1972, pp.55-58.

11. B.R. Pelly, *"Latest developments in static high frequency power sources for induction heating"*, IEEE Trans. on IECI, Vol. 7, 1970, pp.297-312.

12. J.S. Ioffe and V.V. Morgoun, *"Thyristor frequency converters as power source for medium frequency electro-heating plants"*, UIE, VII, 1972, Paper No. 702.

13. R. Thomson, *"High-frequency silicon-controlled-rectifier sinusoidal inverter"*, Proc. IEE, Vol. 110, No. 4, April 1963, pp.647-651.

14. A. Kusko and G.V. Voodley, *"30 kW industrial SCR inverter power supply"*, Electromechanical Design, Nov. 1963, pp.36-39.

15. R. Thomson, *"Designing series SCR inverters"*, Electronic Design, Pt. 1, June 7, 1963.

16. A. Kusko and B. Szpakowski, *"Load ranges of series SCR inverters"*, Electro-Technology, April 1965, pp.76-80.

17. C.A. Sabbah, *"Series-parallel type static converters,* Gen. Elec. Rev., May/October/December 1931.

18. R. Kasturi, *"An analysis of series inverter circuits"*, IEEE Trans. on IECI, Vol. IECI-22, No. 4, November 1975.

19. R. Thomson, *"An audio-frequency high-power generator employing silicon controlled rectifiers"*, Proc. IEE, May 1962, pp.249-258.

20. S.R. Durand and J.B. Rice, *"Mercury-arc furnace converter for induction heating of metals"*, American IEE Technical Paper No. 48-287, September 1948.

21. D.L. Smart and J.J.L. Weaver, *"Use of steel-tank mercury-arc inverters for generating medium frequencies for induction heating"*, IEE Proceedings, Pt. A, Vol. 105, No. 23, October 1958, pp.461-74.

22. W.R. Light, *"A step-up cycloconverter"*, MSc, Thesis, 1965, The University of Virginia.

23. W.R. Light and E.S. McVey, *"A synchronous tap changer applied to step-up cycloconverters"*, IEEE Trans. on IGA, Vol. IGA-3, pp.244-249, May/June 1967.

24. See reference 19.

25. R.J. Wurm and L.J. Stratton, *"Step-up frequency changer"*, AIEE Transactions, Pt. II, (Applications and Industry), Vol. 79, November 1960, pp.426-31.

26. S.B. Dewan and P.P. Biringer, *"Frequency and phase conversion with thyristor converters, Part I"*, IEEE Summer Power Conference, New Orleans, 10 July 1966.

27. S.B. Dewan and P.P. Biringer, *"Frequency and phase conversion with thyristor converters, Part II"*, IEEE Summer Power Conference, New Orleans, 10 July 1966.

28. G.N. Revankar and S.A. Gadag, *"A high-frequency bridge inverter with series parallel compensated load"*, IEEE Trans. on IECI, Vol. IECI-21, No. 1, Feb. 1974, pp.18-21.

29. B.D. Bedford and R.G. Hoft, *"Principles of inverter circuits"*, New York, Wiley, 1964.

30. W.E. Frank, *"New developments in high-frequency power sources"*, IEEE Trans. on IGA, Vol. IGA-6, No. 1, January/February 1970, pp.29-35.

31. F.C. Schwarz, *"A method of resonant current pulse modulation for power converters"*, IEEE Trans. on IECI, Vol.IECI-17 No. 3, May 1970, pp.209-221.

32. H. Suganuma, *"A thyristor inverter for induction heating"*, UIE Congress VII, 1972, Paper No. 628.

33. W.F. Peschel, *"Load power matching of high-frequency power supplies for induction heating"*, IEEE Trans. on IA, Vol. IA-10, No. 3, May/June 1974.

34. F.C. Schwarz, *"An improved method of resonant current pulse modulation for power converters"*, IEEE Trans. on IECI, Vol. IECI-23, No. 2, May 1976.

35. R.F. Dyer, *"The rating and application of SCRs designed for power switching at high frequencies"*, IEEE Trans. on IGA, Vol. IGA-2, No. 1, Jan/Feb. 1966, pp.5-15.

36. T. Tani and T. Horigome, *"Dynamic characteristics of thyristors"*, IEEE Conf. Rec. of IAS 1972 7th Annu. Meet., pp.455-461.

37. F.C. Schwarz and N.C. Voulgaris, *"A wideband wattmeter for the measurement and analysis of power dissipation in semiconductor switching devices"*, IEEE Trans. Electron Devices, Vol. ED-17, September 1970.

38. J.P. Landis, *"A static power supply for induction heating"*, Conference Record of 1970 IEEE Solid State in Industry Conference.

39. J.P. Landis, *"A static frequency converter for 10 kHz power"*, Pillar Corporation, West Allis, Wisconsin, USA.

40. R.W. Brachold, *"Application for 50 kHz solid state induction heating applications"*, 8th Annual Meeting, IEEE Industry Application Soc., Milwaukee USA, 8-11 Oct. 1973, pp.525-9.

41. J.M. Peter, *"Design of a 40 kHz inverter using fast thyristors"*, Electronique and Microelectron Ind. (France), No. 216, March 1976, pp.45-50.

42. I. Horvat, *"A 180 kW 8-11 kHz thyristor frequency converter for induction heating"*, Westinghouse Electric Corporation Research and Development Center, Pittsburgh, Pa.15235.

43. F. Brichant, *"The medium frequency inverters"*, Rev. Gen. Electr. (France), Vol. 86, No. 2, 1976, pp.161-4.

44. I. Nagy, *"Solid state high frequency power supply for induction heating"*, Elektrowarme International, Vol. 31, August 1973, pp.164-170.

45. I. Nagy, *"Investigation of a high frequency power supply for induction heating"*, Elektrowarme International, Vol. 31, No. 6, 1973, pp.281-87.

46. E. Kolbe and W. Reiss, *"Distribution in space of current density induction heated bodies under consideration of the temperature field"*, Elektrowarme 25, 1967, pp.243-250.

47. P.E. Burke, P.P. Biringer, P.F. Ryff and E. Solger, *"The prediction and measurement of current distribution in coaxial circular geometries"*, Sixth PICA Conference Proceedings, 1969.

48. K.M. Makhmudov and A.E. Slukhotsky, *"Calculation of electric parameters of heating inductors by means of the method of induced emf's"*, Proceedings VNII TVCh, iss.11, Mashinostroenye, 1970.

49. R.M. Baker, *"Design and calculation of induction heating coils"*, AIEE Trans. Vol. 76, March 1957, pp.31-39.

50. A.E. Slukhotsky, V.S. Nemkov and K.M. Makhmudov, *"Calculation of electrical parameters of heating inductors"*, UIE Congress VII, 1972, Paper No. 604.

51. H. Barber, *"Induction heating - general principles and theoretical considerations"*, Interdepartmental paper, Department of Electronic and Electrical Engineering, Loughborough University of Technology.

52. G. Havas and R.A. Sommer, *"A high frequency power supply for induction heating and melting"*, IEEE Trans. on IECI, Vol. IECI-5, 1969, pp.686-692.

53. E. May, *"High frequency electric heating"*, Chapman and Hall Ltd., London, 1949.

54. H. Geisel, *"Operating behaviour of oscillatory static frequency changers for induction heating equipment"*, Elektrowarme International, Bd. 27, No. 6, June 1969.

55. R.J. Kasper, *"Induction heating system design"*, IEEE Conf. Record, 5th Ann. meeting of IGA group, Chicago, 5-8 Oct. 1970, pp.289-97.

56. B. De Miramon, *"Application of medium frequency inverters to induction heating and melting"*, Rev. Gen. Electr. (France), Vol. 86, No. 2, 1976, pp.165-174.

57. B.Caussin, *"Static power supply of medium frequency furnaces"*, Rev. Jeumont - Schneider (France), No. 19, Dec. 1974, pp.33-38.

58. R. Youn, *"High frequency SCR inverter"*, IEE Conf. Record 7th Ann. Meeting of Ind. Appl. Soc., 9-12 Oct. 1972, pp.423-8.

59. F.C. Schwarz and J. Ben Kaassens, *"A controllable secondary multi-kilowatt d.c. current source with constant maximum power factor in its three phase supply line"*, PESC Record, 1975, pp.205-215.

60. F.C. Schwarz, *"Switch modulation techniques Parts I and II"*, Proc. of Power Sources Conf. 1962 and 1963, Atlantic City, N.J.

61. J.J. Biess, J.H. Inouye and J.H. Shank, *"High voltage series resonant inverter ion engine screen supply"*, Proc. of IEEE Power Electronics Specialists Conf. 1974.

62. G.N. Revankar and D.S. Karande, *"Voltage-fed, high-frequency bridge inverter circuits"*, IEEE Trans. on IECI, Vol. IECI-21, No. 4, November 1974, pp.226-29.

63. I.I. Szekely, *"Medium frequency thyristor inverter"*, Bul. Univ. Brasoc, Vol. 15, 1973, pp.211-19.

64. H.R. Lowry, *"Controlled rectifier manual"*, Gen. Elec. Company, New York, 1960, Chapter V.

65. N. Mapham, *"An SCR inverter with good regulation and sine-wave output"*, IEEE Trans. on IGA, Vol. IGA-3, No. 2, March/April 1967, pp.176-187.

66. W.C. Fry, *"An ultrasonic power source utilising a solid-state switching device"*, 1961 IRE International Conv. Rev. pt.6, Vol. 8, pp.213-218.

67. N. Mapham, *"Low cost ultrasonic frequency inverter using single SCR"*. IEEE Trans. on IGA, Vol. IGA-3, No. 5, Sept/Oct. 1967.

68. ————, *"SCR manual 5th edition"*. General Electric Corporation, Syracuse, N.Y. 1972, pp.354-356.

69. R.M. Davies, *"Power diode and thyristor circuits"*, Cambridge University Press, 1971, pp.184-187.

70. See reference 29, Chapter V and Section 7.6.

71. W. Guggi, *"Sine wave inverter system"*, IEEE/IGA Conf. Record, 1970, pp.517-24.

72. J.D. Harnden and F.B. Golden, *"Power semiconductor applications"*, IEEE Press, New York, 1972.

73. R.R. Ott, *"A filter for SCR commutation and harmonic attenuation in high power inverters"*, Communications and Electronics, May 1963, pp.259-262.

74. C.W. Young, *"Optimisation of thyristor inverter circuits for induction heating"*, MSc Thesis, University of Toronto, 1968.

75. See reference 68, pp.123-126.

76. E.D. Wolley, H.J. Ruhl and R. Knaus, *"Development of 1000 ampere r.m.s. 4 kHz, 1500 volt thyristorsand rectifiers"*. Conf. Record, 1972 Power Processing and Electronics Specialists, Atlantic City, N.J., pp.146-159.

77. T. Tani, T. Horigome, T. Nakagawa, O. Hashimoto, and M.Suzuki, *"Measuring system for dynamic characteristics of semiconductor switching elements and switching loss of thyristors"*, IEEE Trans. on IA, Vol. IA-11, No. 6, Nov/Dec. 1075, pp.720-727.

78. R.F. Dyer, *"The rating and application of SCR's designed for switching at high frequencies"*, Application Note 660.13, General Electric Company, Syracuse, New York.

79. B.R. Pelly, *"Thyristor phase controlled converters and cycloconverters"*, Wiley, New York, 1971.

80. See reference 69, pp.138-139.

81. S.B. Dewan, P.P. Biringer and G.J. Bendzsak, *"Harmonic analysis of a.c.-to-a.c. frequency converter"*, IEEE Trans. on IGA, Vol. IGA-5, No. 1, Jan/Feb. 1969.

82. S.B. Dewan and M.D. Kankam, *"A method for harmonic analysis of cycloconverters"*, IEEE Trans. on IGA, Vol. IGA-6, Sept/Oct. 1970, pp.455-462.

83. B. Dewan, R.S. Segsworth and P.P. Biringer, *"Input filter design with static power converters"* , IEEE Trans. on IGA, Vol. IGA-6, No. 4, 1970, pp.378-83.

84. F.E. Terman, *"Electronic and radio engineering"*, New York, McGraw Hill, 1955, p.49 and p.402.

85. J. Shepherd, A.H. Morton and L.F. Spence, *"Higher electrical engineering"*, Pitman Publishing, London, 1975.

86. C.J. Amato, *Analog computer simulation of an SCR as applied to a cycloconverter"*, Proc. of NEC, 1965, Vol. 21, pp.933-37.

87. H. Conrad and G. Schneider, *"Simulation of thyristor converters for induction heating by means of analogue computers"*, Conf. Record, UIE VII, 1972, Paper No. 629.

88. A.S. Charlesworth and J.R. Fletcher, *"Systematic analogue computer programming"*, Isaac Pitman and Bath Univ. Press, 1970.

89. J.S.C. Htsui and W. Shepherd, *"Method of digital computation of thyristor switching circuits"*, Proc. IEE, Vol. 118, No. 8, August 1971, pp.993-998.

90. G.N. Revankar, *"Digital computation of SCR chopper circuits"*, IEEE Trans. on IECI, Vol. IECI-20, No. 1, February 1973, pp.20-23.

91. G.N. Revankar and S.A. Mahajan, *"Digital simulation for mode identification in thyristor circuits"*, Proc. IEE, 1973, Vol. 120, No.2, pp.269-272.

92. G.N. Revankar, *"Topological approach to thyristor circuit analysis"*, Proc. IEE, Vol. 120, No. 11, November 1973, pp.1403-5.

93. Y. Muraka, N. Kasaka, M. Nishimura and N. Sakuma, *"Simulation program for thyristor circuits and its applications"*, Elec. Eng. Jap. 1971, Vol. 91, pp.51-59.

94. G.N. Revankar, P.K. Srivastava and R.N. Jawle, *"Computer analysis of SCR circuits"*, IEEE Trans. on IECI, Vol. IECI-22, No. 1, February 1972, pp.48-54.

95. D.J. Comer, *"Computer analysis of circuits"*, USA, International Textbook Company, 1971, pp.207-213.

96. T. Kutman, *"A method of digital computation for SCR circuits"*, IEEE Trans. on IECI, Vol. IECI-21, No. 2, May 1974, pp.80-83.

97. D.F. Mayers, *" Numerical solution of ordinary and partial differential equations"*, Fox, Pergamon, 1962.

98. P.W. Williams, *"Numerical computation"*, T. Nelsons and Sons Ltd., 1972.

99. D. McCracken and W.S. Dorn, *"Numerical methods and Fortran programming"*, John Wiley and Sons, Inc., 1966.

100. J.W. Cooley and J.W. Tukey, *"An algorithm for the machine calculation of complex Fourier series"*, Math. Comput., 19, 90, 1965, pp.297-301.

101. P.P. Biringer and S.B. Dewan, *"Analysis of a filter circuit for non-linear loads"*, IEEE Trans. on Magnetics, Vol. MAG-3, No. 1, March 1967, pp.34-38.

102. A. Emanuel-Eigeles and M.S. Erlicki, *"New aspects of power factor improvement, Part I and II)"*, IEEE Trans. on IGA, Vol. IGA-4, No. 4, July/August 1968, pp.441-455.

103. T.M. Hambin and T.H. Barton, *"Cycloconverter control circuits"*, IEEE Conf. Record, 5th Annual IGA Meeting, Oct. 1970, pp.29-33.

APPENDIX 1

TRANSIENT ANALYSIS OF THE SINE-WAVE INVERTER

In the following analysis the switching elements are assumed to be perfect switches, with instantaneous changes of state and zero reverse current flow. The analysis is performed separately for each possible mode of operation of the inverter.

MODE 1

The equivalent circuit when thyristor S1 is conducting, i.e. Mode 1, is shown in Figure A1.1 and in matrix form the Laplace equations of the configuration are:

$$\begin{vmatrix} I_I \\ I_L \\ I_{Lo} \end{vmatrix} \quad \begin{vmatrix} \frac{2}{sC} & -\frac{1}{sC} & 0 \\ -\frac{1}{sC} & \frac{1}{sC} + sL + \frac{1}{s\,C_o} & -\frac{1}{s\,C_o} \\ 0 & -\frac{1}{sC} & R_o + sL_o + \frac{1}{s\,C_o} \end{vmatrix} = \begin{vmatrix} 0 \\ \frac{V_c(0)-V_{co}(0)}{s} \\ \frac{V_{co}(0)}{s} + L_o I_{Lo}(0) \end{vmatrix} \qquad (A1.1)$$

Solution of these equations for the input current yields:

$$I_I = \frac{b_3 s^3 + b_2 S^2 + b_1 s + b_0}{a_4 s^4 + a_3 s^3 + a_2 s^2 + 1}$$

where:

$$a_1 = R_o C_o + 2 L_o C \qquad a_2 = L_o C_o + 2 L_o C + 2 LC$$

$$a_3 = 2 R_o LC C_o \qquad a_4 = 2 L L_o C C_o$$

and:

$$b_0 = 2 C V_c(0) + C_o V_{co}(0) \qquad b_1 = 2 L_o I_{Lo}(0) + L_o I (0) C_o$$

$$b_2 = 2 V_{co}(0) L C C_o \qquad b_3 = 2 L L_o I_{Lo}(0) C C_o$$

Similarly, the tank load-current may be obtained in the form:

$$I_{Lo} = \frac{d_2 s^2 + d_1 s + c V_c(0)}{a_4 s^4 + a_3 s^3 + a_2 s^2 + a_1 s + 1}$$

where:

$$d_1 = L_o C_o C (V_c(0) - V_{co}(0))$$

$$d_2 = C [C_o R_o V_c(0) - C_o R_o V_{co}(0) + L_o I_{Lo}(0)]$$

To obtain the time domain solutions for i_I, i_L, i_{Lo} the Heaviside Expansion Formula is employed, and the inverse Laplace transformation is obtained subsequently, as shown in the computer program given at the end of this section. On so doing, the circuit currents become:

$$i_L = 4\,[E\,e^{\alpha_1 t}\,\mathrm{Cos}\,w_1 t - F\,e^{\alpha_1 t}\,\mathrm{Sin}\,w_1 t + G\,e^{\alpha_2 t}\,\mathrm{Cos}\,w_2 t - H\,e^{\alpha_2 t}\,\mathrm{Sin}\,w_2 t\,]$$

$$i_I = i_L/2$$

$$i_{Lo} = 2\,[P\,e^{\alpha_1 t}\,\mathrm{Cos}\,w_1 t - Y\,e^{\alpha_1 t}\,\mathrm{Sin}\,w_1 t + S\,e^{\alpha_2 t}\,\mathrm{Cos}\,w_2 t - U\,e^{\alpha_2 t}\,\mathrm{Sin}\,w_2 t]$$

(A1.2)

where w_n and α_n are the real and imaginary parts of the nth root of the characteristic equation and the coefficients E, F, G, F and P, Y, S, U are the Heaviside coefficients as defined in the main program. With the circuit known, the equations for v_{co} and v_{c1} can easily be derived as

$$v_{c1}(t) = V_c(0) - \frac{1}{C}\int_o^t i_I\,dt$$

and

$$v_{co}(t) = V_{co}(0) - \frac{1}{C_o}\int_o^t (i_L - i_{Lo})\,dt$$

Mode 1 ends at the end of the positive half cycle of the output current, given by:

$$i_L(t_c) = 0$$

MODE 2

When the flow of current in S1 ceases, the circuit transforms itself to Mode 2, during which the reactive energy trapped in the output circuit is fed back to the source. During Mode 2, the equivalent circuit remains unchanged, and the transient analysis can easily be obtained by extending the analysis of Mode 1 until S2 is fired, or the output current completes its negative half cycle.

MODES 3 and 4

The equivalent circuit for Modes 3 and 4 is shown in Figure A1.1b. From the symmetry of the power circuit, it can be shown that the matrix equations for these modes may be obtained by changing the signs of the mode initial conditions, $V_{co}(0)$ and $I_{Lo}(0)$, and replacing $V_{co}(0)$ by $E - V_c(0)$ as shown in the main program. Any further analysis is therefore unnecessary.

MODE 5

Since i_{Lo} is the only current now circulating, the mode equation is easily obtained from Figure A1.1c as

$$i_{Lo} = e^{-\alpha t} \left(I_{Lo}(0) \cos w_o t + \frac{2 V_{co}(0) - I_{Lo}(0) R_o}{2 w_o L_o} \sin w_o t \right)$$

where: $$w_o^2 = \frac{1}{L_o C_o} - a^2$$

and

$$a = \frac{R_o}{2 L_o}$$

The systematic solutions for the circuit quantities during each subsequent mode, and until the steady-state conditions are reached, can best be obtained via a digital simulation.

PROGRAM LISTING

(Extracted from a computer program prepared for the digital simulation of the sine-wave inverter)

PERFORMING INVERSE LAPLACE TRANSFORMATION

COEFFICIENTS OF THE CHARACTERISTIC EQUATION

```
A(1)=2.*AL1*AL*C*C1
A(2)=2.*R*AL1*C1*C
A(3)=AL*C+2.*AL*C1+2.*AL1*C1
A(4)=R*C+2.*R*C1
A(5)=1
```

DETERMINING THE ROOTS OF THE CHARACTERISTIC EQUATION

```
      N=5
      IFAIL=0
      TOL=X02AAF(0.1)
      CALL C02AEF (A,N,REZ,DIMZ,TOL,IFAIL)
      DIMZ(1)=ABS(DIMZ(2))
      DIMZ(3)=ABS(DIMZ(4))
      DIMZ(2)=-DIMZ(1)
      DIMZ(4)=-DIMZ(3)
      WRITE(6,881)  (REZ(I),DIMZ(I),I=1,3,2)
881   FORMAT(1H ,4F20.5)
```

COEFFICIENTS b_n and d_n AT THE BEGINNING OF MODE 1OR3

```
      B(1)=AL*AL1*C*C1*AI20
      B(2)=AL*C*C1*(VC10-VC0)
      B(3)=R*C*C1*(VC10-VC0)+AL*C1*AI30+AL1*AI20*C1
      B(4)=C1*VC10
      D(1)=2.*AL*AL1*C1*C*AI30
      D(2)=2.*VC0*AL1*C1*C
      D(3)=AL*AI30*(C+2.*C1)+2.*AL1*C1*AI20
      D(4)=2.*C1*VC10+C*VC0
```

PERFORMING THE PARTIAL FRACTION OF THE CURRENT EQUATIONS TO DETERMINE THE TIME DOMAIN COEFFICIENTS

```
   18 DO19 I=1,3,2
      RT(I)=CMPLX(REZ(I),DIMZ(I))
      F1RT(I)=B(1)*RT(I)**3+B(2)*RT(I)**2+B(3)*RT(I)+B(4)
      XR=REAL(F1RT(I))
      XI=AIMAG(F1RT(I))
      F2RT(I)=4.*A(1)*RT(I)*RT(I)*RT(I)+3.*A(2)*RT(I)*RT(I)+2.*A(3)
     1*RT(I)+A(4)
      YR=REAL(F2RT(I))
      YI=AIMAG(F2RT(I))
      F3RT(I)=D(1)*RT(I)*RT(I)*RT(I)+D(2)*RT(I)*RT(I)+D(3)*RT(I)+D(4)
      VR=REAL(F3RT(I))
      VI=AIMAG(F3RT(I))
      IF(I.EQ.3)  GO  TO  777
      CALL A02ACF(XR,XI,YR,YI,E,F)
      CALL A02ACF(VR,VI,YR,YI,P,Y)
  777 CALL A02ACF(XR,XI,YR,YI,G,H)
      CALL A02ACF(VR,VI,YR,YI,S,U)
   19 CONTINUE
```

/Continued

TIME DOMAIN EQUATIONS FOR VARIOUS CIRCUIT VOLTAGES AND CURRENTS

```
21  DO64 M=1,3,2
    V(M)=DIMZ(M)
    W(M)=V(M)*(T-T2)
    SW(M)=SIN(W(M))
    CW(M)=COS(W(M))
    Q(M)=EXP(REZ(M)*(T-T2))
    X(M)=(Q(M)*(V(M)*SW(M)+REZ(M)*CW(M))-REZ(M))/(REZ(M)**2+V(M)**2)
    KM=M+1
    X(KM)=(Q(M)*(REZ(M)*SW(M)-V(M)*CW(M))+V(M))/(REZ(M)**2+V(M)**2)
64  CONTINUE
    TI1=2.*(E*Q(1)*CW(1)-F*Q(1)*SW(1)+G*Q(3)*CW(3)-H*Q(3)*SW(3))
    TI3=2.*(P*Q(1)*CW(1)-Y*Q(1)*SW(1)+S*Q(3)*CW(3)-U*Q(3)*SW(3))
    TVC=2./C*((2.*E-P)*X(1)-(2.*F-Y)*X(2)+(2.*G-S)*X(3)-(2.*H-U)
   1*X(4))+VCU
    TVC1=VC10-2./C1*(E*X(1)-F*X(2)+G*X(3)-H*X(4))
    VC(I)=TVC*SS
    VC1(I)=TVC1*SS+VE*(1.-SS)/2.
    AI2(I)=2.*TI1*SS
    IF(2.*TI1.GT.AI2MAX)    ILIMIT=1
    AI3(I)=TI3*SS
```

A(I), B(I), D(I)	a_n, b_n, d_n
AI2	i_L
AI3	i_{Lo}
AI2MAX	limiting value of i_L
AL, AL1	L_o, L
C, C1	C_o C_1
DIMZ(I)	w_n
R	R_o
REZ(N)	α_n

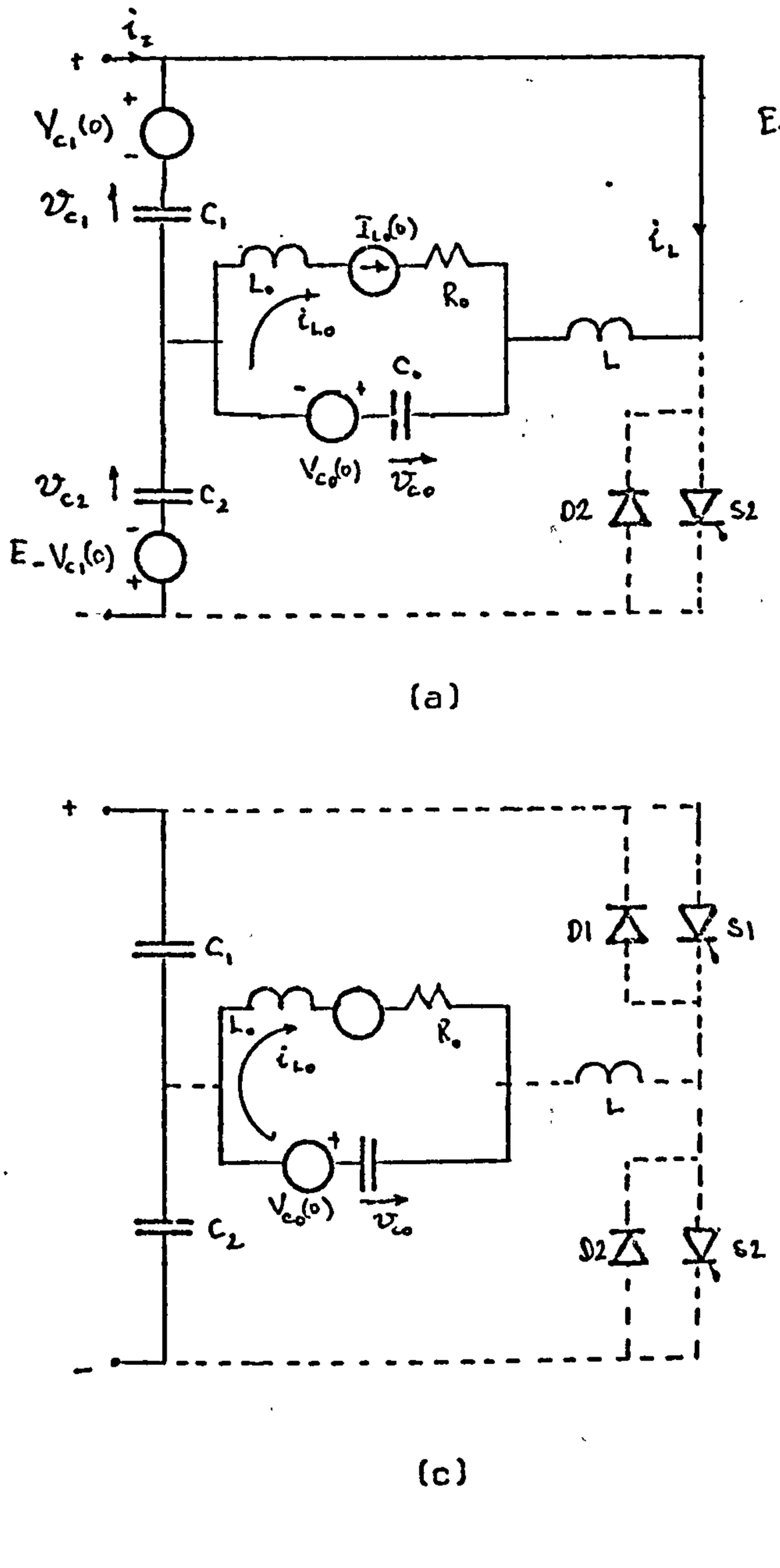

Figure A1.1 Equivalent circuit of the sine-wave inverter in:

a) Mode 1 and 2

b) Mode 3 and 4

c) Mode 5

APPENDIX 2

PROGRAM LISTING, THE ANALYSIS OPTIMISATION OF THE PERFORMANCE OF THE SINE-WAVE INVERTER

```
      MASTERMAIN
C
CC    THE ANALYSIS OPTIMISATION OF THE PERFORMANCE OF
C     THE SINE-WAVE INVERTER
C
      REAL IL,IS,ID,NEWDIF
      DIMENSION IL(20),GIL(20),VO(20),GVO(20),SIL(20),LOAD(5,3)
      COMMON IL,GIL,VO,GVO,NO,R,A,Y,XC,XL
      EQUIVALENCE(Y,QL)
      EXTERNAL CURRENT,VOLTAGE,VC1,DIDT1,DIDT2,SQIL
      READ(1,1) WOB,THYOFF,((LOAD(I1,I2),I1=1,4),I2=1,3)
    1 FORMAT(14F0.0)
      DATA DELXL,DELXC,XLMAX,XCMAX/0.4,0.05,3.,2.,4./
      XL=0.5
C
CC    READ LOAD CONDITIONS
C
 1001 II=1
 1000 WPU=LOAD(II,1)
      REQ=LOAD(II,2)
      QL=LOAD(II,3)
      WO=WOB*WPU
      TO=2.*3.141592/WO
      R=REQ/QL**2
      IF(II.GT.1) GO TO 2000
C
CC    STEP II
C     CALCULATE THE VARIATION OF XC WITH XL WHICH GIVES TOFF=THYOFF
C
  999 XL=XL+DELXL

      IF(XL.GT.XLMAX) GO TO 301
      XC=0.6
  998 XC=XC+DELXC
      IF(XC.GT.XCMAX) GO TO 999
      DO 9 K=1,13,2
      A=K
      CALL ZINPUT(ZR,ZL,ZI,G,ZIN)
      IL(K)=0.9/A/ZIN
    9 GIL(K)=ATAN(G)
      IF(CURRENT(0.).LT.0.) GO TO 998
      IF(CURRENT(TO/2.)*CURRENT(0.4*TO/2.).GT.0.) GO TO 998
      CALL COSAAF(TO/2.*0.4,TO/2.,0.0000005,0.005,CURRENT,TC,1)
      IF(IFAIL.NE.0) GO TO 998
      TOFF=TO/2.-TC
      IF(ABS(TOFF-THYOFF).LT.0.0000015) GO TO 1999
      GO TO 998
 1999 XLB=XL
      XCB=XC
C
```

```
C       STEP  III
C       EVALUATE THE INVERTER PERFORMANCE
C
 2000 XL=XLB*WPU
      XC=XCB/WPU
      WRITE(6,666) XLB,XCB,REQ,WO
  666 FORMAT(1H ,'.....  XL  XC  REQ  WO  =',4F10.2)
      DUMY,CAV,ALAV,RMSI,RMSVO=0.
      DO  10  I=1,13,2
      A=K
      CALL ZINPUT(ZR,ZL,ZI,G,ZIN)
      IL(K)=0.9/A/ZIN
      GIL(K)=ATAN(G)
      VO(K)=IL(K)*ZL
      GVO(K)=ATAN(ZI/ZR)+GIL(K)
      RMSI=IL(K)**2+RMSI
      PT=IL(K)**2*ZR+PT
      RMSVO=VO(K)**2+RMSVO
      VAL=IL(K)**2*XL*A+VAL
      VAC=IL(K)**2*XC/A+VAC
   10 CONTINUE
      RMSI=SQRT(RMSI)
      RMSVO=SQRT(RMSVO)
      CALL C05AAF(TO/2.*0.4,TO/2.,0.0000005,0.005,CURRENT,TC,1)
      TOFF=TO/2.-TC
      PO=IL(1)**2*REQ
  913 DF=IL(1)/RMSI
      DPF=COS(GVO(1))
      OPF=DF*DPF
      PF=PO/RMSI
      VC1PP=VC1(-TOFF)+VC1(-TOFF+TO/2.)
      LOSS=1./DF**2
C
C       CALCULATE RECTIFIER DERATING
C
      CALL D01ABF(TC,TO/2.,SQIL,00.005,128,NN,ID,0)
      CALL D01ABF(0.,TC,SQIL,00.005,128,NN,IS,0)
      IS=SQRT(IS/TO)
      ID=SQRT(ID/TO)
      DS=4.*PO*(ID+IS)
C
C       CLACULATE  DIL/DT
C
      CALL C05AAF(0.,TO/2.,0.000001,0.005,DIDT2,TH,1)
      IF(IFAIL.NE.0)  GO  TO  700
      MDIDT=DIDT1(TH)
  700 WRITE(6,400) IL(1),IL(3),IL(5),GIL(1),RMS1,PO,PF,CAV,ALAV,DPF,
     1OPF,IS,ID,DS,TOFF,LOSS,VC1PP,MDIDT
  400 FORMAT(1H ,19F15.7)
C
```

```
C       CALCULATE OUTPUT CURRENT WAVAFORM
C
        DUMY=0.
        DO  222    I=1,20
        X=DUMY*T0/40.
        DUMY=I
  222   SIL(I)=CURRENT(X)
        WRITE(6,12) SIL
   12   FORMAT(1H ,20F6.2)
C
C       STEP IV
C       VARY LOAD CONDITIONS
        II=II+1
        IF(II.EQ.5)  GO  TO  1001
C
        GO  TO  1000
  301   STOP
        END
```

SEGMENT, LENGTH 754, NAME MAIN

```
        SUBROUTINE ZINPUT(ZR,ZL,ZI,ANGZIN,ZIN)
        REAL IL,LOSS,LOAD,IS,ID,NEWDIF
        COMMON   IL(20),GIL(20),V0(20),GV0(20),W0,R,A,Y,XC,XL
        H=R*Y/((1.-A**2)**2*Y**2+A**2)
        ZR=H*Y
        ZI=H*(A*Y**2*(1.-A**2)-A)
        ZL=SQRT(ZR**2+ZI**2)
        ZINI=XL*A-XC/A+ZI
        ANGZIN=ZINI/ZR
        ANGZIN=ATAN(ANGZIN)
        ZIN=SQRT(ZR**2+ZINI**2)
        RETURN
        END
```

SEGMENT, LENGTH 150, NAME ZINPUT

```
        FUNCTION CURRENT(X)
        REAL IL,LOSS,LOAD,IS,ID,NEWDIF
        COMMON   IL(20),GIL(20),V0(20),GV0(20),W0,R,A,Y,XC,XL
        CURRENT=0.
        DO 454  I=1,13,2
        U=I
  454   CURRENT=CURRENT+IL(I)*SIN(U*W0*X+  GIL(I))*1.4142
        RETURN
        END
```

```
      FUNCTION VOLTAGE(X)
      REAL IL,LOSS,LOAD,IS,ID,NEWDIF
      COMMON    IL(20),GIL(20),VO(20),GVO(20),WO,R,A,Y,XC,XL
      VOLTAGE=0.
      DO  448  I=1,17,2
      U=I
  448 VOLTAGE=VOLTAGE+VO(I)*SIN(U*WO*X+  GVO(I))*1.4142
      RETURN
      END
```

```
      FUNCTION VC1(T)
      REAL IL,LOSS,LOAD,IS,ID,NEWDIF
      COMMON    IL(20),GIL(20),VO(20),GVO(20),WO,R,A,Y,XC,XL
      VC1=0.
      DO  990  I=1,13,2
      U=I
  990 VC1=VC1+1.4142*XC/U*IL(I)*COS(U*WO*T+GIL(I))
      RETURN
      END
```

```
      FUNCTION DIDT1(T)
      REAL IL,LOSS,LOAD,IS,ID,NEWDIF
      COMMON    IL(20),GIL(20),VO(20),GVO(20),WO,R,A,Y,XC,XL
      DIDT1=0.
      DO  495 I=1,13,2
      U=I
  495 DIDT1=DIDT1+IL(I)*WO*U*COS(U*WO*T+GIL(I))*1.4142
      RETURN
      END
```

```
      FUNCTION DIDT2(T)
      REAL IL,LOSS,LOAD,IS,ID,NEWDIF
      COMMON    IL(20),GIL(20),VO(20),GVO(20),WO,R,A,Y,XC,XL
      DIDT2=0.
      DO  496  I=1,13,2
      U=I
  496 DIDT2=DIDT2-U**2*WO**2*IL(I)*SIN(U*WO*T+GIL(I))*1.4142
      RETURN
      END
```

LISTING OF PROGRAM VARIABLES

CURRENT(T)	function statement for $i_L(t)$
DIDT1, DIDT2	function state to calculate $\dot{i}_L$ and $\ddot{i}_L$ respectively
DPF	DP
GIL(N)	β_n
GVO(N)	ϕ_n
IL(N)	I_{Ln}
LOAD (I,3)	two dimensional array. On entry it should contain the load data. LOAD (1,J) contains the load data at worst operation condition.
OPF	PF_o
VOLTAGE (T)	function statement for $v_{co}(t)$
w_{oB}	base value of w_o
w_{pu}	w_o/w_{oB}
ZINPUT	subroutine to calculate Z_{In}

(The remaining variables are given in the list of principal symbols)

APPENDIX 3

SINE-WAVE INVERTER IN APPLICATION

The sine-wave inverter in a typical induction heating application is provided with both:

i) Automotive frequency control

and ii) Output power control

schemes.

The control electronics also include a current limit and a protective system to prevent the simultaneous conduction of thyristors S1 and S2 under all regular and irregular conditions of operation.

3.1 Automatic Frequency Control

In achieving this, the control unit senses the variation in the resonant frequency of the tank load, and changes the switching rate of the thyristors accordingly. The tuning of the tank load is usually detected by monitoring the phase difference between the fundamental components of the load voltage and current. The phase signal is subsequently converted to d.c. and fed to a voltage controlled oscillator, which may also be controlled manually, to generate the required firing frequency. This system also offers a ready means for setting limits to the range of operating frequency, by clamping the input signal to the oscillator at suitably chosen levels.

3.2 Output Power Control

Power control by varying output frequency: The power delivered to the tank load can easily be reduced, by changing the tuning. However in practice such a procedure results in a poor power factor and poor utilisation of the inverter power components. Evidently, the power factor deteriorates sharply as the operating frequency departs from the natural resonant frequency of the load. This also adversely affects the output current, resulting in an increase in both the harmonic content and the power losses.

Power control by current limiting: A block diagram of one possible circuit providing this form of control is given in Figure A3.1. The control unit derives its input from the current transformer CT, and after rectification the voltage signal ki_L is processed through an integrator before comparison with a reference signal e_r. The comparator prevents the firing of the next thyristor whenever the reference level is attained.

Power control by input d.c. voltage control: Power control by adjustment of the input voltage is a well-accepted, reliable and flexible technique, although requiring an additional controlled rectifier. The principal advantage offered is that a ready means is provided for the continuous control of the high-frequency output voltage and power without affecting significantly

the output current waveform. Additionally, the input current to the inverter may be rapidly controlled and limited as desired.

A reliable thyristor protection scheme is suggested in Figure A3.1. The reverse-bias sensors detect the duration of a reverse-bias condition of the thyristor to which they are attached. A reverse-bias signal is then fed to the next block, where its continuity is checked for an interval equal to the minimum thyristor turn-off time. Whenever $t_{rb} < T\,H_{off}$, e_1 is reset to its zero level. Information on the existence of a completely clear signal is fed to the *clear signal storage*, which holds the signal to enable the AND gate when required.

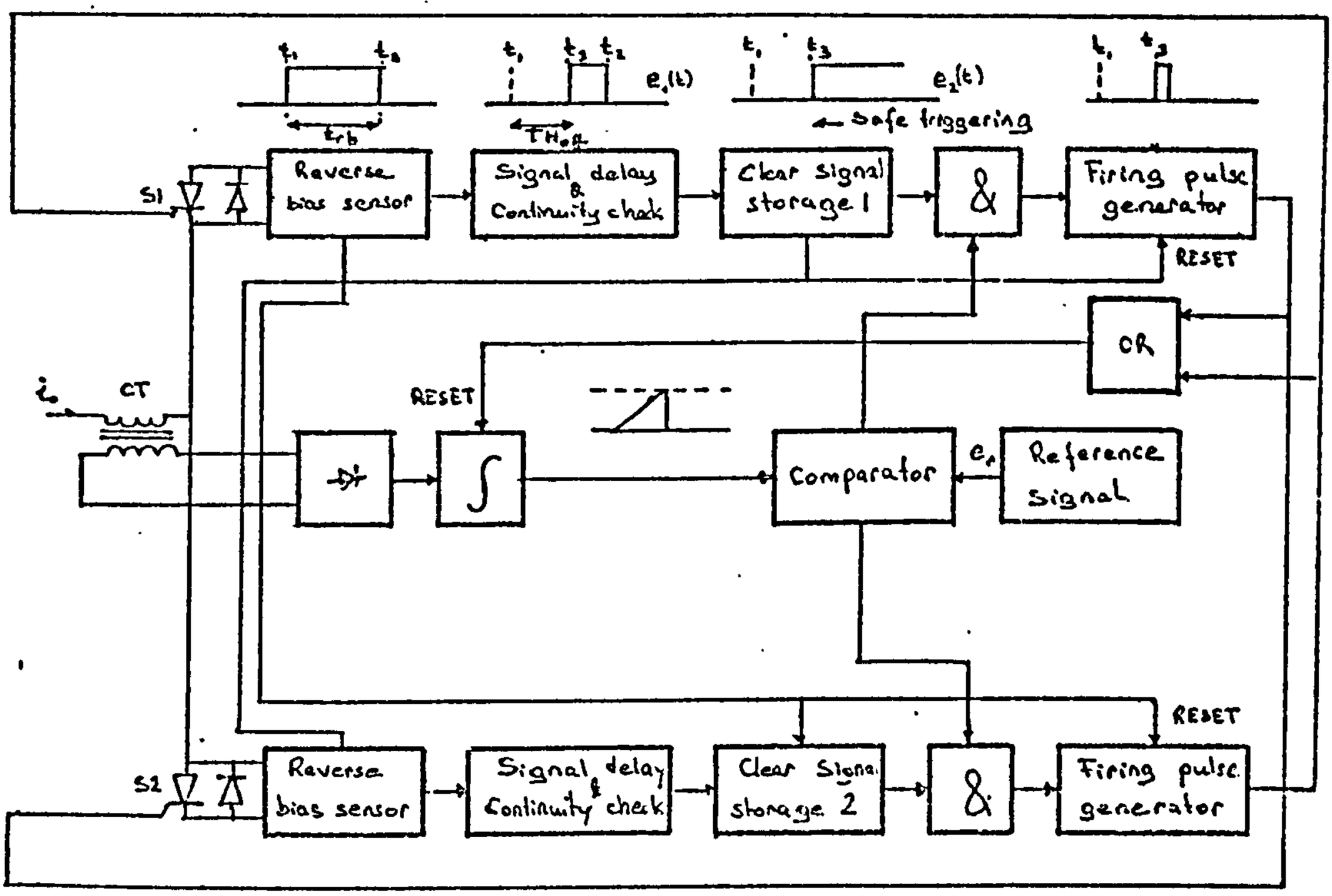

Figure A3.1 Block diagram of protection and control circuit for the sine-wave inverter

APPENDIX 4

PROGRAM LISTING, SIMULATION OF THE FULL-AND HALF-BRIDGE CYCLOINVERTER

```
      MASTERMAIN
C
C     SIMULATION OF THE CYCLOINVERTER
C     LTYPE=1    FULL-BRIDGE
C     LTYPE=0    HALF BRIDGE
C
      REAL L,LO,IS,IO,IL,ILO,I1,LTYPE
      LOGICAL LISJ,LVSJ,LJNEG,LJPOZ
      DIMENSION VC1(1500),IL(1500),VCO(1500),ILO(1500),VS1(1500),S(6),
     1TIME(1550),VA(1550),VB(1550),VC(1550),VL(1550),
     1Z(4),Y(4),O(4),P(4),X(4),Q(4),G(4),I1(1550),FILO(200)
      DIMENSION ILIST(20),VO(200),CS(550),SN(550),FIL(200),GIL(200)
      COMMON R,L,LO,C,CO,U,E12,E23,E31,E11,A,S
      EXTERNAL DERIV
C
C     3-PHASE INPUT
C
      V1(T)=50.0*SIN(314.16*T)
      V2(T)=50.0*SIN(314.16*T-2.0944)
      V3(T)=50.0*SIN(314.16*T+2.0944)
      V11(T)=1570.8.*COS(314.16*T)
      V21(T)=15708.*COS(314.16*T-2.0944)
      V31(T)=15708.*COS(314.16*T+2.0944)
      CALL LU1934
C
C     PER UNIT BASE
C
      VMAX=50.
      REFV=VMAX/1.4142
      REFR=5.
      REFI=REFV/REFR
C
C
C     INPUT DATA
C
      WI=314.1592
      TI=0.020
      RATIO=21.
 1    WO=WI*RATIO
      DELT=TI/1024.
      XL=0.7
      XC=1.35
      L=XL/WO*5.
      C=1./3./5./WO/XC
999   READ(1,10) QF,TETA,LTYPE,WPU,R,LO,CO
10    FORMAT(7F0.0)
```

```
      IF(QF.EQ.0.)  GO  TO  555
      W0=W0*WPU
      F0=W0/2./3.1416
      T0=1./F0
      WRITE(6,11)  LTYPE,QF,TETA,R,C0,L0,F0,L,C
   11 FORMAT(1H ,3F7.2,6F12.7)
C
CC    INITIALLING  VARIOUS  PARAMETERS
C
      NSAY=0
      I0,V0=0.
      VC10=60.
      S(1),S(2),S(3),S(4),S(5),S(6)=0.
      TETA=TETA*3.1416/180.
      TS=TETA/WI
      T=TS
      ISAY,N=0
      N=1
      S(1)=1.
      J=1
      Z(1)=VC10
      Z(3)=V0
      Z(4)=I0
      RMSI1,RMSIL=0.
      COUNT,U,SHORT=0.
      TSTART=TS
   99 TB=COUNT*T0/2.+TSTART
      Z(2)=0.
      TETA=T*WI*180./3.1416
      WRITE(6,166)  TB,Z,COUNT,TETA,S
  166 FORMAT(1H ,E20.4,10X,4F7.3,10X,F5.2,5X,7F5.1)
      COUNT=COUNT+1.
  100 E12=V1(T)-V2(T)
      E23=V2(T)-V3(T)
      E31=V3(T)-V1(T)
      E11=V11(T)
      A=S(1)+S(2)+S(3)+S(4)+S(5)+S(6)
C
CC    SOLVING  STATE  EQUATIONS
C
      CALL D02AAF(Z,Y,T,DELT,4,DERIV,0,P,X,Q)
      IF(T.GE.TI+TSTART)  N=N+1
      IF(N.GE.1024) GO  TO  331
C
CC    VARIOUS   CIRCUIT  VOLTAGES  &  CURRENTS
C
      VA(N)=V1(T)
      VB(N)=V2(T)
      VC(N)=V3(T)

      VC1(N)=Z(1)
      IL(N)=Z(2)
      VC0(N)=Z(3)
      ILU(N)=Z(4)
      Z21=(S(1)*(Z(1)-U)+S(2)*(E31+Z(1)+U)+S(3)*(-E12+Z(1)-U)+S(4)*(Z(1)
     1+U)+S(5)*(E31+Z(1)-U)+S(6)*(-E12+Z(1)+U)-A*Z(3))/L
      I1(N)=C*V11(T)+((S(1)+S(4))*2.-(S(2)+S(5)+S(3)+S(6)))*Z(2)/3.
```

```
      VL(N)=-Z21*L
      A=1.-A
      VS1(N)=S(1)*U-S(4)*U+S(3)*(E12+U)+S(6)*(E12-U)+S(5)*(-E31+U)+S(2)
     1(-E31-U)+A*(Z(1)-Z(3)-L*Z21)
C
C     CHECK POLARITY OF THE OUTPUT CURRENT, IL
C
  108 IS=-(-1.)**J*Z(2)
      IF(IS) 31,32,33
   31 Z(2)=0.
   32 IF(J.EQ.0) GO TO 832
      S(J)=0.
  832 LISJ=.FALSE.
      GO TO 34
   33 LISJ=.TRUE.
C
C     FIRING PULSE GENERATION & THYRISTOR SQUENCING
C
   34 IF(T-TB+DELT.GT.T0/2.) GO TO 338
      IF(T-TB.LT.T0/2.) GO TO 100
  338 IF(IFJ.GT.0) GO TO 339
      LJNEG=LJPOZ
      LJPOZ=.NOT.LJNEG
      GO TO 340
  339 LJNEG=J.EQ.0.OR.J.EQ.2.OR.J.EQ.4
      LJPOZ=J.EQ.1.OR.J.EQ.3.OR.J.EQ.5
  340 J=0
      IF(T.GE.TS+TI) TS=TS+TI
      IF(LTYPE.EQ.1.) GO TO 1111
      IF(V2(T).LT.V3(T).AND.V2(T).LT.V1(T).AND.LJPOZ) J=6
      IF(V3(T).LT.V2(T).AND.V3(T).LT.V1(T).AND.LJPOZ) J=2
      IF(V1(T).LT.V3(T).AND.V1(T).LT.V2(T).AND.LJPOZ) J=4
      IF(T.LT.TS+TI/3..AND.V1(T).GT.V3(T).AND.LJNEG) J=1
      IF(T.GT.TS+TI/3..AND.V2(T).GT.V1(T).AND.LJNEG) J=3
      IF(T.GE.TS+2.*TI/3..AND.V3(T).GT.V2(T).AND.LJNEG) J=5
      GO TO 187
 1111 IF(T.LT.TS+TI/3.)J=1
      T=T+4.*DELT
      IF(T.GE.TS+TI/3..AND.T.LT.2.*TI/3.+TS) J=3.
      IF(T.GE.TS+2.*TI/3..AND.T.LT.TI+TS) J=5
      T=T-4.*DELT
      IF(T.LT.TS+TI/6..AND.LJPOZ) J=6
      IF(T.GE.TS+TI/6..AND.T.LT.TS+TI/2..AND.LJPOZ) J=2
      IF(T.GE.TS+TI/2..AND.T.LT.TS+TI*5./6..AND.LJPOZ) J=4
      IF(T.GE.TS+TI*5./6..AND.T.LT.TI+TS.AND.LJPOZ) J=6
C
C     FIRED THYRISTOR IS S(J)
C
  187 IF(J.EQ.0) S(1),S(2),S(3),S(4),S(5),S(6)=0.
      IF(J.EQ.0) GO TO 99
C
C     CALCULATE VOLTAGE ACRUSS THE FIRED THYRISTOR
C
      GO TO (41,42,43,41,42,43),J
   41 VSJ=VS1(N)
```

```
      IF(J.EQ.4)  VSJ=-VSJ
      GO TO 44
   42 VSJ=E31+Z(1)-Z(3)
      IF(J.EQ.2) VSJ=-VSJ
      GO TO 44
   43 VSJ=-E12+Z(1)-Z(3)
      IF(J.EQ.6)  VSJ=-VSJ
C
C     CAN THE FIRED THYRISTOR CONDUCT ?
C
   44 IF(VSJ.GT.0.)  GO TO 45
      LVSJ=.FALSE.
      IF(T.LT.TI/2.+TSTART)  GO  TO  45
      GO  TO  145
   45 LVSJ=.TRUE.
  145 S(1),S(2),S(3),S(4),S(5),S(6)=0.
      IF(LVSJ)  S(J)=1.
      IF(LISJ.AND.LVSJ) GO TO 500
      GO TO 99
  500 WRITE(6,19) T,IL(N)
   19 FORMAT(1H ,'**********SHORT CIRCUIT*******',F10.6,F16.3)
      IL(N)=0.
      IL(N-1)=0.4
      GO  TO  99
  331 SAY=0.
C
C     PREPEARING CIRCUIT QUANTITIES FOR GRAPHICAL OUTPUT
C
      J=1
      DO  770  I=1,512
      IL(I)=IL(J)/REFI
      I1(I)=I1(J)/REFI
      VC(I)=VC(J)/REFV
      VB(I)=VB(J)/REFV
      VA(I)=VA(J)/REFV
      VL(I)=VL(J)/REFV
      VC0(I)=VC0(J)/REFV
      VC1(I)=VC1(J)/REFV
      VS1(I)=VS1(J)/REFV
      J=J+2
      TIME(I)=SAY*DELT*2.
  770 SAY=1
C
C     PRODUCING GRAPHICAL OUTPUT
C
      NN=512
      Y1=1.5
      Y2=5.
      Y3=6.
      Y4=4.
      CALL ERRMAX(2)
      CALL DEVPAP(210.,297.,1)
      CALL AXIPOS(1,50.,074.,125.,1)
      CALL AXIPOS(0,50.,74.,45.,2)
      CALL AXISCA(3,6,0.0,0.020,1)
      CALL AXISCA(3,12,-Y1,Y1,2)
```

```
      CALL AXIDRA(2,1,1)
      CALL AXIDRA(-1,-1,2)
      CALL GRAPOL(TIME,VC0,NN)
      CALL AXIPOS(1,50.,134.,125.,1)
      CALL AXIPOS(0,50.,134.,45.,2)
      CALL AXISCA(3,6,0.0,0.020,1)
      CALL AXISCA(3,12,-Y4,Y4,2)
      CALL AXIDRA(-1,-1,2)
      CALL AXIDRA(2,1,1)
      CALL GRAPOL(TIME,I1,NN)
      CALL AXIPOS(1,50.,194.,125.,1)
      CALL AXIPOS(0,50.,194.,45.,2)
      CALL AXISCA(3,6,0.0,0.020,1)
      CALL AXISCA(3,12,-Y2,Y2,2)
      CALL AXIDRA(-1,-1,2)
      CALL AXIDRA(2,1,1)
      CALL GRAPOL(TIME,IL,NN)
      CALL AXIPOS(0,50.,254.,45.,2)
      CALL AXIPOS(1,50.,254.,125.,1)
      CALL AXISCA(3,6,0.0,0.020,1)
      CALL AXISCA(3,12,-Y1,Y1,2)
      CALL AXIDRA(2,1,1)
      CALL AXIDRA(-1,-1,2)
      CALL GRACUR(TIME,VA,NN)
      CALL GRACUR(TIME,VB,NN)
      CALL GRACUR(TIME,VC,NN)
      CALL PICCLE
      CALL DEVPAP(210.,297.,1)
      CALL AXIPOS(1,50.,074.,125.,1)
      CALL AXIPOS(0,50.,74.,45.,2)
      CALL AXISCA(3,6,0.0,0.020,1)
      CALL AXISCA(3,12,-Y3,Y3,2)
      CALL AXIDRA(2,1,1)
      CALL AXIDRA(-1,-1,2)
      CALL GRAPOL(TIME,VC1,NN)
      CALL AXIPOS(1,50.,134.,125.,1)
      CALL AXIPOS(0,50.,134.,45.,2)
      CALL AXISCA(3,6,0.0,0.020,1)
      CALL AXISCA(3,12,-Y3,Y3,2)
      CALL AXIDRA(2,1,1)
      CALL AXIDRA(-1,-1,2)
      CALL GRAPOL(TIME,VS1,NN)
      CALL PICCLE

      CALL DEVEND
      STOP
      END
```

```
      SUBROUTINE DERIV(G,Z,T)
      REAL L,LO
      DIMENSION G(4),Z(4),S(6)
      COMMON R,L,LO,C,CO,U,E12,E23,E31,E11,A,S
      G(1)=E11-Z(2)/3./C
      G(2)=(S(1)*(Z(1)-U)+S(2)*(E31+Z(1)+U)+S(3)*(-E12+Z(1)-U)+S(4)*(Z(1
     1)+U)+S(5)*(E31+Z(1)-U)+S(6)*(-E12+Z(1)+U)-A*Z(3))/L
      G(3)=(Z(2)-Z(4))/CO
      G(4)=(Z(3)-R*Z(4))/LO
      RETURN
      END
```

FINISH

LISTING OF PROGRAM VARIABLES

DERIV Subroutine to evaluate the derivatives of the state variables

G(N) $\dot{Z}_n$

REFI, REFR, REFP, REFV I_B, R_B, P_B, V_B

VA, VB, VC v_{ab}, v_{bc}, v_{ca}

VMAX V_{lp}

V11(T) $\dot{v}_1(t)$

(The remaining variables are given in the list of principal symbols).

APPENDIX 5

RELATION BETWEEN THE FULL LOAD RMS INPUT LINE CURRENT AND THE OUTPUT CURRENT IN A HIGH-FREQUENCY CYCLOINVERTER

Equation 4.11 indicates that the input current pulses are approximately equal to either $\mp \frac{2}{3} i_L$ or to $\mp \frac{1}{3} i_L$. Assuming a homogeneous output current waveform (approximately the case at full output power) and if K_1 and K_2 correspond to the number of higher and lower amplitude pulses respectively, the r.m.s. input line current is given approximately by:

$$I_1 = \sqrt{\frac{2}{KT_o} \left[K_1 \int_{t_1}^{t_1+T_o/2} [\frac{2}{3} i_L]^2 dt + K_2 \int_{t_1}^{t_1+T_o/2} [\frac{i_L}{3}]^2 dt\right.}$$

where t_1 is the starting instant of a current pulse and $K = K_1 + K_2$.

Substituting:

$$I_L^2 = \frac{2}{T_o} \int_{t_1}^{t_1+T_o/2} i_L^2 \, dt$$

in the above equation results in

$$I_1 = \sqrt{\frac{4K_1 + K_2}{K}} \quad \frac{I_L}{3}$$

Further, if the frequency conversion ratio $\frac{f_o}{f_I}$ is high, K_1 and K_2

are approximately given by the nearest integer values of:

$$K_1 = \frac{T_I}{3\ T_o} \quad , \qquad K_2 = \frac{2\ T_I}{3\ T_o}$$

which simplifies the input line current equation to:

$$I_1 = \frac{\sqrt{2}}{3} \quad I_L$$

APPENDIX 6

PROGRAM LISTING, SIMULATION OF THE INPUT FILTERED CYCLOINVERTER

```
      MASTERMAIN
C
C     SIMULATION OF THE INPUT FILTERED CYCLOINVERTER
C     LTYPE=1   FULL-BRIDGE
C     LTYPE=0   HALF BRIDGE
C
      REAL LTYPE,I2,I3,LF
      REAL L,L0,IS,IO,IL,IL0,I1
      LOGICAL LD1,LD2,LD3,LS1,LS2,LS3,LS4,LS5,LS6
      LOGICAL LJPOZ,LJNEG,LISJ,LVSJ,DIODE
      DIMENSION TIME(512),UB(512),I2(512),I1(1540),I3(1540),
     1Z(8),Y(3),O(8),P(8),Q(8),G(8),H(8),
     2VA(1540),VB(1540),VC(1540),VL(1540),UA(1540),UC(1540),
     3VC1(1540),IL(1540),VC0(1540),IL0(1540),VS1(1540),S(6)
      DIMENSION F1(550),F2(550),LIST(30),ILIST(20),CS(300),SN(300)
      COMMON R,L,L0,C,C0,U,A,S,U1,U2,U3,Z61,PF,LF,CF
      EXTERNAL DERIV
C
C     3-PHASE INPUT
C
      V1(T)=50.0*SIN(314.16*T)
      V2(T)=50.0*SIN(314.16*T-2.0944)
      V3(T)=50.0*SIN(314.16*T+2.0944)
      CALL LU1934
C
C     PER UNIT BASE
C
      VMAX=50.
      REFV=VMAX/1.4143
      REFR=5.
      REFI=REFV/REFR
      REFP=REFI**2*REFR
```

```
C
C     INPUT DATA
C
      WI=314.16
      RATIO=21.
      WO=WI*RATIO
      XL=0.7
      XC=1.35
      L=XL/WO*5.
      C=1./3./5./WO/XC
      TI=0.02
      DELT=TI/1530.
      READ(1,109)LTYPE,RF,LF,CF,CO
  109 FORMAT(5F0.0)
  999 READ(1,10)  TETA,L0,R,Z,WPU
   10 FORMAT(12F0.0)
      IF(TETA.EQ.0.)  GO  TO  1001
```

```
      W0=WI*RATIO
      W0=W0*UPU
      F0=W0/2./3.1416
      T0=1./F0
C
CC    INITIALLING  VARIOUS  PARAMETERS
C
      N=0.
      N=N+1
      S(1),S(2),S(3),S(4),S(5),S(6)=0.
      S(1)=1.
      J=1
      LJPOZ=.TRUE.
      ISAY=0
      TS=TETA*3.1416/180./WI
      T=TS
      TSTART=TS
      RMSI1,RMSIL=0.
      COUNT=0.
      WRITE(6,11) LTYPE,RF,TETA,R,F0,CF,LF,Z
11    FORMAT(1H ,5F10.1,2F14.7/8F6.2)
99    TB=COUNT* T0/2.+TSTART
      U=0.5
      Z(6)=0.
      TETA=T*WI*180./3.1416
      WRITE(6,166)  TB,Z,COUNT,TETA,S
166   FORMAT(1H ,F10.5,10F7.2,8F5.2)
      COUNT=COUNT+1.
100   U1=V1(T)
      U2=V2(T)
      U3=V3(T)
      IF(J.EQ.0)  GO  TO  82
      IF(LTYPE.EQ.1..OR.S(J).EQ.0..OR.LJPOZ)  GO  TO  82
      S(J)=0.
      DIODE=.TRUE.
      GO  TO  80
81    S(J)=1.
      DIODE=.FALSE.
82    A=S(1)+S(2)+S(3)+S(4)+S(5)+S(6)
C
CC    SOLVING  STATE  EQUATIONS
C
      CALL D02AAF(Z,Y,T,DELT,08,DERIV,0,P,H,0)
      U=U+0.01*Z(6)
      IF(N.EQ.1530)  GO  TO  331


      IF(T.GT.3.*TI+TSTART)  N=N+1
C
CC    VARIOUS  CIRCUIT  VOLTAGES  &  CURRENTS
C
      VA(N)=U1/REFV
      VB(N)=U2/REFV
      VC(N)=U3/REFV
      I1(N)=Z(1)/REFI
      I3(N)=Z(2)/REFI
      UA(N)=Z(3)/REFV
```

```
      UC(N)=Z(4)/REFV
      VC1(N)=Z(5)/REFV
      IL(N)=Z(6)/REFI
      VCU(N)=Z(7)/REFV
      ILU(N)=Z(8)/REFI
      VL(N)=-Z61*L
      E12=Z(3)
      E31=Z(4)
      A=1.-A
      VS1(N)=S(1)*U-S(4)*U+S(3)*(E12+U)+S(6)*(E12-U)+S(5)+(-E31+U)+S(2)
     1(-E31-U)+A*(Z(5)-Z(7)-L*Z61)
C
C     CHECK POLARITY OF THE OUTPUT CURRENT, IL
C
  108 IS=-(-1.)**J*Z(6)
      IF(IS) 31,32,33
   31 Z(6)=0.
   32 IF(J.EQ.0) GO TO 832
      S(J)=0.
  832 LISJ=.FALSE.
      GO TO 34
   33 LISJ=.TRUE.
C
C     FIRING PULSE GENERATION & THYRISTOR SQUENCING
C
   34 IF(T-TB+DELT.GT.T0/2.) GO TO 338
      GO TO 100
  338 LJNEG=LJPOZ
      LJPOZ=.NOT.LJNEG
      J=0
      T=T+3.*DELT
      IF(T.GE.TS+TI) TS=TS+TI
      IF(LJPOZ) GO TO 722
      IF(LTYPE.EQ.1.)          GO TO 1111
   80 LD1=V1(T).LT.V3(T).AND.V1(T).LT.V2(T)
      LD2=V2(T).LT.V3(T).AND.V2(T).LT.V1(T)
      LD3=V3(T).LT.V2(T).AND.V3(T).LT.V1(T)
      LS4=.TRUE.
      IF(LD1.AND.LS4)     J=4
      IF(LD2.AND.LS4)     J=6
      IF(LD3.AND.LS4)     J=2
      IF(DIODE) GO TO 81
      GO TO 187
 1111 LS6=T.LT.TS+TI/6.
      IF(LS6) J=0
      LS2=T.GE.TS+TI/6..AND.T.LT.TS+TI/2.
      LS4=T.GE.TS+TI/2..AND.T.LT.TS+TI*5./6.
      LS6=T.GE.TS+TI*5./6..AND.T.LT.TS+TI
      IF(LS6) J=0
      IF(LS2) J=2
      IF(LS4) J=4
      GO TO 187
  722 LS1=T.LT.TS+TI/3.
      LS3=T.GE.TS+TI/3..AND.T.LT.TS+2.*TI/3.
      LS5=T.GE.TS+2.*TI/3..AND.T.LT.TI+TS
      IF(LS1) J=1
      IF(LS3) J=3
      IF(LS5) J=5
  187 T=T-3.*DELT
C
```

```
C       FIRED  THYRISTOR  IS  S(J)
C
        IF(J.EQ.0)S(1),S(2),S(3),S(4),S(5),S(6)=0.
        IF(J.EQ.0)  GO  TO  99
C
C       CALCULATE VOLTAGE ACROSS THE FIRED THYRISTOR
C
        GO TO (41,42,43,41,42,43),J
 41     VSJ=VS1(N)
        IF(J.EQ.4)  VSJ=-VSJ
        GO TO 44
 43     VSJ=-E12+Z(5)-Z(7)
        IF(J.EQ.6)  VSJ=-VSJ
        GO TO 44
 42     VSJ=E31+Z(5)-Z(7)
        IF(J.EQ.2) VSJ=-VSJ
C
C       CAN  THE  FIRED  THYRISTOR  CONDUCT ?
C
 44     IF(VSJ.GT.0.)  GO TO 45
        WRITE(6,18) J,VSJ
 18     FORMAT(1H ,'**************TRIGGERED SCR CANNOT CONDUCT********',
       1I2,10X,F5.2)
        LVSJ=.FALSE.
        GO  TO  145
 45     LVSJ=.TRUE.
 145    S(1),S(2),S(3),S(4),S(5),S(6)=0.
        IF(LVSJ)  S(J)=1.
        IF(LISJ.AND.LVSJ) GO TO 500
        GO TO 99
 500    WRITE(6,19) T,IL(N)
 19     FORMAT(1H ,'*****************SHORT CIRCUIT*******',F10.6,F16.3)
        IL(N)=0.
        IF(N.GT.2)  IL(N-1)=0.15
        GO  TO  99
  331   SAY=0.
C
C       NUMERICAL  FOURIER  ANALYSIS  OF  I1  AND -IL
C
        J=1
        NN=512
        DO  770  I=1,NN
        VA(I)=VA(J)
        VB(I)=VB(J)
        VC(I)=VC(J)
        I1(I)=I1(J)
        I3(I)=I3(J)
        I2(I)=-I1(I)-I3(I)
        UA(I)=UA(J)
        UC(I)=UC(J)
        UB(I)=-UA(I)-UC(I)
        VC1(I)=VC1(J)
        VCU(I)=VCU(J)
        VS1(I)=VS1(J)
```

```
      ILO(I)=ILO(J)
      VL(I)=VL(J)
      F1(I)=IL(I)
      F2(I)=IL(NN+I)
      IL(I)=IL(J)
      J=J+3
      TIME(I)=SAY*3.*DELT
  770 SAY=I
      M=9
      N=2**M
      M1=M*2+2
      N1=N+1
      F1(N1),F2(N1)=0.
      CALL COGAAF(F1,F2,N1,.FALSE.,M1,LIST)
      M=8
      N=2**M
      M1=M*2+2
      N1=N+1
      DO  508  I=1,N
      CS(I)=I1(I)
  508 SN(I)=I1(I+N)
      CS(N+1)=0.
      SN(N+1)=0.
      CALL COGAAF(CS,SN,N1,.FALSE.,M1,ILIST)
      FILN,FI1N=0.
      DO 155 M=2,40
      FILN=75.+FILN
      FI1N=50.+FI1N
      FIL=SQRT(F1(M)**2+F2(M)**2)
      FI1=SQRT(CS(M)**2+SN(M)**2)
      IF(F2(M).EQ.0.)  GO  TO  153
      GIL=F1(M)/F2(M)
      FILG=ATAN(GIL)
  153 IF(SN(M).EQ.0.)  GO  TO  155
      GI1=CS(M)/SN(M)
      FI1G=ATAN(GI1)
  155 WRITE(6,759) FI1N,FI1,FI1G,FILN,FIL,FILG
  759 FORMAT(1H ,F3.1,10X,2F5.2,30X,F3.1,10X,2F5.2)
C
C     PRODUCING  GRAPHICAL  OUTPUT
C
      Y1=1.5
      Y2=2.
      Y3=4.
      Y4=3.
      Y5=6.
      Y6,Y7,Y8=9.
      CALL ERRMAX(9)
      CALL DEVPAP(210.,297.,1)
      CALL AXIPOS(1,50.,074.,125.,1)
      CALL AXIPOS(0,50.,74.,45.,2)
      CALL AXISCA(3,4,0.,0.02,1)
      CALL AXISCA(3,3,-Y4,Y4,2)
      CALL AXIDRA(2,1,1)
      CALL AXIDRA(-1,-1,2)
      CALL GRACUR(TIME,VCO,NN)
```

```
      CALL AXIPOS(1,50.,134.,125.,1)
      CALL AXIPOS(0,50.,134.,45.,2)
      CALL AXISCA(3,4,0.,0.02,1)
      CALL AXISCA(3,4,-Y3,Y3,2)
      CALL AXIDRA(-1,-1,2)
      CALL AXIDRA(2,1,1)
      CALL GRAPOL(TIME,I1,NN)
      CALL AXIPOS(1,50.,194.,125.,1)
      CALL AXIPOS(0,50.,194.,45.,2)
      CALL AXISCA(3,4,0.,0.02,1)
      CALL AXISCA(3,4,-Y2,Y2,2)
      CALL AXIDRA(-1,-1,2)
      CALL AXIDRA(2,1,1)
      CALL GRACUR(TIME,I1,NN)
      CALL GRACUR(TIME,I2,NN)
      CALL GRACUR(TIME,I3,NN)
      CALL AXIPOS(0,50.,254.,45.,2)
      CALL AXIPOS(1,50.,254.,125.,1)
      CALL AXISCA(3,4,0.,0.02,1)
      CALL AXISCA(3,3,-Y1,Y1,2)
      CALL AXIDRA(2,1,1)
      CALL AXIDRA(-1,-1,2)
      CALL GRACUR(TIME,VA,NN)
      CALL GRACUR(TIME,VB,NN)
      CALL GRACUR(TIME,VC,NN)
      CALL PICCLE
      CALL DEVPAP(210.,297.,1)
      CALL AXIPOS(1,50.,194.,125.,1)
      CALL AXIPOS(0,50.,194.,45.,2)
      CALL AXISCA(3,4,0.,0.02,1)
      CALL AXISCA(3,3,-Y6,Y6,2)
      CALL AXIDRA(2,1,1)
      CALL AXIDRA(-1,-1,2)
      CALL GRACUR(TIME,VC1,NN)
      CALL AXIPOS(0,50.,254.,45.,2)
      CALL AXIPOS(1,50.,254.,125.,1)
      CALL AXISCA(3,4,0.,0.02,1)
      CALL AXISCA(3,3,-Y5,Y5,2)
      CALL AXIDRA(2,1,1)
      CALL AXIDRA(-1,-1,2)
      CALL GRACUR(TIME,UA,NN)
      CALL GRACUR(TIME,UB,NN)
      CALL GRACUR(TIME,UC,NN)
      CALL PICCLE
      GO TO 999
 1001 CALL DEVEND
      STOP
      END
```

```
      SUBROUTINE DERIV(G,Z,T)
      REAL L,LO,LF
      DIMENSION G(8),Z(8),S(6)
      COMMON R,L,LO,C,CO,U,A,S,U1,U2,U3,Z61,RF,LF,CF
      G(1)=(3.*U1-Z(3)+Z(4)-3.*RF*Z(1))/LF/3.
      G(2)=(3.*U3-Z(3)-2.*Z(4)-3.*RF*Z(2))/LF/3.
      G(3)=(2.*Z(1)+Z(2)-(S(1)+S(4)-S(3)-S(6))*Z(6))/(C+3.*CF)
      G(4)=(Z(2)-Z(1)-(S(2)+S(5)-S(1)-S(4))*Z(6))/(C+3.*CF)
      G(5)=(G(3)-G(4)-Z(6)/C)/3.
      G(6)=(S(1)*(Z(5)-U)+S(4)*(Z(5)+U)+
     1S(3)*(Z(5)-Z(3)-U)+S(6)*(Z(5)-Z(3)+U)
     2+S(2)*(Z(5)+Z(4)+U)+S(5)*(Z(5)+Z(4)-U)-A*Z(7))/L
      G(7)=(Z(6)-Z(8))/CO
      G(8)=(Z(7)-R*Z(8))/LO


      Z61=G(6)
      RETURN
      END

      FINISH
```

(Program variables are as defined on page 463 and in the list of principal symbols).